Rijksuniversiteit Groningen

Probing Cosmic Velocity Flows in the Local Universe

Proefschrift

ter verkrijging van het doctoraat in de
Wiskunde en Natuurwetenschappen
aan de Rijksuniversiteit Groningen
op gezag van de
Rector Magnificus, dr. F. Zwarts,
in het openbaar te verdedigen op
vrijdag 8 oktober 2004
om 13.15 uur

door

Emilio Romano Díaz

geboren op 17 augustus 1973
te Teziutlán, México

Promotores:	Prof. dr. M. A. M. van de Weijgaert Prof. dr. R. H. Sanders
Beoordelingscommissie:	Prof. dr. T. S. van Albada Prof. dr. J. M. van der Hulst Prof. dr. M. Plionis

ISBN-nummer: 90-367-2146-6

Inin tonatiuh itoca naollin ye tehuantin tonatiuh
in tonnemi axcan.
Auh inin inezca in nican ca inic tlepanhuetz in tonatiuh
in teotexcalco in oncan in Teotihuacan.
Ye no ye itonatiuh catca in topiltzin in tolla in
Quetzalcoatl.
Y Ynic macuilli tonatiuh a Ollin yn itonal
mitoa olintonatiuh ypampa molini in otlatoca.

Aztec poem of the creation of the Fifth Sun (fragment).
Códice Chimalpopoca.

A mis madres: Inés y Tita

Cover – An Aztec astronomer observes the matter distribution and its velocity field in our local Universe as inferred from the PSCz redshift catalog. The field reconstructions were performed with the Delaunay Tessellation Field Estimator method. The illustration was created using the GIMP software with the help of Miguel Angel Aragón Calvo. The Aztec image was taken from the Códice Mendocino, 1541-1542. Bodleian Library, Oxford University.
Back cover – Image of a Mixtec astronomer inside of a prehispanic observatory. The "x"-shape device was used to measure positions of celestial objects in the sky. Códice Bodley. Bodleian Library, Oxford University.

Contents

1 Introduction **1**

1.1 Motivation . . . 2
1.2 Cosmological Background: The homogeneous Universe . . . 4
1.3 The inhomogeneous universe . . . 6
1.3.1 The Linear regime . . . 7
1.3.2 The velocity field . . . 9
1.3.3 The power spectrum . . . 10
1.3.4 The mildly non-linear regime . . . 10
1.3.5 The Zel'dovich approximation . . . 11
1.3.6 The non-linear regime: Cosmological simulations . . . 11
1.3.7 Cosmic flows . . . 13
1.4 The Least Action Principle . . . 14
1.5 Continuous velocity fields: the DTFE velocity algorithm . . . 15

2 Local Supercluster Dynamics: External Tidal Impact of the PSC*z* sample traced by Optimized Numerical Least Action Method **17**

2.1 Introduction . . . 18
2.1.1 Cosmic Force Fields and Supercluster Dynamics . . . 18
2.1.2 Strategy . . . 20
2.1.3 Outline . . . 21
2.2 Cosmic Flows: Probes of cosmic matter distribution . . . 21
2.2.1 The Large-Scale Universe: Linear flows . . . 21
2.2.2 Internal and External influences . . . 22
2.3 Cosmic Flows: The mildly nonlinear dynamics of superclusters . . . 24
2.3.1 Structure formation: Mildly nonlinear dynamics . . . 25
2.3.2 Least Action Principle in Cosmology . . . 25
2.3.3 Fast Action Minimization . . . 26
2.3.4 Ordered reconstructions . . . 28
2.3.5 LAP and External forces . . . 29
2.4 Cosmological scenarios . . . 31
2.5 Mock catalog Construction and Analysis . . . 35
2.5.1 *N*-body simulations . . . 35
2.5.2 Mock Catalog Construction . . . 35
2.5.3 Mock Catalog Analysis . . . 40
2.6 FAM velocity vector maps . . . 41

2.6.1 N-body sample: The "observed" velocities . . . 41
2.6.2 NBG samples: FAM_{30} velocity vector maps . . . 43
2.6.3 PSCz samples: FAM_{100} velocity vector maps . . . 45
2.7 Point-to-point comparison . . . 45
2.7.1 Systematics . . . 46
2.7.2 Velocity Scatter Diagrams Analysis . . . 46
2.7.3 Inventory . . . 47
2.7.4 Power Spectrum Dependence . . . 53
2.7.5 Nonlinearities . . . 53
2.8 Bulk Flow and Tidal Shear: Velocity Flow Multipole Components . . . 53
2.8.1 Velocity Field Multipole Decomposition . . . 54
2.8.2 Velocity Multipole Analysis: Results . . . 57
2.8.3 Velocity Multipole Contributions: Maps . . . 57
2.8.4 Multipole Scale Dependence . . . 60
2.8.5 Multipole Velocity Flow Model . . . 61
2.8.6 Point-to-Point Comparison . . . 61
2.8.7 Surrounding Matter Distribution: Tidal Source . . . 63
2.8.8 Multipole Components: Summary . . . 68
2.9 Conclusions . . . 69

3 Dipole & Quadrupole moments of the local cosmic velocity field 73
3.1 Introduction . . . 74
3.2 Theoretical framework . . . 76
3.2.1 The velocity bulk flow . . . 77
3.2.2 The velocity shear . . . 78
3.3 Setting the environment: Initial conditions . . . 78
3.3.1 Constrained Simulations . . . 79
3.3.2 Reconstructing the Initial Density Fields . . . 80
3.4 N−body simulations . . . 83
3.4.1 The particle distribution . . . 83
3.5 Observing the simulated Universe: Mock catalogs . . . 85
3.6 Testing the Mock Universe . . . 89
3.6.1 The gravity dipole . . . 90
3.6.2 Shot-noise effects . . . 92
3.6.3 Dipole direction and convergence . . . 93
3.7 The velocity field . . . 95
3.7.1 Modeling the peculiar velocity field . . . 95
3.8 Results . . . 97
3.8.1 Multipolar velocity decomposition . . . 97
3.8.2 The expected velocity bulk . . . 98
3.8.3 The reconstructed velocity bulk . . . 99
3.8.4 The velocity Shear . . . 104
3.9 Conclusions . . . 107
3.A Constrained Realizations . . . 109
3.B The Wiener Filter . . . 112

4 Modeling the local cosmic peculiar velocity field II: Constrained Simulations 115
4.1 Introduction . . . 116
4.2 The external influence over the Local Supercluster . . . 117
4.2.1 Decomposing the peculiar velocity field . . . 118

4.3 $N-$body simulation of the Local Universe . . . 119
4.3.1 Constrained N-body simulations . . . 119
4.3.2 Mimicking the universe: Mock Catalogs . . . 120
4.4 The velocity fields . . . 121
4.4.1 The "observed" velocity field . . . 121
4.4.2 The FAM velocity fields . . . 123
4.4.3 The FAM$_{CNBG}$ velocity field . . . 124
4.4.4 The FAM$_{CPSCz}$ velocity field . . . 125
4.4.5 The residual velocity field . . . 125
4.5 Correcting for external effects . . . 127
4.5.1 The Local Group Environment . . . 129
4.5.2 The corrected velocity field : FAM$_{CNBG}$ + B + S . . . 130
4.5.3 Point-to-point comparisons . . . 132
4.6 Conclusions . . . 135
4.A Smoothing effects . . . 137

5 FAM for real:
PSC*z* as probe of the Local Universe **139**
5.1 Introduction . . . 140
5.2 The data: The PSC*z* catalog . . . 141
5.2.1 Real space distribution . . . 141
5.3 FAM modeling of the peculiar velocity field . . . 143
5.3.1 Redshift space considerations . . . 143
5.3.2 Least Action Principle and FAM analysis . . . 144
5.3.3 Optimum FAM softening . . . 144
5.3.4 Error estimates from mock catalogues . . . 145
5.3.5 Dependence on the β parameter . . . 145
5.4 Analysis . . . 145
5.4.1 Bulk flow . . . 145
5.4.2 FAM$_{PSCz}$ bulk flow *vs* observed bulk flows . . . 150
5.4.3 Velocity shear . . . 150
5.4.4 FAM$_{PSCz}$ shear *vs* other estimates . . . 154
5.5 Conclusions . . . 155

6 DTFE & Cosmic Flows:
Tessellation Interpolation and Reconstruction of Cosmic Velocity Fields **157**
6.1 Introduction . . . 158
6.2 Reconstructing continuous fields from discrete fields . . . 160
6.3 Conventional interpolation schemes . . . 161
6.3.1 Eulerian grid-based interpolation scheme . . . 162
6.4 The DTFE method: Velocity field tessellation-interpolation . . . 163
6.4.1 The Delaunay triangulation . . . 165
6.4.2 DTFE Reconstruction of the peculiar velocity field . . . 165
6.4.3 The velocity-gradient matrix: divergence, shear and vorticity . . . 166
6.4.4 DTFE velocity field procedure illustrated . . . 167
6.4.5 Boundary conditions . . . 169
6.5 Delaunay Velocity Fields: Performance . . . 169
6.5.1 $N-$body simulations . . . 170
6.5.2 The virtues of DTFE velocity field . . . 170
6.5.3 Reconstructed Delaunay velocity Fields: Problems . . . 171
6.5.4 Velocity reconstruction in voids . . . 171
6.5.5 Velocity reconstruction in filaments . . . 172

6.5.6 Velocity reconstruction in clusters . . . 174
6.6 Errors and Sampling effects . . . 174
6.6.1 Sparse sampling effects . . . 175
6.6.2 Perturbing velocities . . . 176
6.7 The density-velocity relation . . . 178
6.7.1 Density-Velocity divergence evolution . . . 179
6.7.2 The Zel'dovich density-divergence relation . . . 181
6.8 The velocity divergence probability distribution function . . . 182
6.9 Void expansion: constraints on Ω_m . . . 184
6.10 From velocity divergence to density field . . . 186
6.11 Shear and Vorticity . . . 187
6.11.1 The density-shear relation . . . 189
6.11.2 Shear matrix and eigenvalues . . . 191
6.11.3 Time evolution of the shear eigenvalues . . . 193
6.11.4 The density-vorticity relation . . . 194
6.12 Conclusions . . . 195
6.A Triangular Shaped Cloud [TSC]: description . . . 199

7 The coldness of the Local Cosmic Environment 201
7.1 Introduction . . . 202
7.2 The Cosmic Mach number . . . 205
7.3 Mimicking the Local Supercluster environment . . . 206
7.3.1 $N-$body, Mock-observed and FAM modeled peculiar velocity fields . . . 207
7.4 Continuous Velocity Fields . . . 208
7.4.1 Resolution effects on the DTFE velocity fields . . . 210
7.4.2 Sampling effects on the DTFE velocity fields . . . 211
7.5 The "thermal" state of the Local cosmic neighborhood . . . 212
7.5.1 The bulk flow . . . 213
7.5.2 The velocity dispersion . . . 215
7.5.3 The Mach number . . . 217
7.6 The Mach statistics at the discrete particle positions . . . 219
7.6.1 The particle distribution case: mass-weighted . . . 220
7.6.2 The particle distribution case: the DTFE . . . 222
7.6.3 $\mathcal{M}$ mass-weighted vs $\mathcal{M}$ volume-weighted: a point-to-point comparison . . . 222
7.7 Discussion and Conclusions . . . 224
7.A Volume & Mass weighted quantities . . . 225
7.B The catalog sample . . . 227

8 Weak lensing reconstruction of filaments 231
8.1 Introduction . . . 232
8.2 Constrained Realizations . . . 233
8.2.1 The Hoffman-Ribak formalism . . . 234
8.2.2 The cluster-bridge-cluster configuration . . . 235
8.3 Constrained initial density fields . . . 235
8.3.1 Imposing CR constraints . . . 235
8.3.2 The real system . . . 237
8.4 $N-$body simulations . . . 239
8.4.1 Quantifying Filaments . . . 240
8.5 Lensing Simulations using $N-$body Data . . . 241
8.6 Fitting Elliptical Profiles to Galaxy Clusters . . . 242
8.6.1 Fitting Elliptical Profiles to the Simulated Surface Mass Density . . . 243
8.6.2 Fitting Elliptical Profiles to the Reconstructed Surface Mass Density . . . 244

8.6.3 Fitting Non–Singular Isothermal Ellipses to the Shear 244
8.7 Using Aperture Multipole Moments to Quantify the Presence of a Filament 246
8.7.1 Defining Cluster and Filament Regions 249
8.8 Conclusions 251
8.A Aperture multipoles moments 252
8.A.1 Definitions 252
8.A.2 Multipole moment in terms of the shear 253

9 The DTFE density and velocity fields of the PSC*z* catalog 255
9.1 Introduction 256
9.2 The DTFE method 257
9.2.1 DTFE density and velocity fields 257
9.2.2 The DTFE general reconstruction 258
9.3 The PSC*z* catalog 258
9.3.1 The linear modeled PSC*z* catalog 259
9.4 DTFE reconstruction of the PSC*z* density and velocity fields 260
9.4.1 The DTFE PSC*z* density field: Cosmography 260
9.4.2 The DTFE PSC*z* velocity field 261
9.4.3 Small-scale details in the DTFE reconstructed fields 263
9.5 DTFE velocity-gradient related fields 266
9.5.1 The DTFE PSC*z* velocity divergence 266
9.5.2 The DTFE PSC*z* velocity shear 266
9.6 Conclusions 267

Nederlandse Samenvatting 269

English Summary 285

Bibliography 301

Acknowledgments 309

Do we speak something truthful here, Giver of life?
We only dream, we only get up from the dream.
It is only like a dream...
Nobody speaks the truth here...
Aztec poem (fragment).

1

Introduction

Probably from even before the dawn of civilization humans have been gazing at the starry nights and wondered about the world in which they found themselves living. Questions that have occupied humanity were ones like How did the universe begin? How had everything come into being? What is the universe made of? Was there a beginning? Will there be an end?. Many explanations have been given throughout the eons, as nearly every culture and society forwarded its own cosmogony and understanding of the universe. This quest has been vigorously pursued up to the modern age. Indeed, for the first time humanity appears to come close to an all-encompassing scientifically justified answer to these age-old questions, on the basis of a vast body of scientific knowledge supported by an ever-increasing and impressive amount of observational evidence.

Within the current cosmological model, it is assumed that the universe we inhabit came into being 13.7 billion years ago, born in a massive expanding fireball which we have named the *Hot Big Bang* (Hoyle 1950). In this event space and time, as well as all the matter and energy that the universe contains came into being. The pristine universe was extremely hot and dense, gradually cooling and diluting as it expanded. Under the gravitational instability scenario of structure formation, the present structure and motions in the universe are due to the growth of gravitational fluctuations from the initially highly homogeneous background (Peebles 1980).

Although by now it seems we have a fairly good idea of how the universe came into being and its dynamics at large scale (tens of Megaparsecs), this is not yet the case at smaller scales. Surveys of galaxies have shown that the universe is rather structured. Stars, gas, dust, planets are not randomly distributed in space but form larger gravitational-bound systems called *galaxies*. These in general are also clustered: some in small groups, others in big clusters with hundreds of galaxies. Moreover the clusters themselves are grouped in filamentary or sheet-like superclusters. Since the early galaxy surveys this highly-structured cosmic web shape of the universe has been observed (e.g. Joeveer & Einasto 1978; de Lapparent et al. 1986; Geller & Huchra 1989). The present galaxy surveys reaching even deeper regions of the universe (e.g. PSCz, 2dF, SDSS, 2MASS, 6dF) have shown that indeed the universe is well organized (see Figure 1.1).

Accompanying this foam-like pattern is the peculiar velocity field of galaxies. These migration flows of cosmic matter are one of the major physical manifestations together with the emergence and growth of structure out of the almost homogeneous primeval universe. The cosmic flows move out matter toward regions where ever more matter accumulates, ultimately assembling the structures we observe in the universe.

In order to understand the large-scale matter structures that form our universe and to have a complete view of the structure formation process, it is necessary to know how the velocity and density fields evolve and affect each other along the temporal and dynamical evolution of the universe.

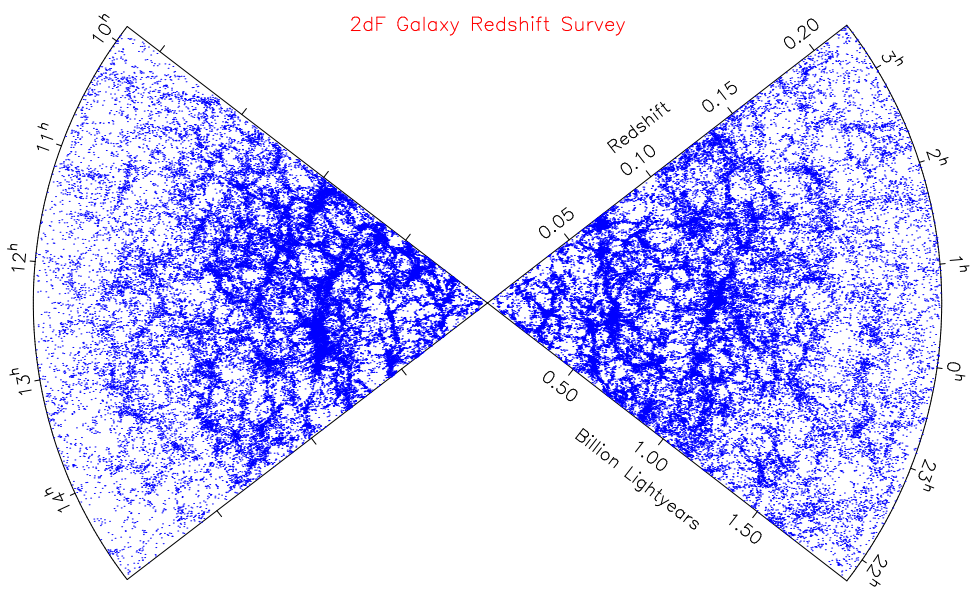

Figure 1.1 — Map of how galaxies are distributed in space as a function of distance from us according to the 2dFGR Survey. Notice how matter is clumped at some specific regions (clusters & superclusters of galaxies), while there are also empty regions (voids). (credits: 2dF Galaxy Redshift Survey team).

1.1 Motivation

The main topic of this thesis is the study of the peculiar velocity field of galaxies, its influence over the matter distribution and its reconstruction or modeling from the galaxy distribution.

Cosmic flows have the potential of determining the density of the universe by an estimation of Ω_m (the ratio of the observed density to the critical density), how galaxies trace mass, and to test the Gravitational Instability paradigm by determining if the initial cosmic density fluctuations were Gaussian. As an important characteristic, the velocity field is sensitive to all of the mass, including any dark matter and baryons that did not end up in galaxies.

Major efforts from the observational side have been carried out in order to accurately measure the distances and peculiar velocities of galaxies. Some systematic errors derived from the observational techniques (e.g. Malmquist bias, redshift distortions) are understood and we have a fair idea of how to correct for them. Still, effects due to the non-linearity of some systems and inhomogeneous sampling cannot be properly corrected for.

From the theoretical point of view, linear theory and its high order perturbation extensions seem to explain reasonable well the dynamics of structures up to the mildly non-linear regime, and in some ideal cases up to the non-linear regime. On the computational side, with the advent of powerful computers and smart numerical codes, cosmologists have been able to solve numerically the equations of motion and to follow the evolution of structures until the non-linear regime. However, this approach only works from one side to another in the arrow of time of the universe. This is, given an initial smooth mass distribution, it is only possible to follow its evolution forward in time. The opposite situation, i.e., to reconstruct the initial smooth mass distribution from the present clumpy mass distribution, it is not always possible since the virialized characteristics of the systems have erased any trace of their initial state.

Theoretical predictions of structure formation usually refer to continuous density and velocity fields. However, matter as traced by the galaxy distribution is rather discrete. Thus, one has to resort to artificial methods in order to construct continuous fields from the discrete observed fields, and to interpolate information to regions devoid of data. A major problem is that the actual galaxy distribution and peculiar velocity surveys suffer from shot-noise effects. This is an important source of

error mainly at large distances where sampling is rather poor. The present available interpolation techniques cannot properly deal with all these sources of errors in order to estimate continuous density and velocity fields, and to establish a fair comparison between theory and observations. Under such circumstances, one usually needs to make use of other extra techniques like smoothing algorithms. This results mainly in smearing out small scale features in the data, allowing only studies from the linear point of view. Because the universe presents small and large scale features in both density and velocity fields, it is highly desirable that such methods could keep the properties of such fields at both regimes if one really wants to have a complete picture of the dynamical processes in the Universe.

The main questions to answer in this thesis could be summarized as follows:

- **Can we properly model the velocity field from a given matter distribution? If so, up to what scales? Can we reproduce its main characteristics?**
- **How important are the tidal effects in the reconstruction or modeling of the peculiar velocity field in our cosmic neighborhood? Can we account for them?**
- **Is it possible to map continuous velocity fields from discrete peculiar velocities preserving its characteristics at both large and small scales?**

Answering completely these questions is beyond the scope of this work. This thesis is a theoretical and computational effort carried out in order to help understanding the peculiar velocity field of our nearby universe and the role that the different large scale structures play in moulding our universe as we see it. We will mainly make use of computer-simulated data which resembles statistically, morphologically and dynamically the cosmic neighborhood. The use of controlled and specifically purpose designed numerical simulations will be of great help to test our methods and hypothesis under controlled circumstances. The further application of these methods to real data will also be explored. In particular, over the PSC*z* catalog whose characteristics such as full-sky coverage, effective deep and homogeneous sampling make it a fair map of the matter distribution of our nearby cosmic environment.

We will asses how well currently available all-sky, flux limited redshift surveys of galaxies can account for the major share of mass concentrations inducing the external tidal forces. We will focus on reconstructing the peculiar velocity field from the galaxy distribution inferred from $N-$body simulations and real data with the characteristics that they will account for linear and mildly non-linear motions. In particular, on the Local Supercluster region since this is the cosmic vicinity where the quality, quantity and spatial coverage of the peculiar velocity field is the best available.

An important ingredient of this work will be the Delaunay Tessellation Field Estimator method for peculiar velocities designed for computing volume-weighted peculiar velocity fields from a discrete set of peculiar velocities. This method is based on the stochastic and geometrical properties of the particle distribution itself, the Delaunay tessellations. We will show that this method will allow a direct comparison with the theoretical predictions. This method guarantees reconstructed continuous volume-covering velocity fields, suppressing shot-noise effects and preserving the large and small scale characteristics of the discrete velocity field. We will make use of this technique to study the small scale characteristics of the peculiar velocity field in the nearby cosmic vicinity.

Finally, we will investigate the necessary conditions that prevailed in the primitive density and velocity fields in order to produce some of the cosmic structures we observe nowadays. We will assess the statistical significance of the possible identification of such structures via their gravitational effects over the light from the background matter distribution.

We assume along this thesis that the universe satisfies the standard homogeneous and isotropic Hot Big Bang model. The framework of Gravitational Instability assumes that gravity is the only agent at large scales responsible for the collapse and formation of structures dominated by dark matter. Before proceeding with this thesis, we review only the basic facts and the theoretical background that will be used along this work. For more complete and detailed formalism we refer the reader to the textbooks Peebles (1980, 1993a); Padmanabhan (1993); Peacock (1999); Coles & Lucchin (2002); Liddle & Lyth (2000).

1.2 Cosmological Background: The homogeneous Universe

Understanding the large-scale structure of the universe is one of the main goals of cosmology. It is well accepted that Gravitational Instability plays a central role in giving rise to the structures we see in galaxy surveys.

The standard Hot Big Bang model relies on three basic assumptions: (1) The universe is homogeneous and isotropic (Cosmological principle). Thus, its geometrical and dynamical properties can be described by the Robertson-Walker [RW] metric. (2) The evolution of the space-time can be described by the General Relativity equations of motion. (3) On scales smaller than the horizon the universe can be described by a perturbed RW model in which metric fluctuations are small.

The evolution of a homogeneous, isotropic expanding universe can be expressed in terms of its metric, specifying the distance between two points in space-time. The Robertson-Walker metric is given by:

$$\mathrm{d}s^2 = c^2\mathrm{d}t^2 - a^2(t)\left(\frac{\mathrm{d}r^2}{1-kr^2} + r^2\,\mathrm{d}\Omega^2\right). \tag{1.1}$$

Here spherical coordinates (r,θ,ϕ) are used to describe the spatial positions, and $\mathrm{d}\Omega^2 = \mathrm{d}\theta^2 + \sin^2\theta\mathrm{d}\phi^2$ is the square of the solid angle. The coordinates are comoving with the expansion of the universe, whose spatial extent grows proportional to the expansion factor $a(t)$. For convenience, at the present time t_0, $a(t_0) = 1$. The curvature k parameterizes the global geometry of the universe, commonly referred to as closed ($k > 0$), flat ($k = 0$) and open ($k < 0$).

The RW metric predicts that a monochromatic wave emitted by a receding object (e.g. galaxy, quasar) is systematically Doppler-shifted toward larger frequencies, in other words *red-shifted*. The redshift "z" of a source is given by

$$z = \frac{\lambda_0 - \lambda_e}{\lambda_e}\,, \tag{1.2}$$

where λ_0 is the wavelength of the radiation detected at t_0 (observed), and λ_e is the wavelength emitted from a distant source at the time t_e. This cosmological quantity can be directly measured from observations of object's spectra. The relation between the redshift of light and the expansion factor at which it was emitted is given by

$$1 + z = \frac{a_0}{a_e}\,. \tag{1.3}$$

Thus, measuring the redshift of an object, we can determine the scale factor a at the moment when the light was emitted, and then the cosmological time and finally infer its spatial distance.

Introducing the RW metric in the Einstein's field equations and under the assumption that the universe can be described as an ideal fluid, one obtains the Friedmann [FRW] equations, which describe the expansion and evolution of the universe:

$$\frac{\ddot{a}}{a} = -\frac{4\pi G}{3}\left(\rho + \frac{3p}{c^2}\right) + \frac{\Lambda}{3}\,, \tag{1.4}$$

$$\frac{\dot{a}^2}{a^2} = \frac{8\pi G\rho}{3} - \frac{kc^2}{a^2} + \frac{\Lambda}{3}\,. \tag{1.5}$$

In these equations, G is the Newton's gravitational constant, ρ is the mass density, p is the pressure and Λ is the vacuum energy or cosmological constant. The Hubble parameter, or the rate of expansion, is defined as

$$H(t) = \frac{\dot{a}}{a}\,. \tag{1.6}$$

H_0 refers to the expansion rate at the present, and is often expressed as $H_0 = 100\,h$ km s^{-1}Mpc, where h is a dimensionless factor.

In order to solve the Friedmann equations, an equation of state for the cosmic fluid needs to be specified. For substances of cosmological relevance, the equation of state has the form: $p(\rho) = w\rho c^2$. Here, w is a dimensionless constant which indicates the kind of matter component we are dealing with,

and c represents the speed of light. There are three main components of the material content of the universe: baryons (normal matter), non-baryonic dark matter (e.g. WIMPs, axions) and relativistic matter (photons and neutrinos). In the early universe, the energy density is dominated by radiation and relativistic particles ($w = 1/3$), then the equation of state is given by $p = \frac{1}{3}\rho c^2$. However, as the universe expands, the energy density decays as a^{-4}, while that of non-relativistic matter, which is assumed to be pressureless ($w = 0$), scales as a^{-3}. Dark energy has $p = -\rho c^2$ with ρ constant in time and $w = -1$. This energy causes an accelerating universe if $w < -\frac{1}{3}$. The cosmological constant Λ is usually identified with this dark energy. It is possible to show that matter dominated over radiation for most of the history of the universe. In this thesis we will only be concerned about the universe in this matter-dominated phase.

The matter content of the universe can be expressed in terms of the critical density

$$\rho_c = \frac{3H_0^2}{8\pi G}\,. \tag{1.7}$$

A universe with density above this critical value will be *"spatially closed"*, whereas a lower density universe will be *"spatially open"*. This critical density allows the definition of the following density parameters:

$$\Omega_m = \frac{\rho_m}{\rho_c}\,, \qquad \Omega_{rad} = \frac{\rho_{rel}}{\rho_c}\,, \qquad \Omega_\Lambda = \frac{\Lambda}{3H_0^2}\,, \qquad \Omega_k = -\frac{kc^2}{a_0^2 H_0^2}\,, \tag{1.8}$$

to refer to the density of ordinary matter, relativistic matter (radiation), vacuum energy and curvature. Note that these quantities are evaluated at present time, t_0. Dividing by H_0 the Friedmann Eqn. 1.5 and evaluating it at the present time becomes

$$\Omega_m + \Omega_k + \Omega_\Lambda = 1\,, \tag{1.9}$$

while Eqn. 1.4 takes the form

$$q_0 = \frac{1}{2}\Omega_m - \Omega_\Lambda\,, \tag{1.10}$$

where q_0 is known as the deceleration parameter $q_0 = -(\ddot{a}a/\dot{a}^2)|_{t_0}$, which can be used to parameterize cosmological models.

With all these definitions, matter-dominated universes can be completely characterize by the cosmological parameters $(H_0, \Omega_m, \Omega_\Lambda)$ or (H_0, Ω_m, q_0). Once this set of numbers is known, the evolution of a cosmological model is given by

$$H(a) = \frac{\dot{a}}{a} = H_0\, E(a)\,, \tag{1.11}$$

where E is the normalized Hubble function defined as

$$E^2(a) = \Omega_m a^{-3} + \Omega_k a^{-2} + \Omega_\Lambda\,. \tag{1.12}$$

There is a large range of possible FRW universe models. Over the decades many different ones were forwarded, gained popularity and subsequently dropped out of the scene. Perhaps the simplest solution is the Milne model with $\Omega_m = \Omega_\Lambda = \Omega_k = 0$ which describes an empty expanding universe. One of the most popular models is the so-called Einstein-de-Sitter model characterized by $\Omega_m = 1$, $\Omega_\Lambda = \Omega_k = 0$. For these scenarios Eqn. 1.11 has exact analytical solutions (also other models with $\Omega_m \neq 1$). In the general case ($\Omega_i \neq 0$ with $i = m, \Lambda, k$), the equation has to be solved numerically.

A continuously rising flood of new cosmological observations, stemming from larger and larger depths in the Universe, has lead to a converging consensus regarding the Universe we are living in. With impressive accuracy a rather remarkable set of values for the crucial cosmological parameters has emerged, now commonly known by the name of *"Concordance Model"*. Satellite experiments such as COBE and WMAP, in conjunction with balloon-borne experiments such as Boomerang, have

showed the validity of the Hot Big Bang model, and that the Universe is *flat* ($\Omega_k = 0$), with an age of 13.7 billion years. In combination with the ground-based mapping efforts of large redshift surveys of galaxies (2dFGRS and SDSS), we have been able to track the (dark) matter content of the Universe with $\Omega_m = 0.27$. Supernova SnIa surveys have showed evidence of the presence of the "Dark Energy", which represents 73% of the energy content of the Universe ($\Omega_\Lambda = 0.73$). Ever since it started to dominate the dynamics of our Universe, only as recent as some 7 Gigayears after the Big Bang, it has been propelling an acceleration of the expanding Universe.

The successes of the Hot Big Bang model are that it has been able of explaining:

1. Why the night sky at night is dark (Olbers' paradox). Only in a Universe with a finite age and with a finite velocity of light this may be understood.

2. The expansion of the universe. Hubble (1929) found that galaxies are receding from us with a velocity proportional to their distance (v = Hr).

3. The abundances of light chemical elements (H, He, Li,...) shortly after the Big Bang (primordial nucleosynthesis).

4. The Cosmic Microwave Background Radiation [CMB], which is the relic blackbody radiation when the temperature of the universe dropped sufficiently ($3000°K$) to allow protons and electrons to combine to form Hydrogen atoms.

1.3 The inhomogeneous universe

So far we have discussed the dynamics of a homogeneous and isotropic universe. However, the observed universe is far from homogeneous. Even the mere existence of galaxies is inhomogeneous. There is a richness of structure ranging from dwarf galaxies, to groups and clusters of galaxies, and to the huge superclusters of galaxies (see Fig. 1.1). This would imply that the cosmological principle is violated at small scales. The standard model, however, will still be valid provided that the metric fluctuations are small within the Hubble radius[1], in other words, provided that the universe is a perturbed FRW universe. At scales somewhat larger than hundreds of Mpc homogeneity is approached. If the universe is smoothed on larger scales, it will appear homogeneous. Despite the small-scale clumpiness of the universe, its global dynamics can still be described by the Friedmann models.

The canonic theory of structure formation in the universe assumes that structure grows due to Gravitational Instability [GI]. Primordial fluctuations in the primeval homogeneous density field are amplified through gravity (e.g. Peebles & Yu 1970; Weinberg 1972; Peebles 1980). Such gravity perturbations induce cosmic flows of matter. High-density regions start to contract and finally experience collapse, amassing more and more matter from their surroundings. In the same way that there are matter surpluses in particular regions, there are regions characterized by densities lower than the average density of the universe. They become emptier and expand with respect to the background, turning into empty voids. Gradually, as matter is displaced, cosmic structures emerge to form the universe as we see it today. Figure 1.2 illustrates the gravitational instability scenario and the emerging of structure. The GI implements the Jeans instability theory in an expanding medium and considers isocurvature and adiabatic longitudinal solutions to describe the growth of initially small density perturbations. Under such conditions, structure formation theories are completely specified by their initial conditions, i.e., by the form the of the initial power spectrum and the values of the cosmological parameters ($H_0, \Omega_m, \Omega_\Lambda, \Omega_k$).

The main force driving the dynamics and evolution of galaxies, and the large-scale structure formation process in the universe is gravity. Although gas physics plays an important role in the galaxy formation process, it only plays a minor role for the dynamics of the large-scale of the universe. Observational measurements indicate that there is a large fraction of "unseen" matter called *dark matter*,

[1]The Hubble radius is the radius of the observable universe. At actual time $d_H = \frac{c}{H_0} \approx 3000\ h^{-1}$Mpc.

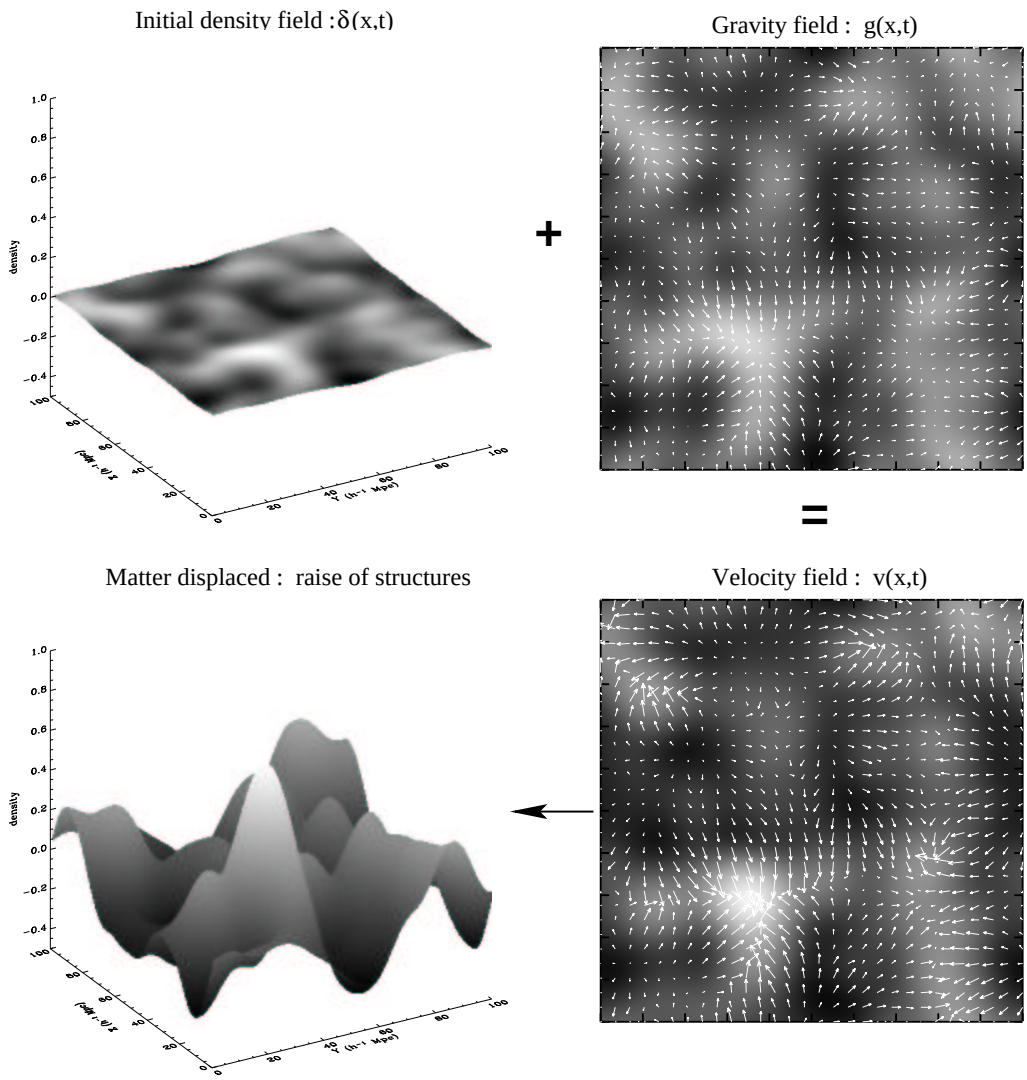

Figure 1.2 — The Gravitational Instability scenario. An initial Gaussian smooth density field is gravitationally perturbed, inducing cosmic flows of matter, ending up in the emergence of structure.

and it is believed that can *only* be detected by their gravitational effects on luminous matter. This assumption implies that the dynamics of dark matter can be treated by using the laws of gravity alone. Observational evidence seems to suggest that the energy content of the universe consist of 4% of its total content by baryonic matter, 23% by non-baryonic dark matter and the rest (73%) is dominated by the dark energy.

1.3.1 The Linear regime

The study of the growth of density perturbations is one of the major topics in cosmology. When fluctuations are small, the equations of motion can be linearized by expanding around the homogeneous solution. The resulting *Linear theory* together with its high-order perturbation extensions are among the best methods to study the large-scale structure formation process.

Dark matter is assume to behave as a collisionless fluid for most of the time of the universe.

At any given time t, we may distinguish between the regime in which the proper wavelength of the perturbations modes $\lambda(t)$ is much smaller than the Hubble radius $d_H(t)$ (horizon), and that in which $\lambda(t) \gtrsim d_H(t)$. In the former regime, the evolution of inhomogeneities can be analyzed with Newtonian dynamics, whereas in the later case the full relativistic treatment is needed. Since we are interested in scales much smaller than the horizon scale, the Newtonian approach can be applied. In order to describe the perturbations of an ideal FRW-model, we scale out the uniform expansion by transforming to a comoving frame. A particle moving with the (hypothetical) homogeneous background universe is defined to have constant coordinates in such frame. The comoving position $\mathbf{x}$ is defined as $\mathbf{r} = a\,\mathbf{x}$ where a is the expansion factor, and $\mathbf{r}$ is the position in the static coordinate system. The physical velocity $\dot{\mathbf{r}}$ of a particle can be written as $\dot{\mathbf{r}} = \dot{a}\mathbf{x} + a\dot{\mathbf{x}}$, where the motion relative to the comoving frame, $\mathbf{v} \equiv a\dot{\mathbf{x}}$, is the peculiar velocity component, and $\dot{a}\mathbf{x} = H\mathbf{r}$ is the Hubble flow. It is also convenient to define the density fluctuation field $\delta(\mathbf{x})$:

$$\delta(\mathbf{x}) = \frac{\rho(\mathbf{x}) - \rho_b}{\rho_b}\,. \tag{1.13}$$

In a statistical sense, $\delta(\mathbf{x})$ is considered as a random field, i.e., as a set of random variables, one for each point $\mathbf{x}$. In this way, the universe is a random realization chosen from a statistical ensemble of universes. In this framework, ρ_b represents an average over the ensemble (background density).

The equations of motion for the matter fluid are the continuity and Euler equations and the Poisson equation. The first and second equations state the conservation of matter and momentum, respectively. The third equation states that the density fluctuations originate by metric perturbations given the Newtonian potential ϕ. These set of equations in an expanding universe in the comoving coordinate system and ignoring relativistic effects are given by:

$$\begin{aligned} \frac{\partial\delta}{\partial t} + \frac{1}{a}\nabla\cdot(1+\delta\mathbf{v}) &= 0\,, \\ \frac{\partial\mathbf{v}}{\partial t} + \frac{1}{a}(\mathbf{v}\cdot\nabla)\mathbf{v} + \frac{\dot{a}}{a}\mathbf{v} &= -\frac{1}{a}\nabla\phi\,, \\ \nabla^2\phi &= 4\pi G\rho_b a^2\delta\,. \end{aligned} \tag{1.14}$$

We have not considered terms depending on pressure because we assume them negligible. This is because the last stages of fluctuations growth occur after $z = 100$, when the pressure is negligible. The *peculiar gravitational potential* ϕ is related to the peculiar gravitational field $\mathbf{g}$ by:

$$\mathbf{g}(\mathbf{x}) = -\frac{\nabla\phi}{a} = G\,a\rho_b \int \frac{\delta(\mathbf{x}')\,(\mathbf{x}'-\mathbf{x})}{|\mathbf{x}'-\mathbf{x}|^3}\mathrm{d}\mathbf{x}' \tag{1.15}$$

This equation shows that density fluctuations are responsible for the motions in the Newtonian limit.

Combining the set of Eqns. 1.14, linearizing them and with some algebraic manipulation one obtains a single equation for the density perturbation (Peebles 1980):

$$\frac{\partial^2\delta}{\partial^2 t} + 2\frac{\dot{a}}{a}\frac{\partial\delta}{\partial t} = 4\pi G\rho_b\,\delta\,. \tag{1.16}$$

This equation is a linear second-order ordinary differential equation in δ and therefore, each mode is decoupled and evolves independently from each other. The general solution consists of two modes,

$$\delta(\mathbf{x},t) = A(\mathbf{x})D_1(t) + B(\mathbf{x})D_2(t)\,, \tag{1.17}$$

where $D_1(t)$ and $D_2(t)$ are the two independent time solutions. They are called the *growing* and *decaying* solutions, respectively. As the universe evolves the decaying mode damps away, so one can focus only on the growing mode D_1 , often called the *linear growth factor*. This is given by,

$$D_1(z) = E(z)\int_z^\infty \frac{1+z'}{E^3(z')}\mathrm{d}z'\,, \tag{1.18}$$

where $E(z)$ is the normalized Hubble function defined in Eqn. 1.12. Normally the values for D_1 have to be found numerically. Although analytical expressions have been found for $\Omega_\Lambda = 0$ models (Peebles 1993a; Sahni & Coles 1995). In an Einstein-de-Sitter universe, the growing mode is given by $D_1(t) = t^{2/3}$. So the density field can be expressed as $\delta(\mathbf{x}, t) = \delta(\mathbf{x})\, t^{2/3}$. As we can see, the evolution of δ is proportional to the scale factor. However, the structure formation growth stops when structures become non-linear (voids and clusters of galaxies) at the redshift,

$$1 + z \approx \frac{1}{\Omega_m} - 1\,, \tag{1.19}$$

at which they decouple from the Hubble expansion. At this redshift, structures experience first contraction and collapse, followed by virialization to turn finally into genuine cosmic objects. For a flat Universe with $\Omega_m = 0.3$, this happens at $z \approx 1.3$ ($a = 0.43$).

This is the main problem of structure formation in the linear regime. In an expanding universe density perturbations grow as a power law in time, while in an static universe they do exponentially. One therefore needs substantial fluctuations in the early universe to produce the structures we see at present. Guth (1981) proposed the idea that the universe experienced an *inflationary* epoch in which, the universe went through a phase of exponential expansion. This model provides a way to generate density fluctuations of the desired type and amplitude to act as the seeds of the structures we see nowadays in the universe.

1.3.2 The velocity field

The equations of motion (Eqns. 1.14) also involve the velocity field. This field is very important in cosmological studies since it is directly observable. This together with the density field, is one of the most prominent physical manifestation of the dynamical growth of structure in the universe.

The linear peculiar velocity field in the linear perturbation approximation with zero pressure satisfies the equations (Peebles 1980):

$$\frac{\partial \mathbf{v}}{\partial t} + H\mathbf{v} = \frac{1}{a}\frac{\partial (a\mathbf{v})}{\partial t} = \mathbf{g}\,, \tag{1.20}$$

$$\frac{\nabla \cdot \mathbf{v}}{a} + \frac{\partial \delta}{\partial t} = 0\,, \tag{1.21}$$

with $\mathbf{g}$ the peculiar gravity field. The velocity field can be decomposed as the sum of a longitudinal (non-rotational) field and a transverse (rotational) field $\mathbf{v} = \mathbf{v}_L + \mathbf{v}_T$, with $\nabla \times \mathbf{v}_L = 0$ and $\nabla \cdot \mathbf{v}_T = 0$. Combining these results with the continuity equation we can immediately distinguish that only the longitudinal component of the velocity field is able to generate matter displacements and hence gravitational perturbations. Primordial rotational motions usually decay rapidly with time, and we therefore will go along the usual assumption that the primordial velocity field is vorticity free. Therefore, and according to the Kelvin's circulation theorem[2], the velocity field will remain curl-free as long as the flow continues laminar.

Eqn. 1.21 is particularly important since it gives the $\delta(\mathbf{x})$ once the velocity field, $\mathbf{v}(\mathbf{x})$ is known. Peebles (1980) introduced the dimensionless growth rate f,

$$f = \frac{d\log D_1}{d\log a} \approx \Omega_m^{0.6} + \frac{\Omega_\Lambda}{70}\left(1 + \frac{\Omega_m}{2}\right), \tag{1.22}$$

to express the time dependence in the continuity equation: $\delta(\mathbf{x}) = -\nabla \cdot \mathbf{v}/(aHf)$. The approximation in Eqn. 1.22 shows that in the general case f depends weakly on the cosmological constant at actual time (Lahav et al. 1991).

Since the peculiar velocity field is considered to be irrotational, it can be expressed as the gradient of a scalar function $\psi_{\rm v}$ called the *velocity potential*, $\mathbf{v} = -\nabla\psi_{\rm v}/a$. Substituting this equation into the

[2]This theorem states that for isentropic flow the fluid circulation around a closed contour fixed in the fluid is conserved.

continuity equation (Eqn. 1.21) gives $\nabla^2\psi_{\rm v} = H f a^2 \delta$, that compared with the Poisson equation, shows that $\phi \propto \psi_{\rm v}$ and therefore $\mathbf{v} \propto \mathbf{g}$:

$$\mathbf{v} = \frac{H_0\, f}{4\pi G \rho_b}\mathbf{g} = \frac{2f}{3H_0\,\Omega_m}\mathbf{g}, \tag{1.23}$$

from which the evolution of $\mathbf{v}$ can be deduced. This equation indicates that in the linear regime the peculiar velocity is proportional to the local gravitational acceleration.

1.3.3 The power spectrum

As we have seen, initially small perturbations grow by gravitational instability. It remains to characterize the spatial dependence of those initial perturbations. It is assumed that (and according to the central limit theorem) such initial fluctuations are described by a Gaussian random field in agreement with the Inflation predictions (e.g. Kolb & Turner 1990). There are other feasible mechanisms for generating primordial fluctuations, for example cosmic defects such as cosmic strings or textures. However, their initial fluctuations may not be necessarily Gaussian.

In this work we assume that Inflation is correct and therefore, the initial density field was Gaussian (Bardeen et al. 1986). In general, it is convenient to represent the perturbations in terms of its Fourier transform

$$\delta(\mathbf{x}) = \frac{1}{(2\pi)^3}\int \mathrm{d}\mathbf{k}\; \tilde{\delta}(\mathbf{k})\, e^{-i\mathbf{k}\cdot\mathbf{x}}. \tag{1.24}$$

Because of the isotropy assumed in the Cosmological principle (i.e. primordial fluctuations concern to isotropic stochastic process of random spatial fluctuations), the statistical properties of $\tilde{\delta}(\mathbf{k})$ are independent of the direction of $\hat{\mathbf{k}}$, and so we can define the *power spectrum* $P(k)$ as:

$$\langle \tilde{\delta}(\mathbf{k})\, \tilde{\delta}^*(\mathbf{k}')\rangle = (2\pi)^3\; P(k)\, \delta^D(\mathbf{k}-\mathbf{k}'). \tag{1.25}$$

Here, δ^D represents the Dirac delta function. Hence, specifying $P(k)$ determines all the properties of the Gaussian random field since this is fully characterized by its second order moment (Bardeen et al. 1986). In linear theory, the shape of the power spectrum is independent of time. The initial power spectrum depends on the way the initial fluctuations were generated. The simplest inflationary models predict the so-called *scale-invariant* power spectrum

$$P(k) \;\propto\; k, \tag{1.26}$$

i.e., the metric fluctuations in the early universe had the same amplitude on all scales. This is also called the Harrison-Zel'dovich spectrum. This model was predicted well before inflation has been suggested (Peebles & Yu 1970; Harrison 1970; Zel'dovich 1972). However, other models with tilted power spectra ($n \neq 1$) are also consistent with Inflation. In this thesis we will only refer to the Harrison-Zel'dovich one.

The adopted power spectrum is generic for universes in which the dark matter is non-relativistic, i.e., *cold*. The initial power spectrum evolves as the universe expands and perturbations grow, hence the processed linear power spectrum at late times will depend on the geometry of the universe and the nature of the matter.

1.3.4 The mildly non-linear regime

The linear relations just described are only valid when $\delta \ll 1$. This can lead to non-negligible errors if they are used to describe the matter perturbations beyond this regime. At the mildly non-linear regime ($\delta \approx 1$), before virialization takes place and erases all linear characteristics of the system, there are still some very useful approximations that can help us to understand the general case that cannot be solved exactly. Zel'dovich (1970) was among the first to explore analytically the non-linear regime. He proposed an extrapolation of linear gravitational instability theory into the non-linear regime. This approach is generally called the *Zel'dovich approximation*.

1.3.5 The Zel'dovich approximation

This method is a purely *kinematic* approach of the formation of structure. The starting point of the Zel'dovich approximation is the result from the linear theory for the growth of small perturbations. The essence of this approximation scheme is a prescription for the displacement of a particle from its initial (Lagrangian) comoving position $\mathbf{q}$ to an Eulerian comoving position $\mathbf{x}$,

$$\mathbf{x}(t) = \mathbf{q} - D(t)\nabla\psi(\mathbf{q}) \,. \tag{1.27}$$

In this mapping, the time dependent function $D(t)$ is the growth rate of linear density perturbations (Eqn. 1.18). The time-independent spatial function $\psi(\mathbf{q})$ is related to the *linearly extrapolated* gravitational potential ϕ. The Zel'dovich approximation also implies that a particle's peculiar velocity $\mathbf{v}$ is proportional to its displacement,

$$\mathbf{x}(t) - \mathbf{q} = \dot{D}(t)\,\nabla_{\mathbf{q}}\psi(\mathbf{q}) = a\,H\,f\,\mathbf{v}\,, \tag{1.28}$$

where f is the dimensionless growth factor. The corresponding evolution of the density field can be obtained from considerations of mass conservation, which requires that the Eulerian and Lagrangian density be equal, $\rho(\mathbf{x},t)d\mathbf{x} = \rho(\mathbf{q})d\mathbf{q}$. Hence

$$1+\delta = \frac{\rho(\mathbf{x},t)}{\rho_b} = \left\| \frac{\partial \mathbf{x}}{\partial \mathbf{q}} \right\|^{-1} = \frac{1}{(1+D\lambda_1)(1+D\lambda_2)(1+D\lambda_3)}\,, \tag{1.29}$$

where the vertical bars denote the Jacobian determinant. $\lambda_1, \lambda_2, \lambda_3$ are the eigenvalues of the deformation tensor $(\partial\psi_i/\partial q_j)$ along the three eigenvectors. These are called the *contraction* or *expansion* coefficients. In the linear regime (small perturbations, $D \ll 1$), the amplitude of the density contrast will be determined by the sum of the eigenvalues of the deformation tensor, $(\delta = -D(\lambda_1+\lambda_2+\lambda_3))$. At later times, the amplitude will be given only by the most negative eigenvalue. Then, the density contrast grows along the direction of this eigenvalue faster than in any other direction, $\delta \sim (1-\alpha D)^{-1}$, and it reaches infinity when $D = \alpha$. Thus, the Zel'dovich approximation predicts the collapse of matter into planes (sheets) called *pancakes*. The further evolution of the density field will be dictated by the second largest eigenvalue and its respective collapse along its eigenvector to form filaments. The third collapse along the third eigenvalue will result in the formation of clusters. The Zel'dovich approximation is completely valid until the moment when shell-crossing occurs, well beyond the linear regime $(\delta > 1)$. This approximation is widely used to describe large scale motions and for setting up initial conditions for numerical modeling since it is only necessary to generate one scalar function $\psi(\mathbf{q})$ to calculate all the other needed initial fields. In this thesis, we will use this technique for both purposes.

1.3.6 The non-linear regime: Cosmological simulations

The equations of motions are non-linear. We have presented solutions so far in the limit of linear and quasi-linear perturbations. The proper evolution of the density and velocity fields can be performed by means of numerical models. There are two main ways of addressing the density field, as a fluid (continuous field) or as a discrete field composed by particles. In principle, one could attempt to solve the "fluid" equations of motion for a continuous matter field (e.g. Peebles 1987). The second approach samples the density distribution in terms of a large number of particles, matter elements. Basically, a Lagrangian approach where the evolution is simulated by following the trajectories of these particles under their mutual gravity. This type of approach is called *N−body simulations*. In this thesis we will make an extensive use of $N-$body simulations in order to address specific problems of the structure formation scenario.

The purpose of cosmological simulations is to model the growth of structure in the universe. Numerical $N-$body techniques offer an effective tool for investigating the non-linear gravitational evolution. Since the region of the universe modeled is much smaller than the horizon volume, Newtonian equations of motions are adequate to describe the particle dynamics and evolution of structure. These

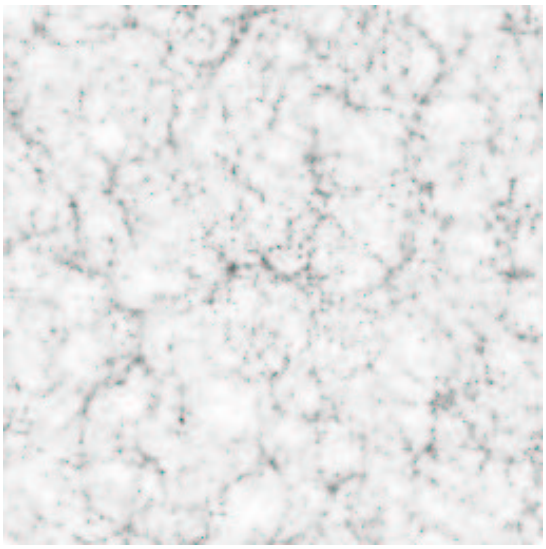

Figure 1.3 — Representation of a portion of the Universe created by a computer simulated model.

numerical methods can -in principle- simulate the evolution of dark and baryonic matter under a specific cosmological model. In the present thesis we will only focus in the evolution of dark matter. With the current powerful computers it is common nowadays to follow the evolution of $\sim 10^{6-7}$ particles in large enough volumes which are a fair representation of the universe at large scales (see Figure 1.3). The actual dynamic range in numerical simulations allows detailed studies of the structure formation process and of the ultimate goal in cosmology, galaxy formation.

The $N-$body simulations considered in this thesis start shortly after the Hot Big Bang, usually at $z = 49$ ($a = 0.02$), with a mass distribution that is close to be homogeneous. The initial Lagrangian particle positions are perturbed according to the fluctuation spectrum predicted by inflationary cosmology. Three main models are being considered along this thesis: the old standard, flat, scale-invariant cold dark matter model (SCDM); a flat tilted model (τCDM) and the flat low-density model with cosmological constant (ΛCDM). As a major characteristic of the initial density and velocity fields used as input for the $N-$body simulations will be the use of Constrained Random Field theory (Bertschinger 1987; Hoffman & Ribak 1991; van de Weygaert & Bertschinger 1996). This allows to generate constrained initial Gaussian random density and velocity fields. With this technique is possible to specify the presence and characteristics of one or more initial "seeds" that generated the large scale structures of the universe. Such constrained fields, completely consistent with the imposed cosmological scenario, allow to study systematically and under controlled circumstances the dynamical evolution of structures in the universe.

In universes dominated by cold dark matter, primordial fluctuations survive on small scales. Thus, the first objects to form are the smaller ones. The larger ones form through the merging of smaller ones that had already formed. This process of *hierarchical structure formation* seems indeed what we observe: *galaxies* are much older than the more massive and more recently collapsed *clusters* of galaxies. On an even larger scale, *Superclusters* have not even reached a collapse stage, at best they started to contract. The way in which these hierarchically embedded structures have arranged themselves in the Universe contains a wealth of information on the structure formation process. They appear to be grouped in planar or filamentary partially contracted superclusters, interconnected into a vast web-like configuration, interspersed by huge and empty void regions, stretching out along the observable Universe (see Figures 1.1 and 1.3).

1.3.7 Cosmic flows

Cosmic flows or Large-scale motions is a term used to describe the motions of galaxies, relative to the overall expansion of the universe, that are coherent over size scales much larger than the typical sizes of galaxy groups ($\sim 2\ h^{-1}$Mpc) in the form of bulk flows or streaming flows and shearing motions. Under the gravitational instability scenario of structure formation, such motions are driven by gravity and are the result of non-random motions imprinted at early epochs of the universe. The amplitude of such coherent large-scale motions are therefore among the most sensitive probes of both the large-scale structure of the universe and of the initial conditions of galaxy formation (Peebles 1980).

In order to measure peculiar velocities of galaxies, astronomers need to know the physical distance of such galaxies. Hubble's law tell us that the distances of galaxies are proportional to their observed recession velocities ($\mathrm{v} = H_0 r$). However, this is not exactly correct. galaxies have peculiar velocities above and beyond the Hubble flow: $\mathrm{v} = H_0 r + u$. Generally, distance indicators relate two quantities: one of them is distance dependent (e.g. galaxy luminosity), and the other is distance independent (e.g. galaxy rotational velocity). Two well known relations have been widely used for these purposes, the Tully & Fisher (1977) and Faber & Jackson (1976) relations applied to spiral and elliptical galaxies, respectively. Other type of distance indicators have also been used to measure cosmological distances, such as SN, Cepheids, surface brightness fluctuations, brightest cluster galaxies, PNe, etc.

While the confirmation of the gravitational instability scenario and determination of Ω_m are probably the most important goals of peculiar velocity surveys, they are also very helpful in characterizing the mass distribution in large scales. The discrete and nonuniform characteristics of wide-angle redshift surveys severely limitate them in order to measure density fluctuations at distances beyond $\approx 200\ h^{-1}$Mpc. On the other hand, large amplitude coherent peculiar velocities ($\gtrsim 500$ km s^{-1}) on large scales can be detected with relatively modest samples (e.g. Lauer & Postman 1994; Dekel 1994). The reason for this is that the peculiar velocity field on a given scale is more sensitive to components of the power spectrum on larger scales than is the density field, and thus is a useful probe of the large scale power.

The first evidence of large-scale streaming was reported by Rubin et al. (1976a,b) who found a bulk flow relative to the local group of 600 km s^{-1} in the direction of $(l,b) = (160,-10)^\circ$. Astronomers were skeptic about this result since it was nearly orthogonal to the Local Group velocity vector (e.g. Fall & Jones 1977). It was until Lilje et al. (1986) and Dressler et al. (1987) reported a bulk flow of 600 ± 100 km s^{-1} relative to the CMB frame, in the direction of $(l,b) = (312,6)^\circ \pm (12,10)^\circ$ that astronomers payed attention to large-scale cosmic flows. Lynden-Bell et al. (1988) analyzing the same data from the previous studies found the apex of the apparent bulk flow. They interpreted this as due to infall into an attracting point, which they modeled as a spherical density perturbation called the *Great Attractor* [GA]. Also the local group has been found to display an infall motion of ~ 230 km s^{-1} to the center of the Local Supercluster (e.g. Schechter 1980; de Vaucouleurs & Peters 1981; Aaronson et al. 1982b), in particular towards the Virgo cluster. This motion is called the *Virgocentric infall*. Further observational evidence has confirmed these two large-scale motions (e.g. Kraan-Korteweg et al. 1984). There are indications that the GA is not the primary source of inducing large scale motions in our cosmic neighborhood (e.g. Mathewson & Ford 1994), but there are other bigger structures located beyond this region which could induce bulk flows at very large-scales. The Shapley supercluster, a massive cluster-rich region located at $\sim 140\ h^{-1}$Mpc, has been pointed out as one of the possible main sources of the very large-scale motions (Raychaudhury 1989; Plionis & Valdarnini 1991). However, large uncertainties are present in the distance measurements due to inhomogeneous Malmquist bias and other effects.

While the Local Group of galaxies participate in a coherent flow of 600 km s^{-1} toward the Great Attractor region, the galaxy velocity dispersion around our local vicinity (in a volume of 5 h^{-1}Mpc) is of ~ 60 km s^{-1}. Such "coldness" of the flow provides a challenging contrast to the expectations from the current cosmological model and its explanation remains somewhat uncertain. Ostriker & Suto (1990) characterized such coldness by defining the *Cosmic Mach Number* as the ratio of the flow velocity to the small-scale velocity dispersion of galaxies. The estimate of such quantity, in particular

of the small-scale galaxy velocity dispersion, is an indication of the true gravitational potential of the matter responsible for such motions and of the shape of the power spectrum of density fluctuations (Ostriker & Suto 1990). However, the computation of such quantity is severely affected by two-body relaxation processes, together with the fact that its measurement is biased toward well sampled regions. These effects have raised problems in the interpretation of the cosmic Mach number, mainly because of the bias sampling. In this thesis, we will study the coldness of the flow by estimating it in a fair way, independent of the matter distribution.

Because peculiar velocities enable a reconstruction of the large scale matter distribution independent of galaxy surveys, one can compare the measured velocity field and the inferred velocities from the matter distribution (velocity-velocity comparison), or the measured density field to the inferred density from the peculiar velocity field (density-density comparison). In these comparisons, one makes the assumption of a biasing model which specifies how galaxies trace the underlying total matter distribution. The simplest model assumes a linear relation of the form:

$$\delta_g = b\,\delta_m\,, \tag{1.30}$$

where δ_g is the observed galaxy density contrast and b is the linear bias parameter. However, reality is more complicated than this and other (non-linear) models have been suggested. In this thesis we will assume that such model is valid. In practice, one does not directly measure b, but rather the combination

$$\beta = \frac{f(\Omega_m, \Omega_\Lambda)}{b}\,. \tag{1.31}$$

Here f is the dimensionless growth factor defined in Eqn. 1.22. In the present thesis, we make the assumption that the galaxy distribution follows the same behavior as the dark matter, i.e. $b = 1$ and $\beta \approx 0.5$ for a Λ dominated universe.

1.4 The Least Action Principle

A complete study of the large scale structure implies the knowledge of both density and velocity fields at any epoch. However, one usually knows one of these fields and needs to infer the "missing" field by any available method. The dynamical evolution of the universe represents a *mixed boundary condition* problem, some of them are specified at the present epoch and some at early times. The problem of mixed boundary conditions can be solved analytically in the linear regime, where a unique solution exists for both density and velocity fields (Peebles 1976). However, the actual density contrast is larger than unity, even when smoothed on scales of 10 h^{-1}Mpc. The associated velocities therefore need to be computed non-linearly. Unfortunately, the non-linear calculation of the growth of density fluctuations of arbitrary geometries is not simple, and $N-$body methods are not very helpful since their use is restricted to initial value problems. A further complication of the non-linear problem of mixed boundary conditions is the multivalued nature of the solutions. Orbit crossing makes identification of the correct orbits difficult, and impossible after virialization has erased the memory of the initial conditions. Often, one is restricted to laminar flow in the quasi-linear regime where orbit crossing has not erased yet the correspondence between the final and initial positions.

The Zel'dovich approximation is a good first order approximation to deal with laminar flows, but it fails at nonlinear regions. Peebles (1989, 1990, 1994) noticed that mixed boundary conditions led to a natural application of Hamilton's principle, the Least Action Principle [LAP], in which one seeks stationary variations of an action, subject to fixed boundary conditions at both the initial and final time.

The principle can be stated as: *the motion of a system from time t_1 to a later time t_2 is such that the integral:*

$$S = \int_{t_1}^{t_2} L\,\mathrm{d}t = \int_{t_1}^{t_2} \mathrm{d}t \sum_i \left[\frac{1}{2} m_i\, a^2\, \mathbf{v}^2 - m_i\, \phi(\mathbf{x}_i)\right], \tag{1.32}$$

where L is the Lagrangian of the system, has a stationary value for the correct path of the motion. m_i represents the mass of the ith particle, and S is referred as the action of the system. This principle

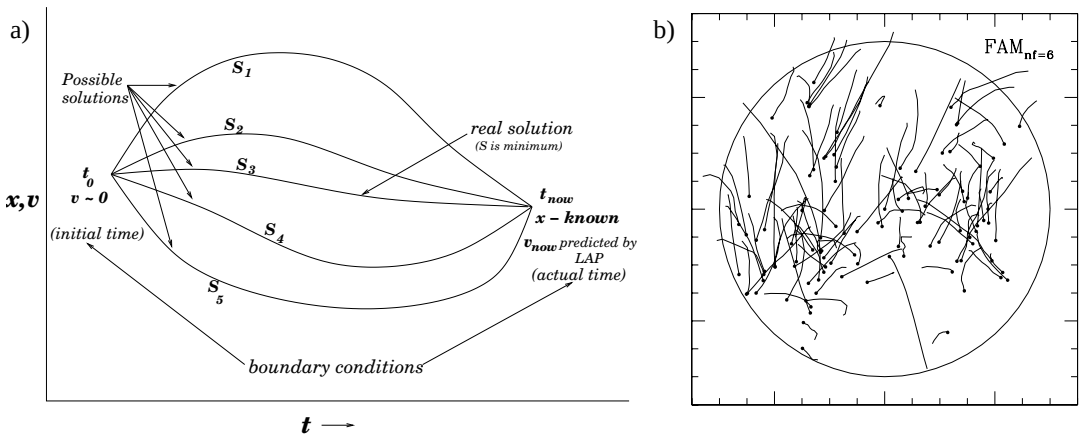

Figure 1.4 — The Least Action Principle. From all possible trajectories for a particle to go from its position at t_0 to its position at t_{now}, LAP predicts that the correct path is along the action S is a minima (Left-hand panel). Reconstruction of galaxy orbits by means of the LAP (Right-hand panel). The dots represents the actual galaxy positions, while the stream lines their trajectories back in time.

implies that from all possible paths by which the system could travel from its position at time t_1 to its position at time t_2, it will travel along the path for which the value of the integral is stationary (see left-hand panel of Figure 1.4 for a schematic representation). In other words:

$$\delta S = \delta \int_{t_1}^{t_2} L \, \mathrm{d}t = 0 \, . \tag{1.33}$$

Solving this equation will lead then to find the peculiar velocity field given the actual mass distribution in the system. The LAP describes the motion of a system for which all the forces are derivable from scalar potentials, that may be function of the coordinates, velocities and time. The LAP technique can be numerically implemented as a non-linear Lagrangian method to reconstruct orbits of objects from their present positions and therefore, to obtain a model of its velocity field (see right-hand panel of Figure 1.4) or, when the distribution of objects is properly smoothed, to recover the primordial density field from the observed one.

In the present thesis we will make use of a cosmological implementation of the LAP technique in order to estimate (model) the peculiar velocity field from the corresponding actual positions of objects in an expanding universe. Under such scenario the mixed boundary conditions are specified by knowledge of the present-day location of galaxies and the value of their velocities at an initial time.

1.5 Continuous velocity fields: the DTFE velocity algorithm

Comparison of observed or simulated velocity fields with predictions from theoretical models is possible only if one makes the assumption that the observed fields faithfully trace the underlying velocity field. In reality this is not the case. One only knows the peculiar velocities at the positions of observed galaxies or simulation particles. Theoretical predictions are based on the assumption that the velocity field is continuous and well defined within the considered volume. The resulting comparison with theoretical predictions is therefore not always clearly defined. The compared fields may not really be the same thing.

Fixed “Eulerian” grid-based methods have been commonly used to carry on such comparison. These methods make use of rigid kernel sizes which in essence “average” the velocities of the particles contained within the kernel (see Hockney & Eastwood 1988). The recovered information can be extrapolated to regions within the size of the kernel at regions devoid of data at the cost of erasing

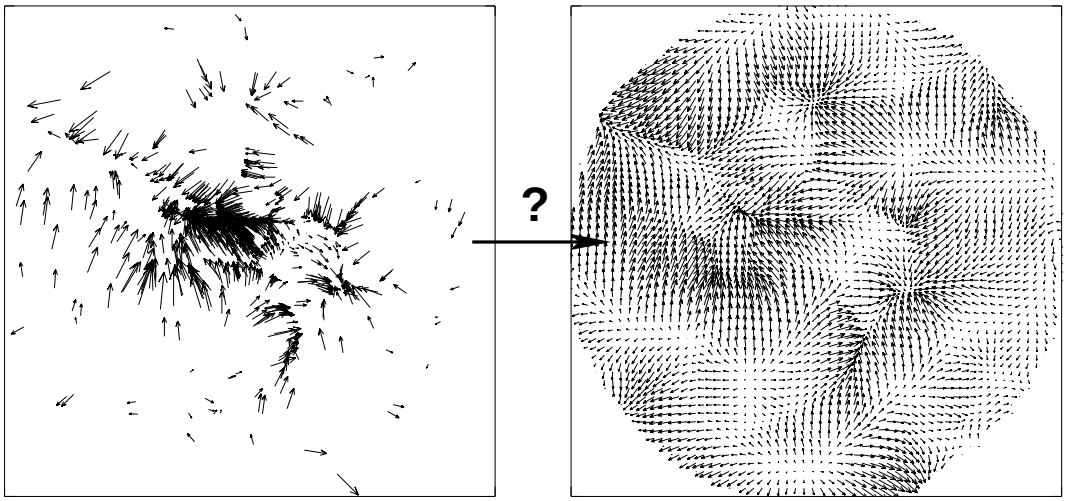

Figure 1.5 — How to get a continuous volume-covering velocity field from a discrete set of peculiar velocities? The use of the Delaunay Tessellation Field Estimator for peculiar velocities is a very promising technique to reconstruct such fields.

any signal smaller than the kernel size. There is therefore, a compromise between the large scale and the small scale signals and the kernel size of the employed interpolation method. In many cases the interpolation procedure alone is not enough, mainly where the sampling is very poor. Hence, one is forced to apply smoothing algorithms in order to obtain more coherent velocity fields and to minimize shot-noise effects, at the cost of erasing the signal of structures smaller than the smoothing kernel.

Adaptive methods have also been implemented. In this "Lagrangian" approach, the locations of the interpolation are confined to or defined by the point distribution itself. Of this type, of which the "SPH-type" schemes are the best known in astronomy. The latter refers to the abundantly used Smooth Particle Hydrodynamics technique (Lucy 1977; Gingold & Monaghan 1977) to follow the hydrodynamical evolution of astrophysical systems. This approach is not restricted to a specific geometry because it does not make use of a mesh, hence with an unlimited (ideally) spatial resolution. In practice, this is not possible and one has to make use of a "softening length". Although, this is usually smaller than the cell size of an Eulerian scheme. Therefore the spatial resolution of the Lagrangian technique can be significantly higher. However, the main difficulty of this technique is that it relies on stochastic arguments which means that it yields only approximate solutions at a given spatial position.

Ideally, one would like to preserve the large and small scale regimes in order to allow consistent studies of the peculiar velocity field. For example, the analysis of the small scale peculiar velocity dispersion contains information on the total matter content and dynamical state within a given region. When directly determined from the particle distribution itself it will lead to misleading conclusions since the study will be biased toward well sampled regions. A far better approach, assigning equivalent significance to the poorly sampled low density regions is to determine a continuous velocity field.

In this thesis, we work out an advanced tessellation interpolation scheme which adapts itself automatically to the geometry of the particle distribution, resolving both small and large scale velocity fields. The method is based on the Delaunay Tessellation Field Estimator [DTFE] (see Schaap 2005) technique. This approach for peculiar velocities has been demonstrated to have very reliable velocity field statistics (Bernardeau & van de Weygaert 1996). The DTFE is based upon a triangular network, known as Delaunay tessellation, which connects neighbouring points in a fully adaptive and objectively defined fashion (see Okabe et al. 2000). Moreover, the intrinsic characteristics of the method will allow us to perform studies of velocity-related quantities such as the expansion or contraction of the velocity field, its rotation, stretching and compression, and the evolution of the structure formation process in the universe.

2

Local Supercluster Dynamics: External Tidal Impact of the PSC*z* sample traced by Optimized Numerical Least Action Method

E. Romano-Díaz, E. Branchini & R. van de Weygaert.

We assess the extent to which the flux-limited IRAS PSC*z* redshift survey encapsulates the complete or major share of matter inhomogeneities responsible for the external tidal forces affecting the peculiar velocity flow within the Local Supercluster and its immediate surroundings. We here investigate this issue on the basis of artificially constructed galaxy catalogs. Two large unconstrained N-body simulations of cosmic structure formation in two different cosmological scenarios form the basis of this study. From these N-body simulations a set of galaxy mock catalogs is selected. From these a variety of datasets is selected imitating the observational conditions of either the local volume-limited Local Supercluster mimicking NBG catalog or the deeper magnitude-limited PSCz catalog. The mildly nonlinear dynamics in the "mock" Local Supercluster and PSC*z* velocities are analyzed by means of the Least Action Principle technique in its highly optimized implementation of the Fast Action Method. By comparing the velocities in these reconstructions with the "true" velocities of the corresponding galaxy mock catalogs we assess the extent and nature of the external tidal influence on the Local Supercluster volume. We find that the dynamics in the inner 30 h^{-1}Mpc volume is strongly affected by the external forces. Most of the external forces can be traced back to a depth of no more than 100 h^{-1}Mpc. This is concluded from the fact that the FAM reconstructions of the 100 h^{-1}Mpc PSCz volume appear to have included most gravitational influences. In addition, we demonstrate that for all considered cosmological models the bulk flow and shear components of the tidal velocity field generated by the external distribution of PSC*z* galaxies provides sufficient information for representing the full external tidal force field.

2.1 Introduction

Migration flows of cosmic matter are one of the major physical manifestations accompanying the emergence and growth of structure out of the virtually homogeneous primordial Universe. The cosmic flows displace matter towards the regions where ever more matter accumulates, ultimately condensing into the objects and structures we observe in the Universe.

Within the gravitational instability scenario of structure formation, the displacements are the result of the cumulative gravitational force exerted by the inhomogeneous spatial matter distribution of continuously growing density surpluses and deficits throughout the Universe. This establishes a direct causal link between gravitational force and the corresponding peculiar velocities. Given a suitably accurate measurement of peculiar velocities within a well-defined "internal" region of space, V_{int}, we may invert these velocities and relate them to the inducing gravitational force. Hence, the source of the measured motions may be traced and possibly even reconstructed. In principle, it may even allow us to infer the total amount of mass involved and thus estimate the value of the cosmological density parameter Ω_m and other fundamental cosmological parameters.

The practical execution of such studies of cosmic velocity flows is ridden by various complicating factors. One major complication is that the cosmic regions in which peculiar velocities have been determined to sufficient accuracy may have a substantially smaller size than what may be deemed appropriate for a dynamically representative volume. Ideally, in order to account for almost the complete flow in our local cosmic neighbourhood we should have probed the density field in a sufficiently large cosmic volume. This should involve a region of space substantially superseding that of the characteristic scale of the largest coherent structures in the Universe. Only then the magnitude of the gravitational influence of inhomogeneities at larger distances will represent a negligible contribution and, as well, start to even out against each other.

The size of this dynamically effective volume depends sensitively on the structure formation scenario which is prevailing in our Universe. Hence, it will be closely affiliated to the spatial distribution, characteristic size and coherence scale of cosmic structures, and its size will therefore be in the order of the scale of the largest pronounced structures in the Universe. Within the conventional structure formation models, based on Gaussian initial density and velocity fields, this is fully specified through the scenario's fluctuations power spectrum $P(k)$. When the power spectrum involves a substantial large-scale component and the survey volume is rather limited we have to be aware of significant external influences. Although not yet exactly determined, observational evidence suggests its size to be in the range of $\approx 100 - 200\ h^{-1}$Mpc (where h denotes the Hubble constant in units of 100 km s^{-1} Mpc^{-1}).

An equally important consideration concerns the spatial resolution at which the velocity field is studied. Available samples of galaxy peculiar velocities extend out to reasonable depth of $\approx 60\ h^{-1}$Mpc. Yet, they involve a rather coarsely and inaccurately sampled cosmic velocity field. By absence of precise distance estimators, more accurately and densely sampled velocity information is therefore mostly confined to a rather limited region in and around the Local Supercluster [LS]. As a consequence, most analyses of large-scale cosmic flows are necessarily confined to spatial scales at which the evolving cosmic structures are still residing in a linear phase of development. The dynamics in more advanced stages of cosmic structure formation are as yet poorly constrained by measurements.

2.1.1 Cosmic Force Fields and Supercluster Dynamics

In this work we wish to extend the analysis of cosmic flows to the more advanced evolutionary stages pertaining within supercluster regions. Only within the local cosmic neighbourhood of our Local Supercluster, the quality, quantity and spatial coverage of the peculiar velocity data are sufficiently good to warrant an assessment of the cosmic velocity field and the corresponding dynamics at a sufficiently high spatial resolution. On these quasi-linear or mildly nonlinear scales we hope to find traces of the onset towards the more advanced stages of cosmic structure formation. In order for this to yield a meaningful and successful analysis, two major questions have to be addressed. Both form the main focus of this contribution.

The first issue, that of the rather restricted sample volume, constitutes the major incentive behind this work. The volume of the galaxy catalog that best samples our local cosmic neighbourhood, the Nearby Galaxy Catalog (Tully 1988, hereafter NBG), is certainly substantially smaller than what may be considered dynamically representative. Any analysis of the (internal) velocity field in our Local cosmic neighbourhood should therefore take into account the impact of external gravitational influences.

We focus on two related problems. In the first place, there is the need to quantify the effect of neglecting the external gravitational influence $\mathbf{g}_{ext}$ when modeling the cosmic velocity field on scales comparable to that of the Local Supercluster. Various studies have attempted to determine cosmological parameters on the basis of a comparison between modeled versus measured velocity field in the Local Universe (Tonry & Davis 1981; Tully & Shaya 1984; Shaya et al. 1995; Tonry et al. 2000). For this it is crucial to understand in how far local density perturbations may account for the local peculiar gravity field within the Local Supercluster. Directly related to this is the need to have a sufficiently accurate description of the external force field $\mathbf{g}_{ext}$, in terms of its nature and spatial extent, in order to properly model the total measured gravity field $\mathbf{g}_{tot}$. For studies intent on a comparison of modeled versus observed peculiar velocities on scales larger than the Local Supercluster this is an essential requirement (Faber & Burstein 1988; Han & Mould 1990; Yahil et al. 1991; Webster et al. 1997; Branchini et al. 1999). Similar considerations are equally relevant for the inverse problem, in which one attempts to infer the external gravitational influence $\mathbf{g}_{ext}$ from peculiar velocities measured within the Local Supercluster (e.g. Lilje et al. 1986; Lynden-Bell & Lahav 1988; Kaiser 1991; Hoffman et al. 2001). Indeed, both problems concerning the restricted galaxy sample volume have figured prominently in previous cosmic velocity field studies and were addressed in a variety of publications. However, usually these tend to discard the fact that the local cosmic region in which we have access to high quality velocity data has already reached an advanced quasi-linear dynamical state.

Referring to the latter, the second major issue concerns the innovative way in which we evaluate the dynamical state of superclusters. These structures reside in a mildly nonlinear evolutionary stadium, having evolved significantly beyond their initial linear phase. Unlike the vast majority of previous studies, we seek to probe into the more detailed and informative kinematic aspects of these structures. A conventional linear analysis will not be able to provide an adequate description, and for the most evolved circumstances not even the Zel'dovich approximation (Zel'dovich 1970) may be expected to do so. In order to be able to optimally exploit the available velocity information – without suffering the loss of valuable high-resolution information through a filtering process – we apply the Least Action Principle [LAP] formalism (Peebles 1989) for dealing with the individual galaxy velocities. To that end, an optimal implementation developed by (Nusser & Branchini 2000, hereafter NB), the Fast Action Minimization [FAM] proved an essential tool.

Elaborating on the first issue of the external gravitational influence, one of the as yet undecided issues is the extent to which a LAP analysis of a cosmological self-gravitating system is dependent on a proper representation of the external gravitational influence. Various strategies have been followed, ranging from a complete neglect of external forces (Peebles 1989), or taking account of the influence of merely a few nearby objects (Peebles 1989, 1990; Dunn & Laflamme 1993; Peebles et al. 2001), towards methods involving approximate descriptions of external influences. The latter mostly incorporated the wider external influence through a frozen, linearly evolving, external tidal field estimated on the basis of the present-day locations of a extended sample of objects deemed representative for the external matter distribution (e.g. Shaya et al. 1995; Schmoldt & Saha 1998; Sharpe et al. 2001). This study does include the influence of force fields, but does so in a fully systematic and self-consistent fashion, enabled by the FAM method to take into account the evolution of the full sample of external matter concentrations.

The principal conclusion of our study is that the gravitational forces exacted by the matter inhomogeneities encapsulated by the IRAS-PSC*z* redshift survey sample (Saunders et al. 2000) are indeed able to account for all motions within our local Universe. In addition, we demonstrate that its external influence may almost exclusively be ascribed to the bulk and shear flow components.

2.1.2 Strategy

This study is based on a number of artificial galaxy samples mimicking the properties of genuine catalogs. They consist of several well-defined and well-selected model catalogs of galaxies and galaxy peculiar velocities. These mock samples are extracted from a set of extensive $N-$body simulations: for the nearby Universe models they adhere to the characteristics of the Nearby Galaxy Catalog, for the deep galaxy redshift samples they are modeled after the IRAS-PSC*z* catalog. These model samples allow us to thoroughly investigate the various strategies forwarded for a successful and conclusive analysis.

Two sets of realistic mock catalogs of galaxies are extracted. The first set, the "local" one, is meant to mimic the mass distribution within the LS as traced by galaxies in the Nearby Galaxy Catalog of Tully (1988). It consists of a volume-limited galaxy sample within a (spherical) interior region with radius 30 h^{-1}Mpc. Each of these interior samples is embedded within a larger mock sample, the "extended" sample which covers a larger cosmic region. In addition to the interior volume-limited sample in the inner 30 h^{-1}Mpc they contain an enclosing outer flux-limited sample covering the surrounding spherical region located between 30 h^{-1}Mpc $< x <$ 100 h^{-1}Mpc. This exterior sample mimics a flux-limited galaxy catalog whose characteristics are modeled after the IRAS PSC*z* sample.

For both the "local" and "extended" mock samples we model the peculiar velocity field at the positions of the particles in the "local" cosmic region, i.e. for the objects out to a radius $x < 30\ h^{-1}$Mpc. These model predictions result from the application of Fast Action Minimization method (Nusser & Branchini 2000). As our FAM reconstruction procedure only takes into account the gravitational forces between the particles in the mock samples – i.e. does not include contributions from outside objects – the differences in predicted velocities between the "local" and "extended" samples will reflect the influence of the mass concentrations in the surrounding region 30 h^{-1}Mpc $< x <$ 100 h^{-1}Mpc. The comparison with the corresponding N-body velocities, representing the "real" velocities, will inform us in how far "sky-covering" samples of galaxies with a depth of $\approx 100\ h^{-1}$Mpc may be expected to represent a proper cosmic region as far as its dynamics are concerned. The strategy of analyzing and comparing the velocity models obtained from the small "local" mock catalogs, the large "extended" mock catalogs, and the "real" velocities in the original N-body simulations, will yield a solid understanding of the effect of neglecting the externally induced peculiar gravitational acceleration $\mathbf{g}_{ext}$ (see Eqn. 2.1).

When analyzing a dataset of galaxy peculiar velocities in the local Universe. The analysis of the larger PSC*z* mimicking catalogs should elucidate if and to what extent such samples will be able to account for $\mathbf{g}_{ext}$. If the galaxies in these samples indeed appear to be responsible for the major share of the external forces, we may feel reassured to use the PSC*z* sample of galaxies for a proper representation of $\mathbf{g}_{ext}$.

One aspect of this question concerns the investigation of the question whether the external tidal influence may be explicitly framed in an analytical approximation consisting of a dipolar and quadrupolar term. Our fully self-consistent FAM reconstructions, in which the "extended" mock catalogs are processed with the inclusion of all external matter concentrations, enable us to estimate the bulk and shear components in the induced "local" galaxy motions. By comparing the resulting velocity fields in the "local" and "extended" samples we will be able to judge the quality of the approximate methods, and quantify and investigate the possible presence of systematic trends throughout the "local" cosmos.

To account for possible systematic effects due to global cosmology, the mock galaxy catalogs are extracted from N-body simulations in two different cosmic structure formation scenarios. One involves a ΛCDM Universe with a characteristic large-scale dominated power spectrum, while the other concerns a τCDM cosmology. The more small-scale dominated character of the latter leads to a different character of its gravitational field fluctuations, the smaller coherence scale of the density field fluctuations yielding a comparatively smaller influence of the external (quadrupolar) tidal field (the induced bulk flows are similar, as the smaller τCDM fluctuations are exactly compensated by the larger mass involved). The resulting comparisons of FAM velocity field reconstructions are expected to reflect these velocity field differences.

In the end, this study of artificial galaxy samples should allow us to appreciate the manifestations of the real physical effects we wish to grasp. In this, we also should learn how to deal with the complications due to the host of measurement uncertainties which beset the observational data. The scope is to quantify the systematic errors which might have affected similar, local, comparisons based on real data and to judge whether the information on the external mass distribution available to these analyses is indeed sufficient to account for $\mathbf{g}_{ext}$.

2.1.3 Outline

In the next section, we will elaborate on the astrophysical background of this study, the study of velocity flows on cosmological scales, and in particular the issue of internal and external gravitational influences. Ensuingly, we address the specific problem of treating the dynamics and related cosmic motions within mildy nonlinear structures such as the Local Supercluster. This brings us to a brief exposition on the LAP analysis for dealing with the complications of mildly nonlinear orbits and the technical issue of the FAM technique which allows us to apply this to a system composed of many objects. Special emphasis is put on the inclusion of external gravitational influences within the LAP/FAM formalism. In section 4 we describe the cosmological setting of the simulations on which this study has been based. As a guidance towards interpreting our calculations, we address a variety of theoretical aspects and predictions concerning cosmic velocity fields in these cosmological scenarios. The basis of this work is the set of two "parent" N-body simulations and the mock catalogs extracted from these simulations, forty in total. They are presented in section 5. In the subsequent sections we present the results obtained from the various FAM computations. In section 6 we analyze the velocity vector maps for the FAM reconstructions. These maps allow a direct and visually illuminating appreciation of the effects we wish to address. This is followed by a first quantitative assessment in section 7. This consists of a comparison between the FAM velocity field reconstructions of the Local Supercluster volume($r < 30\ h^{-1}$Mpc), the FAM reconstructions for the corresponding PSCz sample and the complete "real world" N-body velocity field. The comparison is mainly based on a point-by-point evaluation through scatter diagrams of velocity-related quantities. To encapsulate these results into a spatially coherent description of the large scale external velocity and gravity field, in section 8 we turn to a decomposition of the peculiar velocity field into multipolar components. In particular, we demonstrate that a restriction to its dipolar and quadrupolar components, i.e. the bulk flow and velocity shear, does represent a good description. Thus having looked at the issue of cosmic velocity fields from different angles, the summary of section 9 will focus on the repercussions of our analysis and its relation to the study of the (relatively nearby) surrounding matter distribution. On the basis of these conclusions we provide a description of the various projects which follow up on this work, together with some suggestions for additional future work.

2.2 Cosmic Flows: Probes of cosmic matter distribution

2.2.1 The Large-Scale Universe: Linear flows

Over the past two decades a major effort has been directed towards compiling large samples of galaxy peculiar velocities. These samples made it possible to obtain a rather impressive view of cosmic dynamics on scales $\gtrsim 10\ h^{-1}$Mpc. In particular the Mark III catalog, with an effective depth $\approx 60\ h^{-1}$Mpc, stands as a landmark achievement (Willick et al. 1997a; Dekel 1994; Strauss & Willick 1995). Further progress has been enabled by the assembly of additional and partially complementary samples of galaxy peculiar velocities, of which the SFI late-type galaxy and ENEAR early-type galaxy samples are noteworthy examples. The SFI Catalog of Peculiar Velocities of Galaxies (Giovanelli et al. 1997b,a; Haynes et al. 1999b) consists of around 1300 spiral galaxies with I-band Tully-Fisher (TF) distances, out to $cz < 7500$ km s^{-1}. The ENEAR sample (da Costa et al. 2000b) contains around 1600 early-type galaxies, out to a distance $cz < 7000$ km s^{-1}, with $D_n - \sigma$ distance estimates available for nearly all of them.

Tracing cosmic motions over larger volumes of space is a rather more cumbersome affair and attempts to do so are mainly based upon the peculiar motions of galaxy clusters. The claim of a puzzlingly large flow over scales of 150 h^{-1}Mpc by Lauer & Postman (1994) could not be corroborated. Nonetheless, flows on such large scales may indeed be a reality, as has been inferred from the far better defined "Streaming Motions of Abell Clusters" (SMAC) sample of Hudson et al. (2001). They did recover a bulk flow in the order of 687 ± 203 km s^{-1}, of which 225 km s^{-1} may arise from sources at a distance larger than 100 h^{-1}Mpc (Hudson et al. 2004). One prime objective of most analyses of these large samples of peculiar velocities has been the determination of the cosmological mass density parameter Ω_m The determination of the the cosmological mass density parameter Ω_m has been a prime objective of most analyses of these large samples of galaxy peculiar velocities (Davis et al. 1996; Willick et al. 1997b; Willick & Strauss 1998; Nusser et al. 2001; Branchini et al. 2001). Such assessments are based on a comparison of observed velocities to a model velocity field. A basic requirement for obtaining self-consistent estimates of Ω_m is that the velocity samples concern a "representative" volume of space.

However, even while such studies appear to succeed in attuning the large-scale matter distributions and velocity fields in a reasonably self-consistent fashion, doubts remain with respect to a variety of practical and systematic problems. Firstly, in these comparisons the random errors on the observed velocities are substantial, much larger than those in the structure formation models. Considerable effort has been directed towards quantifying and minimizing errors on the observed peculiar velocities (Dekel 1994; Strauss & Willick 1995, and references therein). These involve random measurement errors as well as more subtle systematic, yet reasonably well understood, errors. Secondly, there remain various systematic effects which have not been addressed and corrected for in an equally convincing fashion. Even though they also tend to play a role with respect to the model predictions they are often overlooked.

A major systematic factor concerns the incomplete information on the spatial mass distribution within the region of the sample itself. This prevents an adequate treatment of artifacts due to the incomplete sky coverage and limited depth of the available samples, and effects systematic errors stemming from luminosity and density effects. These systematic errors are usually accounted for by using large, all-sky redshift surveys, such as the Optical Redshift Survey of Santiago et al. (1995) or the 1.2 Jy and PSC*z* surveys of IRAS galaxies (Fisher et al. 1995a; Saunders et al. 2000). In particular when using IRAS based surveys the effects of incomplete sky coverage are greatly reduced.

Even more problematic for a successful handling of luminosity and density related effects is our incomplete knowledge with respect to the relationship between the observable galaxy distribution and the underlying mass distribution. By absence of a compelling theory of galaxy formation this "galaxy bias" is usually encapsulated in heuristic formulations. The rather ad-hoc and possibly unrealistic or inadequate nature of the latter may seriously affect the significance of the inferred conclusions. Most studies make the simplifying assumption of a galaxy population fairly tracing the underlying density field. This is usually embodied in a global and linear "galaxy bias" factor. A large variety of results suggest that this may be a reasonable approximation on scales in excess of a few Megaparsec. Moreover, while this bias may be problematic in the case of early-type galaxies, it has proven to be quite succesfull with respect to the later type galaxies which figure prominently in IRAS based samples (Verde et al. 2002).

2.2.2 Internal and External influences

Unlike most studies of cosmic flows which seek to assess and analyze the nature and source of dynamical influences within a confined region of space, we try to get an impression of the cosmic dynamics on mildly nonlinear scales of only a few Megaparsec. We focus on the Local Supercluster region and its immediate neighbourhood. The galaxy sample of the NBG catalog is taken to be representative for this region. Because the catalog entails a volume which is substantially smaller than what may be considered dynamically representative, the peculiar velocities of the galaxies are partially due to the gravitational action by outside matter concentrations. That is, the peculiar velocities are not only due to

the gravitational force induced by the matter concentrations within the "internal" survey volume V_{int}, but also reflect the gravitational influence by the "external" matter density distribution, $\mathbf{g}_{ext}$. Because it does not constitute a truely representative volume of the Universe, a meaningful dynamic analysis of the Local Universe on the basis of the NBG sample is substantially complicated by its limited depth, which is one of the major systematic problems besetting the analysis of virtually all available surveys of galaxy peculiar velocities. Theoretical models of peculiar velocities nearly always involve the implicit assumption of the mass being homogeneously distributed outside V_{int}, so that its gravitational effect may be neglected. Even in the case of having a sufficiently large volume at one's disposal, this approximation is only valid in the central part of V_{int}, certainly not near its edges.

The distinction between external versus internal gravitational force may be best appreciated by noting that the total (peculiar) gravity field $\mathbf{g}_{tot}(\mathbf{x})$ is the netto sum of the individual contributions by all patches of matter throughout the visible Universe. At any position within the internal volume V_{int}, we may then decompose the full gravitational field into an "internally" induced component $\mathbf{g}_{int}$ and an "externally" generated contribution $\mathbf{g}_{ext}$,

$$\mathbf{g}_{tot}(\mathbf{x}) = \mathbf{g}_{int}(\mathbf{x}) + \mathbf{g}_{ext}(\mathbf{x}) \ . \tag{2.1}$$

In this way we have defined the internal gravitational force $\mathbf{g}_{int}$ as the integrated contribution from the density fluctuations $\delta(\mathbf{x})$ within the volume V_{int}, while the external gravitational force $\mathbf{g}_{ext}$ concerns the combined gravitational force generated by the density fluctuations outside the realm of V_{int}, so that

$$\begin{aligned}\mathbf{g}_{tot}(\mathbf{x},t) = & \frac{3\Omega_m H^2}{8\pi}\int_{V_{int}} \mathrm{d}\mathbf{x}'\,\delta(\mathbf{x}',t)\frac{(\mathbf{x}'-\mathbf{x})}{|\mathbf{x}'-\mathbf{x}|^3} \\ & + \frac{3\Omega_m H^2}{8\pi}\int_{V_{ext}} \mathrm{d}\mathbf{x}'\,\delta(\mathbf{x}',t)\frac{(\mathbf{x}'-\mathbf{x})}{|\mathbf{x}'-\mathbf{x}|^3}\end{aligned} \tag{2.2}$$

The peculiar velocities of galaxies within V_{int} bear the mark of both the acceleration due to the matter concentrations within the volume itself, $\mathbf{g}_{int}$, as well as that of the combined gravitational influence of the external mass distribution, $\mathbf{g}_{ext}$. A comparison of predicted internally induced velocities with the observed local velocity field should therefore enable us to infer the magnitude and nature of the external field $\mathbf{g}_{ext}$. This analysis is usually facilitated by the fact that the fine details of the external force contribution are largely negligible. The contributions by the various external matter concentrations to the combined gravitational force mostly average out such that what remains noticeable is mainly confined to the low order components of the multipole decomposition of $\mathbf{g}_{ext}$. This can be most readily appreciated from a description of the external gravitational force field in terms of its successive multipole components. When we expand $\mathbf{g}_{ext}$ around some central location in V_{int} – here defined to be the origin of the coordinates $\mathbf{x}$ – we find that to second order

$$g_{ext,i}(\mathbf{x}) = g_{bulk,i} - \sum_{j=1}^{3} \mathcal{T}_{ij} x_j \tag{2.3}$$

In this, we assume that the additional divergence term $\frac{1}{3}(\nabla\cdot\mathbf{g}_{ext})\,x_i$ has been embedded into the (zeroth) order *monopole* term. In essence, it corresponds to a "breathing mode" affecting the "local" Hubble expansion within the volume, and therefore can not possibly be inferred from the local measurement of the internal gravity field $\mathbf{g}_{int}$.

The leading term in the overall external gravitational acceleration is the bulk gravity term $g_{bulk,i}$. This *dipole* term constitutes the uniform acceleration of the matter within V_{int},

$$\mathbf{g}_{bulk} = \frac{3\Omega_m H^2}{8\pi}\int_{V_{ext}} \mathrm{d}\mathbf{x}'\,\delta(\mathbf{x}',t)\,\frac{\mathbf{x}'}{|\mathbf{x}'|^3} \tag{2.4}$$

Evidently, when considering peculiar velocities relative to the centre of mass inside the volume V_{int} instead of absolute velocities this constant vector disappears. The first term whose magnitude and configuration is independent of the reference frame is the *quadrupolar* term $\mathcal{T}_{ij}$.

If the contribution to the gravitational potential by the external mass inhomogeneities is ϕ_{ext}, the quadrupolar tidal tensor $\mathcal{T}_{ij}$ is the trace-free part of $\partial^2\phi_{ext}/\partial x_i \partial x_j$, evaluated at the centre of V_i. It is determined by the external matter distribution through,

$$\mathcal{T}_{ij}(t) = \frac{3\Omega_m H^2}{8\pi} \int_{V_{ext}} \mathrm{d}\mathbf{x}'\, \delta(\mathbf{x}', t) \left\{ \frac{3x'_i x'_j - |\mathbf{x}'|^2 \delta_{ij}}{|\mathbf{x}'|^5} \right\} \tag{2.5}$$

It should be noted that the effects of the quadrupolar component rapidly increase as x^4 towards the edges of sample.

The integral expressions for the dipole and quadrupole components of the external gravity field (Eqn. 2.4 and 2.5), illustrate that it is unfeasible to exploit the observed local cosmic velocity field to recover the detailed and complete spatial distribution of the external matter inhomogeneities. On the other hand, it does indicate how it is that we can infer some overall characteristics of the external matter distribution from an analysis of the local velocity field. From this we may extract interesting and significant information on the nature and even distribution of the large scale cosmic matter distribution and set constraints on the values of some of the fundamental cosmological parameters. The pioneering work by Lilje, Yahil, & Jones (1986) in which the velocity field of the Local Supercluster was exploited to infer the presence of a major external source of gravitational attraction has shown the potential of this approach. Ultimately, it inspired the analysis of Lynden-Bell et al. (1988) that lead to the discovery of the Great Attractor.

2.3 Cosmic Flows: The mildly nonlinear dynamics of superclusters

Even though a structure's evolution may have progressed to a dynamical stage at which a first-order description of cosmic velocity fields will no longer be adequate, it may still be possible to find a direct link to the structure's initial configuration. This is in particularly true for the early and mildly nonlinear phases of evolution. The exemplary archetype of a structure in which such mildly nonlinear circumstances are prevalent is that of superclusters, the filamentary or wall-shaped elements of the cosmic foam-like matter distribution.

Over the past two decades intriguing foam-like patterns have gained prominence as a prime characteristic of the cosmic matter distribution. The first indications for the actual existence of a foam-like galaxy distribution were provided by CfA2 redshift slices (de Lapparent, Geller, & Huchra 1986) and established as a universal cosmic pattern with the Las Campanas redshift survey (Shectman et al. 1996). With the arrival of the large recent and ongoing systematic galaxy redshift surveys, the 2dF galaxy redshift survey ($\approx 250,000$ redshifts, see e.g. Peacock & The 2dFGRS Team 2001) and the Sloan Digital Sky Survey (SDSS, will determine $\approx 1,000,000$ redshifts, see e.g. Zehavi et al. 2002, for an overview of present-day status wrt. galaxy clustering), we may hope to have entered the stage in which we will be enabled to explore the formation and the dynamics of these characteristic spatial structures in the cosmic matter distribution. The typical elements of the cosmic foam – filamentary and wall-shaped superclusters – are precisely at the youthful yet mildly nonlinear phase of development mentioned earlier. They were identified as such within the context of Zel'dovich' "pancake" theory of cosmic structure formation (see e.g. Shandarin & Zeldovich 1989). The significance of the cosmic foam-like network for the understanding of the process of cosmic structure formation has since been generally recognized. This may be appreciated from the widespread use of the concept of the 'cosmic web', coined by Pogosyan, Bond, Kofman, & Wadsley (1996) in their study of the dynamics underlying its formation (see van de Weygaert 2002, for a recent general review).

Mildly nonlinear cosmic features such as superclusters have recently turned their initial co-expansion into a genuine physical contraction (or are on the brink of doing so), marking the emerging structure as a truely identifiable entity. Once it has surpassed this "turn-around" stadium the complexity of its internal kinematics quickly increases. At first moderately, and ultimately dramatically as the

virialization process advances, the matter orbits inside the structure become more and more complex. Even in the more moderate early phases of this process, an appropriately sophisticated treatment of the mildly nonlinear dynamics appears to be a necessary requisite for any study based upon kinematic information. In and around emerging nonlinear structures a simple linear analysis for reconstructing initial conditions will therefore no longer suffice. In other words, a sufficiently detailed and profound understanding of the emergence of these key elements in the cosmic matter distribution cannot be obtained without the development of a more elaborate technique for the analysis of cosmic velocity fields.

2.3.1 Structure formation: Mildly nonlinear dynamics

A linear analysis simplifies the dynamical evolution of a system into an initial conditions problem. It implies the reconstruction of the primordial density and velocity field by means of a simple linear inversion of the observed matter distribution and galaxy peculiar velocity field. Such an approach may even be followed towards a slightly more advanced stage. The Zel'dovich formalism, a Lagrangian first-order approximation for gravitationally evolving systems, has been remarkably successful in describing the early nonlinear evolution of a supercluster (for a review, see Shandarin & Zeldovich 1989). Substantially surpassing its formal linear limitations, it proved to be a highly versatile medium for analyzing and explaining the overall spatial morphology and characteristics of emerging structures. The Zel'dovich approximation elucidated and explained qualitatively the fundamental tendencies of gravitational contraction in an evolving cosmos. Perhaps most noteworthy this concerned the tendency of gravitational collapse to proceed anisotropically, together with its predictive power with respect to location and timescales of the first phase of collapse into planar mass concentrations, "pancakes". This offered the basic explanation for the foamlike morphology of the cosmic matter distribution, stressing its existence many years in advance of its discovery through observational programs to map the galaxy distribution (for an extensive review of various nonlinear approximation schemes seeking to expand upon the Zel'dovich approximation see Coles & Sahni 1996).

In line with the above, the Zel'dovich approximation proved a highly versatile tool for the analysis of the cosmic matter flows. It was successfully applied to the nonlinear situation of mixed boundary conditions – tested and calibrated using N-body simulations – by Nusser et al. (1991); Nusser & Dekel (1992). However, its validity remains restricted to the early stages of nonlinearity at which there is still a linear and direct relation between velocity and gravity field. Once matter inside the emerging structures starts to reach densities so high that local interactions become dominant, the Zel'dovich scheme quickly ceases to lose its applicability. Once matter elements start to cross each each others path the interaction between the nonlinear matter concentrations within the realm of the contracting structure will more and more deflect the orbits away from their initial linear trajectory. The linear kinematics of the Zel'dovich approximation will therefore no longer be able to follow the orbits of the matter elements. Higher order approximations based on perturbation theory have been advocated in order to follow such more advanced nonlinear circumstances. However, the improvement over simple first order Zel'dovich approximation turns out to be quite limited and not warranting the effort invested at each successive perturbation step. This is particularly so as with the onset of nonlinearity the rate at which successive perturbative orders terms become significant rapidly accelerates.

2.3.2 Least Action Principle in Cosmology

In more advanced nonlinear circumstances we encounter a more generic dynamical situation than a simple *initial value problem*. Typically, one seeks to compute the velocity field consistent with an observed density structure at the present epoch or, reversely, one deduces the density from the measured peculiar galaxy velocities. In the case of generic systems, the dynamical evolution represents a *mixed boundary condition* problem. This implies the system to be sufficiently constrained by complementing the incomplete dynamical information regarding the initial conditions with that pertaining to the dynamical state of the system at a different epoch. While N-body codes are particularly con-

cerned with the ideal circumstances usually embodied in terms of *initial value problems*, a different kind of technique needs to be invoked to exploit the typical *mixed boundary* information yielded by observations.

A more profound and direct exploitation of the available information to follow the physics of such a cosmological nonlinear system was forwarded by Peebles (1989, 1990). He pointed out that finding the orbits that satisfy initial homogeneity – and by implication vanishing initial peculiar velocities – and match the (present-day) observed distribution of mass tracers constitutes a mixed-boundary value problem. Such problems lend themselves naturally to an application of Hamilton's principle. This naturally leads to the formulation of the Least Action Principle, based on a variational analysis of the action S of an isolated system of M particles, which at a cosmic expansion factor $a(t)$ is given by

$$S = \int_0^{t_0} L dt = \int_0^{t_0} dt \sum_i \left[\frac{1}{2} m_i a^2 \dot{\mathbf{x}}_i^2 - m_i \phi(\mathbf{r}_i) \right], \tag{2.6}$$

in which L is the Lagrangian for the orbits of particles with masses m_i and comoving coordinates x_i and corresponding peculiar gravitational potential $\phi(\mathbf{x})$. For a system of particles interacting by gravity alone, embedded within a uniform cosmological background of density $\rho_b(t)$, this yields the following explicit expression for the action S,

$$S = \int_0^{t_0} dt \left[\sum_i \frac{m_i a^2}{2} \left(\frac{d\mathbf{x}_i}{dt} \right)^2 + \frac{G}{a} \sum_{i \neq j} \frac{m_i m_j}{|\mathbf{x}_i - \mathbf{x}_j|} + \frac{2}{3} \pi G \rho_b a^2 \sum_i m_i \mathbf{x}_i^2 \right] \tag{2.7}$$

The *exact* equations of motion for the particles are then obtained from finding the stationary trajectories, in particular the minima, amongst the variations of the action S subject to fixed boundary conditions at both the initial and final time. Confining oneself to a feasible approximate evaluation in this *Least Action Principle* approach, one describes the orbits of particles, $\mathbf{x}_i(t)$, as a linear combination of suitably chosen universal functions of time with unknown coefficients specific to each particle presently located at a position $\mathbf{x}_{i,0}$. For instance, by using the linear growth mode $D(t)$ as time variable (Giavalisco et al. 1993; Nusser & Branchini 2000), one can parametrize the orbit $\mathbf{x}_i(D)$ of a particle as

$$\mathbf{x}_i(D) = \mathbf{x}_{i,0} + \sum_{n=1}^{N_f} q_n(D)\, \mathbf{C_{i,n}} \,, \tag{2.8}$$

where the functions $q_n(D)$ form a set of N_f time-dependent basis functions. The factors $\mathbf{C}_{i,n}$ are then a set of free parameters, whose value is determined from evaluating the stationary variations of the action.

The functions $q_n(D)$ satisfy both two orbital constraints, necessary and sufficient to define solutions in agreement with evolution in the context of the Gravitational Instability theory for the formation of structure in the Universe: $q_n(1) = 0$ ensures that at the present time the galaxies are located at their observed positions $\mathbf{x}_i(1) = \mathbf{x}_{i,0}$ and $\lim_{D\to 0} D^{3/2} q_n(D)\theta(D) = 0$ (with θ the peculiar velocity with respect to the time variable D) guarantees vanishing peculiar velocities at early epochs which, in turns, ensures initial homogeneity.

2.3.3 Fast Action Minimization

The successful application of the *Least Action Principle* towards probing the kinematics and dynamics of an evolving cosmological system depends to a large extent on the specific implementation. This will be dictated by the characteristics of the physical system. In order to enable a meaningful LAP analysis of large samples of galaxies, like the Local Universe samples studied in this work, an optimized procedure is necessary for dealing with the large number of objects. Nusser & Branchini (2000) developed an optimized version of Peebles' original LAP formalism, the *Fast Action Minimization* method. The various optimization aspects of the FAM implementation proved to be crucial for our purposes. The relevant optimization hinges on three major aspects of the FAM scheme.

The first FAM improvement involves the choice of time basis functions $q_n(D)$. Its convenient choice of time basis functions yields a simple expression for the action of the system and for its derivatives with respect to $\mathbf{C}_{i,n}$. Both quantities relate to the internal gravity term $\mathbf{g}_{int}$ of the system. Once the action and its derivatives are evaluated numerically, the minimum of the action is determined by means of the conjugate gradient method (Press et al. 1992b). The orbits of the system are then fully specified through the set of parameters $\mathbf{C}_{i,n}$ found in correspondence to the minimum.

Closely related to the first aspect is that of tuning the choice of the time basis functions $q_n(D)$ such that only a limited number N_f of basis functions is needed to successfully parameterize the orbits of the system. This is in particular beneficial to the the physical configuration we are studying here, involving Megaparsec scale dynamics characterized by quasi-linear or mildly nonlinear motions.

A final major aspect of the FAM implementation involves the efficient computation of the internal (self-consistent) gravity $\mathbf{g}_{int}$ from the particle distribution in the sample. To this end, the gravitational forces acting on the particles at the different epochs are computed by means of the TREECODE technique (Bouchet & Hernquist 1988). By proceeding in this fashion, the FAM method is able to reconstruct the orbits of $\approx 10^4 - 10^5$ mass tracing objects back in time. This makes FAM numerically fast enough to perform a large number of orbit reconstructions, essential for performing the intended statistical analysis presented in the following sections.

In this work we use $N_f = 6$ basis functions to parameterize the orbits, choosing a tolerance parameter $tol = 10^{-4}$ to search for the minimum of the action S and setting a softening parameter of 0.27 h^{-1}Mpc to smooth the gravitational force in the TREECODE. In addition, the cosmological context of our evaluations translates into an orbit search restricted to solutions which do not deviate too much from the Hubble flow. Therefore, we set the initial guess for $\mathbf{C}_{i,n}$ according to linear theory prescription and search for the minimum of the action to avoid stationary points which might describe passing orbits (Peebles 1994) and set $\mathbf{C}_{i,n} = 0$ for $n > 1$ and $\mathbf{C}_{i,1}$ obtained from solving the action at $D = 1$. We have checked that this choice of parameters is optimal in the sense that decreasing tol, increasing N_f or changing the input set of $\mathbf{C}_{i,n}$ does not modify the final results appreciably.

Distortions in the resulting FAM-predicted peculiar velocities mainly arise from two systematic artefacts (Branchini et al. 2002). One is the discrete sampling of the mass distribution within V_{int}. The second, and overriding one, is the failure of FAM in reproducing the virial motions within high-density regions. This deficiency of the FAM reconstructions is clearly illustrated by the residual velocity vector maps (see Eqn. 2.20) in Fig. 2.7 and Fig. 2.8 (bottom row). These show the velocity vector differences between the "real" measured, i.e. N-body, velocities and the corresponding FAM reconstructions (here based on either the galaxy distribution in a 30 h^{-1}Mpc central region or the extended 100 h^{-1}Mpc region). The maps show how the largest residuals are the ones found in the high density regions: although the FAM_{30} and FAM_{100} velocity fields do show pronounced velocities near these regions they are not the proper "real" virialized velocities they should have been. The residual fields thus underline the fact that FAM's inaptitude to deal with regions characterized by large virial motions. Instead, in those situations it will lead to a false prediction of coherent inward streaming velocities, an effect pointed out by Nusser & Branchini (2000) and which can be also noted in our images when carefully studying them. Because this "virial effect" is local and restricted to $\sim 5\%$ of the points located in the most nonlinear regions, we partially circumvent this problem by applying a modest spherical tophat smoothing of 2 h^{-1}Mpc to the FAM-predicted velocities. This tophat filter has been specifically important for the quantitative aspects of our study, where such systematic problems may sort distorting conclusions. This smoothing has been invoked in quantitative comparisons between FAM and N-body velocities presented in this work, in particular in the regression analyses.

Finally, for practical reasons, since we are merely interested in measuring the effect of external gravity fields we make two simplifying hypotheses. We ignore redshift distortion effects by working in real space and we neglect the biasing problem by assuming that all particles within the sample fairly trace the mass of the system.

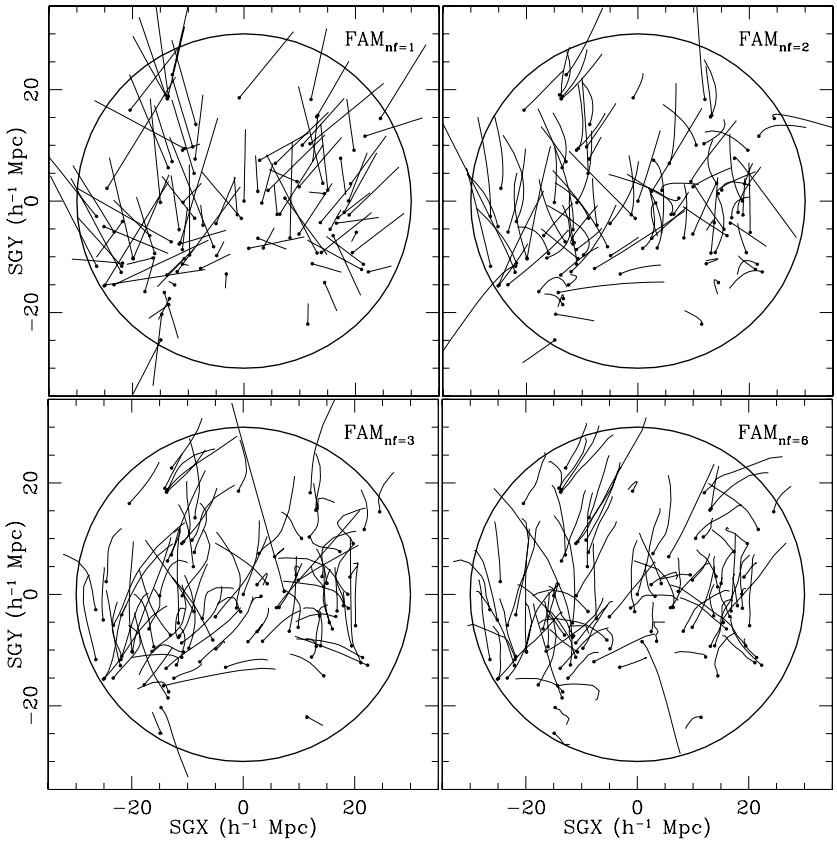

Figure 2.1 — 2D projected reconstructed FAM orbits for different values of N_f. The black dots represent the final (present) positions of each object. The solid lines indicate the trajectories followed by the objects as a function of time. The top-left panel shows FAM reconstructed orbits with $N_f = 1$ (Zel'dovich approximation). The top-right with $N_f = 2$, the lower-left $N_f = 3$ and the lower-right $N_f = 6$.

2.3.4 Ordered reconstructions

To obtain an idea of the level of improvement obtained through the use of successively higher order FAM evaluations, Figure 2.1 depicts 2D projections of the corresponding FAM particle orbit reconstructions within a local spherical volume of $\approx 30\ h^{-1}$Mpc. The black dots indicate the positions for each object in the sample, while the lines emanating from each dot represent the computed trajectories followed by these objects as they moved towards their present location. The illustrated configuration is taken from one of constructed mock catalogs, and resembles that of the Local Universe (see section 2.5.2.1). Each successive FAM reconstruction is based on the same (present-day) particle distribution. The four frames correspond to successively higher order FAM approximations, involving an increasing number N_f of basis functions $q_n(D)$. The top-left panel shows FAM reconstructed orbits with $N_f = 1$, which in fact corresponds to the conventional first order Zel'dovich approximation and thus represent the orbits that would have been obtained by the PIZA method (Croft & Gaztanaga 1997). These are followed by panels with $N_f = 2$ (top right), $N_f = 3$ (bottom left) and $N_f = 6$ (bottom right). They show a clear and steady improvement towards the $N_f = 6$ FAM evaluation. Testing proved that even higher order computations did not yield improvements significant enough to warrant the extra computational effort.

In summary, the galaxy orbits in our Local Universe environment are found at a minimum of the

action which is not too far, yet different, from linear theory predictions. The FAM technique thus yields a significant modification of the recovered galaxy orbits and peculiar velocities for configurations that evolved well beyond the linear regime (see e.g. Figure 2.1).

2.3.5 LAP and External forces

The original cosmological Least Action Principle formulation by Peebles (1989) considered a fully self-consistent, i.e. isolated, system of point masses. For practical reasons, the original implementation had to be restricted to systems of at most a few dozen objects. Almost exclusively, the Local Group of galaxies formed the focus of these LAP studies (Peebles 1989, 1990, 1994; Dunn & Laflamme 1993).

While these studies did indeed yield a substantial amount of new insight into the dynamical evolution of the Local Group, the issue of incorporating the dynamical influence exerted by external mass concentrations remained a major unsettled question. External forces do represent a significant component of the dynamics of the Local Group, as had been shown by Raychaudhury & Lynden-Bell (1989). They established beyond doubt that the Local Group cannot be considered a tidally isolated entity, and demonstrated that the Local Group is acted upon by an appreciable quadrupolar tidal force. The resulting tidal torque appears to be responsible for the large angular momentum of the Local Group as a whole, as Dunn & Laflamme (1993) showed in an elegant and pioneering analysis using orbits computed by the LAP variational method. They confirmed that the tidal influence of the external matter distribution is indeed essential to explain its present angular momentum.

In the course of time various strategies emerged to include external dynamical influences. The nature of these methods are mainly set by the character of the physical system under consideration, and to some extent was dependent on the available computational resources. Three strategies are outlined below.

2.3.5.1 Directly Including External Masses

To incorporate the external tidal influence within the LAP analysis the work by Peebles (1989, 1990, 1994) and Peebles et al. (2001); Dunn & Laflamme (1993) attempted to identify a few principal external mass concentrations which would be responsible for the major share of the external gravitational influence. While in his first LAP study Peebles (1989) considered the Local Group mainly as an isolated system, sequel studies (Peebles 1990; Peebles et al. 2001) attempted to assess the possible external influence by neighbouring matter concentrations. In (Peebles 1990) he attempted to condense the external tidal force into two nearby mass concentrations, the Sculptor and Maffei group, each modeled as a single mass. Both were incorporated as 2 extra particles, with properly scaled masses, within the action S in order to take them along in a fully self-consistent variational evaluation. A similar approach was followed by Dunn & Laflamme (1993), be it that they included five galaxies/groups in the local cosmic neighbourhood which arguably contribute a significant torque on the Local Group. Also in a later application (Peebles et al. 2001) this approach was followed, be it with an extensive outer region between $4h_{75}^{-1}$Mpc and $20h_{75}^{-1}$Mpc whose mass distribution was condensed into a coarse sample of some 14 major external objects.

This "self-consistent" strategy is feasible to pursue within the context of the original, computationally intensive, LAP implementation. This approach may therefore be followed in LG resembling situations in which a few objects suffice to represent the main aspects of a system's dynamical evolution. On the other hand, cosmic systems of a considerably larger scale than the Local Group would in general be too demanding for. Supercluster sized regions, with scales of up to a few tens of Megaparsec, count many more individual objects than a galaxy group. These systems have also not yet reached a formation stage so advanced that they have already largely decoupled from the global Hubble expansion, so the resulting external gravitational influence is usually the shared responsibility of a large number of external matter concentrations. Accounting for large-scale tidal field would quickly become prohibitively expensive in terms of the computational effort for conventional LAP analyses.

2.3.5.2 Inserting External Tidal Potential

An alternative strategy is to incorporate the external gravity in the LAP scheme via an approximate expression for the external contribution. This may be most directly achieved by inserting an extra external tidal potential term $\Phi_{tidal}(t)$ in the action S (Eqn. 2.6). As on sufficiently large, Megaparsec, scales we may expect this term to evolve according to linear gravitational instability perturbation growth,

$$\Phi_{tidal}(t) \;=\; D_\phi(t)\,\Phi_{tidal}(t_0) = \frac{D(t)}{a(t)}\Phi_{tidal}(t_0) \tag{2.9}$$

in which $\Phi_{tidal}(t_0)$ is the tidal term at the present cosmic epoch and $D_\phi = (D/a)$ the linear growth term for the gravitational potential (the growth factor D_ϕ and cosmic expansion factor $a(t)$ are set to be equal to unity at the present epoch, $D(t_0) = a(t_0) = 1$.). Thus, instead of evolving it self-consistently along with the considered system, the external field is determined at one epoch – usually the present one – and then incorporated as an extra linearly growing gravity field term $\Phi_{tidal}(t)$ in the action S:

$$S = \int_0^{t_0} dt\,\left[\sum_i \frac{m_i a^2}{2}\left(\frac{d\mathbf{x}_i}{dt}\right)^2 + \frac{G}{a}\sum_{i\neq j}\frac{m_i m_j}{|\mathbf{x}_i-\mathbf{x}_j|} + \frac{2}{3}\pi G\rho_b a^2\sum_i m_i\mathbf{x}_i^2 - \Phi_{tidal}(t)\right]. \tag{2.10}$$

There are various possibilities to compute the tidal potential term Φ_{tidal}, usually from the current mass distribution. One option is to compute it directly from a sample of M_{ext} external objects which is deemed responsible and representative for the major share of the external tidal force field,

$$\Phi_{tidal}(t_0) = \sum_i\, m_i\,\left\{\frac{G}{a}\sum_{j=1}^{M_{ext}}\frac{m_j}{|\mathbf{x}_i-\mathbf{x}_j|}\right\}. \tag{2.11}$$

Note that none of these external objects ($j = 1,\cdots,M_{ext}$) is taken into account as far as the action of the system and the computation of their orbits is concerned, except for their "passive" role in determining Φ_{tidal}. An alternative approach is to insert an approximate analytical expression for Φ_{tidal}, in particular one including the dipolar and quadrupolar contributions, $\mathbf{d}$ and $\mathbf{T}$, to the tidal potential,

$$\Phi_{tidal}(t_0) \;=\; \sum_i\left[\mathbf{d}\cdot\mathbf{x}_i \;+\; \frac{1}{2}\mathbf{x}_i\cdot\mathbf{T}\cdot\mathbf{x}_i\right]. \tag{2.12}$$

Equivalently, one may chose to insert the corresponding expressions directly into the expression for the derivative of the action with respect to an expansion coefficient, $\partial S/\partial C^{\alpha}_{i,n} = 0$, evidently equal to zero within this variational approach.

The first, "direct", procedure (Eqn. 2.11) was followed by Shaya, Peebles, & Tully (1995), who for the purpose of studying the velocity field within the surrounding 30 h^{-1}Mpc modeled the relevant external mass distribution after the distribution of rich Abell clusters from Lauer & Postman (1994). To some extent, Sharpe et al. (2001) operated along the same lines, be it that they added the resulting tidal term directly to the reconstructed velocities produced by the LAP procedure. However, while in principle exact, such a concentrated and static mass distribution may involve considerable uncertainties and can be highly sensitive to the uncertainties in the location of a few dominant point masses. As this spatial point distribution is supposed to form a suitable model for the underlying large scale matter distribution this may be even more worrisome.

Potentially more elegant may therefore be the modelling of a smooth tidal field along the line of the second procedure (Eqn. 2.12), as suggested by Schmoldt & Saha (1998). The corresponding dipolar and quadrupolar term may then be based on the best available determinations of these parameters. On the other hand, when the LAP volume is comparatively large, the analytical approximation may represent an oversimplification of the force field, neglecting potentially important local variations within the external force field.

Cosmology	Ω_m	Λ_0	Γ	σ_8	box length	N_{obj}
ΛCDM	0.3	0.7	0.25	1.13	345.6	192^3
τCDM	1.0	0.0	0.25	0.55	345.6	192^3

Table 2.1 — N-body simulation parameters. Column 1: cosmological model. Column 2: Ω_m mass density parameter. Column 3: Λ, cosmological constant parameter. Column 4: Γ, power spectrum shape parameter. Column 5: σ_8, density perturbation amplitude spectral normalization. Column 6: size of the computational box in h^{-1}Mpc. Column 7: number of particles in the simulations.

2.3.5.3 Self-consistent and Direct FAM approach

The indirect "potential" approach which we described above (Eqn. 2.11 or Eqn. 2.12) may not properly account for the temporal evolution of the external field in the case of nonlinearly evolving systems. The formalism assumes a static, merely linearly evolving, gravitational potential. However, the matter concentrations which generate the external tidal forces will themselves get displaced as the cosmos evolves. These displacements may be relatively minor for distant masses, but for the more nearby entities this may be entirely different. A detailed treatment of the external mass distribution will be necessary when the influence of the nearby external objects on the evolution of small "interior" regions is comparable to or even dominant over the self gravity of the region. It will be equally crucial to follow the detailed whereabouts of nearby matter concentrations in the case of a large "interior" region in which a marked contrast between the central regions and the outer realms may result in a significantly different dynamic evolution.

This prompted us to follow an alternative and direct approach, a fully self-consistent strategy in which also the external matter concentrations are accounted for in the computation of the system of evolving particle orbits. Alongside that in the "local" region for which we seek to reconstruct the velocity field, also the system of objects in the exterior regions (30 h^{-1}Mpc $< x <$ 100 h^{-1}Mpc) are considered. Non-uniform manifestations of the external influence can only be included by pursuing such a direct and systematic approach. It is only through the availability of the FAM technology that we were enabled to do so for a Megaparsec system consisting of a large number of objects.

2.4 Cosmological scenarios

The mock catalogs on which we apply our Fast Action Minimization analysis are extracted from N-body simulations in two different cosmological settings. Their characteristics, in terms of their relevant parameters, are listed in Table 2.1. The table also lists the simulation specifications. The first scenario is a flat ΛCDM model with a cosmological constant term $\Omega_{\Lambda,0} = 0.7$ ($\Omega_m = 0.3, \Omega_m + \Omega_{\Lambda,0} = 1.0$, h=0.83, n=1). The second model is a τCDM Einstein-de Sitter ($\Omega_m = 1.0, \Omega_{\Lambda,0} = 0, h = 0.5, n = 1$) model, motivated by the decaying particle model proposed by Bond et al. (1991). Both scenarios were chosen to be viable with respect to the current observational constraints, implying similarities in many overall properties and appearances, yet with some significant differences with respect to their dynamical repercussions. This may provide indications on whether the galaxy motions in our local cosmic neighbourhood do contain information on the structure formation scenario.

In both cases the amplitude of density fluctuations is normalized on the basis of the observed abundance of rich galaxy clusters in the local universe. This abundance depends on the magnitude of the matter field fluctuations on the mass scale characteristic for galaxy clusters. This translates into a dependence on the amplitude of density fluctuations on cluster scales modulated by the mean global

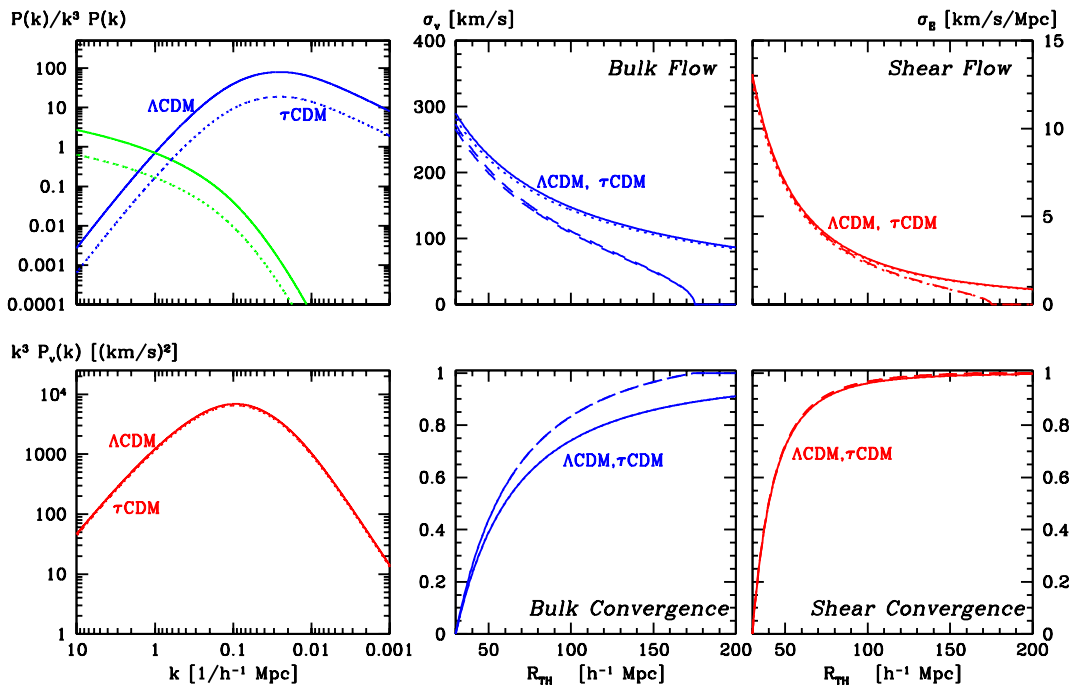

Figure 2.2 — Spectral characteristics for the two studied cosmological scenarios. Upper left: Power spectrum for the ΛCDM and τCDM cosmological scenario used in this study. Lower left: velocity power $k^3 P_{\rm v}(k)$, the amount of velocity power per logarithmic waveband interval. Upper centre: expected bulk flow velocities (kms) over a spherical (tophat) volume of radius R_{TH}. The solid line is the real theoretical prediction, the dashed one concerns the restricted power spectrum represented in the simulation box. Centre low: the convergence of the bulk flow, defined according to Eqn. 2.16. Upper left: Expected shear flow (km s^{-1} Mpc^{-1}) over a spherical (tophat) volume of radius R_{TH}. Similar to bulk flow, the solid line concerns the full theoretical power spectrum while the dashed corresponds to the restricted power spectrum represented in the simulation box. Lower right: convergence of the shear flow, defined according to Eqn. 2.16. Note that for the righthand frames the corresponding ordinate axis are the ones on the righthand side of the plotbox, while for the central frames it is the one on its lefthand side.

matter density. A variety of studies (e.g. White et al. 1993; Eke et al. 1996) found that in order to yield the present-day cluster abundance the amplitude of density fluctuations in spheres of radius 8 h^{-1}Mpc, σ_8, and Ω_m are related by

$$\sigma_8 = 0.55\Omega_m^{-0.6}\,, \tag{2.13}$$

The resulting power spectra are depicted in Figure 2.2 (top left). On all scales, the density fluctuations in the τCDM scenario, represented by the dotted lines (for both $P(k)$ and $k^3P(k)$), are less pronounced than those of the ΛCDM scenario: the two power spectra have a similar shape and differ by a simple scaling factor over the entire wavelength range. Visually, this is immediately reflected in the stark differences between the spatial galaxy distribution in the resulting mock catalogs. Figure 2.3 provides such a visual comparison. It shows the "external" PSCz catalog mimicking galaxy distribution in three mutually perpendicular central slices in the case of the ΛCDM scenario (top row), together with the same set of frames for a τCDM mock galaxy catalog (bottom row). On all scales, the τCDM galaxy distribution looks considerably more uniform than that in the ΛCDM Universe. Not only is the clustering of galaxies in the ΛCDM scenario more pronounced, it also delineates considerably larger structures, a manifestation of the power spectrum's amplitude at the corresponding large wavelengths.

Because the higher average matter density in the $\Omega_m = 1$ τCDM Universe does almost fully compensate for the lower amplitude of the density fluctuations the resulting gravity and velocity perturbation fields in the ΛCDM and τCDM scenarios are very similar. The velocity power spectra $k^3P_v(k)$

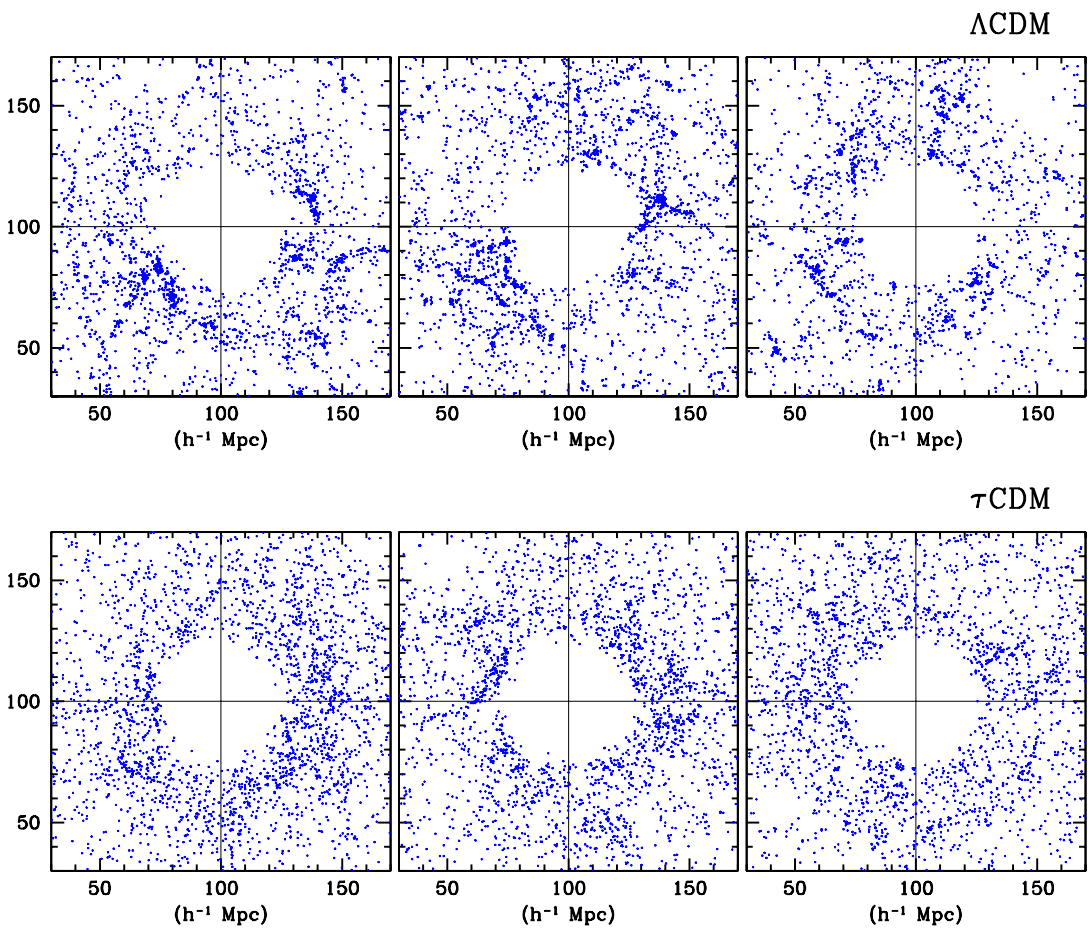

Figure 2.3 — Central slices through a mock galaxy catalog realization. Depicted is the galaxy distribution in the external ($r > 30\ h^{-1}$Mpc) volume. For each catalog, we show the $x-y$ (left), $x-z$ (centre) and $y-z$ (right) plane. Top row: ΛCDM mock catalog; Bottom row: τCDM catalog.

are shown in the bottom lefthand panel of Figure 2.2: their functional dependence is the same over the entire wavelength range. The larger mass corresponding to a given density excess in the τCDM Universe evidently effects a stronger gravitational force. The resulting large scale motions scale as $f(\Omega_m) \propto \Omega_m^{0.6}$. This happens to be almost exactly the inverse of the average density perturbation amplitude scaling (Eqn. 2.13), which is proportional to $\Omega_m^{-0.6}$ (Eqn. 2.13). While this is exactly the factor involved in the normalization of the power spectrum, in terms of σ_8, the lower level of density fluctuations gets precisely compensated by the higher amount of mass involved with them. This can be directly observed from the velocity power spectra $P_v(k)$ for the two scenarios (Fig. 2.2, lower lefthand frame). The velocity power spectra for both scenarios are exactly equal over the entire wavelength range, both in functional dependence as well as in amplitude. Note that also the gravity perturbations in the ΛCDM scenario are substantially stronger than those in the τCDM cosmology: because they scale with $\frac{3}{2}\Omega_m H_0^2$ and the amplitude of the density perturbations, which according to Eqn. 2.13 is $\propto \Omega_m^{0.6}$, the average peculiar gravitational acceleration is proportional to $\Omega_m^{0.4} H_0^2$.

The comparison between $k^3 P(k)$ (Fig. 2.2, top panel) and $k^3 P_{\rm v}(k)$ (Fig. 2.2, bottom panel) in the same figure shows the shift of the velocity perturbations, with respect to the density perturbations, towards a more large-scale dominated behavior. This follows directly from the continuity equation, connecting the velocity and density perturbations such that the velocity power spectrum relates to $P(k)$ through $P_{\rm v}(k) \propto P(k)\, k^{-2}$.

The large-scale behavior of the (linear) velocity perturbation field immediately illuminates the difficulty in tracing the full array of matter inhomogeneities responsible for the cosmic motions within a specific cosmic region. To account for all noticeable contributions it is necessary to probe out to large depth. This is manifestly evident for the first order component in the externally induced flow, the "bulk flow" v_{bulk}. A measure for the expected bulk flow within a (tophat) spherical region of size R_{TH},

$$\mathbf{v}_{bulk}(\mathbf{x}) \equiv \int_V \mathrm{d}\mathbf{x}'\, \mathbf{v}(\mathbf{x}')\, W_{TH}(\mathbf{x}-\mathbf{x}', R_{TH}), \tag{2.14}$$

is represented by the (root square) average value σ_v, whose value may be inferred from the Fourier integral

$$\begin{aligned} \sigma_{\mathrm{v}}(R_{\mathrm{TH}}) &= H_0\, f(\Omega_m)\, \sigma_{-1} \\ &\equiv H_0\, f(\Omega_m) \sqrt{\int \frac{\mathrm{d}\mathbf{k}}{(2\pi)^3}\, P(\mathbf{k})\, \hat{W}^2_{TH}(\mathbf{k})\, k^{-2}}\,. \end{aligned} \tag{2.15}$$

In these relations, $W_{TH}(\mathbf{x}, R_{TH})$ and $\hat{W}_{TH}(\mathbf{k})$ are the expressions for the tophat window filter, spatially and in Fourier space (see Bardeen et al. 1986, henceforth BBKS).

How substantial the large scale origin of the bulk flow is may be readily appreciated from Figure 2.2 (top centre). Because the linear character of fluctuations on large scales, the spectral σ_{v} (Eqn. 2.15) does provide a reasonable order-of-magnitude estimate of the magnitude of the large-scale bulk motions. The figure shows the estimated bulk flow amplitudes, $\approx \sigma_v$, as a function of the (tophat) window radius: the bulk flow is clearly a large scale phenomenon, converging only very slowly towards large spatial scales. In both the ΛCDM scenario and the τCDM scenario the externally induced bulk flow on a scale of 30 h^{-1}Mpc will be in the order of 200 km s^{-1}. Of this overall bulk flow, more than 100 km s^{-1} has to be ascribed to inhomogeneities on scales exceeding 200 h^{-1}Mpc ! When assessing the motions in a local volume of 30 h^{-1}Mpc radius, in terms of relative external contributions, inhomogeneities on a scale larger than 100 h^{-1}Mpc still contribute more than 25% of the total while the ones larger than 200 h^{-1}Mpc are still responsible for more than 10% (see Fig. 2.2, centre bottom). We should therefore expect to find substantial external contributions in the ΛCDM and τCDM simulations. Note that this relative contribution to the bulk flow, the "bulk convergence", is defined as the relative contribution by matter perturbations within a radius R_{TH} to the externally induced bulk flow on a scale of 30 h^{-1}Mpc (the size of the NBG volume):

$$\mathcal{F}_{\mathrm{bulk}} \equiv 1 - \frac{\sigma_{\mathrm{v}}(R_{TH})}{\sigma_{\mathrm{v}}(30\, h^{-1}\mathrm{Mpc})}\,. \tag{2.16}$$

The second order aspect of the velocity field which we seek to study is the induced velocity shear s_{ij},

$$\sigma_{ij} = \frac{1}{2}\left\{\frac{\partial \mathrm{v}_i}{\partial x_j} + \frac{\partial \mathrm{v}_j}{\partial x_i}\right\} - \frac{1}{3}(\nabla\cdot\mathbf{v})\, \delta_{ij}\,. \tag{2.17}$$

Also the velocity shear reveals interesting and distinguishing differences between the ΛCDM and the τCDM scenario. In the linear regime the expected magnitude of the shear tensor s_{ij}, on a tophat scale R_{TH}, may be evaluated through its direct proportionality to the tidal shear $\mathcal{T}_{ij}$. Quantifying s_{ij} by means of its (root square) average σ_s (van de Weygaert & Bertschinger 1996), we find

$$\sigma_s = H_0\, f(\Omega_m)\sigma_0(R_{TH}) \sqrt{\frac{1-\gamma^2}{15}} \tag{2.18}$$

in which the (dimensionless) spectral parameter $\gamma \equiv \sigma_1^2/\sigma_0\sigma_2$ is defined through the 0th, 1st and 2nd spectral moments σ_j (see BBKS). The predictions for the two cosmological scenarios are shown in topright frame of Fig. 2.2. With respect to the bulk flow there is a marked difference in coherence scale: the major contributors to the tidal shear are located at considerably closer distances than the

sources of the bulk flow (fig. 2.2, cf. lower right with lower centre). Most of the shear inducing matter inhomogeneities are found within a radius of 100 h^{-1}Mpc, accounting for more than 95% of its value (fig. 2.2, lower right). On a scale of 30 h^{-1}Mpc we expect an external tidal shear of ≈ 7 km s^{-1} Mpc^{-1} for both the ΛCDM scenario and the τCDM model.

2.5 Mock catalog Construction and Analysis

2.5.1 N-body simulations

The two N-body simulations used in this work were carried out by Cole et al. (1998) within the context of an extensive study of PSCz catalogue resembling galaxy mock samples in a large variety of cosmological structure formation scenarios. They consist of 192^3 particles in a computational box of 345.6 h^{-1}Mpc. They are dynamically evolved using an AP3M code in which the force is smoothed with a softening parameter of 0.27 h^{-1}Mpc.

The purpose of this study is a demanding task for truely representative N-body simulations. The N-body simulations should provide an optimal compromise between a high mass resolution on the small scale side and, on the large-scale side, a cosmic volume large enough to be dynamically representative. The large dynamic range requirement involves a mass resolution refined enough to resolve mass entities comparable to galaxies. This translates into an average inter-particle separation that needs to be smaller or comparable to that of galaxies in real observational catalogues. On the other hand, the simulations have to extend over a cosmic volume which is large enough to incorporate the major share of the gravitational influence exerted by the inhomogeneous cosmic matter distribution. Given the slow convergence of the bulk flow and its large coherence scale this is particularly challenging, and will be in the order of several hundreds of Megaparsec (see discussion in the previous section and Fig. 2.2). Although hardly any current N-body simulations would fully fulfil the dynamic range requirements, the used N-body simulations do appear sufficiently adequate for a meaningful investigation of the relevant systematic trends and effects. This remains true in a qualitative sense, even though on the basis theoretical arguments (see e.g. Fig. 2.2) and observational indications (e.g. Hudson et al. 2004) we know there may be substantial bulk flow contributions stemming from even larger spatial scales.

In this respect it is important to note is that the mock catalog realizations in this work are constrained by the finite size of the simulation box. The practical repercussions of being confined to a limited simulation volume may be inferred from the dashed curves in Fig. 2.2. They show the corrections to the expected bulk flow and velocity shear predictions (solid curves) when only the inhomogeneities in the restricted volume of the 345.6 h^{-1}Mpc simulation box are incorporated. Because perturbations on scales exceeding the fundamental scale of the box are absent, the realized power spectrum has a rather sharp and artificial large-scale cutoff: the limited boxsize L_{box} implies a cutoff in the power spectrum at low wavenumber $k_{box} = 2\pi/L_{box}$. From Fig. 2.2 we can conclude that this correction is particularly apt for the bulk flow, predictions for the velocity shear seem hardly affected. As a consequence, on scales over ≈ 100 h^{-1}Mpc the bulk flows in the realized N-body simulations will be severely repressed and far from representative. Although large-scale mode adding procedures have been proposed to partially remedy this situation (Tormen & Bertschinger 1996; Cole et al. 1997), our τCDM and ΛCDM simulations did not include such MAP (mode adding procedure) extensions. Conclusions with respect to the convergence of the FAM reconstructed velocity flows should therefore be referred to with respect to the suppressed velocity power spectrum indigenous to our N-body simulations (notice that this dynamic range issue is truely cumbersome to nearly any study attempting to assess velocity flows in computer simulations).

2.5.2 Mock Catalog Construction

From the full N-body simulations we extract mock catalogs made to resemble the local Universe. The ΛCDM and τCDM N-body simulations are processed through specified observational masks to imprint the required characteristics on the resulting mock catalogs. We distinguish two types of mock

Cosmology	Set	Number of catalogs	$\langle N_{obj} \rangle$	Maximum radius
ΛCDM	NBG	10	2740	30
	PSC*z*	10	10900	100
τCDM	NBG	10	2803	30
	PSC*z*	10	11207	100

Table 2.2 — Characteristics of the mock catalogs. Column 1: label of the catalog. Column 2: cosmological model. Column 3: for each mock catalog type: number of generated catalogs. Column 4: average number of particles $\langle N_{obj} \rangle$ in each catalog. Column 5: external radius of the catalog in units of h^{-1}Mpc.

catalogs. From each N-body simulation we extract ten different "local" mock catalogs mimicking the NBG catalogue and, with these "local" samples representing their interior, ten different "extended" samples resembling the PSC*z* catalogue.

The "local" class of mock samples is meant to sample the mass distribution within a 30 h^{-1}Mpc region in and immediately around the Local Supercluster. These catalogs constitute *volume-limited* galaxy samples mimicking the Nearby Galaxy Catalog of Tully (1988). Mock catalogs of the second type are designed to account for the mass distribution out to distances of 100 h^{-1}Mpc. These "extended" samples represent *flux-limited* samples, for which we take the IRAS PSC*z* galaxy catalog (Saunders et al. 2000) as template. The PSCz sample is not only ideal for our purposes in that it covers one of the largest volumes of the Universe amongst the available galaxy redshift surveys, but also in that it concerns a survey covering a large fraction of the sky and involves a well-defined uniformity of selection. Assuming that on large linear scales IRAS galaxies define an unbiased tracer of the underlying dark matter, Hamilton et al. (2000) found that its real-space power spectrum is consistent with that of a COBE-normalized, untilted, flat ΛCDM model with $\Omega_m = 0.3$ and $\Omega_\Lambda = 0.7$. In Table 2.2 we have listed the main characteristics of all mock catalogs used in this work.

In constructing the mock galaxy samples the simulation particles were selected randomly, exclusively according to the catalog selection criteria. We did not attempt to include *bias* descriptions to model possibly relevant differences in the spatial distribution of dark matter and galaxies. This is different from the original use of the simulations (Cole et al. 1997), in which various bias descriptions were invoked to construct artificial galaxy samples whose two-point correlation function and large-scale power spectrum largely matched that of the APM survey (Maddox et al. 1996). The analysis of the small-scale nonlinear power spectrum of the PSCz by Hamilton & Tegmark (2002) even implies the bias on small scales to be very complex, involving a scale-dependent galaxy-to-mass bias. We, however, prefer not to include an extra level of modelling prescriptions. Our interest concerns the kinematics and dynamics of the matter distribution in the Local Universe, and the velocities of galaxies are thought to reflect these almost perfectly: they are mere probes moving along with the underlying dark matter flows, irrespective of their particular bias relation with respect to the dark matter distribution. The sole strict assumption is therefore that of having no velocity bias (Carlberg et al. 1990), which on the large-scale Megaparsec scales at hand should be a more than reasonable approximation.

2.5.2.1 Mock NBG catalogs

The mock NBG catalogs are obtained by extracting spherical volumes of 30 h^{-1}Mpc from the N-body simulation particle distribution. The positions of the spheres in the parent simulations are not

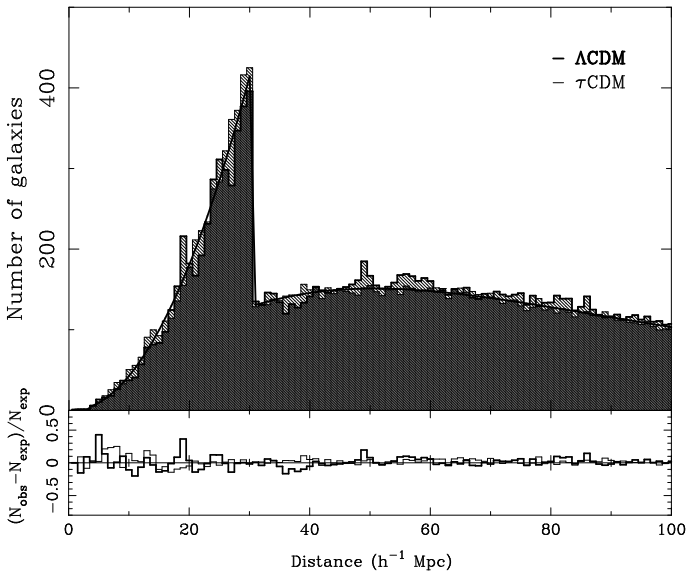

Figure 2.4 — Object counts as a function of distance in the PSC*z* mock catalogs. Upper panel: the two histograms show the average counts in the mock samples for the τCDM and ΛCDM cosmological models. The continuous line represents the expected counts. Lower panel: the histograms show the fractional difference between the observed and expected counts averaged over all PSC*z* mock samples in the two cosmological models explored.

random but chosen to mimic as close as possible the characteristics of a Local Group look-alike region. Therefore, each mock catalog is centered on a particle moving at a speed of 625 ± 25 km s^{-1}, residing in a region in which the shear within 5 h^{-1}Mpc is smaller than 200 km s^{-1}, where the fractional overdensity measured within the same region ranges between -0.2 and 1.0.

The velocity vector of the central particles defines a Galactic coordinate system and a Zone of Avoidance. Particles within the Zone of Avoidance are removed and substituted with a population of synthetic objects distributed using a random-cloning technique (Branchini et al. 1999). The Zone of Avoidance [ZA] in the mock samples is designed to mimic that of the PSC*z* catalog (Saunders et al. 2000) and is smaller than the one of the real NBG catalog (Tully 1988).

Each spherical region contains on average 2×10^4 particles. This set of particles is randomly resampled in order to produce a catalog of around 2800 objects, a number that matches that of the galaxies in the real NBG catalog (Table 2.2). These NBG mimicking mock catalogs define *volume-limited* galaxy samples, so that the number of objects within a distance x therefore increases as x^3. This is indeed what the resulting realizations yield, as may be discerned from the central part of the corresponding histogram in Figure 2.4 ($x \leq 30$ h^{-1}Mpc).

2.5.2.2 Mock PSC*z* catalogs

The second set of mock catalogs was obtained by carving out spherical regions of radius 100 h^{-1}Mpc from the N-body simulations. Each of these new mock samples is centered on the same central position as that of corresponding NBG mock catalogs, with which they share the objects within the central 30 h^{-1}Mpc.

While the central 30 h^{-1}Mpc region coincides with the NBG mock sample, the particle distribution in the external region (30 h^{-1}Mpc $< x <$ 100 h^{-1}Mpc) is supposed to mimic that of galaxies in the *flux-limited* IRAS PSC*z* catalog. To achieve this the objects beyond 30 h^{-1}Mpc were selected from the

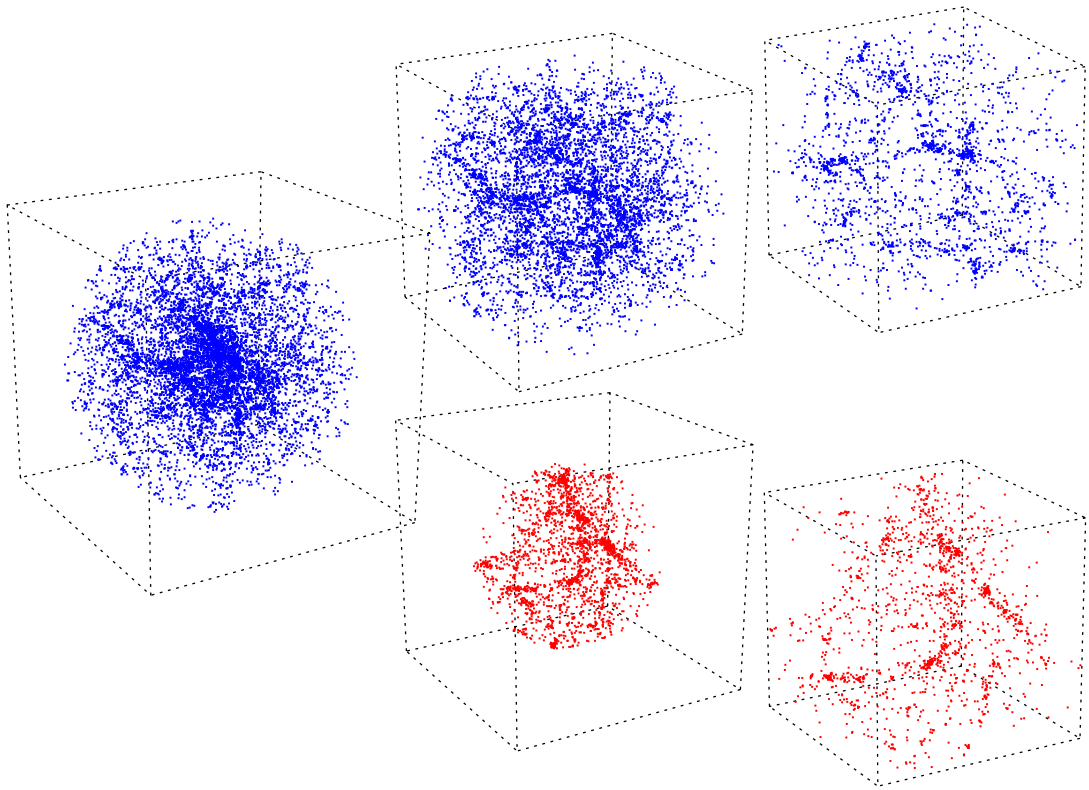

Figure 2.5 — Compilation of cubic subregions and various mock subsamples of the object distribution in one of the ΛCDM PSCz mock catalogs. The full mock catalog of objects, the PSCz look-alike volume and the NBG look-alike volume out to a radius of 100 h^{-1}Mpc, is shown in the large lefthand cubic box (with size 200 h^{-1}Mpc). The boxes along the top row and those along the bottom row represent mutually exclusive object samples. The lower ones represents the inner cosmic region ($x < 30\ h^{-1}$Mpc)), the top row represent a corresponding part of the exterior PSCz region (30 h^{-1}Mpc $< x <$ 100 h^{-1}Mpc). Emanating from the complete cubic volume and running along the top row are two successive boxes which zoom in on the external PSCz mock catalog objects, with cubic sizes of 160 h^{-1}Mpc (middle right cube) and 80 h^{-1}Mpc (lower right cube) respectively. The lower row of two cubic volumes the central (inner) NBG mimicking object sample. The full inner sample, comprising a sphere of radius 30 h^{-1}Mpc is shown in the lower central cubic volume, whose size of 80 h^{-1}Mpc is equal to the central PSCz box, while the righthand cube focusses in on the 40 h^{-1}Mpc size central region.

N-body particle samples according to the PSCz selection function used by Branchini et al. (1999):

$$\psi(x) = Ax^{-2\alpha}\left(1 + \frac{x^2}{x_*^2}\right)^{-\beta} \quad \text{if } x > x_s\ . \tag{2.19}$$

In this expression x is the distance of the galaxy in h^{-1}Mpc, while the parameters have the values $\alpha = 0.53$, $\beta = 1.8$, $x_s = 10.9\ h^{-1}$Mpc, and $x_* = 84\ h^{-1}$Mpc (Branchini et al. 1999). The selection function $\psi(x)$ defines the relative *number* density of the galaxy sample with respect to the *number* density of the N-body particle simulation. While the number density of PSCz galaxies is equal to that of the particles in the simulation at 10.9 h^{-1}Mpc, the amplitude A of $\psi(x)$ is normalized such that $\psi(10.9) = 1$.

Two additional steps concern the treatment of "Zone of Avoidance" objects and the evening of the matter density throughout the full external sample volume. A first step is the processing of sampled objects in the Zone of Avoidance such that the resulting sample conforms to a reality resembling situation. The ZA "removal+substitution" is implemented in the same way as in the case of the NBG

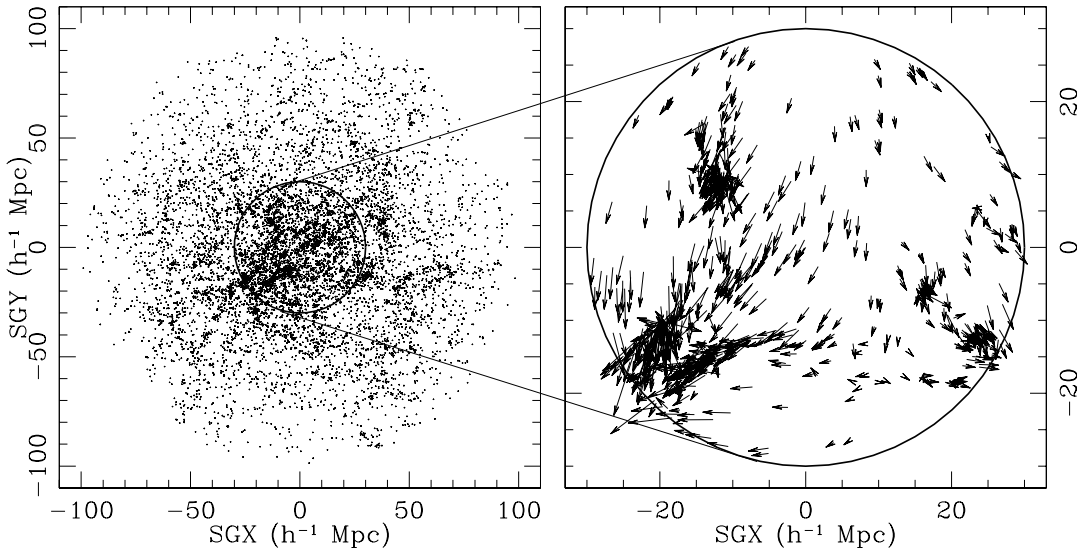

Figure 2.6 — 2D projection of the particle distribution in one of the ΛCDM PSCz mock catalogs (left panel). The inner circle divides the NBG look-alike volume-limited region from the PSCz flux-limited one. The right panel shows the 2D projected velocities in a slice of 10 h^{-1}Mpc cut through the inner part of the catalog.

mock catalog construction, with the replacement achieved with the same random-cloning technique. Finally, in order to guarantee a uniform average *mass* density throughout the volume, the mass of the objects in the *flux-limited* external object sample (30 h^{-1}Mpc $< x <$ 100 h^{-1}Mpc) has been scaled by the inverse of the selection function $\psi(x)$.

2.5.2.3 Mock catalog realizations

From both Figure 2.5 and Figure 2.6 one can obtain an impression of the spatial context of the local NBG mock sample within the wider environment of the surrounding 100 h^{-1}Mpc PSCz sample. To visually appreciate the selection criteria of the catalogs, and their interrelationship, Figure 2.5 shows a three-dimensional view of one set of the ΛCDM mock catalogs, extracted from the particle distribution in the N-body simulation of structure formation in a ΛCDM scenario. Emanating from the full PSCz + NBG mimicking galaxy samples in the top righthand cube is a row of two cubes showing the content of the external PSCz mock catalog (righthand) and the content of the central NBG mock catalog (left-hand). Figure 2.6 elaborates on this, and shows the projected particle distribution in the same PSCz + NBG mock catalog (left panel) while focussing in on the central region (right panel). The circle (left panel) indicates the boundary of the volume-limited region comprised by the mock NBG galaxy sample, which in the right panel has been enlarged to show the corresponding velocity field within this NBG region. Velocities of objects within a 10 h^{-1}Mpc thick slice are shown by means of arrows whose size is proportional to the amplitude of the galaxy velocity components within this slice.

As a matter of test, we checked the distance distribution of the resulting mock galaxy samples. The histograms of the resulting mock catalog distributions are shown in Figure 2.4. The upper part of Figure 2.4 shows the number of galaxies – averaged over all PSCz mock catalogs for both two cosmological models – as a function of distance x over the full range $x \leq 100\ h^{-1}$Mpc. Clearly visible is the discontinuity at 30 h^{-1}Mpc, marking the transition from volume-limited NBG-like region to the PSCz-like flux-limited outer region. For comparison, the solid line shows the theoretically expected counts (Eqn. 2.19). The generated mock samples appear to match the expected distance distribution rather well. This is further underlined by the fractional difference between observed and expected counts, $N_{obs}/N_{exp} - 1$, shown in the lower part of Figure 2.4. The fractional difference between mock

samples displays a perfect featureless scatter pattern: Poisson noise free of systematic effects.

2.5.3 Mock Catalog Analysis

2.5.3.1 FAM velocity field reconstructions

On the basis of the FAM reconstructions of the galaxy velocities and the comparison with the true velocities – i.e. those in the original N-body simulation – we assess to what extent the matter distribution within the confines of each different mock galaxy sample does contribute to the total velocity of the galaxies. In these idealized circumstances of the N-body world the galaxy positions and velocities are known to perfect accuracy, thus circumventing the need to investigate the effects of measurement errors and deceptive systematic biases in the galaxy peculiar velocities. This should provide us with a better understanding of the nature and magnitude of genuine physical influences.

Three different velocities are accorded to each galaxy located within the "local" spherically shaped 30 h^{-1}Mpc NBG region. The first velocity is that of the "true", N-body, velocity. For each of the in total 20 NBG mimicking galaxy mock catalogs, the FAM reconstructions produce two additional velocity estimates. One FAM velocity results from the application of the FAM analysis to the restricted inner 30 h^{-1}Mpc NBG-like region itself. The second FAM based velocity is obtained on the basis of the FAM analysis on the extended, "full", 100 h^{-1}Mpc PSCz survey resembling sample (in which the "local" NBG sample occupies the interior central region). In the following, we will indicate these FAM velocities by the names of FAM_{30} and FAM_{100} velocities.

2.5.3.2 FAM_{30} versus FAM_{100} reconstructions

The mutual comparison between each of the three different galaxy velocities – the FAM_{30}, the FAM_{100} and the full N-body velocities – is expected to yield abundant information on the dynamics and development of the structure in the interior 30 h^{-1}Mpc region.

The FAM_{30} velocities are the galaxy velocities which would have been the product of the combined gravitational interaction of – solely – the matter concentrations within the central 30 h^{-1}Mpc volume. Any deficiency with respect to the "real" N-body velocity of each galaxy has to be ascribed to the gravitational impact of matter inhomogeneities outside the local NBG region.

By tracing the mass distribution further out to a distance of 100 h^{-1}Mpc, invoking the matter distribution in the complete PSCz mimicking mock samples, we will then evaluate the extent to which matter inhomogeneities within a 100 h^{-1}Mpc scale are able to account for the motions within the local 30 h^{-1}Mpc region. From this we can infer in how far the external influence over the local region can be ascribed to matter fluctuations situated between a radius of 30 h^{-1}Mpc and 100 h^{-1}Mpc.

In this study we also have to take into account the fact that a single 30 h^{-1}Mpc region cannot be considered representative for the whole Universe, and generic conclusions on the basis of the kinematics within a single 30 h^{-1}Mpc volume cannot be drawn. This is also true for the the NBG mock samples in this work, even though they were selected according to some strict criteria (see Section 2.5.2). Analysis and conclusions will therefore be based on a straightforward average over the 10 different 30 h^{-1}Mpc mock samples which were constructed for each cosmological scenario. The dispersion in the extracted parameter values will provide a reasonable estimate for their significance.

2.5.3.3 Analysis of Reconstructions

The basic product of the FAM reconstructions are velocity maps, in essence a velocity vector at the location of each galaxy in the sample. Our analysis consists of three different but complementary tracks. The first and most straightforward one is the visual inspection of the resulting velocity vector maps. It provides a direct impression of the extent to which a FAM reconstructed field reproduces the true velocities. Also, it will provide a direct impression of a spatial coherence in the differences between true and reconstructed field, which is an incisive way to uncover systematic contributions like e.g. a bulk flow component.

The second examination is a strictly local analysis, a pure point-to-point comparison between the velocities predicted by the FAM reconstructions on the one hand and the "true" N-body velocity of the same object on the other hand. To some extent, the analysis by means of scatter plots is the most direct and objective quantitative comparison between two fields. Various velocity related quantities will be assessed in this fashion. Note that these localized comparisons cannot address the presence of spatial coherence in the cosmic flows (even though they may uncover systematic effects caused by external influences).

Finally, the third track is targeted towards a factual description of the spatial coherence within the velocity fields or, rather, in the residual fields between the "true" velocities and the reconstructed velocities. Systematic trends in these residual fields are interpreted as manifestations of external forces. Of these we shall determine the first-order – bulk flow – and second order – velocity shear – components.

2.6 FAM velocity vector maps

For reasons of consistency and to achieve optimal transparency the illustrated velocity vector maps in the following discussion all concern the same mock sample of NBG calculations. For the illustration of the FAM_{30} (Fig. 2.7) and the FAM_{100} (Fig. 2.8) reconstructions we use one of the ΛCDM 30 h^{-1}Mpc NBG mock catalogs. It is the same galaxy sample that was shown in 3-D in Fig. 2.5 and in projection along the "x-y" plane in Fig. 2.6.

The vector maps in Figure 2.7 and Fig. 2.8 depict the projections of the raw unsmoothed galaxy velocities, for galaxies within a central slice of 10 h^{-1}Mpc. The size of the arrows is proportional to the amplitude of the peculiar velocity component within this slice, each arrow starting at the location of the galaxy. Both figures consist of three successive rows. The velocity maps in the first row correspond to the "real" world of the N-body simulation. The second row depicts the velocity maps for the FAM reconstructions, the FAM_{30} reconstruction in Fig. 2.7 and the FAM_{100} reconstruction in Fig. 2.8. The last row shows the resulting residual velocity vector fields,

$$\mathbf{v}_{\mathrm{res}} \equiv \mathbf{v}_{\mathrm{FAM}} - \mathbf{v}_{\mathrm{Nbody}}\,, \tag{2.20}$$

the vector difference between the N-body velocities and the corresponding FAM velocity reconstructions, [N-body - FAM_{30}] and [N-body - FAM_{100}].

Each row has three panels, containing the vector maps in the three mutually perpendicular "central" slices. Each plane is identified by means of the index combination "x-y", "x-z" or "y-z" (top figure), the index pair identifying the horizontal and vertical axis along which the panel is seen. Imagining these three planes passing through the centre of the 30 h^{-1}Mpc NBG volume provides a spatial impression of the full 3-D velocity field. Note that here the choice of Cartesian coordinate system does not have any special significance, arbitrarily set by the axes of the total 345.6 h^{-1}Mpc simulation box (the "fundamental" box) from which the mock catalogs were distilled. This is unlike vector maps (e.g. Fig. 2.12) in some later sections.

2.6.1 N-body sample: The "observed" velocities

The velocity vectors in the top row vector maps depict the "real" N-body velocities of the "galaxies" located within the three "central" slices (the same for Fig. 2.7 and Fig. 2.8). The galaxy distribution is characterized by a few dense, massive and virialized clumps, visible as high concentrations of large and randomly directed velocity vectors. The truely massive concentration visible in the lower left of the $x-y$ panel is part of a superstructure extending beyond the boundaries of the NBG region. It represents a major and dominant source for the motions in this area. This may be appreciated from the observed velocity flow towards this clump and the overall distortion of the flow in its vicinity. The large configuration visible in the "y-z" slice contains several dense compact regions embedded in a ridge-like structure running curvedly from the lower right-hand corner to a location slightly left from

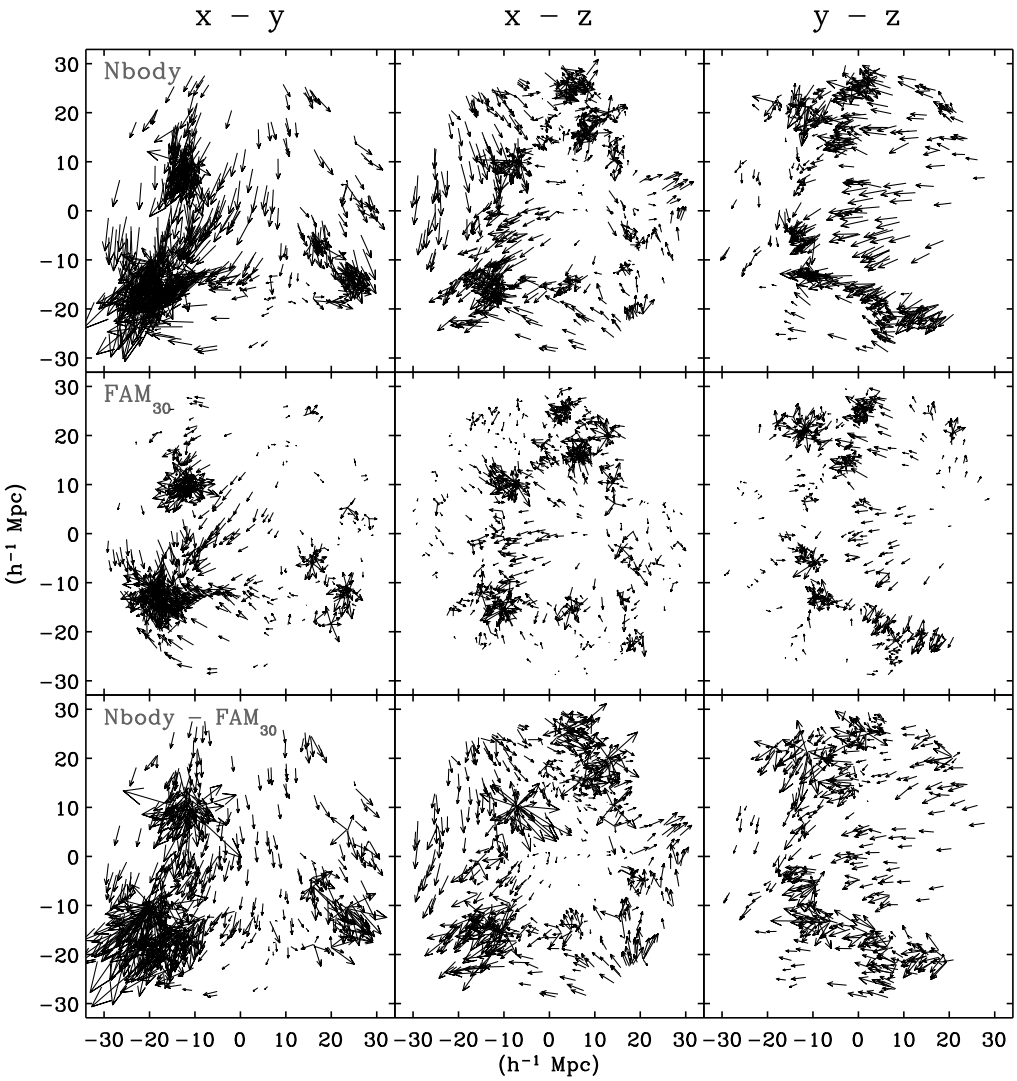

Figure 2.7 — 2D projected, unsmoothed velocities at each particles position in one of the NBG-ΛCDM mock catalogs. Each row contains three frames, corresponding to the central $y-z$, $x-z$ and $x-y$ plane through the point sample. Bottom row: projected N-body velocities. Central row: projected FAM_{30} velocities. Bottom row: residual N-body-FAM_{30} velocities.

the centre. At least partially related to this mass concentration in and around the ridge is the bulk flow along the right-to-left direction.

Overall, the "x-y" and "y-z" vector maps indicate the presence of a dominant coherent "bulk flow" pattern which can be traced throughout the whole NBG volume. By coincidence, the orientation of the coordinate axes is such that the direction of the bulk flow is almost perfectly aligned along the "y"-axis: for this particular mock sample the "y"-axis does represent a physically significant direction defined by the streaming pattern itself. The bulk flow seems to be directed towards some (fictitious) point outside the local 30 h^{-1}Mpc region.

A dominant and conspicuous coherent flow pattern also characterizes the "x-z" velocity vector map. While the flow in the two other planes seems to be almost exclusively dominated by a bulk flow, here the pattern has a more complex geometry, readily recognizable as a typical "velocity shear" pattern. The specific shearing motion in this plane consists of a compressional component along the top

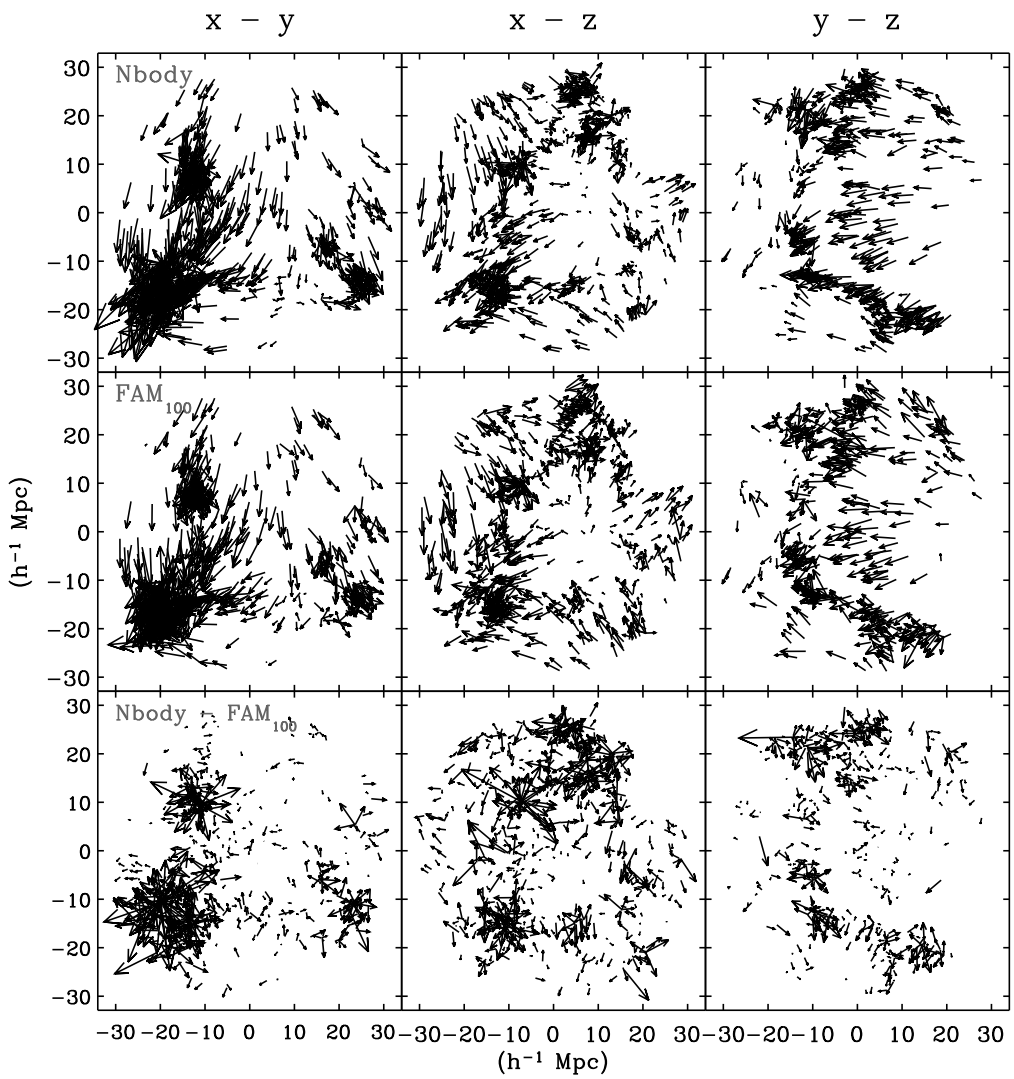

Figure 2.8 — Same as Fig. 2.7, for the PSCz based FAM_{100} reconstructions. Shown are the 2D projected, unsmoothed velocities at each particles position in the central NBG mimicking volume of the full PSCz-ΛCDM mock catalogs, the same region as depicted in Fig. 2.7. Each row contains three frames, corresponding to the central $y-z$, $x-z$ and $x-y$ plane through the point sample. Bottom row: projected N-body velocities. Central row: projected FAM_{100} velocities. Bottom row: residual N-body-FAM_{100} velocities.

left-hand to lower right-hand direction, in combination with a dilational stretch along the perpendicular direction from the lower left-hand towards upper right-hand corner.

2.6.2 NBG samples: FAM_{30} velocity vector maps

The role of the local cosmic matter distribution on the motions in the local Universe is assessed on the based of the "FAM_{30} velocities". They are the peculiar velocities computed by FAM on the basis of the local matter distribution, supposedly reflected by the galaxies within the NBG catalogs. The corresponding reconstructed velocities are shown in the second panel row of Figure 2.7. With their final position as boundary condition, each velocity vector is located at the same galaxy position as in the N-body maps (top row). Note that the vector maps in Figure 2.7 and Figure 2.8, and also the

later ones in Fig. 2.12. Fig. 2.7 and Fig. 2.8, show the pure unsmoothed velocity vectors (and do not "correct" for the virialized regions).

The FAM_{30} velocity maps are distinctly different from the corresponding N-body velocity maps (top row): a coherent flow pattern is almost entirely absent. The FAM_{30} reconstructions obviously did not recover the strong bulk flow observed in the N-body velocity maps, nor the striking shear pattern in the $x-z$ plane. Because the FAM_{30} velocity field reconstructions solely relate to the matter distribution within the inner 30 h^{-1}Mpc NBG region, this indicates that the major share of coherent bulk flow and the velocity shear are due to the matter distribution outside the central 30 h^{-1}Mpc. This is most readily apparent in the velocity residual maps [N-body - FAM_{30}], the difference between the N-body and the FAM_{30} velocity vector fields (bottom row of Fig. 2.7). In the residual field [N-body - FAM_{30}] we recognize the same characteristic flow patterns, strong spatial correlation, long-range coherence and overall morphology as in the full N-body velocity field. This represents convincing evidence for the external origin of the large-scale "bulk" and "shear" component in the local velocity flow.

Prominently visible in the residual velocity field is the strong bulk flow along the "y"-axis. Overall, the spatial pattern of the residual bulk flow appears to reproduce that of the N-body flow field. However, some minor yet significant differences between the residual and the full N-body bulk flow can be discerned. The amplitude of the corresponding velocities in the residual map is somewhat smaller than the equivalent N-body velocities: apparently part of the bulk flow is induced by the local NBG matter distribution. This does not seem to be true for the velocity shear: the shear patterns in the "x-z" plane of the residual and N-body velocity fields are almost identical (except for the virialized motions in high-density clumps). Apparently, the velocity shear component is almost exclusively due to external matter distribution. As a locally flattened matter configuration would induce an internal shear flow, this appears to imply a local matter distribution whose geometry is hardly flattened or elongated.

Closer inspection of the FAM_{30} velocity field provides a more detailed view of the small-scale flow pattern mentioned above. In the "x-y" plane the large-scale (N-body) bulk flow has virtually completely disappeared. Instead, the dominant motion in the "x-y" plane is a streaming flow towards a prominent matter concentration within this region (lower left). On the other hand, in the "y-z" slice a trace of the N-body bulk flow along the "y" axis remains, be it that the corresponding velocities have considerably smaller amplitudes than their N-body counterparts. These local motions appear to be effected by the matter located along the lower ridge, supporting the impression that this feature is a local extension or outlier of the large-scale matter configurations responsible for the full bulk flow. Examination of the panels in Fig. 2.5 and Fig. 2.6 indeed seems to suggest that the density ridge in the lower half of the "y-z" plane is indeed connected to structures just outside the NBG volume, while this perhaps may be true for the massive matter clump in the "x-y" plane too. This may not come as a surprise: the local matter distribution will to some extent be correlated with the external matter configuration so that the locally induced bulk flow is expected to reflect at least partially the full N-body bulk flow.

In summary, the inability of the FAM_{30} reconstruction to recover the large-scale bulk flow and velocity shear is a consequence of the fact that they are a result of the action of the mass distribution on scales larger than the internal 30 h^{-1}Mpc size region while the FAM_{30} velocities are entirely and self-consistently determined by the mass distribution within this interior region. The residual [N-body - FAM_{30}] maps, which are a model for the possible findings of a real-world observational campaign, provide the most elucidating illustration of their "external" origin. Even though they do provide convincing evidence for their external nature, they do not provide sufficient information to infer the identity and nature of the main source of the flow patterns. In principle, however, we may deduce a substantial amount of information on the basis of a careful quantitative analysis: the work by Lilje, Yahil, & Jones (1986) still sets a prime example. To this end, we will investigate the external matter distribution in the PSCz 100 h^{-1}Mpc sized regions.

As a final note, we point to the rather artificial nature of velocity vectors in the vicinity of the massive clump in the "x-y" slice as indicative for the self-consistent nature of the FAM reconstructions. Its location near the edge of the NBG volume even appears to have generated the rather contrived infall motions along the rim of the NBG sphere.

2.6.3 PSC*z* samples: FAM_{100} velocity vector maps

The contribution by the relatively nearby external matter agglomerations, within a distance of 100 h^{-1}Mpc, to the motions in the local Universe is investigated on the basis of the "FAM_{100} velocities". FAM produces these peculiar galaxy velocities on the basis of the galaxy sample in the full mock PSC*z* galaxy sample, extending out to 100 h^{-1}Mpc around the center of our local region. The corresponding reconstructed velocities are shown in the second panel row of Figure 2.8. It is the analogy for the "FAM_{100} velocities" of Figure 2.7, and concerns the same 30 h^{-1}Mpc central region (the NBG region is the central subregion of the PSC*z* mimicking catalog). The FAM_{30} maps showed the dominant influence of externally induced forces on the motions in the local 30 h^{-1}Mpc NBG region: on the basis of the FAM_{100} maps we seek to assess whether the major share of the responsible external matter agglomerations may be identified within the realm of a PSC*z* like volume.

Comparison of the first and the second row of panels in Fig. 2.8 shows the large degree of similarity between the FAM_{100} velocities (panels 2nd row) and the N-body velocities (panels top row). Unlike the FAM_{30} maps in Fig. 2.7 we find that the FAM_{100} maps successfully reproduce most of the large-scale behavior and most of the finer details of the N-body velocity field. The degree of similarity is particularly evident in the corresponding residual velocity field [N-body - FAM_{30}] (bottom row panels). With the exception of the high-density virialized regions the residual velocities are very small and mostly randomly oriented: no significant spatial correlations and spatial coherence can be detected.

The detailed similarity between the N-body and the FAM_{100} maps shows that it is sufficient to take account of the mass distribution out to 100 h^{-1}Mpc for explaining, in considerable detail, the velocity flows in the local NBG volume. Moreover, the detailed rendering of the velocity field by FAM is a convincing demonstration of the capacity of the FAM technique to accurately describe the dynamics implied by the observed local galaxy distribution. The quantitative comparisons in the following sections will provide ample support to this claim.

Of course, the above conclusion is partially related to the realizations of the cosmological scenarios we have studied. The behavior of the power spectrum $P(k)$ on large scales will considerably influence the generality of our findings. A power spectrum with more power on large scales would modify our findings: potentially it may be so that we need a representation of the matter distribution out to larger radii than 100 h^{-1}Mpc. In this respect it is important to note that the used N-body velocity fields do not have any contributions from wavelengths larger than ≈ 175 h^{-1}Mpc (both for τCDM as well as ΛCDM simulations, see Fig. 2.2). This merely for the technical reason of the simulation box imposing an upper limit to the scale on which we can represent $P(k)$. The extent to which this may influence our conclusions may be readily appreciated from Figure 2.2 (right column, top and bottom panel: compare solid lines with dashed ones). The velocity field perturbations of τCDM and ΛCDM carry out considerably further than the fundamental scale of the simulation box, in particularly affecting the resulting bulk flows.

2.7 Point-to-point comparison

Scatter diagrams are used to assess the point-to-point comparisons between quantitative aspects of the "real" galaxy velocities in the original N-body samples and the computed velocities in the FAM_{30} and FAM_{100} reconstructions. This analysis is meant to be a direct, in principal local, assessment of systematic trends in the velocity flows in a volume of the NBG sample. The comparisons involve a component of the "true" N-body velocity (abscissa) versus the equivalent quantity for either the FAM_{30} or FAM_{100} velocities, or of the corresponding residuals (ordinate). Since the objects had been artificially added to the Zone of Avoidance, any particles inside this region (see sec. 2.5.2.2) are excluded from these diagrams.

2.7.1 Systematics

If we neglect the small-scale sources in the deficiencies of FAM reconstructions, the differences between FAM_{30} and FAM_{100} scatter plots are mainly to be ascribed to the corresponding differences in the external gravitational influence acting over the two corresponding sample volumes. In the external gravitational influence the the corresponding leading velocity terms are the bulk flow $\mathrm{v}_{\mathrm{bulk}}$ and the velocity shear s_{ij},

$$\mathrm{v}_{\mathrm{Nbody},i} \approx \mathrm{v}_{\mathrm{FAM},i} + \mathrm{v}_{\mathrm{bulk},i} + \sum_{j=1}^{3} s_{ij} x_j + \dots . \tag{2.21}$$

In the above i, j denotes the Cartesian component indices. The vectors $\hat{x}_j$ represent the vector components along the Cartesian j direction of the spatial unity vector oriented along the object position vector $\mathbf{x}$. Following this definition, $x\hat{x}_j$ is the j-component of the position vector $\mathbf{x}$, with x the distance of the object.

Systematic differences in FAM velocity-N-body velocity scatter diagrams are therefore to be attributed to differences in bulk flow, shear and possibly higher order contributions. Because each of these large-scale phenomena will manifest themselves in distinctly different ways, we seek to identify them from the scatter diagrams. An horizontal offset in the scatter diagram would be the trademark for a bulk flow component. Velocity shear would manifest itself as a distinctly characteristic correlation between residuals and velocities, although the prominence of this signal will be dictated by shear magnitude, configuration, and orientation with respect to the reference system (as is true for the bulk flow). In reality, the situation will be more intricate. Subtle correlations between small-scale and large-scale contributions will bring about a change in the slope of the scatter diagram of FAM reconstructed velocity components against their full N-body values (see 2.7.3.2).

2.7.2 Velocity Scatter Diagrams Analysis

Scatter diagrams are presented in three successive figures. The depicted scatter diagrams all relate to a ΛCDM mock catalogue, and each of these point-to-point analyses relates to a different aspect of the velocity field reconstructions. Figure 2.9 contains four different panels, of which each contains two scatter diagrams: FAM_{30} versus N-body quantity (left) and the equivalent FAM_{100} versus N-body quantity (right). The diagrams in Fig. 2.10 focus on the correlations between these quantities and the scatter around regression relations. The figure addresses three velocity-related quantities, each taking one column of each 2 panels: the top one for the comparison of the FAM_{30} components with their N-body counterparts, and the same for the FAM_{100} components in the bottom frame.

A straightforward comparison is that between the Cartesian velocity components v_i of the FAM reconstructed velocities and the N-body velocities (Fig. 2.10, right-hand column). The choice of the Cartesian reference system is arbitrary and may not form an optimal reflection of the local physical circumstances. Complementary regressions involve coordinate system independent aspects of galaxy velocities. These involve the velocity amplitude $|\mathrm{v}_{\mathrm{FAM}}|$ (Fig. 2.9, top left-hand panel), the component of each FAM velocity parallel to the corresponding N-body velocity, $\mathrm{v}_{\parallel}$ ($\equiv \mathrm{v}_{\mathrm{proj}}$), and the additional perpendicular component $\mathrm{v}_{\perp}$ (Fig. 2.10, first column). Misalignments between the real N-body velocity and the FAM velocity reconstructions should indicate in how far a reconstruction has been failing to take into account all relevant gravitational forces along the path of a particle. Systematic misalignments reveal themselves in the scatter diagram of the angle θ between the FAM velocity and the N-body velocity (in Fig. 2.9 we plot $\mu \equiv \cos(\theta)$, bottom right-hand panel). In terms of the character and systematics of the underlying physics and dynamics the residual velocities, [N-body - FAM], represent highly informative aspects in our analysis. They are assessed in Fig. 2.9 (top right-hand panel) and Figure 2.11.

The significance and strength of correlations between the N-body and FAM velocity components in the scatter diagrams are analyzed by means of a linear regression and correlation analysis. To circumvent excessive pollution of the computed parameters by the virialized motions in high-density

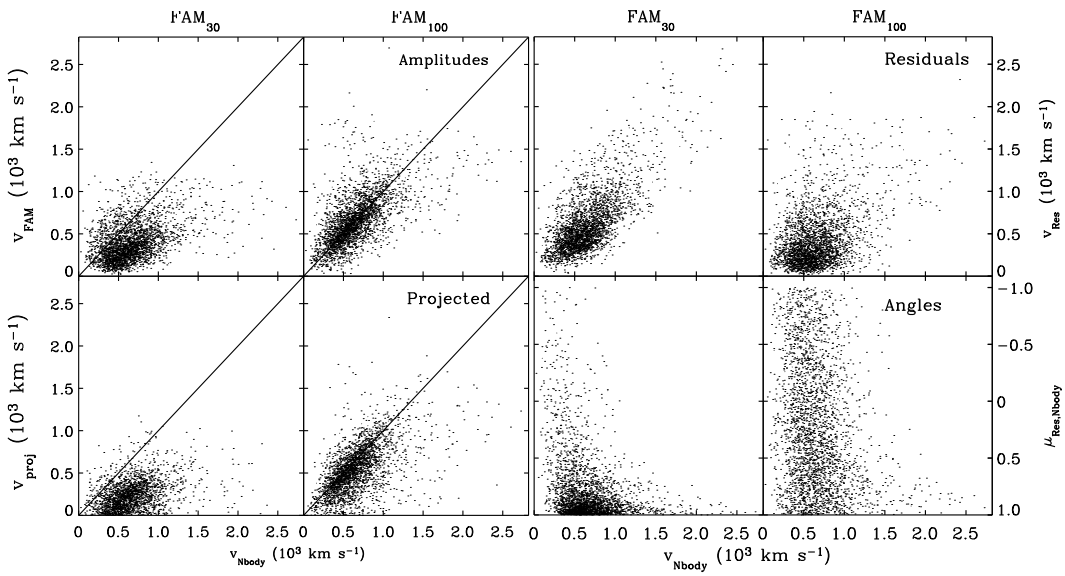

Figure 2.9 — Point-to-point comparison (scatter plot) of four quantities related to FAM reconstructed velocities and the corresponding "real" object velocity in the underlying N-body samples. The N-body realization, and the mock sample, concern the ΛCDM scenario. For each quantity two panels are shown: the lefthand one is the one for FAM_{30} reconstruction, the righthand one for the FAM_{100} reconstruction. Top lefthand: the amplitude of the velocities. Top righthand: residual velocity amplitudes FAM-N-body. Bottom lefthand: FAM velocity component projected along the N-body velocity. Bottom righthand: angle between FAM velocity and N-body velocity, in terms of $\mu = \cos(\theta)$.

regions (see sect. 2.3.3), the galaxy velocity components in these regression analyses involve 2 h^{-1}Mpc tophat filtered velocity fields. The resulting numerical values of the correlation parameters are listed in Table 2.3. This Table is organized in two separate sections, one for the regression analysis results of the ΛCDM mock samples (top section) and a second for the τCDM samples (bottom section). For both the ΛCDM and the τCDM section we list the results for four velocity related quantities, each separately for the FAM_{30} and the FAM_{100} reconstructions.

The presence of significant correlations between FAM reconstructions and their N-body counterparts is evaluated on the basis of the nonparametric Spearman correlation coefficient R_{Spear}. The linear regression parameter R_{lin} quantifies the linearity of the relation. Prevailing in most situations, the linear regression parameters are used to characterize the relation between reconstructed and real N-body velocities: the zero-point (offset) a_0, the slope a_{lrg} and the dispersion σ_{lrg} around the linear regression relation. We assume equal errors in FAM and N-body velocities, as both are affected by similar shot noise errors (while 2 h^{-1}Mpc top hat smoothing significantly reduces the impact of virial motions on FAM velocity predictions). In addition, we also list the rms scatter of the parameters, estimated on the basis of the results for the 10 different mock catalogs (for each of the four different configurations).

2.7.3 Inventory

2.7.3.1 Velocity Amplitude

In the top left-hand frame of Fig. 2.9 the FAM_{30} and FAM_{100} velocity amplitudes are compared with their N-body counterpart $|v_{Nbody}|$. The FAM_{30} diagram differs considerably from the FAM_{100} diagram: the FAM_{30} velocities are systematically smaller than their FAM_{100} counterparts. Also, while the latter have a strong one-to-one correlation to the N-body velocities, the FAM_{30} diagram shows a systematic offset with respect to this relation (the solid line) and a somewhat larger scatter.

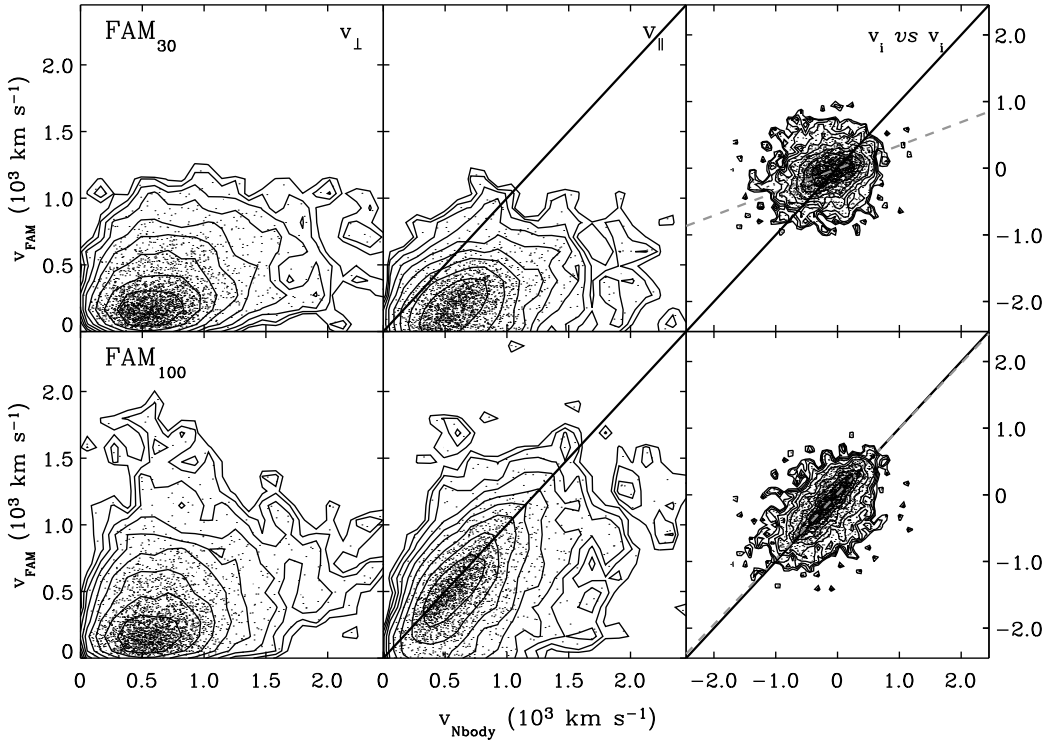

Figure 2.10 — point-to-point comparison of the perpendicular (first column) and parallel (second column) components of the reconstructed FAM_{30} (top-row) and FAM_{100} (lower-row) velocities with respect to the "real" N-body velocities for one ΛCDM mock catalog. The continuous lines represent the one-to-one relation for eye guidance. The third column shows the $N-$body *vs*. FAM velocities for one Cartesian component. The dashed lines represent the best linear fit. The contours are lines of equal point densities.

While the FAM_{100} diagram tapers out to higher velocities and even shows a few points with $|v_{FAM}| > 2000$ km s^{-1}, there is a firm ceiling of $|v_{FAM}| \approx 1300$ km s^{-1} for the FAM_{30} velocities. It is a direct reflection of the FAM_{30} reconstructions *missing out on the gravitational force contributions by the external mass distribution*. The asymmetric nature of the scatter in both diagrams is due to particles in high density regions: the discrepancy between N-body and FAM velocities in these highly virialized regions reflects itself in the substantially higher amplitudes of the corresponding N-body velocities.

To a good approximation, the correlation between the FAM_{100} velocity amplitudes and $|v_{Nbody}|$ is that of a linear identity relation: the solid line, $|v_{Nbody}| = |v_{FAM}|$, forms a good fit to the scatter diagram (see Table 2.3: $a_{lrg} \to 1$). The significantly higher value of Spearman's correlation coefficient (Table 2.3: $R_{Spear} \approx 0.68$ vs. $R_{Spear} \approx 0.54$ for FAM_{30}) indicates and confirms the visual impression of Fig. 2.8) of the tight correspondence between the FAM_{100} and N-body vector velocity fields. The FAM_{30} results stand in marked contrast: the majority of the FAM_{30} velocities have a systematically lower amplitude than their N-body counterparts. It results in a relation with a significantly shallower slope than that of the identity relation $|v_{Nbody}| = |v_{FAM}|$ (also see Table 2.3): objects with a higher velocity have a larger discrepancy. The contribution by the missing large-scale velocity component $\mathbf{v}_{lss}$ to the amplitude of the FAM velocity includes a cross-term $(-\mathbf{v}_{Nbody} \cdot \mathbf{v}_{lss})$, a term dependent on the velocity $\mathbf{v}_{Nbody}$ of the galaxy. Most of the missing large-scale velocity component $\mathbf{v}_{lss}$ is due to the absence of a bulk flow term in the FAM_{30} reconstructions. Subtle and/or higher order external gravitational effects play an additional role: the velocity vector diagrams did already reveal that the

presence of shear should be one of the main contributors (cf. Eqn. 2.21).

When comparing the ΛCDM FAM velocity amplitudes with those of the τCDM reconstructions it is evident that in the case of the FAM_{30} reconstructions the latter adhere considerably better to the corresponding N-body values. The linear fitting slope a_{lrg} (see Table 2.3) is considerably closer to unity for the τCDM samples than for the ΛCDM samples. Over a 30 h^{-1}Mpc volume the external density inhomogeneities in the ΛCDM cosmology will induce considerably higher bulk flows than the more moderate τCDM perturbations, which is entirely in line with the theoretical expectation (fig 2.2). In the case of the FAM_{100} reconstructions the qualitative differences are far less prominent. On the scale of $\sim 100\ h^{-1}$Mpc the mass distribution in both the τCDM and ΛCDM simulation volumes have converged to homogeneity and no major bulk flows are to be expected.

2.7.3.2 Velocity Decompositions

In the two right-hand frames of Fig. 2.10 we show the scatter diagrams for the x-component of the FAM_{30} (top) and FAM_{100} velocities (bottom). Although with a significant level of scatter, the FAM_{100} diagram can be fitted quite well by a straight line with a slope close to unity (linear regression line: dashed, unity line: solid). That the equivalent FAM_{30} diagram may also be fitted by a straight line, be it with a slope significantly smaller than unity is not entirely straightforward. It stems from an intricate interplay between the small scale velocity field and its larger scale contributions, which in most circumstances are not uncorrelated (Berlind et al. 2000).

Table 2.3 lists the linear regression parameters. Although the average best fitting slopes for the FAM_{100} velocities are either larger (τCDM) or smaller (ΛCDM) than unity, the deviation from unity is considerably smaller than that for the FAM_{30} velocities, well within the $\sim 1\sigma$ uncertainty interval. In all, these regression results do adhere to the expected and noted trend of FAM_{100} velocities accounting for practically all contributions to the local velocity field and FAM_{30} velocities systematically neglecting significant external contributions. Notice that the scatter around the regression lines for the FAM_{30} and FAM_{100} reconstructions is of comparable magnitude (as may be inferred from the superposed number density contours). It indicates the corresponding origin, the failure of FAM to properly account for nonlinear (virial) motions.

While the choice of any Cartesian coordinate system is an arbitrary one we have also adressed the decomposition of the particle velocities in one defined by the system itself. The FAM velocities are decomposed in a component projected along the corresponding N-body velocity, v_{proj} (or $v_{\|}$) and the complementary perpendicular component, $v_{\perp}$. The second column of figure 2.10 contains the scatter diagrams for the parallel component of the FAM_{30} (top) and FAM_{100} (low) velocities. Qualitatively, the behaviour of both diagrams resembles that of the velocity amplitude scatter diagrams in Fig. 2.9. A $1-1$ relation between FAM_{100} velocities and N-body velocity amplitude represents a reasonable fit (solid line: slope $a_{lrg} \approx 0.99$). The FAM_{30} diagram not only appears to deviate strongly from such a $1-1$ relation, it may even fail to fit any linear relation. Also, none of the projected FAM_{30} velocity components appears to supersede a value of ≈ 1200 km s^{-1}. Given the fact that the equivalent FAM_{100} component even surpasses values of ≈ 2000 km s^{-1}, this confirms the systematic deficiency of the gravitational field in the FAM_{30} evaluations.

From the scatter diagrams for the perpendicular FAM velocity components, $v_{\perp}$, one can infer that almost all systematic effects are confined to the parallel components $v_{\|}$. For both FAM_{30} and FAM_{100} the complementary perpendicular component lacks a systematic correlation with the N-body velocity. It mainly represents unrelated scatter, with a magnitude concentrated around values of $\sim 200-250$ km s^{-1}. The only difference between the FAM_{30} and FAM_{100} reconstructions is that for the latter $v_{\perp}$ involves considerably higher values, reflecting the higher amplitude of the FAM_{100} velocities. FAM_{30} velocities, on the other hand, involve stronger misalignments (Section 2.7.3.3).

Cosmology	Component	Set	R_{Spear}	R_{lin}	a_0 (km s^{-1})	a_{lrg}	σ_{lrg} (km s^{-1})
	$\|v\|$	FAM_{30}	0.54 ± 0.11	0.56 ± 0.11	-29.43 $\pm$ 84.28	0.66 ± 0.21	198 $\pm$ 73
		FAM_{100}	0.68 ± 0.12	0.62 ± 0.16	83.38 $\pm$ 156.39	0.85 ± 0.26	212 $\pm$ 89
ΛCDM	$v_{\|\|}$	FAM_{30}	0.43 ± 0.14	0.37 ± 0.20	-198.21 $\pm$ 173.86	0.65 ± 0.30	251 $\pm$ 114
		FAM_{100}	0.59 ± 0.23	0.52 ± 0.29	-135.98 $\pm$ 242.78	0.99 ± 0.40	281 $\pm$ 158
	v_i	FAM_{30}	0.54 ± 0.20	0.48 ± 0.29	19.35 $\pm$ 140.90	0.66 ± 0.25	240 $\pm$ 130
		FAM_{100}	0.71 ± 0.27	0.61 ± 0.31	5.96 $\pm$ 78.94	0.86 ± 0.23	233 $\pm$ 107
	$v_{res,i}$	FAM_{30}	0.65 ± 0.11	0.66 ± 0.11			
		FAM_{100}	0.40 ± 0.14	0.47 ± 0.19			
	$\|v\|$	FAM_{30}	0.56 ± 0.05	0.59 ± 0.05	-54.10 $\pm$ 67.09	0.84 ± 0.18	203 $\pm$ 57
		FAM_{100}	0.66 ± 0.10	0.59 ± 0.13	-146.58 $\pm$ 140.40	1.34 ± 0.26	289 $\pm$ 80
τCDM	$v_{\|\|}$	FAM_{30}	0.52 ± 0.09	0.48 ± 0.15	-313.16 $\pm$ 134.10	1.04 ± 0.24	272 $\pm$ 100
		FAM_{100}	0.63 ± 0.14	0.55 ± 0.19	-430.59 $\pm$ 302.29	1.60 ± 0.46	360 $\pm$ 171
	v_i	FAM_{30}	0.68 ± 0.13	0.63 ± 0.15	-4.75 $\pm$ 107.95	0.80 ± 0.19	221 $\pm$ 81
		FAM_{100}	0.79 ± 0.17	0.69 ± 0.13	27.60 $\pm$ 70.70	1.12 ± 0.11	255 $\pm$ 87
	$v_{res,i}$	FAM_{30}	0.55 ± 0.15	0.57 ± 0.13			
		FAM_{100}	0.22 ± 0.13	0.27 ± 0.14			

Table 2.3 — Results of the linear regressions in the tests with the mock catalogs. Col. 1: Cosmological model. Col. 2: Component Col. 3: label of the set. Col. 4: average Spearman correlation coefficient of the point distribution and its 1σ scatter. Col. 5: average correlation index of the best fitting line and its 1σ scatter. Col. 6: average zero point of the best fitting line and its 1σ scatter. Col. 7: average slope of the best fitting line and its 1σ scatter. Col. 8: average dispersion around the fit and its 1σ scatter.

2.7.3.3 Velocity Alignments

Misalignments between the reconstructed FAM velocities and the N-body velocity vectors are the result of a few effects. A major source is that of localized small-scale effects. These are not expected to lead to systematic offsets: they will have a *noisy* character and reflect random motions in highly nonlinear environments, in particular those of dense virialized regions. Because these have no preferred direction, they behave like randomly oriented "residual" velocities wrt. to the real N-body velocities of galaxies. Of an entirely different nature are misalignments stemming from the systematic neglect of the external gravitational forces. Because the resulting residual velocity vectors comprise systematic components along one or a few preferred directions, a distinctly anisotropic distribution is the result. This reflect itself as a systematic trend for total N-body galaxy velocities to be aligned along the residual velocity components.

For both the FAM_{30} and FAM_{100} reconstructions we computed the angles between the N-body velocity vector and the FAM velocities. The lower righthand panel in Figure 2.9 confirms that the alignments of "residuals" and total velocity is indeed considerably stronger for the FAM_{30} reconstructions than the FAM_{100} ones. The figure plots, for each galaxy in the sample, the misalignment angle θ (or, rather, $\mu = \cos(\theta)$) versus the N-body velocity magnitude $\mathrm{v}_{\mathrm{Nbody}}$. For the FAM_{100} velocities we see a near isotropic distribution of angles. With the exception of a minor concentration near perfect alignment, $\cos(\theta) = 1$, the distribution is sweeping out nearly uniformly over the full range of $\mu \equiv \cos(\theta) = 1 \rightarrow -1$. If at all there is a trend in velocity amplitude, it appears to be the weak tendency for large velocities to be better aligned.

The above results reflect the observation that FAM_{100} residual velocities do mainly consist of small-scale random effects. The FAM_{30} residuals form a telling contrast. They are heavily aligned along the full N-body velocities, with a very strong concentration near $\theta = 0$. Although occasionally there are serious misalignments, their occurrence diminishes rapidly towards large θ. When they occur it almost exclusively concerns small velocities, mostly corresponding to serious misalignments between the locally induced velocity and the added external velocity component.

2.7.3.4 Velocity Residuals

The residuals accumulate all systematic physical effects as well as random artefacts which the FAM procedure does not (properly) take into account. They are therefore an excellent source of information on the dynamical role of matter concentrations in the various galaxy sample volumes. If there are large external contributions to the galaxies' velocity these will constitute a major part of the residuals. On the other hand, if most of those influences are contained within the sample volume treated by FAM, the residuals may mainly reflect localized nonlinearities and artefacts of the FAM method. Scatter diagrams involving the residual velocities will indicate systematic trends and are well suited for elucidating the character and underlying dynamics of external influences.

Figure 2.11 elaborates on this observation. In two successive rows, the top one for the FAM_{30} reconstructions and the bottom one for the FAM_{100} reconstructions, it displays the residuals $\mathbf{v}_{res}$ for each of the three Cartesian velocity components, v_x, v_y and v_z. Each panel plots the velocity component residual as a function of the corresponding N-body velocity component.

The mark of a bulk velocity is a constant offset of the scatter diagram, a translation of all FAM velocities by a constant term. This is indeed what is observed in the FAM_{30} v_y scatter diagram: the vast majority of points is located beneath the $\mathrm{v}_y = 0$ km s^{-1} Mpc^{-1} line. It is a telling confirmation of the impression yielded by the corresponding velocity vector fields in Fig. 2.7. The velocity vector field revealed the presence of strong bulk flow oriented almost perfectly along the y-axis: clearly visible in the N-body velocity field, hardly present in the corresponding FAM_{30} velocity field, and representing a major component of the residual field [N-body - FAM_{30}]. When turning to the equivalent FAM_{100} diagram, the indicative offset for a bulk flow has almost completely disappeared. This implies that the source(s) for the bulk flow should be found within the region between 30 h^{-1}Mpc and 100 h^{-1}Mpc. The equivalent v_x and v_z FAM_{30} residual scatter diagrams do confirm the visual impression of there hardly being a bulk flow contribution along the x- and y-directions.

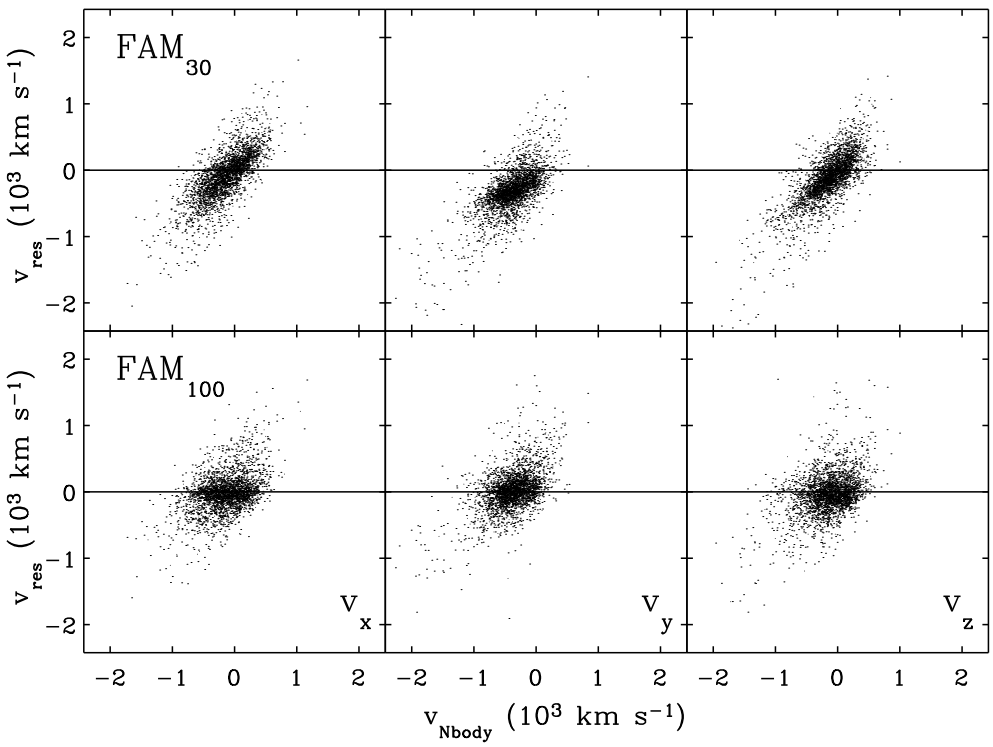

Figure 2.11 — point-to-point comparison (scatter plot) of the Cartesian components of the residual velocity $\mathbf{v}_{FAM} - \mathbf{v}_{N-body}$ components against corresponding N-body velocity $\mathbf{v}_{N-body}$. From left to right: v_x, v_y and v_z. Top row: FAM_{30} reconstructed velocity. Bottom row: FAM_{100} reconstructed velocity.

Additional systematic behavior is readily apparent in Fig. 2.11: the diagrams show an almost linear increase of residual velocity with N-body velocity. Also, we find that the v_x scatter is skewed towards negative v_{res} values while the v_z diagram is skewed towards positive v_{res} values. In the equivalent FAM_{100} scatter diagrams the linear increase of v_{res} and the asymmetry in the v_x and v_z diagram has almost disappeared: the dense core of points has turned into a compact and nearly horizontal bar symmetrically distributed around the $\mathrm{v}_{res} = 0$ km s^{-1} line. To a large extent this is explained by the much smaller contribution of external tidal shear to the flows over 100 h^{-1}Mpc volumes (cf. Fig. 2.2).

The mark for external shear is a near linear increase of residual velocities as a function of their N-body (or measured) velocity. Depending on the location $\mathbf{x}$ of a galaxy within the sample volume and with respect to the shear configuration its participation in a shear flow will involve a velocity component $\mathrm{v}_s \equiv \sum s_{ij} x_j$. This may involve a negative or a positive contribution. With such shear contributions representing a non negligible component to the total velocity, its systematic contribution to a largely random local residual signal reshuffles the velocities such that on average the largest velocity involves the largest residual contribution.

With prominent large-scale bulk and shear motions at large, the FAM_{100} residual scatter diagram has largely transformed into a featureless and purely random point distribution. The residuals mainly involve uncorrelated small-scale effects and are nearly independent of the amplitude of the N-body velocity. Some additional artefacts are seen upon closer inspection: the presence of diffuse "S"-shaped point clouds in both the FAM_{30} and FAM_{100} residual diagrams, tapering off towards a steep tail at both the negative and positive side of the plots. Given their presence in the FAM_{100} diagrams, they seem to be manifestations of the nonlinear motions FAM fails to take into account properly.

The corresponding scatter diagrams for the velocity residual amplitudes $|\mathbf{v}_{\mathrm{res}}| = |\mathbf{v}_{\mathrm{FAM}} - \mathbf{v}_{\mathrm{Nbody}}|$

represents a summary of the systematic trends (Fig. 2.10). The FAM_{30} velocity residuals show a near linear increase as a function of the N-body velocity, starting with an offset, indicative of the ingredients of bulk and shear flow in the residuals. The lack of any clear correlation between $|\mathbf{v}_{\mathrm{res}}|$ and $|\mathbf{v}_{\mathrm{Nbody}}|$ in the case of the FAM_{100} residuals confirms the absence of such systematic components. More clearly than in the case of the individual Cartesian components, the presence of local nonlinear motions may be discerned from the extensive surrounding clouds of outliers.

2.7.4 Power Spectrum Dependence

The contrast between FAM_{30} and FAM_{100} scatter diagrams is more pronounced in the case of the ΛCDM mock catalogs than in those assembled for the τCDM universes. This clearly reflects the fact that within the ΛCDM scenario cosmic structure is characterized by a larger coherence scale. It implies the presence of larger and more coherent structures whose size exceeds 30 h^{-1}Mpc. Their combined gravitation impact will yield a stronger systematic impact in the velocity-velocity comparisons. On the other hand, the dispersions listed in table 3 also show that it would hardly be possible to infer information on the cosmological scenario on the basis of one individual realization. The large dispersion around the average slopes, in particular in the case of the ΛCDM Universe, show that the magnitude of the external dynamical effects may vary appreciably as a function of the location of the (mock) NBG sample within the simulation box. Local measurements will therefore be unable to separate cosmological effects from those stemming from local variations.

2.7.5 Nonlinearities

The point-to-point diagrams discussed above all contain a substantial level of scatter around the inferred regression relations. With a few exceptions the scatter of velocity quantities is in the order of $\sim 200-250$ km s^{-1}, for both the ΛCDM as well as the τCDM FAM reconstructions. The main source for this scatter are the virial motions in the high density and mildly nonlinear environments. Also shot noise provides a substantial additional contribution. In the case of small filter radii, another source of scatter is formed by spurious very close pairs of points in the parent N-body catalog which for artificial reasons failed to collapse into a single object (Branchini et al. 2002). Scatter may also be due to higher order multipole components in the external gravity field. An inspection of the particle configurations and the velocity vector maps does unmistakably show significant systematic variations on top of dipolar and quadrupolar components. However, tests restricting the analysis to points in the central regions of the sample produced no substantial decrease in level of scatter. This seems to argue for a minor role of such contributions.

2.8 Bulk Flow and Tidal Shear: Velocity Flow Multipole Components

In the previous sections we have found that in order to obtain a good representation of the local cosmic velocity field it is necessary to take into account the external gravitational influence. This was accomplished through the incorporation of the fully detailed external mass distribution contained in the (flux-limited) galaxy catalogs. This involved the galaxy distribution out to distances of 100 h^{-1}Mpc. The reconstructions showed that modelling of velocity fields by FAM with the inclusion of matter concentrations on such large scales is indeed rewarding.

In nearly all situations where the local volume V_{int} is suitably large, the small-scale details of the external mass configuration are rather irrelevant for constructing an appropriate model of the flows in the local Universe. An appropriate approximate expression for the the gravitational potential $\Phi_{ext}(\mathbf{r})$ inside the internal volume V_{int} due to the surrounding external matter distribution follows from its expansion in multipole contributions. Assuming a spherical local volume with radius R_{int}, the potential

Φ_{ext} may be written in terms of a multipole expansion of spherical harmonics $Y_{lm}(\theta,\phi)$ (see e.g. Jackson 1975)

$$\begin{aligned}\Phi_{ext}(\mathbf{x}) &= -\int_{R_{int}}^{\infty} \frac{G\rho(\mathbf{x}')}{|\mathbf{x}-\mathbf{x}'|}\,\mathrm{d}\mathbf{x}' \\ &= -\sum_{l=0}^{\infty}\sum_{m=-l}^{m=l} \frac{4\pi G}{2l+1} Q_{lm}\, Y_{lm}(\theta,\phi)\, r^l\,,\end{aligned} \tag{2.22}$$

in which the *multipole moments* Q_{lm} relate to the external density field $\rho(\mathbf{x}')$ as

$$Q_{lm} = \int_r^{\infty} \rho(\mathbf{x}')\, r'^{l-3}\, Y^*_{lm}(\theta',\phi')\,\mathrm{d}\mathbf{x}'\,. \tag{2.23}$$

Most contributions to the external gravity $\mathbf{g}_{ext}$ will be confined to these dipole and quadrupole components, induced by the corresponding large-scale constellations in which the surrounding matter concentrations have grouped themselves. Here we will assess the approximation in which the potential expansion (Eqn. 2.23) is restricted to the monopole term $l = 0$, the dipole term $l = 1$ and the quadrupole term $l = 2$,

$$\Phi_{ext}(\mathbf{x}) \approx \Phi_0(\mathbf{x}) + \Phi_1(\mathbf{x}) + \Phi_2(\mathbf{x})$$

with

$$\Phi_l(\mathbf{x}) = -\sum_{m=-l}^{m=l} \frac{4\pi G}{2l+1} Q_{lm}\, Y_{lm}(\theta,\phi)\, x^l\,. \tag{2.24}$$

To explore the nature of the external component in the total gravitational field in the Local Universe we proceed by probing it through the resulting peculiar velocity field. The amplitude of higher order terms may be assumed to be so small that one cannot expect to deduce any significant value, given the sizeable errors in the available galaxy peculiar velocity datasets, we may expect this to be a reasonable approximation. We investigate the velocity field by decomposing the residual velocity field – i.e. the component in the velocity field which could not be accounted for in the FAM_{30} reconstruction and supposedly induced by external influences – into its multipole components. Once we have determined the bulk flow component and shear tensor components in the tidal velocity field, we will assess whether we can indeed relate this to the external gravitational ("tidal") influence within the local Universe.

Restricting the description of the external gravitational influence to the first few orders of its multipole expansion has several advantages. The large-scale external dipole and quadrupole gravity perturbations retain a largely linear character, simplifying the velocity field analysis and thus retaining the direct linear relation between gravity and velocity field. Also, by discarding its small-scale fluctuating contributions a physically more transparent image of the velocity field is obtained. This allows a straightforward relation and translation towards the corresponding large-scale pattern of the surrounding mass distribution. A final practical issue of some importance is the fact that the dipole and quadrupole characterization is particularly suited for an implementation in FAM. Restricting the external force field to these moments alleviates the need to take into account a large sample of external galaxies. Not only is the latter computationally expensive, in practice it is even not always feasible.

2.8.1 Velocity Field Multipole Decomposition

In the multipole analysis we restrict ourselves to the externally induced velocity components, $\mathbf{v}_{ext}$, which in the following we frequently designate by the term *"tidal"*[1]. For each object, the *"tidal"* velocity vector is determined by subtracting the internally induced velocity field, $\mathbf{v}_{int}$, from the object's full velocity. The latter is usually the N-body velocity of the mock galaxy, although we will assess

[1] in the following we regularly use the word *"tidal"* to shortly indicate the externally induced component of a gravity or velocity field. As it includes a dipolar contribution, strictly speaking this is not an appropriate term. Also see sect. 2.3.5.2.

the possibility of using the FAM_{100} velocity as a reasonable alternative. The internal velocity $\mathbf{v}_{int}$ is deduced by evaluating, through our FAM computations, the impact of the internal matter distribution within the internal catalog volume V_{int}. The resulting (residual) peculiar velocity vector $\mathbf{v}_{ext}$ field may then be expressed in terms of a Taylor series description as function of spatial position $\mathbf{x}$.

For the practical implementation, we follow the general scheme described by Kaiser (1991). The velocity field Taylor expansion is truncated at the quadratic term and is restricted to the dipole and quadrupole moments (and a minor monopole term). The *tidal* velocity field $\mathbf{v}_{ext}$, is then modeled by the the first two components, a bulk flow vector, $\tilde{u}_i$, and a quadratic shear tensor contribution, $\tilde{s}_{ij}$,

$$\mathrm{v}_{ext,i} = \tilde{u}_i + \tilde{s}_{ij} x \hat{x}_j, \qquad \text{where} \qquad i,j = \{1,2,3\}\,, \tag{2.25}$$

in which i, j denotes the Cartesian component indices. As in Eqn. 2.21, the vectors $\hat{x}_j$ represent the vector components along the Cartesian j direction of the spatial unity vector oriented along the object position vector $\mathbf{x}$. Using these notations, we can easily reconfigure Eqn. 2.25 and express the i-component of the velocity of object n into a product of the vectors $F_{n,I}$ and V_{Ii},

$$\mathrm{v}_{n,i} = \sum_{I=1}^{4} F_{n,I}(\mathbf{x}) V_{Ii}$$

in which the data 4-vector F_I and the velocity field component 4-vector V_{Ii} are defined as

$$\begin{aligned} F_{n,I} &= \{1, x\hat{x}_1, x\hat{x}_2, x\hat{x}_3\} \\ V_{Ii} &= \{\tilde{u}_i, \tilde{s}_{i1}, \tilde{s}_{i2}, \tilde{s}_{i3}\}\,. \end{aligned} \tag{2.26}$$

The "dipolar" bulk flow components $\tilde{u}_i$ and "quadrupolar" velocity shear components $\tilde{s}_{ij}$ can then be obtained by solving for the vectors V_{Ii} on the basis of a fitting analysis (to be precise, $\tilde{s}_{ij}$ also includes a minor residual "monopole" expansion/contraction term). We accomplish this by computing for each Cartesian component i the values for the multipole elements $\tilde{u}_i$ and $\tilde{s}_{ij}$ which minimize χ^2

$$\chi^2 = \sum_{n=1}^{N_{objs}} \left(\mathrm{v}_{n,ext,i} - \sum_I F_{n,I}(\mathbf{x}) V_{Ii} \right)^2\,, \tag{2.27}$$

to be evaluated on the basis of the data sample of N_{obj} objects at locations $\mathbf{x}_n$ and with inferred "external" velocities $\mathbf{v}_{n,ext}$. The bulk flow and velocity shear in the externally induced velocity component $\mathbf{v}_{ext}$, along with a residual expansion term,

$$\mathrm{v}_{ext,i} \approx \mathrm{v}_{exp,i} + \mathrm{v}_{bulk,i} + \mathrm{v}_{shear,i} \tag{2.28}$$

will follow directly from the inferred values of the 4-vector components V_{Ii}:

$$\begin{aligned} \mathrm{v}_{exp,i} &= \frac{1}{3} Tr(\tilde{s})\, x\hat{x}_i \\ \mathrm{v}_{bulk,i} &= \tilde{u}_i\,; \qquad \mathrm{v}_{shear,i} = \sum_{j=1}^{3} \tilde{s}'_{ij} x \hat{x}_j \end{aligned} \tag{2.29}$$

in which $Tr(s)$ is the trace of the tensor s_{ij} and $\tilde{s}'_{ij}$ the traceless shear tensor

$$\begin{aligned} Tr(\tilde{s}) &\equiv \tilde{s}_{11} + \tilde{s}_{22} + \tilde{s}_{33} \\ \tilde{s}'_{ij} &= \tilde{s}_{ij} - \frac{1}{3} Tr(\tilde{s})\, \delta_{ij}\,. \end{aligned} \tag{2.30}$$

Field Configuration	Cosmology	v_{bulk} (km s^{-1})	s	s_1	s_2	s_3	$\nabla \cdot \mathbf{v}$	
FAM_{30}	ΛCDM	313 ± 65	13.3 ± 3.8	8.8 ± 3.6	0.6 ± 2.5	-9.4 ± 2.3	1.6 ± 11.7	(km s^{-1} Mpc^{-1})
	τCDM	216 ± 57	13.6 ± 4.6	8.9 ± 3.1	1.1 ± 2.0	-10.0 ± 3.7	1.0 ± 12.4	
	ΛCDM		399 ± 115	264 ± 107	19 ± 76	-283 ± 70	47 ± 351	(km s^{-1})
	τCDM		409 ± 137	267 ± 92	33 ± 60	-300 ± 110	31 ± 373	
FAM_{100}	ΛCDM	81 ± 51	3.7 ± 1.2	2.6 ± 0.9	-0.2 ± 0.8	-2.4 ± 1.0	-2.2 ± 2.8	(km s^{-1} Mpc^{-1})
	τCDM	121 ± 54	4.8 ± 1.1	3.4 ± 1.0	0.0 ± 0.8	-3.3 ± 0.8	-6.2 ± 3.6	
	ΛCDM		110 ± 36	78 ± 27	-6 ± 25	-72 ± 30	-66 ± 84	(km s^{-1})
	τCDM		145 ± 33	101 ± 30	-1 ± 23	-100 ± 23	-187±109	
FAM_{100}-FAM_{30}	ΛCDM	317 ± 89	14.0 ± 4.6	9.4 ± 4.0	0.5 ± 2.9	-9.9 ± 3.0	3.8 ± 12.6	(km s^{-1} Mpc^{-1})
	τCDM	245 ± 60	15.3 ± 4.3	9.8 ± 2.5	1.4 ± 2.9	-11.2 ± 3.8	7.3 ± 13.0	
	ΛCDM		421 ± 138	281 ± 120	15 ± 86	-296 ± 91	113 ± 378	(km s^{-1})
	τCDM		458 ± 128	293 ± 75	42 ± 87	-335 ± 115	218 ± 391	
N−body - FAM_{100}	ΛCDM	81 ± 51	2.4 ± 1.3	-0.6 ± 1.7	-0.2 ± 1.4	0.9 ± 1.3	-5.1 ± 12.7	(km s^{-1} Mpc^{-1})
	τCDM	121 ± 54	2.9 ± 0.8	-0.6 ± 1.6	-0.5 ± 1.6	0.9 ± 1.7	-4.7 ± 16.8	

Table 2.4 — Average results for the tidal bulk amplitude, shear eigenvalues and divergence. The errors represent the 1σ scatter around the average value. Col. 1: Tidal field region where the velocity components were computed. The first two sections refer to the tidal field computed from the N-body - FAM model. Col. 2: Cosmological model. Col. 3: bulk flow, v_{bulk}. Col. 4: shear eigenvalue amplitude, $|s|$. Col. 5: s_1 eigenvalue (stretching). Col. 6: s_2 eigenvalue (middle). Col. 7: s_3 eigenvalue (compressional). Col. 8: velocity divergence.

2.8.2 Velocity Multipole Analysis: Results

The results of our analysis are summarized in Table 2.4. It lists the average quantities for the tidal bulk flow and shear components for the two cosmological scenarios discussed in this work. The table has been organized in four (horizontal) sections. Each corresponds to another "differential" velocity field, the difference between two differently processed velocity fields.

For both the ΛCDM and the τCDM model each of the quoted values in Table 2.4 involve the average and standard deviation determined on the basis of ten different realizations. This adds up to 8 configurations, two cosmologies per section. For each of the 8 configurations, in the third column the table lists the dipole component of the external velocity field, the bulk flow v_{bulk}. Subsequently, the velocity shear is specified in terms of the three eigenvalues s_1, s_2 and s_3 of the traceless shear tensor. This is preceded in the fourth column by the amplitude s of the shear. Finally, in the 8th column, the monopole contribution of the velocity divergence is specified. Note that shear and velocity divergence are each quoted in two units. First, they are specified in proper units of km s^{-1} Mpc^{-1}, followed by the equivalent velocity differential in km s^{-1} over a volume of 30 h^{-1}Mpc radius. The intention of the latter is to offer a directly appreciable comparison between the relative importance of bulk flow and shear contributions.

Each of the four sections specifies the values of the computed monopole, dipole and quadrupole moments of the velocity field of the corresponding sample. The first section relates to a multipole analysis of the differential velocity field between the full N-body velocity field and the FAM$_{30}$ velocity reconstructions of the inner 30 h^{-1}Mpc region, N-body - FAM$_{30}$. Except for the monopole contribution the resulting residual velocity field has been generated by the mass distribution beyond a radius of 30 h^{-1}Mpc. On these linear scales the inferred dipole and quadrupole components of the velocity field may be directly related to the moments of the surrounding mass distribution. The inferred residual velocity divergence (the monopole contribution), on the other hand, is the result of the effective under/over density of the inner 30 h^{-1}Mpc region.

The second section of Table 2.4 does the same for the larger 100 h^{-1}Mpc region. The outcome of similar analyses are presented in the third and fourth section. The third section repeats the analysis of the first section, except that the external tidal influences are determined on the basis of the difference between the FAM velocity reconstructions within the large 100 h^{-1}Mpc region and the inner 30 h^{-1}Mpc region. Earlier, in Section 2.6.3, we have found that the major share of the origin of the external tidal field is confined to this region and that it therefore may well be determined from the residuals between FAM$_{100}$ and FAM$_{30}$. The comparison between the inferred multipole moments of the velocity differences between FAM$_{100}$-FAM$_{30}$ in the third section and those in the first section are therefore expected to be rather similar, any systematic differences originating in tidal effects generated beyond a radius of 100 h^{-1}Mpc. This is emphasized by means of the fourth section in Table 2.4, which refers to the values of the residual tidal velocity field between N-body - FAM$_{100}$. If indeed all significant contributions are located within the inner 100 h^{-1}Mpc, the multipole values in this section are expected to be negligible.

2.8.3 Velocity Multipole Contributions: Maps

For a direct visual appreciation of the various multipole contributions to the tidal velocity field we assess the "tidal" velocity field N-body - FAM$_{30}$, the velocity field generated by the mass distribution beyond a radius of 30 h^{-1}Mpc, for one of the ΛCDM catalogs. The presented maps concern the same ΛCDM catalog as those presented in the maps of Figures 2.7. The map of the projection of this "tidal" velocity flow onto three central planes is shown in the top row of Figure 2.12.

2.8.3.1 Monopole component: Local expansion/contraction

In the above (Section 2.8.1) we have also taken account of the presence of a residual expansion (velocity divergence) term $\mathrm{v}_{exp,i}$ in the velocity flow. While the dipole and quadrupole components are exclusively related to the external matter distribution, the residual monopole term is a result of the

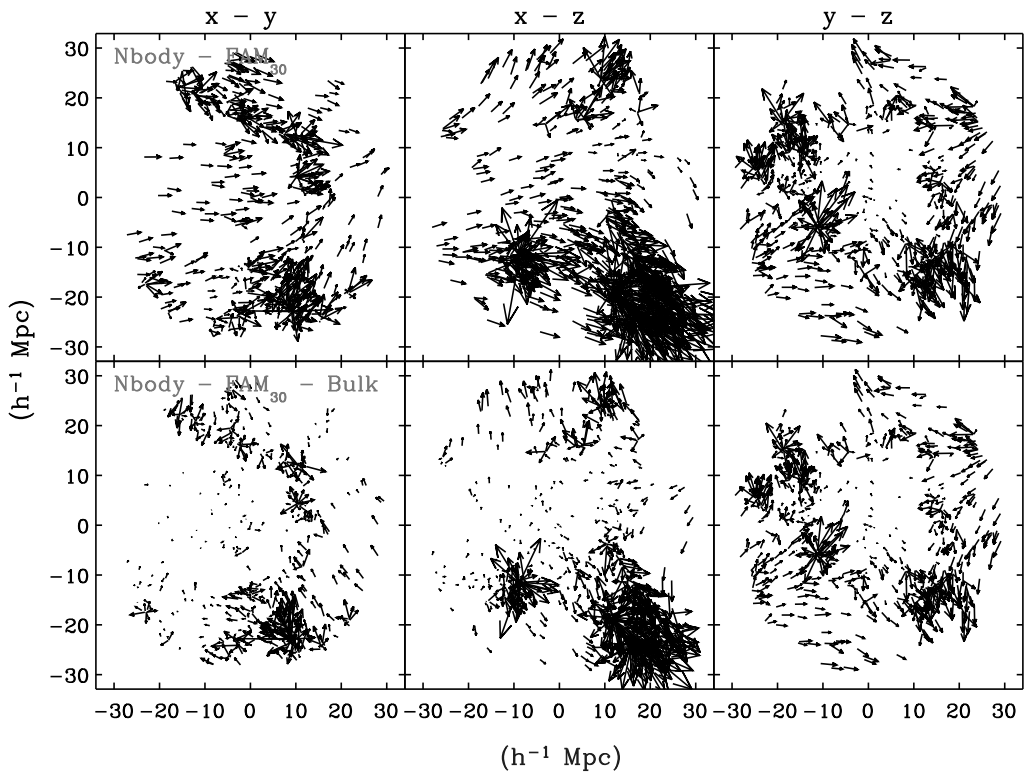

Figure 2.12 — 2D projected peculiar (residual) velocities for the same mock catalog as in Fig. 2.7 and Fig. 2.8 in three perpendicular central planes of 10 h^{-1}Mpc width. The coordinate frame is rotated such that the bulk flow velocity is oriented along the x-direction. Within the plane perpendicular to the x-axis, the y and z axes are chosen arbitrarily. First row: the residual velocity (ie. tidal velocity) $N-$body - FAM_{30}. Second row: residual velocities after subtraction bulk flow component. The resulting residual field is clearly dominated by a shear pattern, most notably in the $y-z$ plane.

effective over- or underdensity of the inner region. The corresponding velocity perturbations tend to be relatively small: even over a region as large as 30 h^{-1}Mpc these density fluctuations tend to be relatively minor, be it not negligible (see Table 2.4).

From the quoted values of the inferred velocity divergences $\nabla \cdot \mathbf{v}$ in Table 2.4 we also notice that there is not only a large variation of values, but that nearly as many values have a positive as a negative sign. This translates into either a local underdensity or overdensity. This is an artefact of our mock catalogs not having been tuned enough towards local cosmic circumstances (see also section 2.5.2.1). By means of better constrained simulations we seek to achieve this in a forthcoming publication.

2.8.3.2 Dipolar component: Bulk flow

The externally generated velocity flow is dominated by its bulk flow component. This is in general true for both cosmologies. The large impact of the bulk flow over the local 30 h^{-1}Mpc volume can be immediately inferred from the values in the first section of Table 2.4, revealing contributions in excess of 200 km s^{-1}.

To facilitate visual appreciation of this observation we have have reoriented the reference system in Figure 2.12 such that the x-axis is oriented along the bulk flow. While the original Cartesian system is an arbitrary one and thus lacks a physical context, the *"bulk flow reference system"* confines the inferred bulk flow $\tilde{u}$ exclusively to the x-direction. As a result there are no bulk flow components in the corresponding y- and z-direction (note that within the $y-z$ plane their direction is arbitrarily

Cosmology	$R_{S\,pear}$	R_{lin}	a_0 (km s^{-1})	a_{lrg}	σ_{lrg} (km s^{-1})
ΛCDM	0.62 ± 0.17	0.58 ± 0.22	-4.03 ± 75.45	0.83 ± 0.20	246 ± 134
τCDM	0.75 ± 0.11	0.71 ± 0.14	-9.31 ± 30.19	0.93 ± 0.13	219 ± 86

Table 2.5 — Average final results for the $N-$body velocities *vs*. the corrected FAM$_{30}$ after adding to it the tidal Bulk and Shear contributions. The errors represent the 1σ scatter around the average value. Col. 1: Cosmological model. Col. 2: non parametric (Spearman) correlation coefficient. Col. 3: linear correlation index. Col. 4: zero point of the best linear fit. Col. 5: slope of the best fitting line. Col. 6: dispersion around the fit.

defined). The pre-eminence of the bulk flow component can be immediately seen in the $x-y$ and $x-z$ frames in the top row of Figure 2.12. Note that the same velocity maps, mostly so the $y-z$ frame, reveal a clear shear pattern.

2.8.3.3 Quadrupolar component: Velocity shear

Seeking to assess the quadrupolar term in the external velocity field we first remove the remaining expansion term from $\tilde{s}_{ij}$. Diagonalization of the resulting traceless shear tensor $\tilde{s}'_{ij}$ yields the shear eigenvalues and eigenvectors. The eigenvalues s_1, s_2 and s_3 are indicative for the strength of the tidal force field induced by the surrounding matter distribution, while the principal directions of this quadrupolar velocity perturbation field are indicated by the corresponding eigenvectors $\hat{e}_{s,i}$.

The *"shear ellipsoid"*, the quadratic surface defined by the shear tensor $\tilde{s}'_{ij}$ with principal axes aligned along the eigenvectors and with axis size set by the corresponding eigenvalue s_i, defines a natural reference system to assess the tidal shear flow field. The coordinate axes of this *"shear reference frame"* are identified with the orthonormal basis defined by the (normalized) eigenvectors. The x-axis is chosen to be aligned along the major axis of the *"shear ellipsoid"*, the direction defined by the largest (positive) eigenvalue s_1 and directed along the strongest dilational (stretching) motion incited by the external tidal field. Likewise the z-axis is chosen to coincide with the lowest (negative) eigenvalue s_3, aligned along the strongest "compressional" component of the tidal velocity flow. This leaves the y-axis as the one coinciding with the intermediate eigenvalue s_2.

The imprint of the shearing motions can be discerned within the $y-z$ plane and, most prominently, along the "x-z" projection of the *"bulk flow reference system"*. After subtraction of the bulk flow component, i.e. N-body-FAM$_{30}$-v_{bulk}, the quadrupolar component of the externally induced velocity flow represents its principal constituent (Fig. 2.12, lower row). This is confirmed by the values quoted in Table 2.4 for the shear contribution. In particular when stated in the velocity equivalent unit of km s^{-1} these shear values suggest that the quadrupolar shear contributions are of a comparable magnitude to those of the bulk flow. The maps in the lower row of Figure 2.12 suggest that there are strong dilational and compressional motions within the $y-z$ plane. By contrast, the shear motions in the x-direction appear to be uncommonly weak. Given the *"bulk flow reference system"*, it implies that for this particular realization we see a bulk flow directed almost perpendicular to the shear flow motions.

Figure 2.13 depicts the same ΛCDM mock sample as presented in Figs. 2.7, 2.8 & 2.12, here in the *"shear reference frame"*. The top row shows the full externally induced flow field, N-body - FAM$_{30}$, in this reference system. The tidal shear flows are almost exclusively confined to the $x-z$ plane. This is most evidently illustrated in the central row of frames showing the velocity field without its bulk flow component: hardly any systematic flow is noticeable in the y-direction of the intermediate shear eigenvalue.

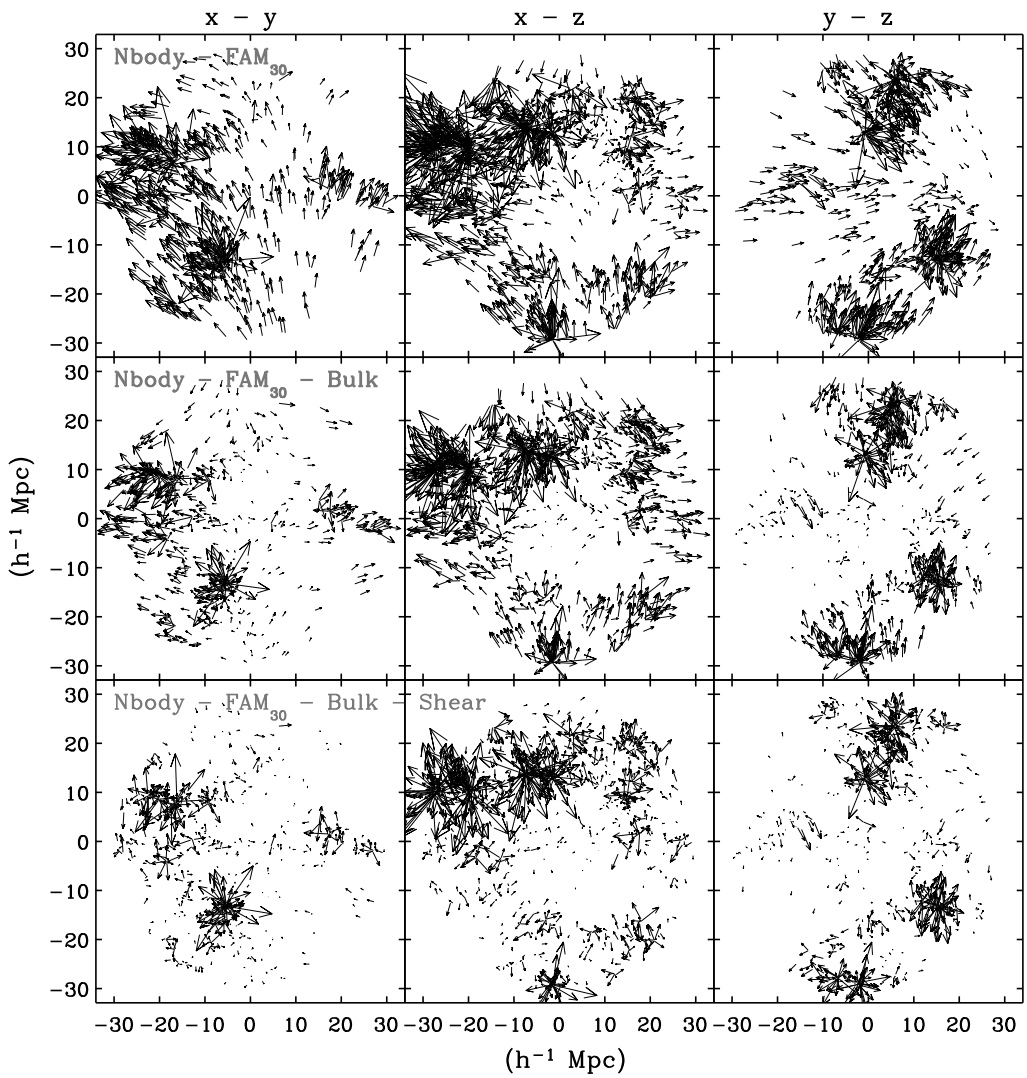

Figure 2.13 — 2D projected peculiar velocities for the same mock catalog as in Fig. 2.7 and Fig. 2.8 in three perpendicular central planes of 10 h^{-1}Mpc width. The coordinate frame is defined by the three eigenvectors of the shear tensor. The x-axis is aligned along the direction of the largest (stretching) eigenvalue, the y-axis is aligned along the middle eigenvalue and the z-axis along the smallest (compressional) eigenvalue. The first two rows are the same as Fig. 2.12, within the "shear reference system". The third row depicts the final residual field after substraction of the quadrupolar shear component.

2.8.4 Multipole Scale Dependence

When turning to the external influences over a large 100 h^{-1}Mpc region, we may conclude from the second section of the table that most of the external contributions are accounted for, both bulk flow and shear are at least a factor of 3-4 smaller than for the inner 30 h^{-1}Mpc region.It is tantalizing to notice that this does not appear to be true for the velocity divergence. The third and fourth section show that the explicit contributions from the regions between 100 h^{-1}Mpc and 30 h^{-1}Mpc and those beyond 100 h^{-1}Mpc are indeed significantly different, those beyond 100 h^{-1}Mpc tending towards zero contributions and as far as the shear is concerned almost an order of magnitude smaller than the equivalent contributions by the $30-100$ h^{-1}Mpc region.

A similar graphical assessment involving the FAM_{100} reconstructions emphasizes the minor significance of tidal contributions stemming from density fluctuations beyond a radius of 100 h^{-1}Mpc. No coherent velocity pattern can be recognized in the residual velocity field between full N-body and FAM_{100} reconstruction. The comparison between this residual velocity field with the velocity maps including the contributions of the inferred bulk flow and shear flow do hardly show any difference. In all cases the velocity fields are dominated by the same thermal motions.

2.8.5 Multipole Velocity Flow Model

Following our argument that the externally induced velocity flow within the inner 30 h^{-1}Mpc mainly consists of a bulk flow and shear contribution, we may expect that the effect of the external gravity field can be sufficiently accounted for by adding these components to a local velocity field model based on the mass distribution in and around the Local Superclusters.

By separating the "internal" FAM velocity field from the "external" multipole contributions of the (monopole,) dipole and quadrupole components of the *"tidal"* velocity field and adding the two, we obtain a total *"FAM-multipole"* model velocity $v_{fammpl,i}$,

$$\mathrm{v}_{fammpl,i} \approx \mathrm{v}_{FAM,i} + \mathrm{v}_{exp,i} + \mathrm{v}_{bulk,i} + \mathrm{v}_{shear,i} \tag{2.31}$$

A visual impression of the extent of the successive multipole contributions may be obtained from Fig. 2.14. The vector plots of the four velocity contributions to v_{fammpl} (Eqn. 2.31) are depicted in four successive rows, each within the mutually perpendicular three central slices (wrt. the shear reference system). The top row concerns the FAM_{30} velocity field reconstruction, followed successively by the expansion/contraction term (monopole), the bulk flow (dipole) and velocity shear (quadrupolar).

From Fig. 2.14 and Fig. 2.13 we conclude that the differences between the "full" N-body velocities and v_{fammpl}, the total sum of the internal FAM_{30} and external dipole and quadrupole contributions, do not appear to show systematic trends. Wherever there are large deviations, these are are mainly confined to the high density virialized regions, where virial motions are known to pose problems for FAM.

2.8.6 Point-to-Point Comparison

A quantitative quality assessment of the *"FAM-multipole"* model is offered by the point-to-point comparison between the full N-body velocity and its difference with respect to the successive modes of the *"FAM-multipole"* velocity in Fig. 2.15. The v_x, v_y and v_z of the various velocity components refer to the *"bulk flow reference system"*. The top row, plotting v_{Nbody} vs. the residual N-body-FAM_{30}, reveals the expected systematic differences due to missing externally induced contributions. Given the fact that the bulk flow in this reference system is confined to the x-component, we may note the uniform systematic shift of the x residuals with respect to the zeropoint $(\mathrm{v}_{Nbody}, \mathrm{v}_{res}) = (0,0)$ (top lefthand frame). The subsequent addition of the dipolar bulk flow contribution to FAM_{30} leads to a systematic downward uniform vertical shift of N-body-FAM_{30}-Bulk (middle row Fig. 2.15): also the residuals in the x-direction now center on $\mathrm{v}_{res} = 0$ (note that by virtue of the bulk flow the N-body velocities in the x-direction are also skewed to values larger than $\mathrm{v}_{Nbody} = 0$).

The three point-to-point diagrams in the middle row of Fig. 2.15 show that even while the bulk flow is taken into account systematic motions remain in all three directions. The point-to-point comparisons still follow a strong correlation with respect to the the N-body velocities. It mainly involves the presence of the quadrupolar velocity shear component (in addition to a minor ingredient contributed by the monopole expansion/contraction term). This can be immediately inferred from the comparison between the diagrams in the central and lower row of Fig. 2.15: once the quadrupole component "Shear" has been added to the "FAM_{30}+Bulk" velocities the systematic effects seem to have largely vanished. What remains in the residuals is mainly random scatter, centered on the $\mathrm{v}_{res} = 0$ km s^{-1} line, with some exceptional outliers originating in the virialized regions (where FAM fails to perform properly).

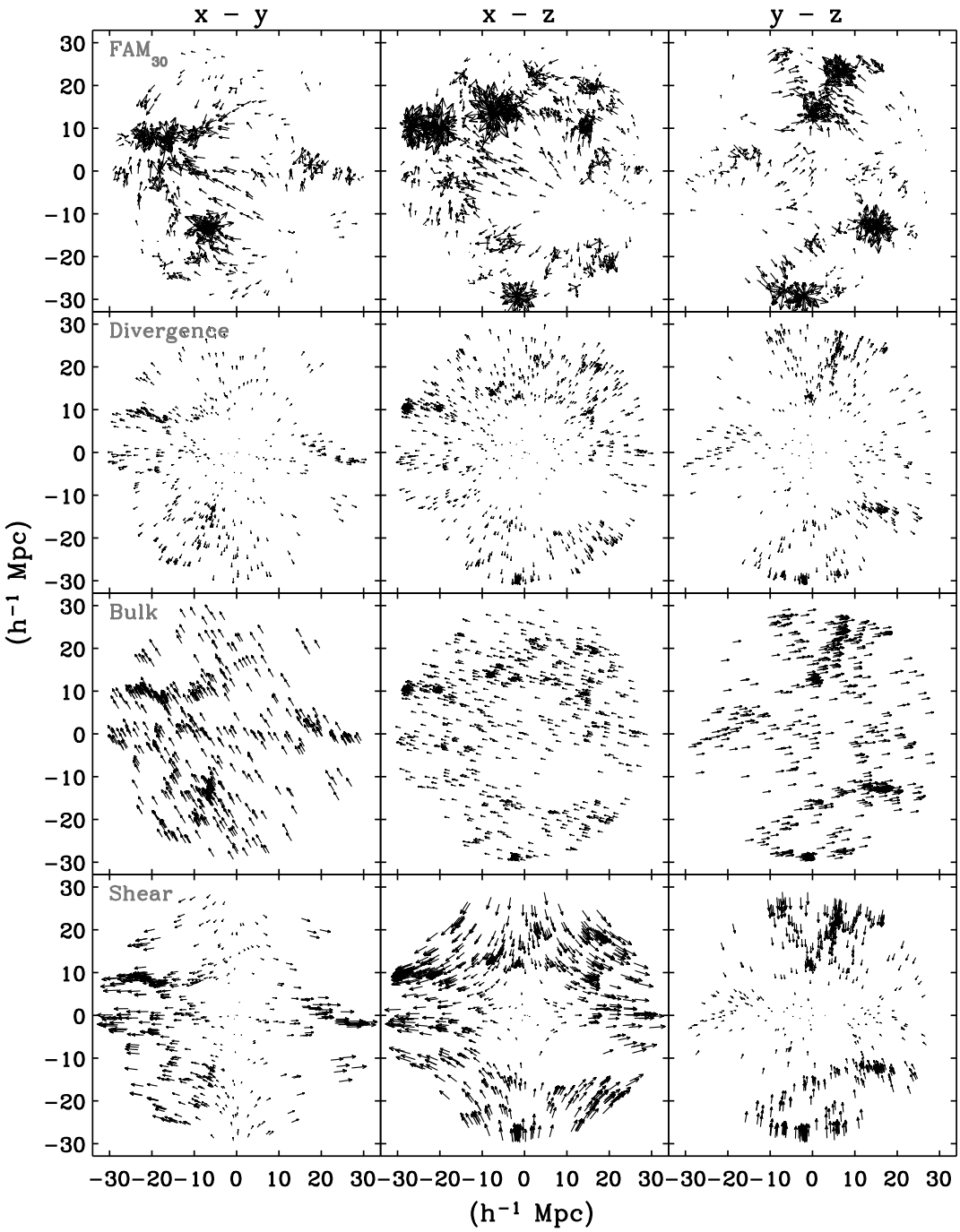

Figure 2.14 — Velocity Field Multipole Decomposition: the total N-body velocity field, involving the same one as in Fig. 2.12 and Fig. 2.13, decomposed into its four different components. The coordinate system is that defined by the tidal shear tensor, see Fig. 2.12. At each row we depict the velocities in the $(x-y)$, $(x-z)$ and $(y-z)$ plane. Top: the locally induced velocity, approximated by the FAM_{30} realization. Second row: the monopole component, a result of the slight local expansion due to its underdensity wrt. the global Universe. Third row: the bulk flow, of which most is concentrated in the $(x-y)$ and $(y-z)$ plane. Fourth row: the shear flow component.

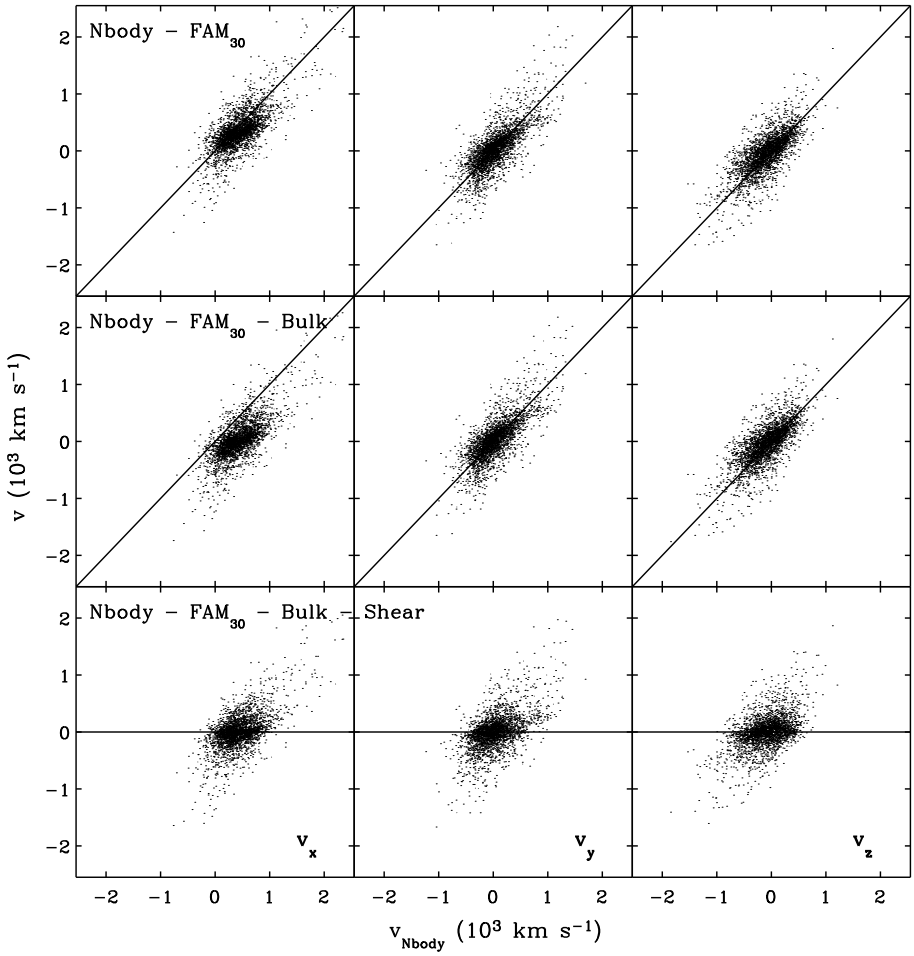

Figure 2.15 — point-to-point comparison between the three successive residual velocities and the corresponding mock catalog N-body velocity. The three panels in each row correspond to the x, y and z velocity components. The coordinate system is the "shear reference system". Top row: the tidal velocity field N-body-FAM. Middle row: residual velocity field after subtraction bulk flow. Bottom row: residual velocity field after subtraction of both tidal bulk and shear components.

We have quantified the point-to-point comparisons by performing linear regressions similar to those presented in Section 2.7. Table 2.5 summarizes the results of this comparison for all catalog samples for both cosmologies. In both cosmological models the slope of the best fitting line is consistent with unity at $\sim 1\sigma$ confidence level. As expected, the scatter around the fit is similar to that of all previous analyses (see Table 2.3). Offsets around the zero-point are consistent with zero, although with a large dispersion. The strength of the point-to-point correlations has increased considerably with respect to their FAM_{30} counterpart (Table 2.3) and it is very similar to the FAM_{100} case.

2.8.7 Surrounding Matter Distribution: Tidal Source

The surrounding external matter distribution is the source for the tidal velocity field which we inferred in the previous sections. For various purposes we wish to relate the computed dipolar bulk flow and quadrupolar shear flow components to the surrounding matter distribution which induced them.

The induced tidal velocities involve spatial scales ranging from 30 h^{-1}Mpc to 100 h^{-1}Mpc. Over

this range the linear theory of gravitational instability holds to good approximation. This translates into a direct linear relationship between induced velocity $\mathbf{v}_{ext}$ and the cumulative external gravitational force $\mathbf{g}_{ext}$,

$$\mathbf{v}_{ext}(\mathbf{x},t) = \frac{2f(\Omega_m,\Lambda)}{3H\Omega_m}\,\mathbf{g}_{ext}(\mathbf{x},t)\,, \tag{2.32}$$

with $f(\Omega_m,\Lambda)$ the linear velocity growth factor. This linear relationship also holds for every component of the velocity and gravity fields, and thus also for the individual dipolar and quadrupolar components of the externally induced velocity field. They are directly proportional to equivalent dipole and quadrupolar components of the gravity field:

$$\begin{aligned} \mathbf{v}_{bulk}(\mathbf{x},t) &= \frac{2f(\Omega_m,\Lambda)}{3H\Omega_m}\,\mathbf{g}_{bulk}(\mathbf{x},t) \\ s_{ij}(\mathbf{x},t) &= -\frac{2f(\Omega_m,\Lambda)}{3H\Omega_m}\,\mathcal{T}_{ij}(\mathbf{x},t) \end{aligned} \tag{2.33}$$

with the (external) gravitational tidal shear tensor $\mathcal{T}_{ij}$ is defined as (see van de Weygaert & Bertschinger 1996),

$$\mathcal{T}_{ij} = \frac{\partial^2\Phi_{tidal}}{\partial x_i \partial x_j}\,. \tag{2.34}$$

Notice that because of its external nature, the term $\frac{1}{3}\nabla^2\Phi_{tidal}\,\delta_{ij}$ is always equal to zero.

Ideally, we would like to infer the external tidal potential Φ_{tidal} directly from the galaxy distribution in a sufficiently large surrounding region. This is specifically true for its dipolar and quadrupolar moments, with the intention to insert these terms directly into the expression for the FAM potential (Eqn. 2.12 and Eqn. 2.10). The required externally induced bulk flow velocity and velocity shear should be the result. The comparison of the FAM computed velocities for the local volume, in combination with the computed tidal velocities (Sec. 2.8.2), and the observed and measured velocities would then enable us to determine the amount of mass and average density in the local volume.

To determine the gravitational influence of the surrounding matter distribution, we set out to assess the sky distribution of galaxies in the local NBG volume, out to $r_{NBG} = 30\ h^{-1}$Mpc, along with the external mass distribution in radial shells out to a distance $r_{PSCz} \leq 100\ h^{-1}$Mpc. A prominent dipolar matter configuration in the sky distribution will translate into a strong bulk gravity force. Similarly, quadrupolar anisotropies will translate into an effective tidal shear force. In Figure 2.16 we have plotted the galaxies in one of our ΛCDM mock catalogs in five successive distance shells. Aitoff projections of the angular positions of the galaxies, as seen from the centre of the local NBG volume, provide an impression of the level of anisotropy in the mass distribution at successive radii.

The first sky plot (top sphere) depicts the sky position of the galaxies in the local NBG-mimicking mock sample. It involves a highly flattened distribution, perhaps reminiscent of the Supergalactic Plane. The four subsequent shells correspond to successive cuts through the PSCz mimicking samples, at sampling depths $d_{sur} = [0-30]$, $[30-55]$, $[55-70]$ and $[85-100]\ h^{-1}$Mpc. The first and direct observation is the deminishing sample density as a function of survey depth, in accordance with the selection function (Eqn. 2.19). Structure is most prominent in the first shell, at $d_{sur} = [30-55]\ h^{-1}$Mpc (central left sphere). The structure contained in this shell also shows a clear affiliation with the matter distribution in the local NBG volume. The compact massive concentration at $l \approx 220°$ is clearly connected to a dense region in the local "plane". A superficial inspection of the angular galaxy distribution reveals the presence of strong dipolar and quadrupolar components, effecting considerable tidal forces. Note that both external shells display a rather strong concentration of galaxies in their southern hemisphere, in the vicinity of $l \approx 180-200°$. Similar but weaker contributions can also be recognized from the galaxy distribution in the shell between $d_{sur} \approx 70-85\ h^{-1}$Mpc. Beyond $d_{sur} > 85\ h^{-1}$Mpc, however, the angular pattern appear to be considerably less pronounced. This is in line with the earlier findings that there were hardly noticeable tidal contributions from large distances.

To see to what extent the depicted galaxy distribution can indeed be held responsible for most of the inferred tidal bulk flow and tidal shear, we have determined the corresponding bulk force $\mathbf{g}_{bulk}$

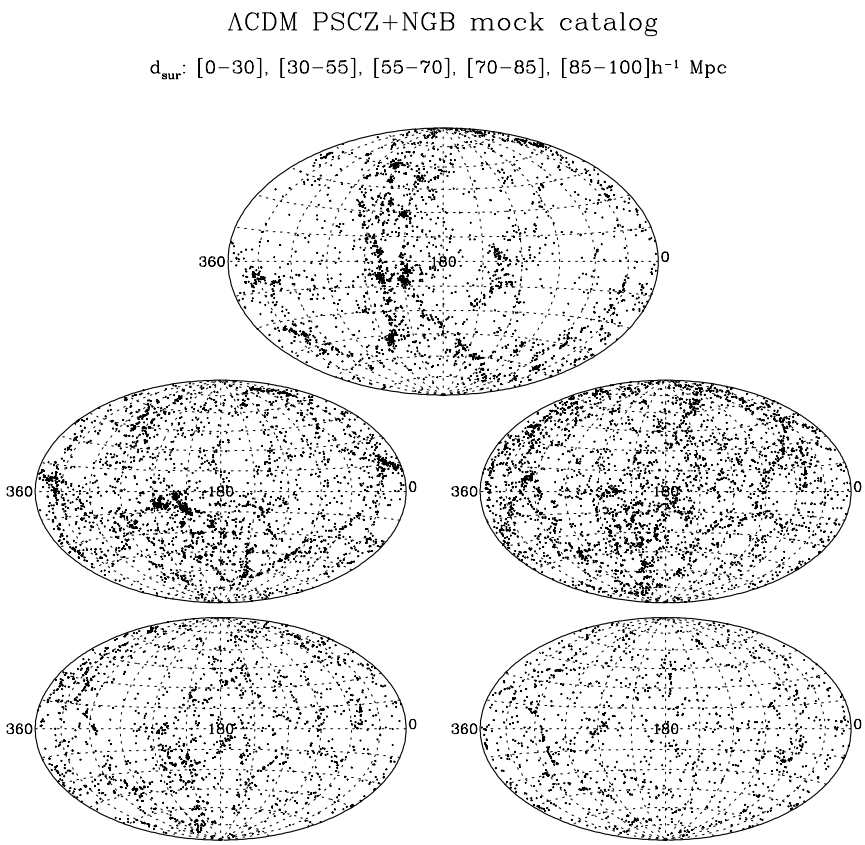

Figure 2.16 — Aitoff projections of the galaxy distribution of a NBG + PSC*z* ΛCDM catalog. The topmost panel shows the corresponding NBG distribution, $d_{sur} = [0, 30]\ h^{-1}$Mpc. The subsequent panels depict the external galaxy distribution enclosed by the shells defined by survey depth $d_{sur} = [30-55]\ h^{-1}$Mpc, $d_{sur} = [55-70]\ h^{-1}$Mpc $d_{sur} = [70-85]\ h^{-1}$Mpc and $d_{sur} = [85-100]\ h^{-1}$Mpc.

(Eqn. 2.4) and tidal shear $\mathcal{T}_{ij}$ (Eqn. 2.5) evoked by the external galaxy distribution ($r > 30\ h^{-1}$Mpc). Since we do not have a continuous density field but the positions of a finite number of objects in our galaxy flux-limited and full mass distribution catalogs, the bulk acceleration on the LG is computed from the discrete equivalent. For a sample of galaxies at locations $\mathbf{x}_i$, with an average number density n of selected objects, this leads to

$$\mathbf{g}_{bulk} = \frac{Hf(\Omega_m, \Lambda)}{4\pi n} \sum_i \frac{1}{\psi(x_k)} \frac{\mathbf{x}_k}{|\mathbf{x}_k|^3} \,. \tag{2.35}$$

where $\psi(x_k)$ is the sample selection function at distance x_k, whose inverse functions as weighting factor. For practical reasons, comparison with the inferred bulk flow $\mathbf{v}_{bulk}$, we have translated the bulk acceleration into equivalent velocity units by means of the transformation $Hf(\Omega_m, \Lambda)/\frac{3}{2}\Omega_m H^2$. The equivalent "discrete" expression for the external tidal shear is

$$\mathcal{T}_{ij} = \frac{Hf(\Omega_m, \Lambda)}{4\pi n} \sum_i \frac{1}{\psi(x_k)} \frac{3\, x_{ki}\, x_{kj}}{|\mathbf{x}_k|^5} \,. \tag{2.36}$$

For the ΛCDM mock galaxy sample depicted in Fig 2.16 we determine the gravity dipole by computing for a set of spherical external shells the resulting bulk flow acceleration (Eqn. 2.35) and the gravity quadrupole by computing external tidal shear (Eqn. 2.36). Recently, a similar approach

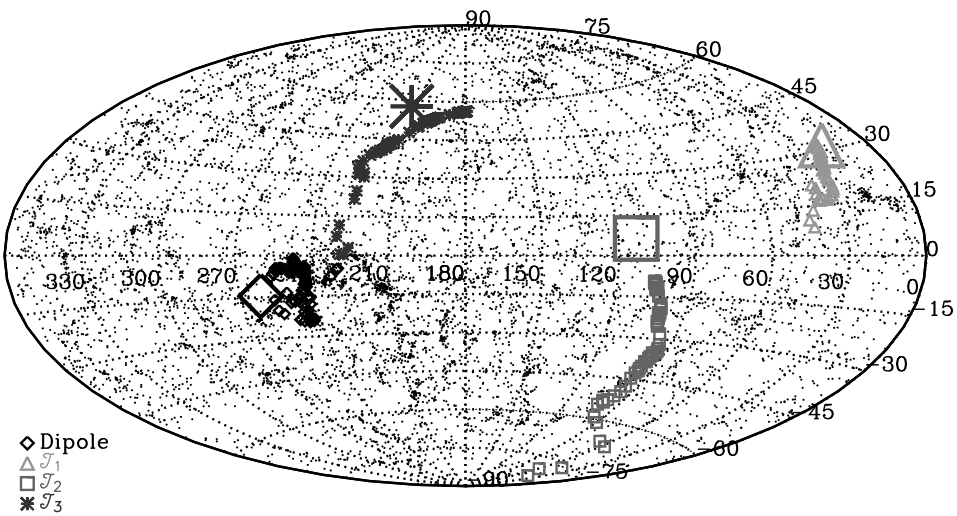

Figure 2.17 — Sky distribution of galaxies in external shell of survey depth $d_{sur} = 30 - 100\ h^{-1}$Mpc. This galaxy distribution should reflect the mass distribution inducing the local tidal velocity flow. By means of symbols we have indicated the track of the gravity dipole and quadrupole eigenvector directions (cf. Eqn. 2.35 and Eqn. 2.36) on the sky, by radially expanding outward the survey depth d_{sur} in steps of 1 h^{-1}Mpc, from $d_{sur} = 30\ h^{-1}$Mpc to $d_{sur} = 100\ h^{-1}$Mpc. For comparison the same symbol, but then enlarged, indicates the directions for the corresponding bulk velocity and velocity shear eigenvector directions. Diamond: dipole. Triangle: stretching component shear. Square: middle component shear. Star: compressional component shear.

was followed by Teodoro et al. (2003). The spherical shell volumes are defined by an inner radius $r_{inn} = 30\ h^{-1}$Mpc and an outer radius r_{out}. The width of the shell is gradually enlarged by increasing r_{out} from $r_{out} = 30\ h^{-1}$Mpc to $r_{out} = 100\ h^{-1}$Mpc. The convergence of the resulting gravity dipole direction on the sky can be observed in Fig. 2.17. The small red diamonds are consistently located near $l \approx 230°$, and converge at a sky location close to the direction of the velocity dipole (large red diamond). To get an idea of the amplitudes involved, Fig. 2.19 (top panel) shows the development of the cumulative gravity dipole as a function of external distance d_{sur} ($30\ h^{-1}$Mpc $< d_{sur} < 100\ h^{-1}$Mpc). By means of symbols the corresponding velocity dipole, for each of the three directions x, y and z, are inserted at the outer radius of $d_{sur} \approx 100\ h^{-1}$Mpc. Note that we have restricted ourselves to a case study example. A more extensive and proper assesment, including a proper error estimate of both gravity dipole and quadrupole as well as the bulk and shear flow, is beyond the scope of the present argument. This issue, involving the shot noise influence on gravity dipole and quadrupole and the role of FAM uncertainties on the velocity flow components, will be treated in more detail in a forthcoming study.

We see that in the x-, y and z-directions of the gravity and velocity dipoles are in reasonable agreement, within a margin of ≈ 30 km s^{-1}. This observation justifies our expectation that the dipole can be estimated to sufficient accuracy from the surrounding external galaxy distribution. These observations form a justification of our expectation that the dipole may be estimated from the surrounding external galaxy distribution, so that the latter can be invoked to correct for the influence of the external tidal field in the dynamics of the local volume.

The situation is comparable for the cumulative tidal shear, in terms of its three eigenvalues and eigenvectors. Also the gravity quadrupole appears to converge relatively smoothly towards the velocity shear. This may be inferred from the plotted directions of the eigenvectors $\hat{\mathbf{e}}_{\mathcal{T}1}$, $\hat{\mathbf{e}}_{\mathcal{T}2}$ and $\hat{\mathbf{e}}_{\mathcal{T}3}$ of the tidal shear $\mathcal{T}_{ij}$. They are indicated by means of three symbols, the triangle corresponding to the stretching component $\mathcal{T}_1$, the star the middle component $\mathcal{T}_2$ and the square the compressional component $\mathcal{T}_3$. The tidal shear tensor wanders extensively across the "sky" as we push the outer radius of the external shell outward, as is shown by the paths of the corresponding eigenvectors. Interestingly, once the shell

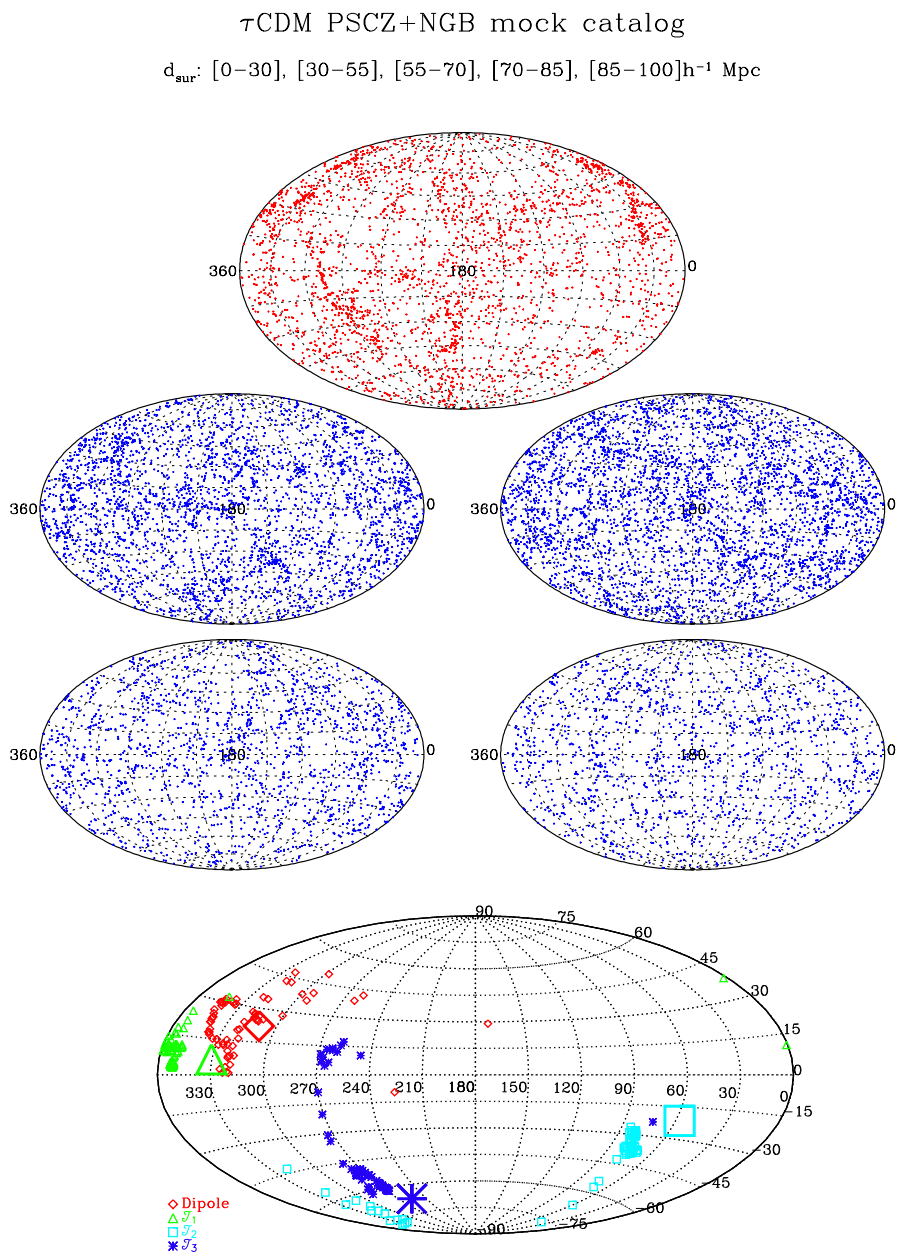

Figure 2.18 — Aitoff projections of the galaxy distribution of a NBG + PSCz τCDM catalog. The top-most panel shows the corresponding NBG distribution, $d_{sur} = [0,30]$ h^{-1}Mpc. The subsequent 4 panels depict the external galaxy distribution enclosed by the shells defined by survey depth $d_{sur} = [30-55]$ h^{-1}Mpc, $d_{sur} = [55-70]$ h^{-1}Mpc $d_{sur} = [70-85]$ h^{-1}Mpc and $d_{sur} = [85-100]$ h^{-1}Mpc. Bottom panel: convergence gravity dipole and quadrupole. By means of symbols we have indicated the track of the gravity dipole and quadrupole eigenvector directions (cf. Eqn. 2.35 and Eqn. 2.36) on the sky, by radially expanding outward the survey depth d_{sur} in steps of 1 h^{-1}Mpc, from $d_{sur} = 30$ h^{-1}Mpc to $d_{sur} = 100$ h^{-1}Mpc. For comparison the same symbol, but then enlarged, indicates the directions for the corresponding bulk velocity and velocity shear eigenvector directions. Diamond: dipole. Triangle: stretching component shear. Square: middle component shear. Star: compressional component shear.

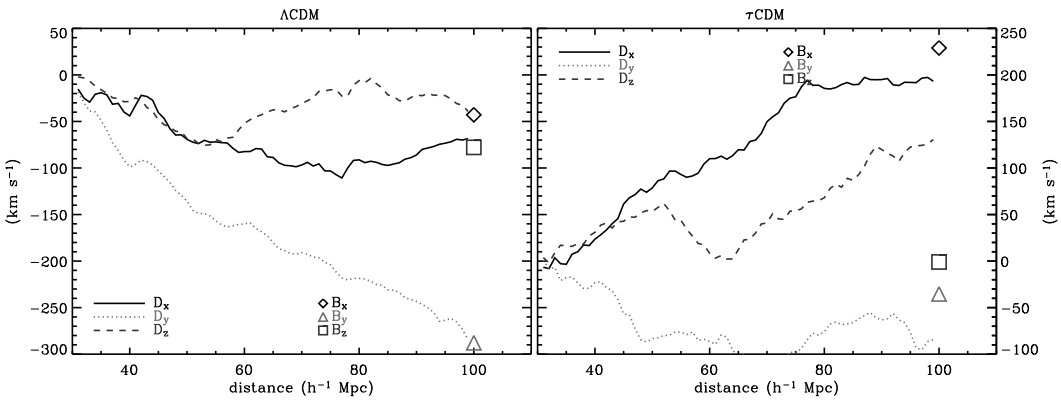

Figure 2.19 — Cumulative gravity dipole and tidal gravity shear. As a function of survey depth d_{sur} the Cartesian components of the gravity dipole, g_x, g_y and g_z is followed (in equivalent velocity unit km s^{-1}). The symbols at d_{sur} indicate the corresponding velocity dipole. Top panel: ΛCDM. Bottom panel: τCDM.

radius starts to approach 100 h^{-1}Mpc, each of the eigenvectors appear to converge near the location of the corresponding stretching, central and compressing velocity shear tensor eigenvectors. However, also here we notice significant deviations in individual cases.

For comparison, we can appreciate the role of the external tidal field on local dynamics for the case of the τCDM cosmology. Figure 2.18 combines the galaxy sky distribution for a τCDM mock galaxy sample, in the same radial shells as in Fig. 2.16. The final frame shows the Aitoff projection of the gravity dipole and gravity quadrupole eigenvectors for a set of gradually increasing radial shells. From the galaxy sky distribution in the four slices at sampling depths $d_{sur} = [0-30], [30-55], [55-70]$ and $[85-100]$ h^{-1}Mpc we notice that these involve considerably more isotropic distributions. Hardly any prominent patterns can be discerned in the sky distribution. This is expressed in a more erratic wandering of gravity dipole and quadrupole directions (lower frame, Fig. 2.16). Even though they appear to converge near the derived velocity dipole and shear flow quadrupole, it agrees less good than in the case of the more prominent anisotropies in the ΛCDM cosmology. In this, we have to realize that the amplitude of dipole and quadrupolar contributions in the two scenarios are not too different (cf. Table 2.5). The less prominent anisotropies in the τCDM catalogues are compensated by a higher average matter density. Possibly the considerable deviations of the τCDM dipole and quadrupole are due to the smaller coherence length of the τCDM fluctuations and the considerably more isotropically oriented contributions by the individual external matter concentrations.

2.8.8 Multipole Components: Summary

The above results reassure the fact that the external tidal field can be well characterized by its main multipole components, the bulk flow and velocity shear. In terms of multipole amplitude convergence, these results show a better agreement for the ΛCDM model than for the τCDM one. This is due to the intrinsic characteristics of both cosmic models. As has been discussed in Section 2.4, and may be directly appreciated from Fig. 2.2, the relatively lower amplitude of the τCDM perturbations is compensated by a higher mass content. It leads to an equally strong external gravitational influence. On the other hand, the smaller spatial coherence of density features in the τCDM scenario causes the orientation of the gravity dipole and quadrupoles to be rather jittery. The direction of the cumulative gravitational force in the τCDM scenario wanders erratically over the sky as we move further out from the local volume. This differs from the situation in the ΛCDM samples, where we observe a consistent, systematic and coherent convergence towards the final dipole direction.

The above results confirm the fact that the external tidal velocity field can be well characterized by its main multipole components, the bulk flow and velocity shear. This depends to some extent on the

cosmology. In terms of multipole amplitude convergence, these results show a better agreement for the ΛCDM than for the τCDM model.

2.9 Conclusions

In this work we have applied the FAM technique to construct model velocity fields using mock catalogs resembling the NBG and IRAS-PSC*z* galaxy catalogs. The mock catalogs were extracted from *N*-body simulations in which the central observer mimics some of the properties of the Local Group environment. Comparing FAM velocities obtained from the NBG mock catalogs with those obtained from the larger PSC*z* mock catalogs and, finally, to the *N*-body velocities, allowed us to quantify the importance of the gravity field generated by the mass distribution within and beyond the LS.

Neglecting the mass distribution outside the LS leads to a systematic underestimate of the gravity field. The amplitude of this bias depends on the amount of power on scales larger than the LS, and thus on the cosmological models. In a τCDM universe model peculiar velocities are $\sim 20\%$ smaller than the true ones. In the case of a ΛCDM model, which has more power on large scales, model velocities are underestimated by $\sim 35\%$.

The results of the described FAM analyses are encouraging in the sense that the presently available all-sky, flux limited catalogs such as PSC*z* appear to be capable of accounting for the major share of the velocity field on the scale of the Local Supercluster. While the 30 h^{-1}Mpc restricted NBG sample showed a substantial deficiency in its capacity to generate the local cosmic motions, in particular in the case of the ΛCDM Universe models, in both cases the 100 h^{-1}Mpc mock samples appear to embody nearly all matter concentrations responsible for the generated velocities in our local (NBG catalog) neighbourhood.

Also we notice a telling difference between the performance of both FAM_{30} and FAM_{100} reconstructions for the case of the ΛCDM cosmology catalogs on the one hand and the τCDM model catalogs on the other hand. The fact that the ΛCDM model involves substantially more power on large scales, $r > 30\ h^{-1}$Mpc, than the τCDM model is reflected in the better quality of the FAM_{30} reconstructions for the τCDM catalogs. The presence of substantial mass inhomogeneities with a scale in excess of that of the local Universe regions implies a larger external contribution to the local velocity field. This is also borne out by the fact that for the ΛCDM catalogs we see a considerable improvement in velocity field reconstruction quality going from the FAM_{30} to the FAM_{100} reconstructions (see Table 2.4), while this is far less so for the τCDM catalogs.

Of course, whether the resulting models do indeed form an unbiased representation of the actual velocity field will to some extent also depend on whether the galaxy distribution in the flux limited galaxy catalogs does represent an unbiased reflection of the actual (external) mass distribution surrounding the Local Supercluster resembling region. The results of recent studies (Verde et al. 2002; Lahav et al. 2002; Tegmark et al. 2001) are quite encouraging in this respect. They seem to indicate, certainly on scales larger than $\approx 5\ h^{-1}$Mpc, that both IRAS and 2dF galaxies trace the underlying mass distribution in an unbiased fashion.

Nonetheless, observations along the lines of the presented mock catalogs seem to suggest that a proper analysis of Local Universe dynamics based on a combination of information of local small-scale (peculiar) galaxy velocities and a rough yet well-founded idea of the matter distribution on scales of a few hundred 100 h^{-1}Mpc may help us towards acquiring far more insight into the dynamical history of the emergence and assembly of the striking nonlinear patterns we have discovered in the large scale matter distribution. Moreover, we have uncovered evidence that a meticulous point-to-point analysis of such velocity samples may help towards modelling the total local force field, including a proper model for the external forces.

When modeling the peculiar velocity of a LS look-alike region by only considering the matter distribution within 30 h^{-1}Mpc, the end product is a biased velocity field lacking of any large scale signature. This bias can be eliminated by accounting for the mass distribution beyond the LS. Our experiments demonstrate that sampling the mass distribution out to scales of 100 h^{-1}Mpc, in a flux

limited fashion, is sufficient to account for the large scale contribution to the peculiar velocities in our cosmological neighborhood. More precisely, we have found that the cosmic velocity field within the LS, modeled by FAM using the mass distribution traced by PSC*z* galaxies out to 100 h^{-1}Mpc is unbiased. The differences between true and FAM velocity field are random and mainly occur in high density environments which are dominated by virial motions that are not modeled correctly by FAM.

The gravity and velocity fields generated by the mass distribution beyond the scale of the Local Supercluster are well characterized by their bulk flow and shear components. Therefore, one can obtain an unbiased model velocity field by superimposing a local model velocity field within the Local Supercluster to the bulk flow and shear components of the velocity field generated by the mass distribution between 30 and 100 h^{-1}Mpc.

These considerations suggest that velocity models which only consider the dynamics within the Local Superclusters (e.g. that of Shaya et al. 1995), might have been affected by systematic errors. In particular, our work suggests that, when compared with observed velocities, they might have underestimated the value of the density parameter, Ω_m, by $15-25\%$. A more precise evaluation of this bias will be performed in a future work in which we will perform the same analysis presented here using a new set of mock catalogs that are constrain to reproduce the distribution of the mass in our local Universe (see e.g. van de Weygaert & Hoffman 2000; Mathis et al. 2002; Klypin et al. 2003).

Furthermore, our analysis shows that all model velocity fields of the Local Supercluster which are based on the PSC*z* catalog (e.g. Branchini et al. 1999; Schmoldt et al. 1999; Valentine et al. 2000; Sharpe et al. 2001) are free from systematic biases arising from having neglected the large scale contribution from scales beyond its realm. Moreover, since the IRAS PSC*z* survey is considerably deeper than 100 h^{-1}Mpc, it is reasonable to assume that the PSC*z* catalog can be used to predict unbiased velocities well beyond our Local Supercluster. The plausibility of this hypothesis has been recently confirmed by the analysis of Hoffman et al. (2001) that shows that the bulk and shear components of the external velocity field in the local universe inferred from the peculiar velocities in the Mark III catalog (Willick et al. 1997b; Willick & Strauss 1998) are qualitatively consistent with those expected from the mass distribution traced by IRAS PSC*z* galaxies. On the other hand, the claim on the basis of the SMAC cluster peculiar velocity sample (Hudson et al. 2004) of an extra 225 km s^{-1} bulk flow component generated by matter concentrations on a scale exceeding 100 h^{-1}Mpc should issue some caution with respect to claims of having accounted for all external influences on the local cosmic flow.

Coupling the local velocity model provided by FAM to the large scale contribution provided by linear theory allows to obtain a model velocity field which is unbiased, nonlinear and fast to compute. This means that, for the first time, we are in the position of performing a large number of experiments aimed at studying the nonlinear evolution of cosmic structures, such as filaments and clusters, and explore the role of tidal fields during their gravitational collapse. This relates to the observation that filaments are forming as a consequence of anisotropic collapse, induced a compressional tidal force acting perpendicular to the "axis" of the filament. By tracing out the coherent paths of the compressional modes of the primordial tidal field one can identify the sites of the later nonlinear filaments (Bond et al. 1996; van de Weygaert 2002). In turn this is directly related to cluster locations: the strong primordial tidal shear is the result of a local quadrupolar mass distribution. The corresponding overdensities tend to evolve into rich clusters, explaining the intimate link of clusters and filaments in the cosmic web.

Finally, it is worth stressing that in this work we have neglected the fact that we measure galaxy redshifts rather then positions. By means of an elegant formalism, Phelps (2000) demonstrated the feasibility of working out the action principle in redshift space. With respect to FAM, Nusser & Branchini (2000) have shown that it can be easily implemented in redshift space and Branchini, Eldar, & Nusser (2002) demonstrated that it performs equally well in real and redshift space. Therefore, our unbiased, nonlinear model velocity field also allows to perform an accurate correction for redshift space distortions and thus lead to a precise reconstruction of the mass distribution in real space. Mapping the mass in the local universe down to nonlinear scales and comparing it with the distribution of baryonic mass (in form of stars or diffuse, ionized gas) is of considerable astrophysical interests as it will constrain and help understanding the process of galaxy formation and evolution within the Universe

Acknowledgments

The authors thank Shaun Cole for allowing the use of his N-body simulations. E.R.D. thanks W. E. Schaap for stimulating discussions. E.R.D. thanks the Università di Roma TRE for its hospitatility while part of this work was done. E.R.D. has been supported by The National Council for Research and Technology (CONACyT, México) through a scholarship. San Crispino provided unique and inspiring guidance.

3

Dipole & Quadrupole moments of the local cosmic velocity field

E. Romano-Díaz, R. van de Weygaert, E. Branchini & Y. Hoffman.

We have compared the bulk flow and velocity shear components of reconstructed peculiar velocity fields with respect to the expected values within a volume of 60 h^{-1}Mpc centred at the Local Group. The velocity reconstructions were performed by means of the Zel'dovich approximation, linear theory and our implementation of the Least Action Principle, FAM. The velocity fields where extracted from mock galaxy catalogs that mimic as close as possible the real mass distribution up to 150 h^{-1}Mpc from the Local Group from constrained $N-$body simulations of our nearby Universe. These catalogs were constructed to sample properly the LS region (30 h^{-1}Mpc), and the large scale structure following the selection function from the PSC*z* catalog ($30-150$ h^{-1}Mpc). Our mock catalogs successfully reproduce the main structures of our nearby cosmic region such as, the Local Supercluster, Great Attractor, Perseus-Pisces supercluster, Coma, Cetus. The reliability of the catalogs was assessed by computing their dipolar moment of the mass distribution. The velocity component's comparison show that the 3 methods give similar results (provided a smoothing procedure) and consistent with the expected values within the 1σ errors. However, the FAM technique proved to give more accurate and reliable results along the whole range in distances than the other two methods, proving in this way to be the *tool* to study the dynamics of the Local Group and the Local Supercluster.

3.1 Introduction

Within the Gravity Instability [GI] scenario for the growth of cosmic structures, the peculiar velocity field of galaxies provides a direct and reliable probe of the matter distribution, under the natural assumption that these objects are unbiased tracers of the large scale, gravitationally induced, velocity field. Furthermore, since peculiar velocities are non-local and have contributions from many different scales and regions, their respective analysis provides information on regions not covered by the data, e.g. the Zone of Avoidance (e.g. Kolatt et al. 1996; Zaroubi et al. 1999), and on scales larger than the sampled regions (Hoffman et al. 2001).

The present large scale structures of our Universe and their motions are due to the growth of gravitational instabilities from an initially homogeneous Gaussian density field. This implies that peculiar velocities at early epochs were negligible. Under this assumption, the peculiar velocity of cosmic regions like our Local Group is mainly due to the gravitational pull of the mass distribution surrounding them.

An important characteristic of the peculiar velocity field is that if GI is valid, then the large scale velocity field is expected to be irrotational, i.e. $\nabla \times \mathbf{v} = 0$. Any vorticity mode would have decayed during the linear regime as the Universe expanded, and based on Kelvin's circulation theorem the flow remains vorticity-free (irrotational) in the quasi-linear regime, even in the presence of nonlinearities, provided these are not so large as to cause dissipative processes (e.g. Peebles 1990; Dekel 1994). This property of the velocity field will prove to be very useful along this chapter.

The dipole anisotropy of the cosmic microwave background (CMB) radiation is generally interpreted as a Doppler effect due to the motion of the Sun with respect to the CMB rest frame. The velocity of the Local Group [LG, hereafter] is now well determined from *COBE* (Kogut et al. 1993), 627 ± 22 km s^{-1} toward $l = 276 \pm 3°$, $b = 30 \pm 3°$. Less well known is the depth and degree to which nearby galaxies share in this motion and the scales and amplitudes of the mass fluctuations responsible for the flow. The boundaries of the LG are not very clear and they change from study to study. A common one is to consider a spherical volume of radius of 5 h^{-1}Mpc around the galaxy-pair-system: Milky way - Andromeda. A dynamical definition is given by determining the zero-velocity surface separating the LG from the local Hubble expansion flow. With a total mass of $\sim 3 \times 10^{12}$ $M_\odot$, and an internal velocity dispersion ~ 60 km s^{-1} (Sandage 1986), such a region has a radius ~ 1.8 h^{-1}Mpc.

Provided that the acceleration is dominated by long wavelength modes, implying that linear theory is applicable, the velocity and acceleration vectors should be parallel with a constant of proportionality from which we may determine the density parameter Ω_m. In biased theories of galaxy formation light does not trace mass, but on large scales at least the fluctuations on light should be proportional to the underlying fluctuations in mass, so one can still expects that the velocity and gravity vectors to be parallel, but now the constant of proportionality is the *bias* parameter b.

The analysis of peculiar velocities plays a major role in Cosmology and the formation of structure in the Universe. Some of the most important goals of peculiar velocity fields and their surveys are the confirmation of the gravitational instability picture, the determination of Ω_m, to find whether initial fluctuations were Gaussian, if so, then if the power spectrum was scale-invariant, and the characterization of the mass distribution on very large scales. Because of shot noise, existing redshift surveys cannot account properly for fluctuations at distances larger than 150 h^{-1}Mpc. Nevertheless, large amplitude coherent peculiar velocities on very large scales can be detected at such distances with modest samples (e.g. Lauer & Postman 1994; Dekel 1994). This is one of the most important features of peculiar velocities, the detection of large scale flows (dipole) due to matter concentrations. Hence, the peculiar velocity field of galaxies and clusters provides a direct and reliable probe of the matter distribution, under the natural assumption that these objects are unbiased tracers of the large-scale, gravitationally induced, velocity field. In order to measure peculiar velocities of galaxies, observers use a variety of distance indicators. In general, these indicators relate two quantities, one of those is distance dependent (*e.g.* galaxy luminosity), and the other one is distance independent (*e.g.* galaxy rotational velocity). The best known examples of such relations are the Tully-Fisher (Tully & Fisher 1977) and Faber-Jackson (Faber & Jackson 1976) relations, although in the last decade many others

distance indicators have been employed to measure cosmological distances (e.g. SNIa, Cepheids, etc.). The availability of an increasing number of galaxy peculiar velocity catalogs, some of them with few thousand objects, have turned cosmic flows to one of the main probes used to study the large scale structure in the nearby Universe.

On scales large enough, where the dynamics is dominated by gravity and the deviations from homogeneity are small, the velocity field reflects the dynamical evolution of structure and the total underlying mass distribution, observed and unobserved. On more nearby and shorter scales, it can serve to help us to understand the dynamics of our own Local Group and to realize the role and influence of the large scale structure over the LG. One way to achieve these goals is by *reconstructing or modelling* the full dynamical structure in the local cosmic neighborhood.

Spatial variations in the mass distribution in our Universe induce (as a consequence) variations in the gravitational force field measured by an observer. These, in turn, induce a peculiar velocity field characteristic of this particular cosmic region, hence exhibiting corresponding spatial variations, which are manifested as a velocity shear.

Our Local Group is located in a very peculiar cosmic location in our Universe. Indeed, as it has been shown by different analysis of surveys (e.g. IRAS 1.2 Jy, MARK III, etc.), the LG is situated at a saddle point between two huge structures, from one side, the Great Attractor [GA], and at the opposite site the Perseus-Pisces supercluster [PP]. Furthermore, the LG is just at the edge of a bridge connecting these two structures, the Local Supercluster [LS]. Even more amazing is the fact that all these structures reside almost along the same plane, the supergalactic $x-y$ plane. This particular and unique situation gives a special flavour to the dynamics of the LG. Within this large scale mass configuration, the LG moves towards the direction of the GA.

The influence of the structures conforming the LS, more in concrete the Virgo Cluster, over the dynamics of the LG is of considerable importance. There is a net peculiar motion of the LG towards Virgo, known as the *Virgocentric infall* (see Pierce & Tully 1988). This motion accounts for $\sim 46\%$ of the total amplitude of the LG motion (Davis & Peebles 1983b). The LS has the shape of a wall located right in front of the LG at the $x-y$ supergalactic plane, and at a distance of about 15 h^{-1}Mpc. The LS is similar in shape to a flattened ellipse (pancake), with the Virgo Cluster near its center its extent in the longest direction is about $40-50$ h^{-1}Mpc.

The fact that galaxies within a volume enclosing the LS seem to fall into Virgo is a mere coincidence. They are directed towards a rather central, wide region of the LS which coincides with the positions of the Virgo cluster and the Ursa Major cluster (Burstein et al. 1990). It has been measured that galaxies within the plane of the LS are falling towards this central region with velocities that increase with distance outward. The LG, which lies near the edge of the LS, has a velocity ~ 300 km s^{-1} to its centre, but only 150 km s^{-1} is directed towards the central region of the LS.

Lilje, Yahil, & Jones (1986), estimated that at the LG location the velocity shear had a value ~ 200 km s^{-1} with respect to the Virgo cluster. They argued that the source of this shear had to be a considerable mass concentration at a distance of ~ 3 times the distance to the Virgo cluster. This study uncovered the source of our local velocity flow, the Great Attractor, from a sample of peculiar velocities of galaxies within a radius of 60 h^{-1}Mpc around the LG. Hoffman et al. (2001) reconstructed the tidally induced component of the cosmic velocity field out to a distance of 60 h^{-1}Mpc. Their results revealed that the Shapley supercluster is a major tidal source even at scales of ~ 140 h^{-1}Mpc, although it is not the only relevant external perturbation. With a constructed toy model composed by a big mass concentration (Shapley supercluster), and two voids, they were able of fitting the observed results given by the Mark III catalog (Willick et al. 1997a) and SFI data (Haynes et al. 1999b).

Several methods for modelling peculiar velocity fields from galaxy positions have been proposed in the last decades. Most of these methods fail in reproducing the velocity fields even at mildly non-linear regions, being their predictions only valid at the linear regime. Hence, the success of the methods is limited by the results of linear theory or some first order approximation (Zel'dovich approx.). The necessity of an algorithm capable of dealing with the mildly non-linear regime and predicting/reconstructing/modelling bias-free peculiar velocity fields is of great importance. Such a method would help us to understand in a more consistent, systematic and complete way, the inter-

play between the different structures that shape the portion of Universe under study, our local cosmic neighborhood. Furthermore, it would allow us to make more realistic estimates of the real velocity field even at the mildly non-linear regime without loosing generality by applying large smoothing procedures. A method that has proved to be able to overcome the problems mentioned above is the Fast Action Minimization algorithm [FAM] (Nusser & Branchini 2000). This method is a very efficient implementation of the Least Action Principle introduced by Peebles (1989, 1990). Some of its advantages over other methods are the capability to deal with a large number of objects, an efficient computing gravity method (making it as a consequence a fast method), and the ability to deal with the mildly non-linear structures (clusters and superclusters of galaxies).

In this Chapter we will address two main questions. The first one is how well we can construct synthetic mock galaxy catalogs from specific purpose constrained $N-$body simulations aimed to mimic as close as possible our nearby Universe. We will assert the degree of confiability by computing one of the most characteristic statistical quantities, the gravity dipole. After having asserted the reliability of our mock catalogs, we will ask ourself how well we can recover the main characteristics of the peculiar velocity field of galaxies from the galaxy mocks even at the mildly non-linear regime, the bulk flow and shear velocities. To do so, we will apply two standard reconstruction techniques: linear theory and Zel'dovich approximation, together with the FAM technique presented in Chapter 2. We will compare the estimated modeled velocity quantities with respect to those from the real velocity field. We will show that the estimates derived with the FAM algorithm are in good agreement and closer to the real measured bulk flow and shear velocities than the ones computed by means of the linear and Zel'dovich approximations.

We will assume in this Chapter that the motion of our Local Group has been generated by gravitational perturbations. Because of these reasons and in order to minimize errors like the *"Kaiser effect"* (Kaiser 1987), we will simplify our approach by working in *"real"* space instead of *redshift* space.

A very important quality of our analysis is that we attempt to model as realistically the actual observations by using constrained simulations of our nearby Universe. For this reason, we will limit our analysis up to distances of 60 h^{-1}Mpc from the LG location.

3.2 Theoretical framework

In linear perturbation theory, initial peculiar velocities are damped by the expansion of the universe, and the peculiar velocity field $\mathbf{v}(\mathbf{x})$ is directly proportional to the gravitational acceleration due to the matter distribution around the position $\mathbf{x}$ (Peebles 1980). We can express such acceleration due to matter with density contrast $\delta(\mathbf{x})$ in a given volume like:

$$\mathbf{g}(\mathbf{x}) = \frac{3}{4\pi}\int \mathrm{d}\mathbf{x}\,\delta(\mathbf{x})\frac{\mathbf{x}'-\mathbf{x}}{|\mathbf{x}'-\mathbf{x}|^3}\ . \tag{3.1}$$

The acceleration $\mathbf{g}$ is related to the peculiar velocity according to the relation (Peebles 1980):

$$\mathbf{v}(\mathbf{x}) = \frac{1}{3}\,f\,H_0\,\mathbf{g}(\mathbf{x}), \tag{3.2}$$

where H_0 is the Hubble constant measured in units of $100h$ km s^{-1} Mpc^{-1}. The quantity $f = d\ln D/d\ln a$ is the logarithmic derivative of the amplitude of the growing mode of density perturbations with respect to the scale factor a. This factor carries information about the underlying cosmological model, and is related to the cosmological matter density parameter Ω_m, cosmological constant Ω_Λ and z (redshift). A common approximation is given by $f(\Omega_m) \approx \Omega_m^{0.6}$ (Peebles 1980), while a more complete approximation in the general case at $z = 0.0$ is given by Lahav et al. (1991)

$$f(\Omega_m,\Lambda) = \Omega_m^{0.6} + \frac{\Omega_\Lambda}{70}\left(1+\frac{1}{2}\Omega_m\right). \tag{3.3}$$

In the present study, we will adopt this form for being the most complete approximation for f.

Following Eqn. 3.2, the peculiar velocity field $\mathbf{v}(\mathbf{x})$, and the linear mass density contrast $\delta(\mathbf{x})$, are then related to one another according to the local differential relation (the continuity equation)

$$\nabla \cdot \mathbf{v}(\mathbf{x}) = -H_0 \, f \, \delta(\mathbf{x}) \,, \tag{3.4}$$

which has as a solution or global (integral) representation, valid under the GI regime for an irrotational field

$$\mathbf{v}(\mathbf{x}) = \frac{H_0 f}{4\pi b} \int \mathrm{d}\mathbf{x} \, \delta(\mathbf{x}) \frac{\mathbf{x}' - \mathbf{x}}{|\mathbf{x}' - \mathbf{x}|^3} \,, \tag{3.5}$$

where b is the "linear biasing" factor, which transforms the observed galaxy density into a mass density: $\delta_{gal} = b\,\delta_{mat}$. Along this analysis we will make the assumption that b is constant, independent of position or smoothing scale. Notice that the peculiar velocity field is determined by the distribution of the matter with all its components, especially by the dominant dark matter component.

It is well known that the peculiar velocities of nearby galaxies are not randomly oriented but they rather participate in a coherent flow (bulk motion) together with our LG, at least for a volume of radius $\sim 60\ h^{-1}$Mpc. However, there should also exist velocity components related to the linear and non-linear local dynamics of each region acting over the nearby galaxies and cluster of galaxies. In this way, we can understand peculiar velocities as a composition of several modes coming from the large scale distribution which will be reflected in a coherent flow and local contributions.

When expanding the peculiar velocity field in a multipolar decomposition, the first component is related to the Hubble expansion, this monopole term introduces a "breathing mode" which affects the Hubble expansion within the volume, hence having no measurable effect. The second term is the dipolar moment, this term presents a very coherent pattern within the sample that disappears when considering peculiar velocities relative to a central observer instead of absolute velocities. This term is known as the **"bulk flow"**. The next term in the velocity expansion is the quadrupole, which effects rapidly decrease with distance. This component of higher order in the decomposition is the outcome of the linear and non-linear configuration of the mass distribution. In the case of the peculiar location of the LG (as shown in Figs. 3.3, 3.4 & 3.5), the configuration between the GA and PP introduces a distortion pattern in the peculiar velocity field, plus the influence of the LS. This term is well known like the **"shear"** velocity. The other higher order terms will be related to the highly non-linear regime (e.g. cluster dynamics). The influence of these terms will be very local because of their strong dependence in distance. So, we can fit a model to the several components that conform the velocity field of the sort:

$$\mathrm{v}_i(\mathbf{x}) = \mathbf{V}_{bulk,i} + \varsigma_{ij}\hat{x}_i + O(\mathbf{x}) \,, \tag{3.6}$$

where i, j refer to the 3 Cartesian components and $\hat{x}_j$ refers to the distance component along the j direction. $\mathbf{V}_{bulk}$ represents the bulk component, and ς_{ij} is the second order velocity component, the other higher terms are included in $O(\mathbf{x})$.

Before proceeding, we want to make a distinction between the dipolar moment computed from the mass distribution and the one computed from the peculiar velocity field; we will call **dipole** to the quantity inferred from the mass distribution, while we will call **bulk flow** the one obtained from the velocities.

3.2.1 The velocity bulk flow

The Bulk flow is defined as the average streaming motion within certain volume. The motion direction and amplitude of this bulk flow on different scales are the simplest quantities to measure from peculiar velocity data. Nevertheless, they provide constraints on the power-spectrum of mass fluctuations. Theoretically, the mean square bulk velocity within a sphere of radius R, is given by,

$$\langle \mathrm{v}^2(R) \rangle = \frac{H^2 f^2}{2\pi^2} \int_0^\infty P(k) \tilde{W}^2(kR) \, \mathrm{d}\mathbf{k} \,, \tag{3.7}$$

where $P(k)$ is the mass fluctuation power spectrum and $\tilde{W}(kR)$ is the Fourier transform of a top-hat window of radius R. The *rms* expected bulk velocity is then given by,

$$V_b(R) = \sqrt{\langle \mathrm{v}^2(R) \rangle}. \tag{3.8}$$

It is interesting to compare the fluctuations in the bulk flow velocity within a sphere of radius R with the corresponding mass fluctuations within the same sphere,

$$\left\langle \left(\frac{\delta M(R)}{M(R)} \right)^2 \right\rangle = \frac{1}{(2\pi)^3} \int_0^\infty P(k) \tilde{W}^2(kR) \, \mathrm{d}\mathbf{k}. \tag{3.9}$$

Both Eqns. 3.8 and 3.9 differ with two powers of k in the integrand. This means that the peculiar velocity field on a given scale is more sensitive to components of the power spectrum on larger scales than is the density field, and thus is a useful probe of the large scale power. Therefore, the *rms* velocity includes contributions from much larger scales than do the *rms* mass fluctuations (dipole).

In practice, the bulk flow is computed from velocity surveys in the following way; let v_i be the radial peculiar velocity of the ith galaxy in the sample and ϵ_i the uncertainty on that quantity. The bulk flow vector $\mathbf{V_b}$ will be obtained from minimizing the merit function (e.g. Lynden-Bell et al. 1988)

$$\chi^2 = \sum_i w_i \left(\frac{\mathrm{v}_i - \mathbf{V_b} \cdot \hat{\mathbf{x}}_i}{\epsilon_i} \right)^2, \tag{3.10}$$

where $\hat{\mathbf{x}}_i$ is the unit vector in the direction of the ith galaxy, w_i is a weight given by the selection function of the sample, and ϵ_i is obtained from the distance indicator used in the catalog (*e.g.* Tully-Fisher, SNIa, Faber-Jackson relations, etc.)

3.2.2 The velocity shear

The second term in the expansion of the peculiar velocity field is conformed by 3 components and it can be expressed as:

$$\varsigma_{ij} = \frac{\partial \mathrm{v}_i}{\partial x_j} = \Theta \frac{\delta_{ij}}{3} + s_{ij} + \omega_{ij}, \tag{3.11}$$

in the matrix representation of this tensor we can understand them as 3 different components: the symmetric part, trace, and antisymmetric part. ω_{ij} represents the antisymmetric part, known as the *vorticity* term, but because we have assumed that the peculiar field is irrotational, this term is equal to zero. The trace-free symmetric part s_{ij} is the *shear tensor*. Θ accounts for possible local isotropic perturbations about the Hubble expansion (δ_{ij} is the identity matrix), and it represents the *divergence* of the velocity field $\Theta = \nabla \cdot \mathbf{v}$.

The gravitational source of ς_{ij} is the tidal field determined by the structures surrounding the observer. In the case of the LG the possible structures responsible for this cosmic shear are mainly: the GA, PP, Coma, Cetus, the local void.

3.3 Setting the environment: Initial conditions

Because we are interested in studying how well we can model the main components of the peculiar velocity field of our cosmic neighborhood, we not only demand that the $N-$body simulations should resemble the statistical properties of our "real" Universe, but also should be able of reproducing the distribution and spatial configuration of matter at linear and weakly non-linear scales. The standard approach for producing the desired realizations is to assume a cosmological model and to use the appropriate primordial power spectrum to construct a random realization of the density field within a desired simulation volume and to evolve them via $N-$body machinery. This method was followed in

Chapter 2. An alternative approach is to find a way of producing simulations which reproduce and mimic the matter distribution at large and intermediate scales of our real Universe. Our intention is to reproduce the matter distribution as close as possible up to considerable large volumes ($\gtrsim 60\ h^{-1}$Mpc) as revealed by the actual large scale surveys. This can be done by setting up the initial density fields by constrained realizations of Gaussian fields (Bertschinger (1987); Hoffman & Ribak (1991) and its implementation van de Weygaert & Bertschinger (1996)), thereby constructing the density and velocity fields in such a way that both agree with the observed large scale structures and the assumed cosmological model. This procedure is usually referred as *"constrained simulations"* [CS, hereafter]. For these reasons, we have adopted this technique for the present study. In the following subsections we will introduce the procedure of the CS while a more rigorous and complete mathematical description can be found at the end of this chapter (Appendix 3.A and 3.B) and Chapter 8.

3.3.1 Constrained Simulations

CSs have been performed in the past by several authors with the purpose of investigating several properties of our local Universe (Kolatt et al. 1996), the morphology of the density field and dynamics (Klypin et al. 2003), the coldness of the local flow (van de Weygaert & Hoffman 1999), the formation of the local galaxy population (Mathis et al. 2002), etc. Nonetheless, none of the previous studies have tackled the problem of the kinematics of the LG & LS and its origins, the origin of the bulk flow velocity, the structures responsible for this motion and their influence range.

Within the GI scenario, the primordial perturbations responsible for the large scale structure constitute a Gaussian Random field, which is defined by its power spectrum and a normalization power. It is assumed that in these random fields, the density peaks are the progenitors of objects like galaxies and clusters, while their minima will correspond to the centers of voids. The theory specifies only the statistical properties of the amplitudes and phases in the plane waves representation. Thus, for Gaussian fields the real and imaginary parts are independently normally distributed around zero with a variance given by half of the power spectrum, which implies that the phases are uniformly distributed. This is being used in setting up the initial conditions for large $N-$body simulations. Nevertheless, there are many interesting problems where one is interested in generating special-purpose initial conditions, which are designed to obey some given constraints (see van de Weygaert & van Kampen 1993; van Haarlem & van de Weygaert 1993; van de Weygaert & Babul 1994). This is the case for the present Chapter where we are interested in modelling the main components of the velocity field of our Local Universe. A very successful tool for reconstructing the Large scale structure of our Universe and setting up the initial conditions that prevailed at the primeval Universe is the combined use of the Wiener filter (Wiener 1949; Rybicki & Press 1992; Lahav et al. 1994; Bond 1995; Fisher et al. 1995b; Zaroubi et al. 1995, 1999) and Constrained Realizations (Bertschinger 1987; Hoffman & Ribak 1991; van de Weygaert & Bertschinger 1996).

The present available redshift and radial velocity surveys provide us with relevant information that enables the reconstruction of the large scale mass distribution of our nearby Universe. An efficient algorithm for reconstructing such density and velocity fields from incomplete, sparse and noisy data from observations is provided by the formalism of the Wiener filter (WF, Lahav et al. 1994; Fisher et al. 1995b; Zaroubi et al. 1995, 1999). The application of the WF requires some model for the power spectrum that defines statistical properties of the perturbation field. In particular, this method holds on scales where the linear theory is valid and the underlying perturbation field is Gaussian.

The Wiener filter provides an optimal estimator of the underlying field in the sense of a minimum-variance solution given the data (*e.g.* peculiar velocity data) and an assumed prior model. The *prior* defines the data autocorrelation and the data-field cross-correlation matrices. In the case where the data are drawn from a random Gaussian field, the WF estimator coincides with the conditional mean field and with the most probable configuration given the data. In the case of Gaussian fields where quadratic entropy can be assigned, the WF also coincides with the maximum entropy solution (Zaroubi et al. 1995).

The WF is a very conservative estimator, in the absence of good data (regions where the data

is sparse and/or noisy) it attenuates the estimate toward its unbiased mean field. This means that by construction the WF suppresses some of the power spectrum that is otherwise predicted by the assumed model. As a consequence the WF often produces an estimated field that is much smoother than the typical random realization of the assumed power spectrum would be. Furthermore the WF estimator is not statistically homogeneous. A way of providing the missing power and regaining statistical homogeneity consistent with the data and the theoretical model is provided by the method of Constrained Realizations [CR] of Gaussian fields (Bertschinger 1987; Hoffman & Ribak 1991; van de Weygaert & Bertschinger 1996). The CR method provides a realization of the underlying field made of two parts. The first one is dictated by the data and the model (provided by the WF approach) and the second one is random in such a way that in those places where the WF suppresses the signal, the random component compensates for it.

The WF and CR are constructed assuming that linear theory is valid on all scales. Hence, in principle it can be done with any desired resolution, even on scales that at present lie in the non-linear regime. This means that the WF/CR algorithm provides a reconstruction of how the present-day structures would appear if the linear regime is still valid.

The Initial conditions were then generated by using data on scales where the linear regime is still valid, so we could apply it to recover the large scale fluctuations and to supplement them with fluctuations due to a random realization of a specific power spectrum on small scales. These fluctuations are then extrapolated back in time using linear theory to provide the reconstruction of the initial conditions.

The WF/CR approach has been applied to several data catalogs and with different purposes: to study the two-dimensional IRAS galaxy distribution (Lahav et al. 1994), the velocity potential out of POTENT (Ganon & Hoffman 1993), the COBE/DMR cosmic microwave background mapping (Bunn et al. 1994), etc.

3.3.2 Reconstructing the Initial Density Fields

3.3.2.1 Parent catalog data

The WF/CR algorithm was applied to the MARK III catalog (Willick et al. 1997a). This catalog has been compiled from several data sets of spiral, elliptical and SO galaxies with the direct Tully-Fisher and the $D_n - \sigma$ distances. The sample consist of ≈ 3400 galaxies and provides radial velocities and inferred distances with fractional errors around $17 - 21\%$. It has an anisotropic and non-uniform density that is a strong function of the distance. The sampling of the density field is reliable out to $\sim 60\ h^{-1}$Mpc in most directions outside the Galactic plane, and out to $\sim 70\ h^{-1}$Mpc in the direction of the GA and PP. In some other directions the data extends out to $\sim 80\ h^{-1}$Mpc. The data has been corrected for the Malmquist biases. This sample enables a reasonable recovery of the dynamical fields with $\sim 12\ h^{-1}$Mpc smoothing.

The cosmological model assumed is the currently popular flat low-density cosmological model ΛCDM with $\Omega_\Lambda = 0.7$, $\Omega_0 = 0.3$, where Ω_Λ measures the cosmological constant Λ in units of the critical density and Ω_0 is the cosmological density parameter. The Hubble constant is $h = 0.7$ (measured in units of 100 km s^{-1} Mpc^{-1}) and the power spectrum is normalized by $\sigma_8 = 0.9$. The ΛCDM model assumed here is consistent with the newest and current observational constraints (WMAP Spergel et al. 2003). This model is also consistent with the radial velocity surveys including the MARK III.

Zaroubi et al. (1999) performed a detailed analysis of the Large scale structure reconstructed from the Mark III survey. The most robust features of the structures recovered from this catalog are the Great Attractor (GA), the Perseus-Pisces (PP) supercluster, the filamentary local supercluster connecting GA and PP, and the local void.

3.3.2.2 Reconstruction of the density field

The WF/CR algorithm has been applied to the MARK III catalog with the assumed cosmological model. This was done on a 128^3 grid with a grid size of 2.5 h^{-1}Mpc, thus reconstructing the density

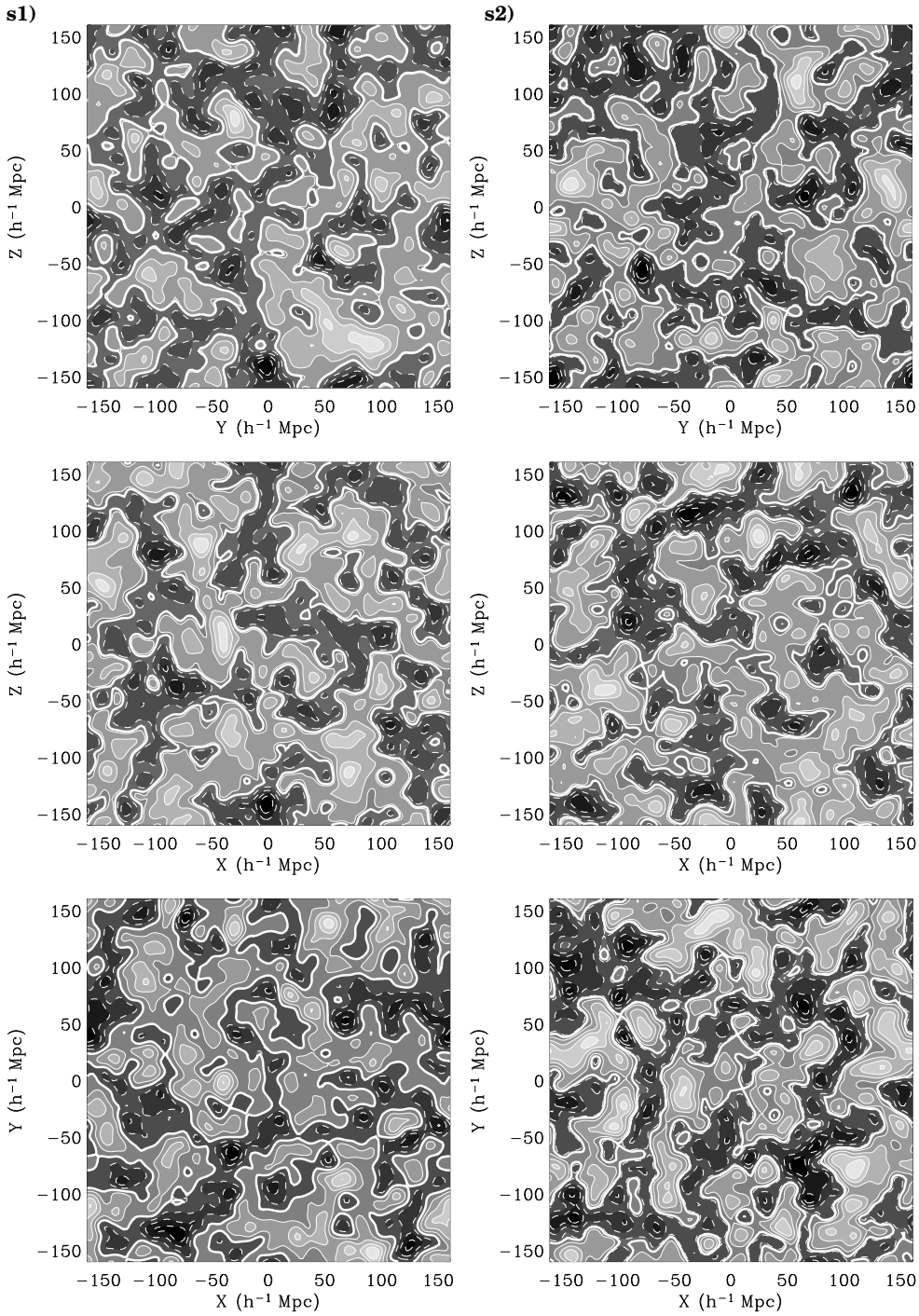

Figure 3.1 — Initial constrained density fields for two catalogs of our sample (S1 & S2). The panels show projections along the 3 supergalactic planes. The top panel corresponds to the *x*-axis projection, the middle one to the *y*-axis, while the bottom one to the *z*-axis. The density fields have been smoothed with a Gaussian filter of 5 h^{-1}Mpc radius.

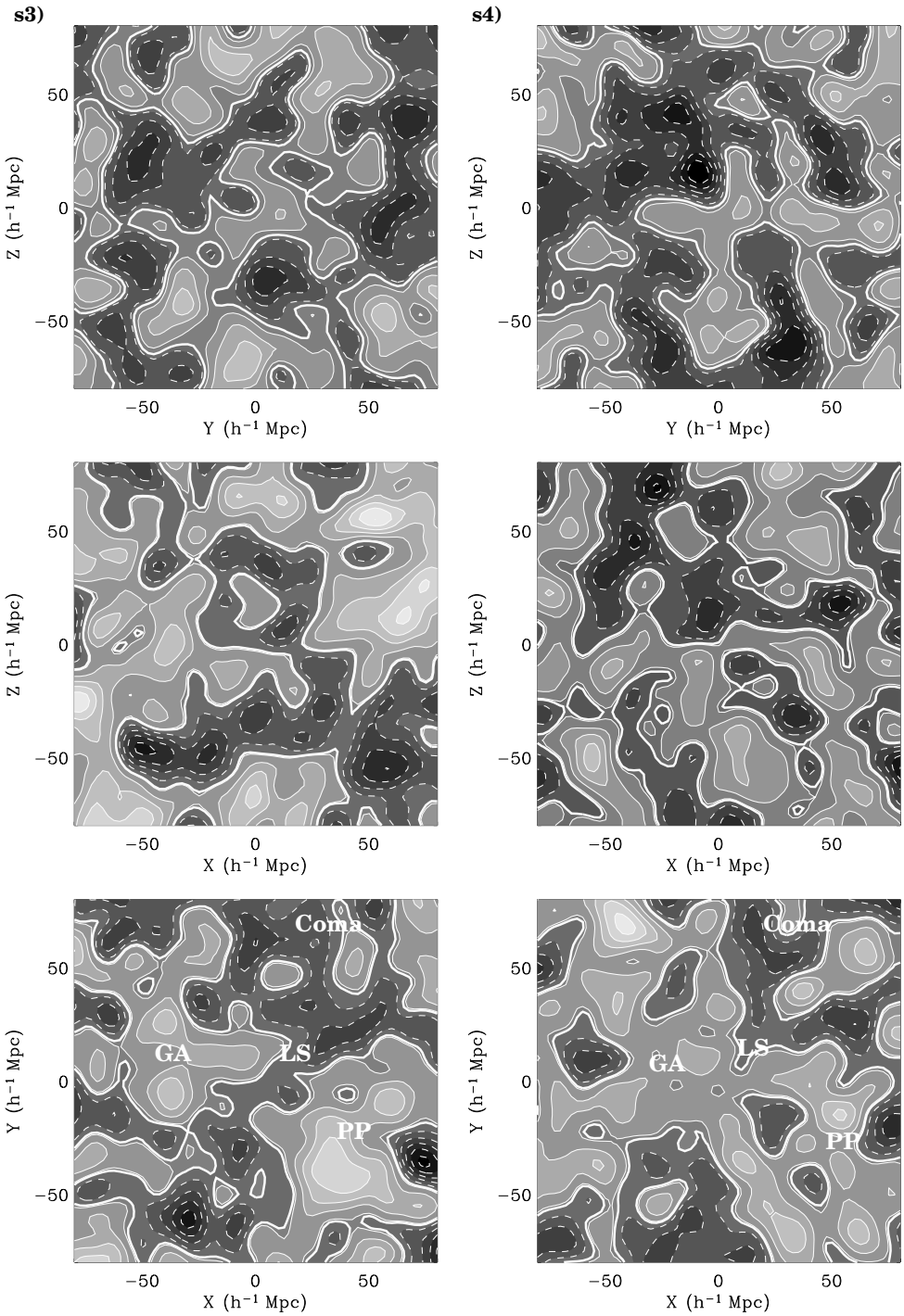

Figure 3.2 — Initial constrained density fields for the other two catalogs of our sample (S3 & S4). The panel distributions are the same as in Fig 3.1. The panels show only the central regions of the catalogs within a radius of 80 h^{-1}Mpc from the center (LG). The initial seeds of the main structures surrounding the LG can be better noticed. The density fields have been smoothed with a Gaussian filter of 5 h^{-1}Mpc radius.

and velocity field within a box of 320 h^{-1}Mpc on a side with the LG located at the center of the simulation box.

For statistical purposes we have made four WF/CR realizations. All of them have been produced for the same cosmological scenario. The variations among the CRs thus provide an interesting representation of the uncertainty in the reconstructing algorithm, and the CRs provide clear indications for the robustness of the various structures. Furthermore, this also will allow us to estimate the statistical significance of our results. In the regions where the data dominates over the noise ($\lesssim 70\ h^{-1}$Mpc), the WF maps are characterized by a high S/N (Zaroubi et al. 1999), and there is little variation between the different CRs. At small scales ($< 12\ h^{-1}$Mpc), the properties of the structures, depend on the nature of the *prior* model, hence the CRs exhibit high variations, consistent with the low S/N. All these can be better noticed in Figures 3.1 & 3.2. These figures show the linear density fields resulted from the outcome of the WF/CR algorithm after being extrapolated back in time (initial density fields). The 3 panels in each column represent projections along the 3 different supergalactic planes. Each density field has been convolved with a Gaussian kernel of $R_G = 5\ h^{-1}$Mpc. The top panel of each figure corresponds to slides which coincide with the supergalactic $y-z$ plane. The middle one to the supergalactic $x-z$ plane, while the bottom panel to the $x-y$ supergalactic plane. All slides have been centered at the Local Group position. In all plots the lines corresponds to regions of equal densities, the continues lines represent the high density regions while the broken lines to under-dense regions. The thick continues line indicates the mean density.

Figure 3.1 shows for simulations S1 & S2 the full planes $[-160, +160]\ h^{-1}$Mpc. In these plots can be noticed that the distribution and shape of structures at large scales ($> 80\ h^{-1}$Mpc from the LG, and correspond to the unconstrained random realization part of the method), differ from catalog to catalog. Still, their statistical properties will be similar because they are given by the same prior assumed cosmological model. Nevertheless, the central regions of the catalogs contain similar kind of structures which correspond to the constrained realization part of the method, these regions are strongly constrained by the data. This can be better noticed in Fig. 3.2 which shows the inner regions ($[-80, +80]\ h^{-1}$Mpc) of the initial density fields for the simulations S3 & S4. The locations of the original seeds of the massive structures like the GA and PP superclusters do not change in spatial location substantially from catalog to catalog. The conspicuousness of the density peaks and voids are also very similar between the different catalogs.

Finally, a useful feature of the WF/CR reconstruction method is that it can relate two data sets that differ in many ways. As an example it can translate velocities into densities allowing comparisons between velocity and density data, even if the data have been sampled with different resolutions and not exactly the same positions (van de Weygaert & Bertschinger 1996; Zaroubi et al. 1999).

We are aware of the fact that all constraints are within a radius of $< 80\ h^{-1}$Mpc from the LG, and that structures smaller than $12\ h^{-1}$Mpc cannot be resolved properly in the maps as a consequence of the previous smoothing procedure on the MARK III data. Beyond the $> 80\ h^{-1}$Mpc radius the velocity constraints in the local volume still work out, as the velocity is a non-local constraint. Any similarly between the structures at these ranges ($< 12\ h^{-1}$Mpc, or $\gg 80\ h^{-1}$Mpc) with the real Universe will be a consequence of the random constrain procedure, e.g. mere chance.

3.4 $N-$body simulations

3.4.1 The particle distribution

The evolution of the WF/CR initial density fields was performed by means of the public numerical code HYDRA (Couchman, Thomas, & Pearce 1995). This code uses an adaptive P^3M code as a gravity solver, and a SPH algorithm to solve the hydrodynamic equations. Here we restrict ourselves to trace only the mass distribution of our Universe. Therefore, we have performed pure $N-$body analysis carrying out simulations of dark matter alone.

The initial particle positions were interpolated from a uniform grid which covers the whole computation box of side $L = 320\ h^{-1}$Mpc. The amplitude of the initial displacements are proportional to

the computed WF/CR initial density fields. The initial velocities (peculiar velocities) are proportional to their respective displacements in accordance with the Zel'dovich approximation (Zel'dovich 1970).

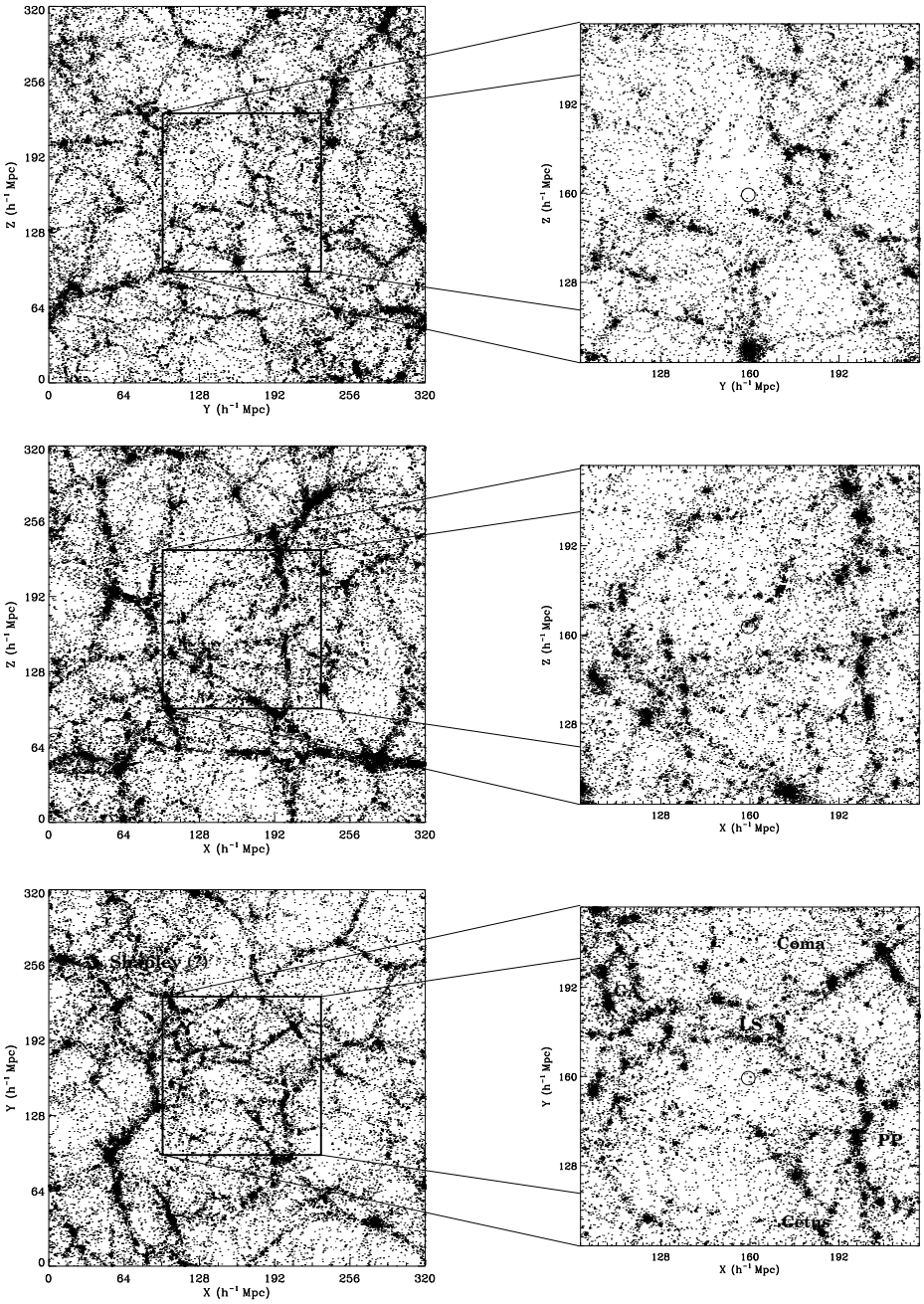

Figure 3.3 — Particle distributions along the three Supergalactic Planes for the S4 simulation at the final output time (actual time). The left-column slides are 40 h^{-1}Mpc thick while the right-side plots are zooms of the central marked areas. The top panels correspond to projections along the supergalactic *x*-axis, the middle panels to projections along the supergalactic *y*-axis, while the bottom panels to the *z*-axis projection. The LG is located at the center of each computational box and marked by a circle. The position of the main structures like GA, PP, Coma, Cetus and Shapley are also indicated.

The four simulations were started at $z = 50$ and evolved up to actual time $z = 0$ (with z being the redshift). We have started the simulations at that initial time to assure the validity and linearity of the initial input density fields.

The simulations were run with 128^3 particles of equal mass, with a mass resolution of $6.4 \times 10^{11} h^{-1} M_{\odot}$. The force computation was done on a grid of 256^3, and a spatial resolution of 25 h^{-1}kpc. Figure 3.3 shows for the S4 simulation slides of the 3 Cartesian projections centered along the 3 Supergalactic planes. The top panels correspond to projections along the supergalactic x-axis. The middle panels refer to projections along the y-axis, while the bottom panels to the z-axis projection. The left-hand boxes correspond to the full simulation box length (320 h^{-1}Mpc), and a thickness of 40 h^{-1}Mpc. The right-hand plots are zooms of the central regions. The position of the LG is marked on the zooms by the central circles. One may clearly notice how well the $N-$body simulation traces the Local Supercluster as well as the presence of the GA, PP, and similar structures like Cetus and Coma. It is interesting to notice how it seems that the LS is connected with the GA and PP superclusters. Another interesting feature is the presence of a Shapley-alike structure located at the region where the real Shapley supercluster resides, although this region correspond to the weakly constrained part of the WF/CR algorithm.

The similarities and differences between the different simulations as a consequence of the WF/CR algorithm can be better noticed in Figure 3.4, where zooms of the central regions ($[-80, +80]$ h^{-1}Mpc) of the S1 & S4 simulations are presented. For comparison purposes the fields have been convolved with different Gaussian kernels of radius $2 \& 5$ h^{-1}Mpc (S1 & S4 respectively). We have done this in order to resolve the small scale structure (S1) and the LG. Despite the different map resolutions, the similarities between the two simulations are quite remarkable; the location and geometry of the structures (peaks and voids) between the two set of maps are very similar. The prominence of the LS can be clearly seen in the z-projection of S4, and how this structure connects with the GA and PP superclusters. The presence of the Coma cluster can also be located at the top right of the z-projection, the Cetus region at the bottom central part of the same slides. We can also compare the smoothed S4 density fields with its initial density maps showed in Fig. 3.2. As can be noticed between the two set of plots, the linear regime remained almost intact, the location, prominence, shape and geometry of peaks and voids are quite similar between the 2 density fields. The final outputs of the four simulations have reproduced the Local Supercluster, the Great Attractor region, the Perseus-Pisces supercluster, the Coma cluster and the Cetus region.

The location of the LG in our nearby Universe is confirmed to be found at a saddle point of the density field between two big nearby surrounding structures, the Great Attractor and Perseus-Pisces superclusters. This situation is depicted in Figure 3.5 where surface plots of the same slides of Fig. 3.4 for the S4 simulation are presented. The plotted planes (± 60 h^{-1}Mpc) coincide with the three supergalactic planes and have a thickness of 2.5 h^{-1}Mpc. The peaks correspond to high density regions (like the GA and PP structures). The location of the LG is at the center of the plots and marked in black. Notice that the location of the LG is very close to a minima in the three projected density field surfaces.

3.5 Observing the simulated Universe: Mock catalogs

Our aim is to study how well we can model the main characteristics of the full, real local cosmic peculiar velocity field. For these reasons we construct mock galaxy catalogs from the final output of the $N-$body simulations aimed to resemble the real mass distribution as revealed by galaxy surveys. For statistical purposes, we have produced four sets of mock catalogs, one set from each $N-$body realization. We follow the mock catalog procedure presented in Chapter 2 (Sect. 2.5.2). The only difference is that this new set of mock catalogs extends up to volumes of 150 h^{-1}Mpc. We will only mention here the main characteristics of the catalogs.

Each catalog consists of two different sampled regions. The first one (internal region) is a volume-limited sample and is aimed to trace the mass distribution within a region of 30 h^{-1}Mpc, mimicking the

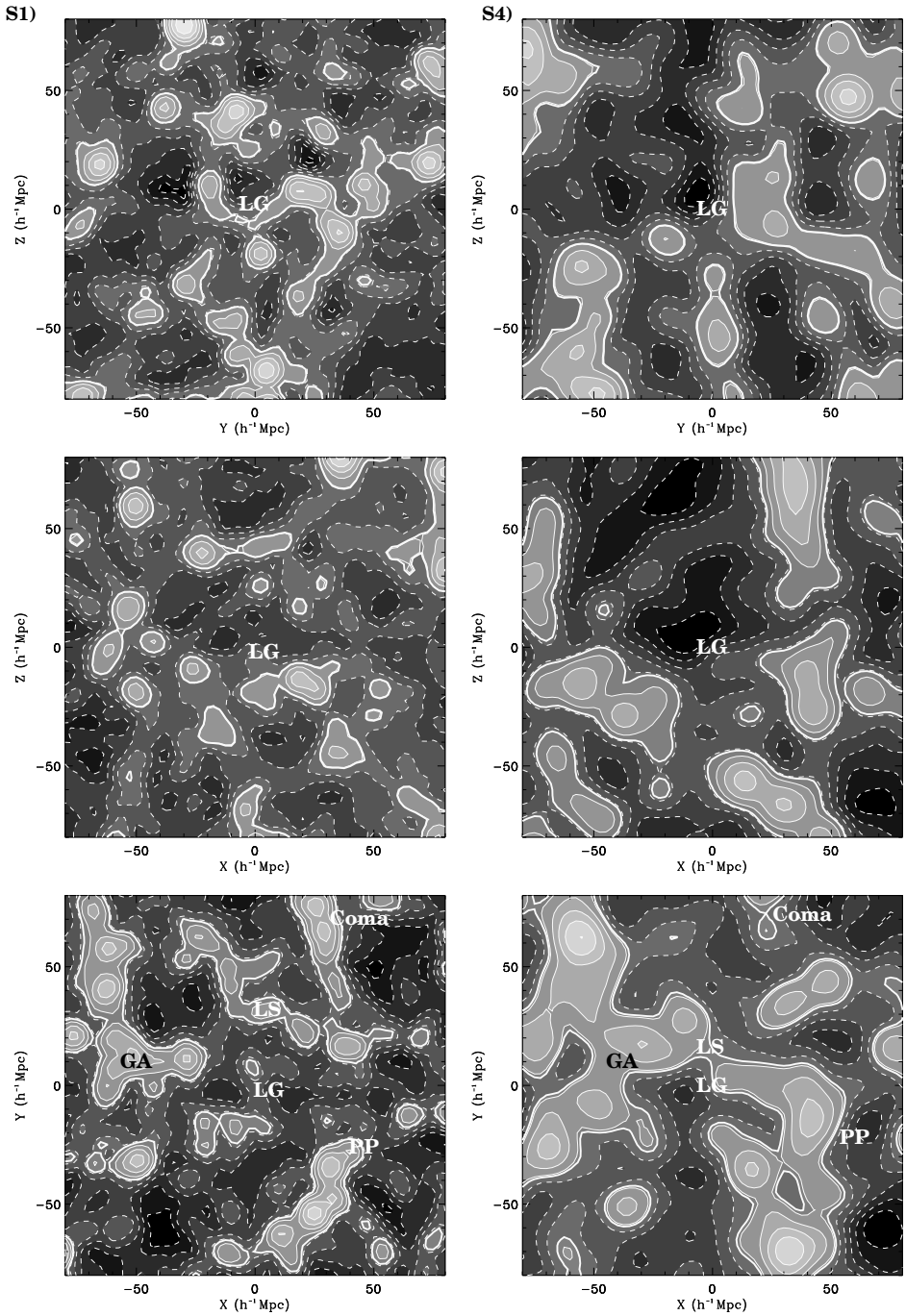

Figure 3.4 — Final output projected density fields for simulations S1 & S4. The plots show zooms of the central regions of the simulations (±80 h^{-1}Mpc) centered at the location of the LG. The main structures (LS, GA, PP & Coma) have been also labeled for reference. The slides are 5 h^{-1}Mpc thick and coincide with the 3 supergalactic planes. The fields have been smoothed with Gaussian filters of $R_G = 2\,\&\,5\ h^{-1}$Mpc respectively for comparison purposes.

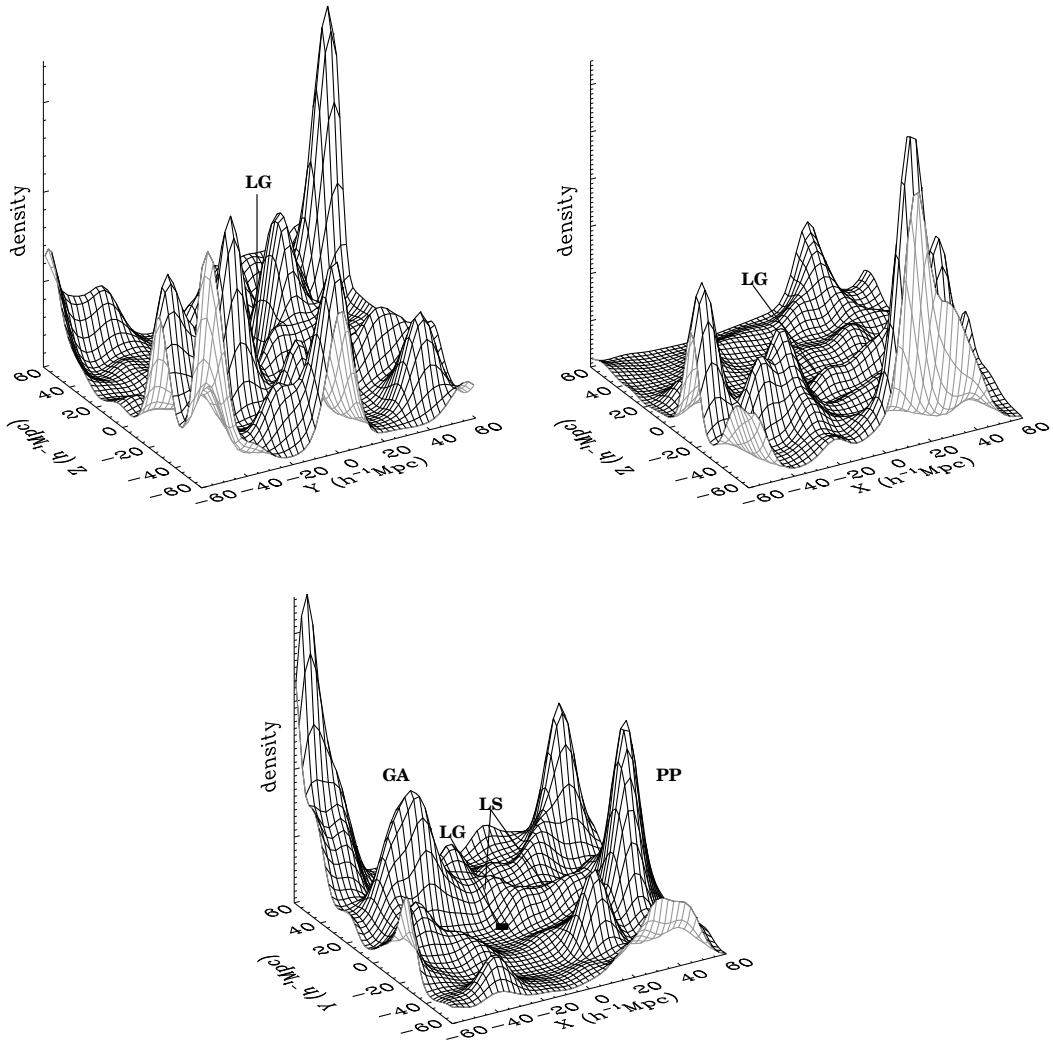

Figure 3.5 — Surface plots corresponding to the plots shown in Fig. 3.4 for the S4 simulation. The peaks shown the prominence of the structures in terms of the average density. The location of the main structures have been identified and labeled.

Nearby Galaxy Catalog of Tully [NBG] (Tully 1988). This catalog includes around 2800 galaxies and it can be considered as a fair volume-limited sample of our Local Supercluster and its surroundings. The second region is a flux-limited sample and it is aimed to trace the mass distribution of regions super exceeding the LS from 30 up to 150 h^{-1}Mpc. This region mimics the IRAS-PSC*z* galaxy catalog (Saunders et al. 2000). To do so, we have chosen objects beyond 30 h^{-1}Mpc from the real mass distribution according to the PSC*z* selection function used by Branchini et al. (1999, see Chapter 2, Sec. 2.5.2.2). The catalog-making algorithm can be described as follows:

1. We select all particles within a radius of 150 h^{-1}Mpc from the closest galaxy located at the geometrical centre of the parent $N-$body simulation.

2. We proceed to split the parent catalog into a “Volume” and “flux” limited regions.

3. For the volume-limited region NBG, we enclose all particles within a radius of 30 h^{-1}Mpc.

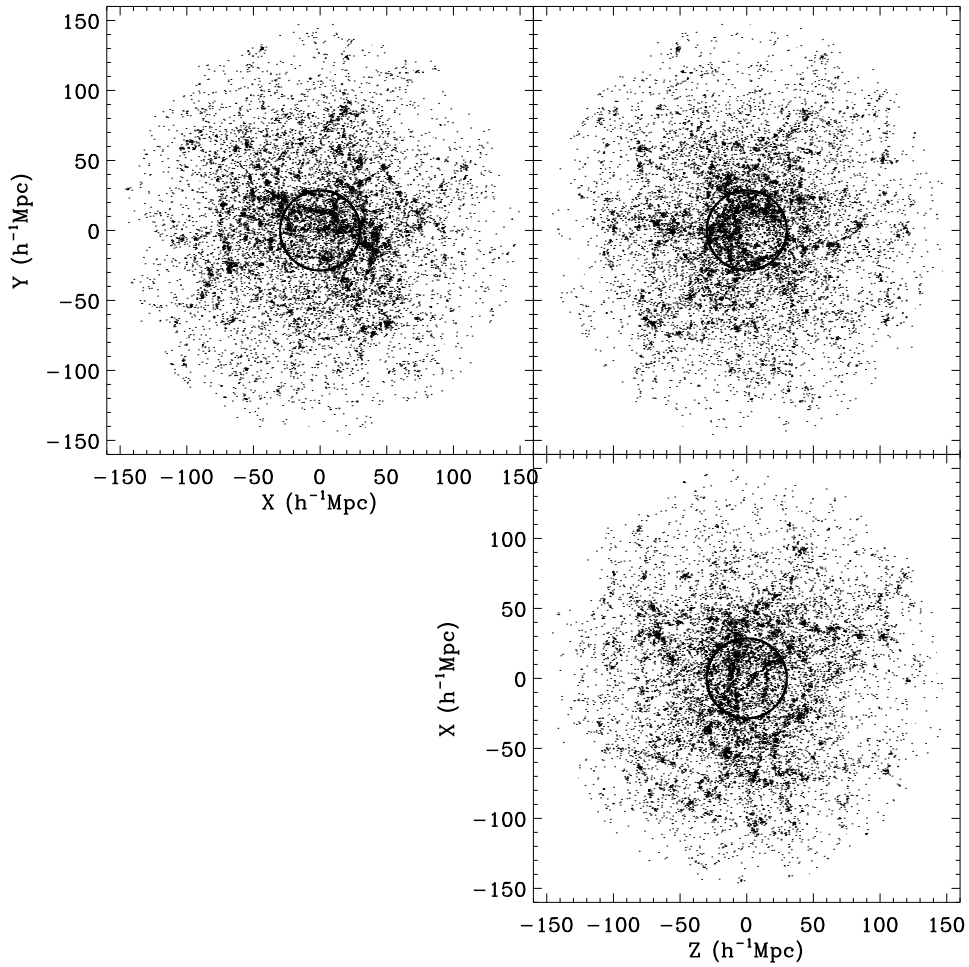

Figure 3.6 — 2D projections of one Mock catalog particle distribution from our sample (S4). The plane projections correspond to the 3 supergalactic planes centered at the LG position.

Because the total number exceeds the one of the NBG, we proceed to re-sample this region by a Monte Carlo selection process to match the observed number of galaxies.

4. For the flux-limited region ($30-150\,h^{-1}$Mpc), objects were selected accordingly to the following IRAS-PSC*z* Selection Function, (Branchini et al. 1999, Chapter 2, Sec 2.5.2.2).

$$\psi(x) = Ax^{-2\alpha}\left(1+\frac{x^2}{x_*^2}\right)^{-\beta} \quad \text{if } x > x_s\ . \tag{3.12}$$

where x is the distance of the galaxy expressed in h^{-1}Mpc, and $\alpha = 0.53$, $\beta = 1.8$, $x_s = 10.9\ h^{-1}$Mpc, and $x_* = 84\ h^{-1}$Mpc (Branchini et al. 1999). The total number of selected objects is in good agreement with the expected number of objects (Figure 3.7).

5. The zone of avoidance was treated in the same way that in Chapter 2.

We justify the first step in the catalog-making procedure by noting that the WF/CR initial density fields were constructed in such a way that the LG would be located at the center of the simulation box, and that the linear regime still prevails at actual time. Therefore, the position of the Local Group

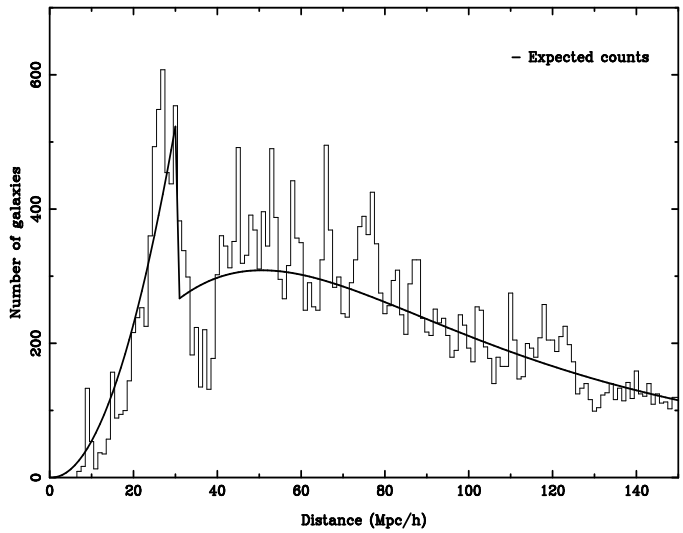

Figure 3.7 — Number density of the PSCz mock galaxies as a function of distance. The histogram shows the average counts of the four mock samples. The continuous thick line show the expected counts in a homogeneous Universe.

in the evolved density fields should also be located at the center. This can be noticed in Figures 3.3 & 3.4. Under these assumptions we have chosen the geometrical centers of the original simulation boxes to be the geometrical centers of our mock catalogs. Nevertheless, this assumption is not totally valid because of the fact that the region corresponding to the LG corresponds to the small scale part of the power spectrum, and as we have pointed out earlier, this part has been produced by random realizations. However, from Figures 3.3 & 3.4 we can see that the LG is located at the centre of the simulation box, so our assumption is not far from reality.

Figure 3.6 shows the outcome of this procedure, the projected spatial distribution of objects along the three supergalactic planes for one of our catalogs (S4). The centre of each projection corresponds to the location of an observer situated at the LG position. As can be noticed, the number of objects decreases with distance from 30 h^{-1}Mpc outward. The inner circle represents the transition part from volume to flux limited regions. It has been noticed before that there are several structures that expand beyond the 30 h^{-1}Mpc region, this is the case for the LS filament and others.

Figure 3.7 shows the average object counts as a function of distance for the four set of catalogs. As can be noticed, there is a good match between the theoretical expected counts (solid line) and the galaxy catalogs (histogram). The discontinuity at 30 h^{-1}Mpc where the transition from volume-limited to flux-limited regions can be clearly seen. The distribution of mock-galaxy objects projected along the sky can be noticed in Figure 3.8, where we have plotted in galactic coordinates the particle distribution of the same mock catalog shown in Fig. 3.6.

3.6 Testing the Mock Universe

In this section we want to asses the confidence of our $N-$body simulations and their corresponding mock catalogs. In particular, we are interested in checking that our Mock catalogs have been sampled properly and that they have accounted for the whole mass distribution. We have already seen that the simulations have been able of reproducing the cosmography of our nearby Universe. Nevertheless a more rigorous and quantitative analysis is necessary. Zaroubi et al. (1999) studied in detail and performed several statistical tests for the WF/CR method. In our case we will do so by estimating a dynamical characteristic of the galaxy density field, the *dipole* moment.

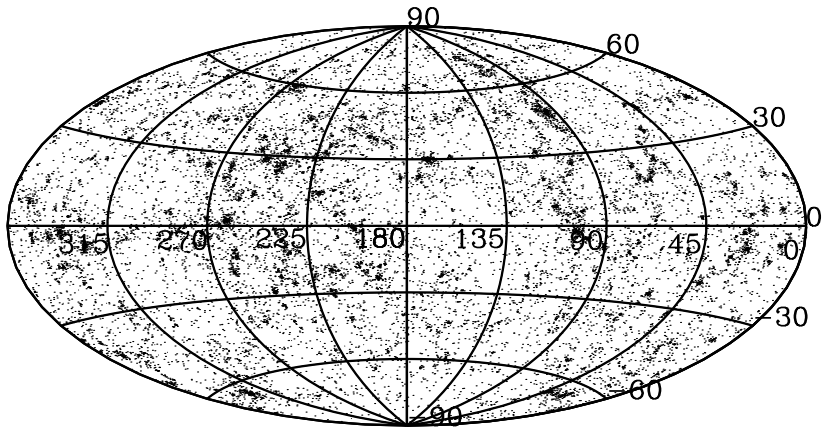

Figure 3.8 — Aitoff projection in galactic coordinates for the mock catalog of Fig. 3.6.

We would like to make clear that while we will consider only the dipole moment from the mass distributions for testing the reliability of our catalogs, we do not assume that this alone provide a good description of the inhomogeneity around us. The dipole is a convenient statistics for which it seems to be reasonable to compare with the real observed mass distribution.

We will focus on 2 aspects of the gravity dipole, its amplitude and direction. The amplitude will give us information about how large the contributions from structures located at different distances from the central observer are, while the direction will point the region towards the central observer is moving.

The direction of the LG is that given by the dipole component of the cosmic microwave background radiation field. In principle, any sample of objects (catalog) that traces the mass distribution "fairly" should converge to this velocity and direction as the samples get deeper. This phenomenon is known as the *dipole convergence*, and the distance at which the shells' dipole motions begin to match the LG motion is call the *convergence depth*. This distance (R in Eqn. 3.13) is to be believed in the order of $150-200\ h^{-1}$Mpc.

3.6.1 The gravity dipole

The mass distribution of galaxies exerts a pull over an object due to gravity effects. The amplitude and direction of this pull is determined by the distribution, concentration and distances of galaxies around the observer's vicinity.

The dipole moment provides an estimate of the gravitational acceleration acting on the LG, and hence of the large scale mass distribution around the LG. In linear theory, the peculiar acceleration dipole vector is given by the following expression:

$$\mathbf{g}_D(\mathbf{x}) = \frac{3\Omega_m H^2}{8\pi}\int_0^R \mathrm{d}\mathbf{x}'\,\delta(\mathbf{x}')\frac{\mathbf{x}'}{|\mathbf{x}'|^3}. \tag{3.13}$$

In this equation, the inferred acceleration vector must be aligned with the LG velocity vector. But, while this is a necessary condition to apply, it is not sufficient, one must also be sure that the radius of the sample (R) of mass tracers is sufficiently deep that it does not miss any contribution from distant density fluctuations. This means that the dipole vector of the mass distribution must converge to its total value within the effective depth of the sample R.

The peculiar configuration of our cosmic vicinity imposes strong characteristics in $\mathbf{g}_D$, this region which is enclosed within a volume of $\sim 40-50\ h^{-1}$Mpc is responsible of at least 60% of the dipole.

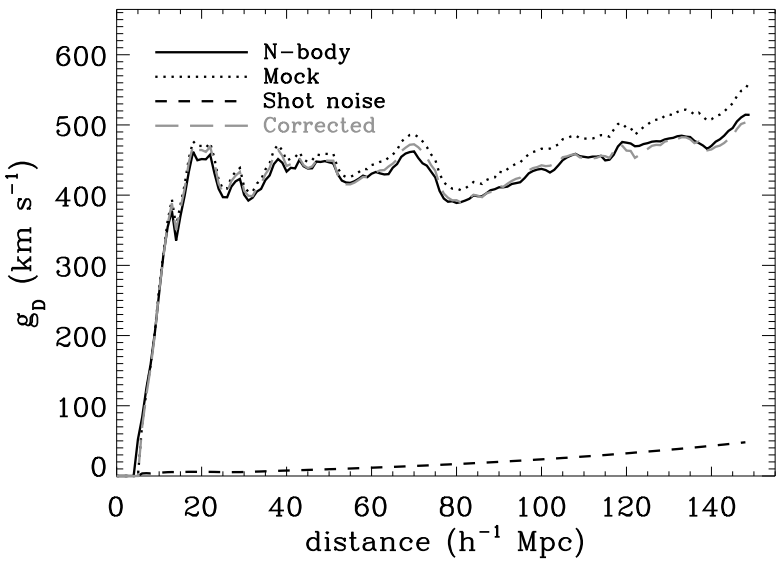

Figure 3.9 — Cumulative gravity dipole for the full $N-$body (continues line) and mock (dotted line) galaxy mass distributions corresponding to the S4 simulation. The bottom dashed line represents the shot-noise contribution to the dipole. The long-dashed gray line represents the dipole after being corrected for shot-noise effects.

Since we do not have a continuous density field, but the positions of a finite number of objects in our galaxy flux-limited and full mass distribution catalogs, our estimate of the acceleration on the LG is given by a discrete form of Eqn. 3.13 in velocity units (relation valid only in the linear regime),

$$\mathbf{g}_D = \frac{f(\Omega_m, \Lambda) H_0}{4\pi n} \sum_i \frac{1}{\psi(x_i)} \frac{\mathbf{x}_i}{|\mathbf{x}_i|^3}, \tag{3.14}$$

where n is the average number density of objects selected in the sample, and $\psi(x_i)^{-1}$ is a weighting factor associated to the selection function evaluated at the distance x_i. This weighting factor is equal to 1 for all objects inside the volume-limited region. Despite the discreteness of the Eqn. 3.14, the estimate of $\mathbf{g}_D$ does not loose generality in the sense that the weighting factor corrects for the relative number density of objects with respect to the number density in the "real" ($N-$body) mass distribution.

We have computed then the gravity dipole from Eqn. 3.14 for the $N-$body and mock catalogs. Figure 3.9 shows the cumulative $\mathbf{g}_D$ computed for the $N-$body mass distribution (continues line) and for the mock galaxy distribution (dotted line) from the S4 simulation. We started the calculation from an initial radius of 5 h^{-1}Mpc and up to 150 h^{-1}Mpc. This was done due to two reasons, the first one is due to the lack of objects to compute the dipole inside this region (which introduce a large dispersion in the calculation), and the second and most important one is because we want to determine the origin and influence radius which is responsible for the movement of the LG. As it can be noticed, the estimate inside the inner zone $[0-30\ h^{-1}$Mpc$]$ of the mock catalog matches the one from the full distribution showing an almost perfect sampling. Deviations from the $N-$body estimate start to arise around 30 h^{-1}Mpc and they become more pronounce at larger radii. This effect is due to the fact that these regions represent the tail of the selection function which does not account properly for all objects. We observe a rapid raising in the dipole in the first $10-30\ h^{-1}$Mpc, after which it remaining almost flat up to 60 h^{-1}Mpc. This quick increase (≈ 400 km s^{-1}) means that the mass distribution enclosed in this region exerts most of the gravitational pull onto the LG. Indeed, as seen in the corresponding mass distributions maps of Figs. 3.4 & 3.6 and reflected in the corresponding velocity maps, the particular configuration between the Local Supercluster, the GA and PP structures over the LG are responsible of this movement, matching the observational results. Nevertheless, after remaining almost constant for a range of distances, the dipole amplitude continues raising as the volume increases, meaning that there are still mass concentrations at those distances which also play a major role into the dynamics of the LG. In the real world, a similar phenomenon is observed. Several authors (e.g. Rowan-Robinson et al. 2000; Plionis & Kolokotronis 1998; Basilakos & Plionis 1998) have pointed out that the Shapley su-

percluster is a very likely candidate responsible for this increase in amplitude which contributes almost 20 to 30% to the total cumulative dipole. This huge mass overdensity is located at $\approx 140\ h^{-1}$Mpc in the direction of the Hydra-Centaurus supercluster (GA). In all our catalogs the dipole amplitude does continue raising at the limit of our catalogs (150 h^{-1}Mpc). This effect can be explained in terms of the WF/CR initial density maps. The input velocity field used to generate the WF fields has imprinted on itself the influence of the mass distribution at very large scales. Hence, registering a general flow towards the direction of GA and Shapley (Hoffman et al. 2001). In this sense the evolution of the WF/CR has successfully reproduced the observations in the sense that there might be still structures influencing over the LG (e.g. Hoffman et al. 2001). Nevertheless, the region which corresponds to the location of the Shapley concentration, corresponds to the weakly constrained part of the WF/CR algorithm, so the real presence of this structure in our simulations is dubious, although we have measured the same effect.

The speculation that the Shapley supercluster is not the major contributor to the motion of the LG but that it is coming even from larger distances was proposed by Raychaudhury (1989) and Plionis & Valdarnini (1991). These authors speculated that large structures like the Horologium supercluster still plays an important role over the LG. Nevertheless, Rowan-Robinson et al. (2000) used the PSC*z* catalog to compute the dipole even at scales up to 300 h^{-1}Mpc. They found that there is indeed a rise in the dipole after 150 h^{-1}Mpc but it finds a convergence before the 200 h^{-1}Mpc with no evidence for a significant contribution to the dipole, excluding in this way the speculation about the Horologium supercluster. This result should be met with caution in the sense that the errors in the PSC*z* catalog and its selection function increase considerable with distance, so that the reliability of the result at these very large scales decreases accordingly.

3.6.2 Shot-noise effects

It has already been pointed out that the discreteness and sampling effects introduce uncertainties in the calculation of the dipole. Furthermore, these effects introduce an additive dipole term, the *shot-noise dipole*. In order to correct for this extra dipole, we need to compute the corresponding shot-noise and to correct for it our dipole estimates.

There are two alternative approaches to correct for shot-noise effects. The first one concerns to generating several Monte Carlo realizations of mock catalogs and keeping the number of objects and selection function unchanged, while the second one is by computing the shot-noise by the analytic estimate of Strauss et al. (1992). Due to the fact that we are also interested in reconstructing their corresponding peculiar velocity fields, it will be very cumbersome and expensive in consuming computing time to use the Monte Carlo approach. The latter would imply necessary to produce a large amount of catalogs per set. We will therefore resort to the second method, supported also by the demonstration by Basilakos & Plionis (1998), who showed that both methods seem to give equivalent results.

From the Appendix A of Strauss et al. (1992) it follows that the shot-noise is given by the expected variance between the contributions to the acceleration from all galaxies on a shell at distance x and the galaxies within the flux-limited sample at the same shell. In this case, the expected value is given by:

$$\sigma^2 = \left(\frac{H_0\beta}{4\pi n_1}\right)^2 \sum_{\text{galaxies}\, i} \frac{1}{\psi(x_i){x_i}^4}\left[\frac{1}{\psi(x_i)} + 1\right], \tag{3.15}$$

where n_1 is the average density of galaxies, $\psi(x_i)$ is the selection function at the distance x of the shell and β is the bias factor, that for our case is equal to $f(\Omega_m, \Lambda)$. In Figure 3.9 the effects of shot-noise are shown. The dashed line is the shot-noise contribution according to Eqn. 3.15 to the dipole. This is almost zero at the inner 30 h^{-1}Mpc due to the fact that this region is volume-limited sampled. The shot-noise starts to be noticed from the 30 h^{-1}Mpc outward. This effect is due to the fact that the selection function depends strongly on distance, so as a consequence the shot-noise will increase at larger distances. The gray long dashed line represents the dipole estimate corrected for shot-noise. The agreement between the real and corrected mock dipole amplitudes, even at large distances, is quite remarkable.

In general, the shot noise amplitudes represent almost the 10% – 15% of their total magnitudes for all catalogs in our sample, and they show the same behavior as in Fig. 3.9.

3.6.3 Dipole direction and convergence

The direction and convergence of the dipole will help us to asses the reliability of our samples. Therefore, we have computed the direction of the dipole by using Eqn. 3.14 as a function of depth. This is shown in the left panel of Figure 3.10. The directions for the cumulative $N-$body mass distribution (black diamonds) and for the mock galaxy catalogs (gray triangles) are shown in galactic coordinates.

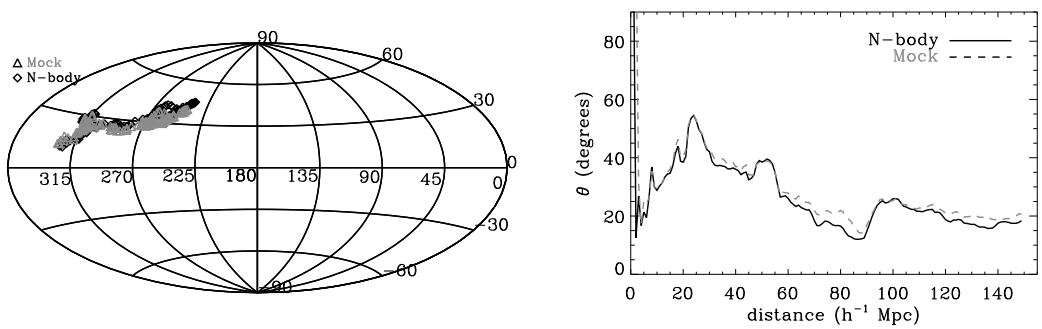

Figure 3.10 — Dipole directions and convergences for the S4 catalog. The left panel shows in galactic coordinates how the dipole wanders around when increasing the computing radius. The diamonds correspond to the full, $N-$body mass distribution, while the triangles to the mock galaxy catalogs. The right panel shows the angle θ between the acceleration vector and the CMB dipole vector for the real mass distribution (continues line), and for the mock galaxy catalogs (broken, gray line).

The convergence of the direction of the dipole has been computed with respect to the one measured by *COBE*. The right panel of Figure 3.10 shows the angle θ between the estimated dipole and the COBE one as a function of depth. These two plots refer to the same catalog shown in Fig. 3.9. Around the first $20-30$ h^{-1}Mpc the angle θ does not converge due to the big influence of the Local Supercluster over the LG (Virgocentric infall). The sudden convergence at $\sim 60-80$ h^{-1}Mpc means that the massive structures like the GA and PP supercluster have been enclosed. This result agrees with those obtained by Strauss et al. (1992) for the 1.2-Jy *IRAS* catalog. The slight rise at 100 h^{-1}Mpc and its convergence at ~ 130 h^{-1}Mpc can be possibly interpreted like the enclose of structures similar to the Shapley concentration at this radius. In effect, as may be seen from the mock catalog particle distribution (Fig. 3.6) and from the density fields (Figs. 3.1 & 3.3, 3.4) the most prominent mass density structure beyond the GA location coincides along the same direction and ~ 110 h^{-1}Mpc far from the LG. It is this Shapley-alike structure responsible for this effect.

3.6.3.1 Averaged Dipole results

The robustness of our results can be noticed from Figure 3.11 where the average cumulative $\mathbf{g}_D$ (top panels) and the average dipole direction (bottom panel) for the four samples are shown. The top-left panel shows the corresponding cumulative dipole for the full $N-$body mass distribution, while the top right panel for the mock galaxy catalogs. The gray shadows represent the $\pm 1\sigma$ dispersion around the average values at each radius. The agreement between the two curves is quite remarkable, meaning that the mock catalogs have successfully traced the real mass distribution. The rapid increase in $\mathbf{g}_D$ for the first 15 h^{-1}Mpc is due to the gravitational attraction of the LS in combination with the GA influence, which is reflected after this radius. The magnitude of this increment varies from realization to realization as may be noticed from the large dispersion around the mean. The almost flat behavior

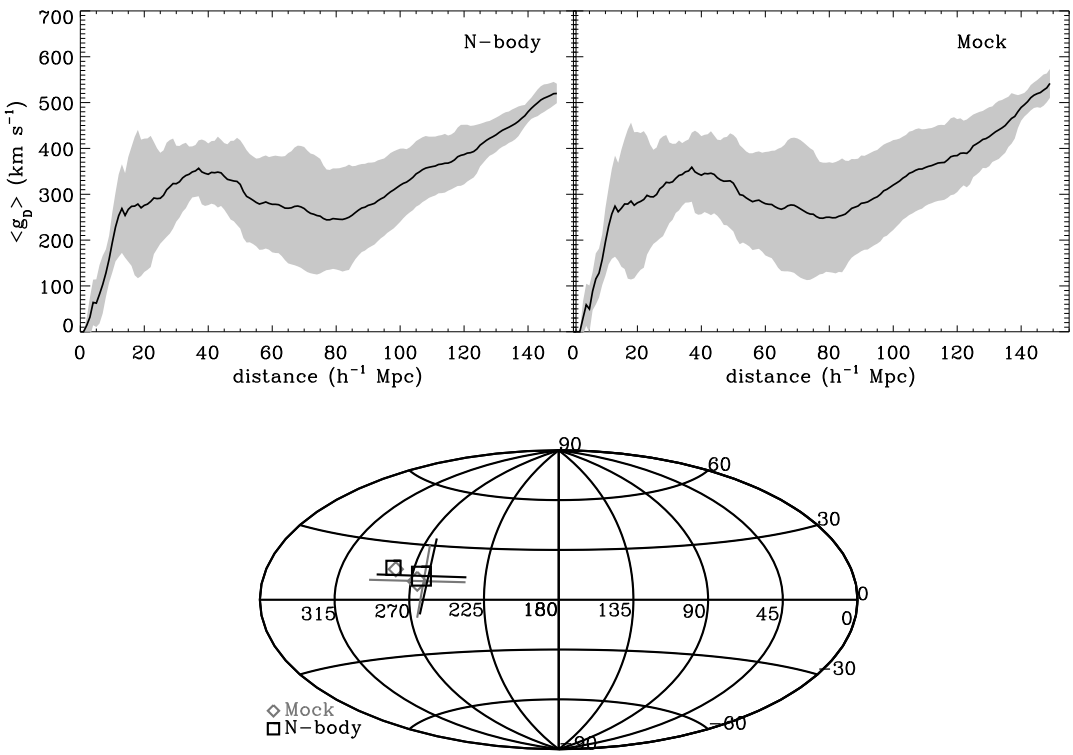

Figure 3.11 — Average cumulative gravity dipole (continues line) for the 4 catalogs of our set (top panels), and average direction (bottom panel) at 150 h^{-1}Mpc and 60 h^{-1}Mpc for both samples in galactic coordinates. The top-left panel corresponds to the full mass distribution, while the top-right panel to the mock galaxy catalogs. The gray shadows represent the 1σ dispersion around the mean value.

after 40 h^{-1}Mpc and up to 80 h^{-1}Mpc means that there are no considerable structures which exert a strong influence over the LG. The sudden raise in the dipole after 80 h^{-1}Mpc without convergence, even at the edge of the catalogs, imply the presence of big(s) structure(s) acting still over the LG. All catalogs show a dipole mass concentration in the density fields along the direction of the GA and Shapley concentration which in turn is responsible for this result. The bottom panel of Fig. 3.11 shows the positions of the average dipole directions computed at 2 different radius, at 60 and 150 h^{-1}Mpc, projected in the sky in galactic coordinates of the $N-$body mass distribution (black square), and the mock galaxy dipole (gray diamond) and their corresponding error bars. The separation between the two quantities gets larger at larger radius. At 60 h^{-1}Mpc both directions differ only 3°, while at 150 h^{-1}Mpc the difference is $\sim 8°$, being this is an effect of the sampling procedure. The dipole at 60 h^{-1}Mpc is $\sim 12°$ far from the real dipole direction, while the one computed at the edge of the sample around 20°. These results agree with those obtained from the literature for the bulk velocity direction and the gravity dipole. Because our initial density fields were computed from real observed velocity fields, then it is expected that our estimates should coincide with those obtained from the velocity bulk flow.

In conclusion, we can say with a high degree of confidence, that our Mock catalogs trace very well the full and real mass distribution got from the $N-$body simulations, and that in principle we have taken into account possible effects that could influence any results obtained from these mock catalogs. Furthermore, the fact that the dipole estimates reproduce quite well the real observed dipole behavior even at very large scales (~ 150 h^{-1}Mpc) justify the use of constrained simulations being extended by unconstrained regions.

3.7 The velocity field

The intricated and very peculiar location of the LG in our Universe is reflected in its corresponding peculiar velocity field. This field not only shows as well the complexity of the local cosmography, but also reveals the entangled dynamical state around the LG.

Figure 3.12 shows slides of the peculiar velocity fields corresponding to the 3 supergalactic planes and centered around the LG position (black central circle) for the S4 simulation. The left-column corresponds to the peculiar velocities at each particle position represented by arrows proportional to their magnitude and pointing towards their projected direction. As can be noticed the structures around the LG influence considerably the dynamics of the surrounding mass distribution. This can be noticed more clearly in the right-column panels. These plots are zooms of the regions enclosed in boxes at the left-hand panels. In these plots, the peculiar velocity field have been interpolated into a grid. The contours correspond to mass density contrast located along the same projections; the continuous line indicate overdensities, while the dotted lines underdense regions, and the thick black line corresponds to the mean density. In these representations, the local flows around the big mass concentrations are more clear. Furthermore, a more general dominant flow along the upper part of $x-y$ direction can be recognized. This is the influence of the GA, and the movement and direction of the LG.

The inhomogeneities in the mass distribution (clusters and superclusters of galaxies) are the origin of the local flows. The configuration of those inhomogeneities also plays an important role. The clumpiness of the mass distribution distorts the amplitude and direction of the peculiar velocities. These distortions have the shape of a shear pattern. These shear patterns can be more easily recognized in the left-hand panels of Fig. 3.12 around the non-virialized structures.

In all panels of the Fig. 3.12, it can be noticed that the LG participates in a very general velocity flow (indicated by the size of the arrows), and it is very well defined towards the direction of the GA region. The influence of the PP supercluster can also be recognized at the lower right of the LG position in the $x-y$ supergalactic plane. Even more, the LS also participates in this intricate game. It exerts a gravitational influence over the LG (indicated by the verticality component of the arrows), the Virgocentric infall. Another peculiarity of this scenario is the elongation of the LS along the same direction of the dominant flow, towards the GA location.

3.7.1 Modeling the peculiar velocity field

Several methods have been proposed to reconstruct/model the peculiar velocity fields. The common approach is to construct the peculiar velocity field from galaxy catalogs (mass densities) using the results of linear theory, or a higher order approximation (quasilinear) like the Zel'dovich approximation. In the present study, we will use these two methods and the advanced implementation of LAP (FAM) to model the peculiar velocity field.

The large scale mass distribution is within the linear regime. Therefore, the inferred bulk flow using linear, Zel'dovich or FAM methods should in principle reproduce the $N-$body bulk flow. In the more local neighborhood, the structures are within the weakly non-linear regime, so the reconstruction of the velocity shear component will tell us what kind of method performs better at this regime. At these scales, linear theory is not totally valid and Zel'dovich could in principle reproduce properly the main characteristics. In the case of FAM, as shown by Romano-Díaz, Branchini, & van de Weygaert (2004, see Chapter 2), this could be the ideal scenario to test it.

3.7.1.1 Linear Theory

Within linear theory, Eqn. 3.2 relates the velocity and gravity fields. The linear peculiar velocities are proportional to $H_0 f(\Omega_m, \Lambda)\mathbf{g}(\mathbf{x})$, where $\mathbf{g}(\mathbf{x})$ is the gravitational force field obtained from the particle distribution (Eqn. 3.14). Hence, we have used this relation to compute the linear peculiar velocity field of our catalogs.

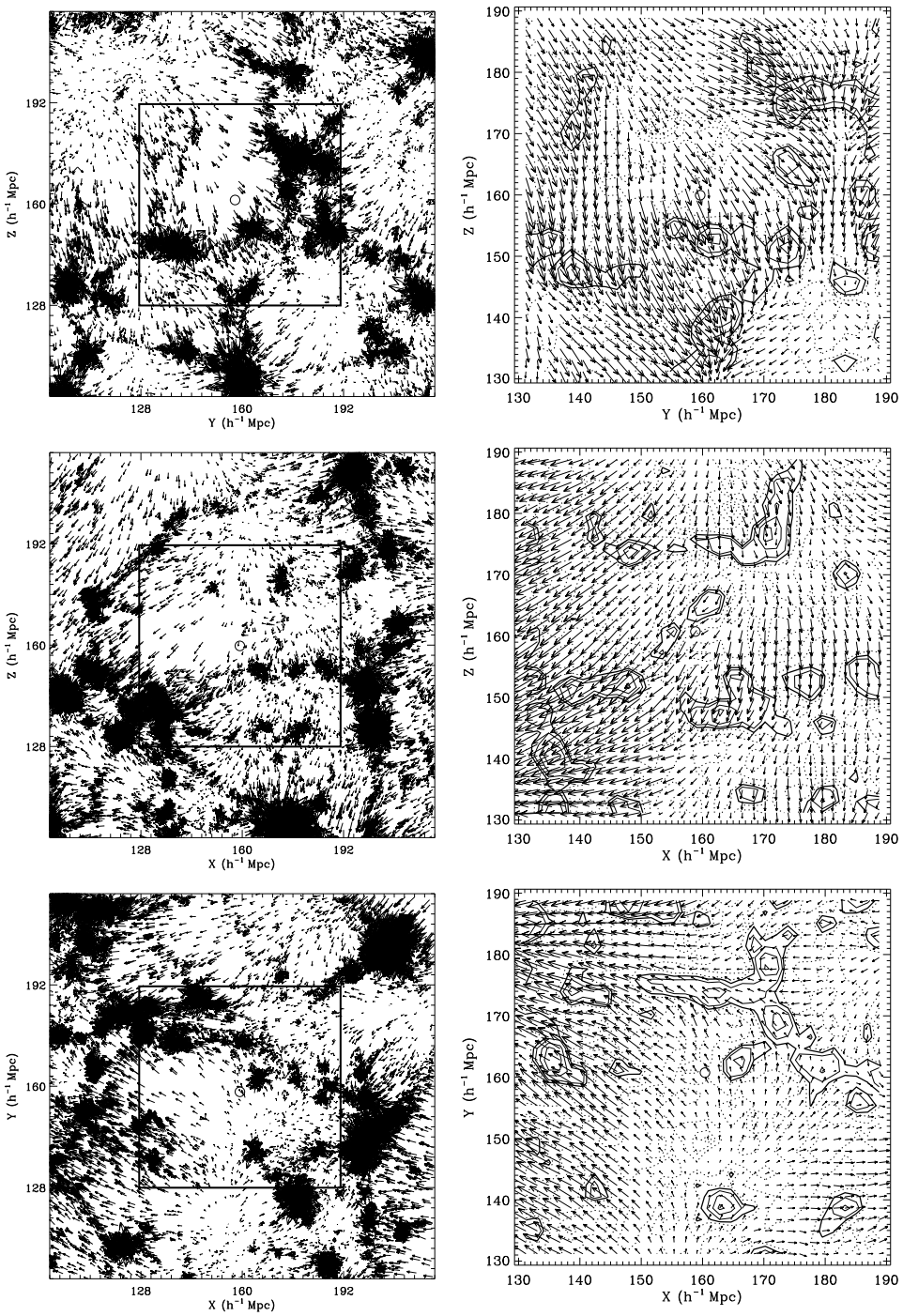

Figure 3.12 — Peculiar velocity fields for the S4 simulation. The left column represents the velocities at the particle positions for $\pm 60\ h^{-1}$Mpc regions around the LG along the 3 supergalactic planes. The right panels show zooms of the velocities interpolated onto a grid for the LS region, $\pm 30\ h^{-1}$Mpc. The position of the LG is marked by a black circle at the center of the maps.

3.7.1.2 FAM approach

We have reconstructed the peculiar velocity fields following the prescription of Romano-Díaz, Branchini, & van de Weygaert (2004) presented in Chapter 2 (Sec. 2.3.3). We have chosen $N_f = 6$ basis functions to parameterize the orbits, a tolerance parameter $tol = 10^{-4}$ to search for the minimum of the action S and setting a softening parameter of 0.25 h^{-1}Mpc to smooth the gravitational force. We have checked that this choice of parameters is optimal in the sense that decreasing tol or increasing N_f does not modify the final results appreciably.

3.7.1.3 Zel'dovich approximation

Velocities in the Zel'dovich approximation can also be obtained by means of FAM (Nusser & Branchini 2000; Romano-Díaz et al. 2004). For this, we set the number of expansion basis functions $N_f = 1$, while keeping the tolerance parameter unchanged. The straight-line orbits are then of the form $\mathbf{x}_i(D) = \mathbf{x}_{0,i} + D\mathbf{C}_{i,1}$, where D is the linear growing mode; $\mathbf{x}_{0,i}$ is the position of the particle at actual time and the vectors $\mathbf{C}_{i,1}$ are the expansion coefficients with respect to which the action in FAM is going to be minimized, the subindex 1 indicates that the gravitational force field at present time is used for the calculation. These velocities should be similar to those that would be obtained by applying the PIZA method (Croft & Gaztanaga 1997).

3.8 Results

In order to extract the bulk flow and the shear component from the peculiar velocity field, we have followed Romano-Díaz, Branchini, & van de Weygaert (2004, see Chapter 2) in using the procedure by Kaiser (1991). This procedure computes the bulk velocity from a multipolar decomposition of the peculiar velocity field of the form of Eqn. 3.6 up to the quadrupolar expansion term.

Because we want to compare our results with respect to the real Universe, we will only present results concerning to the fully constrained part of our catalogs (60 h^{-1}Mpc).

3.8.1 Multipolar velocity decomposition

We decomposed the velocity field by means of a field Taylor expansion truncated at the quadratic term (Kaiser 1991, see also Chap. 2). The velocity field $\mathbf{v}$, is then modeled by the first two components, a bulk flow vector, $\tilde{u}_i$, and a quadratic shear tensor contribution, $\tilde{s}_{ij}$,

$$\mathrm{v}_i = \tilde{u}_i + \tilde{s}_{ij} x \hat{x}_j, \qquad \text{where} \qquad i, j = \{1, 2, 3\}\,, \tag{3.16}$$

in which i, j denotes the Cartesian component indices. The vectors $\hat{x}_j$ represent the vector components along the Cartesian j direction of the spatial unity vector oriented along the object position vector $\mathbf{x}$. Using these notations, we can rewrite Eqn. 3.16 and express the i-component of the velocity of object n into a product of the vectors $F_{n,I}$ and V_{Ii},

$$\mathrm{v}_{n,i} = \sum_{I=1}^{4} F_{n,I}(\mathbf{x}) V_{Ii}$$

in which the data 4-vector F_I and the velocity field component 4-vector V_{Ii} are defined as

$$\begin{aligned} F_{n,I} &= \{1, x\hat{x}_1, x\hat{x}_2, x\hat{x}_3\} \\ V_{Ii} &= \{\tilde{u}_i, \tilde{s}_{i1}, \tilde{s}_{i2}, \tilde{s}_{i3}\}\,. \end{aligned} \tag{3.17}$$

The "dipolar" bulk flow components $\tilde{u}_i$ and "quadrupolar" velocity shear components $\tilde{s}_{ij}$ can then be obtained by solving for the vectors V_{Ii} on the basis of a fitting analysis (to be precise, $\tilde{s}_{ij}$ also includes

a minor residual "monopole" expansion/contraction term). We accomplish this by computing for each Cartesian component i the values for the multipole elements $\tilde{u}_i$ and $\tilde{s}_{ij}$ which minimize χ^2

$$\chi^2 = \sum_{n=1}^{N_{objs}} \left(\mathrm{v}_{n,i} - \sum_I F_{n,I}(\mathbf{x}) V_{Ii} \right)^2 , \tag{3.18}$$

to be evaluated on the basis of the data sample of N_{obj} objects at locations $\mathbf{x}_n$ and with inferred velocities $\mathbf{v}_n$. The bulk flow and velocity shear components of $\mathbf{v}_n$ are then readily obtained from V_{Ii}:

$$\mathrm{v}_{bulk,i} = \tilde{u}_i ; \qquad \mathrm{v}_{shear,i} = \sum_{j=1}^{3} \tilde{s}'_{ij} x \hat{x}_j \tag{3.19}$$

where $\tilde{s}'$ is the traceless shear tensor given by

$$\tilde{s}'_{ij} = \tilde{s}_{ij} - \frac{1}{3} Tr(\tilde{s}) \delta_{ij} , \tag{3.20}$$

and $Tr(s)$ is the trace of the tensor s_{ij}.

3.8.2 The expected velocity bulk

The left panel in Figure 3.13 shows the amplitude of the cumulative bulk flow computed from the S4 catalog for the $N-$body mass distribution (continues line) and the mock galaxy catalog (dotted line). As in the case of the gravity dipole, we have avoided the inner 5 h^{-1}Mpc of the catalogs. The discrepancy between the two bulks in the first 15 h^{-1}Mpc is due to sampling errors (low number of galaxies picked up at the core of the sample). Nevertheless, there is a very good agreement between the two quantities for the following 60 h^{-1}Mpc. Still, there is a small discrepancy between the two quantities which increases with distance. This result is caused by selection effects and sparse sampling, in particular by shot-noise. For these reasons, we have computed and corrected for the shot-noise contribution as described in Section 3.6.2. The shot-noise amplitude is not so large at these scales. For this particular catalog, at the edge of the 60 h^{-1}Mpcits only ~ 20 km s^{-1} . The dot-dashed line in the left panel of Fig. 3.13 represents the mock estimate after being corrected by shot-noise effects. The agreement between the 2 distributions gets better; although some discrepancies beyond 60 h^{-1}Mpc remain. This is ascribed to the fact that the selection function only weights galaxy masses but not their respective velocities. But for our region of interest the distributions match each other very well.

The right panel of Fig. 3.13 shows how the bulk flow directions move around the sky when increasing the volume of the sample. Apart from some disperse points which correspond to the first 15 h^{-1}Mpc, all directions are located around a common area and converge around $l = 270°$, $b = 11°$. This direction is just less than 10° far from its respective gravity dipole direction. The fact that the bulk flow directions are concentrated around a given area, imply that the main structures responsible for the bulk flow are located/aligned around the same direction in the sky.

The average results show in a general way what has been learned from the analysis of the individual catalog. The left panel in Figure 3.14 presents the average bulk flows for the $N-$body mass distribution (broken line), and the galaxy mock catalogs corrected for shot-noise (continuous line). The gray shadow represents the $\pm 1\sigma$ dispersion around the mean mock bulk flow. We have excluded the inner 5 h^{-1}Mpc to avoid non-linear effects and sparse sampling. As in the individual catalog, the mean mock bulk flow distribution follows the same behavior than the corresponding $N-$body flow. Both quantities match each other almost perfectly within the volume-limited region. Differences arise in the flux-limited region, although this mismatch is only ~ 20 km s^{-1}. Nevertheless, both bulk flow amplitude estimates are consistent with each other within the 1σ dispersion error.

The large errors (spikes) around the first 15 h^{-1}Mpc are the result of the position and strength (influence) of the LS in the catalogs. This is also the case for the GA and PP supercluster, where the errors are more pronounced around this region ($40-60$ h^{-1}Mpc). In the case of the directions, they

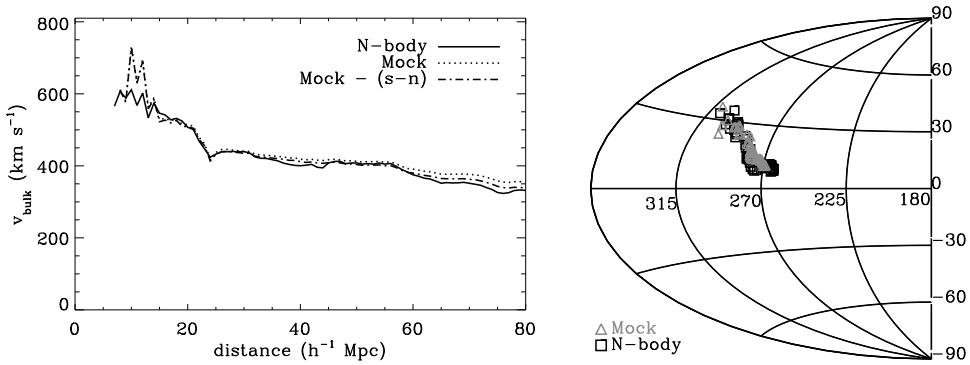

Figure 3.13 — Amplitude and direction of the bulk flow velocity for the S4 catalog. The continuous line in the left panel represents the bulk flow of the $N-$body velocity distribution, while the dotted line the one of the mock galaxy catalog. The dot-dashed line represents the bulk flow corrected for shot-noise. The directions (same range in distances than in the left panel) of the $N-$body and corrected bulk flows are shown in the right panel.

also show a very good agreement. The right panel of Fig. 3.14 illustrates that both bulk flow directions point toward the same direction and just with a relative mismatch of $\sim 5°$. With respect to the direction of the gravity dipole, they are off by $\sim 20°$. This misalignment implies that there is still a considerable influence from the mass distribution beyond 60 h^{-1}Mpc. This result is also shifted with respect to the real bulk direction estimated from the Mark III catalog by $\sim 18°$.

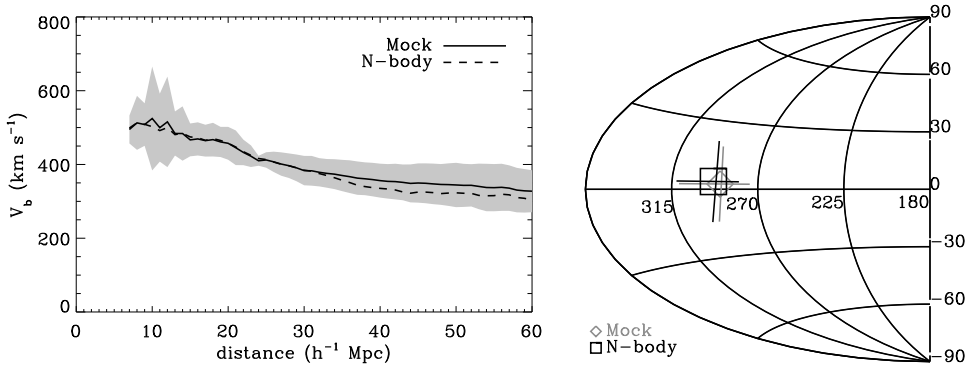

Figure 3.14 — Average amplitudes and directions of the cumulative $N-$body & mock bulk flows. The lines in the left panel represent the average bulk flows, while the gray shadow indicates the 1σ dispersion around the mean. The right panel shows the average directions of the bulk flow computed at the edge of the samples.

In general, these results from both samples at a radius of 60 h^{-1}Mpc agree with previous studies using the WF/CR method (Hoffman et al. 2001) and with the estimates from real velocity catalogs at these scales (e.g. MARK III, SFI catalogs, etc). Furthermore, our bulk flow directions are also consistent with the non-zero vectors of the bulk flow $(l,b) = (280,0) \pm 30°$ (Dekel 1999, and references therein).

3.8.3 The reconstructed velocity bulk

We have reconstructed the peculiar velocity field with the 3 methods listed in Section 3.7.1: linear theory, Zel'dovich approximation and FAM. We extracted the velocity bulk flow from the velocity field in the same way as for the $N-$body and mock bulk flow velocities.

Figure 3.15 shows the comparison between the $N-$body (continuous line), mock (dotted line) and shot-noise corrected FAM ([$\mathbf{V}_{b,FAM}$], dot-dashed line) cumulative bulk flows for one catalog. Clearly, FAM over-estimates the bulk flow, it has suffered a considerable shift toward higher amplitudes. This effect is related to the FAM approach and can be corrected for. When reconstructing the velocity field the FAM technique assumes that inhomogeneities that could influence the dynamical behavior of the sample are contained within the sample itself. The centre of mass *c.o.m* of the mass distribution will therefore coincide with the geometrical centre of the sample. If this is not the case, a spurious bulk component is introduced due to the relative anisotropic mass distribution around the central observer. This will exert an extra pull over the system. For this particular catalog there is a relative displacement of $\sim 10\ h^{-1}$Mpc between the *c.o.m* and the geometrical centers in the mock catalog. Furthermore, the average direction of the *c.o.m.* points toward the direction where the GA and Shapley concentration are located. Juszkiewicz et al. (1990) showed that the contribution due to centre displacements is given by $H_0 f(\Omega_m, \Lambda)\mathbf{x}_{c.o.m.}/3$, where $\mathbf{x}_{c.o.m.}$ is the position of the centre of mass with respect to the geometrical centre. The offset in the bulk flow magnitude in our whole sample is in average 120 km s^{-1} and in the direction of the GA region. The corrected $\mathbf{V}_{b,FAM}$ is the 3dot-dashed line. The agreement between this corrected quantity and the $N-$body bulk distribution is remarkable. The bump in $\mathbf{V}_{b,FAM}$ at $\sim 10\ h^{-1}$Mpc coincides with the location of the LS where FAM cannot reconstruct the velocity field properly due to the fact that this is a non-linear region and the lack of objects available for the reconstruction. At these regions and due to the degeneracy in orbits, FAM chooses from all possible solutions the one which is closest to the one given by linear theory, so that FAM cannot predict properly velocities in this regime (Nusser & Branchini 2000; Branchini et al. 2002; Romano-Díaz et al. 2004).

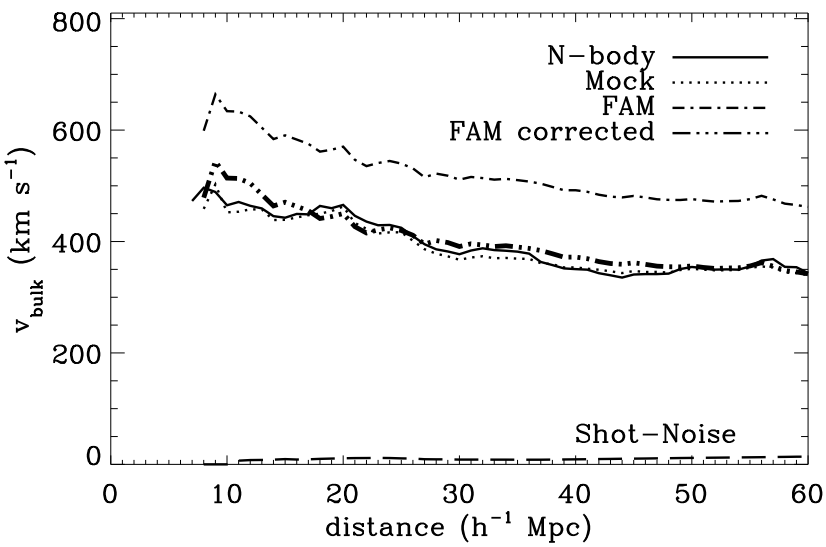

Figure 3.15 — Real (continues line), Mock (dashed line) and FAM bulk flows with its different corrections (shot-noise and *c.o.m.* displacement).

In general, the average results for the four catalogs strengthen the previous results. FAM is able to predict properly the main feature of the peculiar velocity field. The top-left panel in Figure 3.16 shows the mean results for $\mathbf{V}_{b,FAM}$, together with the $\mathbf{V}_{b,Mock}$ for comparison. The gray-shadowed area represents the $\pm 1\sigma$ dispersion error around the FAM mean. The FAM bulk flow follows the same mock bulk flow distribution. This can be better noticed from the upper frame of the bottom-right panel. This frame shows the fractional difference between the mock bulk and the FAM one. As it can be noticed, there is a very good agreement between the 2 quantities. The only major difference is at short scales ($10-15\ h^{-1}$Mpc, region where is located the LS), caused by the failure in FAM in reproducing properly the movements at this non-linear scales, plus the lack of objects sampling such region.

In the same figure, we also display the average results from linear theory and $\mathbf{V}_{b,Mock}$ (top-right panel), together with its dispersion (gray shadows). In this case, we see that the $\mathbf{V}_{b,Lin}$ presents several

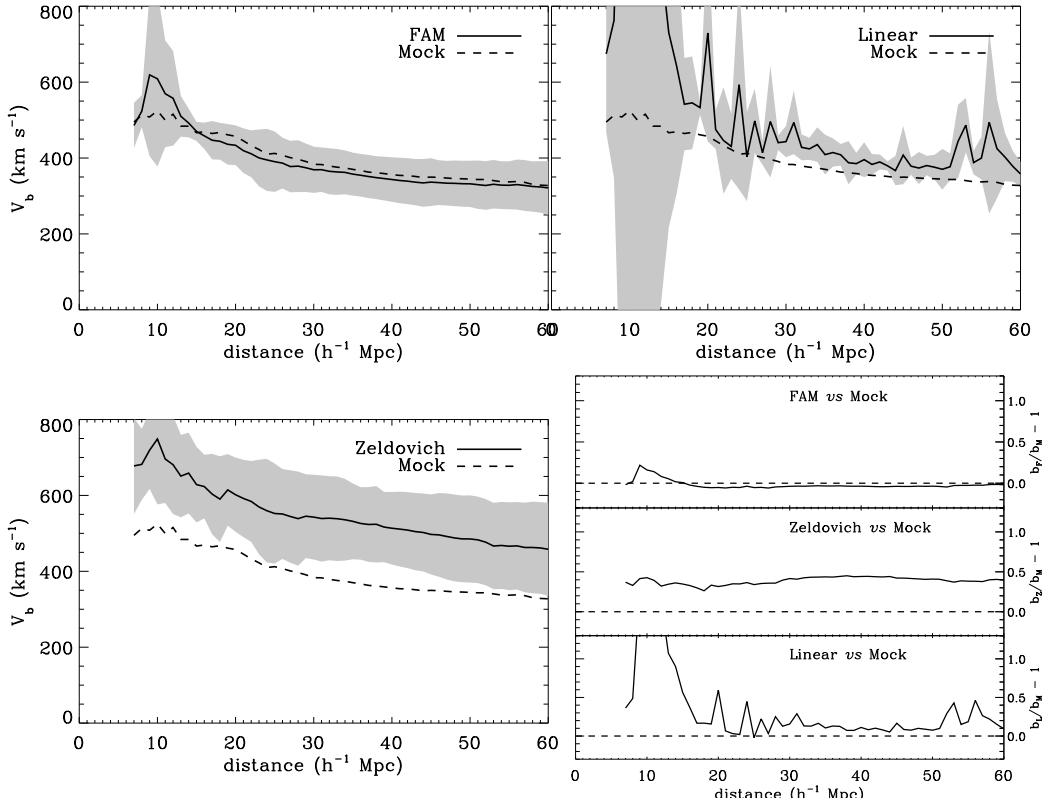

Figure 3.16 — Different bulk flow estimates. The dashed line in all panels represent the Mock bulk flow estimate. The top-left panel shows the FAM bulk flow, the top-right panel the linear bulk flow, while the bottom-left panel the Zel'dovich bulk flow estimate. All the bulk flow estimates have been corrected for shot-noise and *c.o.m.* displacements. The gray shadows represent the $\pm 1\sigma$ dispersion error. The bottom-right panel shows the fractional difference between the different computed bulk flows and the mock one.

spikes along the whole distribution. These spikes are the regions where linear theory is not longer valid (cluster of galaxies). These differences are even more clearly shown in the corresponding fractional-difference panel. The most noticeable difference is around the LS position, while other subsequent spikes are due to considerable mass concentrations, like the GA and PP.

In the case of the Zel'dovich approximation (bottom-left panel), there is a clear mismatch between $\mathbf{V}_{b,Zel}$ and the Mock one. The fractional difference indicates that Zel'dovich overestimates the bulk flow by almost 30%, even after substracting the contribution from the *c.o.m* offset. This mismatch is inherent to the method itself, a consequence of it being a kinematic model. The pull that is exerted over the LG and companying structures is just ruled by the potential well of the mass distribution without taking into account the mutual gravity interaction of the different structures of the system. This introduces a spurious extra bulk flow component into the velocity field.

The bulk flow directions are very similar to each other. Figure 3.17 shows the directions at 60 h^{-1}Mpc for all bulk flow estimates. In particular from the zoom-in we may notice that all directions lie within an area of 20 square degrees. The Zel'dovich direction is the farthest from the rest. In general, all directions are consistent with the Mark III bulk direction, and they point towards the real direction of the bulk flow computed at this distance $(l,b) = (280,0) \pm 30^\circ$ (Dekel 1999). The bulk directions are also consistent with the gravity dipole direction from the mock catalogs (black circle), differing by $17^\circ \pm 5^\circ$. We can conclude that our estimates within the linear regime are consistent, the

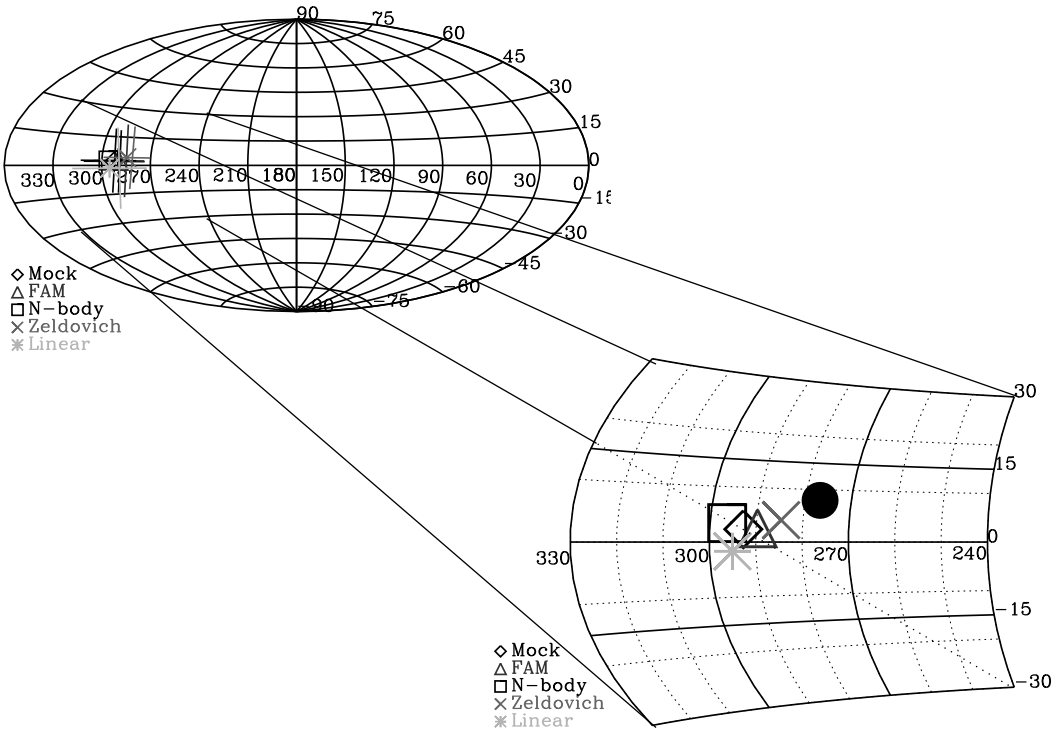

Figure 3.17 — Bulk Flow directions for all the velocity samples studied in this Chapter. The bottom panel is a zoom of the area from the top panel where all bulks reside.

bulk flow and dipole directions do coincide with each other. The three velocity field models,

FAM, linear and Zel'dovich successfully reproduce the direction of the bulk flow. The linear and Zel'dovich directions are within a distance of $\leq 8°$ from the mock one, FAM is only 4°. With respect to direction, FAM appears to be the best performing method.

3.8.3.1 Smoothing Effects

Non-linear effects can also be an important factor. They introduce noise in the different $\mathbf{V}_b$ estimates (e.g. Figs. 3.15 & 3.16). Because our selection procedure follows a Monte Carlo sampling prescription, it could be the case that several particles residing at very dense and clumpy regions with relatively high peculiar velocities have been chosen. At these regions, errors in the velocity estimates are introduced by all methods due to their failure to reconstruct peculiar velocities. In order to clarify this point, we have smoothed the real and reconstructed peculiar velocity fields, convolving the fields with top-hat filters of $R_{TH} = 2$ & $5\ h^{-1}$Mpc. The average cumulative results for all fields are shown in Figure 3.18. The left panel show the unsmoothed $\mathbf{V}_b$ estimates. The central panel displays bulk flows from smoothed velocities with $R_{TH} = 2$, while the right panel exhibits those with $5\ h^{-1}$Mpc. The results show an improvement for the inner cores of the catalogs, the LS region where all small scale structures have been erased. The linear bulk flow estimate is the one who improves best with this smoothing procedure, all spikes have been erased and the distribution coincides better with the real one. The only difference is the central inner region where estimates remain too large. The Zel'dovich quantity does not improve significantly in the sense that the amplitudes are still over-estimated by the same amount than in the unsmoothed case. For the FAM estimate, the only improvement is with respect to the LS, which coincides now with the mock bulk flow estimate. We also computed the relative misalignment angle θ from the smoothed bulk flows results with respect to the unsmoothed case. No significant changes in the bulk flow directions and convergences were noticed. The directions have only been

shifted by $\sim 2^\circ$ closer from their original position. These results show that our bulk flow estimates are not influenced substantially by local non-linearities (except in the case of the $\mathbf{V}_{b,Lin}$) in the mass distribution.

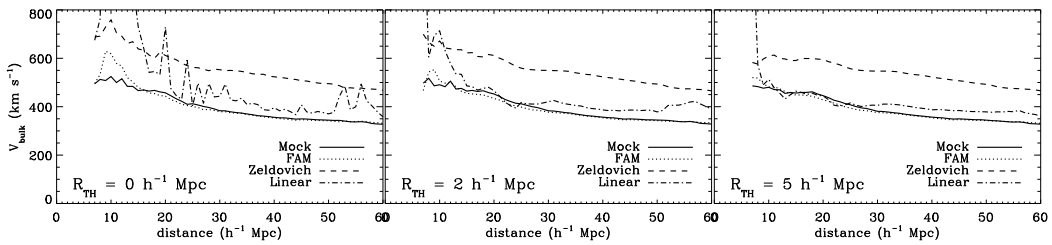

Figure 3.18 — Smoothing effects on $\mathbf{V}_b$ for all methods. The left panel corresponds to the unsmoothed case, the center panel to velocities smoothed with a top-hat filter of 2 h^{-1}Mpc radius and the right panel to velocities smoothed with a 5 h^{-1}Mpc radius.

3.8.3.2 Shell contributions

We have also investigated what the contributions to the total $\mathbf{V}_b$ are from individual shells of thickness (5 h^{-1}Mpc). In this exercise, we have divided the total volume in 30 shells and isolated the velocities of the objects enclosed in each of these shells. For each one of these subsamples we have computed the 3 Cartesian components of their shell-bulk flow. Figure 3.19 shows the average bulk shell Cartesian contributions got from the $N-$body velocities (continues line), mock catalogs (dotted line) and FAM velocities (dashed line). For comparison the gray dot-dashed line represents the $N-$body full average cumulative bulk flow. The gray shadows depict the $\pm 1\sigma$ dispersion errors computed from the FAM Cartesian contributions.

The agreement between the $N-$body, mock and FAM shell Cartesian contributions is very good. All Cartesian-group distributions follow each other very close for almost the whole range in distances. While the y & z Cartesian components remain almost unchanged for the whole range in distances, the behavior along the x component presents more radical changes. This component not only encloses the largest amplitude from the 3 components, but also decreases constantly with radius. Worthy to

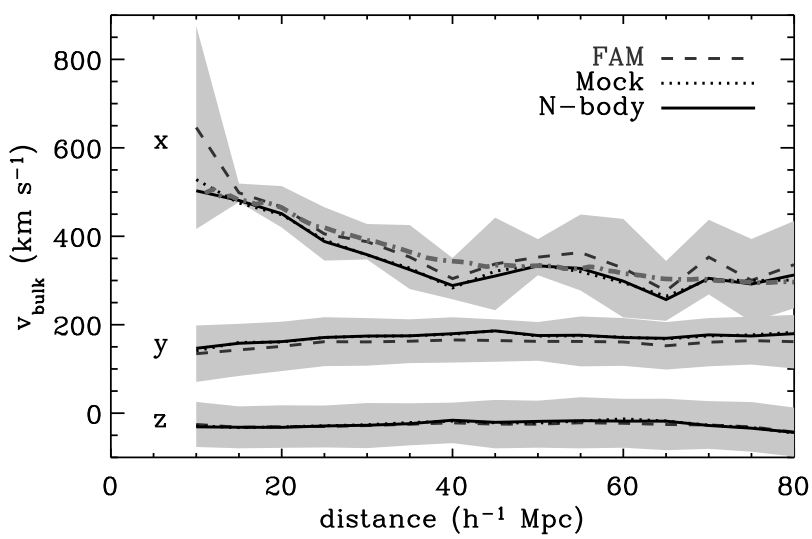

Figure 3.19 — Shell Cartesian contributions to the total $\mathbf{V}_b$. The gray dot-dashed line represents the average $N-$body cumulative bulk flow distribution displayed for comparison purposes.

notice is the fact that this Cartesian bulk shell behavior follows the one prescribed by the full $N-$body bulk distribution (gray dot-dashed line). This means that must of the gravity pull exerted over the LG comes from structures aligned along the x component. The spikes along the FAM $x-$bulk shell distribution represent the location of massive structures that are acting over the LG. Perhaps the most notorious spikes are those located at $\sim 40\ h^{-1}$Mpc (GA), $\sim 50\ h^{-1}$Mpc (PP). At those spikes the FAM components slightly deviates from the mock distribution. Notice as well that there is still a significant contribution of ~ 300 km s^{-1} at the edge of the sample. These results are in good agreement with those obtained by Hoffman et al. (2001) and Dekel (1999).

We have also looked for non-linear effects in the shell contributions. As before, we convolved the different peculiar velocity fields with a top-hat kernel of $R_{TH} = 2$ & $5\ h^{-1}$Mpc. The bulk distributions remain almost intact for the whole distance range.

3.8.4 The velocity Shear

A more demanding comparison between the different reconstructed peculiar velocity fields is the 2nd term in the multipolar velocity decomposition, the velocity shear. The estimate of this term will tell us how well the different techniques deal with the quasilinear regime of our local cosmic neighborhood.

We have computed the velocity shear from the peculiar velocities through the decomposition method exposed in Chapter 2. The matrix representation of the traceless shear tensor is then diagonalized to obtain the eigenvectors (directions) and eigenvalues (amplitudes). We have re-ordered these vectors in such a way that their eigenvalues will be in decreasing order and the sum of all of them will be equal to zero. Hence, the shear eigenvalues follow the following properties:

$$\begin{aligned} &1) \quad s_1 > s_2 > s_3 \\ &2) \quad s_1 + s_2 + s_3 = 0 \\ &3) \quad s = (s_1^2 + s_2^2 + s_3^2)^{1/2} \end{aligned} \tag{3.21}$$

The quadrupole moment of the velocity field informs us about the configuration of the mass distribution. The eigenvalues will tell us how significant the influences of the structures surrounding the LG are. We can visualize these 3 eigenvalues like the 3 main axis of a velocity ellipsoidal, with directions given by their corresponding eigenvectors. These vectors are linearly independent of each other, defining in this way a *shear reference frame*. The s_1 eigenvalue is known like the *dilational (stretching)* mode of the shear velocity and it corresponds to the largest axis of the velocity ellipsoidal. It points towards the direction of the maximum stretch of the ellipsoidal. The s_3 eigenvalue corresponds to the smallest axis of the ellipsoidal, and it is known like the *compressional* mode. Its eigenvector corresponds to the direction where the velocity ellipsoidal is being compressed (like by expanding structures, e.g. voids), and its perpendicular to the dilational eigenvector. The s_2 eigenvalue corresponds to the *middle* mode, and determines the "morphology" of the shear.

Figure 3.20 shows the average 3 eigenvalues and the shear eigenvalue amplitude s for the $N-$body velocity fields (black lines), and the Mock velocity fields (gray lines). The 3 Mock velocity shear components successfully reproduce the behavior of the shear pattern in the $N-$body velocity fields. The velocity field of the mock catalogs trace fairly the $N-$body peculiar velocity field. The mock estimates can be used as genuine representations of the real values. In this plot we present the calculations performed until the edge of the sample radius for displaying purposes. The shear converges to zero much faster than the corresponding bulk flow due to its stronger dependence in distance (x^{-3}). It can be noticed that the gross of the shear influence comes from structures located within $60\ h^{-1}$Mpc, and more specific within $40\ h^{-1}$Mpc. Although there is still some influence (< 10 km s^{-1} Mpc^{-1}) from structures located between $60-80\ h^{-1}$Mpc. The influence of the LS can be clearly seen by the high values at regions $< 15\ h^{-1}$Mpc.

We have computed the value of the 3 cumulative eigenvectors and eigenvalues for all our catalogs with the 3 modeling methods (FAM, Zel'dovich & linear). The left-column panels in Figure 3.21 show the behavior of the eigenvalues for the 3 reconstruction techniques, plus the Mock distributions for

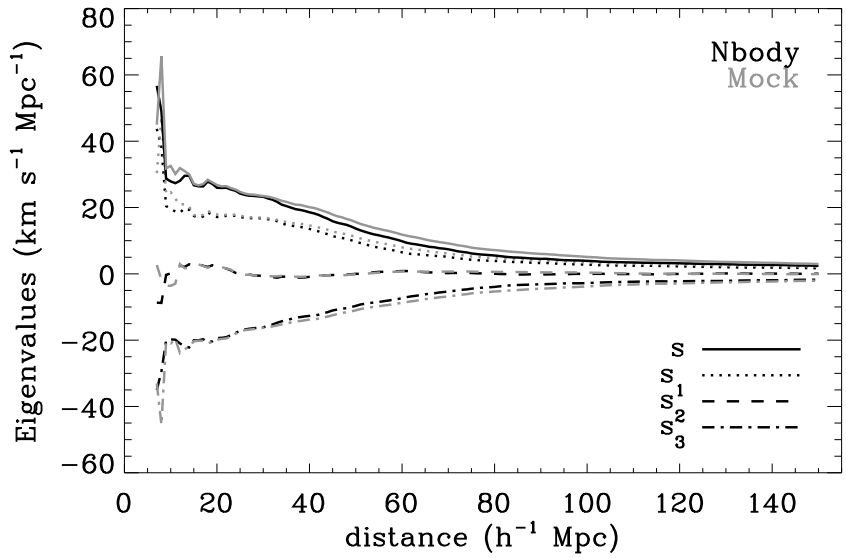

Figure 3.20 — Average eigenvalues for the 4 N-body velocity fields (black lines), and Mock velocity fields (gray lines) as a function of the computation distance.

comparison purposes. The right-column panels show the angular misalignment θ, measured between the mock eigenvectors and those from the reconstruction algorithms at each computing radius. The gray shadows represent the 1σ dispersion errors around the mean values. The darkest gray corresponds to the FAM errors, the half-gray scale the Zel'dovich errors, while the light gray depicts the errors from linear theory. The top panels correspond to the dilational mode, the central to the middle one, and the bottom to the compressional mode. In all panels the linear technique consistently fails in reproducing the expected results. The linear eigenvalue's distributions are full of spikes and deviations from the expected ones; these spikes/deviations are due to the presence of virial motions (linear regime not longer valid) caused by non-linear structures like clusters of galaxies present in the catalogs. This corresponding relative eigenvector's convergences show the same behavior. The large discrepancies in the directions at given positions are correlated with the peaks presented along the eigenvalue distributions, located at the same positions. In general, linear results are barely consistent with the expected values, specially at LS scales. These results make linear theory not very suitable for studying the dynamics of the LG and LS environment. The Zel'dovich approximation gives in general better results than linear theory. Although it underestimates the eigenvalues for regions where the LS and GA ($20-40\ h^{-1}$Mpc) are present, they are still consistent within the errors. With respect to its eigenvectors, they show in general an average constant deviation of 10° for each eigenvector from the mock ones (but again, consistent with the errors). This is a consequence of the method itself (as stated before) of being a kinematic approach. The method suffers from severe problems are regions where the flow is not longer laminar (e.g. cluster of galaxies). This is also reflected in the broad error shadows. The Zel'dovich approximation fails mainly in reproducing the right directions of the non-linear movements, but its performance at middle large scales ($\sim 30-40\ h^{-1}$Mpc) its better than plain linear theory. In the case of FAM, its eigenvalues cannot reproduce properly the expected behavior for the inner regions of the catalogs ($< 20\ h^{-1}$Mpc). This region corresponds to the non-linear regime where FAM (like the other methods) fails in reproducing the corresponding velocities properly. Beyond this radius, the FAM estimates are remarkably good in comparison with the expected ones. This situation is also reflected in the eigenvector's convergence. The direction converges rapidly after the inner region, remaining very close to the Mock directions ($\lesssim 5^\circ$). Furthermore, the better agreement between the FAM and expected quantities is reflected in the error shadows, these are smaller than those given by the other two methods and hence, overshadowed.

With respect to the velocity ellipsoid, the maximum stretch (s_1 eigenvector) points to $(l,b) = (327,14)^\circ \pm (15,8)^\circ$ and its antipode (very close to the one predicted by Lilje, Yahil, & Jones 1986).

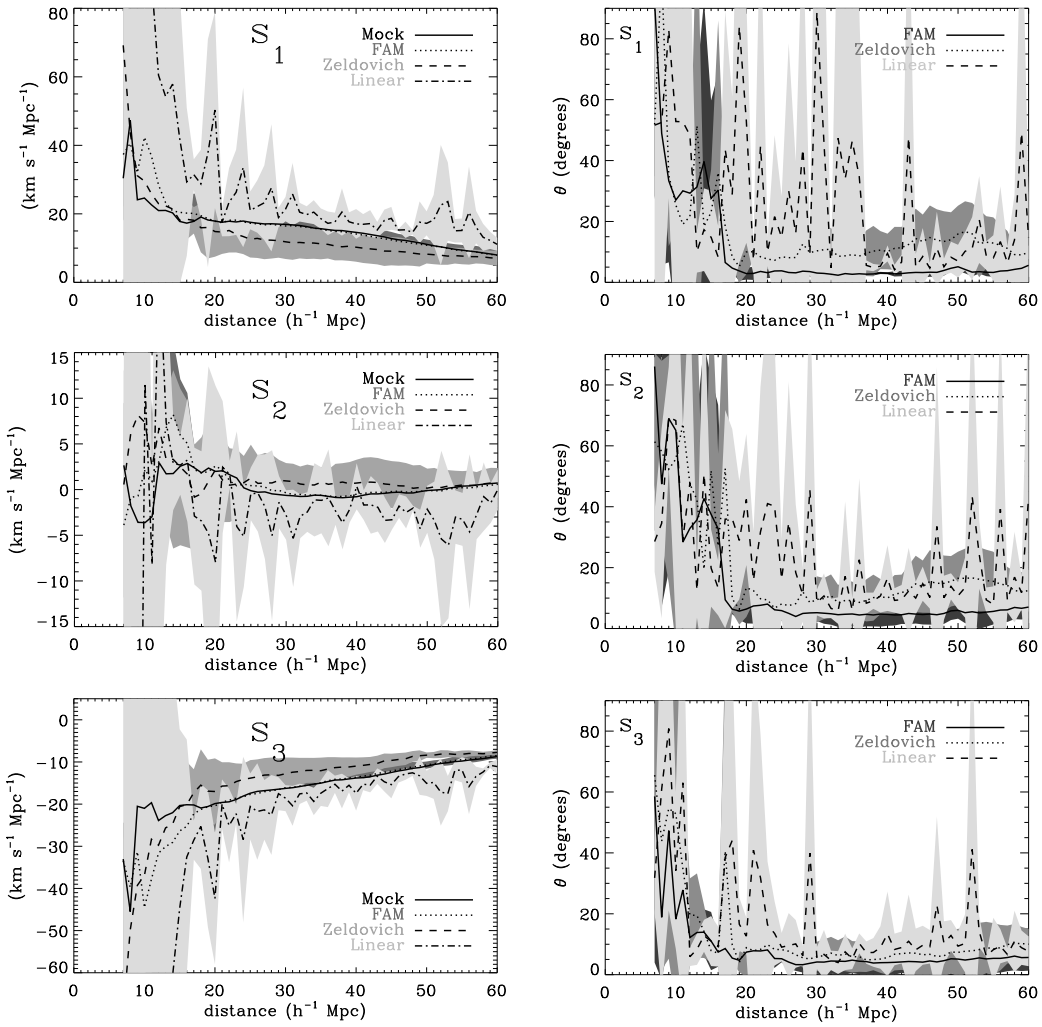

Figure 3.21 — Average shear components for all catalogs and modeling techniques. The Left-column panels represent the 3 eigenvalue amplitudes, while the right-column panels show the convergence of the corresponding eigenvectors with respect to the Mock ones. The gray shadows represent the 1σ dispersion error around the averages.

This indicates a relative offset with respect to the bulk velocity of 43°. This misalignment depends on the configuration of the quadrupolar and dipolar mass distributions. It also indicates that we are still missing contributions from mass concentrations beyond this radius. The contraction (s_3) is pointing towards $(l,b) = (103,2)^\circ \pm (18,10)^\circ$. It is interesting to notice that the expansion points towards the direction of the Hydra-Centaurus cluster (GA).

The last point to consider for the velocity ellipsoid is smoothing effects. Figure 3.22 shows the cumulative eigenvalue's amplitudes (s) of the unsmoothed velocities (left panel), and the $R_{TH} = 5\,h^{-1}$Mpc smoothed velocities (right panel). The gray shadows indicate the $\pm 1\sigma$ dispersion errors. The darkest gray represents the errors from the FAM technique, the middle-gray scale to the Zel'dovich, and the lightest gray to linear theory. Linear theory estimates improve as a result of erasing the small scale signal in the velocities. Nevertheless, it fails in reproducing the virial motions of the LS, but the overall smoothed results are consistent with the expected values. The Zel'dovich approximation un-

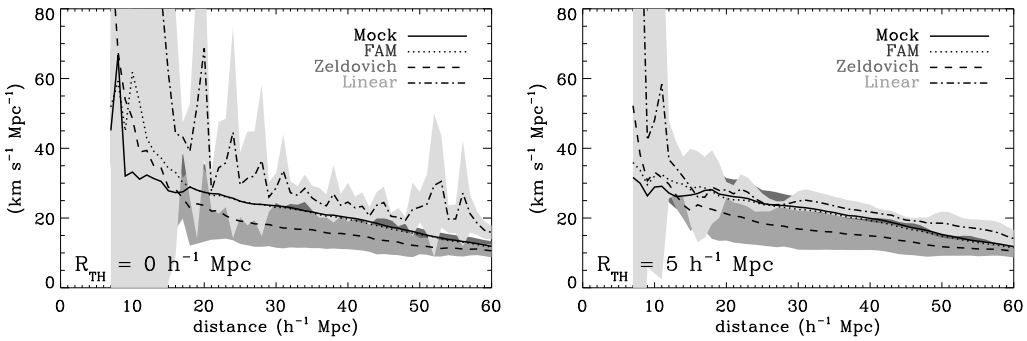

Figure 3.22 — Average shear amplitude eigenvalues (s) for unsmoothed velocities (left panel), and for R_{TH} = 5 h^{-1}Mpc smoothed velocities (right panel) for all catalogs and reconstruction techniques. The gray shadows depict the 1σ dispersion errors around the averages.

derestimates the Mock values by $\sim 20\%$ for both cases, but still consistent within the 1σ errors. It also fails in the LS, although with a better estimate than linear theory. The FAM technique reproduces very well the expected behavior (even in the case of unsmoothed velocities). At the center of the catalogs, FAM still presents some inconsistencies from the expected ones. Nevertheless, they get erased when smoothing velocities, reproducing in this way the inner core of the catalogs. It is worthy to mention that all methods seem to converge at the 60 h^{-1}Mpc edge. This is an intrinsic characteristic from the computed quantity. Indeed, as shown in Fig. 3.20, there are almost none substantial contributions beyond this radius. The case of the eigenvectors show the same behavior, the spikes get erased when applying smoothing, but in general the relative distance between the Mock and the reconstructed quantities remains almost intact.

3.9 Conclusions

In the present study, we have computed the main components of the peculiar velocity field of our local Universe, the bulk and shear moments. The peculiar velocity fields have been modeled from the galaxy positions in mock catalogs. The mock catalogs were extracted from realistic constrained $N-$body simulations of our nearby Universe. The initial density fields used to compute the present mass distributions, were produced from real data through the algorithm of the Wiener Filter and Constrained Realizations. The final outcome of the simulations (4 in total) successfully reproduced the main structures (LS, GA, PP) that surrounds the LG (located at the center of the simulation boxes). The mock catalogs carved out from this simulations are aimed to mimic the mass distribution around the LG, and up to a radius of 150 h^{-1}Mpc. These mock catalogs have been composed by two different sampled regions. An inner region that is volume-limited aimed to mimic the NBG catalog $[0-30\ h^{-1}\text{Mpc}]$, and a flux-limited region following the PSCz catalog selection function $[30-150\ h^{-1}\text{Mpc}]$.

The reliability of the final mass distributions and their corresponding mock catalogs was tested by measuring their dipolar moment and comparing them with respect to the real observed estimates. Results showed that our simulations and mock catalogs successfully reproduce the mass distribution even beyond the constrained dynamical range of the catalogs.

The comparison between the computed gravity dipole for the $N-$body mass distributions and for the Mock galaxy distributions, showed that it is necessary to correct the mock catalogs due to sampling effects for shot-noise effects. These effects become stronger at large distances and can represent more than 10% of the dipole amplitude. The amplitude and direction of the cumulative Mock dipole and the one from the $N-$body mass distribution are very close to each other and follow the same average behavior, at 60 h^{-1}Mpc they are located at $(l,b) = (277,14)^\circ \pm (21,11)^\circ$ and with an amplitude of

542 ± 52 km s^{-1}, being these results in good agreement with those from the literature (e.g. Rowan-Robinson et al. 2000). The evolution of the WF/CR has successfully reproduced the observations in the sense that there might be still structures influencing over the LG at very large scales (e.g. Hoffman et al. 2001).

We have compared the bulk flows from the full $N-$body velocity distribution and the one from the Mock catalog velocities. The results showed that both estimates follow the same behavior for almost the whole range in distances. We have limited our analysis up to 60 h^{-1}Mpc for having similar regions (constrained regions) between the 4 catalogs. Although we have corrected the object distributions for shot-noise effects, we cannot correct for the velocities because of our ignorance of the surroundings around the objects. This means that the objects could be located at a highly non-linear region or in a middle of a void and there is no way to know this in order to correct for. From the selection function, we know that we are dealing with objects that are brighter than a certain limit, but these objects could be located anywhere. A way to overcome this problem, is by increasing the number of chosen objects by modifying the selection function. But because our aim is to produce realistic mock catalogs following (in this case) the real distribution of objects in the PSC*z* catalog, we are limited by this constraint. The position of the computed bulk flows are located in the sky around $(l,b) = (294,3)^\circ \pm (19,14)^\circ$, having an offset of less than 18° from the dipole direction and with an amplitude of 330 ± 62 km s^{-1}. Both results are consistent with observations at this same radius (Dekel 1999; Zaroubi 2002). The fact that there exists a relative misalignment with respect to the real dipole and that the dipole magnitude up to this radius represents $\sim 55\%$ of the total LG bulk amplitude, implies that structures beyond this radius still play an important role in the dynamics of the LG. Between the $N-$body and Mock dipoles, there is an offset of 4°, attributed to the sampling procedure. Nevertheless, the mock catalog velocities represent our best estimate of the real velocity field given a selection function, under the hypothetical case that we can measure the 3D spatial object velocities. The shear components of these two velocity fields show also some interesting features. Both estimates are very close to each other and their directions are comparable. Furthermore, we have measured a significant influence beyond 60 h^{-1}Mpc, evidenced by the amplitude of the eigenvalues at these radii.

The modeling of the peculiar velocity field has been performed by using 3 different algorithms: linear theory, Zel'dovich approximation and the FAM technique. We observed the following:

The linear bulk flow proved to be highly noise dominated, especially at the regions of the LS, GA, and PP where prominent spikes are present in both amplitude and direction. At these regions, linear theory is not longer valid for being non-linear. Nevertheless, these effects can be overcome by applying a smoothing algorithm with a radius of 5 h^{-1}Mpc. These smoothed results were shown to be in good agreement with the expected values, although there was a large discrepancy at the LS region. The corresponding eigenvalues and eigenvectors suffered from the same effects at non-linear regions. Smoothed results proved to be in better agreement, both eigenvectors and eigenvalues are in general closer to the expected values. Nevertheless, at the LS regions, the method fails completely. As in the case of the bulk flow, the linear shear estimates are just barely consistent with the expected values.

In the case of the Zel'dovich and FAM reconstructions, an extra correction had to be done because of the shift between the geometrical centre and *c.o.m.*. This effect introduce an extra-spurious bulk flow because of the different apparent mass distributions when reconstructing the velocity field by means of the FAM technique. Even after these corrections, the Zel'dovich bulk flow had consistently larger amplitudes than the expected estimates. The reason for this is that the method overestimates the velocities in regions where the flow is not longer laminar. These over-predictions have a cumulative effect that is reflected in the bulk flow. The corresponding Zel'dovich bulk direction was much better determined, with an offset of only 9° with respect to the mock one. The eigenvalues always underestimated the Mock values by almost 20% of their total value, but consistent within the 1σ dispersion errors. The average estimates did not show a significant improvement when smoothing apart from the LS region where the amplitudes decreased and converged to the expected ones. The Zel'dovich velocity ellipsoid is slightly distorted with respect to the expected one. There is a misalignment of 8° between the Zel'dovich shear frame and the Mock one.

On the other hand, FAM estimates are in general much closer to the mock estimates than the other

2 reconstruction techniques. Its bulk amplitude is very similar to the Mock one. There is a discrepancy at small radius, the result of the LS influence. The robustness of the method is noticed by the fact that there are no significant changes in the results even when applying a smoothing procedure, plus the fact that errors are considerable small ≈ 60 km s^{-1}. The direction of its bulk flow is remarkably close to the Mock direction, with a misalignment angle of 3°, closer than those obtained from the linear and Zel'dovich approaches. The shear components also follow the expected behavior for regions excluding the LS. If smoothing is applied, then the FAM LS estimates improve considerably. In the case of the eigenvectors, they also remain very close to the Mock ones. The FAM velocity ellipsoidal has a shift of only 4° with respect to the expected one.

We have proved that all methods employed in this study fail in reproducing the LG dynamics for being within the non-linear regime. A smoothing algorithm is necessary in order to overcome this effect, not in all cases results are completely satisfactory (linear theory and Zel'dovich approx.). In the mildly non-linear regime, the 3 methods give acceptable results and comparable to the expected ones within the errors. FAM performs slightly better than the other two methods. It properly reproduces the dynamical behavior of the LS environment and presenting tighter relations with respect to the expected values. At linear scales, the 3 reconstruction techniques give more similar results (provided extra-processing in the peculiar velocity field, like smoothing), and very close to the expected ones. Given these results, we can conclude that the FAM method is the most suitable technique to study the dynamics of the LG & LS cosmic environment. Furthermore, this study showed as well, that the success of FAM will depend on the kind of sample used.

As a last point, the fact that our results match those obtained from observations of our real Universe, is one success of employing the WF/CR algorithm. Even though at scales that have not being strongly constrained due to the lack of good data, the method is able to reproduce the main characteristics of the mass distribution and its corresponding peculiar velocity field, the dipole and bulk flow.

Acknowledgments

The authors thank the HYDRA consortium for making publicly available their $N-$body code. E.R.D. thanks W. E. Schaap for stimulating discussions. E.R.D. has been partly supported by The National Council for Research and Technology (CONACyT, México) through a scholarship.

3.A Constrained Realizations

Bertschinger (1987) realized that a constraint realization of Gaussian random field f is given by the sum of the analytically calculated mean fiend $\bar{f}$ and the random residual field F,

$$f(\mathbf{r}) = \bar{f}(\mathbf{r}) + F(\mathbf{r}). \tag{A3-1}$$

Hoffman & Ribak (1991) presented a straightforward method for the construction of constrained realizations of Gaussian fields based on the defining work of Bertschinger (1987). They realized that, for any constraint that is a linear functional of the field, the problem can be solved exactly and in a simple way, without involving iterations.

van de Weygaert & Bertschinger (1996) exposed in a very detailed way the CR methodology and explored its benefits and advantages on particular realizations. Within this implementation, a peak or dip in the density field can be characterized by a set of 21 physical constraints, including its scale, position and orientation, density, velocity and velocity gradient.

In this appendix we follow the CR prescription of van de Weygaert & Bertschinger and expose its main concepts.

Consider a random homogeneous and isotropic Gaussian field $F(\mathbf{r})$ with zero mean which is defined by its power spectrum $P(k)$. This field is subject to a set of M constraints,

$$\Gamma = \{C_i(\mathbf{r})|_{\mathbf{r}_i} \equiv C_i[f;\mathbf{r}_i] = c_i; \quad i = 1,\ldots,M\}. \tag{A3-2}$$

The constraints are consequently imposed by forcing the field $C_i[f;\mathbf{r}_i],(i = 1,\ldots,M)$, a functional of the field $f(\mathbf{r})$ as well as a function of the point $\mathbf{r}$, to have the specific value c_i at the given position. The constraints C_i are assumed to be linear functionals, clear examples are the values of the field itself at the point $\mathbf{r}_i$, the derivative of the field $f(\mathbf{r})$ or a convolution over $f(\mathbf{r})$ with some function $g(\mathbf{r})$,

$$\begin{aligned} C_i[f;\mathbf{r}_i] &= f(\mathbf{r}_i) = c_i \\ C_j[f;\mathbf{r}_j] &= \frac{\partial}{\partial r} f(\mathbf{r})|_{\mathbf{r}_j} = c_j \\ C_k[f;\mathbf{r}_k] &= \int g(\mathbf{r}-\mathbf{r_i}) f(\mathbf{r}) \mathrm{d}\mathbf{x} = c_k \end{aligned} \tag{A3-3}$$

Since we have limited the field $f(\mathbf{r})$ to those that obey the set of M constraints Γ, the probability of possible realizations of our $f(\mathbf{r})$ is given by the conditional probability distribution function,

$$\mathcal{P}[f(\mathbf{r})|\Gamma] = \frac{\mathcal{P}[f(\mathbf{r}),\Gamma]}{\mathcal{P}[\Gamma]} = \frac{\mathcal{P}[f]}{\mathcal{P}[\Gamma]}, \tag{A3-4}$$

where $\mathcal{P}[\ldots]$ is the multivariate Gaussian of the appropriate variables. This comes by virtue of the central limit theorem, the distribution of a Gaussian random field will approach normality, and the multivariate distribution $\mathcal{P}$ is multivariate Gaussian:

$$\mathcal{P}_N = \frac{\exp\left[-\frac{1}{2}\sum_{i=1}^{N}\sum_{j=1}^{N} f_i(\mathrm{M}^{-1})_{ij} f_j\right]}{[(2\pi)^N (det\mathrm{M})]^{1/2}} \prod_{i=1}^{N} \mathrm{d} f_i, \tag{A3-5}$$

where M^{-1} is the inverse of the covariance matrix M, the generalization of the variance σ^2 in a one-dimensional normal distribution. M is completely determined by the autocorrelation function $\xi(\mathbf{r})$ if the field is a Gaussian random field,

$$M_{ij} \equiv \langle f(\mathbf{r}_i) f(\mathbf{r}_j)\rangle, \tag{A3-6}$$

where the brackets $\langle\ldots\rangle$ denotes ensemble averages. Since f is a $N-$dimensional vector, the covariance matrix M can be written as:

$$\mathrm{M} = \langle f f^t\rangle, \tag{A3-7}$$

with f^t being the transpose of f.

Because the constraints C_i are linear functionals, the central limit theorem also assures them to have a Gaussian probability distribution when applied on a Gaussian field $f(\mathbf{r})$. The second equality in Eqn. A3-4 comes from the fact that the constraints are linear functionals of f, so that the joint probability space for f and Γ is the same as the probability space for f.

The conditional probability distribution function can be described as a shifted Gaussian around the ensemble mean field $\bar{f}(\mathbf{r})$ (van de Weygaert & Bertschinger 1996), defined as

$$\bar{f}(\mathbf{r}) = \langle f(\mathbf{r})|\Gamma\rangle = \xi_i(\mathbf{r})\xi_{ij}^{-1} c_j, \tag{A3-8}$$

where summation over repeated indexes is assumed. Hence, $\bar{f}(\mathbf{r})$ is the "most likely" field satisfying the constraints and it equals the 'average density profile' obtained by BBKS. The term ξ_i in the previous equation is given by

$$\xi_i(\mathbf{r}) = \langle f(\mathbf{r}) C_i\rangle, \tag{A3-9}$$

and it represents the cross-correlation between the field and the ith constraint $C_i[f;\mathbf{r}_i]$, while

$$\xi_{ij} = \langle C_i C_j\rangle, \tag{A3-10}$$

is the ijth element of the constraints' correlation matrix, and C_i is evaluated at $\mathbf{r}_i$. In the case where the constraints C_i involve only the field itself, both the correlation matrix ξ_{ij} and $\xi_i(\mathbf{r})$ can be written in terms of the two-point autocorrelation function $\xi(\mathbf{r})$, that is:

$$\begin{aligned}\xi_{ij} &= \langle f(\mathbf{r}_i) f(\mathbf{r}_j)\rangle = \xi(|\mathbf{r}_i - \mathbf{r}_j|)\,,\\ \xi_i(\mathbf{r}) &= \langle f(\mathbf{r}) f(\mathbf{r}_j)\rangle = \xi(|\mathbf{r}_i - \mathbf{r}|)\,,\end{aligned} \tag{A3-11}$$

The residual field $F(\mathbf{r})$ is defined as the difference between the Gaussian field $f(\mathbf{r})$ satisfying the constrain set Γ and the mean field $\bar{f}(\mathbf{r})$:

$$F(\mathbf{r}) \equiv f(\mathbf{r}) - \bar{f}(\mathbf{r})\,. \tag{A3-12}$$

Note that the residual field F is a random Gaussian field because it is the difference between two Gaussian fields. This residual field provides random noise which is added to the signal $\bar{f}(\mathbf{r})$, which is completely fixed by the imposed set of constraints Γ. In terms of the residual field F, the constraint points are expressed as $\{F(\mathbf{r}) = C_i[f;\mathbf{r}_i] = c_i; i = 1,\ldots,M\}$. Any particular constrained realization can be written then as the sum of the analytically calculated mean field Γ (via Eqn. A3-8), and the random residual field $F(\mathbf{r})$:

$$f(\mathbf{r}) = \bar{f}(\mathbf{r}) + F(\mathbf{r}) = \xi_i(\mathbf{r})\xi_{ij}^{-1} c_j + F(\mathbf{r})\,. \tag{A3-13}$$

The "crucial" point in this algorithm is that

$$C_i[F] = C_i[f - \bar{f}] = C_i[f] - C_i[\bar{f}] = c_i - c_i = 0\,, \tag{A3-14}$$

the statistical properties of the residual field are all *independent* of the numerical values of the constraints c_i, and for any particular choice of the constraints a realization of the residual can be straightforward constructed.

The construction of a constrained realization of the field $f(\mathbf{r})$ it can be done in five stages (Hoffman & Ribak 1991; van de Weygaert & Bertschinger 1996)

1. Create a random, unconstrained realization of the field $\tilde{f}$, which is a homogeneous and isotropic Gaussian random field whose statistics is determined solely by the power spectrum $P(\mathbf{k})$.

2. Calculate for this particular realization $\tilde{f}$, the values $\tilde{c}$ of the constraints $\{C_i(\mathbf{r})|_{\mathbf{r}_i}, i = 1,\ldots,M\}$. These variables can be looked upon as defining another set of constraints, $\tilde{\Gamma} = \{\tilde{c}\}$. This a posteriori set of constraints is evaluated at the positions of the original constraints and has the values of this specific realization.

3. Calculate for this "random" constrained set $\tilde{\Gamma}$ the corresponding mean field expected as if the set was chosen initially,
$$\bar{\tilde{f}} = \langle \tilde{f}|\tilde{\Gamma}\rangle = \xi_i(\mathbf{r})\xi_{ij}^{-1}\tilde{c}_j\,. \tag{A3-15}$$

4. Evaluate the residual field $\tilde{F}$ of the realization from the given particular realization and the calculated mean field $\tilde{\Gamma}$ as
$$\tilde{F}(\mathbf{r}) = \tilde{f}(\mathbf{r}) - \bar{\tilde{f}}(\mathbf{r})\,. \tag{A3-16}$$
The residual field $\tilde{F}$ thus generated is the residual field of a particular realization restricted to the desired constraints, Γ

5. Evaluate the desired mean field $\bar{f}$, according to Eqn. A3-8 and add it to the residual field $\tilde{F}(\mathbf{r})$ to obtain a particular realization of the desired constrained Gaussian random field
$$f(\mathbf{r}) = \tilde{f}(\mathbf{r}) + \xi_i(\mathbf{r})\xi_{ij}^{-1}(c_j - \tilde{c}_j)\,. \tag{A3-17}$$

The constructed field $f(\mathbf{r})$ obeys the imposed constraints and replaces the unconstrained field $\tilde{f}(\mathbf{r})$. Note that there is a one-to-one correspondence between the trial field $\tilde{f}(\mathbf{r})$ and the constructed one $f(\mathbf{r})$. Furthermore, the ensemble of realizations produced by this algorithm properly samples the sub-ensemble of all realizations constrained by Γ. The algorithm is exact and involves the creation of only one random unconstrained realization and the calculation of the mean field under the given constraints. There is not restriction over the number of constraints and these can be in a very large number, and they can be imposed on the field itself or on any linear functional of it.

3.B The Wiener Filter

The common use of the Wiener Filter [WF] is for noise suppression. Several authors (e.g. Lahav et al. 1994; Fisher et al. 1995b; Zaroubi et al. 1995, 1999) implemented the WF to reconstruct the density field from the observed radial velocities and to interpolate or extrapolate the reconstruction to regions of poor sampling. The latter can be done in real space, to interpolate into the Zone of Avoidance or to extrapolate into large distances, or it can be used in a reciprocal space, such as the Fourier space or spherical harmonic space to increase the resolution of the data.

The WF multiplying the data to obtain the estimator is schematically $P_k/(P_k+\sigma^2)$ (where P_k is the power spectrum and σ the error). This means that the filter attenuates the estimator to zero in regions where the noise dominates. The reconstructed mean field is thus statistically inhomogeneous. In order to recover statistical homogeneity the use of Constrained Realizations is necessary. In the CR the random realizations of the residual from the mean are generated such that they are statistically consistent both with data and with the prior model (Hoffman & Ribak 1991). In regions (real or any reciprocal space) dominated by "good" quality data, the CRs are dominated by the data, while in the limit of no data the realizations are practically unconstrained.

The general application of the WF/CR method to the reconstruction of large scale structure is described in detail in Zaroubi et al. (1995), see also Fisher et al. (1995b). Here we limit to the description and application of the approach to radial velocity data as stated in Zaroubi et al. (1999).

The data for the WF/CR analysis are given as a set of observed radial peculiar velocities u_i^0 sampled at positions $\mathbf{r}_i$ with estimated errors ϵ_i which are assumed to be uncorrelated. The peculiar velocities are assumed to be corrected for systematic errors. The observed velocities are related to the true underlying velocity field $\mathbf{v}(\mathbf{r})$, or its radial component $\mathbf{u}_i$ at $\mathbf{r}_i$, by the following expression:

$$\mathbf{u}_i^0 = \mathbf{v}(\mathbf{r}_i)\cdot\hat{\mathbf{r}}_i + \epsilon_i \equiv \mathbf{u}_i + \epsilon_i\,. \tag{B3-18}$$

It is assumed that the peculiar velocity field $\mathbf{v}(\mathbf{r})$ and the density fluctuation field $\delta(\mathbf{r})$ are related via the linear gravity instability theory. Under the assumption of a specific theoretical prior for the power spectrum $P(k)$ of the underlying density field, the WF minimum-variance estimator of the reconstructed velocity field can be written as:

$$\mathbf{v}^{WF}(\mathbf{r}) = \langle \mathbf{v}(\mathbf{r})\mathbf{u}_\mathbf{i}^0\rangle\langle \mathbf{u}_\mathbf{i}^0\mathbf{u}_\mathbf{j}^0\rangle^{-1}\mathbf{u}_\mathbf{j}^0\,, \tag{B3-19}$$

where the angle brackets denote an ensemble average. The term $\langle \mathbf{u}_\mathbf{i}^0\mathbf{u}_\mathbf{j}^0\rangle$ is the two-point radial velocity correlation function. The cross-correlation term $\langle \mathbf{v}(\mathbf{r})\mathbf{u}_\mathbf{i}^0\rangle$ is calculated from the two-point velocity correlation tensor (Zaroubi et al. 1999). The WF mass-density fluctuation field $\delta^{WF}(\mathbf{r})$ is given by an analogous expression:

$$\delta^{WF}(\mathbf{r}) = \langle \delta(\mathbf{r})\mathbf{u}_\mathbf{i}^0\rangle\langle \mathbf{u}_\mathbf{i}^0\mathbf{u}_\mathbf{j}^0\rangle^{-1}\mathbf{u}_\mathbf{j}^0\,, \tag{B3-20}$$

where the first term corresponds to the cross-correlation matrix of the density and radial velocity. Note that in linear theory the WF reconstruction of the velocity and density fields is equivalent to first reconstructing one of those fields and then solving the Poisson equation for the other.

The formalism of constrained realizations allows one to create a typical realization of the residual from the WF mean field Hoffman & Ribak (1991). The method is based on creating random realizations, $\tilde{\delta}(\mathbf{r})$ and $\tilde{\mathbf{v}}(\mathbf{r})$, of the underlying fields that are statistically consistent with the assumed power

spectrum and the data via linear theory, and a proper set of errors $\tilde{\epsilon}_i$. The velocity random realization is then "observed" like the actual data to yield a mock velocity data set $\tilde{\mathbf{u}}_i^0$. Constrained realizations of the dynamical fields are then obtained by

$$\mathbf{v}^{CR}(\mathbf{r}) = \tilde{\mathbf{v}}(\mathbf{r}) + \langle \mathbf{v}(\mathbf{r})\mathbf{u}_\mathbf{i}^0 \rangle \langle \mathbf{u}_\mathbf{i}^0 \mathbf{u}_\mathbf{j}^0 \rangle^{-1} (\mathbf{u}_\mathbf{j}^0 - \tilde{\mathbf{u}}_\mathbf{j}^0) \tag{B3-21}$$

and

$$\delta^{CR}(\mathbf{r}) = \tilde{\delta}(\mathbf{r}) + \langle \delta(\mathbf{r}) u_i^0 \rangle \langle \mathbf{u}_\mathbf{i}^0 \mathbf{u}_\mathbf{j}^0 \rangle^{-1} (\mathbf{u}_\mathbf{j}^0 - \tilde{\mathbf{u}}_\mathbf{j}^0) . \tag{B3-22}$$

The average of the CRs is the WF field. Their scatter about the WF field is the uncertainty that it is attributed to the field. The uncertainties are evaluated from the CRs for the purpose of evaluating errors in quantities that are computed later from the WF fields. It is worthy to mention that this type of reconstruction is designed to treat the random errors in an optimal way, thus stressing only robust structures and avoiding fake structures.

4

Modeling the local cosmic peculiar velocity field II: Constrained Simulations

E. Romano-Díaz, E. Branchini, R. van de Weygaert & Y. Hoffman.

We have modeled the peculiar velocity field of our Local Supercluster [LS] in a volume of 30 h^{-1}Mpc radius from the Local Group by means of the FAM method. We have made use of mock catalogs carved out from realistic constrained $N-$body simulations of the nearby universe. The LS mock catalogs were constructed according to the Nearby Galaxy Catalog [NBG] in a volume fashion way. External contributions from the mass distribution beyond 30 h^{-1}Mpc and up to 150 h^{-1}Mpc from the Local Group have been considered by applying FAM to volume+flux limited catalogs. Such catalogs mimic the mass distribution according to the IRAS-PSC*z* selection function. The external contributions have been quantified by a multipolar decomposition of the residual velocity field by substracting the "inner" contributions given by the NBG catalog, from the large scale "external" contributions given by the PSC*z*-alike catalog. Results show that the dipole and quadrupole moments represent the major share of the external matter distribution beyond the LS region. When adding these two components to the LS velocity model, it is possible to obtain a bias-free velocity field for the inner NBG catalog. In an earlier study Romano-Díaz et al. (2004) addressed the same issue by using unconstrained $N-$body simulations for the LS. The accuracy of their results, however, depends on the mass distribution beyond the LG region. In this chapter we do not suffer from this problem since our parent $N-$body samples are effectively constrained according to the matter distribution revealed by the Mark III catalog of peculiar velocities.

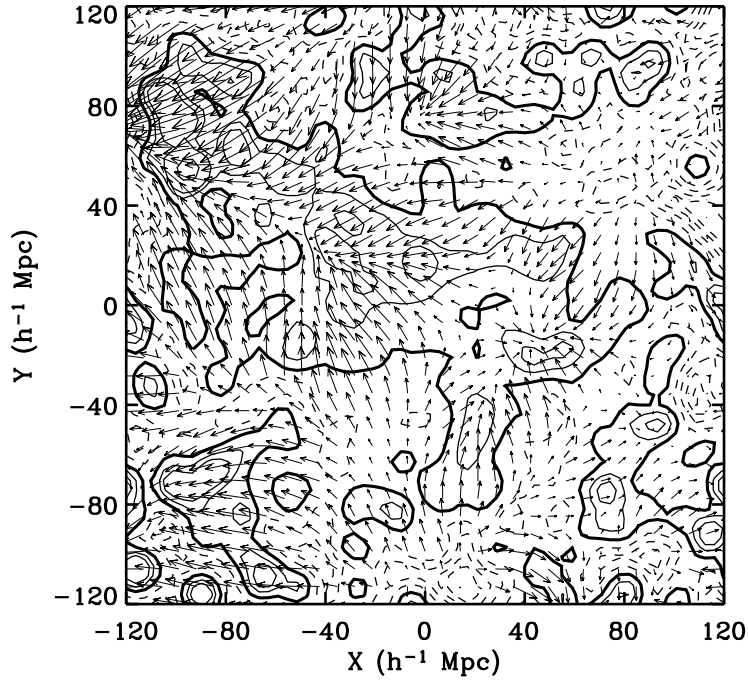

Figure 4.1 — Interpolated density (contour lines) and Peculiar Velocity field (arrows) around the LG and LS within a slice of [±60 h^{-1}Mpc] centered at the LG, and projected along the supergalactic $x-y$ plane. The main nearby structures can be recognized, the Hydra-Centaurus supercluster at (SGX,SGY) = (-35,20). Together with the Pavo-Indus-Telescopium supercluster [(SGX,SGY) = (-40,-15)] the latter makes the Great Attractor. The Perseus-Pisces supercluster at (SGX,SGY) = (45,-20) is the second largest structure on the map. (From Branchini et al. 1999).

4.1 Introduction

Peculiar velocities are an important cosmological tool because they directly probe the matter spectrum rather than the galaxy spectrum. The galaxy velocity field is the result of the gravitational attraction of matter in any form. They can characterize the mass distribution on very large scales because velocities are more sensitive to the low frequency part of the fluctuation power spectrum. They play an important role in the determination of the cosmological density parameter, Ω_m. A comparison of the velocity field with the matter density field allows a test of gravitational instability theory.

Our Local Group of galaxies [LG, hereafter] is located in a rather atypical cosmic region of the Universe. Massive nearby structures such as the Great Attractor [GA] (at $\approx 40\ h^{-1}$Mpc) and at the opposite site the Perseus-Pisces supercluster [PP] (at $\approx 50\ h^{-1}$Mpc) generate a very strong peculiar gravity field. Furthermore, the LG is located just at the edge of a bridge connecting these two structures, the Local Supercluster [LS]. This location is close to a saddle point in the gravity field. The gravitational attraction of the two structures near compensate each other, being of comparable magnitude and pointing in opposite directions. The GA prevails slightly, resulting in a net pull toward the GA region. Another characteristic of this system is that all these structures are positioned in a planar configuration, the supergalactic $x-y$ plane (Fig. 4.1, see also the cosmography section of Chapter 2).

The velocity field of the local cosmic vicinity is a mere reflex of the intricate peculiar mass configuration surrounding the LG. It receives contributions from the local, intermediate and large scale mass distribution. At small scales ($\sim 20\ h^{-1}$Mpc), the local vicinity is strongly influenced by the nearby Virgo cluster (e.g. the Virgocentric infall, Davis & Peebles (1983b) and references therein) and the filamentary Local Supercluster, which itself connects to the Great Attractor (e.g. IRAS density field, Strauss et al. 1992). At intermediate scales ($40-60\ h^{-1}$Mpc) the GA and PP dominate. At large scales the local environment seems still to experience significant influence from structures located even beyond 150 h^{-1}Mpc such as the Horologium supercluster (Raychaudhury 1989; Plionis & Valdarnini 1991) and the Shapley concentration (Plionis & Kolokotronis 1998; Basilakos & Plionis 1998;

Rowan-Robinson et al. 2000; Hoffman et al. 2001). It is therefore necessary to consider all dynamic scales when studying the peculiar velocity field of the LG cosmic neighborhood.

Here we are interested in modeling in an optimal fashion the full peculiar velocity field of our local Universe up to scales of 30 h^{-1}Mpc. This scale corresponds to the volume enclosing the LS and leaves out major cosmic structures such as the GA and PP. In this work we want to address two separate problems concerning to the LS peculiar velocity field. First we want to quantify the effect of neglecting the external contributions beyond the LS volume when modeling only the enclosed mass distribution (LS). Secondly, we want to account for these external contributions in order to obtain an unbiased LS peculiar velocity field free from any external and tidal effects.

We will make use of an improved implementation of the Least Action Principle [LAP], the Fast Action Minimization method (FAM Nusser & Branchini 2000) to model the peculiar velocity field. The LAP technique has been widely used to study the LG dynamics (Peebles 1989, 1990, 1994; Giavalisco et al. 1993; Dunn & Laflamme 1993; Branchini & Carlberg 1994; Shaya et al. 1995; Phelps 2000; Sharpe et al. 2001). However, these implementations suffered mainly from expensive direct force calculations, limiting the number of objects for their analyses. With FAM this is not longer the case, as shown by Nusser & Branchini (2000) and Romano-Díaz et al. (2004). FAM can deal with more than 20 000 objects. This LAP implementation allows one to explore the mildly non-linear regime, the same regime of the Local Supercluster. All these characteristics make FAM a very suitable tool for studying the LS volume.

4.2 The external influence over the Local Supercluster

The power of velocity fields is that they sample scales large enough that density perturbations are fully in the linear regime. Mass conservation in the linear regime of gravitational instability tells us that

$$\nabla \cdot \mathbf{v}(\mathbf{x}) = -H_0 \Omega_m^{0.6}\, \delta(\mathbf{x}), \tag{4.1}$$

where $\mathbf{v}$ is the peculiar velocity vector and δ is the mass density contrast. If we translate this equation into Fourier space we get,

$$\imath \mathbf{k} \cdot \tilde{\mathbf{v}}(\mathbf{k}) = -H_0 \Omega_m^{0.6}\, \tilde{\delta}(\mathbf{k}), \tag{4.2}$$

Thus, it is possible to define a "velocity power spectrum" $P_{\rm v}(k) \sim \langle \tilde{\mathbf{v}}^2(\mathbf{k}) \rangle$ in analogy to the density power spectrum $P(k)$. Both quantities are related via

$$P_{\rm v}(k) = H_0^2 \Omega_m^{1.2}\, k^{-2}\, P(k), \tag{4.3}$$

and therefore $|\tilde{\mathbf{v}}(\mathbf{k})| \propto \tilde{\delta}(\mathbf{k})/k$. This means that the long-wavelength perturbations have a larger impact on large-scale peculiar velocities than they do on mass fluctuations.

The LAP technique has been used to compute the peculiar velocity field of the LS from galaxy positions. But because the peculiar velocity field receives contributions from the large scale mass distribution, even beyond 150 h^{-1}Mpc, these have to be taken into account if one pretends to model such velocity field free from any systematic effect.

Many attempts have been done in order to consider the large scale influence when modeling peculiar velocities in the local vicinity. Shaya et al. (1995) modeled the influence of the external mass distribution by considering the distribution of rich Abell clusters, while Sharpe et al. (2001) accounted for the linear contributions from this mass distribution according to the PSC*z* catalog (Saunders et al. 2000). Schmoldt & Saha (1998) proposed a different approach, they considered a "tidal" potential caused by the influence of objects external to the region considered. They characterized this potential by its dipole and quadrupolar terms based on observational estimates. The linear evolution of this tidal field was taken into account in the evolution of the action in the LAP machinery. However, such characterizations of the external mass influence may not properly account for the evolution of nonlinear systems, such as the massive superclusters Hydra-Centaurus (GA) and Perseus Pisces. Furthermore,

this mass distribution beyond the LS volume (30 h^{-1}Mpc) exerts a strong tidal influence over this "inner" volume. Lilje, Yahil, & Jones (1986) estimated that at the location of the LG the velocity shear had a value ~ 200 km s^{-1} with respect to the Virgo cluster. They argued that the source of this shear had to be a considerable mass concentration at a distance of ~ 3 times the distance to the Virgo cluster, soon after confirmed by the results of Lynden-Bell et al. (1988). Hoffman et al. (2001) reconstructed the tidally induced component of the cosmic velocity field from the Mark III and SFI catalogs out to a distance of 60 h^{-1}Mpc . Their results indicate that there is still non-negligible influence from structures beyond such sample radius.

Romano-Díaz, Branchini, & van de Weygaert (2004, hereafter RBW, see Chapter 2) studied and analyzed the velocity fields of cosmic regions which resemble statistically the cosmic neighborhood. They assessed how well currently available all-sky, flux-limited redshift surveys of galaxies, such as PSCz, can account for the major share of mass concentrations inducing the external tidal forces. They compared the $N-$body velocities for two different cosmological scenarios, ΛCDM and τCDM cosmogonies, with respect to their reconstruction from mock catalogs up to distances of 100 h^{-1}Mpc. The study was centered in spherical regions around LG-alike observers in volumes of 30 h^{-1}Mpc radius (the Local Supercluster region) according to the Nearby Galaxy Catalog of Tully (1988, hereafter NBG). The reconstruction of the peculiar velocity field was done by means of FAM. Results showed that in all plausible cosmological scenarios the mass distribution outside the Local Supercluster does significantly affect the local dynamics: a typical reconstruction of the velocity field around the LS is biased in the sense that it does not account properly for the mass distribution beyond the sampled region. The corresponding external velocity field can be reasonably represented by the two main components (dipole and quadrupole, i.e. Bulk and Shear) of a multipolar decomposition of such field. The modeled LS peculiar velocity fields can be corrected by adding the bulk and shear velocity components of the external tidal velocity field. Despite of the good agreement between the corrected FAM results and $N-$body velocity fields, there is a considerable large dispersion, especially in the case of the ΛCDM scenario. The scatter around the main results implies that the goodness of these corrections depends on the position of the observer and the mass distribution beyond 100 h^{-1}Mpc.

Although RBW used LG-alike observers for their study, this choice only constrained the LG environment. The mass concentrations beyond 5 h^{-1}Mpc were only statistically consistent with the LS environment, and did not fairly represent the mass configuration as presented in the real universe. Structures such as the GA and PP need to be taken into account if one wants to make a faithful model of the velocity field in the LS.

Taking into consideration the large scatter of the fits from the velocity-velocity comparisons between the corrected FAM velocities and $N-$body ones for the ΛCDM cosmology, and taking into account the consideration that this model seems to be the most viable cosmological scenario (WMAP, Spergel et al. 2003), we have addressed this problem in more detail for this particular cosmological scenario. In this chapter we have asked ourselves how important the external influences are when reconstructing the peculiar velocity field of realistic realizations of the LS within a volume of 30 h^{-1}Mpc. As in RBW, we want to characterize this external influence by its bulk and shear flow components. A main difference from the RBW analysis, is the use of constrained $N-$body simulations of the cosmic neighborhood, that effectively represent the real mass distribution as inferred from the reconstructed density field obtained from the Mark III catalog of peculiar velocities (Willick et al. 1997a). With this approach the presence of real structures such as the GA, PP, Coma, Cetus and other structures can be taken into account.

4.2.1 Decomposing the peculiar velocity field

Any given vectorial field can be characterized or decomposed through a multipolar decomposition (around some origin) of the form:

$$F(\mathbf{x}) = M + \alpha D + \beta Q \cdot \mathbf{x} + O \ldots \tag{4.4}$$

where M represents the monopole term, D dipole, Q quadrupole and O the higher order terms, and $\alpha,\beta,\ldots$ are the multipole scalar coefficients.

In the same way, the peculiar velocity field can be decomposed in a multipolar summation of terms. The decomposition can be performed in several ways. One may use a decomposition by using spherical harmonics and Legendre polynomials (e.g. Fisher et al. 1995b). Or, one can take a more straightforward approach like the one adopted here (Kaiser 1991, RBW), where the field is expressed in terms of a Taylor series expansion, as function of spatial positions $\mathbf{x}_i$. Each term of the velocity decomposition carries information on different scale regimes. The monopole term indicates the local underdense of overdensity and does not affect peculiar velocities and can be ignored when considering co-moving coordinates. The dipole term, also referred as the bulk flow, is the average streaming motion within a volume of a characteristic length scale R. The quadrupole term, also known as the velocity shear, is the result of the action (stretching and/or compression) over the enclosed matter distribution of structures located beyond the edge of the sample, and its effects become more pronounced at the edge of the sample. Higher order terms are related to non-linear structures and therefore their influence radius is very limited, mainly around the virialized structures. Thus, they only represent a minor, very local, contribution to the peculiar velocity field.

RBW showed that a multipolar decomposition of the type of Eqn. 4.4 for the "residual" velocity field (the field which is the outcome of extracting the LS "inner" contributions to the "large-scale" velocity field) is a fair characterization of the external gravitational influence over the LS volume. They showed that it is possible to fairly model the LS peculiar velocity field by solely considering the mass distribution within a volume of radius 30 h^{-1}Mpc, and by considering only the dipole and quadrupole moments of the residual velocity field. Here, we apply the present velocity decomposition to the residual velocity field. Because we are interested in studying the large scale structure effects over the LS, we only include up to the quadrupolar moment of the residual velocity field.

4.3 $N-$body simulation of the Local Universe

RBW studied the influence of the mass distribution beyond 30 h^{-1}Mpc over the LS environment. In their analysis they made use of $N-$body simulations which statistically resembled the nearby universe. A challenging problem for this type of statistical approaches is the peculiar velocity field around the LG. The presence of rare objects such as the GA and the specific configuration with PP imprint strong characteristics on the local peculiar velocity field (e.g. Lilje et al. 1986; Lynden-Bell et al. 1988; Bertschinger et al. 1990; Branchini et al. 1999). A very important characteristic of the local peculiar velocity field is the observed low velocity dispersion of nearby galaxies. This has been perceived as one of the challenges for structure formation models (Peebles 1993b), mainly because the typical velocities of galaxies in cosmological simulations turn out to be too large in comparison with those from the LG (Schlegel et al. 1994; Governato et al. 1997).

A very successful technique for making realistic simulations that reproduce the large-scale structures of the nearby real universe as revealed by the large-scale surveys (e.g. IRAS, SDSS, PSCz), and at the same time the small-scale nearby structures is the combined use of Constrained Realizations and the Wiener Filter [WF] technique (Bertschinger 1987; Hoffman & Ribak 1991; van de Weygaert & Bertschinger 1996; Zaroubi et al. 1995, 1999).

4.3.1 Constrained N-body simulations

Constrained simulations [CS] are meant to match as close as possible the kinematics, dynamics, and structure of the mass distribution in our local universe. This can be achieved by imposing certain constraints on the initial conditions in the N-body experiments which guarantee the time-evolved distribution of particles to reproduce some specific properties of the mass distribution in the local cosmos.

Because velocities reflect the mass distribution on large scales, they can be used to map the linear density field of the nearby universe. This can be done by applying the WF algorithm to the Mark III

catalog of peculiar velocities (Zaroubi et al. 1995, 1999). Fluctuations on all scales are given by the constrained random field technique (CRF Bertschinger 1987; Hoffman & Ribak 1991; van de Weygaert & Bertschinger 1996). The WF field is used as the "mean field" in the CRF procedure to constraint the initial Gaussian field. The field is most correlated on scales of constraints. However, since we are using peculiar velocities to constraint the field, the constrained field will be "effectively" constrained at scales larger than the effective radius of the input catalog used (see Eqn. 4.3). The small-scale density fluctuations are generated via the CRF according to a specific power spectrum of fluctuations and adopted cosmology model. This approach guarantees that whether the signal to noise from the data is very high, the information is dominated by the input data, and where the signal is very low the constrained random method provides with the right power according to a *priory* model previously selected.

The combined use of the WF and constrained realizations provides a reconstruction or a realization of how the present day structure would appear if linear theory is valid. This implementation can be used as a tool to recover the initial conditions of structures that prevail nowadays in the nearby universe. Once the small and large scale density fluctuations have been computed, they are extrapolated back in time using linear theory to provide a reconstruction of the initial conditions.

The CSs success in reproducing the main features of our local universe has been shown in Klypin et al. (2003); Mathis et al. (2002), see also Chapter 3. Low and high resolution CSs have been performed for studying several purposes related to the LS (e.g. Kolatt et al. 1996; Bistolas & Hoffman 1998; van de Weygaert & Hoffman 1999; Kravtsov et al. 2002; Klypin et al. 2003). However, none of these authors studied the dynamical influences of the large scale mass distribution over the LS region.

In the present study, we will make use of the $N-$body simulations presented in Chapter 3. They are a set of four constrained $N-$body simulations of our local universe. The CSs methodology was applied to the Mark III catalog of peculiar velocities to generate the initial density fields. The four simulations are fully constrained within a volume of $\approx 60\ h^{-1}$Mpc from the LG region surveyed by the Mark III catalog. The regions beyond this radius will also be correlated at scales within the velocity correlation length of the Mark III catalog. At scales larger than this length, the method weakly constraints such regions obeying the *a priori* model. The simulations not only reproduced the spatial density distribution of the local universe within $\approx 60\ h^{-1}$Mpc, but also its dynamical behavior even beyond $100\ h^{-1}$Mpc. The simulations correspond to a ΛCDM cosmology with $\Omega_\Lambda = 0.7$ and $\Omega_m = 0.3$, where Ω_Λ measures the cosmological constant Λ in units of the critical density and Ω_m is the cosmological density parameter. The Hubble constant is $h = 0.7$ (measured in units of 100 km s^{-1} Mpc^{-1}) and the power spectrum is normalized to $\sigma_8 = 0.9$. The present model is consistent with the current observational constraints (WMAP, Spergel et al. 2003), and also consistent with the radial velocity surveys including the Mark III. The simulations were loaded with 128^3 particles and performed in a box of $320\ h^{-1}$Mpc side with the position of the LG located at the center of the box. The evolution of the initial density fields into the non-linear regime was followed by means of the public available code HYDRA (Couchman et al. 1995).

4.3.2 Mimicking the universe: Mock Catalogs

For our analysis we have considered two different types of mock catalogs from the parent $N-$body simulations. The first ones are meant to sample the mass distribution within a region of the size of the LS in a volume-limited fashion similarly to the Nearby Galaxy Catalog [NBG] of Tully (1988). The second ones are designed to account for the mass distribution out to distances of $150\ h^{-1}$Mpc as traced by the IRAS-PSC*z* galaxies in our universe (Saunders et al. 2000) (for a detailed description of the Mock-construction procedure see Chapter 3).

The NBG catalogs were subtracted from the PSC*z* ones by carving out the matter distribution within $30\ h^{-1}$Mpc, in this way both types of catalogs shear the same inner region. Catalogs have been centered at the center of the simulation box where the LG should reside. Two main aspects concerning the mock-center election should be discussed. The first one concerns the presence of the LG in the linear (initial) density field. This structure corresponds to the small-scale part of the power spectrum

Label	Radius (h^{-1}Mpc)	Number of catalogs	$\langle N_{obj} \rangle$	Characteristic
CNBG	30	4	2 800	Volume limited
CPSCz	150	4	19 000	Volume + Flux limited

Table 4.1 — Characteristics of the constrained mock catalogs. The radius indicates the catalog's size, $\langle N_{obj} \rangle$ the average number of objects for the 4 catalogs.

which is hardly correlated with the constrained scale. Therefore, its presence and mass configuration will be a more fortunate event than a real local structure. Even more, if a LG configuration has formed in any of the simulations, this does not necessary has to be located at the center of the simulation box. The second point is related to the resolution of LG-alike structures in the parent $N-$body simulations. Due to the mass resolution within the simulations ($6.4 \times 10^{11}\ M_{\odot}$), it is not possible to resolve with a high resolution (many particles) a Local Group observer ($M_{LG} \approx 3 \times 10^{12}\ M_{\odot}$). Nevertheless, as we will show in Section 4.5.1 our choice for the mock-centers is not far from reality since the local mock environment within 2 h^{-1}Mpc from the LG-observer is in good agreement with the real observational characteristics for this region.

From the 4 constrained simulations we have constructed 4 volume-limited catalogs (CNBG) and 4 volume+flux limited catalogs (CPSCz). Table 4.1 states the main characteristics for the 4+4 sets of Mock catalogs. The second column indicates the radius of the sample, the third column the average number of objects ($\langle N_{obj} \rangle$) for the 4 catalogs, and the fifth column the main characteristics of each set.

Figure 4.2 depicts 2D projections for one Mock catalog of our sample. The "C4" label at the top-left panel indicates that the catalog has been extracted from the fourth constrained simulation of our CSs set presented in Chapter 3. Each slice has a thickness of 20 h^{-1}Mpc centered along its respective supergalactic plane. The inner circles indicate the transition region between volume and flux limited samples. Clearly visible along the $x-y$ plane, and indicated by labels, are the LS running along the inner circle. It connects with the PP supercluster at the right-hand and the GA at the opposite side, both structures are located just outside of the circled region.

4.4 The velocity fields

In this section we present the different estimates of the velocity fields: the Mock velocity fields and the FAM modeled velocity fields for the two sets of catalogs, CNBG and CPSCz. Because we are interested in performing our analysis for the LS region (30 h^{-1}Mpc), the plots presented here concern only to the objects within this volume. All velocity plots presented here will refer to the unsmoothed velocity fields unless something different is stated. A discussion about smoothing effects is presented in Appendix 4.A at the end of this chapter.

4.4.1 The "observed" velocity field

The "observed" velocity field is defined to be that obtained from the Mock galaxy distribution. This field represents our best estimate for the real velocity field in the hypothetical case that we could measure the full 3D velocity field. Selection effects in the mock-making procedure, such as sparse sampling affect the sampled mass distribution and therefore the velocity field (Chapter 3). These effects become more pronounced at large scales (> 100 h^{-1}Mpc) To avoid these problems, it will be desirable to deal with a sample that covers properly the whole space under study.

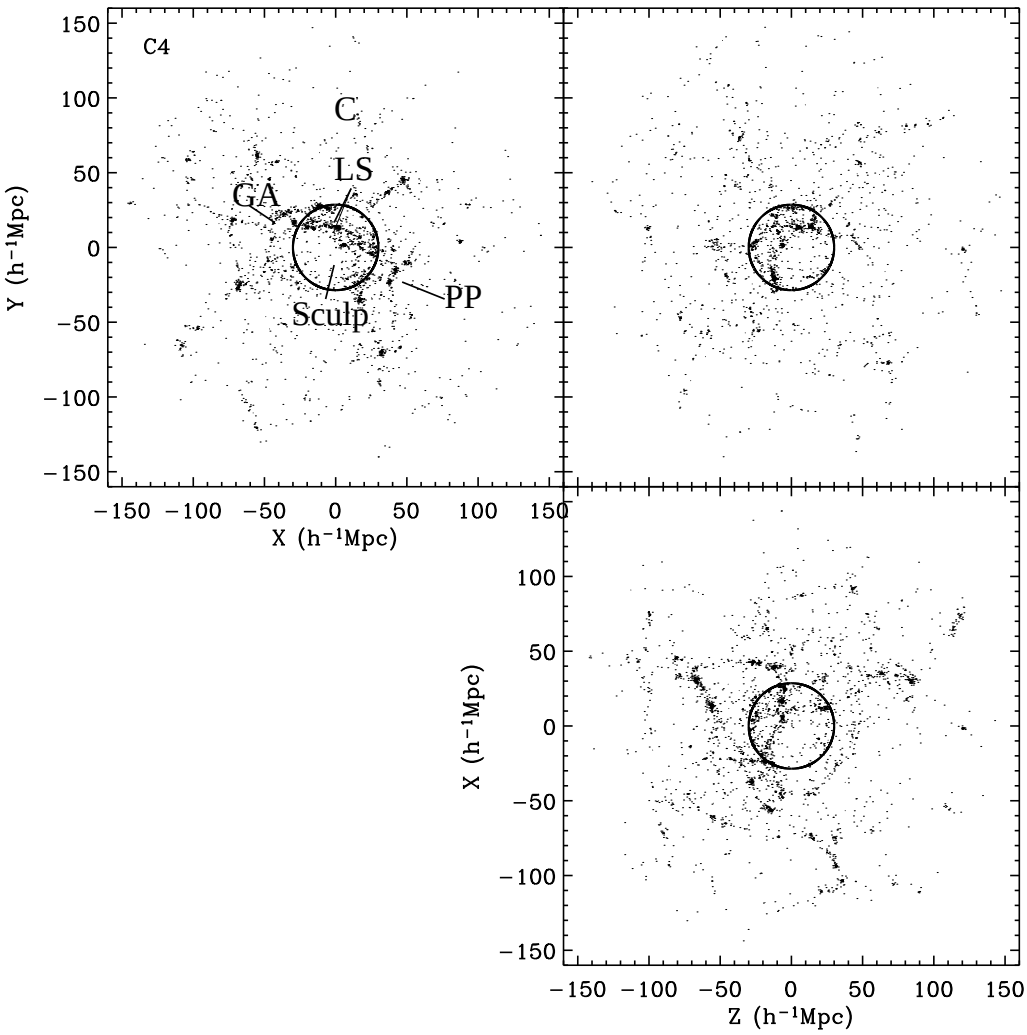

Figure 4.2 — 2D projections along the three supergalactic planes of the particle distribution for one Mock catalog (C4) of our sample. The slices are centered at the LG-observer's position, and with a thickness of 20 h^{-1}Mpc. The circles indicate the transition region between volume-limited and flux-limited regions. The labels indicate some of the most prominent structures presented in the catalog.

Figure 4.3 shows cuts for the mock-observed velocity field along the 3 supergalactic planes from two mock catalogs of our set (C1 & C4). The plots show the unprocessed projected peculiar velocities at the particle positions within a slice of ± 5 h^{-1}Mpc from its respective supergalatic plane. The size of the arrows is proportional to the amplitude of the galaxy velocity components within the 3 slices, with each arrow starting at the location of the galaxy. As expected, the two set of plots show clear similarities between both, the velocity field and the mass distribution. Both catalogs show a strong coherent bulk flow along the $x-y$ plane towards the $-x$ direction -the GA location which lies just outside the considered volume and mainly responsible for this bulk flow. This significant flow is also present along the $x-z$ projection. Apart from the intrinsic flow contained within the sample, there is a clear signal pointing towards the center of this slice, the $x-y$ plane and location of the GA region. The third projection also shows some interesting characteristics, there is (easily noticed) the presence of a filament running from the bottom-left of the projection to the opposite side. Another striking feature is the presence of a shear pattern along the $x-y$ plane and also noticeable, although not so pronounced,

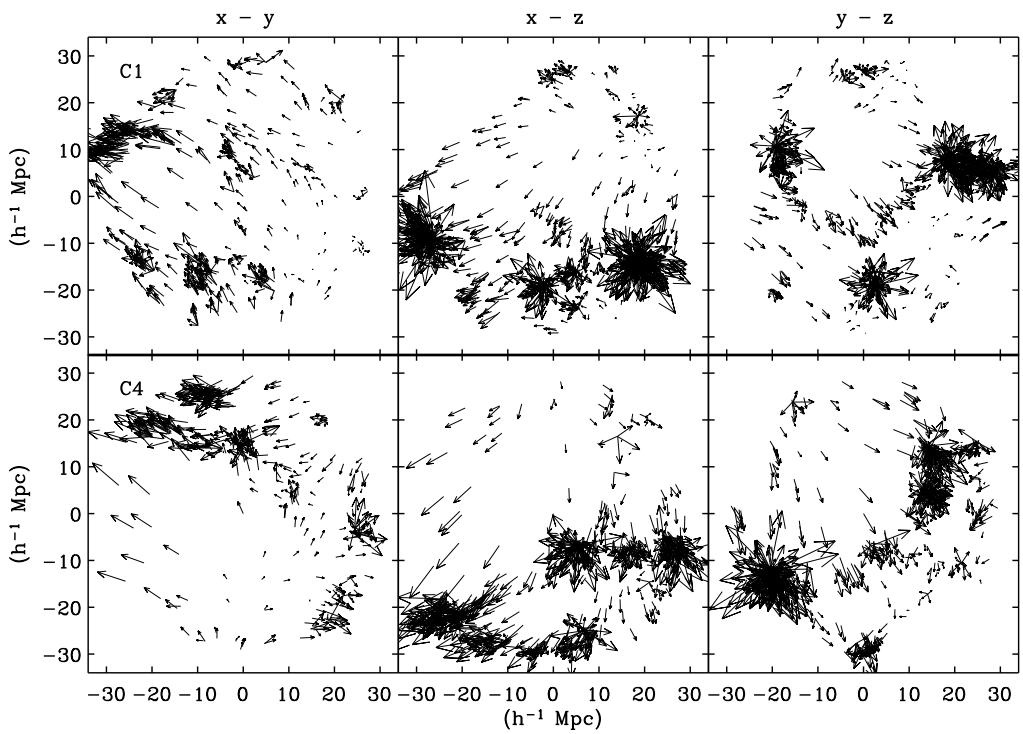

Figure 4.3 — 2D projected velocity fields at the mock-galaxy positions for the 3 central slices of 10 h^{-1}Mpc thick centered along the supergalactic planes for two mock catalogs, C1 & C4, top and bottom panels respectively. The local group is located at the center of slices. The top labels indicate the projected Cartesian axes (abscissa - ordinate).

in the $x-z$ plane. This shear pattern is mainly produced by the quadrupolar mass distribution around the LG and LS. Characteristics of this configuration are the mass concentrations defined by the GA on one side and the PP on the other, with the local void in the midplane (see Fig. 4.2). The maximum stretching direction is oriented along the GA-PP direction. This particular matter distribution also constraints the compressional mode.

The nonlinear regions (clusters of galaxies) can be easily recognized as the sites with clumps of randomly oriented velocities. Another noticeable feature is the Local Supercluster. It is visible in the $x-y$ plane as the running structure from the middle right part of the panel towards the upper-left part of the panel, and along the $y-z$ plane at the right upper part of the panel.

4.4.2 The FAM velocity fields

We have modeled the velocity fields from the particle distributions of the two sets of Mock catalogs by means of the FAM approach. We will refer to the modeled velocity field coming out from the constrained NBG volume-limited catalog (within 30 h^{-1}Mpc) as FAM$_{CNBG}$, while we will call FAM$_{CPSCz}$ to those constrained velocity fields resulted from the volume+flux limited mock catalogs (150 h^{-1}Mpc). All catalogs were modeled using the same FAM parameters, e.g. a tolerance parameter of 0.0001 to search for a minimum of the action S, number of basis functions $n_f = 6$ and a softening parameter for the force resolution matching the one from the original $N-$body simulation of $\epsilon = 0.25\ h^{-1}$Mpc.

The FAM technique suffers from a main problem. It fails in properly model the peculiar velocities at high density regions, the virialized regions where velocities not longer laminar (Nusser & Branchini

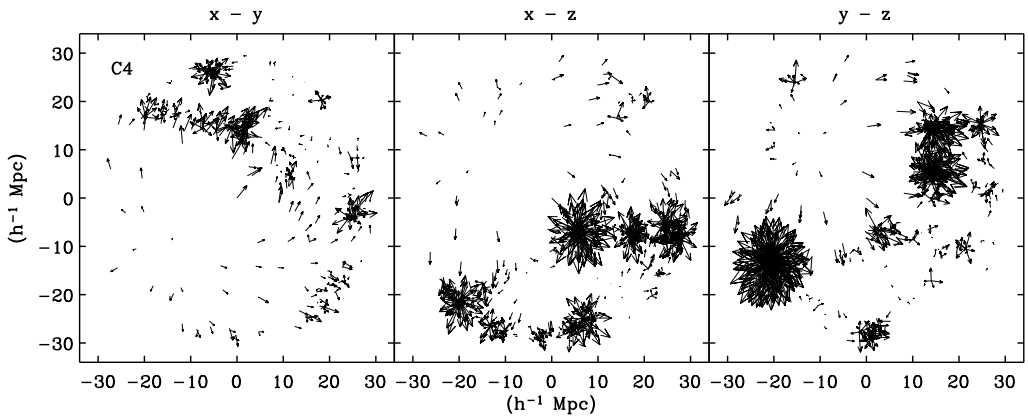

Figure 4.4 — 2D projected FAM velocity fields at the mock-galaxy positions for the C4 CNBG catalog. The slice properties are the same than in Fig. 4.3, and velocities have been normalized with the same parameters than the mock ones.

2000; Branchini et al. 2002, RBW). Therefore, the corresponding velocity scatter around these regions will not correspond to the mock one. However, this is a very local effect that only affects objects' velocities at the high-density regions and not the overall velocity flow (Branchini et al. 2002, RBW).

4.4.3 The FAM$_{CNBG}$ velocity field

Burstein et al. (1990) pointed out that the fact that galaxies within a volume enclosing the LS seem to fall into Virgo is a mere coincidence. They are directed towards a rather central, wide region of the LS which coincides with the positions of the Virgo cluster and the Ursa Major cluster (Burstein et al. 1990). It has been measured that galaxies within the plane of the LS are falling towards this central region with velocities that increase with distance outward. The LG, which lies near the edge of the LS, has a velocity ≈ 300 km s^{-1} to its centre (Aaronson et al. 1982a; Tonry et al. 2000), but only ≈ 150 km s^{-1} is directed towards the central region of the LS (Davis & Peebles 1983b; Tonry et al. 2000). With the present kind of analysis it is possible to address what is the net influence of the LS over the LG.

The FAM$_{CNBG}$ velocity field is solely induced by the matter distribution contained within 30 h^{-1}Mpc without considering any type of inhomogeneities located outside the radius sample. FAM considers a homogeneous matter distribution outside the sampling radius, which has a null effect over the sample's dynamic (Nusser & Branchini 2000, RBW). Figure 4.4 depicts the FAM$_{CNBG}$ velocity field for the same C4 catalog presented in Fig. 4.3 (lower panel). The velocities have been normalized with the same parameter than the mock ones.

The reproduced velocity fields show the so-called *Virgocentric infall* (see Pierce & Tully 1988). This can be most clearly seen in the $x-y$ plane, but also shows to be influenced by structures along the $y-z$ plane. From the $y-z$ projection it is very visible the fact that the structure running along the volume is pulling towards itself the galaxies around it. An important feature present in Figs. 4.3 & 4.4 is the *Local Void*. This "empty" zone is visible along the 3 projections. The galaxies' movements can be clearly pick up by the FAM reconstruction as a zone of expansion. The difference between the observed and FAM modeled velocity fields in the void region shows that while in the observed field the objects' velocities are dominated by the general external bulk flow, this is not so for the FAM$_{CNBG}$ catalog. Instead, the FAM$_{CNBG}$ void gives the impression of a spherical expanding mini-universe. This is in line with theoretical expectations, see e.g. Icke (1984); van de Weygaert & van Kampen (1993). Another important characteristic is the fact that the shear patterns presented in the mock catalogs are not longer present in the corresponding FAM$_{CNBG}$ catalogs.

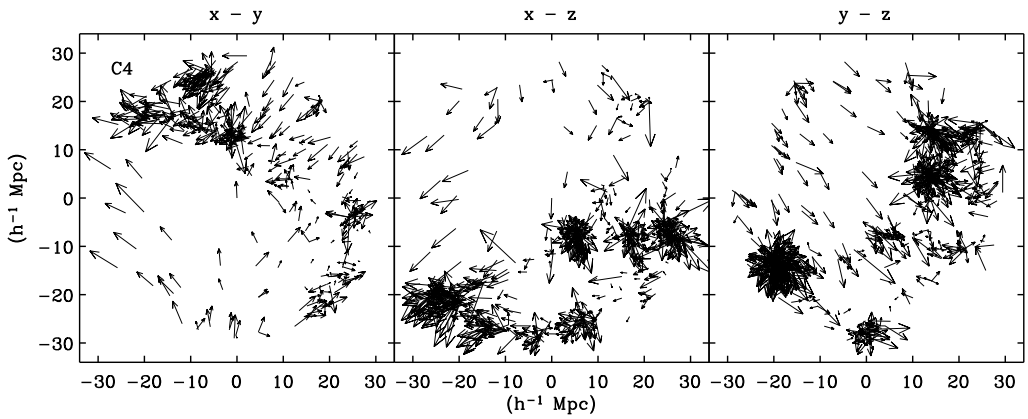

Figure 4.5 — 2D projected FAM velocity fields at the volume-mock-galaxy positions for the corresponding PSC*z* catalog of Fig. 4.4 (C4). The slice properties are the same than in Fig. 4.3.

4.4.4 The FAM$_{CPSCz}$ velocity field

RBW showed that in order to account properly for the external mass influence and depending on the power spectrum of fluctuations, one should take into consideration very large volumes of at least 100 h^{-1}Mpc in radius (see Chap. 2). Such large volumes assure oneself for accounting for the large modes of the power spectrum. In the particular case of the LG it is necessary to consider larger volumes due to the contributions to the local peculiar velocities from structures located beyond 100 h^{-1}Mpc (e.g. Raychaudhury 1989; Plionis & Valdarnini 1991; Hudson et al. 1999).

Figure 4.5 shows the projected FAM$_{CPSCz}$ velocity field corresponding to the same CNBG catalog (C4) presented in Fig. 4.4. The slice characteristics are the same than in the previous velocity field plots, and velocities have been normalized with the same constant parameter than in the previous plots. It can be noticed from the 3 panels that the amplitude and direction of the vectors are very similar to those from the observed ones. The $x-y$ and $x-z$ projections clearly show the presence of a dominant bulk flow towards the GA region. The local bulk induced by the filamentary structure along the $y-z$ projection is also present. The shear pattern in the $x-y$ and $x-z$ has returned and points toward the same directions than in the mock sample. As expected, the incoherent motions at the virialized regions are more pronounced than in the observed maps.

With this visual inspection seems that when we consider the mass distribution of large enough volumes (> 100 h^{-1}Mpc), it is possible to reconstruct LS peculiar velocity fields free from large scale influences. We will discuss this point in more detail in Section 4.5.3 where point-to-point comparisons between mock and FAM velocities will be presented.

4.4.5 The residual velocity field

We define the residual velocity field as the residual velocities between the large scale (full) velocity field and the FAM velocity field computed within 30 h^{-1}Mpc :

$$\mathbf{v}_{res} = \mathbf{v}_{ls} - \mathbf{v}_{FAM_{CNBG}} \,, \tag{4.5}$$

where $\mathbf{v}_{ls}$ is in principle the full large scale velocity field. This residual field contains the missing external large scale contributions when only modeling the LS peculiar velocity field as given by its mass distribution. RBW pointed out that the $\mathbf{v}_{ls}$ may also be replaced by the FAM$_{PSCz}$ velocity field due to the fact that this field adequately accounts for most of the significant influence of the external mass distribution. For the present study, we have adopted the mock-observed $\mathbf{v}_{obs}$ field as the full velocity field.

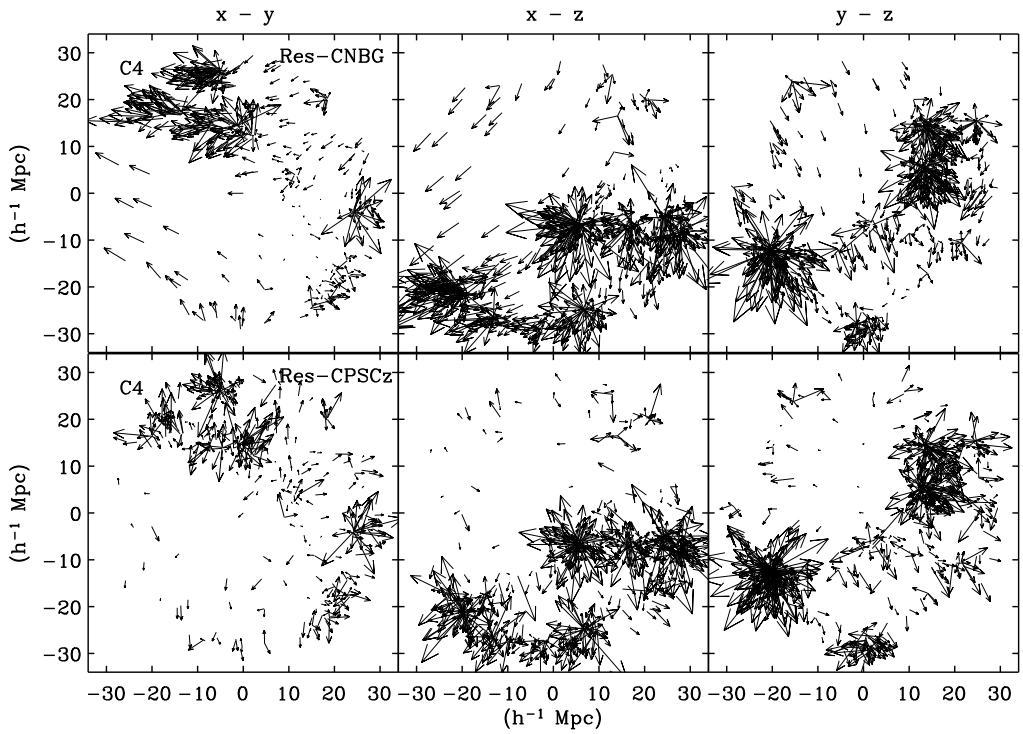

Figure 4.6 — 2D projected residual velocity fields at the volume-mock-galaxy positions. The top row panels show the outcome residual field between the mock-observed and FAM_{CNBG} velocity fields. The low row panels refer to the residual field between the mock and FAM_{CPSCz}. The slice properties are the same as in Fig. 4.3.

Figure 4.6 shows two different residual fields for the same C4 catalog presented in previous plots. The top-row panels refer to the residual field between the mock and FAM_{CNBG} velocities, while the lower panels depicts the residual field from the mock and FAM_{CPSCz}. The plot characteristics are the same as previous plots. From this figure we can make three major observations. The first one concerns the bulk flow. There is a clear bulk flow pattern present in the top panels along the three plane projections. The appearance of those coherent flows is due to the influence of the external mass distribution that was not taken into account when modeling the FAM_{CNBG}. From the $x-y$ plane we can infer that the major share of the large scale bulk in the LGE and LS is due to the structures located along the negative part of this plane, the GA region.

The second point refers to the existence of a shear pattern in the three top projections. This pattern indicates the presence of a quadrupolar mass configuration located outside the studied region along the $x-y$ plane as revealed by the $x-y$ and $x-z$ projections. The velocities in these two projections increase outward, implying an external tidal shear, whose stretching mode is in a direction parallel to the LS. In the $y-z$ plane the velocities decrease inward and they point toward the central filament. This configuration indicates a compression mode along the z-axis, perpendicular to the filament and the stretching mode. All these imply that the shear effects are more pronounced toward the edge of the sample than at the center.

The third point deals with the fact that when modeling the velocity field inside large volumes it is possible to account for nearly all significant dynamical influences exerted by large scale structures located far away from the observer. It results in a velocity field free from any external influence. This may be observed in the lower row panels where the residual velocity field from the mock and FAM_{CPSCz} velocities is shown. It shows how the bulk flow and shear pattern have disappeared and only small thermal-alike motions are presented.

Sample	V_{bulk} $\lvert V\rvert$ (km s^{-1})	l (°)	b (°)	s (km s^{-1} Mpc^{-1})
Mock	390±34	285 ± 23	5 ± 23	16.5±2.9
FAM$_{CNBG}$	66 ±18	248 ± 49	17 ± 18	2.6±1.2
FAM$_{CPSCz}$	389±28	287 ± 24	3 ± 27	15.8±2.9
Res$_{CNBG}$	345±50	290 ± 22	1 ± 25	16.1±3.4
Res$_{CPSCz}$	56±31	173 ± 59	27 ± 41	1.54±0.8
FAM$_{cor}$	390±34	285 ± 23	5 ± 23	16.5±2.9

Table 4.2 — Average bulk flow and shear amplitudes for the different velocity fields. All analyses have been made within a 30 h^{-1}Mpc sphere. The velocity field sample label is presented in Column 1. The bulk flow amplitude ($|V_{bulk}|$) in Column 2, and its direction projected into the sky in galactic coordinates (l, b, Columns 3 & 4). The eigenvalue's amplitude in Column 5.

4.5 Correcting for external effects

The residual field corresponding to FAM$_{CNBG}$ still contains a large amount of information indicated by the presence of a flow and shear pattern. One option for accounting for the external influence is to include mass concentrations in larger volumes. This is a way to compute a faithful velocity field for the LS. RBW studied the characteristics of the missed bulk flow and tidal contributions velocity field for the the LS region. They found that the residual field can be well characterized by its dipole and quadrupole moments, the bulk flow and tidal shear. When adding them to the internal catalog velocities yield to an unbiased velocity field which resembles the mock one.

We have decomposed the residual velocity field according to Eqn. 4.4. The residual field is modeled by its first two components, a bulk flow vector, U_i, and a quadratic shear tensor contribution, s_{ij},

$$\mathrm{v}_{res,i} = U_i + s_{ij}\, x\hat{x}_j\,, \tag{4.6}$$

where $i, j = 1, 2, 3$ denote the Cartesian component indexes. The vectors $\hat{x}_j$ represent the unity vector components along the j direction of the **v** vector. For a more extensive discussion on the procedure to obtain the 3 U_i and the 6 s_{ij} coefficients we refer to RBW (Chapter 2).

Table 4.2 presents the average results for the bulk flow (V_{bulk}), and tidal shear magnitude (s, in units of km s^{-1} Mpc^{-1}) for all catalog samples, FAM$_{CNBG}$, FAM$_{CPSCz}$, Res$_{CNBG}$, Res$_{CPSCz}$ and Mock. Table 4.3 presents the average results for the 3 individual tidal shear eigenvalues : s_1−dilational, s_2−middle and s_3−compressional for the same samples. The quantities have been averaged over the 4 catalogs for each sample. The errors represent the $\pm 1\sigma$ dispersion error around the mean value. In both tables ($|\,|$) represents the amplitude of the velocity component, while (l, b) specifies their direction in galactic coordinates (longitude and latitude).

The external contributions for the FAM$_{CNBG}$ case are very substantial and significant. In the LS volume, the bulk flow is missing $\sim$ 300 km s^{-1}. The amplitude and direction of the corresponding missing bulk flow (Res$_{CNBG}$) coincides with the observed Mock bulk flow. This result clearly indicates that the external mass distribution plays a dominant role in the kinematics of the LS environment. Also of considerable importance is the tidal shear contribution. The FAM$_{CNBG}$ sample lacks an important contributions from pure tidal effects, as may be inferred from the Res$_{CNBG}$ shear results. In Chapter 3

Sample	Dilational			Middle			Compressional		
	$\lvert s_1 \rvert$ (km s^{-1} Mpc^{-1})	l (°)	b (°)	$\lvert s_2 \rvert$ (km s^{-1} Mpc^{-1})	l (°)	b (°)	$\lvert s_3 \rvert$ (km s^{-1} Mpc^{-1})	l (°)	b (°)
Mock	16.9±3.0	317±11	18±2	-0.6±1.2	191±84	-13±25	-16.3±3.8	148±84	29± 59
FAM_{CNBG}	3.1±1.2	89±126	37±30	0.7±0.9	261±93	25±16	-3.8±0.8	191±138	-2±41
FAM_{CPSCz}	16.3±2.9	315±10	17±3	-0.4±0.4	235±9	-28±8	-15.9±3.0	197±2	56±6
Res_{CNBG}	16.3±3.2	272±98	10±15	-2.2±2.6	142±94	-4±21	-14.0±2.5	140±159	-31±67
Res_{CPSCz}	2.0±0.8	76±68	-28±28	0.1±0.2	82±93	-18±34	-2.1±1.0	139±80	36±28
FAM_{cor}	16.9±3.0	317±11	18±2	-0.6±1.2	191±84	-13±25	-16.3±3.8	148±84	29± 59

Table 4.3 — Average eigenvalues and their corresponding directions (eigenvectors) in galactic coordinates for the different velocity fields. AS before, all analyses have been made within a 30 h^{-1}Mpc sphere. Col. 1 Catalog label. Col. 2, 3 & 4 Amplitude and direction for the first eigenmode (Dilation). Col. 5, 6 & 7 Amplitude and direction for the second eigenmode (Middle). Col. 8, 9 & 10 Amplitude and direction for the third eigenmode (Compressional).

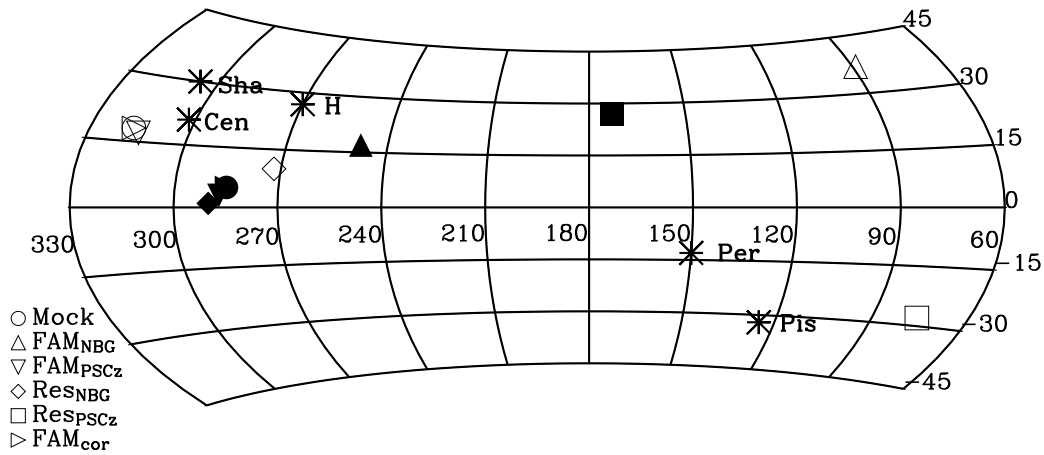

Figure 4.7 — Galactic directions for the different bulk flows (filled symbols) and 1st shear eigenvectors (stretching, empty symbols) from our set of catalogs. The asterisks mark the direction of the large structures that may influence the bulk and shear components, Hydra-Centaurus supercluster (H-C,GA), Perseus-Pisces (Per,Pis) superclusters, Shapley concentration (Sha).

we argue that there are still significant tidal contributions to the LG from structures located around 60 h^{-1}Mpc. Therefore, this non-negligible quantity has to be included in any study concerning LG and LS studies. In the case of the FAM$_{CPSCz}$, we can see how the external contributions are minor. The amplitude and direction of the bulk flow and shear eigenvalues are very close to the mock values. The FAM$_{CPSCz}$ residual bulk and shear contributions are not statistically significant.

From Tables 4.2 & 4.3, we see that the Res$_{CNBG}$ stretching eigenvector is misaligned with respect to the mock V_{bulk} by $13.82° \pm 15.4°$, and $20.03° \pm 17.2°$ with respect to the Res$_{CNBG}$ bulk. This can be better understood by looking at Figure 4.7, where we have plotted the direction in galactic coordinates of the different bulk flows (filled symbols) and first shear eigenvector estimates (empty symbols). The small misalignments can be explained in terms of the main external large scale structures which are responsible for the tidal influence. These estimates point toward the same direction, the Hydra-Centaurus supercluster (GA region), which is one of the main structures responsible for the external bulk and tidal shear. Nevertheless, these results might contrast with the larger misalignment between the mock bulk and its corresponding dilational shear component of $33.86° \pm 19.5°$. This misalignment can be explained as follows: the general bulk flow is mainly dominated by the massive structures beyond the 30 h^{-1}Mpc and up to a distance of ~ 150 h^{-1}Mpc, while the tidal shear is mainly produced for more local (closer) structures, with some of these structures also being responsible for the bulk flow (GA mainly). In such configuration, the tidal shear is aligned with the external bulk flow which is dominated mainly by the GA, but not with the overall large scale structure because there might more than a single nearby structure responsible for the tidal field (Lilje et al. 1986; Hoffman et al. 2001). The Res$_{CPSCz}$ bulk flow and tidal shear estimates are randomly oriented because they involve merely spurious quantities.

4.5.1 The Local Group Environment

With the present analysis and samples, it is possible to investigate in more detail the situation around the LG volume. First we have computed the reliability of the LGE with respect to observations. From the mock catalogs we have considered all particles within a sphere of 5 h^{-1}Mpc from the center of each catalog. These Local Group Environments have on average a peculiar velocity of 600 km s^{-1}, with a fractional overdensity of 1.5 and with a shear of ≈ 200 km s^{-1}. This is consistent with observed physical properties of the real LG (Brown & Peebles 1987). Secondly, we have computed the average

Sample	$\|v_{lg}\|$ (km s^{-1})	l (°)	b (°)
Mock	598± 117	271.1 ± 25.8	13.3 ± 12.3
LGE$_{CNBG}$	330±124	242.3± 46.8	25.3± 12.4
LGE$_{CPSCz}$	660±136	273.2± 34.7	14.8± 26.1
LGE Res$_{CNBG}$	395 ±108	291.5±14.8	-1.1±15.4
LGE Res$_{CPSCz}$	225 ±106	261.6± 87.1	2.4±44.3
FAM$_{cor}$	567± 99	267.8±33.0	16.0±16.4

Table 4.4 — Average results for the LGE velocity for the different velocity fields. All analyses have been made within a 2 h^{-1}Mpc radius sphere. The velocity field sample label is presented in Column 1, LG$_{CNBG}$ stands for the LG motion computed from the FAM$_{CNBG}$while LG$_{CPSCz}$ for the FAM$_{CPSCz}$. The LG velocity amplitude ($|v_{lg}|$) is shown in Column 2, and its direction projected on the sky in galactic coordinates (l, b) in Columns 3 & 4).

velocity amplitude and direction in galactic coordinates for the LGE for each different sample. The analysis was performed by including all objects within a sphere of 2 h^{-1}Mpc from the center of each catalog. We have compared these results with those by enlarging the local volume up to a radius of 5 h^{-1}Mpc to ensure ourselves that there are no significant discrepancies in our estimates.

Table 4.4 presents the average results for the LGE for different samples. The subindices in the first column indicate their respective parent sample to which they belong. It can be noticed that when considering larger volumes it is possible to better model the LGE.

The FAM$_{CNBG}$ sample reveals that if we only consider objects within the inner volume of 30 h^{-1}Mpc, the corresponding LGE velocity vector points toward the direction of the Virgo supercluster (LS). But this structure is not the only one that generates this motion, there are other sources located along the $x-z$ & $y-z$ planes that also influenced considerably the LGE motion (see Fig. 4.4). The direction of the LGE coincides with the direction of the FAM$_{CNBG}$ bulk, indicating that the bulk flow source inside the sample is also responsible for the LGE motion.

When considering larger volumes, the LGE motion matches the one from the expected mock catalog. Even though the LGE$_{CPSCz}$ amplitude is slightly larger than the mock one, it is still consistent with the 1σ error. This difference could be attributed to a poor sampling around the LGE. Still, the direction of the FAM-LGE coincides very well with the expected mock direction, indicating that the FAM-LGE has been properly modeled.

4.5.2 The corrected velocity field : FAM$_{CNBG}$ + B + S

RBW argued that in order to correct for the missing contributions in the peculiar CNBG velocity field, it is enough to add the first two moments of the external velocity contribution: the missing bulk flow [B] and tidal shear [s] components.

Figure 4.8 presents 4 different projected velocity fields for the same C4 catalog presented in previous plots. The fields correspond to the same enclosed particle distribution within a slice of ±5 h^{-1}Mpc thickness centred along the supergalactic planes. The 4 velocity fields have been normalized with the same constant value for a better comparison. The first row presents the external bulk flow computed from the velocity decomposition. Clearly, the bulk glow pattern points towards the GA region as shown in the $x-y$ and $x-z$ planes. Along the $y-z$ the bulk flow is mainly influenced by the inner

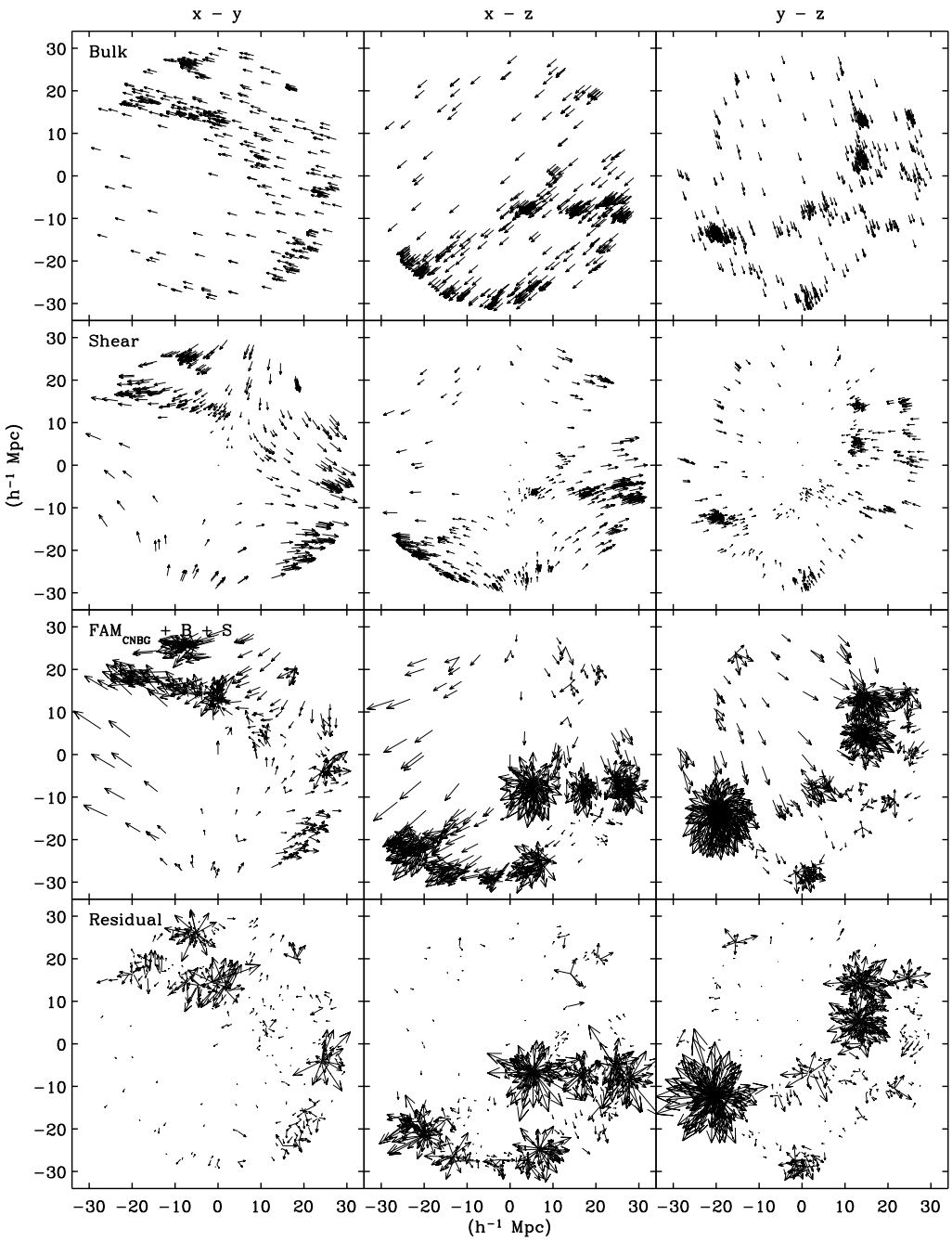

Figure 4.8 — 2D projected velocity fields at the volume-mock-galaxy positions for the C4 catalog. The top panels depict the tidal bulk while the second row presents the tidal shear components. The third row displays the FAM$_{cor}$ velocity field (FAM$_{CNBG}$+ B + S). The final row shows the residual field between the mock-observed velocities and FAM corrected. The slice properties are the same than in Fig. 4.3.

mass distribution but also by the void located at the upper left part of the distribution.

The tidal shear pattern is presented in the second row of the same figure. The shear amplitude and directions are well defined in the three panels. The maximum stretching directions reveal the presence

of two major mass concentrations responsible for such pattern, the GA and PP, both opposite to each other and located along the z-supergalactic plane. In the $y-z$ plane, what appears to be a free-falling pattern or a negative divergence, it is the action of the local void exerting pressure over the LS volume, the compressional shear mode.

We define the *corrected* FAM velocities [FAM$_{cor}$] like:

$$\mathbf{FAM_{cor}} = \mathbf{FAM_{CNBG}} + \mathbf{Missing\ Bulk} + \mathbf{Tidal\ Shear}\,, \tag{4.7}$$

where we have added to the inner FAM velocities the major external contributions, the missing bulk flow and tidal shear components. The third row in Fig. 4.8 shows the corrected velocities after adding the two upper panels to the FAM$_{CNBG}$ velocities. This new velocity field is very similar to the mock-observed one. This can be noticed from the lower row plots, where the residual field between the FAM$_{cor}$ and mock velocities are shown. The FAM$_{cor}$ field presents now the main characteristics of the mock-observed field, the bulk flow toward the GA, the correct inner bulk flow in the $y-z$ plane and the shear pattern exerted by the GA, PP and local void. In the same way, the residual field is not anymore dominated by any large scale pattern. Only random motions are presented, and large velocity dispersion at the high density regions where FAM cannot recover the orbits properly. These results are quantified by the average results presented in Tables 4.2, 4.3 and 4.4. From these tables one can infer that the amplitude and directions of the bulk flow, shear components and LG of the FAM$_{cor}$ samples match very well the mock results.

4.5.3 Point-to-point comparisons

In order to quantify the reliability of our reconstructions we have performed point-to-point comparisons between our FAM fields (CNBG, CPSCz and corrected) versus the Mock catalogs. In order to quantify these comparisons, we have carried out linear fits for each Cartesian velocity component ($\alpha = x, y, z$), allowing errors along both directions, of the form:

$$\mathrm{v}_{obs,\alpha}(x) = \mathrm{v}_{0,\alpha} + a_{\mathrm{v},\alpha}\,\mathrm{v}_{FAM,\alpha}\,, \tag{4.8}$$

by minimizing the χ^2 merit function:

$$\chi^2(a,b)_\alpha = \sum_{i=1}^{N} \frac{(\mathrm{v}_{obs,i} - \mathrm{v}_0 - a_\mathrm{v}\mathrm{v}_{FAM,i})^2_\alpha}{(\sigma_e^2 + a_\mathrm{v}^2\sigma_e^2)_\alpha}\,, \tag{4.9}$$

with respect to v_0 and a_v, where these parameters correspond to the *zero-point* and *slope* of the fit for each α-Cartesian component. The subindexes indicate the respective sample, *obs* for the mock-observed sample and FAM for any of the respective FAM fields. σ_e represents equal standard deviations for all samples.

From the linear fits, we can asses how good our algorithm is in order to correct for the external mass distribution. It give us information about the amount of missing data in the FAM reconstructions. The slope of the fit tell us how good the FAM fields are with respect to the mock-observed one. The zero-point is an indication of the presence of residual or external bulk flows in the FAM field. Together with these two quantities, we have computed the velocity dispersion (σ_v) which measures the deviations from the FAM velocities to the best linear fit.

In addition to the linear fits, we have also computed two different correlation indexes, the *linear correlation coefficient (Pearson's r)* denoted by R_{lin} and given by the formula (see Press et al. 1992b)

$$R_{lin} = \frac{\sum_i (\mathrm{v}_{obs,i} - \overline{\mathrm{v}_{obs}})(\mathrm{v}_{FAM,i} - \overline{\mathrm{v}_{FAM}})}{\sqrt{\sum_i (\mathrm{v}_{obs,i} - \overline{\mathrm{v}_{obs}})^2}\,\sqrt{\sum_i (\mathrm{v}_{FAM,i} - \overline{\mathrm{v}_{FAM}})^2}}\,, \tag{4.10}$$

Sample	$a_{\rm v}$	$\rm v_0$ (km s^{-1})	$\sigma_{\rm v}$ (km s^{-1})	$R_{S\,pear}$	R_{lin}
FAM$_{CNBG}$	0.57±0.27	63.2±89.1	147.8±19.6	0.54±0.14	0.56±0.14
FAM$_{CPSCz}$	1.08±0.25	4.1±109.3	189.4±47.5	0.71±0.14	0.75±0.10
FAM$_{cor}$	0.95±0.08	-6.5±24.2	142.6±18.4	0.79±0.10	0.80±0.09
NBG-PSC*z*	0.93±0.09	-62.1±87.6	142.5±20.0	0.79±0.10	0.80±0.09

Table 4.5 — Average results for the linear fits performed from the point-to-point comparisons between the 3 FAM velocity fields and the Mock one. The last row indicates the results between FAM$_{cor}$ *vs* FAM$_{CPSCz}$ instead of the mock field. The first column indicates the sample used for the comparison. The second column gives the slope of the best fitting line. Col. 3: the zero point of the best linear fit. Col. 4: the dispersion around the fit. Col. 5: the non-parametric (Spearman) correlation coefficient and in Col. 6: the linear correlation index.

and the *nonparametric or Spearman rank-order correlation coefficient* $R_{S\,pear}$ given by

$$R_{S\,pear} = \frac{\sum_i (R_i - \overline{R})(S_i - \overline{S})}{\sqrt{\sum_i (R_i - \overline{R})^2}\,\sqrt{\sum_i (S_i - \overline{S})^2}}\,, \tag{4.11}$$

where R_i correspond to the rank of $\rm v_{obs,i}$ and S_i to the rank of $\rm v_{FAM,i}$.

These indexes are indicators of how well the pair of velocities $(\rm v_{obs}, v_{FAM})_i$ fit the straight line given by the linear fit. They rank from -1 to 1, indicating positive (slopes > 0) or negative (slopes < 0) correlations. If the indexes are close to ± 1, the points lie close to the given straight line. A value near to zero indicates that the compared variables are uncorrelated and have little or no tendency to lie on a straight line. An additional inherent feature is that their values are independent of the measured slope. Therefore, when a correlation is known to be significant, these indexes are one way of summarizing its strength.

Table 4.5 presents the results from the point-to-point comparison parameters and correlation indexes. The numbers represent the mean values from averaging the 3 spatial directions for the 4 catalogs of each set. The errors represent the 1σ dispersion around the mean value. The first column gives the sample used for the comparison, the second column the slope of the best fitting line, the third column the zero-point in units of km s^{-1}, while the fourth column gives an estimate of the velocity dispersion (also measured in km s^{-1}) in the case that all errors were of equal magnitude. The final two columns show the 2 correlation indexes, the linear correlation index R_{lin}, and the nonparametric correlation coefficient $R_{S\,pear}$.

As shown by RBW, when comparing the CNBG *vs* Mock, the missing external information is reflected in recovering slopes considerably lower than unity. The FAM$_{CNBG}$ results are very similar to those found by RBW for unconstrained NBG catalogs. The scatter around the average quantities and velocity dispersion may be somewhat smaller. This is a result of the constrained realization procedure which effectively constrains the dynamical effects of the mass distribution around the CNBG catalogs. The FAM$_{CNBG}$ slopes in Table 4.5 indicate that these velocity fields are missing more than 40% of the total contribution, which is induced by the external mass distribution. The large velocity dispersion is mainly dominated by the contributions from the non-linear regions. These are responsible for a large dispersion around the fit, quantified by small correlation indexes. To appreciate this situa-

tion, Figure 4.9 shows density contours of the point-to-point comparisons between the same Cartesian components for the FAM$_{CNBG}$ and Mock catalogs are presented. The gray scale indicates the density point distribution going from black (lowest densities) to white (highest densities). The dashed lines correspond to the best fitting line between the Cartesian velocities for the two given samples. For guidance we have included continuous lines representing one-to-one relations. The best fitting line is considerably lower than the one-to-one line denoting missing external information. The zero point of the distribution is offset from the zero origin. This is a consequence of the presence of bulk flows not accounted for. The broad contours reflect the large velocity dispersion. A possible solution for overcoming this large dispersion is by smoothing the velocity fields with a Top-Hat filter. The lower panels of Fig. 4.9 refer to the 2 h^{-1}Mpc smoothed velocity fields. This mainly decreases the dispersion around the fit while preserving the main characteristics of the fit.

A different situation prevails for the FAM$_{CPSCz}$ case. Their sufficiently large volumes ($>$ 100 h^{-1}Mpc) properly recover all the information. The corresponding slopes of the best fits are very close to unity. The zero-point is very close to zero, because of the absence of significant unaccounted bulk flows. The Spearman and linear correlation indexes indicate a tight one-to-one correlation between the two fields. The middle panels of Fig. 4.9 show the corresponding FAM$_{CPSCz}$ velocities. They clearly show a better correlation with respect to the Mock velocities. The zero offset has decreased, although the velocity scatter around the fit is of the same order than in the FAM$_{CNBG}$ case, while the smoothed case also shows a much tighter point distribution. These results are similar to the unconstrained PSC*z* catalogs of RBW. We find that the zero point and the two correlation indexes are very similar although, the slopes of the best linear fits are closer to one than in RBW. All these reflect the effect of using $N-$body simulations which effectively constraint the mass distribution up to intermediate scales (60 h^{-1}Mpc), as a difference of the unconstrained simulations where the mass distribution beyond the LG varied from catalog to catalog.

The FAM$_{cor}$ fields present characteristics similar to the FAM$_{CPSCz}$case. Table 4.5 shows that the average slope is close to unity with a small dispersion, a negligible zero-point value, a velocity dispersion of the same order than in the previous two cases (FAM$_{CNBG}$ and FAM$_{CPSCz}$), and correlation indexes indicating a strong correspondence between the mock and FAM$_{cor}$ velocities. The right-hand panels of Fig. 4.9 illustrates these points. The FAM corrected velocities are in very good agreement with the Mock-observed ones indicated by a slope very close to unity, the zero offset is very small.

An interesting point to note is that while the FAM$_{CPSCz}$and FAM$_{cor}$ distributions are skewed toward negative velocity values, this is not the case for the FAM$_{CNBG}$. This reveals the dominant gravitational effect of the GA over the whole LS volume. While in the FAM$_{CNBG}$ sample this effect is not present, as it is excluded from consideration, a more symmetric distribution follows.

We have also investigated what the effects are when computing the external contributions from the residual field between the CPSC*z* and CNBG catalogs and not from the Mock and CNBG. We have characterized this residual field as before by its two main dominant components and add them to the inner CNBG sample. Table 4.5 shows that results are very close to the FAM$_{cor}$ case. The main difference is related to the zero-points which for this case are larger than before. This is a mere reflection of the large scatter present in the FAM$_{CPSCz}$sample. These results show that the Mock mass distribution can be characterized by its Bulk Flow and tidal Shear components.

We have checked the net effect of adding separately each external component to the FAM$_{CNBG}$ sample and compared these new samples with respect to the expected Mock velocities. Figure 4.10 shows the density contours of the point-to-point distributions between the different residual fields and Mock velocities for the 3 Cartesian velocities. For reference we included the one-to-one line, zero residual line (horizontal), and the centre lines (vertical). The top-most panels present the Mock-FAM$_{CNBG}$residual velocities versus the Mock ones. These residual velocities correspond to the external tidal field. From Table 4.5 we infer that this field contains almost 50% of the relevant gravitational contributions. This explains the strong correlation with respect to the Mock catalog. This correlation mainly concerns the *x* and *y* components (main directions of the GA gravitational pull and bulk motion), and is less pronounced along the *z* component.

Because the external missing bulk motion is a constant vector, the net effect of adding it to the

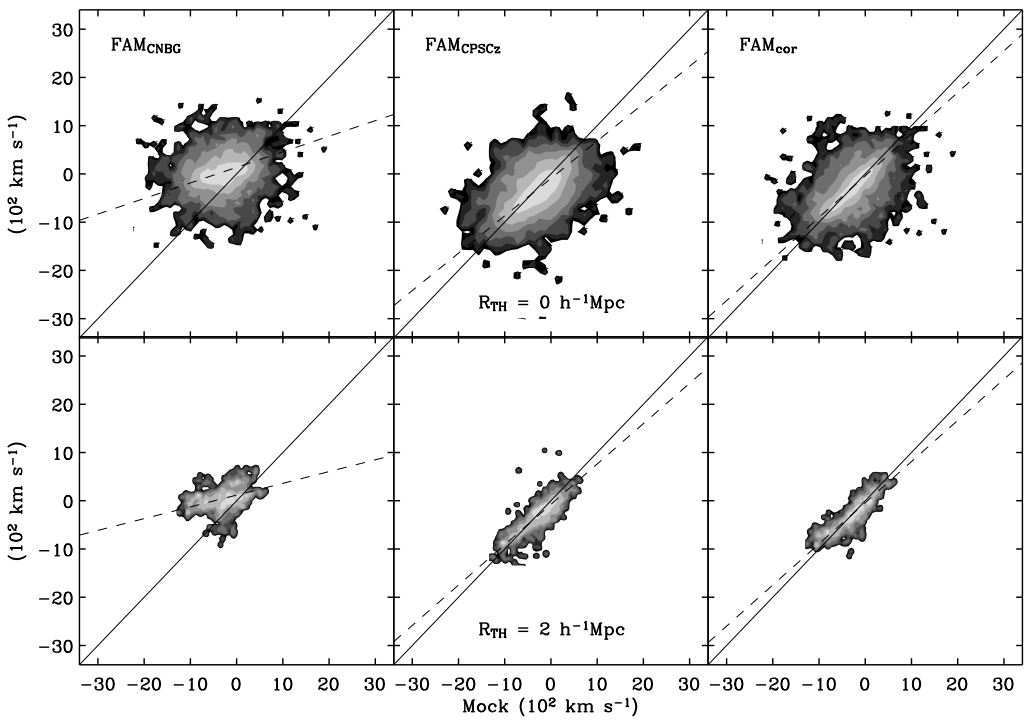

Figure 4.9 — Density contours of the point-to-point distributions for the same Cartesian component for the 3 different FAM samples *vs* the corresponding Mock one. The continuous line represent the one-to-one relation, while the broken line represents the best fitting line from the comparison. The top panels represent the unsmoothed velocities, and the bottom panels refer to the convolved velocities with a Top-Hat kernel of 2 h^{-1}Mpc.

FAM$_{CNBG}$ sample shifts the whole distribution. The corresponding central value of the distribution will move to the zero point. The second row of Fig. 4.10 illustrates this point. The three point distributions have been shifted and are more symmetric than before. Yet, the residual velocities still present a strong correlation with respect to the mock velocities.

The last two rows of Fig. 4.10 represent the unsmoothed and smoothed residual velocity fields of the Mock - (FAM$_{CNBG}$+ missing bulk + tidal shear). After subtracting the shear, the central contours of the residuals tilt toward the zero abscissa line. This is particularly visible along the x and y axes where most of the tidal shear is coming from. This situation is clearer in the smoothed panels, where the bulk of the distributions are aligned along the zero abscissa line. The fact that the z component is only vaguely affected implies that the major external sources are located along the $x-y$ and $x-z$ supergalactic planes.

4.6 Conclusions

In this chapter we have studied the influence of the large scale mass distribution over the peculiar velocity field of the Local Supercluster confined within a volume of 30 h^{-1}Mpc radius, based on constrained realizations of the nearby universe.

We have reconstructed the peculiar velocity fields by means of the FAM technique from Mock catalogs which resemble the mass distribution within the LS volume. Such catalogs were obtained from constrained $N-$body simulations of the nearby universe according to the real mass distribution inferred from the the Mark III catalog of peculiar velocities up to 60 h^{-1}Mpc. The fields are effectively constrained at larger radii since the correlation length of the velocity field extends further away than the physical boundaries of the surveyed data. Constraints were imposed on the initial Gaussian density

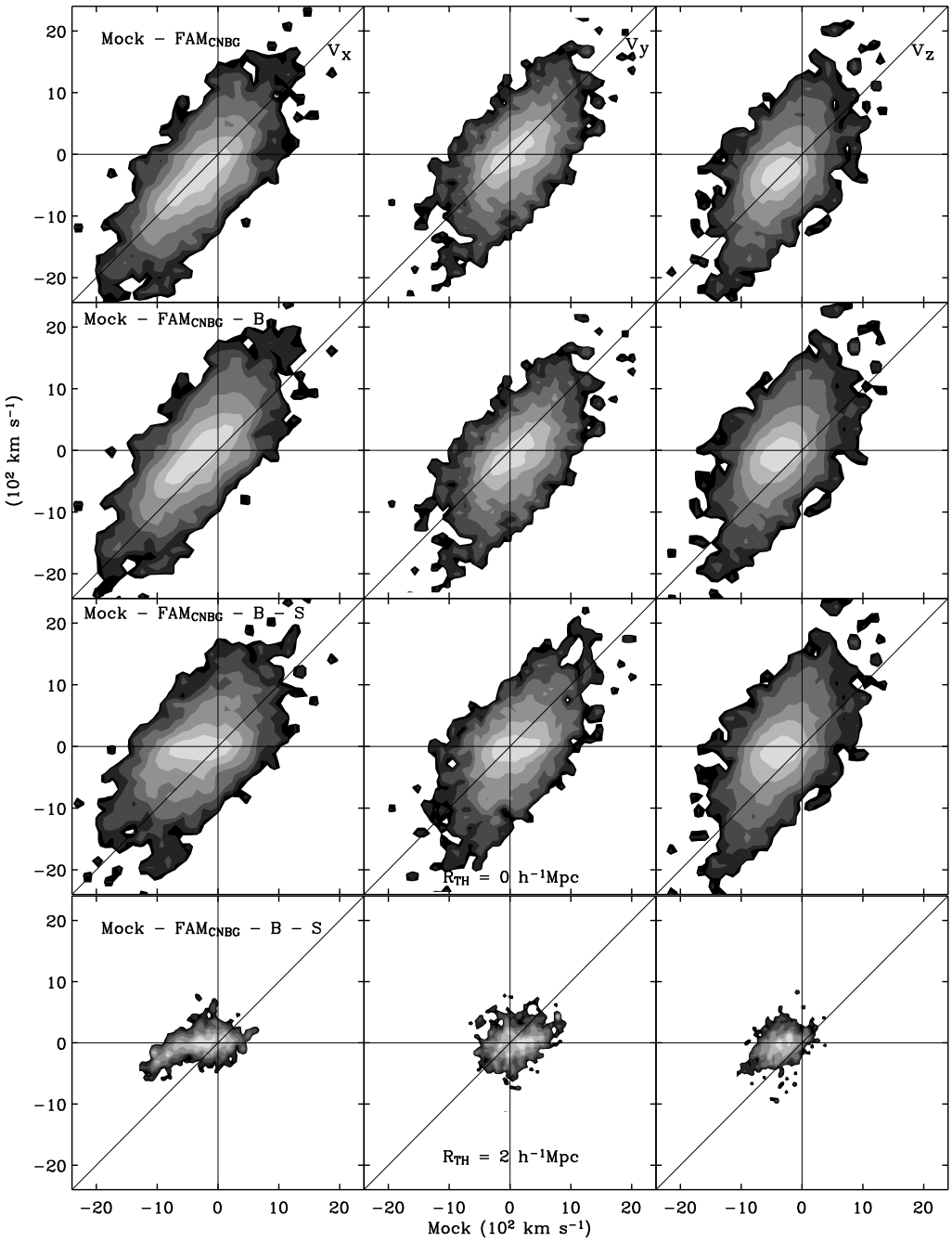

Figure 4.10 — Density contours of the point-to-point comparison for the 3 Cartesian components of the velocity residuals between Mock and FAM$_{CNBG}$, FAM$_{CNBG}$+ Bulk, FAM$_{CNBG}$+ Bulk + Shear. The continuous line in the two top panels represent the one-to-one relation, while the lines in the lower two panels represent the residual-zero line. The top 3 rows represent the unsmoothed velocities, and the bottom row refers to the convolved velocities with a Top-Hat kernel of 2 h^{-1}Mpc.

field by means of the Constrained Realization method. The Mock catalogs were constructed to sample the LS region in a volume-limited way according to the Nearby Galaxy Catalog of Tully (1988), and in

a flux-limited way from $30-150\ h^{-1}$Mpc according to the IRAS-PSCz catalog (Saunders et al. 2000) in order to account for the tidal influence of the large scale structure over the LS volume.

We have divided our velocity modeling in two steps. The first models the local contributions within the LS by considering only the mass distribution enclosed by the volume-limited catalogs. In the second step we modeled the LS + large scale distribution of the nearby universe (volume + flux limited samples).

The Mock catalogs showed that the LS is dominated by a bulk flow induced mainly by the GA. It involves a particular mass configuration around the LG and LS resembles a quadrupolar mass distribution, composed by the GA and PP. Both structures are located at opposite directions from the Local Group and along the same z-supergalactic plane. This mass distribution induces a strong shear pattern along all directions over the LS, but it has its strong components along the $x-y$ and $x-z$ planes. It implies that most of the external tidal influence comes from structures located along the $x-y$ supergalactic plane.

The FAM modeling of the LS region argues that this volume only accounts for $\sim 55\%$ of the total gravitational influence. The rest it is induced by the external mass distribution. Comparisons between FAM_{CNBG} and Mock velocities indicate that the large scale components of the power spectrum are missing when the velocity modeling only refers to the LS region. The average recovered slope from the point-to-point comparisons is 0.57 ± 0.27 with a considerably large deviation from the zero point of 63 ± 89 km s^{-1}. These results indicate that the large components of the velocity field are missing. This information should be added to the LS peculiar velocity field in order to get an unbiased field.

When modeling the LS + large scale structure, we found that the corresponding LS peculiar velocity field has accounted for the missing gravitational influence properly. The modeled fields are bias-free, and therefore trustable with respect to the expected ones. Comparisons of these fields with respect to the mock catalogs showed a good agreement between both fields.

We have characterized the external gravitational influence over the LS by a multipolar decomposition of the residual velocity field between the FAM_{CNBG} and Mock fields. This residual field is exclusively the result of the influence of the unaccounted mass distribution beyond the LS volume. Our results indicate that for an external mass distribution of the nearby universe as measured by the PSCz catalog up to distances of 150 h^{-1}Mpc, can be characterized by the two most dominant components of such field, the dipole and quadrupole (bulk flow and shear). By adding such components to the LS volume-limited peculiar velocities, it is possible to recover an unbiased peculiar velocity field free from any external unaccounted large scale effect.

Comparing our results with those from RBW, we found two main differences. The first one concerns the scatter around the average values, in the present work the measured uncertainty is smaller than in RBW as a result of the use of constrained $N-$body simulations which effectively constrain the mass distribution within 60 h^{-1}Mpc in the four simulations. The second one is related to the tidal eigenvalues, our estimates are slightly larger than those reported by RBW. The reason for this is the specific configuration of the cosmic neighborhood. The presence of the GA and PP superclusters mould in a particular way the local peculiar velocity field.

From these results it can be infer that one can indeed construct an unbiased model for the cosmic velocity field within our Local Supercluster by taking into account the mass distribution traced by PSCz galaxies out to a distance of 150 h^{-1}Mpc, provided that the mass distribution responsible for the dynamics of the LS is indeed contained within this distance.

Finally, the FAM technique has proved to be a good tool to model the peculiar velocity field within the LS volume from the corresponding density field, up to the mildly non-linear regime.

4.A Smoothing effects

The raw Mock velocities are severely affected at the highly clumped regions by two body relaxation processes. These interactions have erased any memory from their initial linear state. Therefore, they are responsible for the large differences between FAM and Mock velocities at the non-linear regions.

Nusser & Branchini (2000) suggested that increasing the number of basis functions will not improve the results because after 6 expansion functions, there are not considerable changes in the FAM performance (Chap. 2 & 3). RBW showed that a simple smoothing procedure (after applying FAM) helps to improve the results, mainly to reduce the large scatter along the average results, but also to decrease considerably the velocity dispersion. Branchini, Eldar, & Nusser (2002) pointed out that by discarding in the analysis galaxies located at high density regions also helps to improve the results substantially, but this will erase small scale signal that could be of importance when performing studies concerning to small scales, e.g., the coldness of the flow. In this chapter we have adopted the RBW approach and applied a Top-Hat smoothing procedure to our velocity fields for all statistical analyses and point-to-point comparisons.

We have convolved the velocity fields with 3 different top-hat kernels of sizes $1, 2$ and $5\ h^{-1}$Mpc. We have found that a kernel of $2\ h^{-1}$Mpc is more than enough for our purposes. Although the velocity dispersions get smaller with a kernel of $5\ h^{-1}$Mpc, the slopes, zero points and correlation indexes do not change considerable with respect to the $2\ h^{-1}$Mpc case.

5

FAM for real: PSCz as probe of the Local Universe

E. Romano-Díaz, E. Branchini & R. van de Weygaert.

We have investigated the two main components of the large scale velocity field (in real space), inferred from the IRAS-PSCz catalogue, the bulk flow and velocity shear. Such catalogue can be considered as a fair representation of the nearby universe. In order to minimize redshift effects, we have used the real spatial catalogues reconstructed from Branchini et al. (1999). The modeling of the peculiar velocity field was performed by means of the FAM technique. The corresponding bulk flow estimates are in very good agreement with other measurements from different catalogues and techniques. The cumulative distributions of the velocity shear indicate that most of the contributions to it come from structures located within a volume of 20 h^{-1}Mpc around the Local Group. Structures located within 20 and 60 h^{-1}Mpc still deform the velocity ellipsoid considerably, and those located beyond 70 h^{-1}Mpc do not contribute to the velocity shear. The radius at which the shear vanishes has been estimated at a distance of 80 h^{-1}Mpc from the Local Group. The shear eigenvectors suggest that the Hydra-Centaurus supercluster is responsible for the largest stretching direction of the velocity ellipsoid, with an anti-apex direction pointing toward the Perseus-Pisces supercluster. This eigenvector is roughly aligned with the bulk flow direction, implying that some of the structures responsible for the bulk flow motion, are also responsible for the velocity shear, i.e. the Hydra-Centaurus supercluster.

5.1 Introduction

The increase of quantity and quality of the galaxy distribution mapping in our nearby universe in the last years has given us the opportunity to study in more detail several aspects of the large scale structure of the universe. Several different techniques have been applied to the available data in order to estimate or characterize such data catalogues, quantifying mainly the magnitude and direction of their dipole or bulk flow.

Within the Gravitational Instability scenario, peculiar velocities are the result of galaxy interactions with their surrounding matter concentrations, such as galaxies, clusters and superclusters of galaxies, voids, etc. On the other hand, peculiar velocities are more prone to the large scale modes of the power spectrum of fluctuations than its corresponding matter distribution. Therefore they can better trace the inhomogeneities in the density field at larger distances than the matter itself.

When characterizing the peculiar velocity field by contributions coming from different scales and regimes within a given volume, two terms are the most dominant : the bulk flow (dipole) and shear (quadrupole) (Chapter 3 Romano-Díaz et al. 2004). The bulk flow represents a robust statistic of the velocity field over a volume of a characteristic length scale R. The convergence radius of the bulk flow is estimated to be in the order of $150-200\ h^{-1}$Mpc from the Local Group (see Zaroubi 2002, for a review about the topic).

The velocity shear measured in a given sample is the result of the action (stretching and/or compression) over the enclosed matter distribution of structures located beyond the edge of the sample. Unless one is dealing with a large enough volume ($\geq 100\ h^{-1}$Mpc), such contributions are not negligible (Chap. 2 & 3), becoming more pronounced at the edge of the sample. The velocity shear convergence radius, the distance at which the shear amplitude vanishes, is more ill-defined than the bulk flow one. In a seminal paper, Lilje, Yahil, & Jones (1986) proved the tidal field in the Local Supercluster ($30\ h^{-1}$Mpc) and predicted the existence of a dominant structure beyond $40\ h^{-1}$Mpc, the so-called "Great Attractor". Tonry et al. (2000) determined from the SBF catalogue, on a surveyed volume of $30\ h^{-1}$Mpc, that structures beyond $40\ h^{-1}$Mpc like the Perseus-Pisces supercluster or Shapley concentration do not play a substantial role in perturbing the velocity field within such catalogue. However, in a preliminary study using the Mark III and SFI catalogues Hoffman et al. (2001) found that the dilational eigenvector of the residual shear tensor is roughly aligned with the bulk velocity, indicating the presence of a major attractor at distances $> 150\ h^{-1}$Mpc, coinciding with the Shapley concentration. In Chapter 2 (Romano-Díaz et al. 2004), it was shown that for a ΛCDM universe the velocity shear (in linear theory) converges at scales larger than $100\ h^{-1}$Mpc. From the flux-limited mock catalogue analysis performed in Chapter 3, we did not find substantial contributions to the shear amplitude from scales beyond $80\ h^{-1}$Mpc.

Studies concerning the velocity shear need to make use of a homogeneous sample, with a large effective radius and depth, and mainly, full sky coverage. The PSC*z* catalogue (Saunders et al. 2000) fulfills these requirements and gives us the opportunity to prove the role of structures beyond the effective radii of the samples mentioned above.

Several studies have been performed with the PSC*z* catalogue concerning to the large scale structure of the Universe, e.g. Branchini et al. (1999) inferred the velocity field, Tadros et al. (1999) studied the real-space power spectrum and redshift distortions, Sutherland et al. (1999) the redshift-space power spectrum, Rowan-Robinson et al. (2000) studied the direction and convergence of the dipole, Plionis et al. (2000) studied the galaxy-cluster bias using the PSC*z* dipole. Nevertheless, none of the previous works have investigated the role and origin of the velocity shear and the structures responsible for deforming the peculiar velocity ellipsoid. Here we address these issues which concern to the peculiar velocity field of galaxies.

In this chapter we apply FAM to the real PSC*z* catalogue mapped from redshift-space to real Cartesian coordinates. We compute the peculiar velocity field from the discrete galaxy distribution and characterize it by means of its main components, the bulk flow and shear. We also investigate the changes of these components when considering different volume sizes in the FAM modeling procedure. Furthermore, we will try to determine the shear convergence radius and explore the effects of tripled-

valued regions on the FAM velocity models. The error estimates have been assessed from the results of Chapter 3. We will compare our results with the expected theoretical predictions and with respect to those obtained from other samples and techniques.

In order to have a more realistic estimate of the bulk flow and velocity shear quantities, it would be preferable to perform the analysis from velocities inferred directly from their redshift distribution. However, we apply FAM to the real space galaxy distribution of the PSC*z* catalogue because we have fully tested it, and we have control over the possible systematic error sources of the method. In the future, we intend to use the FAM technique in redshift space (Branchini et al. 2002) to estimate the peculiar velocity field from the redshift distribution of the PSC*z* survey. This chapter represents a first step toward a better determination and understanding of these two important quantities (bulk flow and shear) of the large scale peculiar velocity field.

5.2 The data: The PSC*z* catalog

The flux-limited IRAS-PSC*z* all sky redshift catalogue is described in detail by Saunders et al. (2000) and we only summarize its main features here.

This catalogue is basically an extension of the IRAS $1.2-Jy$ survey (Fisher et al. 1995a). The catalog contains ~ 15500 galaxies with $60\mu m$ flux $f_{60} > 0.6Jy$ covering a large part of the sky $\sim$ 84%. The median redshift is 8500 km s^{-1}, with a mean galaxy separation within 10 000 km s^{-1} of $\langle l \rangle \sim 1000$ km s^{-1}. A major improvement with respect to the IRAS $1.2-Jy$ catalogue which has $\langle l \rangle \sim 1500$ km s^{-1}. These characteristics ensure a depth and dense sample.

Because of the flux-limited nature of the catalogue, there is a degradation of sampling as a function of distance from the observer, causing the number density of objects to decrease with distance. This decrease is measured by a radial selection function. In order to recover the true galaxy density from the observed flux-limited sample, each galaxy has been weighted by the inverse of the selection function $\phi(r)$. This function has been defined as the fraction of galaxies that can be seen out to a redshift distance $r = cz/H_0$ (expressed in h^{-1}Mpc) given the survey flux limit. Various authors have used different estimators to compute the selection function (e.g. Canavezes et al. 1998; Sutherland et al. 1999; Branchini et al. 1999). Nevertheless, Branchini et al. (1999, hereafter B99) found that different selection functions induce variations smaller than 5% in the model density and velocity fields within a distance of 20 000 km s^{-1}. In the present study, we have adopted the selection function of the form assumed by B99:

$$\phi(r) = Ar^{-2\alpha}\left(\frac{1+r^2}{r_*^2}\right)^{-\beta} \qquad \text{for} \quad r > r_s \tag{5.1}$$

with $\alpha = 0.52$, $\beta = 1.92$, $r_s = 6.0\ h^{-1}$Mpc, and $r_* = 90.75\ h^{-1}$Mpc. The fitting parameters were computed via likelihood analysis including only objects within 100 000 km s^{-1} and they provide a good description of the data. B99 showed that the value of the normalization value A, does not affect the modeling of peculiar velocities. In their implementation, the selection function was arbitrarily set $\phi(r) = 1$ for $\mathrm{r} \leq \mathrm{r_s}$. This is equivalent to imposing a lower cut-off in the $60-\mu m$ luminosity in order to avoid too much weight to faint, nearby galaxies that may not trace the galaxy distribution reliably in the nearby volume (Rowan-Robinson et al. 1990).

5.2.1 Real space distribution

In order to take into account (1) the 16% of the missing sky de-voided of data due to high cirrus emission areas and unobserved regions, and (2) to correct for redshift-space distortions that affect the observed galaxy distribution and to obtain the real spatial Cartesian positions, we have made use of the corrected galaxy catalogue of B99. In this catalogue, B99 followed a method similar to the Yahil et al. (1991) approach to fill the galactic plane with synthetic objects that reproduce the mean density of galaxies of the nearby regions. In the cases of masked regions at larger latitudes, these are filled in with a random distribution of synthetic galaxies having the observed mean number density of PSC*z* galaxies.

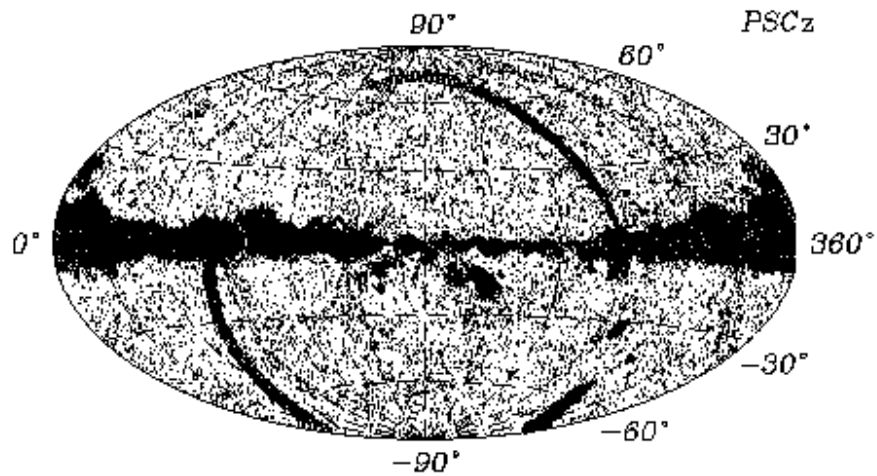

Figure 5.1 — Aitoff projection of the IRAS-PSCz galaxy distribution in galactic coordinates. The dark regions shown unobserved or obscured regions. The horizontal strip surrounding the Galactic plane is the Zone of Avoidance (from Branchini et al. 1999).

Tests performed by B99 on mock catalogues showed that the only bias introduced by this filling-in technique is a spurious bulk motion of < 60 km s^{-1}. In order to minimize the "Kaiser effect" and to recover the real spatial Cartesian positions, B99 applied an iterative algorithm in order to solve for the positions and velocities. Such method is based on three main assumptions: (a) the gravitational instability scenario is valid (Peebles 1980), and therefore cosmic structures have grown by gravitational amplification of small-amplitude fluctuations in the density field at early epochs. (b) The linear or mildly non-linear theory is applicable once the density field is smoothed. (c) Galaxies are assumed to trace the underlying mass density field according to a linear biasing model of the form: $\delta_{gal} = b\delta_{mat}$, where δ_{mat} is the mass overdensity, δ_{gal} is the fluctuation in the number of galaxies and b the biasing parameter. Under these assumptions, a redshift survey enables an independent reconstruction of the density and velocity fields. However, this method is only valid in the linear regime, where a one-to-one mapping between distance and redshift is guarantee. Therefore the force field needs to be smoothed to eliminate non-linear effects, shot-noise, distance uncertainty, and tripled-valued zones.

Although the catalogue contains objects with recession velocities as large as 30 000 km s^{-1}, the sample is not very reliable at these ranges. B99 considered all PSCz galaxies out to a radius of 200 h^{-1}Mpc in their reconstruction procedure, beyond this radius galaxies are severely affected by shot-noise effects.

Around high-density regions, like clusters of galaxies, there may occur shell crossing. Hence there may be tripled-valued regions in which the same redshift is observed at three different positions along the line of sight. B99 adopted the same procedure as in Yahil et al. (1991) by collapsing the tripled-valued regions by using two different data sets. Their results showed that the collapsing procedure only affects the infall pattern around the clusters. Nevertheless, with the level of smoothing used here, such effects are not considerable. In order to check if tripled-valued regions have a considerable effect, we have used two different PSCz catalogues from B99. One without collapsing the tripled-value regions, and another with collapsing the galaxies.

The reconstruction technique recovers the main cosmic features of the PSCz catalogue as shown by B99, and we will address readers to this work for a detailed cosmographic tour of the local universe. We want to stress, as it can be noticed from Figure 5.2, that structures like the Virgo cluster, Hydra-Centaurus supercluster (Great Attractor), Coma, Perseus-Pisces and Camelopardalis superclusters, the Pavo-Indus-Telescopium complex, the Cetus wall, the Shapley concentration and voids like the Sculptor void and the voids in the foreground of Coma, in the background of Perseus-Pisces complex and

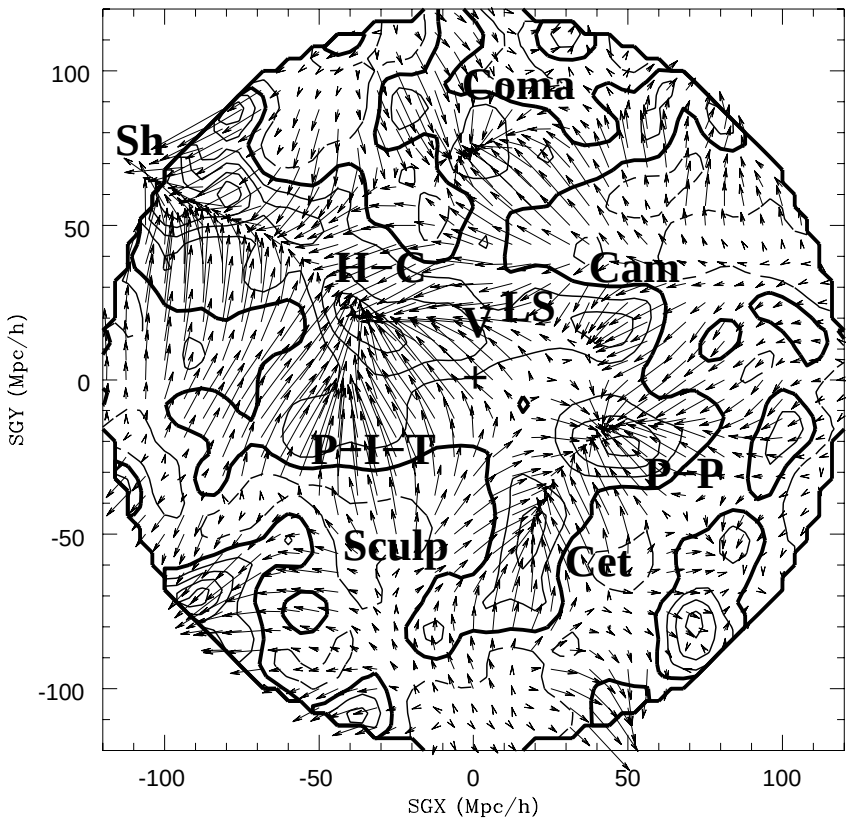

Figure 5.2 — Real space density and velocity fields derived from the PSC*z* survey. The fields, smoothed with a Gaussian filter $R_G = 6\ h^{-1}$Mpc, are shown in a slice along the Supergalactic plane. The thick continuous line represents the $\delta = 0$ contour. The continuous lines represent overdensity regions, while dashed lines underdense regions. Contours are plotted at steps of $\Delta\delta = 0.5$. The labels mark the position of the largest structures along the Supergalactic plane. V: Virgo cluster, LS: Local Supercluster, H-C: Hydra-Centaurus, Sh: Shapley, P-P: Perseus-Pisces superclusters, P-I-T: Pavo-Indus-Telescopium complex, Cet: Cetus wall, Sculp: Sculptor void. (from Branchini et al. 1999).

behind the Great Attractor are clearly recognizable in the reconstructed density field maps. Figure 5.2 shows the PSC*z* model density and velocity fields reconstructed up to 120 h^{-1}Mpc smoothed with a 6 h^{-1}Mpc Gaussian filter in a slice through the Supergalactic plane. The central crux denotes de position of the Local Group. Notice how the Local Group is located between two massive structures, the Hydra-Centaurus and Perseus-Pisces superclusters. The modeled linear velocity field is strongly distorted by these two matter concentrations.

5.3 FAM modeling of the peculiar velocity field

We have modeled the peculiar velocity field by using our implementation of the Least Action Principle [LAP], the Fast Action Minimization method [FAM] (Nusser & Branchini 2000, Chapters 2 & 3).

5.3.1 Redshift space considerations

It is necessary to mention that the application of FAM over the real space Cartesian galaxy distribution represents a refinement over the linear reconstruction method to model the peculiar velocity field. FAM

represents an improvement over the B99's method in the sense that it extends the velocity modeling into the mildly non-linear regime.

In order to have a more consistent non-linear peculiar velocity field from redshift catalogues, e.g. PSC*z*, it could be preferable to apply a modified version of FAM, directly applicable to redshift space. Such modification of the FAM formalism was indeed introduced by Branchini et al. (2002). Their analysis from mock catalogues proved that this new algorithm could be applied to redshift galaxy distributions such as the PSC*z* catalogue.

Here we applied FAM to the real space galaxy distribution of the PSC*z* catalogue because we have fully tested it, and we have control over the possible systematic error sources of the method. In the future, we intend to use the FAM*z* technique to estimate the peculiar velocity field from the redshift distribution of the PSC*z* survey. refinement

5.3.2 Least Action Principle and FAM analysis

The LAP technique has been applied to predict the orbits of galaxies within the Local Group (Peebles 1989, 1994; Phelps 2000), and to predict the peculiar velocities of nearby PSC*z* galaxies contained in a volume of 2 000 km s^{-1} from the LG (Sharpe et al. 2001). The main limitation of the previous implementations is the small number of objects used in the calculations due to the expensive force algorithms employed (direct summation). As discussed in Chapter 2, FAM overcomes this problem by using the TREECODE technique (Bouchet & Hernquist 1988) to speed up the gravity calculations. Our LAP implementation has proved to be a very suitable algorithm to be applied on large cosmologic data sets. Furthermore, the force calculation algorithm implemented on FAM gives it the especial advantage of handling particle distributions in spherical regions as in the case of whole-sky galaxy catalogues (e.g. PSC*z*).

FAM needs 3 basic input parameters: (1) the number of basis expansion functions N_f, to parametrize the orbits. (2) A tolerance parameter to search for the minimum of the action. (3) A softening parameter to smooth the gravitational force in the TREECODE. In Chapters 2 & 3 (see also Nusser & Branchini 2000) we have shown that a $N_f = 6$ basis functions and a tolerance parameter $tol = 10^{-4}$ are the optimal choices. Nevertheless, we still have to look for the best suitable softening employed in the force calculation. The role of the softening is to impose the limiting scale on the FAM calculations, below which the FAM cannot model accurately the structure of orbits.

5.3.3 Optimum FAM softening

In Chapters 2 & 3 we set the force resolution to match the one given by the $N-$body simulations. Nevertheless, we face here the problem of finding an optimum "natural" softening for the real galaxy distribution. An obvious choice would be to set it to the minimum inter-particle separation. Nevertheless, such softening could introduce extra noise in the modeled velocity field since it would lead FAM to calculate interactions at small scales where the method is not completely accurate. Other possible softening prescriptions are the mean of the minimum inter-particle separations or the mean inter-particle separations computed at different radii. They may also be acceptable due to the fact that the 3D-real particle distributions were computed by means of linear theory.

To choose the most suitable softening we performed 5 different runs testing 5 different softenings: the minimum inter-galaxy separation distance (0.014 h^{-1}Mpc); the mean minimum inter-galaxy distance (1.55 h^{-1}Mpc); the mean inter-galaxy distance at a distance of 30 and 60 h^{-1}Mpc (4.57 and 7.14 h^{-1}Mpc respectively); and the $N-$body softening of 0.27 h^{-1}Mpc used in Chapter 3.

Point-to-point comparisons between all test samples indicated that the minimum inter-particle separation and $N-$body softenings present larger scatters in the point distributions with respect to the other 3 options. The two mean inter-particle separation samples are very similar to each other and also with respect to the velocity field computed with linear theory. This is mainly due to the fact that the softening is comparable in length to the smoothing kernel used to compute the Cartesian density and velocity field. Taking into account that our intention is to preserve the mildly non-linear regime, we

have chosen as our optimum softening the mean minimum inter-particle separation of 1.55 h^{-1}Mpc. This choice will keep the shot-noise level low at very high density regions while given an acceptable performance at quasi-linear and low density regions.

After having selected the softening, we proceed to model the two velocity fields by considering galaxies up to 150 h^{-1}Mpc. The choice for this value as the limiting radius is based on two considerations. The first one is that galaxies up to this radius are not seriously affected by shot-noise effects (B99). The second reason is based on the analysis of B99, where they did not find substantial contributions to the bulk flow estimate beyond this radius.

5.3.4 Error estimates from mock catalogues

In order to assess and to quantify random and systematic errors in our modeled peculiar velocity fields, we have used the constrained mock catalogues presented in Chap. 3. These catalogues mimic the main properties of our nearby Universe according to the same adopted PSC*z* selection function. An important consideration is the fact that these catalogues do not contain large scales contributions beyond 150 h^{-1}Mpc.

5.3.5 Dependence on the β parameter

In our actual FAM implementation, the equations of motion expressed in terms of the time variable D (the linear growing mode of the density perturbations), are almost independent of Ω_m and the cosmological constant (e.g. Nusser & Colberg 1998). Our velocity field models will therefore depend linearly on the β parameter ($\beta = \Omega_m^{0.6}/b$, with b the biasing parameter), affecting only the amplitude of the computed velocities. However, the β value should be consistent with the one chosen from the reconstruction procedure, i.e. $\beta = 0.5$.

5.4 Analysis

In order to determine the bulk flow and shear contributions, and the radius at which the shear vanishes, we have considered 5 different volumes for the FAM modeling. The bulk flow and velocity shear were computed by using the same decomposition method presented in Chapter 3 (Kaiser 1991). The first volume was chosen in order to obtain the contributions from the Local Supercluster region (30 h^{-1}Mpc). The second and third volumes were limited at the radii at which most of the existing catalogue samples, 60 and 80 h^{-1}Mpc. B99 estimated that with the depth and frequency of the PSC*z* survey, a reliable density field can be constructed out to a radius of 150 h^{-1}Mpc. Beyond this radius sparsed sampling effects become more important and could affect the field reconstruction. Nonetheless, Tadros et al. (1999) indicated that the PSC*z* catalogue should not be used down to a flux limit of $0.6Jy$ and that a more conservative limit in flux of $0.745Jy$, should be adopted instead. This flux cut translates into a volume of radius 120 h^{-1}Mpc. We have taken into account these two results and decided to model 3 large scale velocity fields with radii of $100, 120$ and 150 h^{-1}Mpc. The 5 FAM catalogues were constructed for the two PSC*z* reconstructions in order to check for possible effects in the reconstruction process. Table 5.1 presents the 5+5 different volume samples for both reconstructed catalogues: those considering tripled-valued regions ("tripcoll"), and those where this effect was not taken into account ("untripcoll"). This table also indicates their respective depths and corresponding number of galaxies enclosed by each subsample.

5.4.1 Bulk flow

The bulk flow is defined as the average streaming motion within a certain volume. Within the linear gravitational instability scenario, the *rms* expected bulk velocity within a sphere of radius R, is given

Label	Sample Volume (h^{-1}Mpc)	Sample Type	N_{gal}
PSCz_{30}	30	untripcoll tripcoll	1875 1789
PSCz_{60}	60	untripcoll tripcoll	5421 5262
PSCz_{80}	80	untripcoll tripcoll	7527 7336
PSCz_{100}	100	untripcoll tripcoll	9300 9098
PSCz_{120}	120	untripcoll tripcoll	10651 10415
PSCz_{150}	150	untripcoll tripcoll	12166 11939

Table 5.1 — PSC*z* subsamples at different depths. Each catalogue has been constructed from the full sample (200 h^{-1}Mpc). Col. 1 indicates the catalogue label. Col. 2 gives the limiting depth of the sample. Col. 3 refers to the sample used: "tripcoll" indicates the reconstruction where tripled-valued regions (collapsed) were treated (see text), while 'untripcoll' to the reconstruction were this effect was not taken into account. Col. 4 presents the number of galaxies contained in the subsample.

by (Peebles 1993a),

$$V(R)_{Exp} = \frac{H_0 f(\Omega_m)}{\sqrt{2}\pi}\Big[\int_0^\infty P(k)\tilde{W}^2(kR)\,\mathrm{d}\mathbf{k}\Big]^{1/2}, \tag{5.2}$$

where $f(\Omega_m) \simeq \Omega_m^{0.6}$ (Peebles 1980), $P(k)$ is the mass fluctuation power spectrum, and $\tilde{W}(kR)$ is the Fourier transform of a top-hat window of radius R.

In order to estimate the effects of tripled-valued regions, we have compared the bulk flow estimates at different radii from the two PSC*z* reconstructions using the PSCz_{150} volume sample. Table 5.2 gives the bulk flow direction and amplitude expressed in galactic coordinates (Columns 3, 4 and 5 respectively), together with their $\pm 1\sigma$ dispersion computed from the mock catalogues. Column 1 indicates the volumes at which the FAM bulk estimates were performed. Column 2 gives the name of the PSC*z* reconstruction used for the analysis. As in Table 5.1, the labels refer to the sample where tripled-valued regions were considered or not. We have only indicated dispersion errors for one reconstruction, because we have found that they are similar for both samples.

From the comparison between the two PSC*z* reconstructions, we can notice that both samples are consistent with each other at any sampled volume. Bulk flow amplitudes are $\sim 10\%$ larger for the collapsed reconstructions than for the uncollapsed ones, but consistent within the 1σ dispersion. However, differences in the bulk flow directions are less pronounced than for the corresponding magnitudes. The different bulk flow directions point consistently toward the same region in the sky. These results indicate that for the case of the bulk flow, tripled-valued regions do not represent an important source of error. It is worth mentioning that this effect has also been minimized by the smoothing procedure in

Sample Volume (h^{-1}Mpc)	Sample Type	V_{bulk} (km s^{-1})	l (°)	b (°)
30	tripcoll	326	253	18
	untripcoll	302±55	250±31	19±30
60	tripcoll	222	249	16
	untripcoll	221±59	247±16	17±19
80	tripcoll	229	250	19
	untripcoll	201±73	246±14	20±19
100	tripcoll	210	249	20
	untripcoll	185±78	247±13	20±17
120	tripcoll	195	250	20
	untripcoll	171±82	247±12	20±16
150	tripcoll	174	251	19
	untripcoll	155±78	247±12	20±14

Table 5.2 — Bulk flow estimates from the two PSC*z* reconstructions computed at different radii from the PSCz_{150} sample. Col. 1 indicates the radius at which the bulk flow estimate was performed. Col. 2 gives the label of the PSC*z* sample used : 'tripcoll' refers to the reconstruction where galaxies were collapsed, while 'untripcoll' to the reconstruction were it was not taken into account. Cols. 3, 4 & 5 present the bulk flow amplitude, and its direction in galactic coordinates.

the catalogue-reconstruction.

Taking into consideration the fact that the bulk flow estimates from the two different reconstructions are equivalent, we will refer from now on to the PSC*z* bulk flow as that quantity computed from the uncollapsed reconstructed catalogue.

Figure 5.3 depicts several aspects of the computed bulk flow. The upper left-hand plot displays the bulk flow amplitudes computed as a function of depth for the different volumes. Each different volume is indicated by different symbols and line styles. Notice that we have changed labels from PSC*z* to FAM. We have done so because the samples represent now velocity fields modeled by means of FAM. The thick continuous line represents the expected theoretical rms bulk flow prediction (V_{Exp}) of a sphere of radius R as given by Eqn. 5.2 for a ΛCDM universe. The lines are a measurement of the contributions from the density fluctuations enclosed by such regions. It is clear that small volumes up to middle size (30 – 100 h^{-1}Mpc) miss the very large scale contributions exerted by the matter distribution beyond the limits of the corresponding samples. Volumes large enough ($\geq$ 120 h^{-1}Mpc) seem to enclose most of the density fluctuations that contribute to the real power spectrum and are consistent with the theoretical expectation of a ΛCDM universe as revealed by the residual bulk flow. This is defined as the expected bulk flow (V_{Exp}) minus the different FAM volume models (V_i). The bottom part of the upper left-hand plot shows the residual bulk flows for the different FAM samples. Because the bulk flow is a characteristic quantity of the enclosed matter concentration, the missing contributions are the same for the whole surveyed region. Furthermore, one would not expect configuration-dependent effects. This brings as a consequence, that the residual bulk flows ($V_{Exp} - V_i$) are almost constant along the sampled volumes.

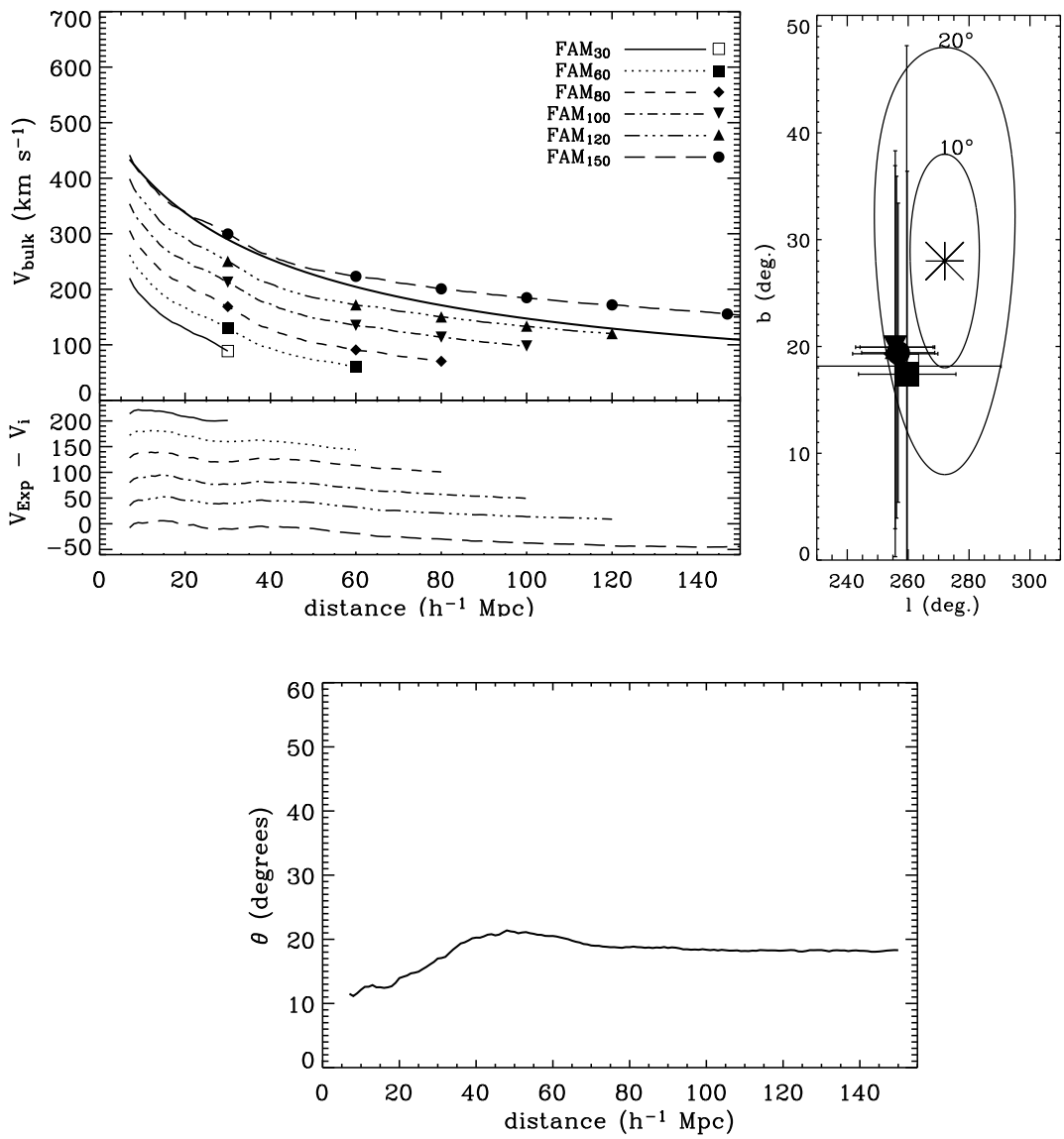

Figure 5.3 — Cumulative bulk flow amplitudes (upper left-hand plot) computed for 5 different volume samples. The top panel indicates the volume contributions to the bulk flow, while the lower panel depicts the residual bulk flows computed between the theoretical expected bulk flow and the 5 subsamples. The upper right-hand plot depicts the bulk flow directions shown in Table 5.2. The asterisk plotted at the center represents the CMB dipole direction. The lower plot shows the angular misalignment between the 150 h^{-1}Mpc volume FAM model and the CMB direction.

The upper right-hand plot of Figure 5.3 depicts the bulk flow directions as stated in Table 5.2. The symbols indicate the corresponding volumes at which the directions were computed from the 150 h^{-1}Mpc volume sample. The error bars represent the 1σ uncertainties computed from the mock catalogues. The central asterisk represents the CMB dipole direction in galactic coordinates as given by COBE, $(l,b) = (276°, 28°) \pm 3°$ and $|V| = 627 \pm 22$ km s^{-1} (Kogut et al. 1993). The contours indicate equidistant regions in steps of 10° from the CMB direction. All computed directions are in very good agreement with respect to each other, indicating that the flow has converged to the CMB frame. This agreement can be better noticed in the lower plot of Fig. 5.3. This plot shows the convergence direction

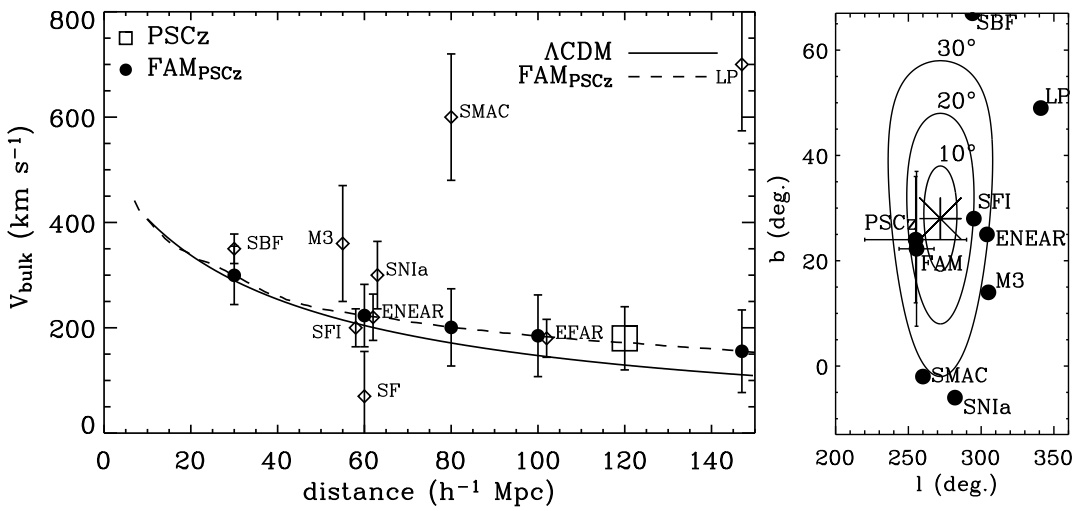

Figure 5.4 — Different bulk flow measurements. The left-hand plot shows the amplitude of the measured bulk flows together with their respective errors. We have over-plotted our FAM estimates at different radii and the PSC*z* estimates from B99. The solid line represents the expected rms bulk flow velocity for a ΛCDM universe, while the dashed line the cumulative FAM_{PSCz} bulk flow. The corresponding directions are indicated at the right-hand plot. The central asterisk indicates the CMB dipole direction.

(misalignment) of the bulk flow with respect to the CMB direction as a function of distance for the 150 h^{-1}Mpc volume FAM model. As can be noticed, there is a clear convergence in the bulk flow

Survey	Sample Volume (h^{-1}Mpc)	Method	V_{bulk} (km s^{-1})	l (°)	b (°)
SBF	30	SBF	350	294	67
FAM_{PSCz}	30	LAP	300	250	19
Mark III	60	TF+FP	370	305	14
SFI	60	TF	200	295	28
SF	60	TF	70	269	27
SNIa	60	SNIa	320	282	-8
ENEAR	60	FP	220	304	25
FAM_{PSCz}	60	LAP	220	247	17
EFAR	100	FP	180 (≈ 0)		
PSC*z*	120	LT	180	255	24
FAM_{PSCz}	120	LAP	172	252	20
SMAC	60-140	FP	630	260	-1
LP	150	BCG	700	341	49
FAM_{PSCz}	150	LAP	150	255	21

Table 5.3 — Different bulk flow estimates. Column 1 gives the survey name. Col. 2 the depth of the sample. Col. 3 specifies the method used to computed the velocity field : SBF-Surface Brightness Fluctuations method; LT-Linear Theory; LAP-Least Action Principle; TF-Tully-Fisher measurements; FP-Fundamental plane; BCG-Brightest Cluster Galaxy method. Bulk flow amplitudes and sky directions are shown in the Cols. 4, 5 & 6 respectively.

direction beyond distances larger than 60 h^{-1}Mpc.

The direction, amplitude and convergence behavior of our bulk flow estimates are consistent with those of B99. This indeed was expected from the fact that our velocity model is based on the real spatial Cartesian reconstruction procedure performed to erase redshift distortions.

5.4.2 FAM$_{PSCz}$ bulk flow *vs* observed bulk flows

We have compared our FAM$_{PSCz}$ bulk flow estimates with others based on different survey catalogues and techniques. We present results based on the 150 h^{-1}Mpc volume sample because this one seems to enclose most of the large scale fluctuations.

We have considered bulk flow estimates from the following surveys : Surface Brightness Fluctuations (SBF, Tonry et al. 2000); SFI (Haynes et al. 1999a,b); Shellflow (SF, Courteau et al. 2000); Supernova type Ia (SNIa Riess et al. 1997); ENEAR (da Costa et al. 2000a); Streaming Motions of Abell Clusters (SMAC, Hudson et al. 1999); Mark III (M3 Dekel et al. 1999); EFAR (Colless et al. 2001), Brightest Cluster Galaxies (LP, Lauer & Postman 1994), and the linear theoretical prediction inferred from the PSCz catalogue (Branchini et al. 1999). Although this list is not complete, our intention is to give a broad view of the different bulk flow measurements at different volumes using different samples and techniques. The different bulk flow measurements are presented in Table 5.3. We have indicated for each survey the sample's depth limit and the method used to compute the velocity field. The methods depend on the kind of sampled objects : Tully-Fisher (TF) for spiral dominated samples; Fundamental Plane (FP) for elliptical dominated surveys; Brightest Cluster Galaxy method (BCG); Surface Brightness Fluctuations (SBF) for early-type galaxies; Linear Theory (LT) and Least Action Principle (LAP) for the models derived from the PSCz catalogue. According to their surveyed volumes, there are 3 main groups of catalogues : nearby samples (30 h^{-1}Mpc), middle scales (60 h^{-1}Mpc) and large scales ($\geq$ 100 h^{-1}Mpc). We have included 5 FAM-PSCz estimates at different radii for comparison purposes.

Figure 5.4 depicts in a more clear way the different amplitudes and directions from the different surveys. In the left-hand plot, the continuous line represents the expected rms bulk velocity in a ΛCDM universe. Almost all bulk flow magnitudes are consistent with the predicted model, except for the well known cases of the SMAC and LP estimates (for a review about their implications see Dekel 1999; Zaroubi 2002). The estimates at 60 h^{-1}Mpc have been slightly shifted for sake of clarity. These quantities are consistent, within their dispersion errors, with each other and the bulk prediction. This is also the case for their directions displayed at the right-hand plot, which are within $\approx 25^\circ$ of the CMB dipole direction (located at the center of the plot). At larger volume samples both direction and magnitude agree with each other. The FAM-PSCz estimates are in good agreement with the different samples at different radii, both in amplitude and direction.

5.4.3 Velocity shear

The velocity shear is given by (Chapter 2 & 3):

$$s_{ij} = \frac{1}{2}\left\{\frac{\partial \mathrm{v}_i}{\partial x_j} + \frac{\partial \mathrm{v}_j}{\partial x_i}\right\} - \frac{1}{3}(\nabla \cdot \mathbf{v})\,\delta_{ij}\,, \tag{5.3}$$

where $i, j = 1, 2, 3$ and δ_{ij} is the Kronecker's delta. With this definition, we are considering a traceless shear tensor. Therefore, when diagonalizing its matrix representation only two eigenvalues are linearly independent.

In order to compute the velocity shear components from the different PSCz catalogues, we have followed the prescription given in Kaiser (1991). We have taken care of re-arranging the eigenvectors in descending order according to the magnitude of their respective eigenvalues. The most positive eigenvalue indicates the largest stretching direction, and it is known as the *dilational* component. The central eigenvalue could be positive or negative, and determines the nature of the shear pattern, i.e. if it is positive indicates an extra stretching component, while if it is negative indicates a compressional

mode. The direction of this eigenmode is by construction perpendicular to the first eigenvalue. The smallest eigenvalue (most negative) indicates the direction of the compressing mode, and it is known as the *compressional* component.

In Sec. 5.4.1, we showed that tripled-valued regions do not have a considerable effect on the bulk flow estimates. Table 5.4 shows the 3 shear components ordered by their amplitudes (dilational, central and compressional) with their respective galactic directions (l, b). Calculations were performed by taking into account only the matter distribution enclosed in 80 h^{-1}Mpc. We considered this limit because it is the radius at which the shear amplitude convergences in the mock catalogues. The amplitude of the 3 eigenvalues for the two reconstructions are very similar for all four volumes, with differences less than 5% for each component. However, directions are more severely affected, except in the case of the dilational component where the angular misalignment is less than 4°. The middle and compressional components experience larger deviations ($\leq 10°$). However, in the case of the 150 h^{-1}Mpc volume, the difference is $\sim 18°$ for both components. Such a difference could be due to big mass concentrations like the Shapley concentration that distort the field as shown by B99. We can therefore conclude that, the effect of tripled-valued regions is not considerable in the case of the velocity shear.

Figure 5.5 depicts several aspects of the velocity shear eigenvalues. The upper left-hand plot shows the cumulative shear amplitude distributions for the FAM models estimated using different sample volumes. From this plot we can distinguish three different regions separated by two points (indicated by arrows) where the slope changes considerably. The shear amplitude values at those points are 20 km s^{-1} Mpc^{-1} at a depth of 20 h^{-1}Mpc and 4 km s^{-1} Mpc^{-1} at 80 km s^{-1} Mpc^{-1} respectively. The first region is an "inner" sector enclosing the matter distribution within the first 20 h^{-1}Mpc (first arrow) from the Local Group, and where most of the shear contributions originate. This region is characterized by a very fast drop in the cumulative distribution up to the edge of this volume. The second region is located between the 2 different slope points (20, 80 h^{-1}Mpc). The cumulative distribution presents a more gentle descent in this region, implying that the corresponding enclosed structures still play an important role. Considering the fact that the shear contributions decrease as r^3, the responsible structures should be very massive in order to affect considerably the velocity shear (e.g. Great Attractor, Perseus-Pisces supercluster, see Fig. 5.2). The third region (> 80 h^{-1}Mpc) is a "convergence" region. All samples larger than 60 h^{-1}Mpc (80, 100, 120, 150 h^{-1}Mpc) show a clear convergence beyond this radius. In fact, we could say that the PSCz-FAM$_{60}$ sample indicates that no substantial contributions are coming beyond this radius.

On the other hand, the 30 h^{-1}Mpc sample clearly and substantially underestimates the shear from the external mass distribution. There is ≈ 10 km s^{-1} Mpc^{-1} shear difference between this sample and the largest samples for the whole distance range. The shear effects become more pronounced at the edge of the sample, where the difference has increased up to ≈ 14 km s^{-1} Mpc^{-1}, due to the more localized nature of shear.

The comparison between the PSCz-FAM velocity shear and the predicted one for a ΛCDM universe is presented at the upper right-hand plot of Fig. 5.5. The gray shadow around the cumulative FAM distribution represents the $\pm 1\sigma$ dispersion error given from the analysis of the mock catalogues. Apart from the bump registered at ≈ 40 h^{-1}Mpc, both curves describe the same behavior for the whole distance ranges. Although this bump is only significant at the 1σ level, it is interesting that it coincides with the GA location.

The lower plot at Fig. 5.5 shows the cumulative distributions for the 3 shear eigenvalues: dilational, central and compressional from the PSCz_{150} sample. The shear component distributions show that matter concentrations beyond 80 h^{-1}Mpc do not distort the velocity ellipsoidal.

The second eigenvalue has a magnitude around zero for the whole range of distances, with the exception of the so-called "inner" region, where it is positive and indicates a stretching mode along the direction given by its corresponding eigenvector.

Sample Volume	Sample Type	Dilational $\lvert s_1 \rvert$ (km s^{-1} Mpc^{-1})	l (°)	b (°)	Central $\lvert s_2 \rvert$ (km s^{-1} Mpc^{-1})	l (°)	b (°)	Compressional $\lvert s_3 \rvert$ (km s^{-1} Mpc^{-1})	l (°)	b (°)
80	tripcoll	2.61	318	28	-0.33	199	43	-2.29	69	34
	untripcoll	2.60	317	27	-0.35	198	43	-2.25	67	35
100	tripcoll	2.95	325	35	-0.39	191	45	-2.66	78	25
	untripcoll	2.97	324	33	-0.38	197	42	-2.59	76	30
120	tripcoll	3.74	328	34	-1.08	182	51	-2.66	70	17
	untripcoll	3.58	327	32	-1.09	187	51	-2.49	70	20
150	tripcoll	3.75	327	38	-0.76	172	49	-2.98	67	12
	untripcoll	3.62	325	33	-0.93	197	44	-2.69	76	29

Table 5.4 — Shear eigenvalues and their corresponding directions in galactic coordinates (eigenvectors) for different volume samples for the two PSCz reconstructions. We have included all objects within a sphere of 80 h^{-1}Mpc radius from the Local Group. Col. 1 indicates the sample volume. Col. 2 The reconstruction method used, 'tripcoll' stands for collapsed objects, while 'untripcoll' for the reconstruction were it was not taken into account. Col. 3, 4 & 5 amplitude and direction for the dilation component. Col. 6, 7 & 8 amplitude and direction for the second component (central). Col. 9, 10 & 11 amplitude and direction for the compressional component.

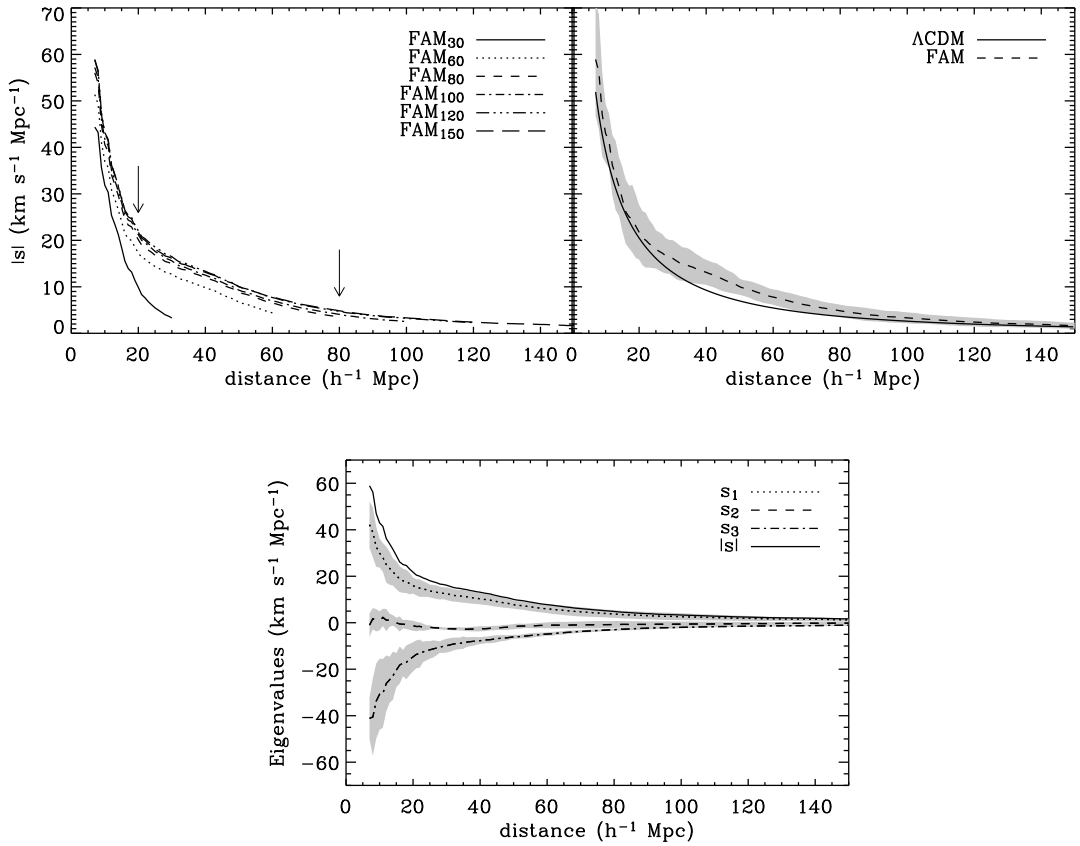

Figure 5.5 — Velocity shear eigenvalues. The upper left-hand plot shows the cumulative distributions of the amplitude of the eigenvalues for the different volume samples. The upper right-hand panel compares the amplitude of the eigenvalues with respect to the expected shear amplitude prediction for a ΛCDM universe. The lower plot depicts the 3 eigenvalue components for the FAM_{150} sample. The gray shadows represent the 1σ dispersion error.

The corresponding directions of the eigenvalues (eigenvectors) are displayed in Figure 5.6. From the cumulative distribution of the largest PSC*z*-FAM reconstruction (FAM_{150}), we have plotted the directions of 15 shells separated every 10 h^{-1}Mpc. The gray symbols indicate their corresponding anti-apex directions. The big black filled circle indicates the CMB dipole direction. The filled inverted triangles represent the position of the major clusters around the Local Group : V-Virgo; C-Coma; UM-Ursa Major; H-Hydra, C-Centaurus and H-C Hydra-Centaurus supercluster; Per-Perseus, Pis-Pisces supercluster; Pav-Pavo, Tel-Telescopium, Ind-Indus supercluster; Scul-Sculptor cluster; Boot-Bootes supercluster; Her-Hercules supercluster; Sha-Shapley concentration; and Hor-Horologium supercluster. The empty triangles correspond to the first eigenmode direction, and they point toward the direction where the velocity ellipsoid suffers the largest stretching. According to linear theory, the bulk flow direction and the first shear eigenvector should point toward the same region. Nevertheless, the dynamics of the nearby universe (< 30 h^{-1}Mpc) is far from being linear. Furthermore, the presence of several massive structures (e.g., PP, GA) strongly gravitationally perturb the local nearby matter concentrations (see Fig. 5.2). The bulk flow points toward the direction where there are several large matter concentrations like the Hydra-Centaurus supercluster and the Shapley concentration. From our analysis, the dilational component points roughly toward the same direction. To be precise, directly to the H-C region. The corresponding dilational anti-apex points toward the Perseus-Pisces supercluster region. This apparent alignment between the shear eigenvector and the directions of the H-C and PP

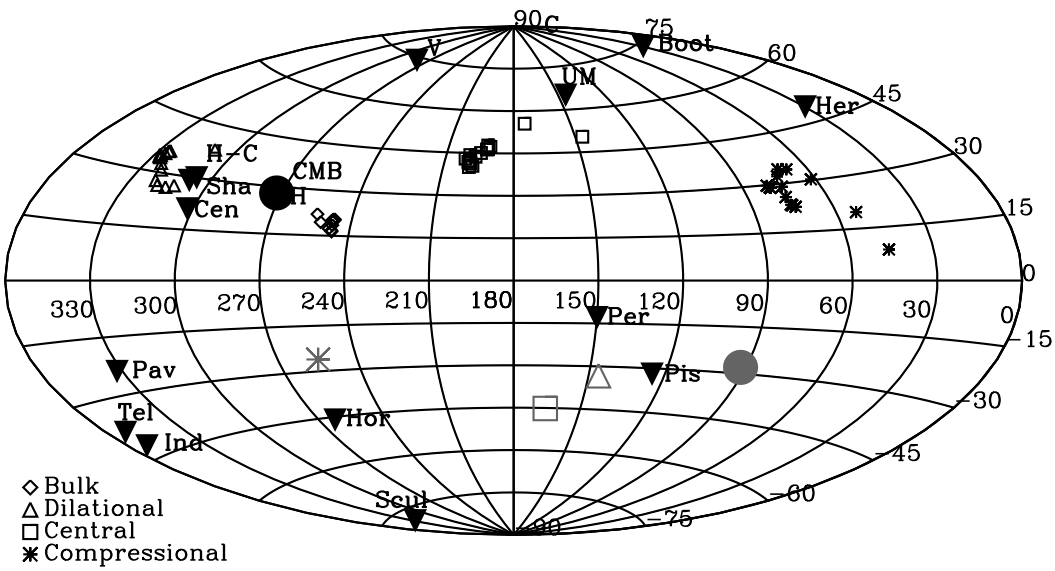

Figure 5.6 — Sky directions of the FAM velocity bulk and the 3 velocity shear eigenvectors. The gray symbols represent their corresponding anti-apex directions. The black circle depicts the CMB dipole direction, while the inverted black triangles the positions of the most prominent clusters and superclusters.

superclusters is more than a simple coincidence. The Local Group resides in a region that is being stretched along the direction of these two giants, H-C (GA region) and PP superclusters (e.g. Fig. 5.2, also B99).

The source of the bulk flow motion is also the source (partially) of the stretching shear eigenmode. From the shear eigenvalues cumulative distribution functions we deducted that most of the shear contributions come from matter distributions within 60 h^{-1}Mpc (i.e. H-C, PP).

The source of the second eigenmode (central) is less well determined. There are no nearby structures (clusters or voids) that could be responsible for this mode. However, any two matter concentrations that stretch along the line connecting them, will compress in a perpendicular direction. Therefore, the direction of this eigenmode is most probably also due to the H-C, PP configuration. However, the two measurements at 10 and 20 h^{-1}Mpc of the cumulative distribution point toward the Ursa-Major cluster. The corresponding eigenvalues for these two eigenvectors are positive, indicating a stretching mode along this direction. This is the very local influence of the Local Supercluster (Virgo + Ursa-Major) over the Local Group (e.g. Tonry et al. 2000).

5.4.4 FAM$_{PSCz}$ shear *vs* other estimates

Figure 5.7 shows the distribution of other different estimates of the velocity shear eigenvectors. The black-filled symbols correspond to our estimates from the FAM modeling (We) as indicated in Table 5.4 for the 150 h^{-1}Mpc volume sample, computed at a radius of 80 h^{-1}Mpc. The gray-filled symbols represent the estimates from the tidal field as inferred from the Mark III catalogue (Hoffman et al. 2001), using two different techniques: POTENT (POT) and the Wiener Filter (WF) to estimate the residual tidal field. The empty symbols represent the estimates from Lilje, Yahil, & Jones (LYJ, 1986) who used the galaxy catalogue of Aaronson et al. (1982a) to infer the direction of the shear in a volume equivalent to the Local Supercluster region, i.e. 30 h^{-1}Mpc. Our FAM estimates are, within the 1σ dispersion, in concordance with those from LYJ, and they roughly agree with the first eigenvector from Hoffman et al. (2001). However, our estimates for the other two eigenmodes do not agree with those from Hoffman et al. There is a misalignment of more than 100° for these two eigenvectors. Although the WF and POT eigenmode estimates are for the tidal field, these should coincide with our estimates

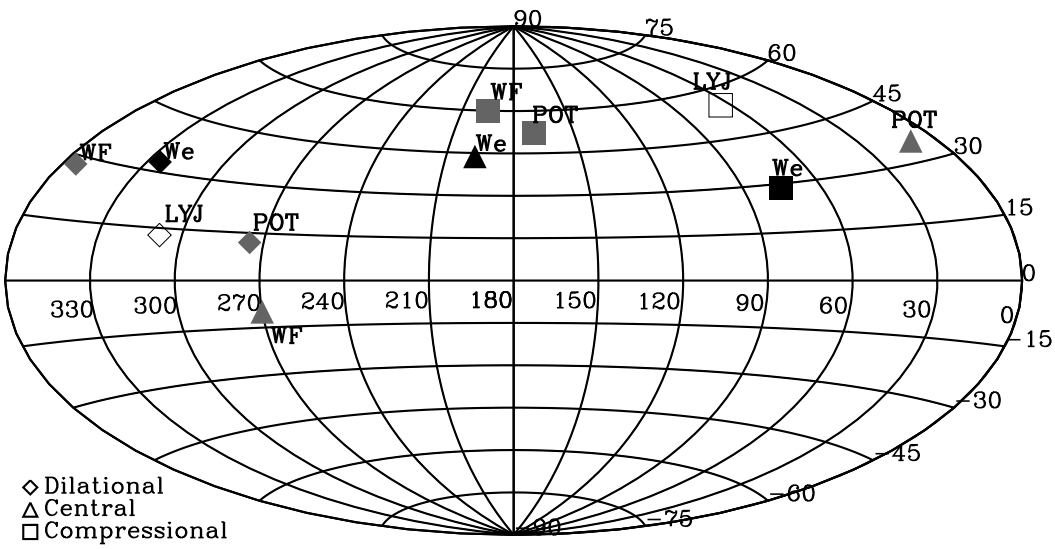

Figure 5.7 — Different shear eigenvector estimates. The black-filled symbols represent our FAM estimates (We). The gray-filled symbols represent the tidal shear eigenvectors from Hoffman et al. (2001), WF refers to those from the Wiener Filter analysis of the Mark III catalogue, while the POT labels refers to those performed with POTENT to the same catalogue. The empty symbols indicate the estimates from Lilje, Yahil, & Jones (LYJ, 1986).

since we do not find contributions to the velocity shear beyond 80 h^{-1}Mpc. Furthermore, the large discrepancy measured with respect to our estimates could be due to the fact that beyond 60 h^{-1}Mpc the amplitude of the second eigenvalue is of the order of zero. The tidal shear is then dominated by the largest eigenmode, making difficult to estimate the other independent direction. This can be noticed by the large dispersion in the mock catalogues of Figure 6 from Hoffman et al. (2001).

5.5 Conclusions

We have modeled the IRAS-PSCz catalogue velocity field by means of the FAM technique from the galaxy distribution in real space. In order to do so, we have used the reconstructed PSCz catalogues from B99. In this sense, the use of the FAM technique was implemented as a refinement in the estimation of the peculiar velocity field over the linear reconstructed velocity field of B99. However, as we have shown, results do not yield a significant improvement to the linear theory analysis.

We have characterized the large scale velocity field by means of its most dominant moments: the bulk flow and velocity shear components.

Our results showed that tripled-valued regions do not have a considerable effect on the bulk flow estimates. We found a difference of less than 10% in amplitude and direction between the sample considering tripled-valued regions and the one without considering them. This effect is more substantial for the velocity shear components. Although the magnitudes of the 3 components remain the same, differences arise for their respective sky directions. Such differences are larger for the direction of the middle and compressional modes (second and third eigenvectors) with an angular misalignment of 18° (largest case) at distances of 150 h^{-1}Mpc. However, directions at smaller scales show a better agreement between the two different samples.

The bulk flow estimates as a function of depth are in good agreement with the different measurements from other catalogues performed with different techniques. Since we have used as input to our FAM the linear reconstruction method to map galaxy positions from redshift-space to real-space, our

results are very similar to those obtained by B99.

From the analysis of the cumulative distribution of the shear amplitude, we found that this curve identifies two radii at which the slope changes considerably. They correspond to regions providing different contributions. The first point is located at $\approx 20\ h^{-1}$Mpc, and gives the range of the largest contributions to the velocity shear. At this region, the cumulative shear experiences a very rapid fall off, meaning that the very nearby structures (Local Supercluster) are markedly responsible for these contributions. The proximity of such structures provoke that their influence would be more pronounced than those registered at larger scales. The second transition occurs at $\approx 60\ h^{-1}$Mpc, and is characterized by a more gentle slope. This region enclosed between $20-60\ h^{-1}$Mpc still contributes considerable to the velocity shear. Such significant contributions come from structures like the Hydra-Centaurus and Perseus-Pisces superclusters. Beyond $60\ h^{-1}$Mpc matter distributions hardly affect the velocity shear. This is indicated by the very good agreement between the models constructed at radii $80, 100, 120, 150\ h^{-1}$Mpc, showing no contributions at all to the velocity shear amplitude. On the basis of this analysis, we roughly estimate that the radius at which the shear amplitude converges (vanishes) is $80\ h^{-1}$Mpc.

The direction of the largest eigenmode (stretching mode) is roughly aligned with the direction of the bulk flow. This indicates that at least some of the sources which produce the gravity bulk are also responsible for the shear contribution, i.e. the Hydra-Centaurus supercluster. Furthermore, the anti-apex direction of this eigenvector point toward the Perseus-Pisces supercluster region, indicating that this structure also plays a major role in molding of the velocity field of the nearby universe, in contradiction with the results of Tonry et al. (2000).

The Local Supercluster also exerts a stretching mode. The amplitude of the second eigenmode is positive for the first $20\ h^{-1}$Mpc from the Local Group. These results are confirmed by the fact that the corresponding second eigenvector within this region points toward the Ursa-Major cluster (the Local Supercluster).

Our results are in agreement with those from LYJ, and only in the case of the largest eigenvector, with those from (Hoffman et al. 2001). We did not find any alignment for the directions of the other two eigenmodes between our estimates and those from Hoffman et al. Such misalignment could be due to the fact that beyond $40\ h^{-1}$Mpc, the amplitude of the second eigenvalue is of the order of zero, making difficult to estimate its direction. Nevertheless, we do agree with the fact that there is more than one source responsible for the shear pattern in our cosmic vicinity.

Some issues should be addressed in order to improve bulk flow and velocity shear estimates. The first one concerns to the quality of the data. Although the IRAS-PSC*z* catalogue represents a good estimate of the cosmic matter distribution up to scales contained within 15 000 km s^{-1}, it would be desirable to have larger and better sampled data bases covering the entire sky, and as uniformly observed as possible. Such survey should have full-sky, uniform sampling in angle and redshift, and a very accurate distance indicator with small intrinsic dispersion (such as the 2MASS survey, Cutri et al. 2003). The second point refers to the inclusion and better treatment of non-linear regions. The extension of FAM to redshift space (Branchini et al. 2002) could be a great advantage in order to estimate the bulk flow and shear in a more consistent way. In the future, we plan to apply directly the FAM implementation in redshift space to the PSC*z* catalogue and other samples.

Acknowledgments

E.R.D. benefited from enthusiastic discussions about tidal fields with Bernard Jones.

6

DTFE & Cosmic Flows: Tessellation Interpolation and Reconstruction of Cosmic Velocity Fields

E. Romano-Díaz, W. E. Schaap & R. van de Weygaert.

DELAUNAY tessellations have proven to be a powerful tool for the interpolation of a discrete number of field values to a fully volume-covering and continuous field estimate (Bernardeau & van de Weygaert 1996; Schaap & van de Weygaert 2000). In this chapter, we have applied the Delaunay Tessellation Field Estimator method [DTFE] to a set of simulations of the cosmic structure formation to obtain continuous, space-covering and volume-weighted peculiar velocity field from a discrete peculiar velocity field sample. The procedure is based upon the determination of the values of the (constant) velocity gradients in each Delaunay tetrahedron from the four known velocities at its vertices. Velocity values at any given point are then computed by a linear interpolation procedure. This method is an improvement over conventional interpolation methods in the sense that one can get fully-covering velocity fields without the use of artificial smoothing procedures, and hence without loosing information at small scales. The method is fully self-adaptive and suppresses shot-noise effects. The velocity-gradient matrix allows to compute velocity-related quantities such as the velocity divergence, shear and vorticity. The estimated quantities are volume-weighted and volume-covering, allowing a direct comparison with theoretical predictions. We have found that the density-velocity divergence relation estimated with our method reproduces the analytical perturbation results at least up to second order. Based on an analysis of the kinematics of voids, we have been able of compute a lower limit for the matter density parameter Ω_m, which is in good agreement with the imposed value on the simulation. Maps of the velocity-related quantities and density fields are shown to elucidate the dynamical state of the cosmic volume. We also analyze errors introduced by the interpolation procedure and method and suggest solutions for a general improvement of the method.

6.1 Introduction

The peculiar velocity flow on cosmological scales provides important information on the formation and evolution of structures in the Universe, it supplies direct information on the dynamics of the universe on scales of more than few Megaparsecs.

In general, the peculiar velocity field is only known at a discrete set of points. In the case of $N-$body simulations this set corresponds to particle positions. In the case of observational data to galaxy positions. Within the Gravitational Instability scenario of structure formation the present large scale structure is the result of tiny fluctuations in the primordial density field that were amplified via gravity (Peebles 1980). This primeval density field is assumed to be Gaussian. Due to gravitational interactions the actual density field is not longer Gaussian. Once regions surpassed a given density threshold they collapse and virialize, attaining high-density excesses. Low-density regions expand and empty asymptotically reaching a density deficit $\delta \approx -1$. Therefore, the actual matter distribution is not distributed uniformly, but it is very skewed (at least on scales less than 200 h^{-1}Mpc). As a consequence the $N-$body or observed velocity field, which is traced by galaxies residing in the high-density regions, is sampled very non-uniformly. Often, for a balanced view and proper statistical evaluation of a field a uniformly sample dataset is necessary. In principle, an alternative to the use of the Lagrangian character of $N-$body codes to simulate the evolution of cosmic density fields is the use of an Eulerian code, often used for solving fluid systems. A notable example for a gravitationally evolving cosmology system whose evolution is followed by such a code, can be found in Peebles (1987). A different approach within the context of Lagrangian systems is to interpolate the discrete velocities into a regular grid via any known interpolation method. With this approach one sometimes needs to make use of large grid sizes in order to obtain a fully volume-covering velocity field and to overcome the problems of sparsely sampled data. This implies the lost of resolution at the high-density regions. In some cases a smoothing procedure is still needed in order to recover a volume-covering velocity field.

Because of the limited nature of the discrete samples it is often of crucial importance to use as much of the relevant information which is present in the data as possible. Bernardeau & van de Weygaert (1996, BW96, hereafter) have shown than in the case of the velocity field conventional reconstructions methods are unable of recovering this field accurately over its whole range of values at both low and large values. They introduced tessellation based methods (the Voronoi and Delaunay tessellation methods) to fully recover volume-covering and volume-weighted velocity fields. While they explicitly showed that the zeroth-order Voronoi estimator is the asymptotic limit for volume-weighted field reconstructions from discretely sampled field values, they showed the better performance of the first-order Delaunay estimator in reproducing analytical predictions. In particular they focussed on testing the validity of the second order perturbative approximation of the velocity divergence-density relation (Bernardeau 1992).

Based on the work by BW96, Schaap & van de Weygaert (2000, SW00, hereafter) and Schaap (2005, S05, hereafter) developed a reconstruction scheme based on the geometrical concept of the Delaunay tessellations (Delaunay 1934), the *Delaunay Tessellation Field Estimator* [DTFE]. The method enables a natural, unbias and volume-covering reconstruction of the density or intensity field from the sampling point set. The method is self-adaptive and does not make use of any artificial smoothing procedure. Delaunay-based reconstruction scheme would also be a natural choice for other kind of fields, and were in fact first designed to process discretely sample velocity fields (BW96). Schaap (2005) also showed the main differences and advantages of DTFE with respect to grid-based schemes and SPH-like (adaptive) methods (see also Pelupessy et al. 2003).

S05 discussed to great extent why conventional density field reconstruction methods have important shortcomings for studies of the large scale matter distribution. These methods are unable to accurately describe a point distribution with a large dynamic range in terms of spatial densities and scales. Furthermore, they also fail in describing highly anisotropic structures, which are a common element of the large scale matter distribution. These effects are a consequence of the use of smoothing kernels (filtering functions) from such interpolation methods. Reconstruction methods of dynamical fields such as peculiar velocity fields are closely related to methods for reconstructing density or intensity

fields. These methods also make use of smoothing kernels whose parameters have to be subjectively pre-defined by the user. Therefore, similar problems, as occur in the density field reconstruction, are expected to appear.

In the present chapter we elaborate on the defining work of BW96 and expand the DTFE method toward a reconstruction/tessellation interpolation scheme of discretely sampled cosmic velocity fields from cosmological $N-$body simulations. The method is based upon the computation of the velocity field gradient matrix. Thus, it allows studies over the velocity divergence, shear and vorticity of the velocity field. These velocity related quantities will automatically acquire the characteristics given by the DTFE approach. We will assess the resulting spatial and statistical characteristics of the reconstructed velocity fields, including the various aspects of velocity gradient field quantities. Subsequently, we combine these DTFE velocity fields with the DTFE density field reconstruction method to develop a scheme for inferring information on the dynamical evolution of the cosmic structure formation process. In this, we explicitly concentrate/illustrate on the density-velocity divergence relation. Suggestions for further expansion of the method will be also discussed.

Because cosmic density and peculiar velocity fields are measured at the galaxy positions, such fields are then mass-weighted. Most analytical relations concern volume-weighted quantities. In addition, the *a priori* unknown bias between dark matter and baryonic matter difficult even more the comparison between measured estimates and theoretical values. It is therefore desirable to use continuous volume-weighted velocity fields, with uniform full-coverage sampling. This characteristic is mainly needed at those regions where the density contrast is less than zero, i.e. voids. These regions, severely affected by Poisson noise, enclose relevant dynamical information, e.g. Dekel & Rees (1994) used voids to constraint a lower limit of Ω_m, the cosmological density parameter.

Within linear theory, the velocity ($\mathbf{v}$) and mass-density fluctuation (δ) fields are related via,

$$\nabla \cdot \mathbf{v}(\mathbf{x}) = -H_0 \; f(\Omega_m, \Lambda) \; \delta(\mathbf{x}), \tag{6.1}$$

where H_0 is the Hubble parameter, and the function f can be approximated by $f(\Omega_m, \Lambda) \approx \Omega_m^{0.6}$ (Peebles 1980). On the other hand, a strong correlation between the galaxy density (δ_g) and velocity divergence fields has been found in observational data analysis (e.g. Hudson et al. 1995; Sigad et al. 1998; Dekel et al. 1999). It is assumed that the galaxy density fluctuation field is related to the mass density one via a linear bias factor b, $\delta_{gal} = b \; \delta_{mat}$. However, in order to obtain such correlation a smoothing procedure with a large kernel size ($R_G = 1000 - 1200$ km s^{-1}) appeared to be necessary for obtaining the linearizing needed, and to reduce distance estimation errors and shot-noise. In the non-linear regime the relation between δ and $\mathbf{v}$ is less trivial. Nonetheless, Bernardeau et al. (1997) used the Voronoi and Delaunay methods of BW96 to show the validity of Perturbative Theory. The moments of the Probability Distribution Function of the local smoothed velocity divergence strongly depend on Ω_m in the quasi-linear regime. Even more, this dependence does not involve the possible bias between the galaxy density field and the underlying mass density field. In this way, by using these tessellation techniques it is possible to get bias-independent values of Ω_m based on reliable determinations of the velocity divergence probability distribution function.

The use of these type of tessellations has been widely exploited in other sciences like geophysics, computing imaging, material sciences, etc. (see Okabe et al. 2000, for a review). The DTFE algorithm as a linear multidimensional field interpolation scheme may be regarded as a first-order version of the natural neighbouring algorithm for spatial interpolation (see Okabe et al. 2000). The use of Delaunay tessellations for solving hydrodynamical equations and in general as self-adaptive grids for solving partial differential equations has been particularly impressive (see Braun & Sambridge 1994; Whitehurst 1995).

The chapter is structured as follows. We first discuss the differences between the mass-weighted and volume-weighted quantities. Then we review traditional velocity interpolation methods and analyze their performance at different resolutions. The DTFE method for the peculiar velocities is introduced in the following section. In section 5 we analyze the performance of the method at linear, quasi and non-linear regions and discuss sources of errors and possible solutions. In sections 6 and 7 we analyze the velocity divergence probability distribution function and its implications in calculating the

matter density parameter Ω_m. The density-velocity divergence relation and its time evolution is analyzed in section 8, and the reconstruction of the density field from the velocity divergence is presented in section 9. The shear and vorticity are investigated in Section 10, and finally the conclusions are presented in Section 11.

6.2 Reconstructing continuous fields from discrete fields

When one seeks to obtain reliable estimates of statistical parameters from a given observed or computer-simulated field (e.g. density, velocity or intensity fields), one faces the problem of dealing with discrete, non-uniform fields. This discreteness forms a major technical obstacle for a successful comparison with theoretical predictions. Analytical/theoretical predictions often concern quantities evaluated uniformly throughout a cosmic volume, while observed or simulated results are biased toward the measured particle (matter) distribution.

The usual strategy to deal with such discrete data sets is to smooth them with a filter to yield a continuous field. In the case of the peculiar velocity field several authors (e.g. Bertschinger et al. 1990; Juszkiewicz et al. 1995; Lokas et al. 1995; Branchini et al. 1999) filtered galaxy velocities with a Gaussian kernel of a fixed length for reducing problems of noisy data, sparsely sampled underdense regions and to obtain the velocity field on a regular grid. The POTENT method (Bertschinger & Dekel 1989; Dekel et al. 1990, 1999) applied to the Mark III catalog of peculiar velocities (Willick et al. 1997a) needs a Gaussian smoothing of $10-12\ h^{-1}$Mpc in order to overcome the previously mentioned problems. If one is interested in performing studies concerning only the large scale structure of the universe such methods provide good estimates. Nevertheless, when one is interested in studying both the large and small scale regimes at once, such methods are not very appropriate. The use of such kernels erases the small scale signal. At sparsely sampled regions field estimates get tunned to obtain unnatural values from better sampled high-density regions.

Often, without explicitly stating so, most smoothing procedures are implicitly mass-weighted. Formally, a mass-weighted field is defined as:

$$\mathbf{v}_{mass}(\mathbf{x}_0) \equiv \frac{\int \mathrm{d}\mathbf{x}\,\mathbf{v}(\mathbf{x})\rho(\mathbf{x})W_M(\mathbf{x},\mathbf{x_0})}{\int \mathrm{d}\mathbf{x}\rho(\mathbf{x})W_M(\mathbf{x},\mathbf{x_0})}\,, \tag{6.2}$$

where $W_M(\mathbf{x},\mathbf{x_0})$ is the used filter function . Effectively W_M determines the weight of a mass element. Usually the filter function is not dependent on the location $\mathbf{x_0}$, but on the distance $\mathbf{x}-\mathbf{x_0}$. The aim of this procedure is to interpolate the velocity field values at random sampling locations to those at a regular grid, weighing the contribution of each sampling point by the filter function value. When the density field has been sampled discretely its effective density field is given by

$$\rho(\mathbf{x}) = \sum_i \delta_D(\mathbf{x}-\mathbf{x_i})\,, \tag{6.3}$$

where $\delta_D(\mathbf{x}-\mathbf{x_i})$ is the Dirac delta function. The resulting mass-weighted filtered field thus becomes

$$\mathbf{v}_{mass}(\mathbf{x}_0) = \frac{\sum_i w_i \mathbf{v}(\mathbf{x}_i)}{\sum_i w_i}\,, \tag{6.4}$$

where $w_i \equiv W_M(\mathbf{x}_i,\mathbf{x_0})$. it is not difficult to appreciate that straightforward and more conventional schemes usually implicitly involve mass-weighted results (BW96). These type of interpolation methods cannot properly reproduce the large dynamic range present in the cosmic matter distribution, erasing mainly small-scale features. The 1-point distribution function of velocity quantities is therefore

shifted to higher values. Because analytical results involving two fluctuation fields, $\rho(\mathbf{x})$ and $f(\mathbf{x})$, are more cumbersome to evaluate, most theoretical work relates to the simpler *volume – weighted* filtered quantities. The volume-weighted velocity field $\tilde{\mathbf{v}}$ is given by

$$\tilde{\mathbf{v}}(\mathbf{x_0}) \equiv \frac{\int \mathrm{d}\mathbf{x}\ \mathbf{v}(\mathbf{x})\mathbf{W_V}(\mathbf{x},\mathbf{x_0})}{\int \mathrm{d}\mathbf{x}\ W_V(\mathbf{x},\mathbf{x_0})}\,, \tag{6.5}$$

where $W_V(\mathbf{x},\mathbf{x_0})$ is the applied weight function. Hence, for a successful comparison of the analytical results with the observed ones, and for a full space determination of the desired quantities, it is of crucial importance to have a reliable estimator of volume-average quantities. The problem turns now to produce a realistic and very accurate interpolation from a sparsely sampled velocity field to the whole sampling volume (regular grid) without loosing information at any scale and without restricting themselves to estimates at a finite number of positions.

BW96 proposed the use of Voronoi and Delaunay tessellations as natural filters and interpolation volumes in multi-D space. They showed that their implementations were capable of probing accurately the velocity field statistics even at regions of low-density, and of utmost importance that these methods provide an optimal estimator for determining the statistics of volume-weighted quantities.

6.3 Conventional interpolation schemes

Several methods have been proposed with the purpose of reconstructing from a discrete set of points a volume-covering field. We can divide these methods into three main groups. The first group is that of the grid-based schemes, also known as Eulerian type, in which the desired field estimates (e.g. density, intensity, velocities, temperatures) are confined to a set of locations defined on a fixed and regular grid, which in principle is defined independently from the point distribution itself. In cosmology these grids are usually regular but various other options are applied depending on the system under consideration. Their main limitation is that their spatial resolution is fixed by the cell size. This limitation is quite severe in cosmology, since many relevant physical processes appear to happen over a range of scales, so that once a gridsize has been defined effective smoothing over the Eulerian cell size usually erases important information about the physical conditions at small scales.

The second group is formed by the Lagrangian scheme[1], in which the locations of the interpolation are confined to or defined by the point distribution itself. Of this type, the "SPH-type" schemes are the best known in astronomy. The latter refers to the abundantly used Smooth Particle Hydrodynamics technique (Lucy 1977; Gingold & Monaghan 1977) to follow the hydrodynamical evolution of astrophysical systems. The main difference between Lagrangian and Eulerian methods is the fact that the former is not restricted to a specific geometry because it does not make use of a mesh. Instead, it follows the trajectories of the displacing matter aggregating into the high-density regions and ideally with an unlimited spatial resolution. In practice, this is not possible and one has to make use of a "softening length". Although, this is usually much smaller than the cell size of an Eulerian scheme. Therefore the spatial resolution of the Lagrangian technique can be significantly higher. However, the main difficulty of this technique is that it relies on stochastic arguments which means that it yields only approximate solutions at a given spatial position.

A third class seeks to combine the virtues of Lagrangian and Eulerian methods. These were first introduced by Noh (1964) and referred as arbitrary Lagrangian-Eulerian [ALE] methods. This technique incorporates the high resolution of the Lagrangian scheme by letting a grid to move along with the system, combined with the Eulerian scheme for computing the physical state of the system within each of the resulting distorted grid cells. Although as yet reluctantly applied in cosmology, there are some noteworthy promising efforts (e.g. Gnedin 1995; Xu 1997; Pen 1998).

[1]Paradoxically, the "Lagrangian" formulation is in fact also due to Euler (1759), who employed this formalism in a letter to Lagrange. Lagrange (1762) used these ideas without crediting Euler.

For the purpose of merely providing a comparison, we restrict ourselves to a grid-scheme as a representative interpolation algorithm. All other Eulerian grid-based methods perform in a similar way. For a general revision of the performance of several grid and Lagrangian methods we refer the reader to Hockney & Eastwood (1988) and S05, and for comparisons of the methods and their use in $N-$body cosmological simulations to Kang et al. (1994) and Bertschinger (1998).

6.3.1 Eulerian grid-based interpolation scheme

The most common methods are the grid-based methods, in which one calculates the desired field quantity (e.g. density, velocities, temperature) at a set of locations defined on a regular grid. The value of each particle is spread over the grid in accordance with a particular weighting function W, leading to a relation of the form (Hockney & Eastwood 1988; Efstathiou et al. 1985)

$$\hat{f}\left(\frac{\mathbf{n}}{M}\right) = \frac{M^3}{N}\sum_{i=1}^{N} f_i W\left(\mathbf{x}_i - \frac{\mathbf{n}}{M}\right), \tag{6.6}$$

where M is the number of grid cells along one dimension, N is the total number of particles in the volume, $\mathbf{n} = (n_x, n_y, n_z)$ denotes the center of each grid cell, $\mathbf{x}_i$ is the position vector of the ith particle and f_i its corresponding value to be interpolated. The units are such that the volume of the cube is equal to unity. The quantity W defines the weighting scheme used to assign the value to the mesh points (smoothing kernel). The choice of W is set by the wish of the resulting interpolated field has the desired resolution and smoothness. A common choice for the grid size is such that on average each grid cell contains at least one particle. There is a large variety of possible schemes, their shape and scale defined by the weighting function. Here we will specifically employ the Triangular-Shaped Cloud [TSC] interpolation scheme, one of the most popular and most commonly used methods.

6.3.1.1 Triangular Shaped Cloud [TSC] method:

The TSC method is described in the Appendix 6.A. Here we will only concentrate in the main characteristics and results from this method. The TSC scheme produces smooth fields which could not be affected considerably by shot noise effects depending on the size of the grid cells at the cost of low spatial resolution. On the other hand, if one desires a high resolution reconstruction there is the risk that the particle density will on average be less than one particle per cell. When this happens, the resulting interpolated field will be dominated by shot-noise.

In order to assure a fully volume-covering field with a grid-based method the usual procedure is first interpolation, and second filtering with a specific kernel of particular scale to relate to analytical predictions. After having defined the interpolated field on the grid points, the resulting field may be applied to a host of processing steps to obtain the required information. The rigid non-adaptive grid characteristic leads to a loss of information. In the case of the TSC scheme implies loosing information in the interpolated field on scales smaller than the size of the TSC kernel or smoothing radius. The anisotropic and caustic features present in the particle's value distribution will therefore not be recovered if their scale is smaller than the grid-cell size.

The problems besetting this particular method are not exclusive to it, but for all grid-based interpolation schemes. These problems are undesirable characteristics for computing full spatial covering velocity fields. The need of having an interpolation scheme that can cope with modeling velocity flows properly at both low and high density regions is highly desirable in order to be able to establish more conclusive studies of the dynamics and the structure formation process in the universe.

Typical TSC reconstructions are presented in Figure 6.1. The left panel shows a discrete $N-$body velocity field at the particle distribution in a slice of 1 h^{-1}Mpc thickness. The slice presents several common structures of a typical large scale structure region of the universe, i.e., a void located at the top-right of the plot and another at the bottom-left, a cluster located almost at the centre, and a filamentary structure at the low-right part. The contiguous two panels depict TSC interpolations of

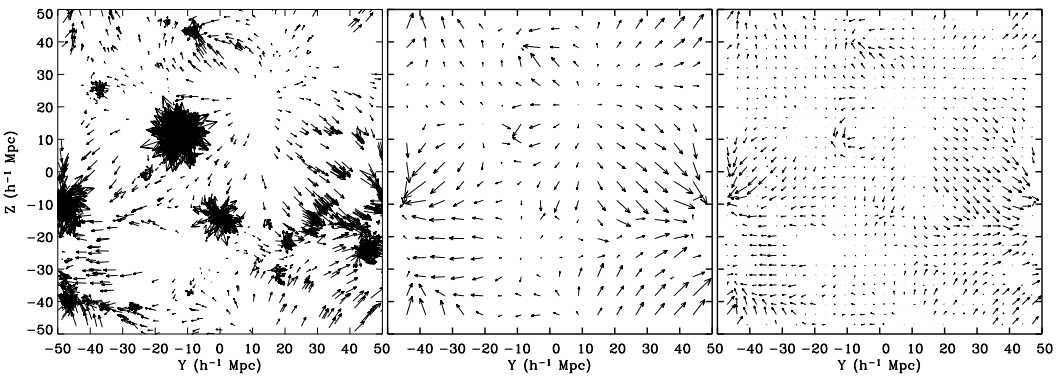

Figure 6.1 — Interpolated TSC Velocity field. The left panel shows the $N-$body velocities at the particle positions. The central panel refers to the TSC interpolated velocity field onto a 64^3 cubic grid. The right panel depicts the same TSC interpolated field but onto a grid of 128^3 grid cells.

the same discrete field at different spatial resolution. The central panel shows a low resolution interpolation with 64 cells per dimension, while the right panel a higher resolution map with 128 grid cells per dimension. For the sake of clarity in visualizing both plots we have lowered their plotted density resolution to a $\frac{1}{4}$ of their original map resolution.

Clear differences can be distinguished between the two maps. The low resolution interpolation assures full volume-coverage maps at the cost of smearing high density regions. Although the main trend of the flows can be distinguished, many of the features visible on the particle velocities are not recovered in the low-resolution interpolated map. Even though a trace of related shearing flow is visible at the bottom-right part of the map, it is more than marginal. We can extract four crucial observations from this map: (1) At high-density regions the interpolation smooths away interesting velocity information because basically all the velocities within the grid-size are averaged. (2) Highly crucial with respect to the ability to reproduce the 1-point velocity distribution function, at low-density regions the sampling is so poor and sparse that there is no strong and significant signal in these regions to be recovered. (3) The field estimates are beset by shot noise effects. Note that if one has less than two or one particles within the kernel estimates of local bulk flow and/or velocity dispersion would even not be possible anymore. (4) Cosmic velocity fields are much more quiet than density fields. Hence, intrinsically features are less prominent and therefore, for the required contrast a better sampling (high-resolution) is preferred at those regions where it is needed.

The high resolution map of Fig. 6.1 (right-hand panel) illustrates the second point. This map does recover structures that the low-resolution map did not. The high density regions can be better noticed in this map. The general flows resemble those from the discrete velocity map. Particularly noteworthy are the low-density regions, devoid of any objects to base velocity interpolations upon. Here the high-resolution TSC is unable to recover any significant information. A possible solution to circumvent this problem is to apply a smoothing procedure in order to extrapolate information to those regions where no information is available. However, the real cost of such operation would be to loose the high sensitivity of the map, degrading it to an equivalent low resolution field.

6.4 The DTFE method: Velocity field tessellation-interpolation

The DTFE interpolation method (SW00, see also S05) was introduced for rendering fully volume-covering and volume-weighted physical fields from a discrete set of sampled field values. The method is self-adaptive and does not make use of any artificial smoothing procedure. It followed the pioneering work by BW96 for using the Delaunay tessellation of the point set as a natural and self-adaptive interpolation frame for recovering the continuous velocity field sampled by the velocities at those

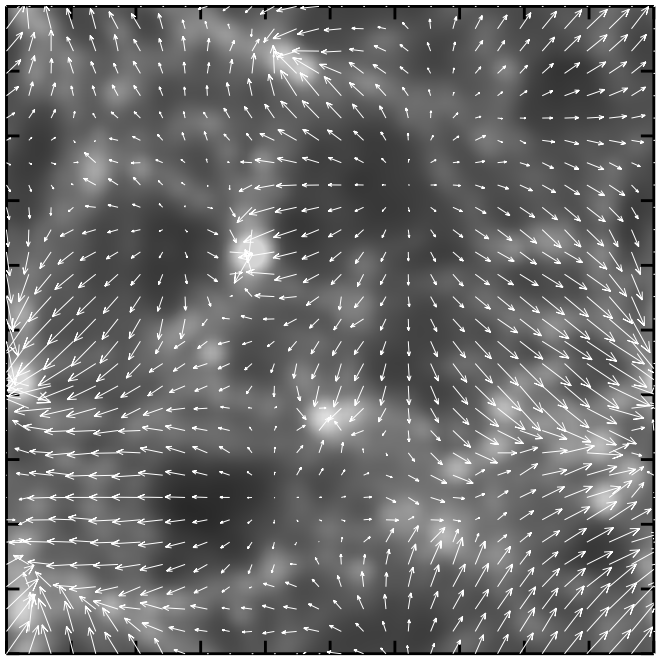

Figure 6.2 — DTFE reconstructed density and velocity fields (contour image and vector field respectively) from the same discrete velocity field presented in Fig. 6.1.

points. SW00 and S05 extended this to the recovery of the density or intensity field when one assumes it to be fairly sampled by the spatial point distribution. The later work by Schaap & van de Weygaert (2003) showed the first results on the successful reproduction by DTFE of the physical and spatial correlation between cosmic density and velocity fields in a large $N-$body simulation (see also S05).

The DTFE algorithm as a linear multidimensional field interpolation scheme is the linear first-order version of the natural neighbouring algorithm for spatial interpolation (see Sibson 1981; Okabe et al. 2000). Related procedures have been implemented in a variety of other applied sciences. Successful examples may be found in geophysics (see e.g. Braun & Sambridge 1994; Sambridge 1999) and engineering mechanics (Sukumar 1998).

Following the work of BW96 and Schaap & van de Weygaert (2003), we apply the DTFE method to reconstruct the full peculiar velocity field from a discrete set of velocities. The DTFE scheme is based upon the minimal triangulation properties of Delaunay tessellations. For a first impression of the method's potential and capabilities see Figure 6.2. It illustrates a typical outcome of the reconstructed DTFE density and velocity fields (contour image and vector field respectively) from the discretely velocity field presented in Fig. 6.1.

In order to obtain full space-covering volume weighted peculiar velocities with the DTFE scheme the following steps have to be carried out:

1. Construction of the Delaunay tessellation from the point distribution.

2. Calculation of the velocity gradient $\widehat{\nabla f}|_j$ in each Delaunay tetrahedron j by inversion on the basis of the field values and positions of the tetrahedron vertices.

3. Processing. This may involve various operations. The most important ones are *image reconstruction* and, subsequently, *filtering*. Image reconstruction consists of two steps:

   (a) For a set of image points (usually grid points) determine in which Delaunay tetrahedra they are located.

   (b) By (linear) interpolation compute field values at each of these points, on the basis of one vertex field value and computed gradient.

This formalism ensures that the reconstructed velocity field will have the same properties as a DTFE reconstructed density field (SW00, S05): it is volume-covering and continuous over the whole sampled space. An important characteristic of the DTFE velocity method is that while a DTFE density reconstruction requires a fair sampling of the underlying density field, a succesfull DTFE velocity field interpolation does not demand it to be uniformly sampled.

The sequence of steps mentioned above is illustrated in Figure 6.4. In the following we will describe each of these steps in some detail.

6.4.1 The Delaunay triangulation

The first step of the procedure involves the construction of the Delaunay tessellation of the point set, defined by the set of measurement locations, galaxy position in an observational sample or simulation particles. The Delaunay tessellation $\mathcal{D}(\mathcal{P})$ of a set point $\mathcal{P}$ is defined to be the tessellation consisting of all the tetrahedra (in 3-Dimensional space) defined by four nuclei which circumscribing sphere is *empty* in the sense that no nucleus of the generating set of nuclei should be inside the circumsphere (Delaunay 1934). In 2-Dimensional space this concerns Delaunay triangles of three nuclei. Figure 6.3 illustrates a 2-Dimensional Delaunay triangulation (right panel) for a set of discrete random points (left panel), where we have implemented continuous boundary conditions in the tessellation construction. For further information see van de Weygaert (1991, 1994); Stoyan et al. (1995) and Okabe et al. (2000).

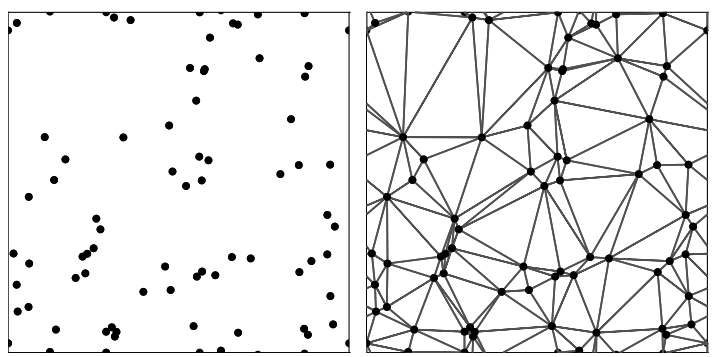

Figure 6.3 — 2-Dimensional Delaunay triangulation (right panel) of a discrete random distribution of 70 points (left panel).

The complete set of Delaunay tetrahedra forms a unique and volume covering framework of mutually disjoint cells as shown by Fig. 6.3 (see also S05). Note that the Delaunay tessellation is the dual of the Voronoi tessellation. This intimate relationship indicated by the fact that the circumcentre of each Delaunay tetrahedron is a vertex in the Voronoi tessellation. The Voronoi tessellation of a point set is the division of space into mutually disjunct polyhedra, each polyhedron consisting of the part of space closer to the defining point than any of the other points (Voronoi 1908). The minimal coverage characteristics of the Delaunay tessellation imply it to be optimal for defining a network of multidimensional interpolation intervals (BW96).

6.4.2 DTFE Reconstruction of the peculiar velocity field

Mathematically the *Delaunay Tessellation Field Estimator* [DTFE] interpolation procedure for peculiar velocities can be formulated as follows: Let the value of a field f be known at a set of N irregularly distributed discrete locations $\mathbf{x}_i$. Let the corresponding Delaunay tessellation consist of N_T Delaunay hypertriangles. The field value $f(\mathbf{x})$ at location $\mathbf{x}$ may then be found by first identifying the Delaunay hypertriangle j inside which $\mathbf{x}$ lies. Let this tetrahedron consist of the $(D+1)$ vertices $\mathbf{x_0}, \mathbf{x_1}, \ldots, \mathbf{x_D}$, in which D is the dimension of the space. Then the value of the function f at location $\mathbf{x}$ is defined as follows:

$$\hat{f}(\mathbf{x}) = f(\mathbf{x_0}) + \widehat{\nabla f}|_j \cdot (\mathbf{x} - \mathbf{x_0}), \tag{6.7}$$

in which $\widehat{\nabla f}$ is the estimated constant field gradient within the tetrahedron. Given the $(D+1)$ field values, $f(\mathbf{x_0}), f(\mathbf{x_1}), \ldots, f(\mathbf{x_D})$, the value of the D components of $\widehat{\nabla f}$ can be computed straightforwardly by evaluating Eqn. 6.7 for each of the D points $\mathbf{x_1}, \ldots, \mathbf{x_D}$

$$f(\mathbf{x}_i) = f(\mathbf{x_0}) + \widehat{\nabla f}|_j \cdot (\mathbf{x_i} - \mathbf{x_0}), \qquad i = 1, \ldots, D. \tag{6.8}$$

In the interior of each tetrahedra each of the velocity gradients $\partial \mathrm{v}_i / \partial x_i$ has one particular constant value, which is determined by the value of the function f at the locations x_i of its four vertices (three in 2D) (BW96).

Therefore the problem reduces to calculate the nine components of the velocity gradient $\partial \mathrm{v}_i / \partial x_i$ in each tetrahedron. They are determined from the location of each of the four vectors, $\mathbf{x_0}, \mathbf{x_1}, \mathbf{x_2}, \mathbf{x_3}$, and the value of the velocity field at each of these locations, $\mathbf{v_0}, \mathbf{v_1}, \mathbf{v_2}, \mathbf{v_3}$. Defining the intervals $\triangle x_n, \triangle y_n, \triangle z_n$ and velocity differences $\triangle \mathrm{v}_{xn}, \triangle \mathrm{v}_{yn}, \triangle \mathrm{v}_{zn}$, for $n = 1, 2, 3$ as:

$$\begin{aligned} \triangle x_n &\equiv x_n - x_0\,, & \triangle \mathrm{v}_{xn} &\equiv \mathrm{v}_{xn} - \mathrm{v}_{x0}\,, \\ \triangle y_n &\equiv y_n - y_0\,, & \triangle \mathrm{v}_{yn} &\equiv \mathrm{v}_{yn} - \mathrm{v}_{y0}\,, \\ \triangle z_n &\equiv z_n - z_0\,, & \triangle \mathrm{v}_{zn} &\equiv \mathrm{v}_{zn} - \mathrm{v}_{z0}\,, \end{aligned} \tag{6.9}$$

we obtain the following linear relations:

$$\begin{aligned} \triangle \mathrm{v}_{xn} &= \frac{\partial \mathrm{v}_x}{\partial x} \triangle x_n + \frac{\partial \mathrm{v}_x}{\partial y} \triangle y_n + \frac{\partial \mathrm{v}_x}{\partial z} \triangle z_n\,, \\ \triangle \mathrm{v}_{yn} &= \frac{\partial \mathrm{v}_y}{\partial x} \triangle x_n + \frac{\partial \mathrm{v}_y}{\partial y} \triangle y_n + \frac{\partial \mathrm{v}_y}{\partial z} \triangle z_n\,, \\ \triangle \mathrm{v}_{zn} &= \frac{\partial \mathrm{v}_z}{\partial x} \triangle x_n + \frac{\partial \mathrm{v}_z}{\partial y} \triangle y_n + \frac{\partial \mathrm{v}_z}{\partial z} \triangle z_n\,. \end{aligned} \tag{6.10}$$

From these equations it can be inferred that the $\partial \mathrm{v}_i / \partial x_i$ components can be calculated from:

$$\begin{pmatrix} \partial_x \mathrm{v}_x & \partial_y \mathrm{v}_x & \partial_z \mathrm{v}_x \\ \partial_x \mathrm{v}_y & \partial_y \mathrm{v}_y & \partial_z \mathrm{v}_y \\ \partial_x \mathrm{v}_z & \partial_y \mathrm{v}_z & \partial_z \mathrm{v}_z \end{pmatrix} = A^{-1} \begin{pmatrix} \triangle \mathrm{v}_{x1} & \triangle \mathrm{v}_{x2} & \triangle \mathrm{v}_{x3} \\ \triangle \mathrm{v}_{y1} & \triangle \mathrm{v}_{y2} & \triangle \mathrm{v}_{y3} \\ \triangle \mathrm{v}_{z1} & \triangle \mathrm{v}_{z2} & \triangle \mathrm{v}_{z3} \end{pmatrix}, \tag{6.11}$$

where we have used the convention $\partial_i = \partial / \partial_i$, and $i = x, y, z$. A^{-1} is the inverse of the matrix:

$$A = \begin{pmatrix} \triangle x_1 & \triangle y_1 & \triangle z_1 \\ \triangle x_2 & \triangle y_2 & \triangle z_2 \\ \triangle x_3 & \triangle y_3 & \triangle z_3 \end{pmatrix}. \tag{6.12}$$

Note that the four points of the interpolation tetrahedron are both necessary and sufficient to fix the value of each of the nine velocity gradient components.

6.4.3 The velocity-gradient matrix: divergence, shear and vorticity

When computing the full spatial peculiar velocity field we need to compute the nine elements of the velocity gradient (see Sec. 6.4.2). By doing so, we retrieve the complete information derived from the gradient matrix. Because this gradient matrix is composed by the partial spatial derivatives of the velocity field, it is straightforward to compute any related derivative-velocity quantity. In particular, as the velocity divergence $\nabla \cdot \mathbf{v}$ is the trace of the velocity-gradient matrix, shear σ_{ij} (with $i, j = x, y, z$) its symmetric and traceless part and vorticity ω_{ij} its antisymmetric part we may immediately infer the

DTFE estimates for these quantities in each Delaunay tetrahedron in the following way:

$$\nabla \cdot \mathbf{v} = \left(\frac{\partial \mathrm{v}_x}{\partial x} + \frac{\partial \mathrm{v}_y}{\partial y} + \frac{\partial \mathrm{v}_z}{\partial z} \right), \tag{6.13}$$

$$\sigma_{ij} = \frac{1}{2} \left\{ \frac{\partial \mathrm{v}_i}{\partial x_j} + \frac{\partial \mathrm{v}_j}{\partial x_i} \right\} - \frac{1}{3} (\nabla \cdot \mathbf{v}) \delta_{ij}, \tag{6.14}$$

$$\omega_{ij} = \frac{1}{2} \left\{ \frac{\partial \mathrm{v}_i}{\partial x_j} - \frac{\partial \mathrm{v}_j}{\partial x_i} \right\}, \tag{6.15}$$

where δ_{ij} represents the Kronecker delta pseudo-tensor, and the vorticity ω_{ij} follows the usual definition $(\nabla \times \mathbf{v})_k = \epsilon_{ijk} \omega_{ij}$, with ϵ_{ijk} the Levi-Civita tensor.

This results in fully volume-covering reconstruction of the divergence, shear and vorticity fields. However, notice that while the velocity field itself is continuous, its linear nature results in a discontinuous velocity gradient because they are constant in each Delaunay tetrahedron.

6.4.4 DTFE velocity field procedure illustrated

The four steps enumerated in Section 6.4 to perform the DTFE reconstruction of the peculiar velocity field are illustrated in Figure 6.4. The top-left panel presents a discrete velocity field. The length of the arrows is proportional to the velocity amplitude of each object, and the arrows' head indicate the direction of the motions. It can be noticed that there is and emerging velocity flow from the right-left corner of the box, which spans over the whole box. The field splits at almost the center of the box and grows in amplitude towards the upper-right and bottom-left parts of the box, but it also continues toward the upper-left corner. This velocity field gives the impression of a velocity shear pattern with the largest stretching direction crossing the box from top-right to bottom-left corners. As a consequence of this velocity pattern, the central part of the box presents a "transition" region between the two dominant flows. We will proceed to describe and analyze the interpolation scheme in such figure.

From the locations of the sample points we construct its Delaunay tessellation (top-right panel). The computed velocity gradient for each triangle is indicated in the middle panels. The gray scale in both panels is proportional to the amplitude of the determinant of the velocity gradient matrix, and it runs from black (maximum gradient amplitude) to white (minimum gradient amplitude). In the central-left panel, a clear dark strip can be recognized running along the transition region. This belt-like zone represents one of the areas where the gradient experiences maximum changes because of the dominance of the two opposite maxima flow regions. The central-right panel represents the corresponding Delaunay-surface of the gradient plot. The height of each point is given by its corresponding velocity amplitude. The hyperboloid-like shape of the surface is determined by the velocity distribution, the two maxima located at the two extremes of the cube and the minima points at the opposite extremes. The middle part corresponds to the so-called transition region.

After the gradient matrix calculation, we proceed to do the image reconstruction. In this case on a rectangular grid of 8 grid-cells per dimension as illustrated at the bottom-left panel (gray broken-line grid). First, we identify where each of the grid points are located within the Delaunay tessellation, this is illustrated by the hatched triangles in the panel. The interpolation of the velocity field follows the linear prescription of Section 6.4.2. The bottom-right panel shows the outcome of the procedure. This interpolated velocity field clearly displays the same characteristics as the input field: it recovers the two maxima regions located at the opposite extremes and the low velocity region at the bottom-right part of the box. Also note that due to the linear interpolation scheme, velocity information has been recovered at the top-left part of the box where no data was available.

Although the method performs very well where the velocity flow presents a laminar behavior, the interpolation scheme will not be valid at regions dominated by incoherent (virialized) motions. We will address this point in more detail in Section 6.5.

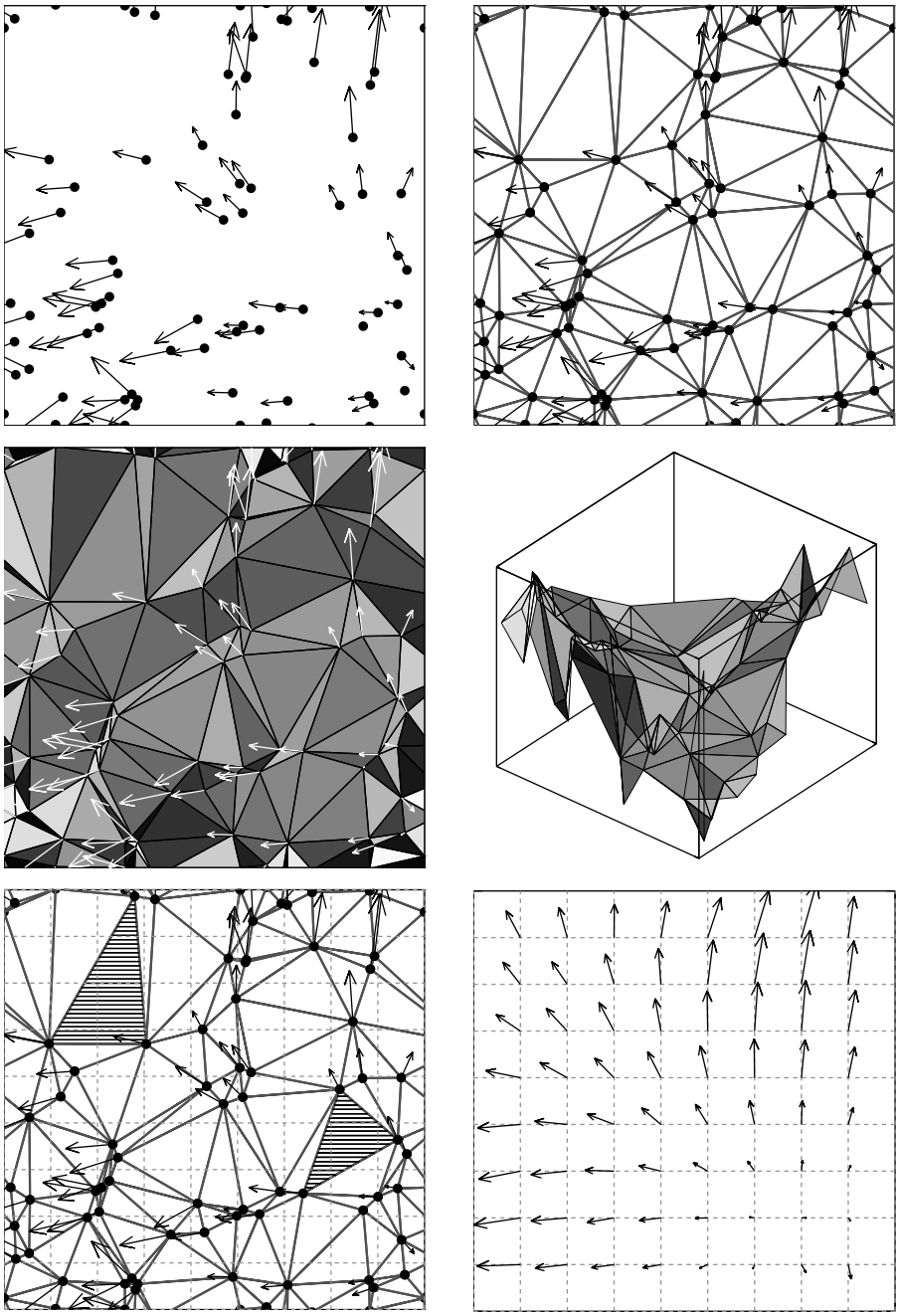

Figure 6.4 — DTFE velocity interpolation procedure. The top-right panel presents the Delaunay triangulation of the discrete particle positions of the velocity field presented at the top-left panel. The central panels show the velocity gradient computed for each triangle. The gray scale corresponds to the amplitude of the determinant of the gradient matrix. The right-hand panel depicts the 3D representation of the gradient surface. The height of each point corresponds to its velocity amplitude. The DTFE velocity field is estimated at the grid points indicated by the gray-colored grid of the bottom-left panel by assuming a linear variation of the velocity field. The bottom-right panel presents the outcome of the DTFE velocity interpolation procedure.

6.4.5 Boundary conditions

An important practical issue for DTFE is that of the boundary conditions. The problem resides in calculating velocity estimates at the border of the data point sample. If we confine the Delaunay triangulation only within "natural" edges imposed by the data set, the reconstructed velocity field at the edges will not be completely correct. In addition, its continuity's characteristic at the edge might also not be conserved. This is because the method will only consider the points within the tessellation. In principle, points at the edge might not be dynamically related to each other leading to incorrect velocity estimates at the edges. This situation is very common in surveys of galaxies whose edges are defined by the selection criteria of the survey itself, mapping objects at the edges that might not be dynamically bounded with the inner mapped matter distribution.

Possible solutions to overcome this edge problem are: cloning techniques, constrained realizations and periodic boundary conditions. The first solution refers to draw random points at the edges of the sample to assure the continuity condition within the field. These points should satisfy two conditions. The first one is that the random distribution of "synthetic" objects should preserve the mean number object density of the data. This technique is similar to the random cloning technique to fill the zone of avoidance and unobserved regions when performing full sky-coverage surveys (Yahil et al. 1991). The second condition is related to the velocities of these synthetic objects. The velocities assigned to these points should follow the velocity distribution function imposed by the data. Although this solution will preserve the continuity condition, velocity field estimates at the edges will not be totally reliable.

An even more advanced and consistent solution would try to make use of the existing correlations in the field. Constrained Field Realizations [CR] (Bertschinger 1987; Hoffman & Ribak 1991; van de Weygaert & Bertschinger 1996) offer a natural solution for this strategy. The use of the CR algorithm is specifically of effectiveness in the immediate neighborhood. This is determined by the correlation length of the field, and therefore be dependent upon the spatial scale. This procedure will assure that the added field will be statistically consistent with the data field at the cost of making an implicit assumption of *a priori* cosmological model used to describe the data. This procedure will certainly improve the field estimates at the edges besides of giving the condition of periodicity. However, this method has only been worked out on linear scales and under the assumption of the chosen cosmological model (see Chapter 3). For processing observational data along these lines, the WF/CR procedure has proved to be very successful (Zaroubi et al. 1995, 1999; Hoffman 2000, Chapter 3).

The periodic boundary conditions solution refers to consider the given point distribution surrounded everywhere by the point distribution itself, just as in the case of cosmological $N-$body simulations. In the present approach we have taken advantage of the periodic boundary conditions imposed by the $N-$body experiment, and implemented this conditional into the procedure. However, this solution is not always feasible because if we want to apply this method to real data this conditional is not longer valid.

6.5 Delaunay Velocity Fields: Performance

The main characteristics of the DTFE velocity scheme over the conventional methods are its self-adaptiveness, completeness of volume coverage and dynamic range, together with the linear interpolation scheme for velocities. These characteristics allow one to apply the method to a velocity field composed by small and large scale features and to recover information at those regions devoid of data. Also, the velocity method shares the property of DTFE of supressing shot-noise and yielding volume-weighted estimates.

However, the interpolation scheme also present problems at given regions, in particular at high-density regions where shell-crossing has occurred. At these regions the linear velocity interpolation scheme is not completely valid anymore.

To get an idea of the method's characteristics and the resulting velocity field reconstruction, we analyze in this section how the DTFE velocity method performs at different density scenarios and cosmic scales drawn from cosmic peculiar velocity fields of $N-$body simulations.

6.5.1 $N-$body simulations

The $N-$body simulations needed to test the DTFE velocity scheme should be able to deal with a velocity field composed by the "typical" structural elements present in the large scale structure of the universe. These range from huge empty voids to mildly non-linear regions like filaments and non-linear structures such as dense galaxy clusters. For the purpose of testing and illustrating this we have performed a cosmological $N-$body simulation of structure formation. The simulation involves the currently popular flat low-density cosmological model ΛCDM with $\Omega_\Lambda = 0.7$, $\Omega_m = 0.3$, $h = 0.7$ (measured in units of 100 km s^{-1} Mpc^{-1}). The power spectrum normalized to the current value of $\sigma_8 = 1$. The simulation was performed in a cubic box of $L = 100\ h^{-1}$Mpc, with 64^3 particles. The linear Gaussian initial conditions were computed on a cubic grid of 64 grid-cells per dimension. Particles were displaced from their original grid position and initial velocities assigned according to the Zel'dovich approximation (Zel'dovich 1970) at redshift $z = 49$. The evolution of the linear initial density and velocity fields into the non-linear regime was carried out by means of the publicly available HYDRA code (Couchman et al. 1995), with a force resolution of 128 grid-cells per dimension.

6.5.2 The virtues of DTFE velocity field

The virtues of the DTFE velocity method can be most clearly appreciated from a study of those regions where the sampled density is relatively moderate or even low. These involve the low density void regions as well as the mildly non-linear. But also at small scales where the method can trace the infalling motions into high-density regions.

The top-right panel in Figure 6.5 presents a full DTFE velocity reconstruction from the discrete velocity field at the top-left panel (same velocity field presented in Fig. 6.1). The field has been interpolated onto a cubic grid of 128 grid-cells per dimension as in the TSC high-resolution plot. As previously, we have decreased the plotted density resolution of the map to $\frac{1}{4}$ of its original resolution. The reconstructed DTFE velocity field retains the main characteristics of the input field. The high density regions can be clearly recognized. In general the outline of the Megaparsec structures can be easily recognized. Particularly outstanding is the performance of DTFE in regions where the sampling is very poor. The contrast offered by grid-based methods could hardly be more stark.

The self-adaptiveness of the code improves substantially its spatial resolution, allowing it to resolve small scale features within the large scale ones. This method's characteristics allows one to produce high-resolution images without loosing spatial information as in the case of grid-based methods. Hence, if we zoom in on a denser region, we will be able to follow the related velocity flows, while retaining the flow's characteristics at underdense regions. The resolution of the method is determined by the point distribution itself and not by the grid-size as in the case of grid-based methods.

In the zoomed panels of Fig. 6.5 (middle and lower rows) we have created a 512^2 image of the areas on which we zoomed in. These regions are indicated by dashed sub-boxes in the discrete velocity field. For visualization purposes we again took a lower plotting density. The regions were chosen on behalf of their density contrast and dynamical state, such that the four frames represent a reasonable variety of cosmological structures. Each region has been framed and labeled according to these criteria: (a) a void-like region located at the top-right of the box; (b) a filamentary structure at the bottom-left; (c) a mildly non-linear region; (d) a collapsed and virialized clump. Each one of the corresponding zooms are indicated by their respective letters.

In addition, we recover a 1-Dimensional profile along a particular line-of-sight through the simulation box. The velocity profiles and zoomed regions will be discussed together in the following subsections in order to point out the benefits and problems of the DTFE method.

Figure 6.6 shows the reconstructed DTFE density and velocity fields for a slice covering a region of $80 \times 5\ h^{-1}$Mpc. We may recognize along the cut a variety of structures, a void, a filament and a cluster. The central-top frame shows the discrete particle distribution along the cut. In the top frame, the 2-Dimensional slice through the 3D DTFE density field is presented. The central frame presents the corresponding discrete velocity field. The central-bottom frame shows the corresponding interpolated

DTFE velocity field, and the lower frame the 2D amplitudes of the velocities. It is important to realize that the DTFE slices cannot be compared directly with the discrete data points depicted because the latter shows the projected particle distribution in a slice of a given thickness, while the DTFE fields represent infinitesimal thin slices. Nevertheless all the structure patterns present in the discrete field have a corresponding counterpart in its DTFE density and velocity fields. Clearly visible are the big cluster, a filament, and two voids. One void is located between the cluster and filament, and the other one to the most-left part of the plot. Each of these structures have an imprint in the velocity field. The bold solid lines plotted along the discrete particle and velocity distribution and DTFE velocity field indicate the line direction along which we have computed the DTFE density and velocity profiles. The resulting density and velocity profiles are plotted in the bottom frame of the same figure, where only the velocity component parallel to the direction of the cut is shown. The density scale is plotted on the left ordinate, while the velocity scale on the right ordinate of the plot.

6.5.3 Reconstructed Delaunay velocity Fields: Problems

While the DTFE has many virtues, the method has its own limitations, specially at the core of high-density regions. The linear interpolation scheme implies that the velocity field behaves as a laminar flow, i.e., the field does not present turbulence. In other words, small-scale (virial) motions are dominated by the large scale characteristics of the velocity field.

Once an object has decoupled from the Hubble flow and has started to collapse, the laminar flow assumption is not valid anymore. Under such circumstances, the DTFE velocity scheme cannot reconstruct a continuous velocity field at those regions. However, the notion of a continuous velocity field within a virialized region is also not physically defined precisely because of virialization, i.e., dominated by random (thermal) motions.

6.5.4 Velocity reconstruction in voids

By their nature, void regions contain a minimum amount of points. This makes notoriously difficult to reconstruct them by conventional methods. When their resolution is too high, shot-noise peaks are induced at the particles' positions. When the resolution is decreased their masses are smeared out over a large volume (see S05). For velocities this tends to be worse (see Fig. 6.1).

The first enclosed region (a) in Fig. 6.5 depicts an expanding void whose center almost coincides with the geometrical center of its respective box. The corresponding DTFE zoom (middle-left panel) shows the reconstructed velocity field. Theoretical models of voids (Icke 1984; van Haarlem & van de Weygaert 1993; Sheth & van de Weygaert 2004) predict that such empty regions are characterized by an inverse tophat density profile. Their dynamics correspond to a low-Ω_m universe, represented as "super-Hubble" expanding bubbles with an almost constant velocity divergence.

DTFE manages to succeed in deriving a natural and continuous void velocity field profile without the application of artificial smoothing procedures, leading to a higher and better resolution maps. In the DTFE algorithm the void is rendered as a slowly varying region of low density (see top-most frame in Fig. 6.6, density image) (S05). Despite the center of the void is "devoid" of particles, the DTFE manages to recover information at that region. Once we reach the boundaries of the voids in the form of clumps or bridges, we see this reflected in the distorted flow. Near those regions the gravitational force is dominated by the overdense features.

The general characteristics of the void's DTFE velocity profiles can be seen in Fig. 6.6. The velocity cut presents two voids, in which their velocities rise almost linearly along the cut. This implies that they are characterized by an almost constant velocity divergence, as predicted by the theoretical void models. The left-side void presents only expanding velocities because we have made the cut from its center, the other side will present an inverted mirror-like behavior with negative velocities.

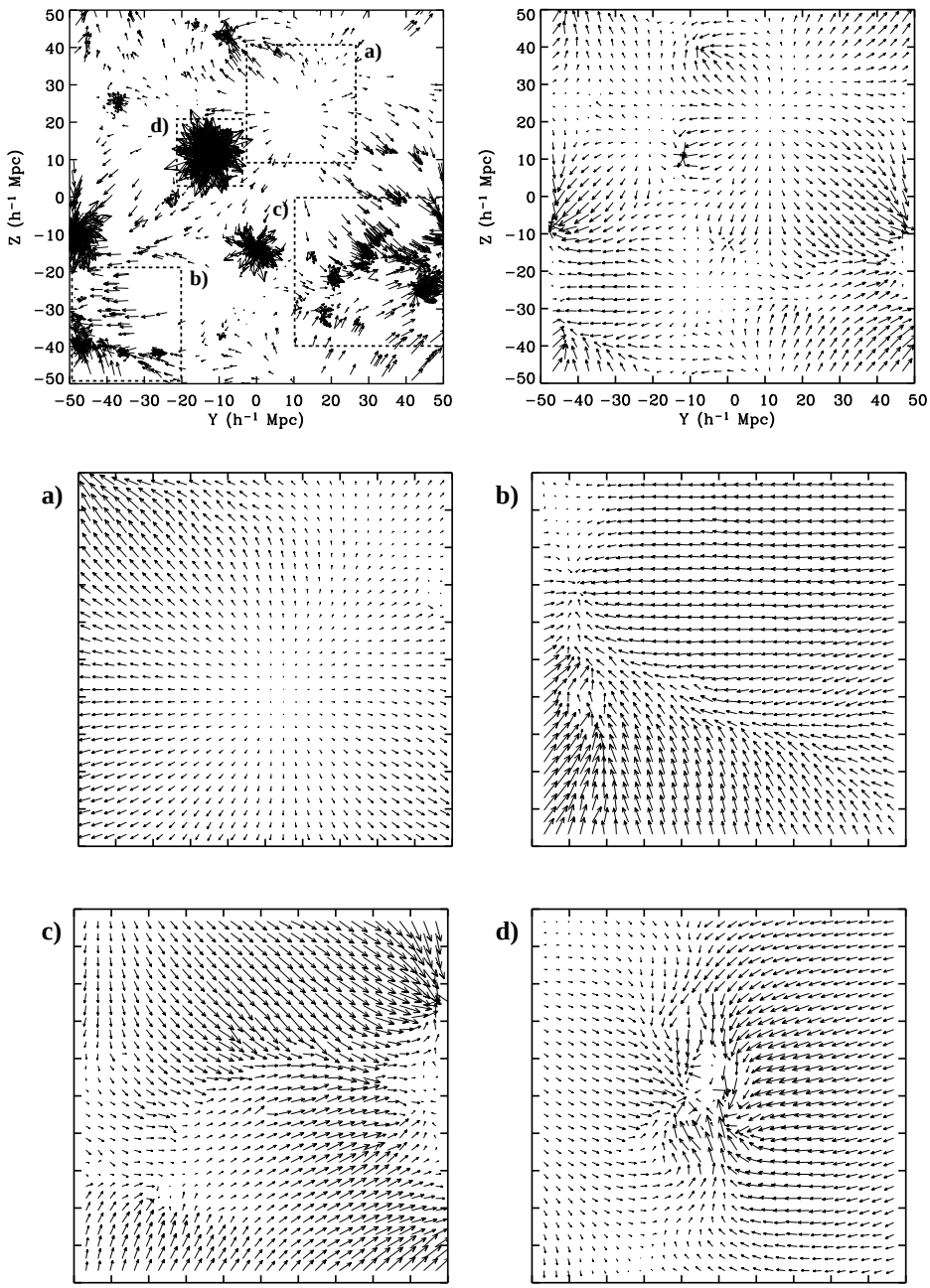

Figure 6.5 — DTFE velocity maps. The top-left panel shows the same discrete velocity field presented in Fig. 6.1. The top-right panel presents the corresponding DTFE velocity map using the same resolution as its TSC counterpart (right panel of Fig. 6.1), notice that the whole field is sampled now. The central and bottom rows are 2D zooms of the corresponding enclosed regions in the discrete map and can be identified by their labels. The selected regions have been chosen according to their density and dynamics characteristics, void, filaments and a cluster. See text for details.

6.5.5 Velocity reconstruction in filaments

Panel (b) of Fig. 6.5 shows a filamentary structure running along the lower part of the box and a seemingly coherent velocity flow pointing toward the left side of the box. Both are clearly reproduced

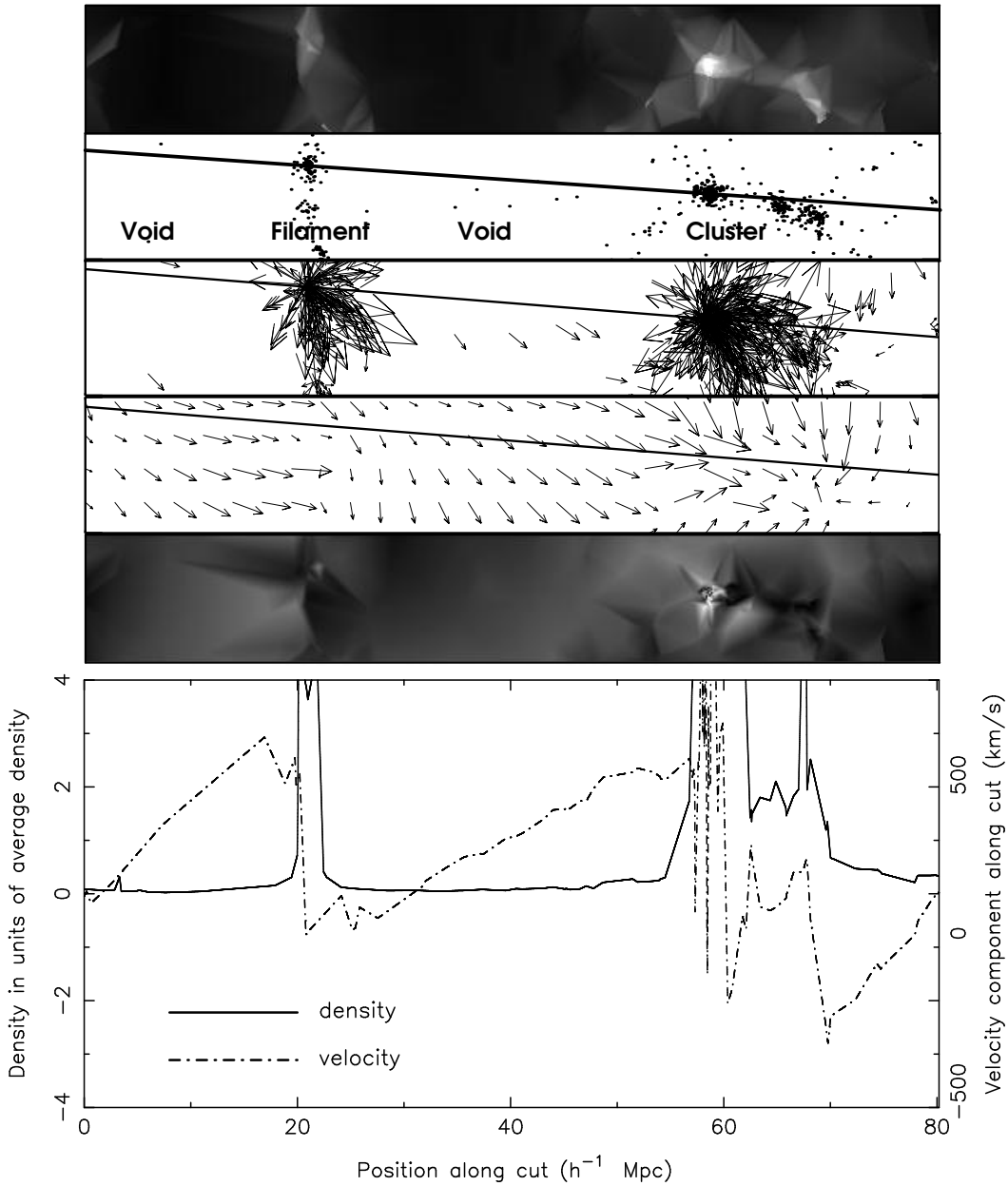

Figure 6.6 — DTFE velocity and density profiles (bottom panel) computed along a cut through the N−body simulation box. The discrete point distribution and its corresponding density field are shown in the two top-most panels. The analogous discrete velocity field, continuous (DTFE) vectorial and image velocity fields are shown in the three intermediate panels. The bold lines crossing the particle and velocity fields indicate the direction along the profiles were computed.

in the zoom-in frame. A clear shearing flow can be identified along the filament's ridge. Toward the massive clump this flow is distorted by the action of the clump itself. Besides the filament within this frame we can recognize two "singularities". One is related to the clump at the left-hand tip of the filament. Its high densities imply mildly virial motions, leading to a breakdown of the interpolation scheme. The second one is an artifact of our use of periodic boundary conditions. Because we find a

cluster at the other side of the full box, some of those clustered points (the most external ones to the cluster) have been used when performing the triangulation procedure. The result is a "saddle" point in the velocity flow toward which the velocities from each direction seem to converge. We will discuss in more detail the boundary condition effects in Section 6.4.5.

The panel (c) presents similar characteristics to the panel (b). It contains a filamentary structure and a mild-dense cluster. The shape of the filament can be well traced in the DTFE velocity field. The shearing infall flow towards and along the filament is clearly recovered. Here and there the discontinuities imprinted by clumps can be clearly recognized.

The respective filament velocity profiles (see Fig. 6.6) also illustrate such discontinuities. After the interpolated velocities raised as a combination of the void's expansion and infalling motions toward the filament, the profile presents a dramatic drop when it crosses the edges of the filament. This is because there are virial motions perpendicular to the filaments. We can notice that the velocity profile presents still irregularities beyond the density filament edge as a result of back infall motions toward the filament.

6.5.6 Velocity reconstruction in clusters

Panel (d) of Fig. 6.5 shows a zoom enclosing a highly non-linear structure. It is clear that the velocity field is not continuous at the core of the cluster and that the DTFE velocities cannot reproduce the real velocities. This plot clearly shows the problems of DTFE at such high-density regions. However, some remarks about the performance of the method around the cluster are worthy to mention.

In any collapsing/collapsed structure, a vorticity velocity mode appears as a natural consequence of such collapse. Apart from this mode, the velocity field around the cluster is also sheared. This distortion is clearly noticeable at both top and bottom ends of the cluster. At regions closer to the cluster's core the flow describes circular trajectories before converging at the cluster itself. Further out from the cluster while virial motions give way to systematic infall motions it can be noticed how the velocity field gets smoother and better behaved. We will treat these vortical modes in more detail in Section 6.11.

The velocity profile also illustrates the problems of DTFE at high-density regions. The density profile peaks at the cluster's location. The sudden and pronounced variations (discontinuities) in the corresponding velocity profile indicate the presence of a very evolved non-linear structure, unveiling the characteristic virial motions in the cluster.

This profile uncovers the "deficiencies" of the method at such dense regions. Because vorticity should be non-existing in regions where shell-crossing did not yet take place. There, vorticity can function as an indicator of the related error. Once collapsed occurred, vorticity can be generated, making hard to judge whether the "measured" vorticity is real or not. We will address this issue in more detail in Section 6.11.4.

6.6 Errors and Sampling effects

So far we have reconstructed the velocity field from the full discrete velocity field. However, in many cases, mainly observationally, one does not deal with the full discrete velocity field but with a sparse sample. Surveys of galaxies are usually magnitude-limited samples. Therefore, they are severely affected by sampling effects. In general, surveys have better sampling at dense regions (clusters and filaments) and a very poor coverage at low density regions (voids), with the number of objects decreasing with distance from the observer.

Another problem related to peculiar velocity surveys is the large measured distance error via the Tully-Fisher or Faber-Jackson relations for spiral and elliptical galaxies. Estimated distances have uncertainties in the order of $\sim 20\%$ accuracy. This translates into large velocity errors proportional to the object's distance. This limits the range of peculiar velocity surveys to distances below which the

errors are substantially smaller. A lot of effort has been devoted to coping with these errors, particularly the systematic ones (see Strauss & Willick 1995, for a review about different correcting methods).

As the statistics of DTFE reconstructions is not trivial, and involves cumbersome Poisson statistics, we resort to a Monte Carlo approach for estimating the influence of a variety of sampling effects. Schaap (2005) studied how the Delaunay triangulation changes when varying the point distribution and its implications for density field reconstructions and we refer the reader to this work.

6.6.1 Sparse sampling effects

Sparse sampling has a direct repercussion when reconstructing the velocity field. Because DTFE relies on the point distribution itself, dilution of samples imply less "observed" (measured) objects to perform the Delaunay triangulation. This affects the density field reconstruction because it is inversely proportional to the contiguous Voronoi cell surrounding such point. A "contiguous Voronoi cell" is composed by the immediate hypertriangles surrounding a given point (see SW00 for further details). S05 argued that one may deal with such effects if one knows the "selection function", which describes the sampling density of the particle distribution.

Despite the density field can be corrected for sparse sampling effects, this is not the case for peculiar velocity fields. In general, peculiar velocity fields are more quiet than density fields. This implies that no sudden variations are present on the velocity field, at least in the linear and mildly non-linear regime where velocities are considered laminar. Provided that the sampled point distribution is still a fair representation of the underlying density field, the linear characteristic of the DTFE velocity method helps to mitigate such sampling effects and to recover a reliable velocity field. At high-density regions and immediate surroundings sampling effects have a more pronounced effect. At these regions objects' velocities may be uncorrelated since such objects have decoupled from the Hubble flow and the velocity field is incoherent. The method cannot properly recover velocities at these regions because of this incoherence in the velocities. Thus, sampling effects will enhance the errors in the reconstruction leading to understimate the velocity field.

In order to measure sparse sampling effects on the DTFE velocity reconstruction, we have diluted the full discrete velocity field by assuming an homogeneous dilution procedure via Monte Carlo sampling. For each one of these sparsed fields we have reconstructed their DTFE velocity fields. In Figure 6.7 we present a comparison between both DTFE diluted and full velocity fields. A direct comparison is possible because diluted fields have been reconstructed with the same resolution than the full velocity field. The top row presents residual DTFE velocity fields computed from substracting the DTFE diluted field from the full DTFE field. Each panel corresponds to a different fraction of objects indicated by the enclosed labels. In the left-hand panel we have only considered 30% of the total number of objects, in the middle panel 60% and in the right-hand panel 80%. The velocity projection and characteristics are the same than in Figs. 6.5 and 6.1. Velocities in the three panels have been normalized by the same factor for a fair comparison. Clearly the larger velocity residuals trace the matter distribution, implying that the velocity reconstruction is more affected at these regions. As expected, errors increase toward more diluted samples. The very low density regions are the least affected ones, also in the most diluted sample. This implies that voids can be reconstructed with very few points by the DTFE method. Typical reconstruction procedures will be seriously affected by shot-noise effects which will become worse at more diluted samples.

Quantitative evidence for the similarity between the diluted and full fields is presented in the bottom row of Fig. 6.7. The panels show density contours from the point-to-point distribution. For reference, one-to-one lines have been drawn. The density contours have been weighted by the real spatial DTFE density field estimates. Therefore, particles located at high-density regions (clusters) can be recognized in the contoured point-distribution like those light-gray spots distributed all over the cloud of points. These "high-density" points are precisely those which are located farther away from the best fitting line, in agreement with the visual inspection of the residual velocity maps.

The top labels in each frame refer to linear fits performed between both fields: $a_{\rm v}$ is the best slope that fits the data, $\rm v_0$ is the zero-point offset, and σ the dispersion around the linear fit. The fact that

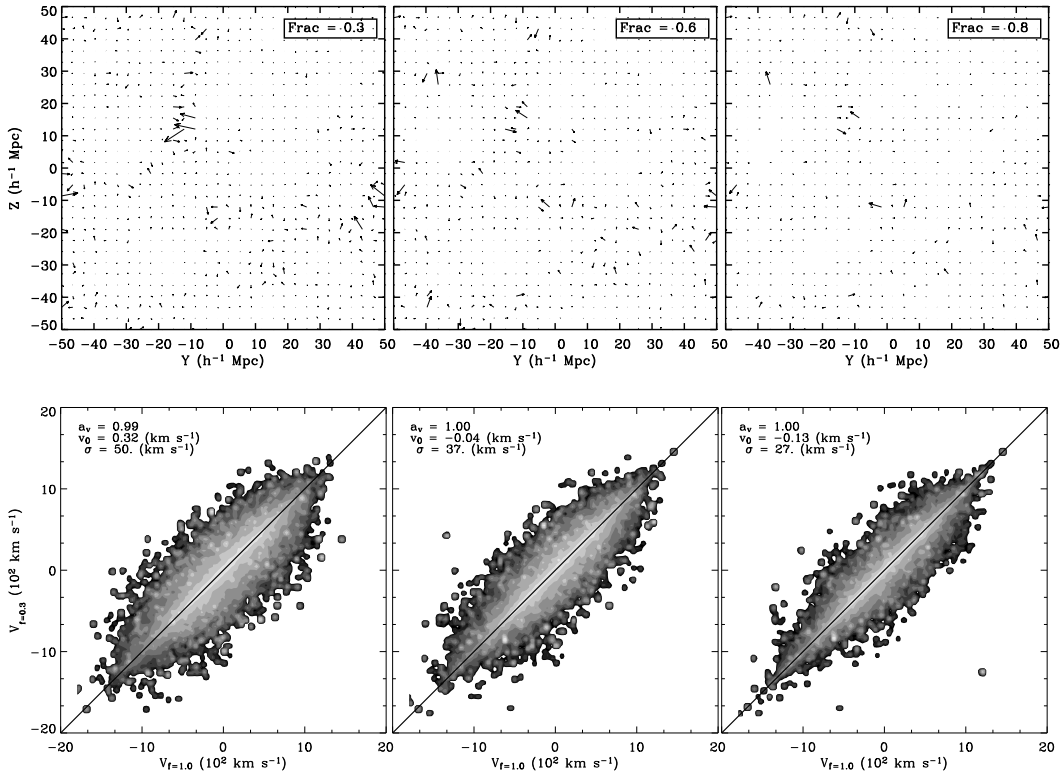

Figure 6.7 — Comparison between diluted DTFE velocity fields and the full DTFE field. The top row panels present residual maps between the full field and diluted fields. The enclosed labels indicate the fraction of objects used to reconstruct each velocity map. The bottom-row panels are qualitative comparisons between diluted and full DTFE velocities for one Cartesian component. See text for further details.

the slopes for the three cases are almost unity implies that there are no systematic differences between the two fields, underlined by the almost zero offsets. Remarkable is that the velocity dispersion does not seem to increase with dilution level. A remarkably point is that the velocity dispersion does not increase considerable when increasing the dilution. The difference between the two extreme diluted samples is only of 23 km s^{-1}. These results justify the validity of our interpolation method.

6.6.2 Perturbing velocities

A second test concerns an evaluation of the influence of uncertainties in velocities for the DTFE velocity field reconstructions. Intrinsically, this error is much more difficult to correct for than the one introduced by sparse sampling. One way to deal with this noise is by assuming that is Gaussian distributed. Then, one could reduce this noise and obtain the most probable field by weighting the contribution of each object inversely by the variance of its velocity measurement error (e.g. Dekel et al. 1999). However, this method is only effective when considering large smoothed fields. Another possible way could be by drawing multiple realizations of the field and measuring the signal-to-noise to find the statistical significance of the method.

Here we only check how Gaussian noise affects our DTFE velocity reconstructions. We have not added errors proportional to their distances since this will only imply that the reconstruction will get worst towards large distances from a particular observer. Since our interest is to check whether this error introduces systematic effects in the DTFE reconstruction, we proceed as follows. To each Cartesian velocity component of the discrete velocity set, we add a random velocity drawn from a

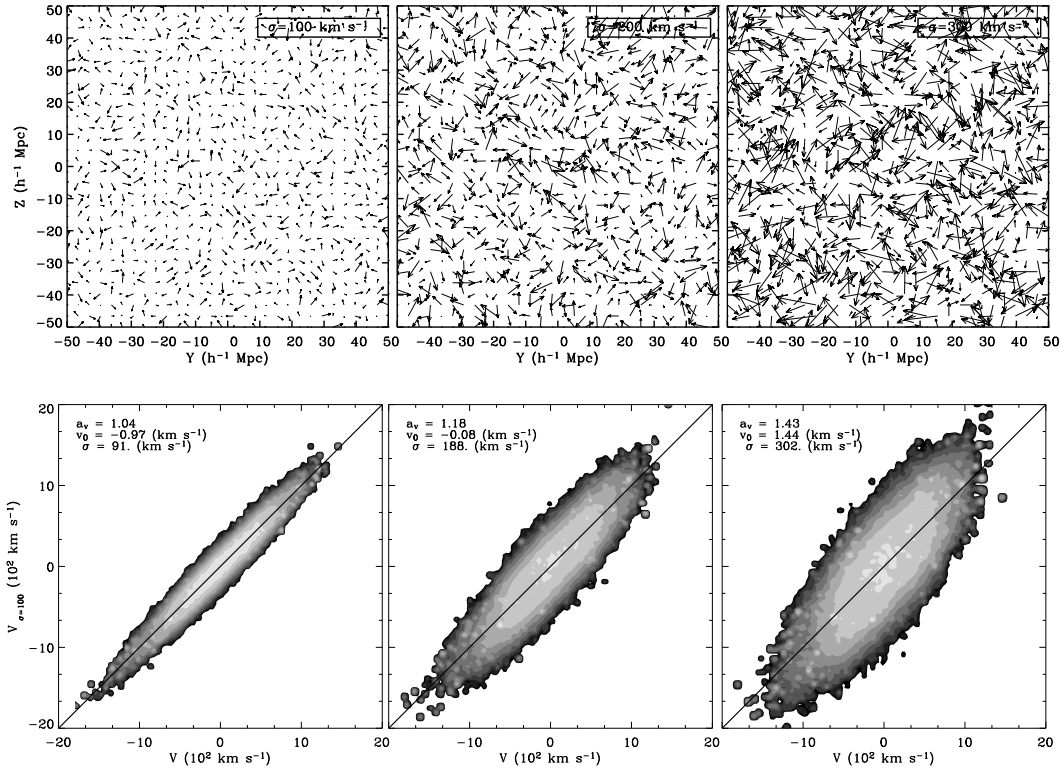

Figure 6.8 — Comparison between reconstructed DTFE perturbed velocity fields and the original field. The top row panels present residual maps between the original and perturbed fields. Perturbed velocities have been computed from adding random error-velocities drawn from a Gaussian velocity distribution of width $\sigma = 100, 200, 300$ km s^{-1}. The bottom-row panels are qualitative comparisons between perturbed and original DTFE velocities for one Cartesian component. See text for further details.

Gaussian distribution function with a given fixed standard deviation σ, and randomly orientated. The top-row panels of Figure 6.8 show the residual velocity fields between the DTFE perturbed velocities and the original DTFE field for three cases, $\sigma = 100, 200, 300$ km s^{-1} (left, middle and right panels respectively). No systematic effects seem to be introduced since the residual velocity fields only show random motions which get larger for larger σs.

The point-to-point comparison between the perturbed and original velocity fields (Fig. 6.8, lower panel) immediately shows two effects: the dispersion increases as σ becomes larger, and the point cloud appears to change its inclination with respect to the one-to-one line. The former is indicated by the fact that the point-density contours are Gaussian distributed with measured velocity dispersions very close to the ones imposed by the errors. The latter is a consequence that velocities have increased their amplitude. This trend is clearly observed along the whole point distribution in the right-hand panel. The fact that the zero-points are consistent with zero and that the point-contours have Gaussian distributions, imply that no systematic effects are introduced by the method itself.

Notice that in this case the points located at high-density regions are not longer dominating the outskirts of the distributions, but they are more equally distributed.

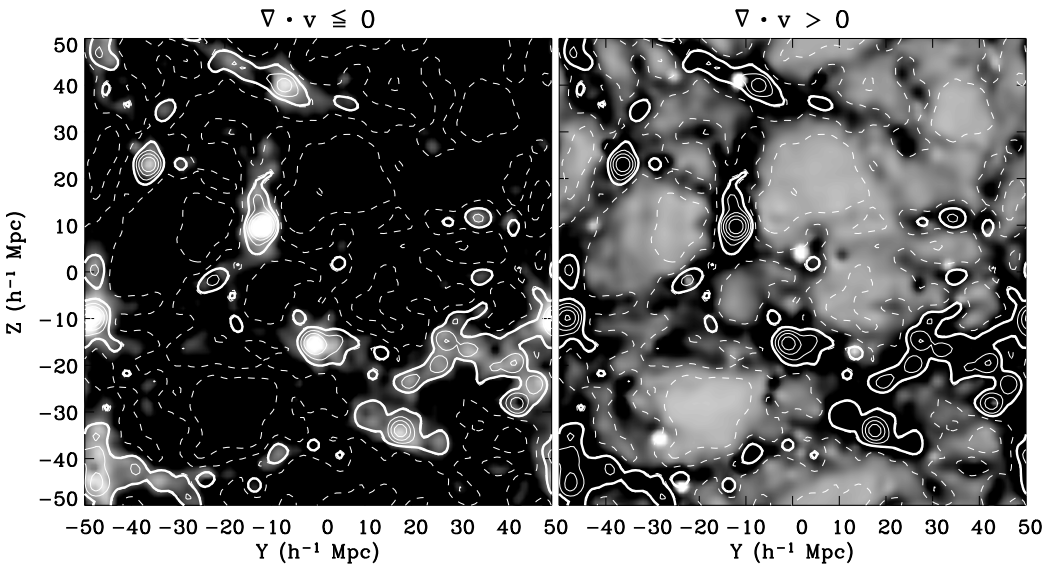

Figure 6.9 — Velocity divergence maps. The plotted slices correspond to the one presented in Fig. 6.5. The left-hand plot depicts regions where inflows are presented, i.e., in and around clusters and filaments. The right-hand plot shows regions with outflows, expanding regions like voids. The contour lines represent the density maps. Broken lines represent low density regions, continuous lines overdensity regions, while the bold line the zero density contrast line.

6.7 The density-velocity relation

An important characteristics of the DTFE method is that the quantities it produces are volume-weighted, allowing a direct comparison with theoretical predictions. BW96 used Delaunay and Voronoi tessellation based-velocity fields to test the validity of the analytical perturbation calculations. Their results showed that their reconstructed fields are in good agreement with the theoretical predictions. Although their results involved quite heavy smoothing, by a top-hat filter of $R_{TH} = 15\ h^{-1}$Mpc.

The velocity divergence and the density contrast are related via the continuity equation (Peebles 1980). In the linear regime this is a strict linear relation (Eqn. 6.1). In the quasi-linear and mildly non-linear regime the one-to-one correspondance between the two fields remains intact, be it that it involves higher order terms (see Bernardeau et al. 2002, for an extensive review).

Since the DTFE method has the ability to resolve both small and large scale features of the density and velocity fields, it gives us the opportunity to test the capacity of DTFE to probe the dynamics in structure formation scenarios. From the density-velocity divergence relation we seek to obtain an idea of the performance of DTFE. By following the evolution of the described density-velocity divergence relation we hope to get an idea of DTFE's performance in different dynamical regimes. Once the reliability of the method has been tested, we could reconstruct the density field from the velocity divergence field.

Figure 6.9 presents a first impression of the intimate relation between the density and velocity divergence fields reconstructed with the DTFE method. The velocity divergence has been computed according to Eqn. 6.13. The figure shows velocity divergence maps for the same projection presented in Fig. 6.5. For a visual impression of the correspondences between high and low density regions, we have splitted the divergence field into two parts, positive and negative divergence regions. On top of the divergence maps we have plotted the density contrast contours. Continuous lines indicate high density regions, the bold continuous line represents the $\delta = 0$, and the dashed lines underdense regions. Both fields, velocity divergence and density have been Gaussian smoothed with a kernel of $R_G = 1\ h^{-1}$Mpc.

The left-hand panel presents those regions where the divergence is negative, i.e., those regions where infall motions are present as in those where matter is being accreted into clusters and filaments. Notice the good correspondence between the high-density regions and the features in the velocity divergence. The most pronounced spots correspond to the two clusters located at the center of the field as expected. The right-hand panel shows regions where the velocity divergence is positive. The expanding regions are, of course, to be identified with the low-density voids in the density field. The gray scale indicates that at the voids' centers, the expansion is slower (lightest gray regions) in comparison with the void edges where tones are darker (higher velocities). As in the previous case, there is a good correlation between the positive velocity divergence areas and the low density regions.

6.7.1 Density-Velocity divergence evolution

A lot of theoretical effort has been devoted to obtain more accurate density-velocity divergence relations than in Eqn. 6.1. On the basis of perturbation theory and assuming Gaussian initial fluctuations, Bernardeau (1992) derived a 2nd order relationship between the velocity divergence and density fields valid for the quasi-linear regime of the form:

$$\frac{1}{H}\nabla\cdot\mathbf{v}(\mathbf{x}) = \frac{3}{2}\, f(\Omega_m)\,[1-(1+\delta(\mathbf{x}))^{2/3}]\,. \tag{6.16}$$

Other higher order perturbative corrections have been also implemented (e.g. Nusser et al. 1991; Nusser & Dekel 1993; Bernardeau et al. 1999; Kudlicki et al. 2000; Bernardeau et al. 2002, and references therein). Here we have computed the density-velocity divergence relation from the reconstructed DTFE velocity and density fields and compared with the 2nd order approximation relation of Bernardeau (1992, Eqn. 6.16) and the empirical quasi-linear approximation of Nusser et al. (1991) based on the Zel'dovich approximation given by:

$$\frac{1}{H}\nabla\cdot\mathbf{v}(\mathbf{x}) = -\,f(\Omega_m)\frac{\delta(\mathbf{x})}{1+0.18\delta(\mathbf{x})}\,. \tag{6.17}$$

Figure 6.10 shows the evolution of the density-velocity divergence relation as a function of the expansion factor, a, reconstructed from our $N-$body simulation. Here, we have plotted the normalized divergence θ of the velocity field given in units of the Hubble parameter,

$$\theta = \frac{\nabla\cdot\mathbf{v}}{H}\,, \tag{6.18}$$

Density and velocity divergence fields have been smoothed with a Gaussian filter of radius $R_G = 5\ h^{-1}$Mpc in order to obtain a tighter correlation. Fields convolved with smaller kernels (e.g. 2&3 h^{-1}Mpc) do show the density-velocity divergence relation but they present a large scatter mainly at regions where $\delta > 0$. We have plotted ten output times linearly scaled in a, from $a = 0.02$ until $a = 1$. In each panel, the continuous line represent the linear theory prediction (Eqn. 6.1), the short-dashed line the 2nd order perturbative approximation (Eqn. 6.16), and the long-dashed line the empirical Zel'dovich-based approximation (Eqn. 6.17).

At early times, the DTFE method cannot recover the relation. This is a consequence of the "artificial" grid-like distortion of the initial point distribution. At early times, the matter distribution still preserves the grid-like configuration, an almost perfect cubic grid. Under these circumstances, the DTFE approach performs poorly since the regular point distribution is clearly not a faithfull reflection of the underlying density field. A possible solution to avoid this effect could be the use of glass-like initial conditions. In this approach, particles sample subrandomly the initial density field with no regular structures on scales greater than the interparticle separation (Baugh et al. 1995).

The dynamical evolution of the system into a more natural configuration, superseding the clear imprint of the grid geometry, helps the triangulation procedure to remove the degenerate cells. For $a \geq 0.2$, the point distribution indeed appears to follow the quasi-linear predictions. At later times, the agreement between the distributions and the theoretical predictions becomes extremely good. The

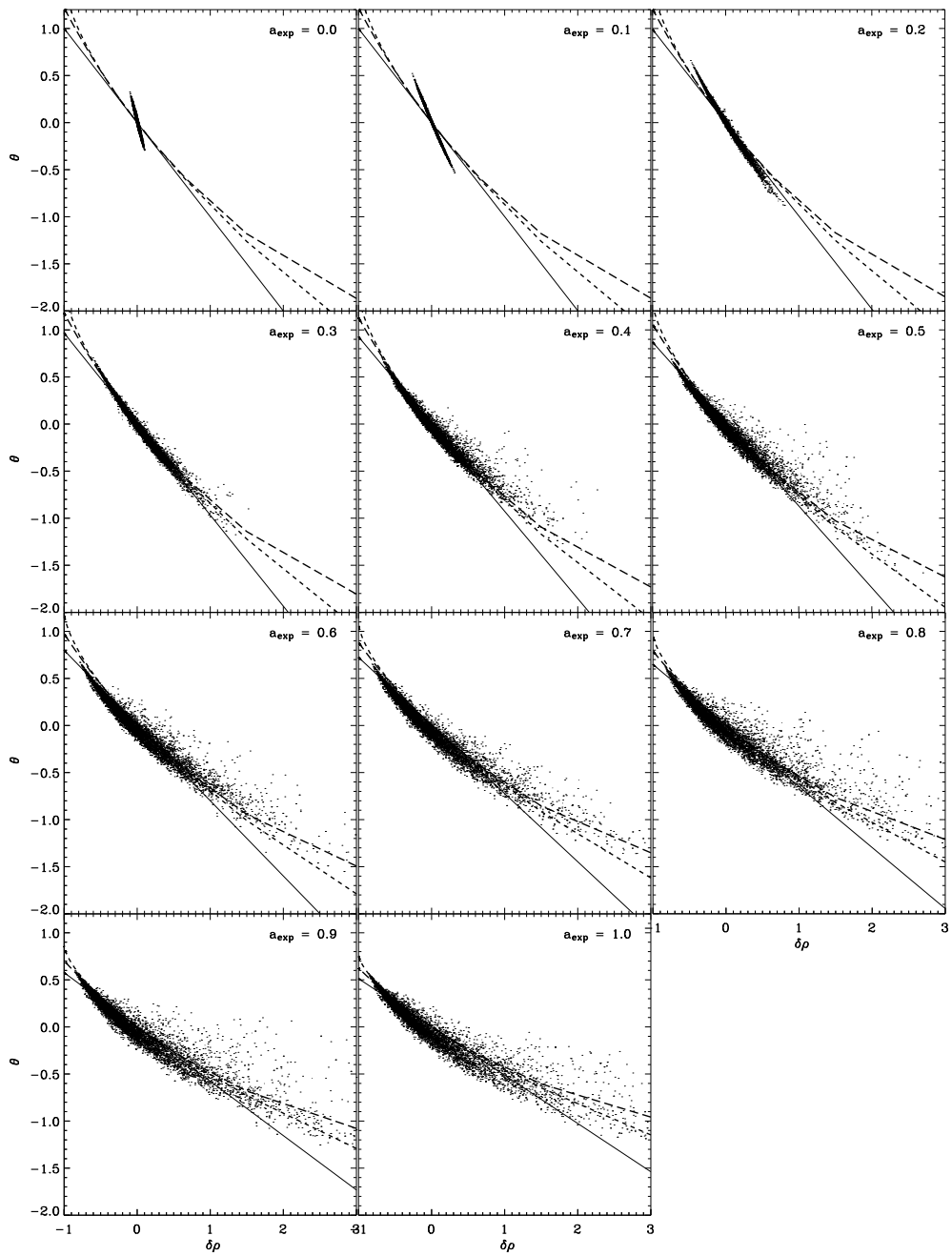

Figure 6.10 — Time evolution of the density-velocity divergence relation. The cloud of points are given by the densities and velocities computed through the DTFE algorithm. The continuous lines indicate the linear theory relation, the broken lines the 2nd order approximation relation, and the long-dashed lines an empirical quasi-linear relation. The velocity divergence (θ) is expressed in terms of the Hubble parameter at the given epochs.

dispersion around the point distributions increases at later expansion times due to the appeareances of virialized motions in and around the highest density regions.

At the tip of the point distributions, which correspond to the low-density regions (voids), the DTFE

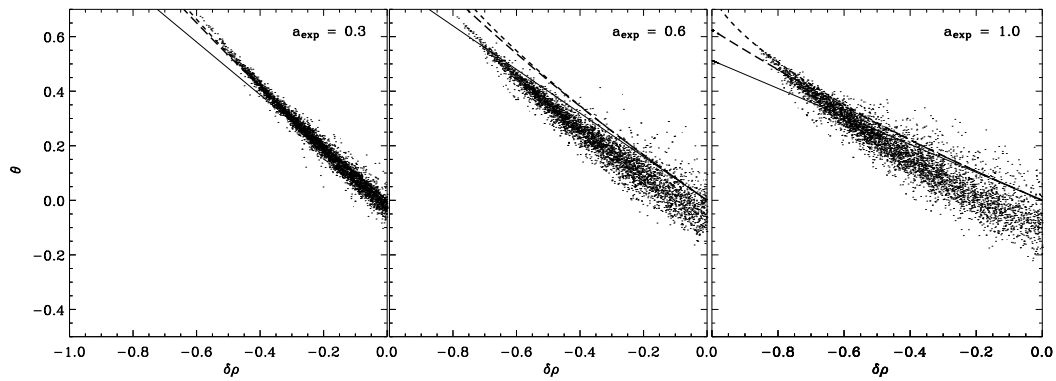

Figure 6.11 — Zooms of three DTFE density-velocity divergence relation snapshots from Fig. 6.10. The continuous lines indicate the linear theory relation between the two fields, the short-dashed lines the 2nd order approximation relation, while the long-dashed the empirical approximation.

estimates are very close to the theoretical predictions. These results justify and confirm also the validity of the linear interpolation DTFE procedure.

However, a peculiar effect can be noticed at the very tip of the distributions as a function of the expansion factor. The point distribution at $a = 0.3$ presents an almost perfect alignment with the theoretical predictions. As the system evolves in time, the tips of the distributions shift toward lower velocity divergence values until $a = 0.6$, where it bounces back to the behavior predicted by the theoretical predictions. All these can be better noticed on Figure 6.11 where we have zoomed in onto the range of underdensities for three expansion factors ($a = 0.3, 0.6, 1.0$). The departures from the perturbed theoretical predictions are clear enough. A possible explanation for such effect could be the fact that these are also non-linear regions and therefore, such perturbative approximations are not valid at this regime. Since voids evolve as homogeneous ellipsoidal underdense regions with a tendency to evolve into a top-hat density profile, the spherical model could offer a better fit at these underdense regions.

In conclusion, we have seen that the performance of the combined DTFE density and velocity method is in general very good. The method is able to follow the dynamical evolution of cosmological structures at both large and small scale regimes. The reliability of the bouncing effect at the tip of the density-velocity divergence point distributions can be tested by means of the Zel'dovich approximation. Within this approximation velocities and densities evolve kinematically from their initial state. Therefore, non-linear effects will not be present.

6.7.2 The Zel'dovich density-divergence relation

Since the Nusser et al. (1991) relation is a higher order Zel'dovich approximation, we have applied the DTFE velocity method to a series of density and velocity fields evolved in time according to the Zel'dovich approximation from the initial Gaussian fields used for the $N-$body simulation. If the effect at low density regions found in Section 6.7.1 is also present with the Zel'dovich approximation evolved fields, this will imply that such effect is not genuine but a systematic error introduced by the DTFE method. If such effect is not found, this will imply that it is truly caused by the non-linear evolution of such structures.

Figure 6.12 shows three snapshots at different expansion factors for the density-velocity divergence relation evolved according to the Zel'dovich formalism. The earliest snapshot (left-hand panel) follows almost the same predicted behavior as the empirical relation, but with larger velocity divergence measurements at the underdense regions than expected. This is mainly due to the grid effects mentioned in

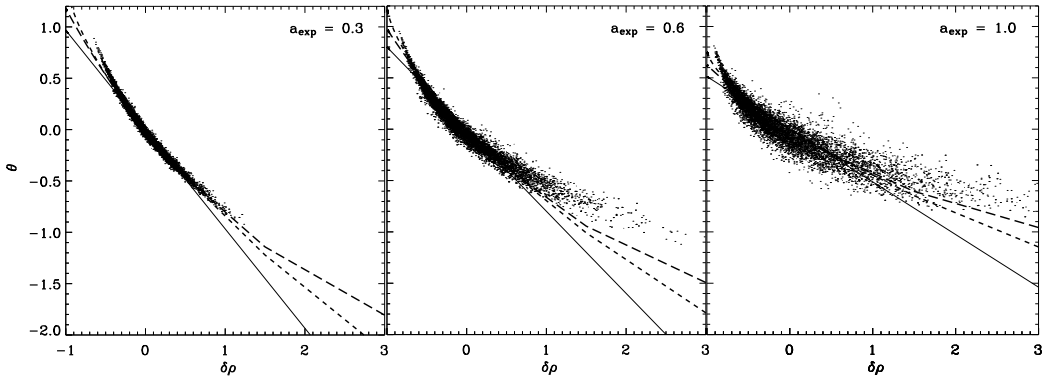

Figure 6.12 — Time evolution of the Zel'dovich density-velocity divergence relation. The cloud of points are given by the densities and velocities computed through the DTFE algorithm. The continuous lines indicate the linear theory prediction between the two fields, the short-dashed lines the 2nd order approximation relation, while the long-dashed the empirical relation.

Sec. 6.7.1. At later times (central panel) the relation still follow the expected behavior but with a larger dispersion toward high density regions. At underdense regions, the point distribution follows much better the empirical relation. The break at regions beyond $\delta < -0.8$ is expected since as was pointed out by Nusser & Dekel (1993) the empirical relation is not accurate in the range $-0.8 \leq \delta \leq 4.5$ because of non-linearity effects. The effect seen in Fig. 6.11 appears to have disappeared. The last frame shows the relation for $a = 1$ with a good agreement in general with the expected behavior. The scatter around the theoretical lines is larger than earlier times as a result of having used a pure kinematic model. At underdense regions smaller than $\delta < -0.8$, the measured relation bends more toward higher values of the velocity divergence. Apart from the problems of the relation at this regime, this effect has been amplified by the use of the kinematic model.

In conclusion, the presence of the bouncing effect at low-density regions seen in the reproduction of the non-linear density-velocity divergence relation has not been found when using the kinematic Zel'dovich approximation. This implies that such effect is genuine and not an spurious or artificial effect introduced by the DTFE velocity method.

6.8 The velocity divergence probability distribution function

BW96 explicitly applied Delaunay tessellations to the velocity divergence field to test the validity of the second order perturbation theory results (Bernardeau 1992). This was in particularly interesting as a mildy non-Gaussian velocity divergence distribution would enable the breaking of the degeneracy between the cosmic matter density Ω_m and the bias b between the matter and galaxy distribution (Bernardeau 1994; Bernardeau et al. 1995). Bernardeau et al. (1997) used the probability distribution function [PDF] of the velocity divergence to constrain the value of Ω_m (see also Bernardeau 1994; Bernardeau et al. 1995). Juszkiewicz et al. (1995) studied the PDF of the mass density contrast and the peculiar velocity divergence from evolved Gaussian initial density fluctuations in the weakly non-linear regime using perturbation theory. Their aim was to derive constraints on the nature of primordial fluctuations, the value of the cosmological density parameter, and the physical processes that govern galaxy formation. Here we present the probability distribution function for the normalized velocity divergence θ, computed from the reconstructed DTFE velocity fields smoothed with a Gaussian filter of $R_G = 5\ h^{-1}$Mpc, and its evolution as a function of the cosmological expansion factor a.

Figure 6.13 shows the PDF of the reconstructed DTFE velocity divergence computed at $a = 1$. Note that DTFE reproduces the expected sharp cutoff at the positives values of θ (see also BW96), which

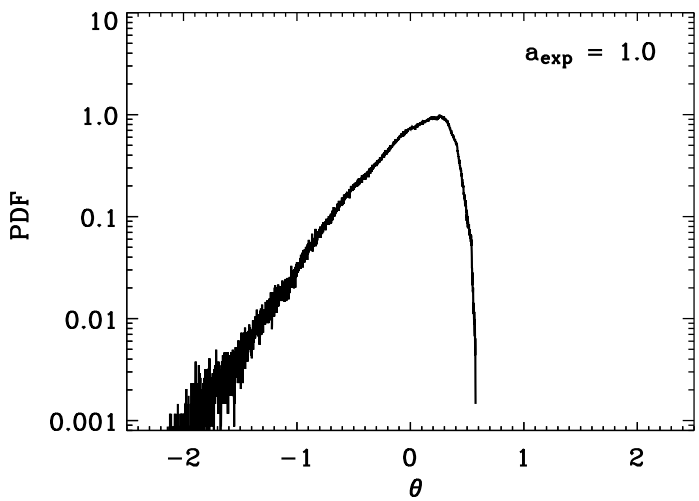

Figure 6.13 — Probability distribution function [PDF] of the normalized DTFE velocity divergence θ at actual time. The velocity divergence has been Gaussian smoothed with a kernel of $R_G = 5\,h^{-1}$Mpc.

corresponds to voids. This sharp cut in the PDF allowed Bernardeau et al. (1997) to reconstruct the value of Ω_m from $N-$body simulations following the work of Dekel & Rees (1994). At the opposite side, the high-density regions, the method manages to trace the PDF down to probabilities of 10^{-3}.

Figure 6.14 presents the evolution of the DTFE PDF velocity divergence as a function of the cosmological expansion factor. Although, the first top panel indicates an $a = 0.$, this is in reality the PDF of the initial Gaussian field used for the simulations set at $a = 0.02$. Since the velocity divergence is an indicator of the amount of structure present on the field, the growth of structure can be traced along the time evolution of the PDF. Notice how the PDF evolve from an almost perfect Gaussian distribution (very early times) into a non-Gaussian shape with negative skewness. This is because in the non-linear regime the inflows to high-density regions are faster than the outflows from low-density regions. Therefore, negative values of the velocity divergence correspond to overdense regions, while the positive values to underdense ones. The appearance of weakly non Gaussian features is shown in the PDF at $z \approx 4$ ($a = 0.2$), where the PDF starts to deviate from a symmetric (Gaussian) distribution. This can be better noticed in Figure 6.15. The distributions in the top panels and bottom-left one represent the first four stages of the evolution of the PDF plotted in a linear scale. The gray lines are the best Gaussian fits to the PDFs. Note that as the structure formation process evolves with time the PDF deviates more from its respective Gaussian distribution. This departure has been quantified in the bottom-right panel of Fig. 6.15. The plot shows the residual excesses between the density-velocity divergence PDF and the best Gaussian fit for the four stages of the PDF. At $a = 0$ and $a = 0.1$ the residuals are less than 5%, at $a = 0.2 \approx 10\%$, and at $a = 0.3 \approx 15\%$. These discrepancies continue raising up to almost 30% at present time. The larger and most notorious differences are located at the positive values of θ. The negative residuals at the most positive values of θ imply that voids evolve into the non-linear regime much faster than high-density regions. The presence of "noise" in Figs. 6.14 and 6.15 and its growth as a function of time at the negative tail of the PDF is an indication of the evolution of clustering of matter into high-density regions, such as cluster of galaxies.

The positive side of the PDF in Fig. 6.14 evolves much more quietly. This is indicated by the almost unchanged shape of the PDF at the positive values of θ. Notice that the shape of the PDF around its maximum becomes sharper as structure grows and it shifts from 0 toward positive values of θ. The shift of the maximum produces the largest discrepancy from the Gaussian fits as can be noticed from the bottom-right panel. Particularly noteworthy is the sharp cut at high-values of the PDF at later times.

The fact that the PDF preserves almost the same shape from $a = 0.6$ ($z = 0.66$) until present time, apart from the increase of noise at the negative tail, is an indication of the quietness of the velocity field and that the growth of structure formation has stopped. Indeed, structures which become non-linear

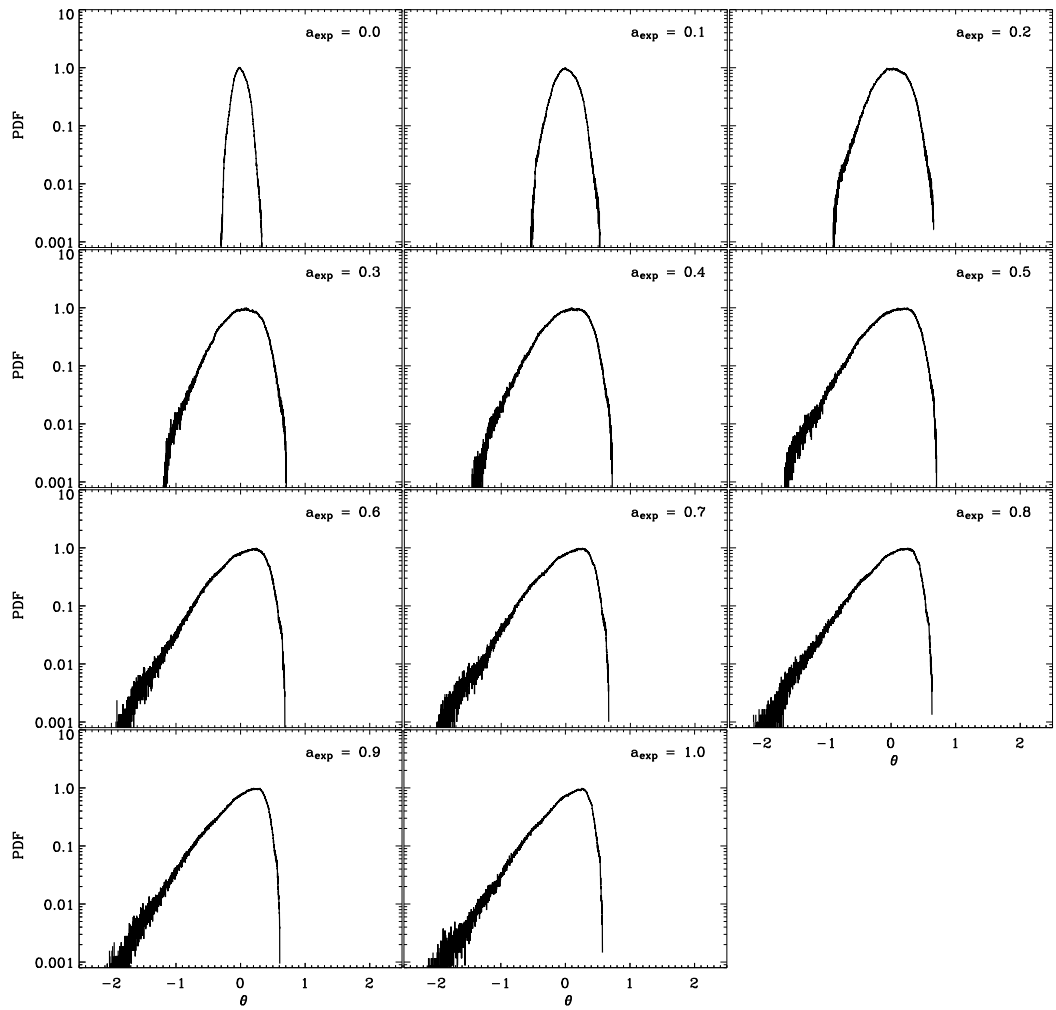

Figure 6.14 — Evolution of the probability distribution function [PDF] of the DTFE velocity divergence as a function of the cosmological expansion factor a_{exp}. Each of the velocity divergence fields has been smoothed with a Gaussian filter of $R_G = 5\,h^{-1}$Mpc.

(voids and clusters of galaxies) stop growing at the redshift,

$$1+z \approx \frac{1}{\Omega_m} - 1\,, \tag{6.19}$$

at which they decouple from the Hubble expansion. At this redshift, structures experience first contraction and collapse, followed by virialization to turn finally into genuine cosmic objects. For our particular $N-$body realization ($\Omega_m = 0.3$), this happens at $z \approx 1.3$ ($a = 0.43$). The same epoch at which the DTFE velocity divergence PDF deviates from a Gaussian distribution.

6.9 Void expansion: constraints on Ω_m

Dekel & Rees (1994) proposed the idea to use the outflow from voids to constrain Ω_m. The idea is based on the observation that large outflows are not expected in a low-Ω_m universe. From the fact that $\delta \approx -\Omega_m^{-0.6}\nabla\cdot\mathbf{v}$ (Eqn. 6.1), the inferred density from a given velocity divergence field becomes

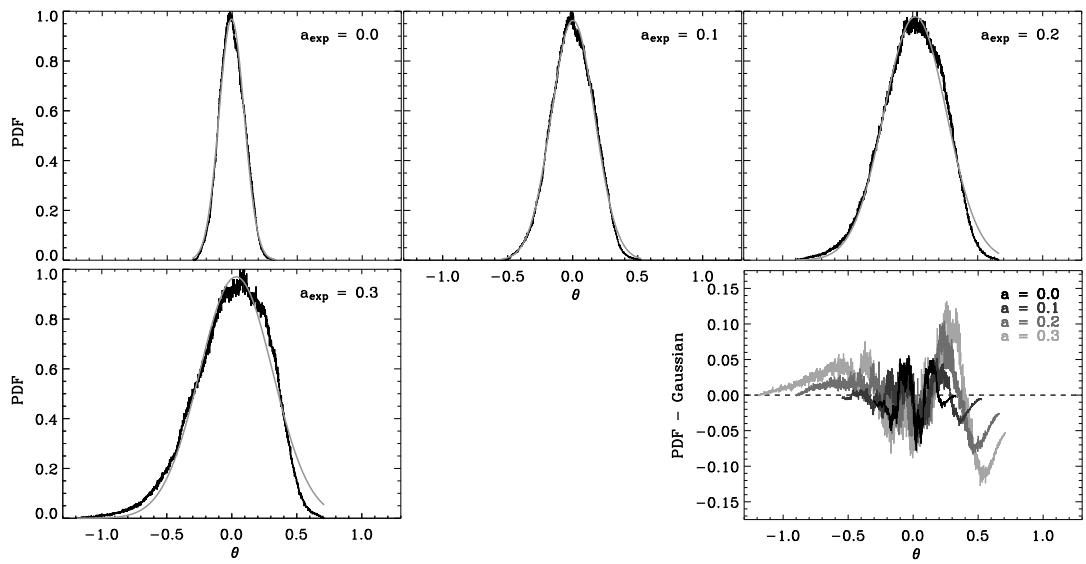

Figure 6.15 — Evolution of the probability distribution function [PDF] of the DTFE velocity divergence for the first four cosmological expansion factors ($a_{exp} = 0., 0.1, 0.2, 0.3$, top row panels and bottom-left). The PDFs are plotted in a linear scale. The gray distributions in each panel correspond to their best Gaussian fits. The bottom-right panel shows the residual excess from the PDFs and their corresponding Gaussian fits. Each of the velocity divergence fields has been smoothed with a Gaussian filter of $R_G = 5\ h^{-1}$Mpc.

more negative if one assumes lower Ω_m values. Under such assumption, one can obtain $\delta < -1$ in void regions. Evidently, this is an impossible value since one cannot get "emptier than empty", providing in this way a lower bound on Ω_m.

Dekel & Rees used this idea and applied a quasi-linear Zel'dovich-based approximation of the continuity equation (Nusser et al. 1991) to the Mark III catalog of peculiar velocities (Willick et al. 1997a) smoothed at 12 h^{-1}Mpc, more in concrete to the Sculptor void, finding that values of $\Omega_m \approx 1$ were perfectly consistent with the data, and that low density universes ($\Omega_m = 0.2, 0.3$) were ruled out at $\approx 2\sigma$ level. Their "high" Ω_m determination is related to the interpolation scheme used in the POTENT algorithm, a fixed grid-based algorithm (see Section 6.3.1). Such methods cannot reproduce the sharp cut-off at the positive side of the velocity divergence PDF. Instead, they suffer from spurious tails at both ends of the distribution (BW96).

By using the results of perturbative theory, Bernardeau et al. (1997) showed that the cutoff location of the velocity divergence PDF θ_{max}, strongly depends on Ω_m, as indicated by Dekel & Rees (1994), and it can be used to constrain such parameter by the following relation:

$$\theta_{max} = 1.5\ \Omega_m^{0.6}\,. \tag{6.20}$$

The value of 1.5 in the later equation is the difference in value in the Hubble parameter between an empty universe ($\Omega_m = 0$) and an Einstein-de Sitter universe ($\Omega_m = 1$).

Here we have used Eqn. 6.20 in order to recover Ω_m from our $N-$body simulations. Our intention is not to give a full statistical proof of the measurements but rather to show the possibilities and capabilities of the DTFE velocity method.

We have used the velocity dispersion PDF shown in Fig. 6.14 to estimate the density parameter. Following Eqn. 6.20 we find that the measured DTFE density parameter from the 5 h^{-1}Mpc smoothed velocity divergence is $\Omega_{m,DTFE} = 0.21$ at present time. This is not very different from the input $N-$body simulation value of $\Omega_m = 0.3$. This measured value should be interpreted as a lower bound as mentioned earlier since Eqn. 6.20 follows the assumption that in void regions δ is strictly

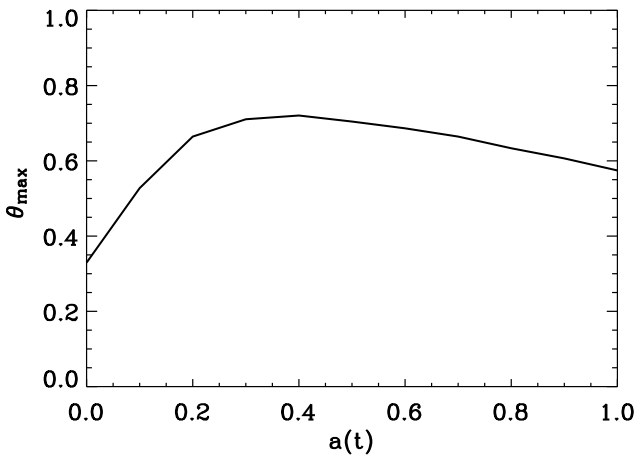

Figure 6.16 — Evolution of the cutoff of the DTFE velocity divergence PDF as a function of the expansion factor a.

equal to -1, which is not necessarily true.

Some comments about the sharp cutoff of the PDF and its time evolution as shown in Fig. 6.14 are noteworthy. The evolution of underdense regions should follow a linear expansion as predicted by the spherical model, until shell crossing occurs. At this point, voids will not expand as fast anymore. Depending on the environment in which voids are embedded, some of them will start to collapse. Figure 6.16 shows the evolution of the PDF cutoff as a function of the cosmological expansion factor.

The curve of the measured maximum of the velocity divergence PDF, θ_{max}, suggests that the underdense regions start to get empty very fast. After $a = 2$ the growth of such regions decreases considerably up to $a \approx 4$, where the curve has an inflection point. This transition region coincides with the appearances of non-linear features in the PDFs (see Fig. 6.15). The inflection point at $a \approx 4$ agress with the theoretical prediction that structure growth stops at $a = 0.43$ (see Eqn. 6.19). However, we should be cautious with this result since the physical box size of our simulation is not large enough (100 h^{-1}Mpc). This could imply that the underdense regions are gravitationally interacting with themselves because the long waves of the power spectrum have exceeded the box size.

6.10 From velocity divergence to density field

Dekel et al. (1999) using the POTENT algorithm and second and third-order corrections to the Zel'dovich approximation derived satisfactory density fields from the smoothed velocity field with kernel sizes of $R_G = 10, 12\ h^{-1}$Mpc based on the Mark III catalog.

While POTENT is based upon linear theory and mildly non-linear approximations, the performance of DTFE with respect to non-linear structures and its reproduction of the non-linear density-velocity divergence relation give us strong confidence to reconstruct the density field from the velocity divergence field.

The intimate relationship between the density and the velocity divergence can be noticed in Figure 6.17. The top-left panel shows the reconstructed density field from the DTFE velocity divergence field smoothed at 2 h^{-1}Mpc, using only the linear prediction. The top-right panel shows the density reconstruction using the 2nd order approximation of Bernardeau (1992) convolved with the same filter. The bottom-left panel presents the DTFE density field as computed from the discrete particle distribution. The similarities between the three maps are indeed remarkably good. The better agreement betwen the 2nd order reconstruction and the density field can be noticed at the bottom-right panel. This plot shows the residual density estimates resulted from substracting the linear and 2nd order reconstructed densities to the real density ($\delta - \delta_{rec}$), black and gray point distributions respectively. As

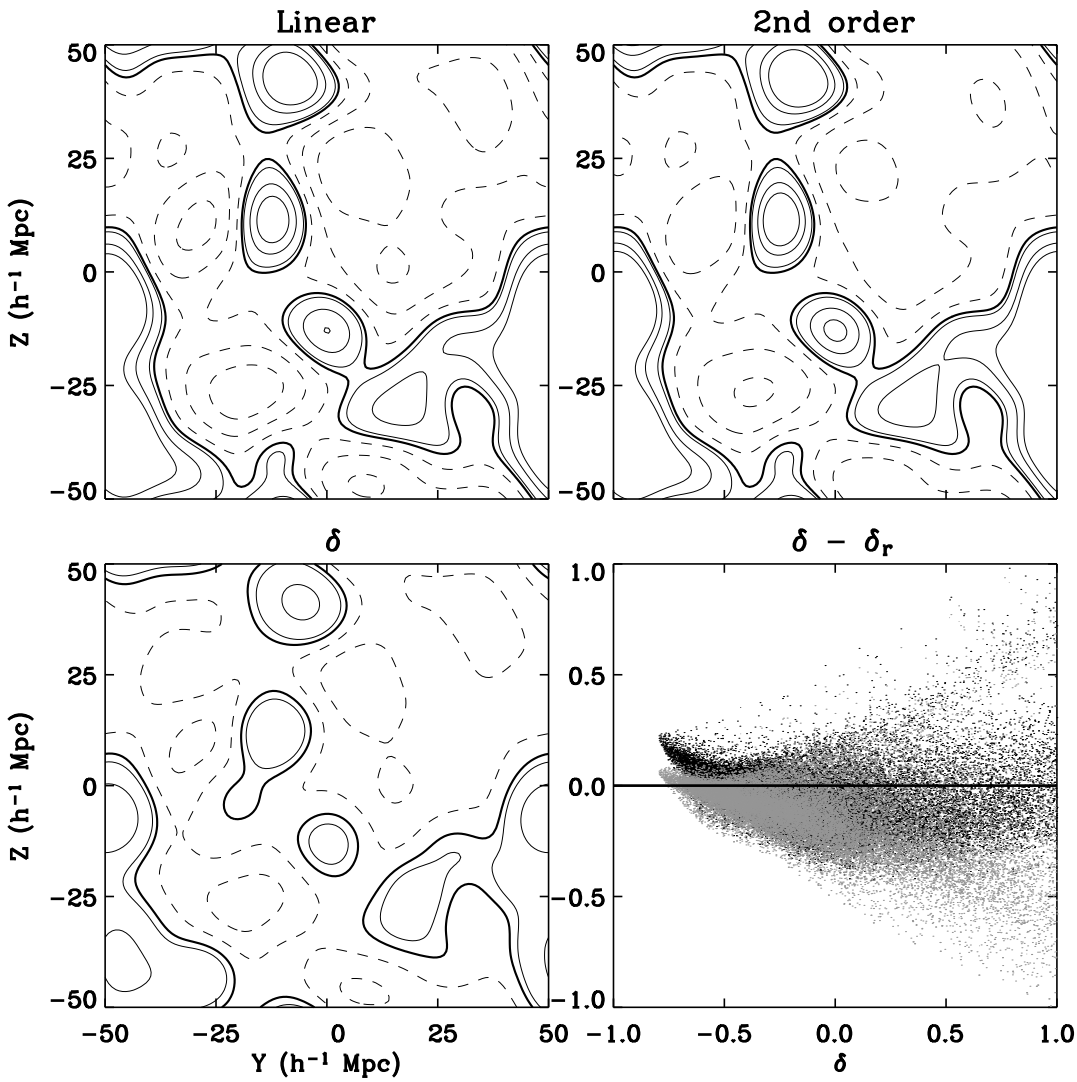

Figure 6.17 — DTFE density field reconstructions from the velocity divergence. The top-left panel shows the denisty reconstructed from the linear density-velocity divergence relation. The top-right panel the reconstruction using the 2nd order perturbative approximation. The bottom-left panel shows the real density field. The bottom-right panel present residual point-to-point comparison between the recontructed density fields and the reald density one. All fields have benn convolved with a Gaussian kernel of 2 h^{-1}Mpc.

can be noticed, high-density regions present a large scatter since both relations are not completely valid at these regimes. At low-density regions the 2nd order reconstruction gives better estimates as expected.

6.11 Shear and Vorticity

The shear and vorticity terms (Eqn. 6.14 & 6.15) are the other two components which are recovered when computing the velocity gradient matrix (see Section 6.4.3). Shear and vorticity patterns are expected to be particularly prominent near high-density regions, where distortions in the velocity flows are particularly strong. In general, vorticity measures the speed of rotation of a fluid element, while

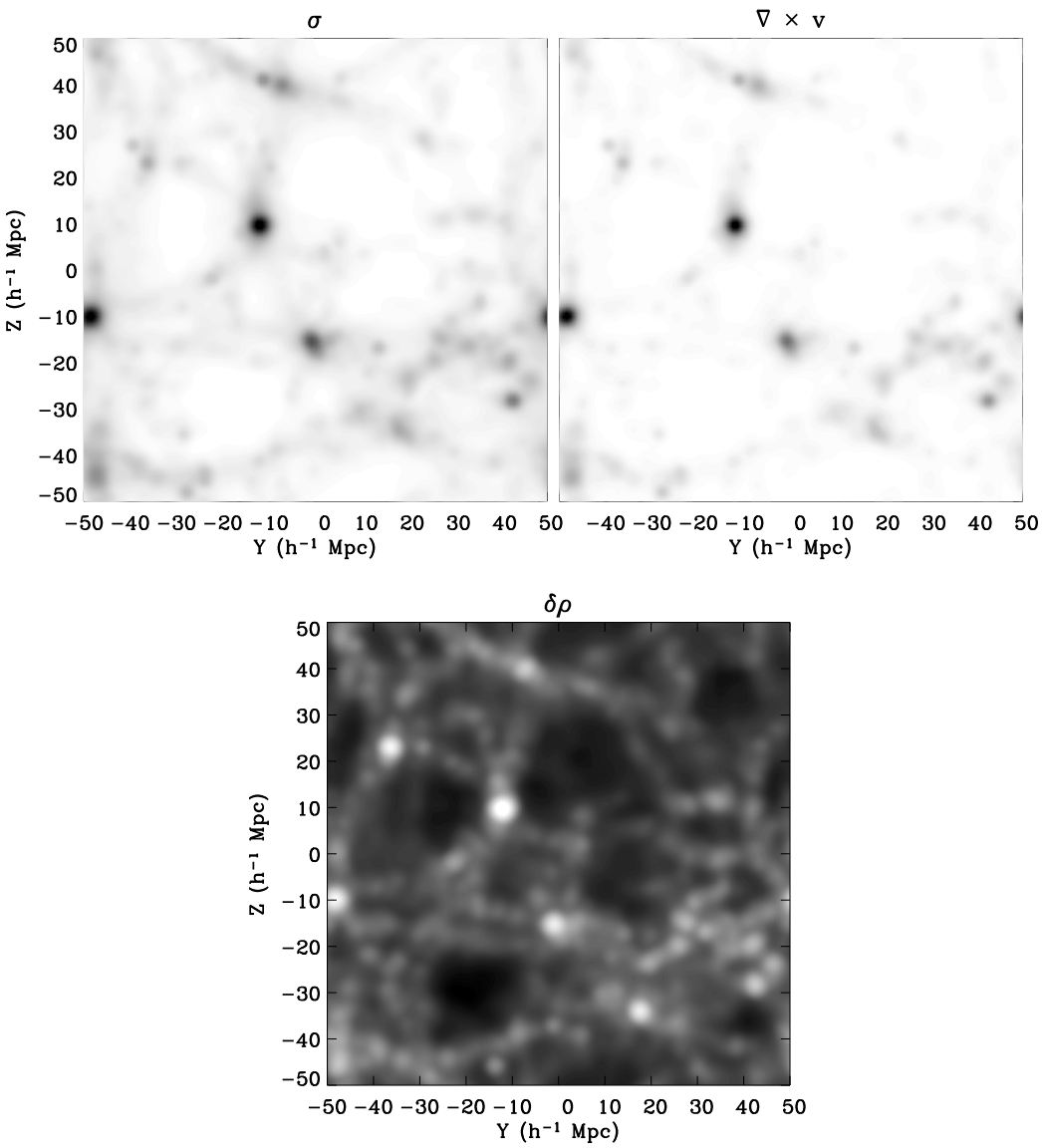

Figure 6.18 — DTFE recovered velocity shear and vorticity amplitudes (top left and right panels respectively) and density field (bottom panel) for the same slice of the velocity field presented in Fig. 6.5. We have inverted the color scales of the shear and vorticity to enhance the contrast between the different structures.

shear measures the anisotropy in its expansion rate. The shear is a dominant factor in shaping the large scale structure (e.g. Hoffman 1986; van de Weygaert & Babul 1994; Bond et al. 1996).

Figure 6.18 shows for the same slice projection presented in Figs. 6.9 & 6.17 the shear and vorticity amplitudes, $\sigma = (\Sigma\sigma_{ij}\sigma_{ij})^{1/2}$, $\omega = (\Sigma\omega_{ij}\omega_{ij})^{1/2}$ (left and right top panels respectively) and the density contrast reconstructed with the DTFE method. Each fields has been convolved with a Gaussian kernel of $R_G = 1\ h^{-1}$Mpc. We have inverted the color scales of the shear and vorticity with respect to the density one in order to get a better enhancement of the shear and vorticity patterns present in the maps. As can be noticed, both top panels trace very well the matter distribution (bottom panel). The velocity shear unveils more the large scale structure pattern of the matter distribution than the

vorticity mode since the shear is more prone to the linear and weakly non-linear matter distribution than vorticity. Because the velocity field is expected to be irrotational, at least in linear theory, vorticity can only appear around non-linear structures like cluster of galaxies where strong infall motions are presented (Peebles 1980). The vorticity plot clearly shows that this term is mainly present at the high density regions. Most of the field is curl-free in accordance with the linear prediction. However, some vorticity is present at not very dense regions, indicating a possible failure of the method in properly reconstructing the velocity field at these regions. We will discuss this in more detail in Section 6.11.4.

6.11.1 The density-shear relation

The shear in the velocity field can be due to the intrinsic asphericity (anisotropic collapse) of evolving structures and/or can be due to tidal forces acting around the local matter distribution exerted by the large scale matter distribution. Therefore, it is expected to be present at linear, quasi and non-linear regions as a result of interaction and the collapse of matter. In fact, the rate of growth of the density field gets amplified in the presence of shear because this increases the rate of growth of fluid convergence $-\nabla\cdot\mathbf{v}$ following a given fluid element (Hoffman 1986; Bertschinger & Jain 1994). This convergence is precisely located around collapsing structures, filaments and clusters (see Section 6.7). Hoffman (1986) and Bond, Kofman, & Pogosyan (1996) pointed out that the filamentary web is a consequence of the distribution and spatial coherence of the shear field in the medium (see also van de Weygaert 2002). Therefore, it is expected that the density and velocity shear should be correlated as a function of time. Although, there is no clear relation between the density and velocity shear like via the continuity equation. In the linear regime, the velocity shear is related to the density excess growth factor $D(t)$ via (van de Weygaert & Bertschinger 1996),

$$\sigma_{ij} \propto D(t)H(t)f(\Omega_m), \tag{6.21}$$

and therefore, to the density field since $\delta(t) \propto D(t)$. In general, the evolution of the velocity shear tensor σ_{ij} is strictly related to the tidal tensor $\mathcal{T}_{ij}$,

$$\mathcal{T}_{ij} \equiv \frac{1}{a^2}\left\{\frac{\partial^2\phi}{\partial x_i \partial x_j} - \frac{1}{3}(\nabla^2\phi)\delta_{ij}\right\}, \tag{6.22}$$

where ϕ is the gravitational potential, and δ_{ij} the Kronecker delta. This evolution can only be calculated by solving the (non-local) Possion equation.

Figure 6.19 shows the evolution of the density-velocity shear amplitude distribution as a function of the expansion factor. The velocity shear is expressed in units of $H(t)$, the Hubble parameter at the given cosmological expansion factor. Since the velocity shear is the result of tides, then it is expected that at early times this term would not be necessary zero, but rather small. The first top panels show that indeed, the amplitude of the velocity shear is very small. Although, as discussed in Section 6.7.1, at these times the density field reconstruction is not very reliable since density is badly sampled by the early particle distribution. However, the reconstruction of the velocities, and thus of shear, does not depend upon sampling process (see Sec. 6.7.1). At early times, the shear growth scales according to the linear prediction of Eqn. 6.21. The sudden rise of the velocity shear amplitude at $z \approx 4$ ($a = 0.2$) coincides with the appearances of weakly non-linear features in the velocity divergence PDF (see Fig. 6.14 & 6.15).

It can be noticed that while the structure formation process grows with time, the density-shear cloud distributions increase in amplitude and bend along the whole range of values. Also, the spread around the distributions increases considerably. At high-density regions this is an indication of the collapse of structures. Around linear and mildly non-linear structures such as filaments, the shear is large enough (> 70 km s^{-1} Mpc^{-1}) indicating that this term is a key element in the formation of filaments (Bond et al. 1996; van de Weygaert 2002). On the other hand, the shear is very small at underdense regions. This is because voids tend to become more spherical as they evolve. This implies that shear is minimized at the voids, while their dynamics is dominated by the expansion mode of the

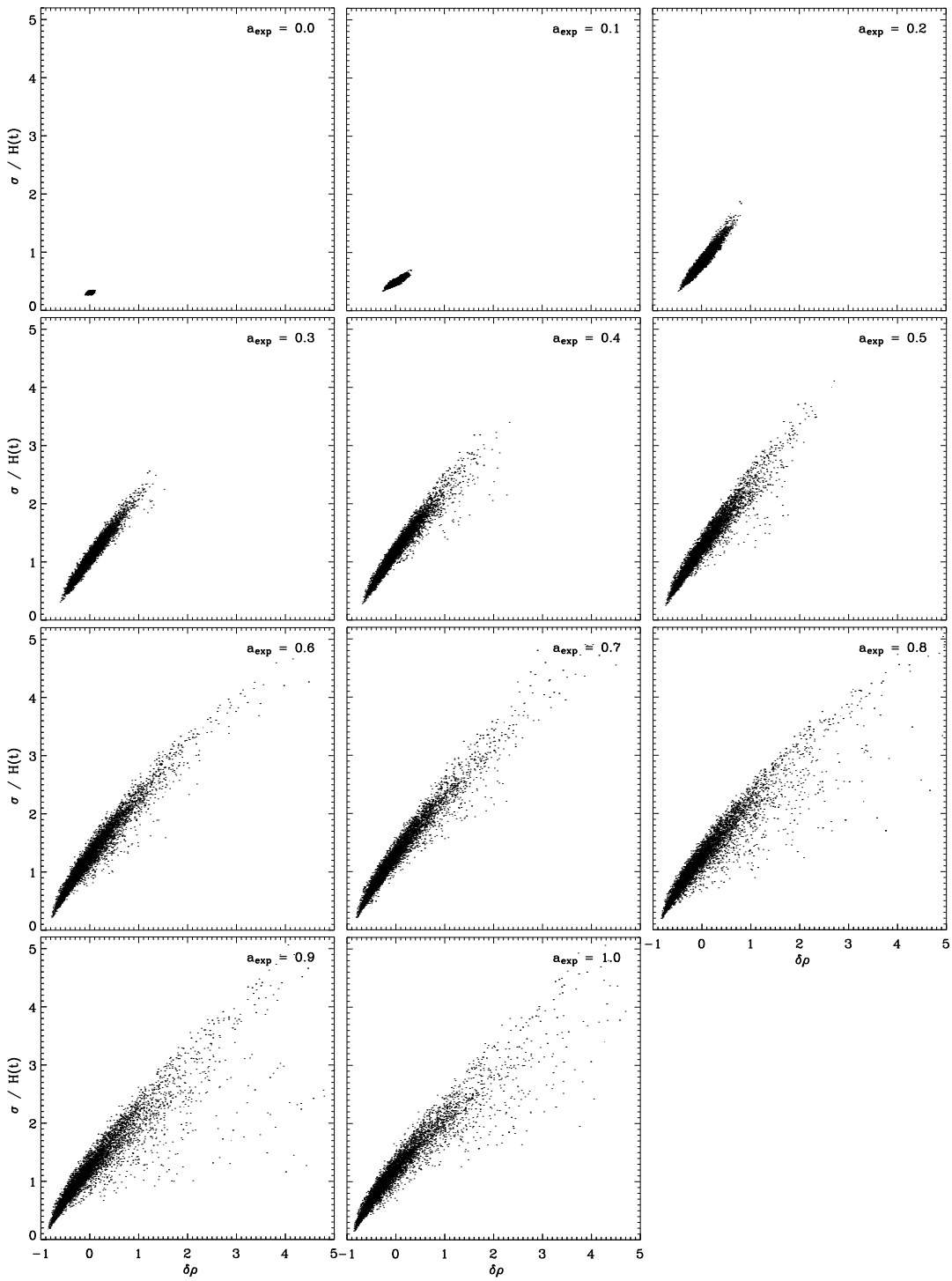

Figure 6.19 — Time evolution of the density-velocity shear amplitude relation computed by means of DTFE. We have expressed the shear in terms of the Hubble parameter.

velocity, positive divergence. If this would not have been the case, underdense regions could have collapsed if the shear is large enough (Bertschinger & Jain 1994). The visual impression from the left panel of Fig. 6.18 helps to clarify all these points.

As in the case of the density-velocity divergence relation, the shape of the density-velocity shear relation does not change considerably from $a \geq 0.4$, apart from the scatter at high-densities. This behavior is an indication that the growth of structures ceases and, that at least, in the linear and quasi-linear regimes, velocity fields are very coherent.

6.11.2 Shear matrix and eigenvalues

The velocity shear is a traceless symmetric tensor. The shear describes how the matter distribution is dynamically affected by its surroundings, i.e., if the matter distribution is being stretched or squeezed along a given direction. This information is contained within the eigenvalues and eigenvectors of the diagonalized matrix representation of the velocity shear tensor. The eigenvalues indicate the strength of the stretching or compression, while their directions are given by the corresponding eigenvectors. Here, we order the eigenvalues (and corresponding eigenvectors) according to their amplitudes, $\lambda_1 > \lambda_2 > \lambda_3$. Because the shear tensor is traceless, only two of its three eigenmodes will be linearly independent, i.e., $\sum \lambda_i = 0$. By construction, the eigenvectors form a unitary and orthogonal system. The amplitude of this shear reference frame will be given by the eigenvalues, and since these are different from each other, this is also know as the *velocity ellipsoid*. The first eigenmode (λ_1) is positively defined and indicates the direction and intensity of the maximum stretching exerted over a given region. The third eigenvalue (λ_3) is always negative, and corresponds to a compression along a direction perpendicular to the stretching one. The second eigenmode (λ_2) could be either positive or negative. The configuration of the tidal field is decided by this eigenmode, with an extra stretching or compression direction perpendicular to the first eigenmode. If $\lambda_1 > \lambda_2 > 0$ the velocity ellipsoidal describes a planar structure, if $\lambda_3 < \lambda_2 < 0$ then it describes a filamentary configuration.

In our approach, one could compute these eigenmodes for each Delaunay tetrahedron. However, for reasons of efficiency we did so from the grid interpolated velocity gradient field. By diagonalizing the shear matrix at each pixel's image, we find its eigenvectors and eigenvalues. Note that since the velocity-gradient matrix is not continuous, the computed eigenvalues and eigenvectors will no so too.

Figure 6.20 shows maps of the amplitude of the two linear independent eigenvalues (λ_1 and λ_2) for the same slice shown in previous map figures. The stretching mode (λ_1) traces the filamentary structure present in the map (see bottom panel of Fig. 6.18). This is larger at the core of the high-density regions than along filaments. As expected, no stretching is found at the void regions. In the case of the second eigenvalue, the brightest regions correspond to a positive mode ($\lambda_2 > 0$) and therefore, where stretching also occurs. Light regions can also be distinguished following the filamentary distribution. Most of the map corresponds to $\lambda_2 \approx 0$ (gray areas), mainly around the voids where almost no shear is present (see Fig. 6.19).

The amplitude of the eigenvectors are very illustrative in displaying the characteristics of the matter distribution. However, they are only part of the total information contained within the shear. In Figure 6.21 we present a more qualitative analysis. For the same slice shown in Figs. 6.18 and 6.20, we have computed a 2D cut of the velocity shear, and its projected eigenvalues and eigenvectors. This is equivalent to consider the intersection of the velocity ellipsoidal with the 2D plane. This has as result an ellipse whose major axis is the stretching mode and the minor axis the compression along such bisecting plane. Both modes are presented in Fig. 6.21 as "shear bars". The left panel represents the stretching mode, while the right panel the compressional mode. The bars are proportional to the amplitude of each eigenvalue and oriented according to their corresponding eigenvectors. The point distribution corresponds to the matter distribution in a slice of 5 h^{-1}Mpc thick centered along the eigenmodes cut. A seemingly correlation between the compressional bars and the filamentary structure of the point distribution can be noticed. This correlation is stronger in the case of the gravitational tidal field (see van de Weygaert 2002). The compressional bars are strong (large) and almost perpendicular to the filamentary structure. The dilational bars tend to be more aligned with the filament. The

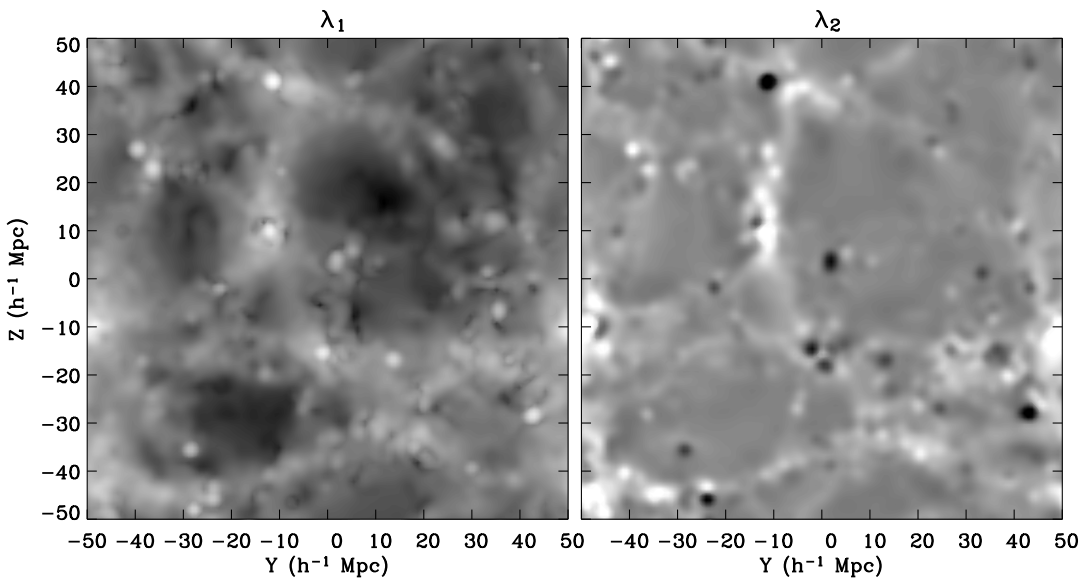

Figure 6.20 — Velocity shear eigenvalue maps of the same slice presented in Fig. 6.18. The left panel corresponds to amplitude of the largest eigenvalue (stretching mode) along the slice. The right panel shows the second eigenvalue which could be either positive (stretching, light regions) or negative (compression, gray-dark regions).

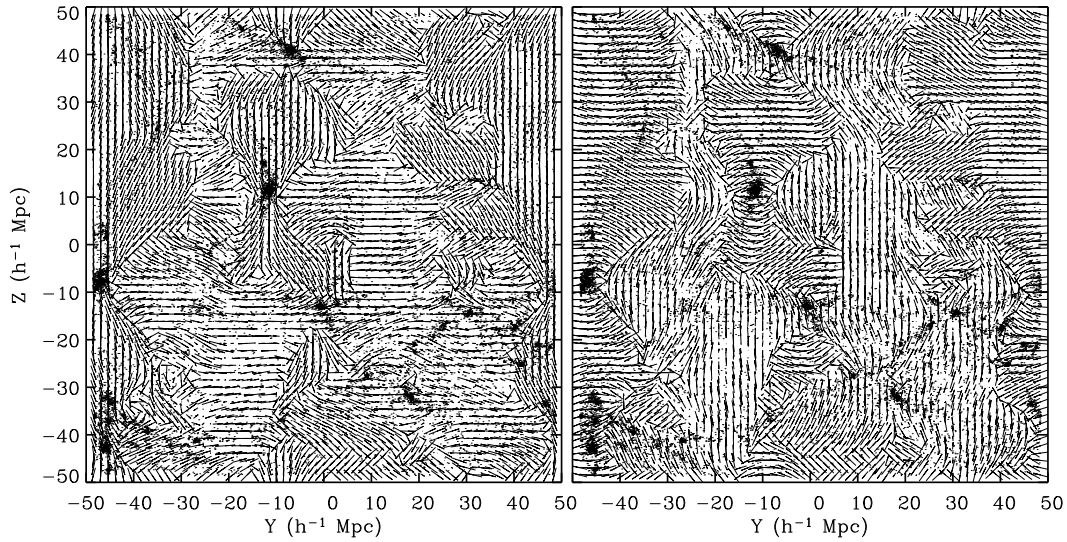

Figure 6.21 — Decomposition of the velocity shear components along the same slice of Fig. 6.20. The dilational (stretching) component is shown at the left panel, while the compressional component at the right panel. The bars are proportional to the intensity of the components and they are aligned along the corresponding eigenvectors' direction. The point distribution along a thicker slice is also present.

presence of more massive structures like clusters are delineated by the compressional bars as a result of infall motions around the cluster. With this representation, clusters are the "nodes" of the filamentary structure. On the other hand, underdense regions are very quiet in both representations. They are clearly recognized as those regions where bars are not perturbed, but rather aligned coherently.

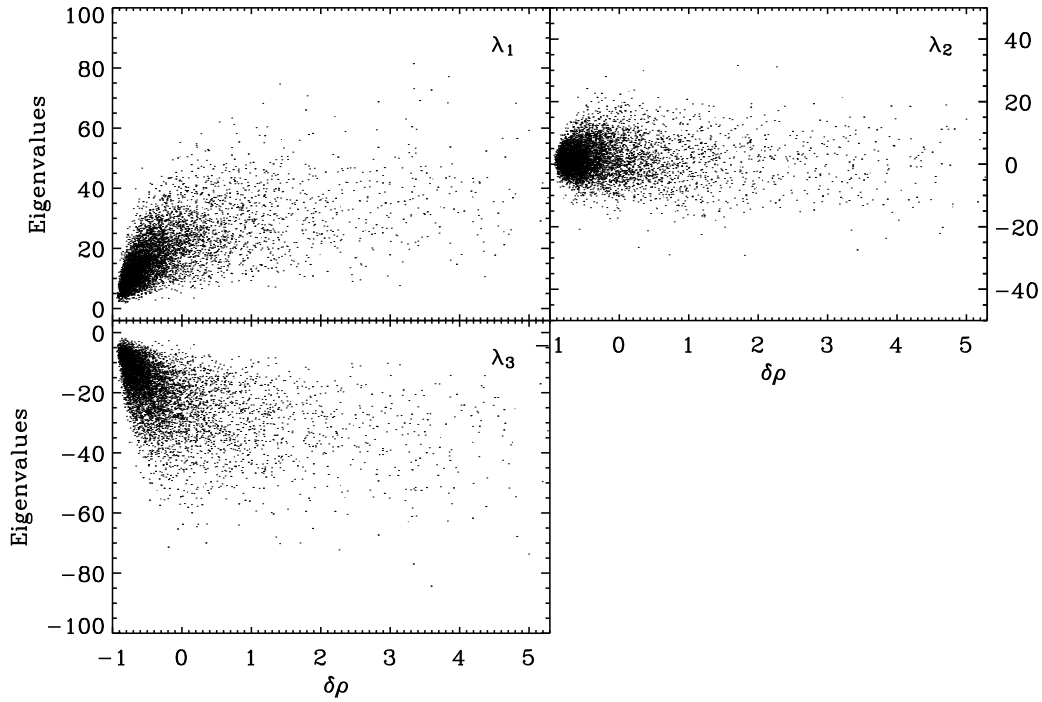

Figure 6.22 — Velocity shear eigenvalues *vs* density contrast. The three panels show the eigenvalue's dependence with density. The top-left panels shows the first eigenvalue, dilation. The top-right panel the second eigenvalue, middle. The bottom panel the third eigenvalue, compressional.

With the shear-bar analysis, we have shown the strong interplay between shear and the filamentary structure of the universe. This confirms the theoretical basis of the Zel'dovich formalism. Hoffman (1986) using such approximation noticed that objects with large initial shear collapse sooner than one would predict. This result can be derived from first principles from the Raychaudhuri equation which connects the velocity divergence evolution, shear and vorticity with the density field. According to the Zel'dovich formalism (Zel'dovich 1970), objects collapse first along the largest eigenvalue forming the Zel'dovich pancake, then along the next eigenmode to form filaments, and finally along the last eigenmode to collapse into clusters. If the primordial Gaussian velocity field was shear-less and irrotational, the velocity-gradient matrix will be isotropic, allowing spherical collapse as predicted by the spherical model.

In Figure 6.22 we plot the eigenvalues-density dependence for $a = 1$. The top-left panel indicates that stretching becomes stronger at higher density regions. The compressional component (bottom plot) also grows as a function of density, with the dense cores of clusters experiencing the largest compression. The middle eigenvalue does not present a clear correlation with density, but a rather symmetric distribution between the two possible modes as shown also in its respective PDF (see Fig. 6.23).

6.11.3 Time evolution of the shear eigenvalues

For the case of a Gaussian random density fluctuation field, Doroshkevich (1970) studied the distribution function of the eigenvalues of the shear tensor. The distribution of the two independent eigenvalues

(λ_1&λ_2) is given by,

$$P(\lambda_1,\lambda_2) = \frac{27}{4\sqrt{2\pi}} \exp\left[-\frac{15}{2}(\lambda_1^2+\lambda_1\lambda_2+\lambda_2^2)\right] \times (\lambda_1-\lambda_2)(2\lambda_1+\lambda_2)(\lambda_1+2\lambda_2)\,, \qquad -\infty < \lambda_2 < -(\lambda_1+\lambda_2) < \lambda_1 < \infty\,. \tag{6.23}$$

This yields a probability of 8% that all eigenvalues are negative, while 92% of the matter has one or more positive eigenvalues.

We have traced the evolution of the shear eigenvalues as a function of the expansion factor, which in principle are linked to the matter structure evolution. It is therefore expected that the eigenvalues will be smaller at early times and grow according to the collapse of density fluctuations at different times. This can be better understood in Figure 6.23 which shows the time evolution of the PDF from the three eigenvalues for three expansion factors. The eigenvalues have been computed from the smoothed velocity shear at 2 h^{-1}Mpc. For comparison purposes we have also plotted the eigenvalues distributions computed according to the Zel'dovich formalism at the given times (gray lines), normalized with respect to the maximum of the $N-$body PDFs. It it clear that the eigenvalue's distributions extend toward higher values at later times as a result of the evolution of the structure formation process. Since it has been proved that the Zel'dovich approximation performs very well even beyond the linear regime, it is not surprising that the two type of distributions for the three eigenvalues are very similar. These similarities are stronger at earlier times where the approximation is still valid (top row). Both distributions peak at the same value for the three eigenvalues, although the $N-$body dilation is somewhat larger than the Zel'dovich. This is expected since the later is just a kinematic approximation which at first order is correct. At later times, differences in the distributions become more pronounced as structures get into the non-linear regime. The $N-$body eigenvalues indicate that there is more stretching than with the Zel'dovich formalism as the result of the non-linear evolution of structures. On the other hand, both $N-$body and Zel'dovich compressional modes are very similar to each other. Although, the compressional contribution from the middle eigenvalue is relatively larger in comparison with the Zel'dovich one.

6.11.4 The density-vorticity relation

According to the linear theory of gravitational instability (Peebles 1980), the large scale velocity field is expected to be irrotational, $\nabla \times \mathbf{v} = 0$. Any vorticity mode would have decayed away during the linear growth of density fluctuations, and the only growing modes are curl-free. Based on Kelvin's circulation theorem, the flow remains vorticity free as long as it is laminar, i.e., with no orbit crossing (Bertschinger & Dekel 1989; Dekel et al. 1990). This condition is expected to hold even in the weakly non-linear regime (Bertschinger & Dekel 1989). Therefore, it is expected that vorticity is only present around the non-linear features of the density field.

Figure 6.24 shows a zoom over the density and velocity field (image and vector field respectively) of a galaxy cluster from the simulation. The gravitational pull onto the surrounding matter distribution of such massive cluster can be recognized in its respective velocity field. At the top and bottom ends of the cluster perturbations to the velocity field (infall motions) are presented as shear and vorticity. Notice how the latter becomes stronger toward the cluster centre indicated by the circulation pattern. The presence of vorticity in the velocity maps has to be ascribed to two effects. The first one is physical and induced by the cluster. The second effect is that the vorticity is partly introduced by the method itself since it cannot recover motions properly at high-density regions where the linear interpolation breaks down. At this stage we cannot disentangle how much vorticity is physical and how much is due to the method's failure. From the "linearized" field (smoothed with $R_G = 5\ h^{-1}$Mpc, right-hand panel) we can notice that the vorticity around the cluster outskirts is real since it is still present. The vorticity mode has diminished considerably, mainly at the center, but it is still present around the cluster, being this a real effect.

As the collapse of structures is responsible for generating vorticity in the velocity field (orbit crossing), it is expected then that vorticity grows as linear structures evolve toward the non-linear regime.

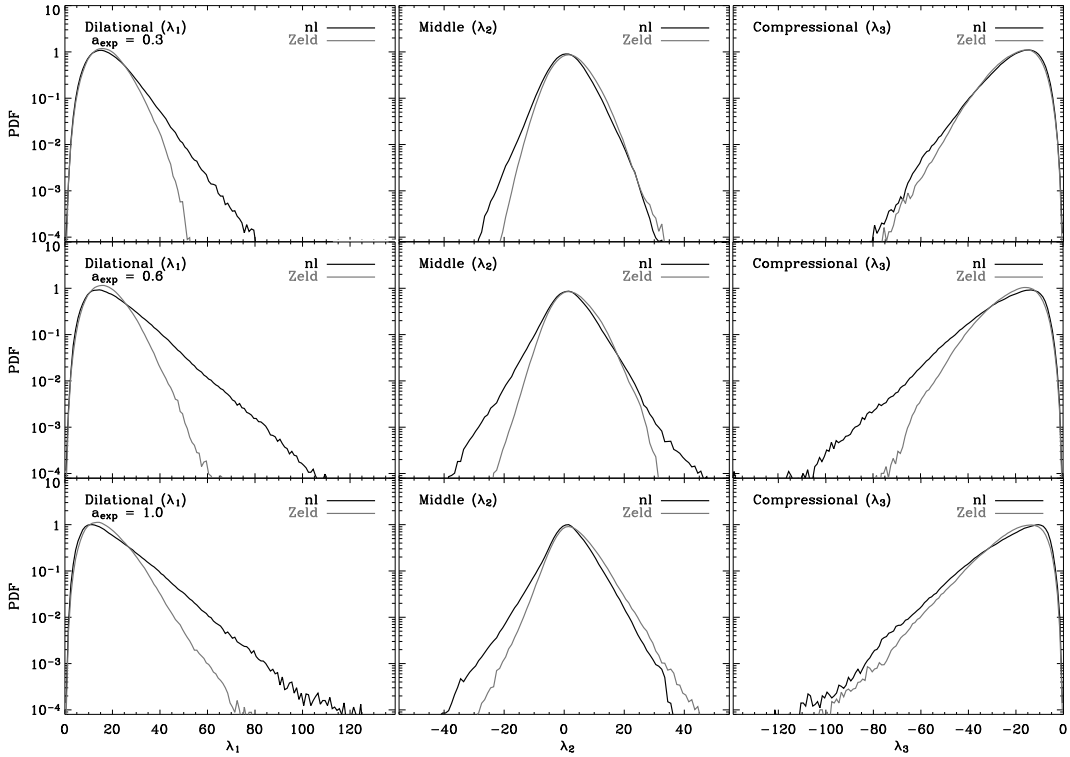

Figure 6.23 — Velocity shear eigenvalues PDF computed at three different expansion factors. The bold lines correspond to the eigenvalues computed from the $N-$body simulation (nl). The gray lines represent the eigenvalues computed from the Zel'dovich approximation (Zeld) at the given expansion factor. The left-hand column shows the dilation (λ_1), the central column the middle (λ_2), and the right-hand column the compressional mode (λ_3).

Figure 6.25 shows the evolution of the density-vorticity relation as a function of the expansion time a, where the vorticity ($\omega = (\Sigma\omega_{ij}\omega_{ij})^{1/2}$) has been expressed in terms of the Hubble parameter $H(t)$ at the given time. Both quantities have been smoothed with a Gaussian filter of 5 h^{-1}Mpc to erase any distortion introduced by DTFE. As expected, at very early times the vorticity is of the order of zero, but almost similar to the shear. It starts to become noticeable when non-Gaussian features are present on the field ($z \approx 4, a = 0.2$), which reflects the behavior of the shear. In general, the vorticity is very small at low density regions and grows almost linearly toward mild density regions (situation present at all panels). At high-density regions, the point distribution spreads over a large range of vorticity values. This becomes more noticeable at latter times. Comparing the shear and vorticity amplitudes (Figs. 6.19 and 6.25), it can be noticed than in general, the vorticity is much smaller than the shear along the whole range of densities as expected. Figure 6.26 shows a contour plot of a point-to-point comparison between the velocity shear and vorticity computed at actual time (both quantities expressed in terms of H_0). In general, the vorticity is ≈ 3 times smaller than the velocity shear. Notice that both terms are related almost linearly. This is not surprising since shear and vorticity are the symmetric-traceless and antisymetric part of the velocity-gradient matrix respectively.

6.12 Conclusions

We have presented a method based on the Delaunay Tessellation Field Estimator algorithm [DTFE] to reconstruct continuous volume-weighted and fully volume-covering peculiar velocity fields from

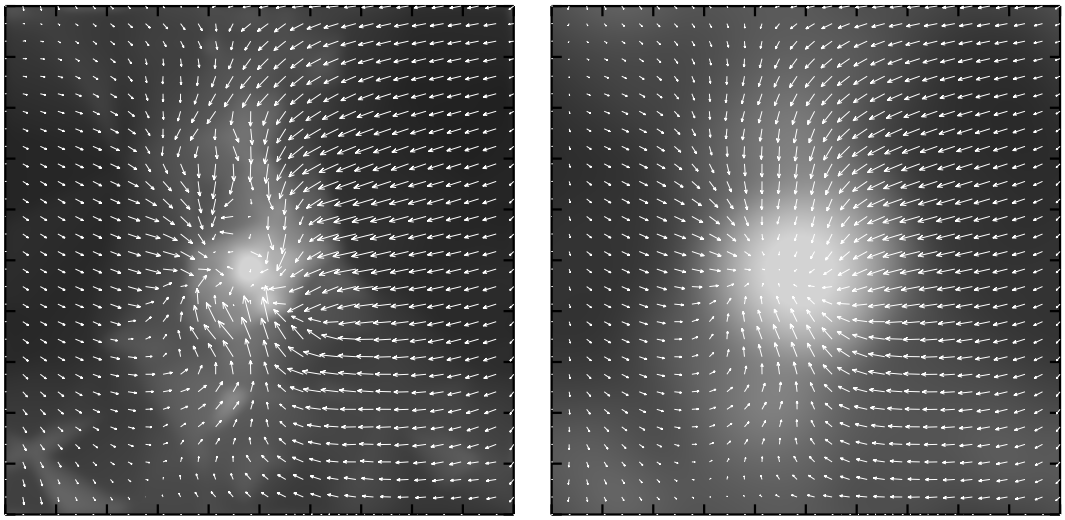

Figure 6.24 — Zoom over a galaxy cluster's density and velocity field (image and vector field respectively) smoothed with a Gaussian filter of $R_G = 1\ h^{-1}$Mpc (left panel) and $R_G = 5\ h^{-1}$Mpc (right panel). Notice how the velocity field is highly distorted by the mass distribution (left panel) introducing vorticity modes around the density field. Such distortions are less pronounced at the linearized (right) panel, still some vorticity can be noticed.

a discrete set of $N-$body peculiar velocities. The method does not make use of any pre-specified smoothing kernel, which allows it to adapt to the geometry of the point distribution sampling the velocity field, and therefore, to resolve velocity fields at both low and high density regions at once. The method involves a scheme based on the Delaunay tessellation defined by the sampling point process, and linear interpolation with Delaunay tetrahedra intervals.

Field value estimates from conventional grid-based methods are usually mass-weighted instead of volume-weighted. Therefore, comparisons with theoretical predictions which refer to volume-weighted quantities are difficult. These methods cannot resolve velocity fields at high-density regions while keeping an acceptable velocity reconstruction at low density regions. The computation of high-resolution reconstructed velocity fields with grid-based methods introduce spurious effects at regions devoid of objects and in high-density ones that one cannot obtain reliable estimates. On the other hand, if one wants to recover information at low density regions, low-resolution interpolations are needed at the cost of smearing high-density regions.

The DTFE velocity reconstruction procedure does not suffer from these problems. The DTFE method offers a higher spatial resolution than conventional methods at high density regions, while preserving the velocity features of low density regions devoid of objects without suffering from shot-noise effects. The velocity field at underdense regions are rendered as realistically slowly varying motions due to the linear interpolation scheme of the method. This interpolation has proven to give correct results in the sense that the void's velocity profile resembles a super Hubble-like linear expansion as predicted by analytical models. At high-density regions, the method traces with high resolution the infalling velocity patterns towards and around these regions. At regions where shell crossing has occurred, i.e., high-density regions such as cluster of galaxies, the interpolation is not completely valid. Virial motions can not be properly recovered and the reconstructed velocity field is discontinuous. However, a simple smoothing procedure helps to improve the field estimates.

We have shown that the DTFE velocity method is in general a very robust method. It does not suffer from sparse sampling effects, provided that the sampled velocity field traces the underlying full field. The reconstructed diluted samples are in good agreement with respect to the full sample.

In the case of Gaussian like velocity uncertainties, the comparison with respect to the true velocities

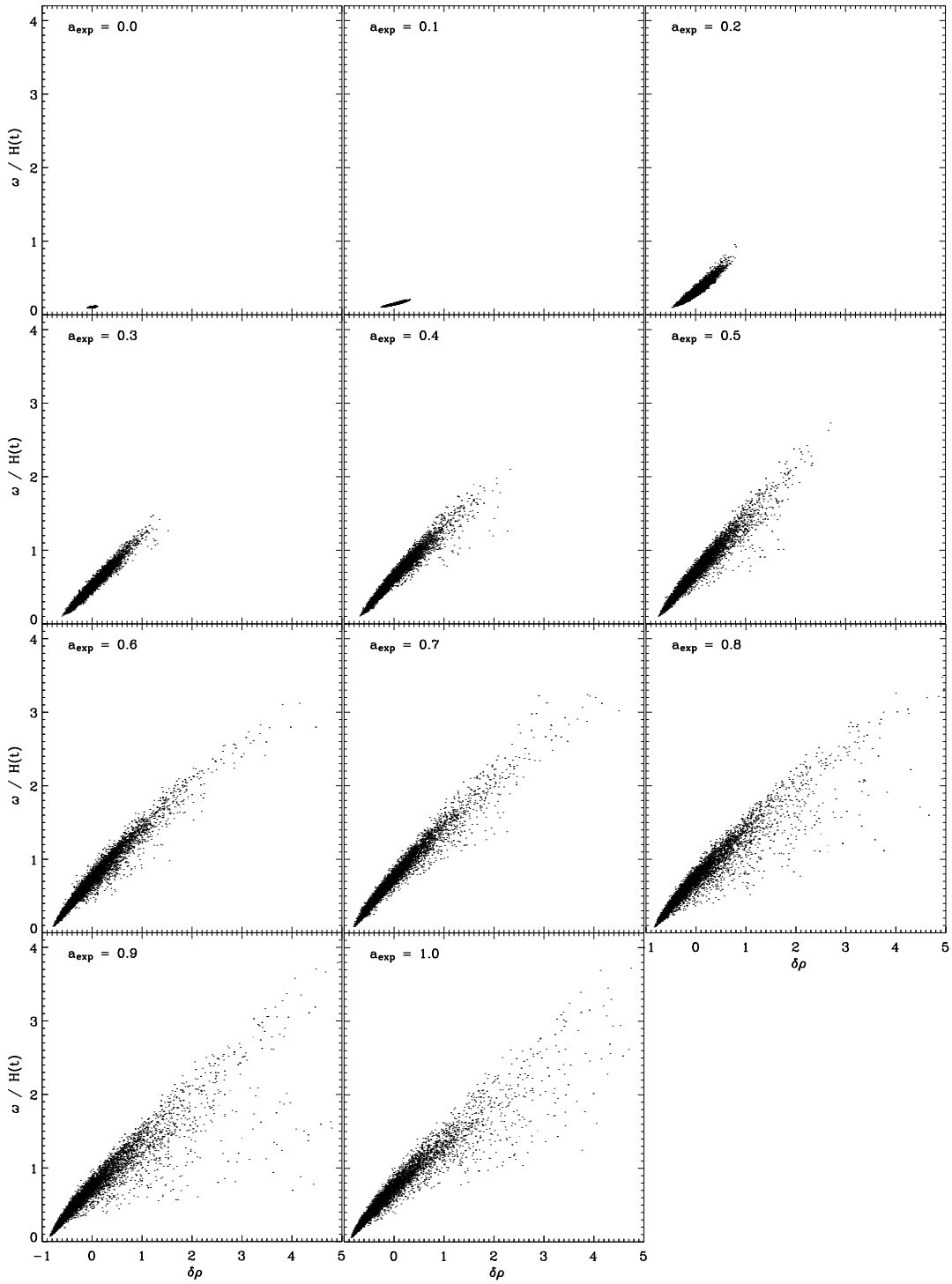

Figure 6.25 — Time evolution of the density-vorticity relation. The cloud of points are given by densities and vorticities computed with DTFE. We have expressed the vorticity in terms of the Hubble parameter $H(t)$.

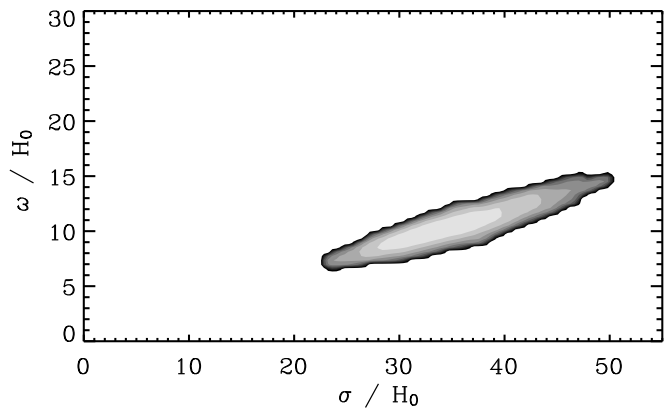

Figure 6.26 — Contours of the point-to-point comparison of the DTFE velocity shear and vorticity computed at present time (a = 1). Both quantities have been expressed in terms of the Hubble paramter H_0 and convolved with a Gaussian kernel of 5 h^{-1}Mpc.

indicate that the reconstructed field does not contain any artificial bias introduced by coupling of the method and the Gaussian errors.

Because the method makes use of the velocity-gradient matrix in order to compute the interpolated velocity field, it is therefore straightforward to compute other velocity-related quantities such as the velocity divergence, shear and vorticity.

Because DTFE reproduces the PDF of the velocity divergence, it is possible to probe the velocity flows around voids, which define a sharply defined maximum in the PDF. Such sharp cutoff allowed us to constraint a lower value for $\Omega_m \approx 0.21$, which is in good agreement with the imposed value in the $N-$body simulations of 0.3. The large dynamic range of the method allowed us to test our estimates for the velocity divergence and density contrast with respect to the 2nd order perturbation theory result of the density-velocity divergence relation. Once the grid imprint of the initial conditions has disappeared the method recovers the density-velocity divergence relation rather well. A particular promising application exploits DTFE's ability to probe the density-velocity divergence relation into advanced clustering situations. This would allow a reconstruction of the density field from peculiar velocity measurements (e.g. POTENT like analisys).

We have found that the recovered shear and vorticity modes are also strongly dependent on the density field. The velocity shear eigenvalues trace very well the density field. In particular, the compressional mode is strongly related to the filamentary structure. Clusters of galaxies are identified as regions with high shear measurements. By contrast, the large void regions present a lack of shear as expected. The vorticity mode is an indication of the method failure at high density regions. The method also recovers physical vorticity since these regions are collapsing and therefore circular motions appear. At this moment, we are unable to disentangle both contributions (real vorticity and method's vorticity). However, the recovered vorticity at the cluster outskirts is for real, as revealed by smoothed fields.

In conclusion, we have shown that the DTFE reconstruction scheme of the peculiar velocities corresponding to a simulation of cosmic structure formation seems to provide a good qualitative and quantitative description of the data under consideration. In particular, we have shown that the use of DTFE enables a meticulously study of the dynamics of the cosmic foam, in which one has to deal with structures of diverse densities and geometries at both small and large scales. Applying the DTFE reconstruction procedure to the analysis of a data set of peculiar velocities will help us understand the formation and evolution of the characteristic elements of the large scale structure of the universe.

Acknowledgments

E.R.D. thanks the HYDRA consortium for making their $N-$body code (HYDRA) public available.

6.A Triangular Shaped Cloud [TSC]: description

The TSC is a quadratic scheme in which the particle value is distributed over all grid points within a distance of at most one and a half grid cells. In this scheme, the value assignment function can be expressed as the product of three functions of the one dimensional displacement of a particle from the cell center

$$\delta\mathbf{x} = \mathbf{x} - \mathbf{n}/M\,, \tag{A6-1}$$

therefore,

$$W(\mathbf{x}) = \prod_{i=1}^{3} w(x_i)\,, \tag{A6-2}$$

and where the one-dimensional weighting function is defined as follows (see Hockney & Eastwood 1988)

$$w(x_i) = \begin{cases} \dfrac{3}{4} - M^2\delta x_i^2, & M|\delta x_i| \le \dfrac{1}{2} \\[2ex] \dfrac{1}{2}\left(\dfrac{3}{2} - M|\delta x_i|\right)^2, & \dfrac{1}{2} \le M|\delta x_i| \le \dfrac{3}{2}\,. \end{cases} \tag{A6-3}$$

With this definition the method produces smooth fields which could not be affected considerably by shot noise effects depending on the size of the grid cells at the cost of low spatial resolution.

7

The coldness of the Local Cosmic Environment

E. Romano-Díaz, R. van de Weygaert & W. E. Schaap.

We have characterized the thermal state of the Local Group and Local Supercluster environments by computing the cosmic Mach number statistics in a volume-weighted fashion. In order to compute volume-weighted quantities from discrete positions of objects, we have made use of the Delaunay Tessellation Field Estimator for peculiar velocity fields. We have addressed the differences for the Mach number estimates when these are computed from $N-$body velocity data, mock-observed velocities and modeled velocities using the FAM method. The parent $N-$body simulations have been constrained in order to give a reasonable mimic representation of the matter distribution in our cosmic vicinity. Results indicates that our local neighborhood is rather chilly, even more so than if this number were computed in mass-weighted way. Here we argue that the coldness of the local flow is a characteristic given by the mass configuration around the Local Group environment. The surrounding velocity field is dominated by the massive structures beyond the Local Supercluster.

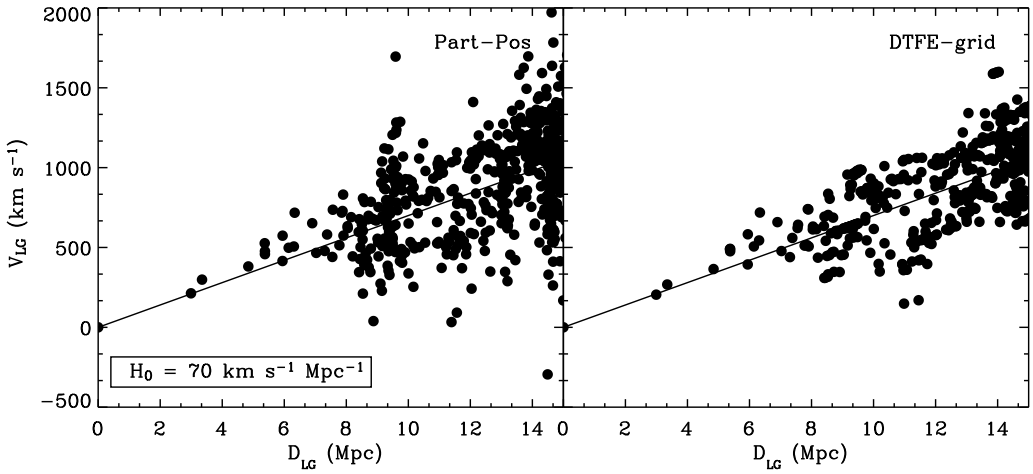

Figure 7.1 — Radial peculiar velocities plotted as a function of distance computed from a discretely (and unevenly) sampled velocity field (left panel). The corresponding radial velocities for the resulting interpolated volume-weighted velocity field is shown at the right panel. The objects are suitable sampled particles from an $N-$body simulation aimed to mimic the mass distribution and dynamical behavior around the Local Supercluster. The continuous lines indicate a pure Hubble flow expansion. Notice how the velocity dispersion around the Hubble flow increases with distance.

7.1 Introduction

Peculiar velocities of galaxies are the velocity deviations from a pure Hubble expansion. They are the result of gravitational interactions that each galaxy has with all surrounding matter concentrations. This makes them a direct probe of the underlying dark matter in the universe and a test for the gravitational instability paradigm. They provide constraints on cosmological models, in particular on the cosmological density parameter, Ω_m. They can characterize the mass distribution on very large scales because with respect to density fluctuations, velocity fluctuations are more sensitive to large scale perturbations and thus, to structures at a larger distance.

The dynamics of the Local Group [LG] and its environment provides a unique challenge to cosmological models. The velocity field within 5 h^{-1}Mpc of the LG is extremely "cold". The deviation from a pure Hubble flow, characterized by the observed radial peculiar velocity dispersion, is measured to be ~ 60 km s^{-1} (Sandage 1986, 1999; Peebles 1988; Schlegel et al. 1994; Ekholm et al. 2001; Karachentsev et al. 2003). Averaged over larger volumes of the Universe this dispersion increases to a few hundred km s^{-1}. While within a volume of 3 h^{-1}Mpc around the LG Karachentsev et al. (2002) reported a velocity dispersion value of $25-30$ km s^{-1}, in a volume of radius 14 h^{-1}Mpc the velocity dispersion raises to 200 km s^{-1} (Groth et al. 1989), and at the scale of 30 h^{-1}Mpc up to 310 km s^{-1} (Groth et al. 1989; Tonry et al. 2000). While the "small-scale" component of the velocity dispersion has a remarkably low value, it is superimposed on a truely impressive "large-scale" bulk flow component. The LG participates in a bulk flow of approximately 600 km s^{-1}, mainly influenced by the Great Attractor [GA] region. The particular location of the Local Group and Local Supercluster in the cosmic vicinity undoubtedly plays a major role in shaping their velocity fields. Figure 7.1 shows the radial peculiar velocities of objects computed from the discrete velocity field (left-hand panel) and from its volume-weighted velocity field (right-hand panel) from a constrained $N-$body simulation that mimics the dynamics of the Local Supercluster and its environment. Notice how the velocity dispersion around a pure Hubble flow (continuous line) increases as a function of distance. The right-hand panel presents smaller dispersions especially at the high density regions because volume-weighted velocities are less affected by virialization effects.

Ostriker & Suto (1990, hereafter OS) suggested combining the large-scale and small-scale characteristics of the peculiar velocity field into a single statistics, the Cosmic Mach Number $\mathcal{M}$. It was introduced in order to characterize the coldness of the observed velocity field data of Aaronson et al. (1982a). The Mach number in physics is the ratio of the flow velocity in some medium to the sound velocity in that medium. In a cosmological context, the equivalent of the sound velocity is the small-scale velocity dispersion of galaxies. The characteristic bulk velocities in a given cosmological model measure the large-scale component of the power spectrum, while the small-scale velocity dispersion depends on the power on small scales. Their ratio is therefore independent of the amplitude of the power spectrum, at least in Linear theory (OS). By comparing small and large scale contributions it is a diagnostic of its shape. Suto & Fujita (1990) extended the results of OS to nonlinear regimes and studied the probability distribution of $\mathcal{M}$ using N-body simulations.

van de Weygaert & Hoffman (1999, 2000) used low resolution constrained $N-$body simulations of the Local Universe to study the coldness of the flow of the LG-alike regions, finding that the local cosmic vicinity is rather cold. Their preliminary results suggested that the local cold flow may be influenced by the mass distribution on much larger scales and be induced by coupling of the small and large scales via the velocity shear.

In a more general study, Nagamine, Ostriker, & Cen (2001) investigated how typical such a cold region, similar to that of the local group, would be in the entire distribution of the cosmic velocity field. Their results suggested either that the LG is in a relatively low density region or that the true value of Ω_m is ~ 0.2, and that the Mach number is a weakly decreasing function of overdensity. They recovered the velocity dispersion using different sphere radius in a box of 20 h^{-1}Mpc. In their approach they corrected the peculiar velocity field from the missing bulk flow due to large scale contributions by using an empirical method. They computed the ratio in Fourier space between the power spectrum of their simulations with respect to the full power spectrum. Although this ad-hoc approach corrects for the missing long waves in the simulation box, it does not take into consideration the distortions in the velocity field produced by structures residing just outside the box that could play an important role in the moulding of the inner velocity field (Chapters 2 & 4).

OS estimated the $\mathcal{M}$ number for different volume sizes. They found that for spiral galaxies $\mathcal{M}(R = 4\ h^{-1}\text{Mpc}) = 4.2 \pm 1.2$, $\mathcal{M}(R = 14\ h^{-1}\text{Mpc}) = 2.2 \pm 0.5$, while for elliptical galaxies $\mathcal{M}(R = 30\ h^{-1}\text{Mpc}) = 1.3 \pm 0.4$. Strauss et al. (1993) used spiral galaxies to determine that $\mathcal{M}(R = 14\ h^{-1}\text{Mpc}) = 1.03$, and that for elliptical galaxies $\mathcal{M}(R = 25\ h^{-1}\text{Mpc}) = 0.57$. Nagamine, Ostriker, & Cen (2001) suggested that the relative high observed $\mathcal{M}$ is an indication that the LG is located in a relatively low cosmic density region.

Suto & Fujita (1990), using $N-$body simulations found that the distribution of $\mathcal{M}$ is close to Maxwellian in linear and mildly nonlinear regimes. Nagamine, Ostriker, & Cen (2001) using higher resolution $N-$body simulations found that the bulk flows are well fitted by a maxwellian distribution, the velocity dispersion is not well fitted by a Maxwellian and that the Mach number is relatively well fitted by a such distribution.

An extra consideration from these studies is the fact that all these measurements are biased toward estimates at high density regions, and therefore, they are mass-weighted. A more "fair" estimate could be the use of volume-weighted quantities. This kind of analysis would allow one to estimate the velocity dispersion independently of the objects positions, avoiding biasing any estimate toward high density regions.

A common problem from previous theoretical studies is that none of them managed to reproduce a realistic mass distribution around the Local group as revealed by the large-scale surveys of the universe, neither Local Group environments with velocity dispersions close to the observed ones (Schlegel et al. 1994; Governato et al. 1997). This point is of utmost importance since the Local Group resides in a rather atypical location of the universe. The presence of the Local Supercluster, the Great Attractor and Perseus Pisces superclusters shape in a very specific way the local peculiar velocity field.

In the present study we investigate how cold the Local Group environment and Local Supercluster [LS] region are when computing the bulk flow, the local velocity dispersion and the cosmic Mach number in a volume-weighted fashion. We will argue that the coldness of the local flow is a characteristic

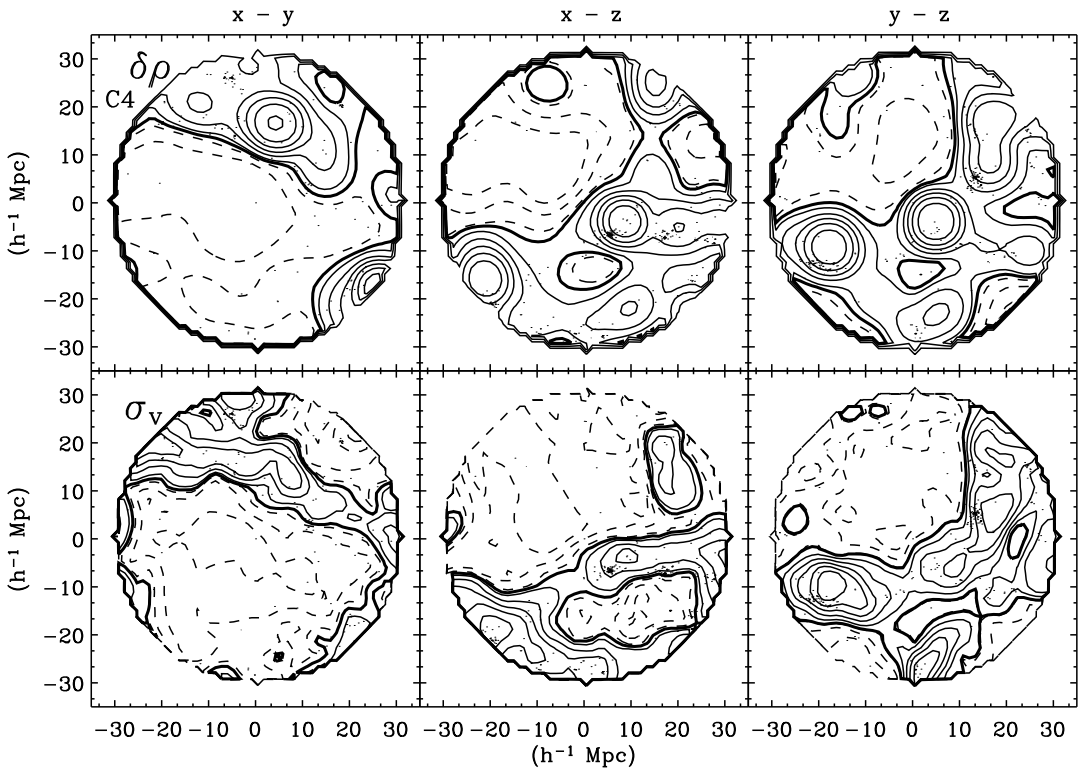

Figure 7.2 — Density field (top row) and velocity dispersion (bottom row) maps for the Local Supercluster region from one catalog of our sample (C4) along the three supergalactic planes. The points represent the galaxy distribution in a 5 h^{-1}Mpc thick slice centered along the respective supergalactic planes (top labels). Notice the good correspondence between the two fields.

of the atypical mass configuration of the cosmic vicinity rather than interpret it as a global property of the Universe. We will make use of realistic velocity fields extracted from constrained $N-$body simulations aimed to mimic as close as possible the mass distribution around the LS. We will assess how the Mach estimates change when considering LS observation-mimicking mock catalogs, such as the Nearby Galaxy Catalog of Tully (1988, hereafter NBG), as well as considering modeled velocity fields as given by the FAM method (Nusser & Branchini 2000). We will also compare our estimates with the "conventional" mass-weighted estimates and address the main differences between the two methods. In order to compute volume-weighted quantities we will make use of the Delaunay Tessellation Field Estimator for peculiar velocities [hereafter DTFE] presented in Chapter 6. This technique is a linear interpolation method that assures full spatial and continuous volume-covering velocity field from a discrete velocity field sample without loosing spatial resolution.

The chapter is organized as follows. The cosmic Mach number statistics is reviewed in Section 2. A description of the different Local Supercluster velocity fields, full, observed and modeled, is presented in Section 3. The construction of continuous velocity fields and side effects in their reconstructions are presented in Section 4. In Section 5 the volume-weighted measurements of the Mach statistics for the three sample sets will be exposed, while in Section 6 a similar analysis but mass-weighted will be presented. Finally, discussions and conclusions will be stated in Section 7.

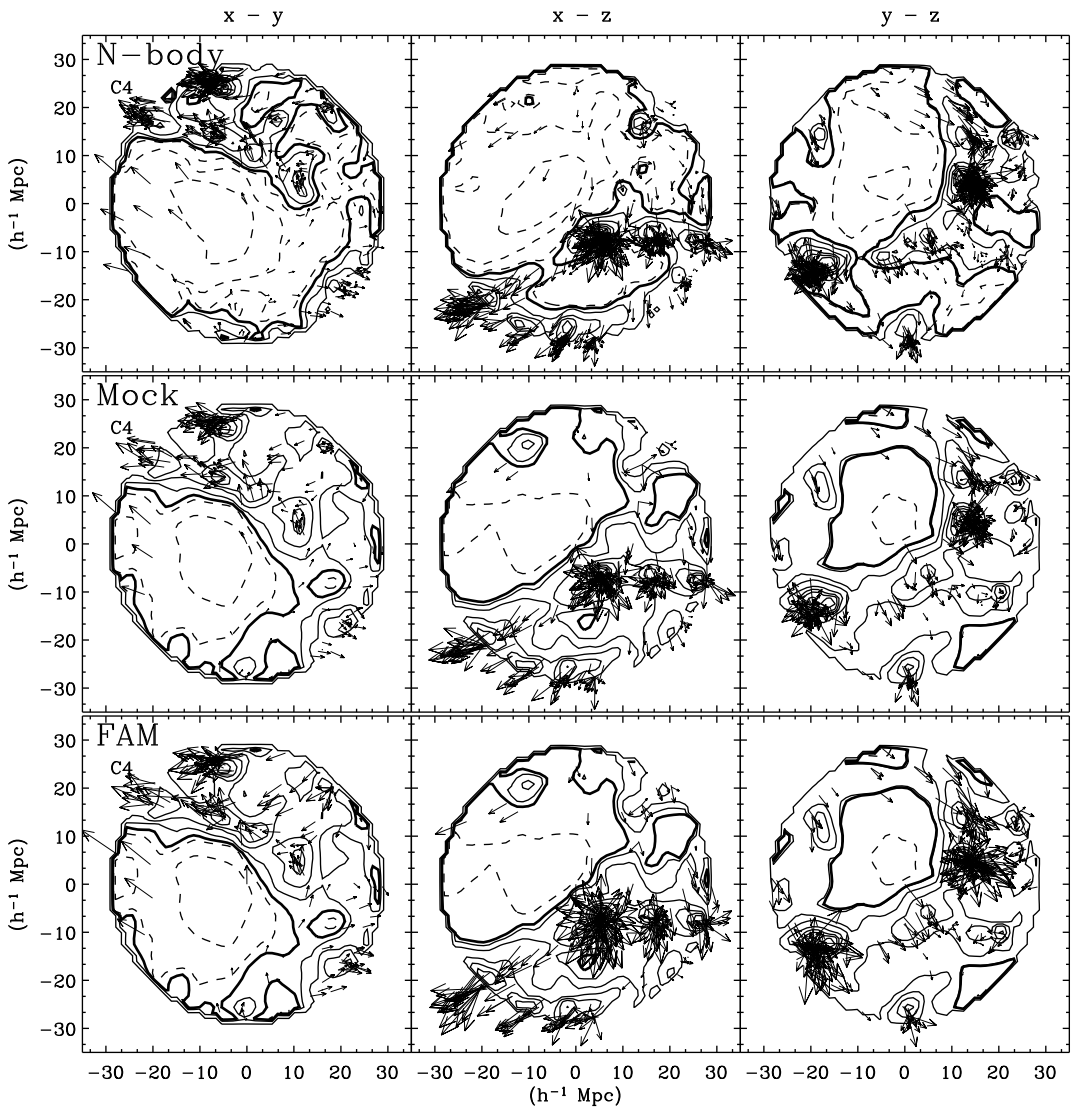

Figure 7.3 — Density fields (contour lines) along the three supergalactic planes, and peculiar velocities for the LS within a slice of 5 h^{-1}Mpc centered along the supergalactic planes from one mock catalog of our set (C4). The top-most labels indicate the plane projections. The top row represents the full velocity and density fields as given by the $N-$body simulation, the middle row for the diluted volume-limited mock-observed catalogs, while the bottom row for the FAM modeled velocity field. The contours in the three rows are scaled in such a way that they represent the same density values.

7.2 The Cosmic Mach number

Under the formalism of Linear theory of gravitational instability, OS defined the expressions for the mean square bulk flow and the mean square velocity dispersion in a window of size R as follows:

$$\langle V^2(R)\rangle = \frac{\Omega_m^{1.2} H^2}{2\pi^2} \int_0^\infty P(k)\, \tilde{W}^2(kR)\, \mathrm{d}k\,, \tag{7.1}$$

$$\langle \sigma^2(R)\rangle = \frac{\Omega_m^{1.2} H^2}{2\pi^2} \int_0^\infty P(k)\, [1 - \tilde{W}^2(kR)]\, \mathrm{d}k\,. \tag{7.2}$$

In other words, in the framework of gravitational instability where peculiar velocities are due to the gravitational attraction of density inhomogeneities (Peebles 1980), the large-scale flows are related to the amount of power in the density field at the largest scales, while the small-scale velocity dispersion is governed more by the small-scale components of the power spectrum and therefore, it will be correlated with the density field (see Figure 7.2). In Eqns. 7.1 & 7.2, Ω_m and H are the cosmological density parameter and the Hubble constant, $P(k)$ is the power spectrum of density fluctuations and $\tilde{W}(kR)$ is the Fourier transform of the window function of size R.

The cosmic Mach number $\mathcal{M}$ is given by the ratio of the rms bulk flow velocity V on some scale R of some sets of objects to the rms velocity dispersion $\sigma(R)$ of the objects in the frame of the bulk flow. In this way, the $\mathcal{M}$ is independent of the amplitude, and therefore the normalization of the power spectrum and is insensitive to the bias between galaxies and dark matter (OS). This quantity characterizes the warmth or coldness of the velocity field by measuring the relative strength of the velocities, and implicitly the gravitational field, at scales larger and smaller than the patch size R.

The rms cosmic Mach number can be defined in two ways, depending in how one does the averaging (OS):

$$\langle \mathcal{M}^2(R)\rangle^{1/2} = \left\langle \frac{V^2(R)}{\sigma^2(R)} \right\rangle^{1/2} \quad \text{or} \quad \left(\frac{\langle V^2(R)\rangle}{\langle \sigma^2(R)\rangle} \right)^{1/2}. \tag{7.3}$$

Since $\mathcal{M}$ is defined as V/σ on a certain scale R, a larger $\mathcal{M}$ implies a smaller σ if the variation of V is weaker than that of σ. Suto et al. (1992) and Nagamine et al. (2001) showed that these ratios present differences between each other and they follow the order-relation:

$$\left(\frac{\langle V^2\rangle}{\langle \sigma^2\rangle} \right)^{1/2} < \left\langle \left| \frac{V}{\sigma} \right| \right\rangle < \left\langle \frac{V^2}{\sigma^2} \right\rangle^{1/2}. \tag{7.4}$$

This order-relation works out into considerable differences when computing the Mach number. Although the intention of the three quantities in Eqn. 7.4 is the same, we adopt in the present study the intermediate relation because we find it is the closest to the physical essence of the Mach number.

7.3 Mimicking the Local Supercluster environment

The fact that the LG resides in a mildly overdense region of the Universe connecting to the nearby Virgo cluster, and its location in between the Local Supercluster [LS], which itself connects to the GA (Strauss et al. 1992) and the Perseus-Pisces supercluster [PP], create a complex gravitational tidal field (see Figure 7.3). This situation has turn out to be very difficult to reproduce via $N-$body simulations. Such experiments cannot naturally reproduce the "coldness" of the local velocity field (Schlegel et al. 1994; Governato et al. 1997). The study of Governato et al. (1997) confirmed that the standard CDM model cannot reproduce the observed low value of the velocity dispersion. In the case of the open CDM model ($\Omega_m = 0.3$) the velocity dispersion was in the order of $\sim 150-300$ km s^{-1}, while for the SCDM model $\sim 300-700$ km s^{-1}. In both cases the measured velocity dispersions were at least twice the observed value. However, the conclusions of these studies should be taken with caution since none of the tested models concerned the actually assumed ΛCDM model and the LG candidates were chosen from a small-size simulation volume.

Therefore, if one wants to address issues concerning the LS it is necessary to reproduce its main characteristics as close as possible. This concerns both its mass distribution and its peculiar velocity field. One particularly promising strategy is the use of Constrained Simulations (Kolatt et al. 1996; Bistolas & Hoffman 1998; Klypin et al. 2003; Kravtsov et al. 2002; Mathis et al. 2002, see also Chapters 2 & 4). With this approach one invokes the observational information yielded by surveys of the large scale structure of the universe. Kolatt et al. (1996); Bistolas & Hoffman (1998) used the IRAS 1.2Jy catalog (Fisher et al. 1995a). van de Weygaert & Hoffman (1999); Klypin et al. (2003); Mathis et al. (2002) used the Mark III catalog of peculiar velocities (Willick et al. 1997a) as a source of the mass distribution within the cosmic neighborhood.

The Mark III catalog has proved to be one of the best available catalog surveys for this study. On large scales peculiar velocities directly reflect the mass distribution, so that they can be used to directly reconstruct the linear density field of the local universe. The application of the Wiener filter algorithm enables one to infer the significant density field features, taking into account the measurement uncertainties (see Zaroubi et al. 1995, 1999). This reconstruction is only valid within the linear regime, so that the input data has to be linearized prior processing. The small scale structures are imposed by applying the technique of constrained random fields (Bertschinger 1987; Hoffman & Ribak 1991; van de Weygaert & Bertschinger 1996). This allows one to add realizations of the small scale density and velocity fluctuations according to *a priori* cosmological model adopted.

The combined use of the Wiener filter and the constrained random field technique guarantees that where the signal to noise from the data is very high, the information is dominated by the input data, and where the signal is very low the constrained random method provides with the right power according to the chosen cosmological model. This combination of methods provides a reconstruction of how the present day structure would appear if linear theory is valid. By extrapolating back in time such fields, this implementation can be used as a tool to recover the initial conditions of structures that prevail nowadays in the nearby universe.

7.3.1 $N-$body, Mock-observed and FAM modeled peculiar velocity fields

In the present study we make use of the four LS constrained simulations presented in Chapter 3. These simulations correspond to a flat ΛCDM cosmological model with $\Omega_\Lambda = 0.7$ and $\Omega_m = 0.3$, $h = 0.7$ (measured in units of 100 km s^{-1} Mpc^{-1}). The power spectrum is normalized to $\sigma_8 = 0.9$. The present model is consistent with the current observational constraints (WMAP, Spergel et al. 2003), and also consistent with the radial velocity surveys including the Mark III. The simulations were performed in a box of 320 h^{-1}Mpc side, loaded with 128^3 particles and with the LG located at the center of the box. The evolution of the initial density fields into the non-linear regime was followed by means of the HYDRA code (Couchman et al. 1995).

Because we are only interested in studying the LS volume, we will only consider the mass distribution within a volume of radius 30 h^{-1}Mpc centered on an observer at the midpoint of the simulation box. Such observer possesses observational characteristics of the Local Group Environment [LGE]. i.e. a velocity amplitude of 600 km s^{-1} in the direction of the GA region, a velocity shear within 5 h^{-1}Mpc of $\sim$ 200 km s^{-1} and a fractional overdensity in the same region between 0.5 and 1.5 (see Chapter 4). For the case of the observation-mimicking mock catalogs and FAM modeled velocity fields we will make use of the constrained NBG and FAM$_{cor}$ catalogs presented in Chapter 4. The former is a volume-limited diluted sample of the total mass distribution within 30 h^{-1}Mpc in order to mimic the NBG catalog (Tully 1988), which represents a fair sample of the LS volume. The FAM$_{cor}$ catalogs contain the same mass distribution as their NBG counterparts, but their velocity fields have been computed with the FAM method and properly corrected for large scale influences (see Chapter 4). Table 7.1 presents the three different sets of catalogs and their main characteristics. The first column gives the name of the set of catalogs: LS$_{Nbody}$ refers to the full Local Supercluster velocity and density fields as given by the simulations, LS$_{Mock}$ to the diluted "observation mimicking" mock catalogs extracted from the parent simulations, and LS$_{FAM}$ to the modeled FAM velocity fields but with the same diluted density field as the mock sample. The second column indicates the radius of the spherical sampling volume, and the third column the number of catalogs in each set. The fourth column gives the average number of objects $\langle N_{obj} \rangle$ within the set and the last column indicates the main characteristics for each set of catalogs.

Figure 7.3 illustrates the main differences between the three set of catalogs for one particular realization, the C4 catalog. This label indicates that all samples have been drawn from the fourth constrained $N-$body simulation. In all panels the contours represent the density contrast along the respective supergalactic planes indicated by the top-most labels (abscissa-ordinate). The bold line represents the average density within the volume, the continuous lines overdensity regions, while the dashed lines underdense regions. The density contours are equivalent between realizations, i.e., they represent the

Label	Radius (h^{-1}Mpc)	Number of catalogs	$\langle N_{obj} \rangle$	Main Characteristic
LS_{Nbody}	30	4	31 000	Full **v** and ρ fields
LS_{Mock}	30	4	2 800	Mimic-observed: diluted **v**, ρ
LS_{FAM}	30	4	2 800	Diluted ρ, modeled **v**

Table 7.1 — Characteristics of the constrained mock catalogs. The first column indicates the label of the set. The second column gives the catalog's size. The third column the number of catalogs that compose the set. In the fourth column the average number of objects for each set is presented, and the main characteristics that distinguish each set of catalogs are stated in column 5.

same density values for the three samples. On top of the density maps we have plotted the velocity vectors at the particle positions in slices of 5 h^{-1}Mpc thick centered along the supergalactic planes. Differences and similarities between the three samples can be recognized from this plot. The density fields for the mock and FAM samples are identical, and both bear a close resemblance to the original $N-$body one.

In all catalogs the presence of the LS is clearly recognized as the filament crossing the $x-y$ projection. The coherent velocity flow pointing toward the left-hand side of this projection denotes the presence of a massive structure located outside the LS volume, the Great Attractor [GA] region. At the opposite side, the emergence of a velocity flow is also noticeable, which is induced by the Perseus-Pisces [PP] supercluster. The prominence of the local void can also be noticed along the 3 projections.

The $N-$body and mock velocity fields are basically the same, both have the same characteristics but the latter contains less objects. The FAM fields contain the same number of objects as the mock ones. Both velocity fields display the same large scale characteristics, but they differ at the high density regions where the FAM velocities do not represent the real velocities. This is because the inability of FAM in properly modeling virialized motions (Nusser & Branchini 2000; Branchini et al. 2002; Romano-Díaz et al. 2004). We have only shown one catalog, the other 3 set of catalogs present a very similar situation. For the complete set of catalogs for the Mock-observed realizations along one particular projection, the $z-$supergalactic plane, see Appendix 7.B.

7.4 Continuous Velocity Fields

When one desires to obtain reliable estimates of statistical parameters from a given observed or computer-simulated field (e.g. density & velocity fields), one faces the problem of dealing with discrete, non-uniform fields. This discreteness forms a major technical obstacle for a successful comparison with theoretical predictions. A major issue concerns the fact that analytical/theoretical predictions involve quantities evaluated uniformly throughout a cosmic volume, while observed or simulated results are biased toward the measured particle (matter) distribution. This issue of volume-weighted versus mass-weighted physical quantities is treated somewhat more detail in Appendix 7.A.

The usual strategy to deal with such discrete data sets is to smooth them with a filter to yield a continuous field. In the case of the peculiar velocity field several authors (e.g. Bertschinger et al. 1990; Juszkiewicz et al. 1995; Lokas et al. 1995) filtered galaxy velocities with a Gaussian kernel of a fixed length for reducing problems of noisy data, sparsely sampled underdense regions and to obtain the velocity field on a regular grid. If one is interested in performing studies concerning the large

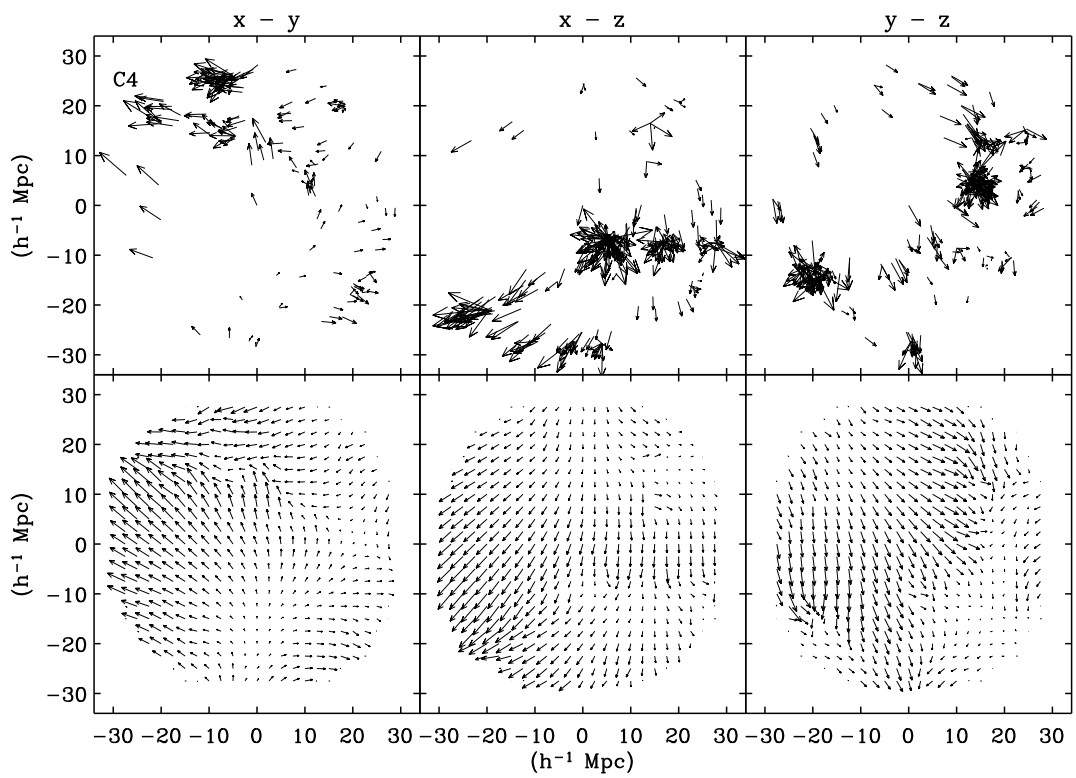

Figure 7.4 — Discrete and continuous velocity fields for one catalog of our set (C4). The top panels present the peculiar velocities at the particle positions on a slice of 5 h^{-1}Mpc thick centered along their respective supergalactic planes. The bottom panels show the corresponding continuous DTFE velocity fields for the same catalog along the supergalactic planes.

scale structure of the universe such methods give good estimates. However, when one is interested in studying the more local (small-scale) qualities of the velocity field, such methods are not very suitable since the use of such kernels erases the small-scale signal, the regime in which one is interested.

Bernardeau & van de Weygaert (1996) proposed the use of Voronoi and Delaunay tessellations as natural filters and interpolation volumes in multi-D space. They first explicitly proved that the zero-order Voronoi estimator is the asymptotic limit for volume-weighted field reconstructions from discreet sampled field values. Subsequently, they extended this to a first-order Delaunay estimator. This showed a superior performance in reproducing analytical predictions.

Schaap & van de Weygaert (2000); Schaap (2005) worked along the same line of Bernardeau & van de Weygaert and extended the Delaunay method into a general map-making and field reconstruction tool, including density fields, the Delaunay Tessellation Field Estimator [DTFE] interpolation method. In Chapter 6 we have expanded the DTFE method to obtain volume-weighted velocity related-quantities.

The main characteristics of this interpolation scheme are:

1. It provides a volume-covering velocity field by a multi-dimensional interpolation routine in adaptive intervals.

2. The resulting velocity field is explicitly volume-weighted and therefore, more closely related to most analytical inferred quantities.

3. It automatically suppresses shot-noise effects.

N_{grid} (1D)	Resolution scale (h^{-1}Mpc)
32	2.5
64	1.25
128	0.625
256	0.3125

Table 7.2 — Grid resolutions for the DTFE velocity interpolation scheme. The left-column indicates the number of grid-cells per dimension, N_{grid}. The right-column gives their corresponding physical size in units of h^{-1}Mpc.

4. It uses a linear interpolation of the velocity field for the Delaunay triangulation to sample the whole space.

5. Processing. This may involve various operations. The most important ones are *image reconstruction* and, subsequently, *filtering*. Image reconstruction consists of two steps:

   (a) For a set of image points (usually grid points) determine in which Delaunay tetrahedra they are located.

   (b) By (linear) interpolation compute field values at each of these points, on the basis of one vertex field value and computed gradient.

Figure 7.4 presents the outcome of the DTFE velocity interpolation scheme for one catalog of our sample (C4). The top panels refer to the peculiar velocities at the discrete particle distribution. These are depicted in the three mutually perpendicular central slices of 5 h^{-1}Mpc thick. The lower panels correspond to the DTFE interpolated velocities along the supergalactic planes. Although a direct comparison between the discrete and DTFE velocity fields cannot be done because they represent different slice thicknesses, one can notice that both fields are very similar to each other. As a result of the linear interpolation scheme of the method, the regions devoid of objects have been filled in with coherent flows. For the sake of clarity we have lowered the resolution in the DTFE velocity maps. The advantages of the DTFE velocity method can be clearly appreciated from this figure.

However, this implementation also presents some features that have to be taken into account in our analysis. These can be divided into two categories, those concerned with the method itself, and those related to the parent sample. The latter concerns in particularly the consequences of using ill-defined samples. It involves the effects of dealing with a sparse sample of how this influence the interpolated velocity field with respect to the full one. The former are related to the grid-resolution and the interpolation scheme of the method which could affect the measurements mainly at high density regions where the flows are not longer laminar.

7.4.1 Resolution effects on the DTFE velocity fields

One of the main characteristics of the DTFE velocity interpolation method is that is self-adaptive. The linear interpolation scheme allows to map velocities at any desired resolution without loosing information. This is an advantage over conventional interpolation schemes where one is restricted to the size of the kernel employed (see Chapter 6, see also Schaap 2005).

In order to check for any resolution effect that could affect our Mach statistics, we have computed the volume-weighted velocity dispersion (see Eqn. 7.6, Sec 7.2) using different grid resolutions in the DTFE interpolation scheme. We have used four different number of grid-cells per dimension, $N_{grid} = 32, 64, 128, 256$. Table 7.2 states the four different grid-sizes and their corresponding physical

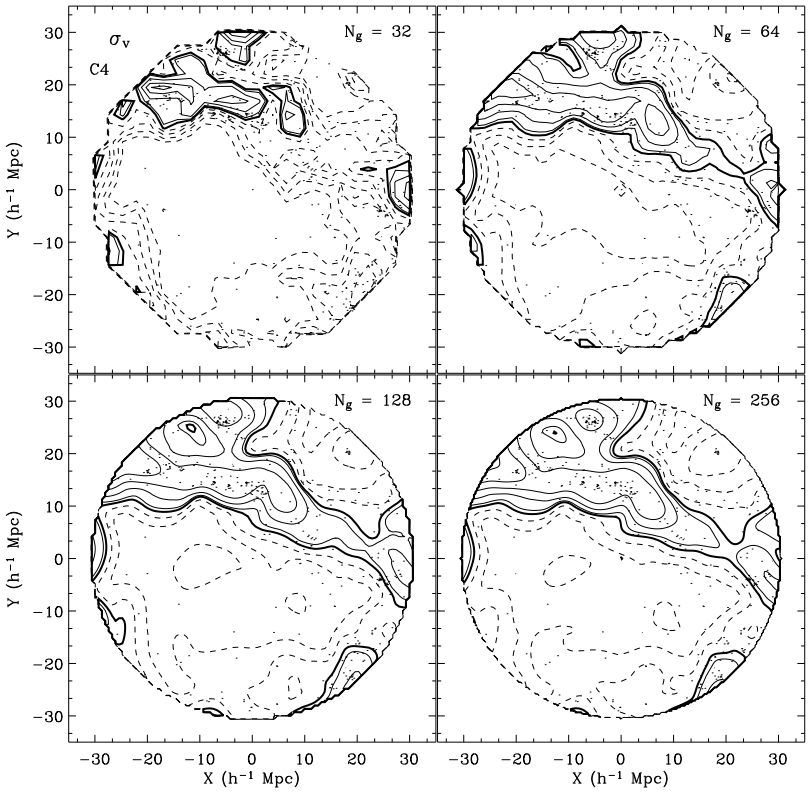

Figure 7.5 — Volume-weighted velocity dispersion maps computed at different grid resolutions with the DTFE velocity interpolation scheme. All panels refer to the same $x - y$ projection of the C4 mock catalog. The top-left panel refers to the velocity dispersion computed on a cubic grid with $Ng = 32$ grid-cells per dimension, the top-right panel to $Ng = 64$, the bottom-left to $Ng = 128$ and the bottom-right to $Ng = 256$ grid-cells. The contours in all panels represent exactly the same velocity dispersion values.

spatial resolutions used in this experiment. Figure 7.5 shows the effects of the grid resolution for the four grid-resolutions, for the same catalog and projection. It concerns the velocities along the $x-y$ plane. The contours represent exactly the same velocity dispersion values for the four panels. The bold contour references the "average" velocity dispersion used to divide regions with high velocity dispersion from those with low dispersions, with a value of 142 km s^{-1}.

The lowest resolution panel ($N_{grid} = 32$) is clearly affected by the grid resolution. Although the map presents the same general features than the other three at the low velocity dispersion regions, this is not the case for the high dispersions zones where there are less areas than in the other cases. The $N_{grid} = 64$ map resembles well enough the high resolution velocity dispersion maps, the main differences are at the very high or very low velocity dispersions regions. Another difference is in the smoothness of the maps as result of the grid resolution.

The differences at high density regions are related to the interpolation scheme of the DTFE procedure. In these regions the velocity field is not longer laminar, so that an interpolation of velocities is no longer possible and DTFE cannot be applied (neither other methods, see Chapter 6). As a consequence of this, the method reduces the velocities by mitigating the virialization processes that take place at these high density regions. This results into reducing the velocity dispersion at these regions, see Fig. 7.1.

Taking into consideration these effects and the fact that we do not find systematic differences between the $N_{grid} = 64, 128, 256$ maps, we chose $N_{grid} = 64$ as a standard grid resolution for reasons of efficiency.

7.4.2 Sampling effects on the DTFE velocity fields

The linear interpolation algorithm of the DTFE velocity scheme overcomes the problem of shot-noise effects. However, sampling effects remain affecting the interpolation procedure. They enter through

the computation of the velocity gradient (see Chapter 6). A denser sampling will assure a more reliable interpolated field.

The sampling effects will be most noticeable at the mildly non-linear regions since is at this regime where the laminar flow could change to virial motions in a small spatial region. If so, the corresponding interpolated DTFE velocities will slightly differ from the real velocity field. Figure 7.6 illustrates the sampling effects. We have computed the residual velocity fields for the C4 catalog along the $z-$supergalactic plane between the $N-$body, Mock and FAM DTFE velocity fields. The $N-$body– Mock residual velocity field traces the high density regions, which are marked by large arrows. The LS filament can be recognized as the region where the largest velocity differences are. Also, the dense region located at the top-left of the plot, which is part of the GA region, presents large velocity residuals. This is the effect of having a diluted sample. On the other hand, the interpolation is much better at the low density regions. The local void does not present any significant residual flow. This can be appreciated from the almost negligible velocity vectors. These results make clear that when computing any velocity related quantity from these two velocity fields, they will only differ in the mildly non-linear regime where the sampling affect the interpolation scheme notably.

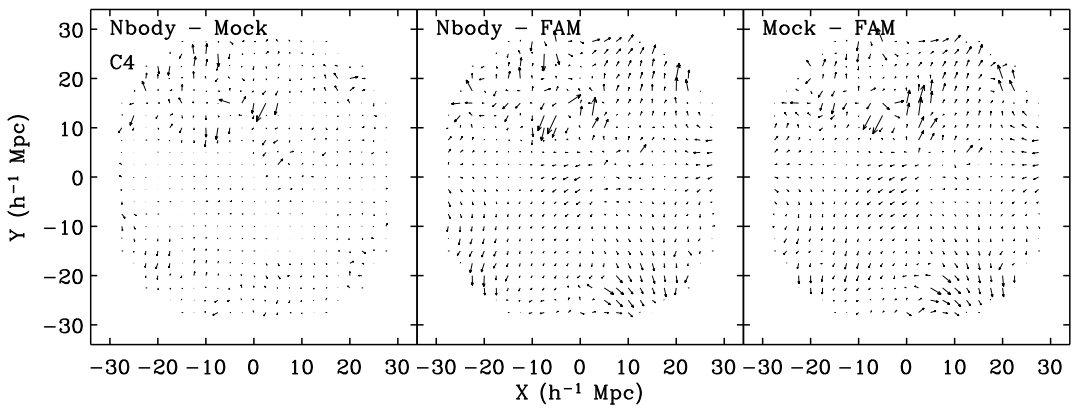

Figure 7.6 — Volume-weighted DTFE velocity residual maps computed between the three samples for the same C4 catalog along the $z-$supergalactic plane. The top labels indicated the DTFE velocity samples used to compute the residual velocities. In all maps velocities have been normalized by the same scale factor.

In the case of $N-$body– FAM and Mock – FAM residual fields two factors affect the interpolation procedure, both affecting in particular the high-density regions. The first one is the intrinsic error of the diluted parent mock sample as mentioned above. The second one is the inability of FAM in modeling virial motions correctly. These two factors enhance the velocity errors mainly at dense regions. This can be noticed along the LS filament where residuals are larger than in the $N-$body– Mock case. The emergence of coherence patterns can be seen at the upper and bottom right sides of the plot. This is an intrinsic error in the FAM modeling because of the presence of two clusters located at the edge of the sample (see Chapter 4, Figure 4.8).

7.5 The “thermal” state of the Local cosmic neighborhood

The “temperature” or “thermal” state of the LS volume are not strictly related to the typical dynamical definition of the temperature of a system since not all structures within the LS volume are virialized. Here we use these terms to characterize the velocity dispersion within a region as a consequence of the small-scale cosmic velocity perturbations.

In order to define the “temperature” of the LS region, we assess the velocity dispersion in spheres of 5 h^{-1}Mpc radius. This smoothing length has been chosen to minimize virial motions at the cores of galaxy clusters. Most virialized groups are small compared to the 5 h^{-1}Mpc radius, and effectively

these groups are replaced by their respective center-of-mass velocities. The spheres were drawn randomly in the volume, for a total of 1000 spheres for each sample. For each sphere we extracted all circled particles or grid values for the analysis corresponding to a top-hat window of size $R = 5\,h^{-1}$Mpc. While the velocity dispersion computed at the particle distribution will lead to a mass-weighted estimate, the latter will yield to a volume-weighted estimate of the same quantity. If $N_i(R)$ is the number of particles or grid-cells inside the sphere of radius R centered at $\mathbf{x} = \mathbf{x}_i$, the center-of-mass (*c.o.m*) velocity $\mathbf{V}(\mathbf{x_i}, R)$ and the residual velocity dispersion $\sigma(\mathbf{x_i}; R)$ are computed as follows:

$$\mathbf{V}(\mathbf{x}_i; R) = \frac{1}{N_i(R)} \sum_{|\mathbf{x}_j|<R} \mathbf{v}(\mathbf{x}_i + \mathbf{x}_j), \tag{7.5}$$

$$\sigma^2(\mathbf{x}_i; R) = \frac{1}{N_i(R)} \sum_{|\mathbf{x}_j|<R} [\mathbf{v}(\mathbf{x}_i + \mathbf{x}_j) - \mathbf{V}(\mathbf{x}_i; R)]^2, \tag{7.6}$$

$$\mathcal{M}(\mathbf{x_i}; R) = \frac{|\,\mathbf{V}(\mathbf{x}_i; R)\,|}{\sqrt{\sigma^2(\mathbf{x}_i; R)}}. \tag{7.7}$$

Notice that the bulk flow computed with this procedure (Eqn. 7.5) is a "bulk flow" on another scale than e.g. the ones discussed in Chapters 2, 4 and 5. In all analyses we will only consider the unsmoothed velocities of each sample set. The application of applying any smoothing algorithm with a kernel of size R will mainly affect the velocity dispersion on scales smaller than R, and will increasing the values of $\mathcal{M}$. In the following we will present images of the bulk flow, velocity dispersion and Mach estimates for one particular catalog for its three representations ($N-$body, Mock and FAM). The situation is very similar for all other catalogs. For a complete overview of all catalogs we refer to Appendix 7.B.

7.5.1 The bulk flow

We have computed the local volume-weighted bulk flow according to Eqn. 7.5 for all catalogs from the three different sets (LS_{Nbody}, LS_{Mock} and LS_{FAM}). Because the bulk flow is a linear large-scale feature which characterizes the average matter displacement within the surveyed volume, its spatial distribution should reflect a dipolar pattern. Since this quantity is the first order moment of the velocity field, it should be the same for all sets. Figure 7.7 shows the volume-weighted bulk flow maps for the same C4 catalog for the three different velocity field samples: the left-panel represents the LS_{Nbody} (full) sample, the middle one the LS_{Mock} (observed), and the right one for the LS_{FAM} (modeled) field. The plots show 2D cuts along the $x-y$ supergalactic plane. The contours represent equal bulk flow velocity regions for the three maps. We have divided the three maps in regions with bulk flows above (continuous lines) and below (dashed lines) the LG bulk flow amplitude of 600 km s^{-1}. In all maps, the LGE, indicated by the central diamond, is clearly dominated by a bulk flow of ≈ 600 km s^{-1}. The differences between the $N-$body and Mock bulk flows are only due to sampling effects since in these two samples the object velocities are the same. The FAM modeled bulk flows are in general in good agreement with the expected Mock ones.

The three maps are very similar to each other and they clearly show a dipolar motion along the whole projection. The bulk flow amplitude grows continuously along the negative x-direction, with the largest bulk flow motions (~ 1000 km s^{-1}, see Fig. 7.8) along the top-left side of the panels, near the GA region. This is a clear indication that the structures located around this region are the main contributors for this bulk flow motion. The shape of the large bulk flow regions indicate that this GA region gravitationally dominates the LS volume. The region opposite to the GA has a "lower" measured bulk flow as a result of the influence of the PP superclusters. At this region the gravitational interactions between the GA and PP even each other out, resulting in small net flows.

The good concordance between the different bulk flow maps is confirmed by their corresponding distribution functions [DF] and cumulative distribution functions [CDF] displayed in Figure 7.8, top and bottom left-most panels respectively. These distributions were constructed by placing 1000

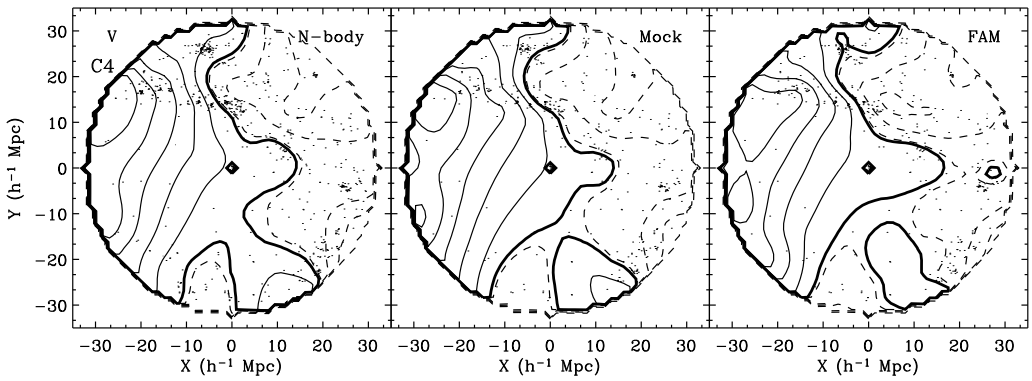

Figure 7.7 — Volume-weighted local bulk flow maps for the C4 catalog of the 3 sets. The thick contour line indicates the average bulk velocity of 600 km s^{-1}. The contours represent equal bulk flow values for the three samples. Notice how the LGE is immerse in the overall motion toward the GA region.

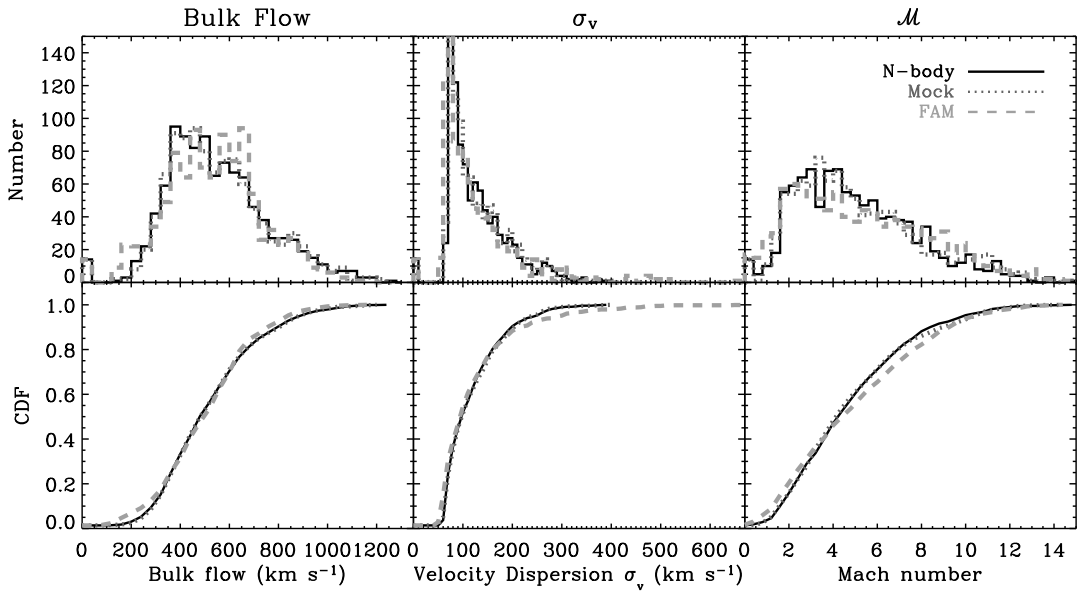

Figure 7.8 — Volume-weighted distributions for the bulk flow, velocity dispersion and $\mathcal{M}$ number for the 3 representations of the C4 catalog. The calculations have been performed at completely random locations within the LS volume, independently of the particle distribution.

spheres at the same locations in the three different representations of the C4 catalog. In both panels the continuous line represent the full LS$_{Nbody}$ sample, the dotted line the LS$_{Mock}$ observed one and the gray-dashed line the LS$_{FAM}$ modeled sample. The three bulk flow DFs are very similar to each other. The only slightly difference is at the mode of the DFs. While the $N-$body and Mock DFs are almost identical, the FAM one indicates that it has relative less regions of low bulk flow, and more high value regions. The spikes presented in the FAM bulk flow distribution at the range of $400-700$ km s^{-1} correspond to contributions from high density regions where FAM fails in reproducing the right velocities. The general agreement between the three distributions is more apparent from their CDFs. These do not show basic differences between the three samples. The CDFs show that most of the LS volume comprises bulk flows between 400 and 800 km s^{-1}. The average bulk flow within the LS region is

535 ± 47 km s^{-1} for the three sets (see Table 7.3, column 4), this is based on the four catalogs of each set.

In order to better understand these distribution functions we have analyzed how the bulk flow is distributed as a function of density. The top row of Figure 7.9 shows point-to-point comparisons between the density contrast and bulk flows for the three different representations of the C4 catalog, LS_{Nbody} (left), LS_{Mock} (middle) and LS_{FAM} (right). These point-to-point distributions are presented in terms of scatter diagram point density contours.

It is clear that there is not a significant correlation between bulk flow and density quantities. Low density regions ($\delta\rho < 0$) are located throughout the whole velocity range. This is because deep underdense regions expand with a constant (positive) velocity divergence. This implies that objects located within these regions are accelerated at high speeds toward the edge of the voids. From the bulk flow maps we can infer that objects located near the GA region experience the largest gravitational attraction and therefore have the largest measured bulk flows. Also at density contrast between $[0,3]$ the same bulk flow range is found. This indicates that even at these densities the large scale velocities are influenced by the large scale structure, e.g., the GA in the case of the LS volume. At very high density regions ($\delta\rho > 3$), there are some isolated point clouds which are separated from the mainstay of the point distribution. These highly non-linear regions have decoupled from the large scale influence, and their internal motions have become more important, i.e., eventually dominated by virial motions. This behavior is most pronounced in the LS_{Nbody} sample. In the other two samples it is slightly weaker because they are diluted samples. In comparison to the Mock distribution, we observe that FAM has a more "continuous" distribution. This is particularly true for the high-density regions ($\delta\rho > 2$) as a result of the intrinsic FAM problems at these regions. This explains the broader FAM bulk flow distribution at $[400,700]$ km s^{-1} range. The virialized cloudy regions can also be recognized in this sample, but they spread over a wider range of bulk flows. Nevertheless, the FAM bulk-density point distribution resembles its parent distribution.

7.5.2 The velocity dispersion

In terms of revealing most clearly the very local characteristics of the peculiar velocity field, the volume-weighted velocity dispersion (σ_{v}) is the most interesting quantity from the $\mathcal{M}$ statistics. The velocity dispersion is defined as the local velocity deviations from the local measured bulk flow (Eqn. 7.6). Within the gravitational instability paradigm migration flows of matter are the result of the primeval tiny perturbations in the density field. These flows are enhanced as the result of the gravitational collapse of the mass distribution in certain regions. Therefore, these velocity deviations are potential tracers of the local gravitational potential. With this, it is expected to measure high velocity dispersions at high-density regions, while small velocity dispersions at low-density regions whose kinematics could be dominated by the large scale structure.

Figure 7.10 shows the σ_{v} maps for the same C4 catalog along the $z-$supergalactic plane as in Fig. 7.7. In all panels contour lines represent exactly the same σ_{v} values. The bold contour represents a "reference" velocity dispersion of $\sigma_{\mathrm{v}} = 140$ km s^{-1}. Regions with values above this σ_{v} are indicated by solid contours, those with smaller values by dashed contours. Although our criterion to divide high velocity dispersions from the low ones is rather arbitrary, we have chosen this value since it is very close to the mean velocity dispersion for the three sets (see Table 7.4 column 4). This is also the velocity dispersion around the LS filamentary structure. In this way, the LS is clearly well defined by "higher" velocity dispersion contours in the three samples. Note that the LS_{Mock} map is not severely affected by the sampling procedure. This map delineates the same high and low velocity dispersion values than the LS_{Nbody} map and therfore, it is a good representation of the "real" velocity dispersion map. The LS_{FAM} modeled sample presents the same overall characteristics than the "real" and "observed" maps. However, the FAM sample contains higher velocity dispersions along the LS-filament than the other two samples as a result of the FAM failure at these regions (see Section 7.4.2).

Low-density regions can be clearly recognized through their low velocity dispersions. The lowest measured σ_{v} value for the three samples coincides with the center of the Local void ([SGX,SGY] $\approxeq$

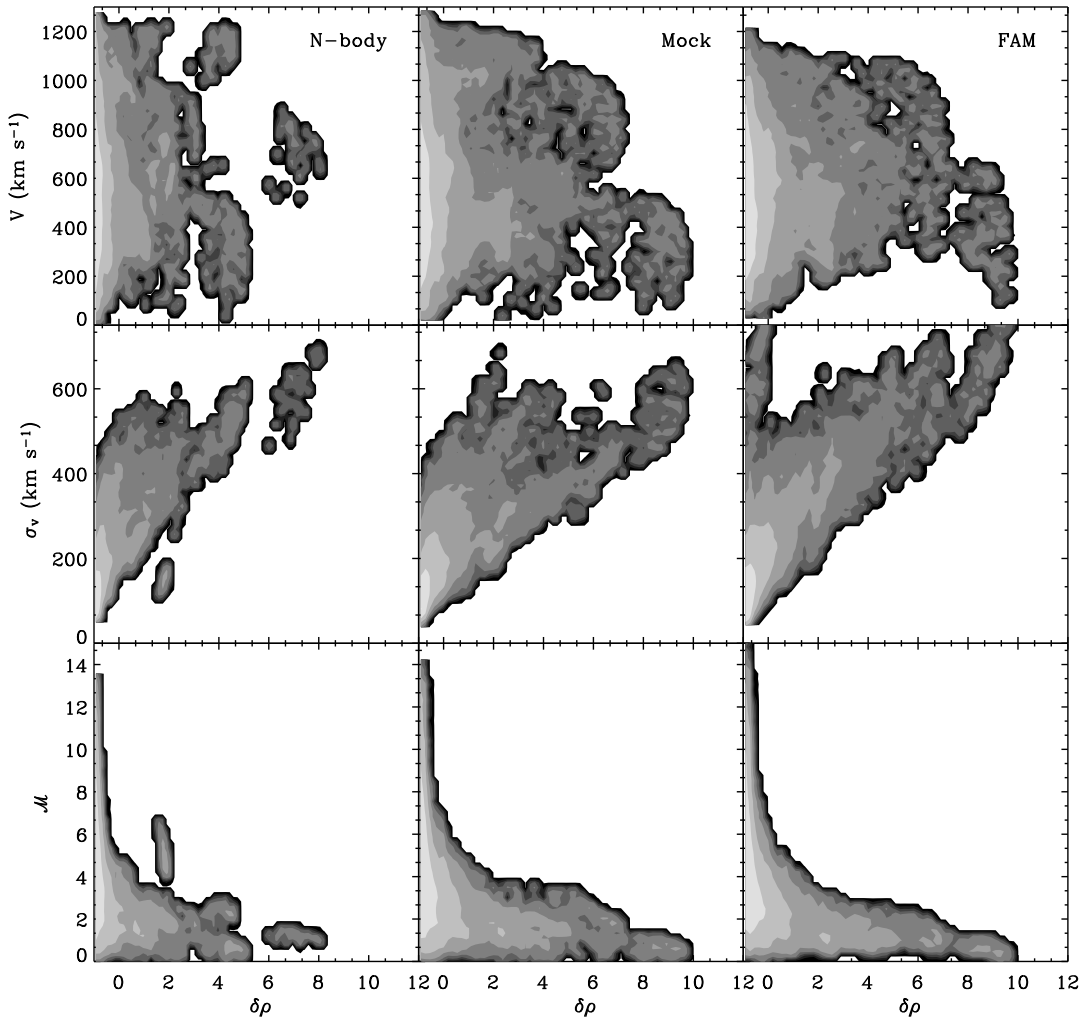

Figure 7.9 — Contour plots of the point-to-point distributions between the density contrast *vs* the bulk flow (upper row), velocity dispersion (middle row) and Mach number (bottom row) for the same catalog of the 3 sample sets (N−body, Mock and FAM). Contours represent equal density points in each panel.

[-10,-5]). The quietness of these regions can be interpreted as the result of their dynamics. Voids evolve as expanding super Hubble-bubbles (Icke 1984) with an almost constant velocity divergence. Therefore there are no velocity perturbations within these regions. However, these "low" velocity dispersion regions are larger in volume than the underdense regions. This is because the mildly non-linear regions, which still have laminar flows, are also dominated by the large scale motions. A point to notice in the three maps is that independently of the "mean" σ_v value chosen, the LGE is located in a region with a very low velocity dispersion of $\sigma_v \approx 60$ km s^{-1}.

We have also investigated how the velocity dispersion and the density field are related. Nagamine et al. (2001) pointed out that the velocity dispersion is an increasing function of overdensity (see also Kepner et al. 1997; Strauss et al. 1998). Willick & Strauss (1998) studied the small scale velocity dispersion from data finding a linear density dependence of this velocity dispersion. The middle row of Figure 7.9 shows the velocity dispersion as a function of density for the C4 catalog. There is a clear correlation between these two quantities as revealed by the three different samples. At the underdense regions there is a wide range of velocity dispersions, although the density of points decreases at higher

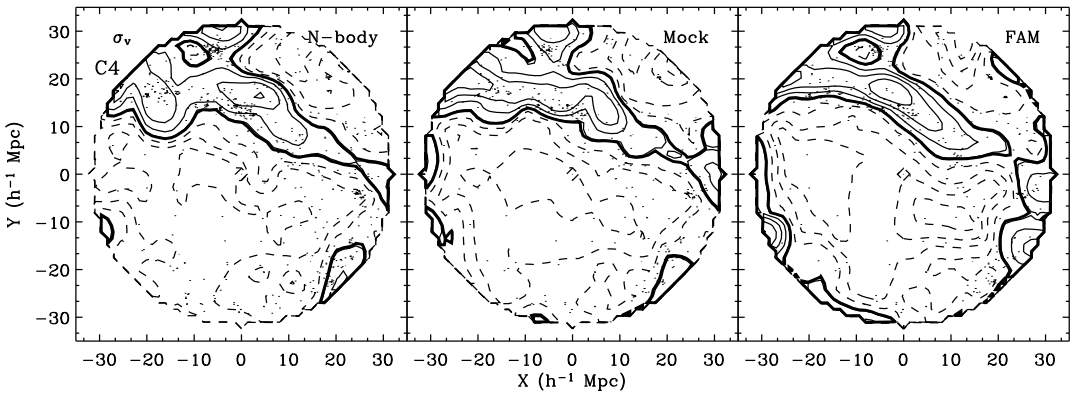

Figure 7.10 — Volume-weighted velocity dispersion maps for the same C4 catalog and projection than in Fig. 7.7 for its three different representations. Contour lines represent the same $\sigma_{\rm v}$ values for the three samples. The thick contour line represents the "average" velocity dispersion of 140 km s^{-1} within the surveyed volume.

$\sigma_{\rm v}$. These high contributions are coming from those low-density regions surrounding the high-density ones where the velocity dispersion increases as a result of the top-hat window size. This could partly include virialized regions hence. In the case of FAM this effect is magnified as a result of its inherent problems. At high density regions, the velocity dispersion increases almost linearly with density. The highest density regions in the $N-$body sample are separate from the rest of the point distribution indicating the virialized nature of such structures. These virialized regions are also clearly identified at the bulk flow panels as those isolated clouds of points from the general distributions.

The similarities and differences between the three different sets are also reflected in their DFs and CDFs presented in Figure 7.8. These distributions were computed from the same 1000 random spheres used to compute the bulk flow distributions (contiguous left panels). The distributions show indeed a very good agreement between the LS$_{Nbody}$ and LS$_{Mock}$ sets. The LS$_{FAM}$ distribution differs from the other two DFs in one main aspect. The tail of the FAM modeled $\sigma_{\rm v}$ distribution extends more than 200 km s^{-1} away than the "real" and "observed" ones. Furthermore, FAM not only predicts regions with larger dispersions, but also less number of $\sigma_{\rm v}$ values above 200 km s^{-1}. At low $\sigma_{\rm v}$s the FAM distribution follows the DF and CDF expected behaviors.

From the CDFs we can notice that most of the LS volume presents velocity dispersions within the range of $[70, 250]$ km s^{-1}. This is a rather "low" range. This may imply that the LS volume is in general not very dense, or that there are not many large matter concentrations that could perturb the velocity field. The mean velocity dispersion value is in the order of ≈ 145 km s^{-1} (see Table 7.4, column 4).

7.5.3 The Mach number

We have computed the volume-weighted cosmic Mach number $\mathcal{M}$ according to Eqn. 7.7. In this way, each $\mathcal{M}$ estimate corresponds to a real local value and not to an average value as given by other $\mathcal{M}$ definitions (see Nagamine et al. 2001). Since the $\mathcal{M}$ number is the ratio between the local bulk flow and velocity dispersion, for a given bulk flow a low $\sigma_{\rm v}$ will imply a high $\mathcal{M}$ value, while a high $\sigma_{\rm v}$ a low $\mathcal{M}$. Regions with low velocity dispersions such as the local void, the LGE and the mildly high density regions will have high $\mathcal{M}$ values, while the filamentary structure concerns a "high" velocity dispersion with a low $\mathcal{M}$ number.

Figure 7.11 shows the corresponding $\mathcal{M}$ maps for the C4 catalog. The contour maps are plotted along the $z-$supergalactic plane. The contour lines represent the same $\mathcal{M}$ values for the three samples. The thick bold line represents the "average" $\mathcal{M}$ contour, which we have computed by dividing the

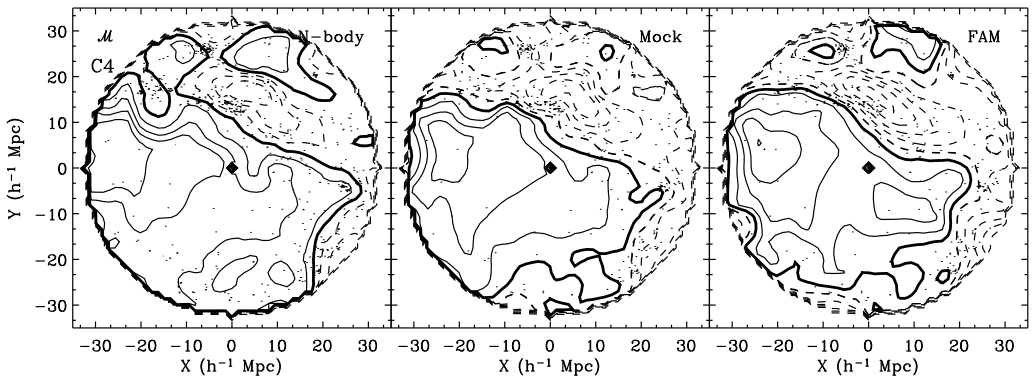

Figure 7.11 — Volume-weighted cosmic Mach maps for the same three representations of the C4 catalog. The projection corresponds to that of Fig. 7.7. The contour lines represent the same $\mathcal{M}$ values for the three panels. The thick contour line represents the "average" value of $\mathcal{M}$= 4.5

average bulk flow in Fig. 7.7 and the average velocity dispersion of Fig. 7.10. As expected, the LS filament may be identified with the low $\mathcal{M}$ number that crosses the map from the $-x$ to $+x$ region. The $\mathcal{M}$ number decreases inward the central regions of the LS. This may hint a density dependence. The local void, the LGE and mildly density regions are enclosed by high $\mathcal{M}$ estimates. The three maps present the same general characteristics: a well delimited LS region, the two cold spots at the top of the maps and the large cold area around the local void. The FAM map presents a smaller cold region (continuous contours) as a result of its larger measured velocity dispersions. Comparing these maps with the those for the velocity dispersions, we see that the former are the negative of the latter ones.

This might imply that the $\mathcal{M}$ number could also depend on the local density. In the bottom row of Fig. 7.9 we evaluate whether there is a possible relation between these two quantities. One can recognize that at the underdense regions ($0 < \delta$), the $\mathcal{M}$ estimates spread over the whole range of values, from 15 down to almost 0. This is a consequence of the same large spread observed in the bulk flow (top row). One of the coldest regions is located just at the border of the map $(SGX, SGY) \approx (-26, 0)$, a low density region close to the GA. The kinematics of this region is completely dominated by this structure as revealed by the corresponding bulk flow maps. At higher overdensities ($\delta > 0$), $\mathcal{M}$ drops drastically and presents a tighter point distribution. Still, there is not a clear correlation between $\mathcal{M}$ and the bulk flow. The virialized regions correspond to those separated clouds at $\mathcal{M} > 2$ in the $N-$body case. In the Mock-observed and FAM samples this is not clear. Despite the differences between the FAM bulk flow and velocity dispersion with respected to the full and observed samples, its $\mathcal{M}$ density point distribution resembles the Mock-observed one.

The Mach distribution functions and cumulative ones from the 1000 random spheres are presented in Figure 7.8 (top and bottom right-most panels). The measured Mock-observed $\mathcal{M}$s show a good concordance with the $N-$body Mach distribution. The FAM distribution reproduces in general the same behavior as the full and observed samples. The CDFs indicate that FAM predicts slightly more "colder" regions and less "hot" regions as a result of the higher measured $\sigma_{\rm v}$s. The strong similarities between these catalogs are strengthened by the average $\mathcal{M}$ numbers from the three catalog sets, $\mathcal{M} = 4.6 \pm 0.6$ (see Table 7.5, column 4).

These results reveal the dominant role of the large scale structure over the LS region. The relative high volume-weighted $\mathcal{M}$ number indicates that the galaxy distribution within a volume of 30 h^{-1}Mpc radius is mainly dominated by a large coherent bulk flow, partly induced by the GA region. However, the quadrupole mass distribution around the LS composed by the GA and PP is also responsible for such velocity quietness within this region, as indicated by the bulk flow and velocity dispersion maps. Under these circumstances is therefore not surprising that the LGE is rather cold. The LS represents a peak in the $\sigma_{\rm v}-$maps or a valley in the $\mathcal{M}$-maps as a result of its dynamical state prone to virialization.

Sample	V (km s^{-1}) M-W	M-W (DTFE)	V-W (DTFE)
$N-$body	551±51	549±53	535±46
Mock	557±54	552±59	533±47
FAM	536±66	555±70	535±47

Table 7.3 — Average local bulk flows (V) for the LS$_{Nbody}$, LS$_{Mock}$and LS$_{FAM}$from the four catalogs of each sample. The quantities were computed in three different ways: mass-weighted at the particle position (M-W), volume-weighted at the same particle positions (M-W DTFE), and volume-weighted at random positions (V-W DTFE).

Sample	$\sigma_{\rm v}$ (km s^{-1}) M-W	M-W (DTFE)	V-W (DTFE)
$N-$body	619±67	278 ±26	139± 14
Mock	609±49	276±16	142± 12
FAM	635±32	400±35	156± 20

Table 7.4 — Average local velocity dispersions ($\sigma_{\rm v}$) computed for the same set of samples as in table 7.3. Quantities were computed in the same ways.

Sample	$\mathcal{M}$ M-W	M-W (DTFE)	V-W (DTFE)
$N-$body	1.6±0.2	2.6±0.3	4.6±0.5
Mock	1.7±0.2	2.6±0.4	4.5±0.6
FAM	1.6±0.2	2.2±0.3	4.6±0.5

Table 7.5 — Average local cosmic Mach numbers ($\mathcal{M}$) computed for the same samples and methods as in tables 7.3 and 7.4.

7.6 The Mach statistics at the discrete particle positions

The volume-weighted analysis gives a fair estimate of the Mach statistics at any spatial position without depending of the galaxy distribution. However, the observational estimates only correspond to

measurements at the discrete galaxy positions. The resulting Mach estimates are then biased toward high-density regions as most observations.

In this section we investigate the effect of performing the Mach statistics only at the discrete object positions. For this we will consider two approaches. The first one is by using only the information given by the object distribution, a mass-weighted statistics. The second one will be by using the volume-weighted estimates of Section 7.5, but performed only at the particle positions.

As before, we have drawn 1000 spheres of 5 h^{-1}Mpc radius for each catalog from the 3 sample sets. The spheres have been centered at a particle position, and only those spheres containing more than 2 elements were included for the analysis. This was done in order to avoid zero velocity dispersions, and therefore undefined $\mathcal{M}$ estimates. The same sample of spheres was used for the $N-$body sample.

7.6.1 The particle distribution case: mass-weighted

We have computed the $\mathcal{M}$ statistics from the discrete particle positions of the 3 sample sets, LS_{Nbody}, LS_{Mock} and LS_{FAM}. The plots in this section refer to the C4 catalog. We only present the maps for the $N-$body catalog because our intention is to illustrate how these maps change when using mass-weighted quantities in comparison with the volume-weighted maps.

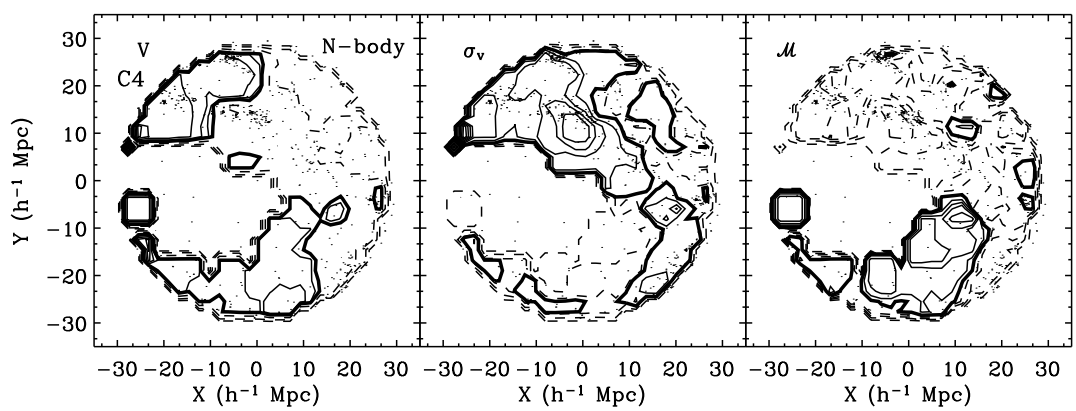

Figure 7.12 — Bulk flow, velocity dispersion and $\mathcal{M}$ mass-weighted maps for the C4 $N-$body catalog along the $z-$supergalactic plane.

Computing the $\mathcal{M}$-statistics at the particle distribution will sample mostly high-density regions, while the low density ones will be avoided. We have illustrated this in Figure 7.12. It concerns the contour maps for the C4 $N-$body catalog for the bulk flow (left panel), velocity dispersion (middle) and Mach number (right panel). The thick "mean" contours in the three panels represent the same average contours of the volume-weighted maps, i.e., $V = 600$ km s^{-1}, $\sigma_{\rm v} = 140$ km s^{-1} and $\mathcal{M} = 4$. The three maps clarify the problems of mass-weighted quantities in the large region devoid of data which corresponds to the Local void ($[SGx, SGY] = [-10, -10]$), and where no information has been extracted. Unlike the volume-weighted case, the LS region does not show a dominant bulk flow. In general there are less regions with bulk flows above the 600 km s^{-1} level. The peak at $V \approx 1000$ km s^{-1} corresponds to the region where the LS connects with the GA ($[SGX, SGY] = [-20, 20]$) and coincides with its volume-weighted counterpart. The velocity dispersion map looks more similar to the volume-weighted one at high-density regions. This is because these are the best mapped regions for the mass-weighted case. Measurements indicate larger $\sigma_{\rm v}$s than the volume-weighted ones (see also Fig. 7.1). As in the continuous case, the LS filament contains the largest measured $\sigma_{\rm v}$. By contrast, no velocity dispersion measurements have been carried out at low-density regions because of the lack of objects to perform this measurement. As a consequence of the discreteness in both quantities (V and $\sigma_{\rm v}$) the $\mathcal{M}$-map is severely affected. Although the LS is presented as a "cold" region, it is less colder than in

its volume-weighted counterpart. From these maps one could conclude that the LS volume is "warm", much more than in the volume-weighted case.

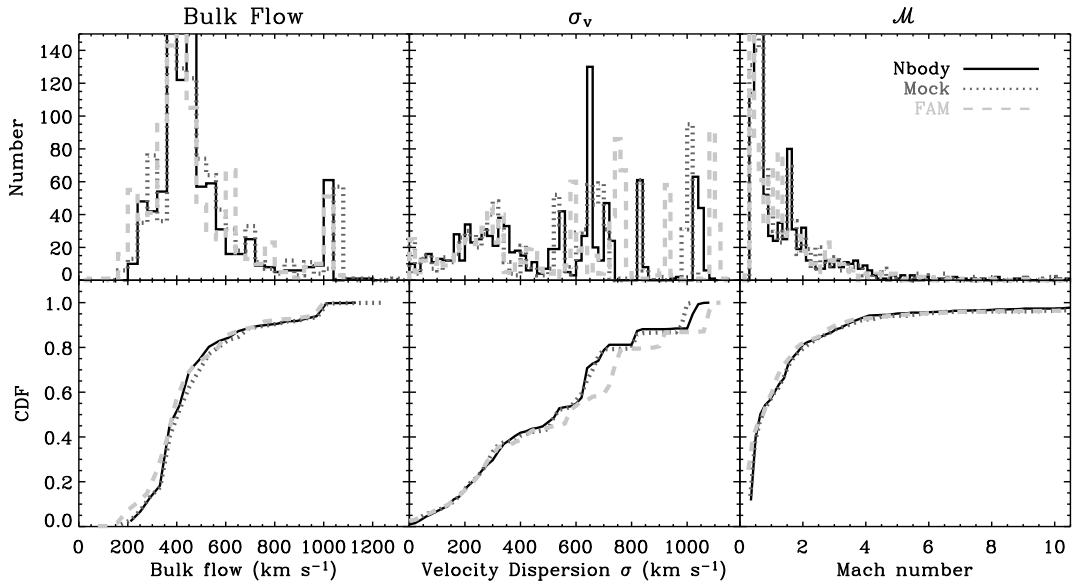

Figure 7.13 — Bulk flow, velocity dispersions and $\mathcal{M}$ distributions for the 3 set of catalogs (top panels). The respective cumulative distribution functions are shown in the lower panels for each quantity.

The discrete behavior of the maps can be noticed in the corresponding DFs and CDFs in Figure 7.13. The left column shows the local bulk flows, the central column the velocity dispersions and the right column the Mach numbers. The $N-$body, Mock and FAM local bulk flow distributions resemble each other. This is because this quantity is a large scale characteristics of the field. The spike at $V \sim 1000$ km s^{-1} corresponds to the region near the GA which is highly overdense and whose kinematics is dominated by the GA. The average measured bulk flows for the three set of samples ($V \approx 550 \pm 60$ km s^{-1}) are consistent with each other and with the volume-weighted case, be it that they are ~ 20 km s^{-1} larger.

The velocity dispersion panels reveal the effects of using a discrete sample. At low σ_vs the three distributions are very similar since these correspond to low density regions. At larger σ_v differences are clearly noticeable. The FAM dispersions at these high-density regions are not related anymore to the real ones as shown by their CDFs. The discrete jumps at high σ_vs correspond to the very local virialized regions, the galaxy clusters. These σ_v distributions are broader than in the volume-weighted case because particle velocities are more affected by two body relaxation processes. The distributions expand over a large range of velocities and with measurements of 400 km s^{-1} larger than in the volume-weighted case. The corresponding average σ_v for the four catalogs ($\sigma_v \approx 620 \pm 50$ km s^{-1}) differs substantially from the volume-weighted ones (see Table 7.4, second column).

The large σ_v values shift the Mach DFs toward lower values which peak at $\mathcal{M} \sim 0.8$. This clearly indicates that such distributions are dominated by the sampling at high-density regions. The long tails of the DFs toward high Mach values (> 4) are the result of small velocity dispersions measured in void regions, introducing noisy estimates of the Mach number.

We can conclude that when using mass-weighted quantities the nearby cosmic region is in general much "warmer" than in the volume-weighted case, as indicated by the average $\mathcal{M}$ estimates of $\sim 1.6 \pm 0.2$ (see Table 7.5, second column).

7.6.2 The particle distribution case: the DTFE

We have performed the same $\mathcal{M}$ statistics as in Sec. 7.6.1 but using the volume-weighted fields. Our intention is to compare in a fairer way the mass-weighted estimates from the discrete particle positions with respect to the volume-weighted quantities at exactly the same locations. For this, each sphere was located at the same position as in the mass-weighted case. This will bias measurements toward the high density regions. Therefore, the Mach DFs and CDFs will be shifted toward lower values than in the volume-weighted case.

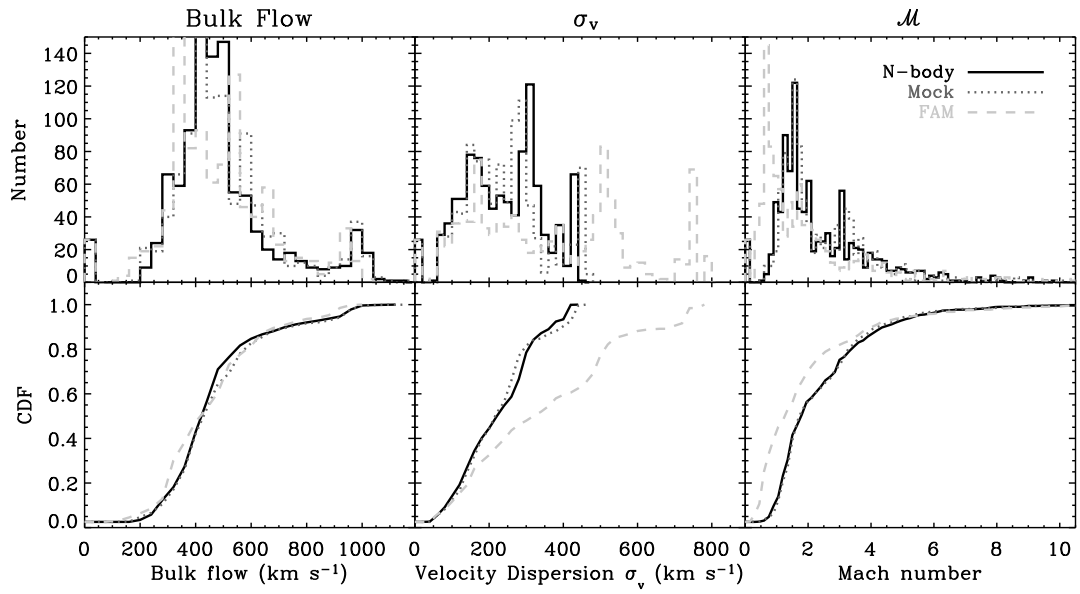

Figure 7.14 — Volume-weighted distributions for the local bulk flow, velocity dispersion and $\mathcal{M}$ for the 3 set of catalogs, computed at the particle positions as in Fig. 7.13.

Figure 7.14 shows the distribution and cumulative distribution functions for the bulk flow, velocity dispersion and Mach number for the three representations of the C4 catalog.

The bulk flow distributions are very similar to each other, and also to the mass-weighted distributions. The small peak at $V = 1000$ km s^{-1} coincides with its mass-weighted counterpart, an indication of the GA effects around its surrounding areas. The average bulk flows are consistent with the other methods, (see Table 7.3, third column). The velocity dispersion DFs are more compact than in the mass-weighted case as a result of mitigating shot-noise and two-body relaxation effects.

The average σ_vs are much smaller than the mass-weighted, but still somewhat larger than the volume-weighted random measurements (Table 7.4). This is a result of performing biased measurements toward high density regions. The large departure in the corresponding FAM CDF indicates that its dispersion is not related at all with the real velocity dispersion.

The fact that the Mach distributions are very similar to each other, despite the σ_v differences, denotes that the surveyed volume is mainly dominated by the bulk flow. This volume-weighted sampling at high-density regions indicates that the LS volume is not so "warm" as indicated by the mass-weighted estimates but "cold" (Table 7.5), where the $\langle\mathcal{M}\rangle = 2.6 \pm 0.4$ for the full and observed cases, while $= 2.2 \pm 3$ for the FAM case.

7.6.3 $\mathcal{M}$ mass-weighted vs $\mathcal{M}$ volume-weighted: a point-to-point comparison

We have performed a point-to-point comparison between the mass and volume weighted methods. We have only used estimates at the same particle positions.

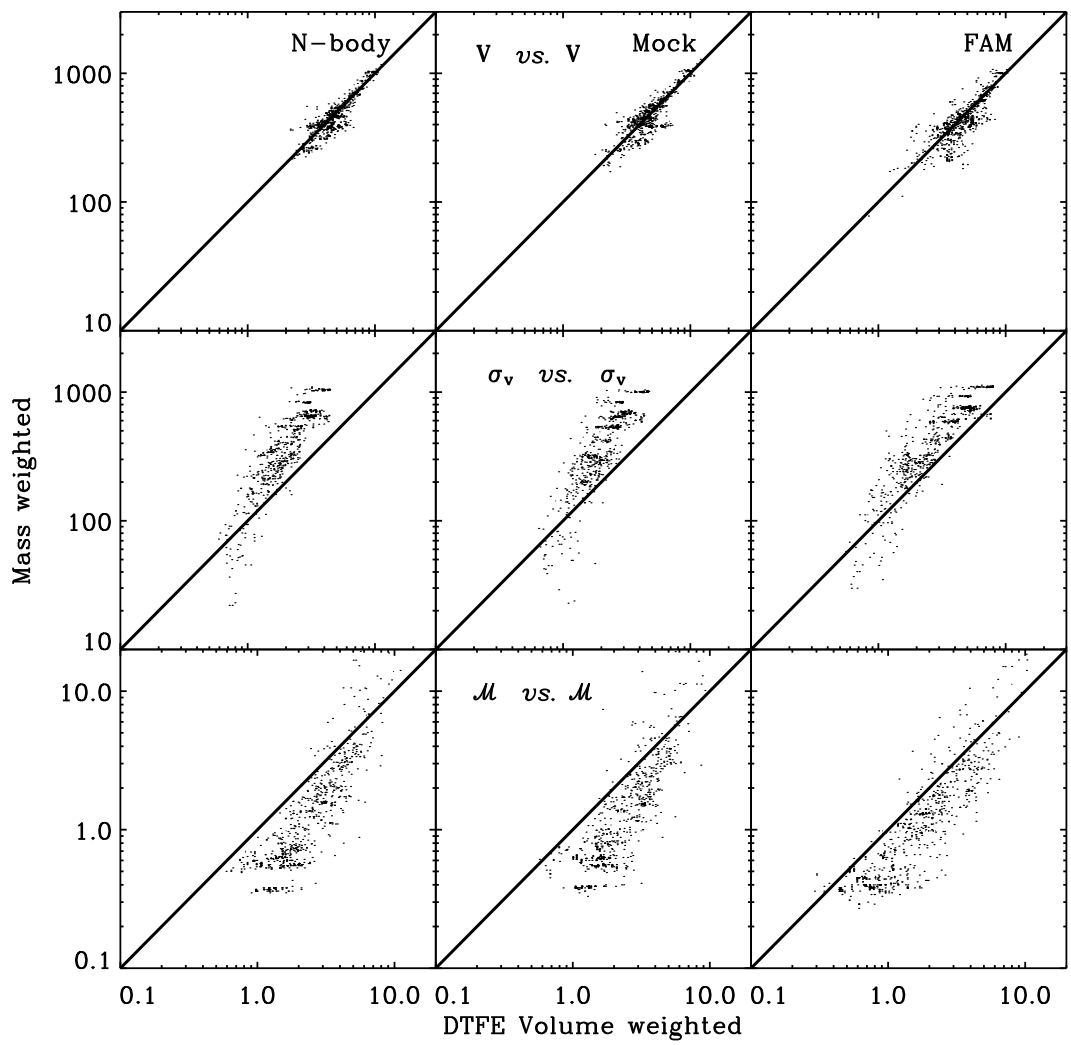

Figure 7.15 — Point-to-point comparisons of the mass-weighted *vs* the DTFE volume-weighted quantities for the 3 representations of the C4 catalog.

Figure 7.15 shows the point-to-point comparisons between the mass-weighted and volume-weighted estimates for the three representations of the C4 catalog. The solid lines delineate the one-to-one relations. Because the bulk flow is a characteristic measurement of the large scale matter distribution, it should not be severely affected by sparse sampling effects, and it should not depend on the very local density contrast of the region under study. This is indeed showed in the top row panels.

The mass-weighted estimates give consistently higher values for the velocity dispersions than the volume-weighted ones. The reason is twofold. The first one concerns sampling covering effects. While the volume-weighted velocity represents a continuous field, it is not for the discrete case. Thus, when the calculation is performed near mildly and non-linear density regions, the DTFE velocities vary more smoothly than in the discrete case. This is also the reason for the horizontal lines of points at high $\sigma_{\rm v}$. While the mass-weighted dispersions are the same within the galaxy clusters, they are not in the volume-weighted case where they vary smoothly. This also explains why at low density regions the mass-weighted velocity dispersions are smaller than the volume-weighted ones. In the

former, only 2-3 enclosed particles could characterize $\sigma_{\rm v}$, while in the latter this is not the case. Each enclosed region will always contain the same amount of grid-cells with smoothly vary velocities to characterize the velocity dispersion. The second effect concerns to the size of the tophat kernel used in the procedure (5 h^{-1}Mpc). This radius is large enough to enclose high density peaks together with lower density regions, introducing an extra noise and bias in the mass-weighted case, increasing the respective estimates.

As a consequence of the differences in $\sigma_{\rm v}$ between the two methods, the volume-weighted estimates predict in general much "colder" regions than in the mass-weighted case for the full, observed and modeled samples. However, the "coldest" regions are much colder in the mass-weighted case than in the volume-weighted one as deduced from their $\sigma_{\rm v}$ behaviors.

7.7 Discussion and Conclusions

We have presented a study of the kinematics of the large-scale *vs* small-scale structure for the Local Supercluster region within a volume of 30 h^{-1}Mpc from the Local Group. For this we have computed the cosmic Mach number. This is defined as the ratio between the bulk flow within a volume to the velocity dispersion within that volume. The bulk flow is a measurement of the large scale perturbations, while the velocity dispersion is a measurement of the small scale components of the power spectrum.

We have used a set of four velocity fields extracted from $N-$body simulations aimed to reproduce the nearby mass distribution of large-scale structures ($\gtrsim 5$ h^{-1}Mpc). These simulations also mimic their main dynamic characteristics. We have addressed how sparse sampling could affect the Mach statistics by constructing Mock "observed" catalogs according to the NBG catalog of Tully (1988). We have also considered the effect of dealing with modeled velocity fields, such as those from the FAM modeling.

We have used volume-weighted quantities to compute the Mach statistics since these are closer to the analytical predictions and suffer less from systematic effects: two-body relaxation and sampling problems. This has been achieved by applying the Delaunay Tessellation Field Estimator [DTFE] for peculiar velocities. We have applied this method to discrete $N-$body, Mock and FAM sets to render full spatial-covering and volume-weighted velocity fields. By studying the velocity dispersion we have found that such DTFE fields are not affected severely by grid-resolution effects. A direct implication of using Mock samples in the DTFE velocity fields is that the interpolated fields would differ more at high density regions than at low density regions. Due to the DTFE characteristics the velocity dispersion at high-density regions are smaller as for any discrete velocity field.

The Mach statistics was performed over spheres of 5 h^{-1}Mpc radius in the LS volume. An unbiased volume-weighted analysis by placing randomly spheres within the volume, showed that our results were not bias toward the sampled regions. Also, they represented a fair estimate of the coldness of warmness of the LS volume. We found that the LS volume is dominated by an average coherent bulk flow of 530 ± 47 km s^{-1} for the three sample sets, illustrated by the bulk flow maps for a given catalog. Furthermore, this is not dependent of the local measured density. The bulk flow increases in amplitude toward the GA region and decreases toward its opposite direction, the PP region. This implies that the GA is an important source for such coherent motion, but also the other major structures around the surveyed volume such as the PP supercluster.

The velocity dispersion proved to be the most interesting quantity of this statistics. In average we measured a $\sigma_{\rm v} = 140 \pm 16$ km s^{-1} for the three sample sets. However, the FAM dispersion were consistently higher than in the other two cases as result of its attached problems. We found that $\sigma_{\rm v}$ strongly depends on the local overdensity, indicating that the density field is the amplifier and source for such velocity dispersions. The highest measured velocity dispersions correspond to the highest density regions. The fact that the average $\sigma_{\rm v}$ is so low for the LS volume is an indication that this volume is filled out by large underdense regions. Indeed, on average within the LS volume the 77% of the density field corresponds to underdense regions, while the other 23% to high-density regions. This is reflected in the $\mathcal{M}$ number. We measured a $\mathcal{M} = 4.6 \pm 0.6$ for the three sets. This implies that the

LS volume is a rather "cold" region dominated by the influence of the large scale structure. Due to the large bulk flow influence, the $\mathcal{M}$ number is a weakly decreasing function of overdensity.

A direct comparison of our results with those reported in the literature is not feasible since the earlier measurements were mass-weighted and heavily weighted by the densest regions. Therefore, we performed the $\mathcal{M}$-statistics by placing spheres only at the particle positions for the discrete and DTFE continuous velocity fields. The bulk flow estimates did not represent any considerable variation with respect to the volume-weighted measurements. Both techniques gave a $V \approx 550$ km s^{-1}.

The velocity dispersion revealed very significant differences between the two techniques. The measured mass-weighted velocity dispersion indicated a $\sigma_{\rm v} = 620 \pm 50$ km s^{-1} for the three samples. This clearly indicates that the sampling is biased toward high-density regions. At these regions, $\sigma_{\rm v}$ is dominated by virialization and two-body relaxation processes. By contrast, the volume-weighted measurements at the same particle locations gave a lower value of $\sigma_{\rm v} = 278 \pm 26$ km s^{-1} for the full and observed fields, but a value of 400 ± 35 km s^{-1} for FAM. This is an indication of the FAM failure for modeling motions at high-density regions. A direct comparison between mass-weighted and volume-weighted velocity dispersions indicated that the largest differences are at high-density regions. The discrete DTFE expected measured $\sigma_{\rm v}$s are in good agreement with those reported by Tonry et al. (2000) from the surface brightness fluctuation (SBF) survey ($\sigma_{\rm v} = 312 \pm 24$ km s^{-1}), and also with the results from (van de Weygaert & Hoffman 1999, $\sigma_{\rm v} \approx 280$ km s^{-1}).

The corresponding $\mathcal{M}$ values are different for both techniques. The mass-weighted measurements give a $\mathcal{M} = 1.6 \pm 0.2$, while the volume-weighted $\mathcal{M} = 2.6 \pm 0.5$. These results could bring a strong discrepancy because while the mass-weighted $\mathcal{M}$-statistics could indicate an open universe (denoted by the high velocity dispersion), the corresponding volume-weighted measurements indicate a low-density universe. However, these measurements correspond to the same low-density universe. Hence, the mass-weighted one is a mere reflex that the statistics has been heavily weighted by the densest regions. The volume-weighted result at the particle position is consistent with van de Weygaert & Hoffman (1999), and in principle also with the mean value reported by Nagamine et al. (2001) (also the mass-weighted one). Because the local cosmic region is in general a low density one, dominated by a large coherent bulk flow, it is then expected to be "cold".

We have shown that the effects of incomplete sampling (Mock catalogs) are not important in the $\mathcal{M}$-statistics provided one deals with the 3D velocity field. However, this statistics is affected when one has to infer the peculiar velocity field by any method, specially for the velocity dispersion where one obtains higher values. Although, the use of volume-weighted quantities circumvent this problem.

The fact that the FAM sample has been corrected for unaccounted large scale influences and tidal effects and that it manages to recover the $\mathcal{M}$-numbers, implies that these two unaccounted external effects should be taken into account for this kind of studies. The analysis from Nagamine et al. (2001) about the cosmic Mach number lacks from tidal information. Although they did correct for the missing very large scale contributions, they did not take into account the more nearby-local contributions like the shear velocity. This tidal velocity component could affect mainly the velocity dispersion of galaxies, mainly in the case of the LGE, giving therefore, different values of the Mach number.

We conclude that the Mach statistics is not a good unbias "temperature" estimator. It strongly depends of how one proposes the analysis, volume-weighted or mass-weighted. A very general analysis independent of the particle positions indicates that the LS volume is rather "cold". By contrast, a volume-weighted biased analysis toward the well sampled regions indicate that the LS is "cold". However, this gets "warmer" when the analysis is performed in a mass-weighted fashion. Nevertheless, all employed methods agree on the fact that the LS is fully dominated by a coherent bulk flow mainly exerted by the GA region.

7.A Volume & Mass weighted quantities

When one wishes to obtain reliable estimates of statistical parameters from a given observed or computer-simulated field, one faces the complication of dealing with discrete, non-uniform fields.

A major issue concerns the fact that analytical/theoretical predictions concern quantities evaluated uniformly throughout a cosmic volume, while observed or simulated results are biased toward the measured particle (matter) distribution.

The usual strategy to deal with such discrete data sets is to smooth them with a filter to yield a continuous field. In the case of the peculiar velocity field several authors (e.g. Bertschinger et al. 1990; Juszkiewicz et al. 1995; Lokas et al. 1995) filtered galaxy velocities with a Gaussian kernel of a fixed length for reducing problems of noisy data, sparsely sampled underdense regions and to obtain the velocity field on a regular grid.

Often, without explicitly stating so, most smoothing procedures are implicitly mass-weighted. Formally, a mass-weighted field is defined as:

$$\mathbf{v}_{mass}(\mathbf{x}_0) \equiv \frac{\int \mathrm{d}\mathbf{x}\, \mathbf{v}(\mathbf{x})\rho(\mathbf{x})\, W_M(\mathbf{x},\mathbf{x_0})}{\int \mathrm{d}\mathbf{x}\rho(\mathbf{x})W_M(\mathbf{x},\mathbf{x_0})}, \tag{A7-1}$$

where $W_M(\mathbf{x},\mathbf{x_0})$ is the used filter function . Effectively W_M determines the weight of a mass element. Usually the filter function is not dependent on the location $\mathbf{x_0}$, but on the distance $\mathbf{x}-\mathbf{x_0}$. The aim of this procedure is to interpolate the velocity field values at random sampling locations to those at a regular grid, weighing the contribution by each sampling point by the filter function value. When the density field has been sampled discretely its effective density field is given by

$$\rho(\mathbf{x}) = \sum_i \delta_D\,(\mathbf{x}-\mathbf{x_i}), \tag{A7-2}$$

where $\delta_D(\mathbf{x}-\mathbf{x_i})$ is the Dirac delta function. The resulting mass-weighted filtered field thus becomes

$$\mathbf{v}_{mass}(\mathbf{x}_0) = \frac{\sum_i w_i \mathbf{v}(\mathbf{x}_i)}{\sum_i w_i}, \tag{A7-3}$$

where $w_i \equiv W_M(\mathbf{x}_i,\mathbf{x_0})$. Because analytical results involving two fluctuation fields, $\rho(\mathbf{x})$ and $f(\mathbf{x})$, are more cumbersome to evaluate, most theoretical work relates to the simpler *volume – weighted* filtered quantities. In this way, the volume-weighted velocity field $\tilde{\mathbf{v}}$ is given by

$$\tilde{\mathbf{v}}(\mathbf{x_0}) \equiv \frac{\int \mathrm{d}\mathbf{x}\mathbf{v}(\mathbf{x})W_V(\mathbf{x},\mathbf{x_0})}{\int \mathrm{d}\mathbf{x}W_V(\mathbf{x},\mathbf{x_0})}, \tag{A7-4}$$

where $W_V(\mathbf{x},\mathbf{x_0})$ is the applied weight function. Hence, for a successful comparison of the analytical results with the observed ones, and for a full space determination of the desired quantities, it is of crucial importance to have a reliable estimator of volume-average quantities. The problem turns now to produce a realistic and very accurate interpolation from a sparsely sampled velocity field to the whole sampling volume (regular grid) without loosing information at any scale.

Bernardeau & van de Weygaert (1996) proposed the use of Voronoi and Delaunay tessellations as natural filters and interpolation volumes in multi-D space. They explicitly showed that the zero-order Voronoi estimator is the asymptotic limit for volume-weighted field reconstructions from discreetly sampled field values. They extended this to the first order Delaunay estimator showing its the superior performance in reproducing analytical predictions. In Chapter 6 an interpolation method for peculiar velocities was described. This is based on the Delaunay Tessellation Field Estimator (Schaap 2005; Schaap & van de Weygaert 2000). This method has the purpose of rendering a fully volume-covering reconstruction of a peculiar velocity field from a set of discrete data velocity points. The method suppresses various discreteness effects such as shot-noise. Combining the volume-average prescription from Bernardeau & van de Weygaert with our velocity interpolation method, it is possible to compute volume-weighted quantities for all space under consideration.

7.B The catalog sample

We present in this appendix the four catalog realizations for one set, the Mock-observed sample. For reasons of simplicity, we only present one 2D-section through the 3D catalogs along the $z-$supergalactic axis for all catalogs and for all maps. Each catalog is indicated by the upper left label: C1,2,3,4. We present maps for the density contrast, δ (Figure 7.16), the bulk flow V (Figure 7.17), the velocity dispersion $\sigma_{\rm v}$ (Figure 7.18) and the Mach number $\mathcal{M}$ (Figure 7.19). For each set of plots the contours represent the same values for the four catalogs. The bold lines represent the respective average quantity, regions above this value are represented by continuous contours, while those below that value by broken lines. All quantities have been computed by top-hat filtering of 5 h^{-1}Mpc radius. As can be noticed, all maps for each quantity share the same large scale characteristics. The main structures such as the LS and Local void are clearly visible in Figs. 7.16, 7.18 and 7.19. In all catalogs the strong influence of a bulk flow exerted by the GA is clearly noticed (Fig. 7.17). The LS is recognized by its large velocity dispersion and therefore its low $\mathcal{M}$ number, while the Local void by its low velocity dispersion and large $\mathcal{M}$ number (Figs. 7.18 and 7.19).

The similitudes and differences between the different catalogs can be noticed on the distribution functions and cumulative distribution functions for the bulk flow, velocity dispersion and Mach number (Figure 7.20). The C2 and C4 catalogs display somewhat larger bulk flows than the other two catalogs, but less regions with the same V values. All catalogs have similar $\sigma_{\rm v}$ distributions. The C2 and C4 $\mathcal{M}$ distributions indicate that these catalogs are colder than the other two.

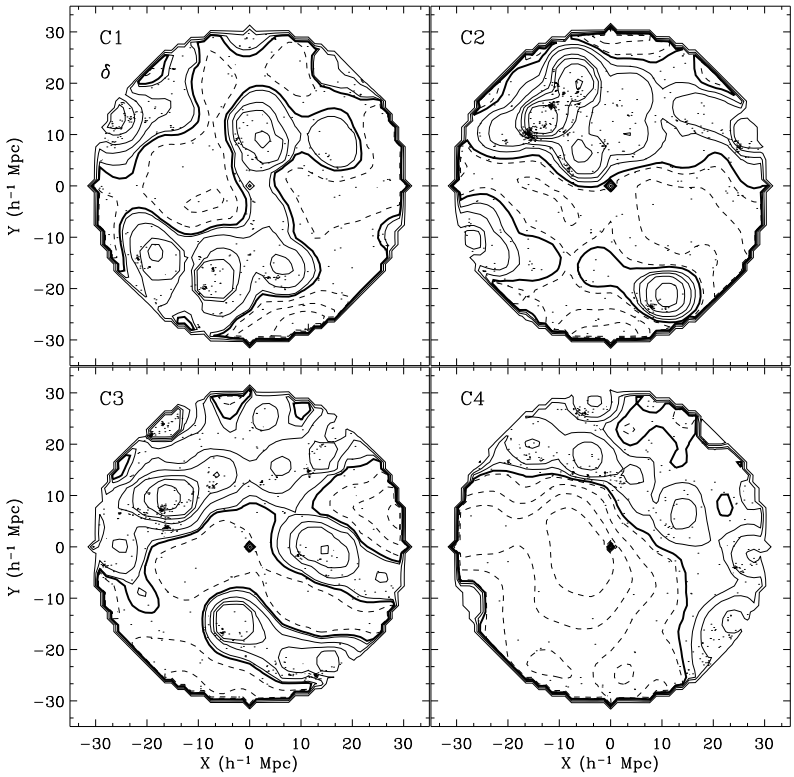

Figure 7.16 — Volume-weighted density contrast maps. The thick continuous line represents the $\delta = 0$ contour.

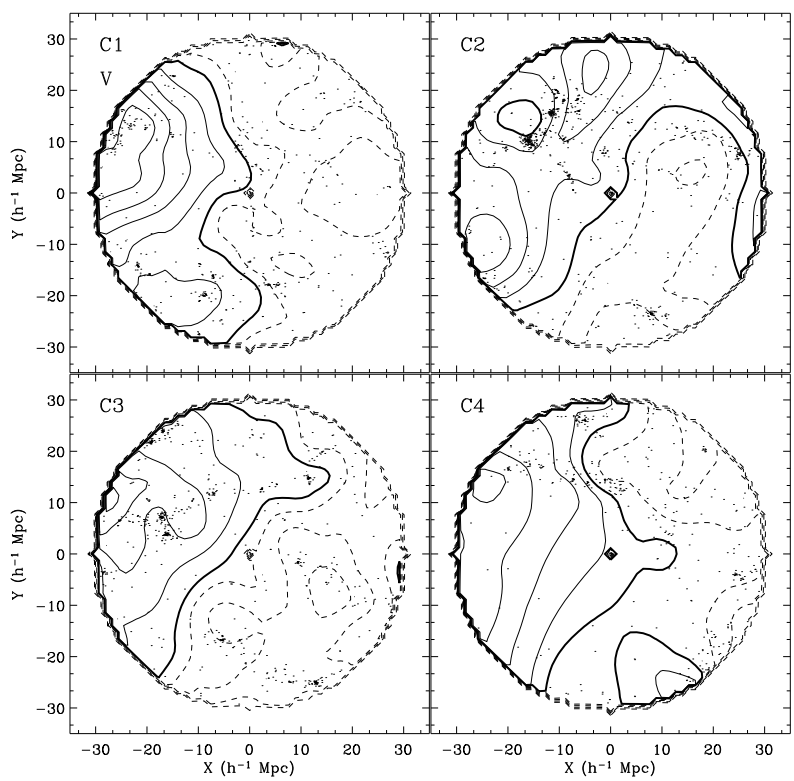

Figure 7.17 — Volume-weighted bulk flow maps. The average contour is the LGE velocity of 600 km s^{-1}.

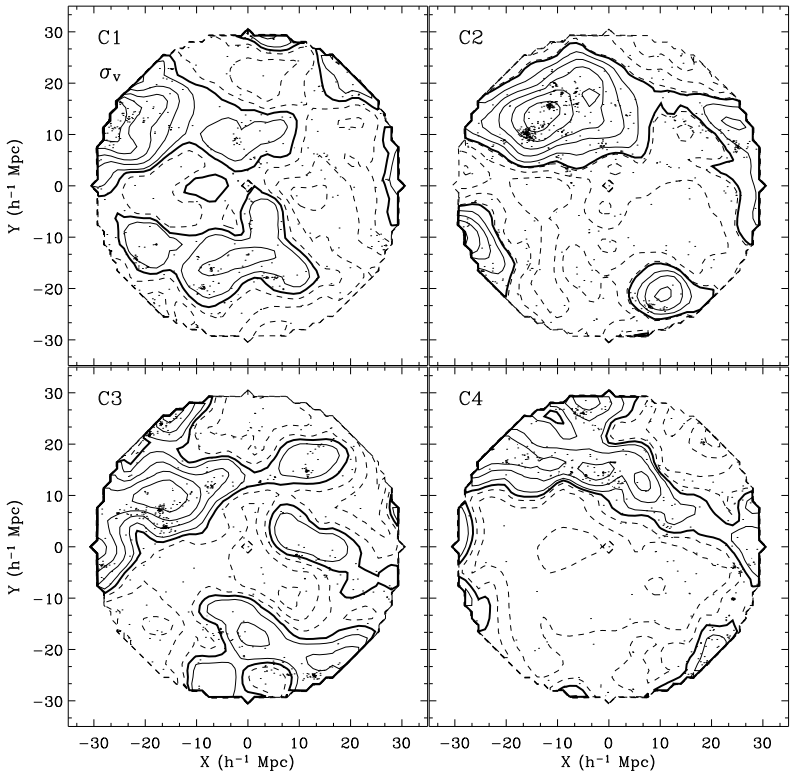

Figure 7.18 — Volume-weighted velocity dispersions maps. The bold line represents the average velocity dispersion of $\sigma_v = 140$ km s^{-1}.

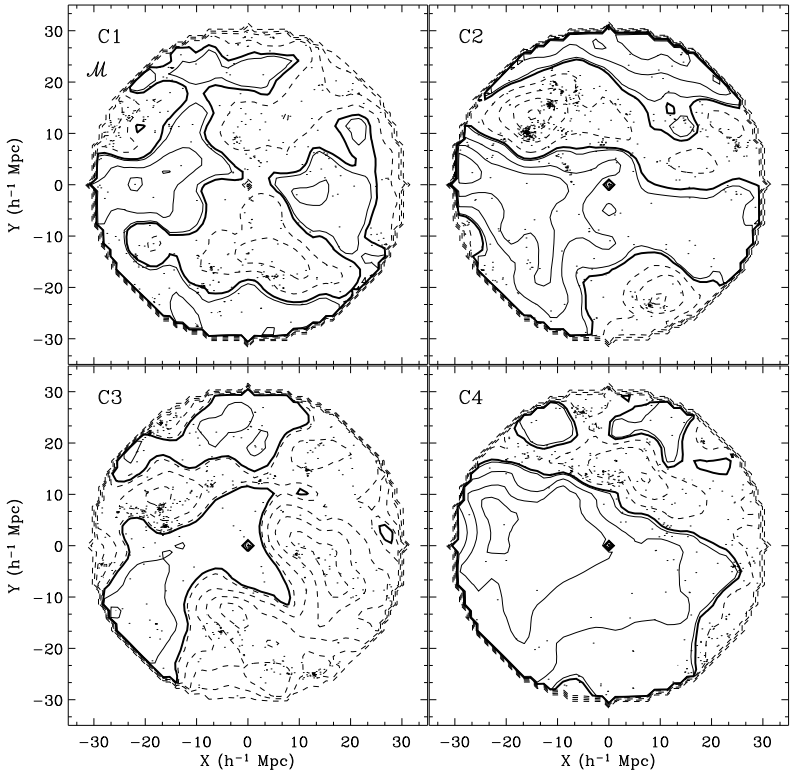

Figure 7.19 — Volume-weighted Mach maps. The average $\mathcal{M}$number is the ratio between the LGE velocity and the average velocity dispersion, hence = 4 (rounded number).

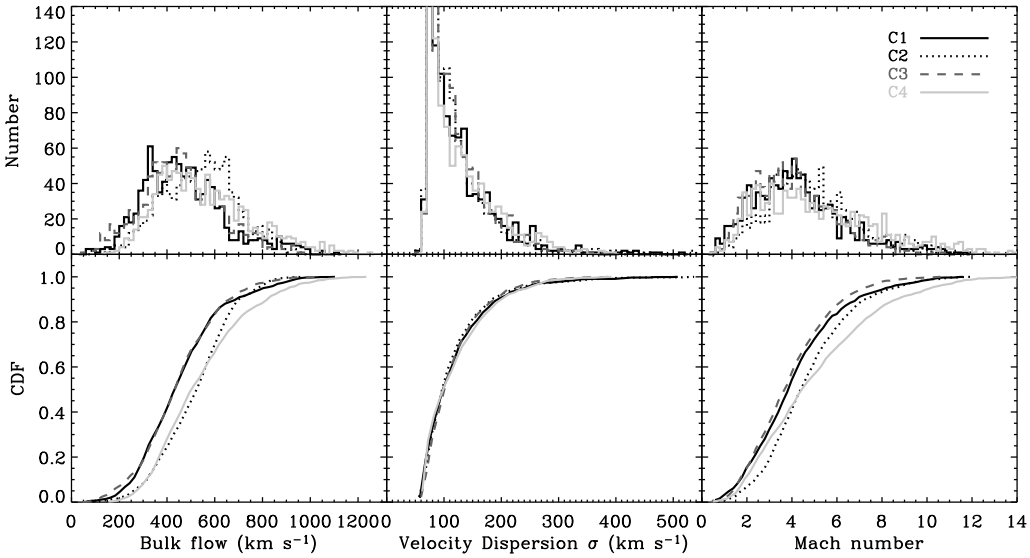

Figure 7.20 — Volume-weighted distributions for the bulk flow, velocity dispersion and $\mathcal{M}$for the 4 catalogs. The calculations have been performed at completely random locations within the LS volume, independently of the particle positions.

8

Weak lensing reconstruction of filaments

J. P. Dietrich, E. Romano-Díaz, & P. Schneider.

We present a study based on weak lensing analysis, the Aperture multipole moments statistics, to detect filaments connecting neighbouring galaxy clusters. Within the large scale structure of the universe, filaments exist between highly clustered and aligned clusters. This should be notable in the reconstructed surface mass distribution around pair of clusters with weak gravitational lensing. Observationally, the characterization of filamentary patterns remains ill-defined by absence of a well defined criterion for identification. The Aperture multipole moments technique is a promising method to quantify observationally the presence of filaments. It is therefore necessary to establish the reliability and confidence level of such method before applying it to real observations. In the present chapter we have applied this technique to quantify the presence of a filament connecting two neighboring clusters in carefully designed constrained $N-$body simulations. Results show that although the weak lensing method employed is not the most ideal technique to detect filaments, there is indeed a small yet detectable lensing signal that can already be observed using available instruments.

8.1 Introduction

Within the Gravitational Instability paradigm the large scale structure in the universe of the distribution of galaxies is the result of initially small Gaussian random density fluctuations which have been amplified by gravity. Objects such as galaxies evolved from "peaks" in the initial density field. This structure of galaxies consists of rich and poor cluster of galaxies connected by filaments and sheets and with large regions devoid of galaxies in between. This filamentary structure which resembles a "cosmic foam", has been observed since the earliest galaxy surveys (e.g. Joeveer & Einasto 1978; de Lapparent et al. 1986; Giovanelli et al. 1986; Geller & Huchra 1989; Vogeley et al. 1994; Shectman et al. 1996) and more recently at higher redshift by Möller & Fynbo (2001), Ebeling et al. (2004) and Baugh et al. (2004); Doroshkevich et al. (2004) on the 2DF and SDSS galaxy surveys.

Zel'dovich (1970) was among the first to realize that shear plays an important role in the structure formation process. The collapsing of density perturbations is not arbitrary but it follows specific directions determined by the axes of the deformation tensor (see also Doroshkevich 1970; Zel'dovich et al. 1982; Shandarin & Zeldovich 1989). Density perturbations collapse first along one direction giving origin to planar pancakes, these drain into filaments (second collapse along the second direction), and finally collapsing into clusters. The validity of the Zel'dovich approximation extends up to regions where the density contrast is within the the linear regime, $\delta \leq 1$ (where $\delta = \rho/\langle\rho\rangle - 1$ is the density contrast, ρ is the local density and $\langle\rho\rangle$ is the average density of the universe), although it gives reasonable results well beyond such limit. Several authors have worked along the Zel'dovich path in order to extend such formalism into the quasi non-linear regime. An extensive review of the different methods may be found in Sahni & Coles (1995). On the other hand, numerical simulations of the growth of initial Gaussian density fluctuations into the non-linear regime have succeeded in reproducing such filamentary structure of the universe (e.g. Klypin & Shandarin 1983; Davis et al. 1985; Bertschinger & Gelb 1991; Evrard et al. 2002).

Bond, Kofman, & Pogosyan (1996) showed that the filamentary "web" that defines the final state in the $N-$body simulations is present in the initial density fluctuations. In other words, the pattern of the web is defined largely by the rare density peaks in the initial fluctuations, with the subsequent non-linear evolution of the structures bringing the filamentary network into sharper relief. Furthermore, the filamentary web is a consequence of the distribution and spatial coherence of the strain (shear) field in the medium. They found that filaments exist between highly clustered and aligned clusters, and that this should be especially notable in the mass distribution around systems of clusters reconstructed with weak gravitational lensing techniques which uses the projected strain field.

Because of the greatly varying mass-to-light ratios between rich clusters and groups of galaxies (Tully & Shaya 1999) it is very challenging to convert the measured galaxy densities without making further assumptions. Dynamical and X-ray measurements of filaments will not yield to accurate mass values, as filamentary structures are probably not virialized. Weak gravitational lensing, which is based on the measurement of the shape and orientation parameters of faint background galaxies, is a model-independent method to determine the surface mass density of clusters and filaments. This method makes no assumption related to the dynamical state of such structures and the nature of the deflecting matter. However, because of the random orientation of the unlensed faint background galaxies, every weak lensing mass reconstruction is unfortunately an inherently noisy process, and therefore the expected surface mass density of a single filament is too low to be detected with current telescopes (Jain et al. 2000).

Bond et al. (1996) showed that the surface mass density of a filament increases towards a cluster. Therefore, filaments connecting neighboring clusters (*bridges*) should have surface mass densities high enough in order to be detected by weak lensing analyses (Pogosyan et al. 1998). There have been some reports that such filamentary structure have been detected through weak lensing studies (Kaiser et al. 1999; Gray et al. 2002; Clowe et al. 1998). Nevertheless, the possible detections remain somewhat uncertain due to several aspects, foreground structures in front of filaments, edge and systematic effects on the observational data, etc.

A significant detection of a bridge between galaxy clusters and the estimation of its surface mass

density is of utmost importance in observational cosmology and would provide important constraints for the theory of structure formation.

In this chapter we address the question of how to identify a bridge between two neighboring clusters using weak gravitational lensing. Normal weak lensing mass reconstructions have strongly correlated error bars and therefore make it difficult to assign a significance level to a limited part of a structure (like a bridge between to clusters). Nevertheless, there is one method to avoid this problem, the aperture mass statistic. Aperture masses are masses inside a circle minus the mass inside an annulus around the circle. This method allows one to easily determine the SN ratio inside the region covered by the weight function. The problem here lies in finding a suitable weight function.

The concept of aperture masses can be generalized to multipoles of the mass distribution inside a circle (Schneider & Bartelmann 1997). In this study, we hope to find a suitable combination of aperture masses and multipole moments to identify a bridge. Furthermore, we need to develop a statistic to quantify the significance of a bridge (or no bridge). For these reasons, we have applied this weak lensing technique to controlled $N-$body experiments of bridges between clusters, where one could know in advance the main characteristics of such configuration. This can be done by using the Constrained Realizations methodology [CR] for $N-$body simulations (Bertschinger 1987). This technique has proved to be very useful for investigating in a very consistent and systematic way the configuration and dynamical evolution of cosmic structures like clusters of galaxies and voids (e.g. van de Weygaert & van Kampen 1993; van Haarlem & van de Weygaert 1993).

In this chapter we have developed a statistics based on weak gravitational lensing to quantify the presence of a filament between two galaxy clusters by using $N-$body constrained realizations aimed to mimic as close as possible the real configuration presented by two Abell clusters, Abell 222 and Abell 223. Observational evidence suggests the presence of a bridge connecting the two clusters (Proust et al. 2000; Dietrich 2002). This configuration seems ideal to test the aperture mass statistic technique.

The chapter is structured as follows, we first review the Constrained Realizations algorithm. In section 3 we present the constrained initial density fields for filaments. In section 4 we evolve the initial fields into the non-linear regime using $N-$body simulations. In section 5 we performed lensing simulations of the given system. The quantification of the clusters and connecting filament is presented in section 6. The application of the aperture multipole moments is presented in section 7 and conclusions in section 8.

8.2 Constrained Realizations

Constrained Realizations [CR] were first explored by Bertschinger (1987) who developed a method to construct a realization of a Gaussian random field which obeys various constraints based on the path integral formalism from quantum field theory. To sample the fourier modes he resorted to Monte Carlo numerical methods. This work extended the statistical treatment of Bardeen et al. (1986, BBKS) of the peaks of Gaussian random fields by allowing one to construct samples of the field subject to constraints. He demonstrated by means of the path integral description that the probability function of the constrained field around a peak given by BBKS is the most likely one, in the sense of maximizing the probability density. He found that a constrained field f, can be written as the sum of a mean field $\bar{f}$, completely fixed by the values and forms of the constraints, and a residual field F. This residual field, F, provides random noise which is added to the signal $\bar{f}$,

$$f(\mathbf{r}) = \bar{f}(\mathbf{r}) + F(\mathbf{r}) \,. \tag{8.1}$$

However, this first implementation was rather elaborated and when the degrees of freedom and the number of constraints increase to more than a few, the system converges so slowly that the algorithm becomes prohibitively expensive and impractical.

Bertschinger's method was extended by Binney & Quinn (1991) to a formalism in which the basis functions are spherical harmonics, rather than plane waves. For a localized set of constraints, such as the presence and shape of a peak at the centre of the simulating box, the problem can be described by

a few spherical harmonics and the problem can be solved exactly and not iteratively. The drawback of this technique is that it can be applied only in the case of quite localized constraints defined around an obvious centre of symmetry.

Hoffman & Ribak (1991) made the crucial observation that the statistical properties of the random field F are independent of the numerical values of the constraints themselves provided that the constraints are linear functionals of the field f. In this way, the problem of generating a constrained realizations of a Gaussian field can be solved exactly and has a simple and elegant solution without involving iterations.

van de Weygaert & Bertschinger (1996) worked out the CR formalism along the lines of the Hoffman-Ribak method for an arbitrary number of density, velocity and gravity field constraints by means of a Fourier space description. With this implementation, a peak or dip in the density field can be characterized by a set of 21 physical constraints, including its scale, position and orientation, density, velocity and velocity gradient.

Appendix 3.A of Chapter 3 contains a description of the general formalism for constraining a Gaussian field. In this chapter we will discuss a particular implementation of this formalism. Here we will first describe the principal aspects and discuss the constraints involved in setting up a cluster-bridge-cluster configuration.

8.2.1 The Hoffman-Ribak formalism

The construction of a constrained realization of the field $f(\mathbf{r})$ subject to a set of M constraints:

$$\Gamma = \{C_i \equiv C_i[(f);\mathbf{r}]|_{\mathbf{r_i}}, i = 1,\ldots,M\}, \tag{8.2}$$

can be done in five stages (Hoffman & Ribak 1991; van de Weygaert & Bertschinger 1996). Equation 8.2 implies that the linear functionals C_i of the field f are imposed to have specific values c_i at $\mathbf{r_i}$.

1. Create a random, unconstrained realization of the field $\tilde{f}$, which is a homogeneous and isotropic Gaussian random field whose statistics is determined solely by the power spectrum $P(\mathbf{k})$.

2. Calculate for this particular realization $\tilde{f}$, the values $\tilde{c}$ of the constraints $\{C_i(\mathbf{r})|_{\mathbf{r_i}}, i = 1,\ldots,M\}$. These variables can be looked upon as defining another set of constraints, $\tilde{\Gamma} = \{\tilde{c}\}$. This *a posteriori* set of constraints is evaluated at the positions of the original constraints and has the values of this specific realization.

3. Calculate for this "random" constrained set $\tilde{\Gamma}$ the corresponding mean field expected as if the set was chosen initially,
$$\bar{\tilde{f}} = \langle \tilde{f} \mid \tilde{\Gamma} \rangle = \xi_i(\mathbf{r})\, \xi_{ij}^{-1}\, \tilde{c}_j\,, \tag{8.3}$$
where ξ_{ij} represents the constraints' correlation matrix, $\xi_{ij} = \langle C_i C_j \rangle$, and $\xi_i(\mathbf{r})$ is the cross-correlation between the field and the ith constraint, $\xi_i(\mathbf{r}) = \langle f(\mathbf{r})\, C_i \rangle$.

4. Evaluate the residual field $\tilde{F}$ of the realization from the given particular realization and the calculated mean field $\tilde{\Gamma}$ as
$$\tilde{F}(\mathbf{r}) = \tilde{f}(\mathbf{r}) - \bar{\tilde{f}}(\mathbf{r})\,. \tag{8.4}$$
The residual field $\tilde{F}$ thus generated is the residual field of a particular realization restricted to the desired constraints, Γ.

5. Evaluate the desired mean field $\bar{f}$, according to $\bar{f}(\mathbf{r}) = \langle f(\mathbf{r}) \mid \Gamma \rangle = \xi_i(\mathbf{r})\, \xi_{ij}^{-1}\, c_j$, and add it to the residual field $\tilde{F}(\mathbf{r})$ to obtain a particular realization of the desired constrained Gaussian random field $f(\mathbf{r})$:
$$f(\mathbf{r}) = \tilde{f}(\mathbf{r}) + \xi_i(\mathbf{r})\, \xi_{ij}^{-1}(c_j - \tilde{c}_j)\,. \tag{8.5}$$

The constructed field $f(\mathbf{r})$ obeys the imposed constraints and replaces the unconstrained field $\tilde{f}(\mathbf{r})$. Note that there is a one-to-one correspondence between the trial field $\tilde{f}(\mathbf{r})$ and the constructed one $f(\mathbf{r})$. Furthermore, the ensemble of realizations produced by this algorithm properly samples the sub-ensemble of all realizations constrained by Γ. The algorithm is exact and involves the creation of only one random unconstrained realization and the calculation of the mean field under the given constraints. There is not restriction over the number of constraints and these can be in a very large number, and they can be imposed on the field itself or on any linear functional of it (see van de Weygaert & Bertschinger 1996).

8.2.2 The cluster-bridge-cluster configuration

Bond, Kofman, & Pogosyan (1996) realized the importance of the tidal field in shaping the overall outline of the web-like pattern in a given region (see also van de Weygaert 2002). This relation may be traced back to a simple configuration, that of a "global" quadrupolar matter distribution and the resulting "local" tidal shear at its central site (see van de Weygaert & Bertschinger 1996). Such a quadrupolar primordial matter distribution will almost by default evolve into a cluster-filament-cluster configuration which appears so prominently in the cosmic foam. The non-local nature fo the tidal shear constraint can be observed from the expression of the tidal tensor expressed in terms of the density distribution,

$$T_{ij}(\mathbf{r},t) = \frac{3\Omega_m H^2}{8\pi} \int \mathrm{d}\mathbf{r}'\, \delta(\mathbf{r}',t) \left\{ \frac{3(r'_i - r_i)(r'_j - r_j) - |\mathbf{r}' - \mathbf{r}|^2 \delta_{ij}}{\mathbf{r}' - \mathbf{r}|^5} \right\} - \frac{1}{2}\Omega_m H^2\, \delta(\mathbf{r},t)\, \delta_{ij}\,, \tag{8.6}$$

one can immediately observe that any local value of T_{ij} has global repercussions for the generating density field. In Eqn.8.6, H represents the Hubble constant in units of km s^{-1} Mpc^{-1}, Ω_m is the cosmological matter density parameter, δ represents the density contrast, and δ_{ij} is the Levi-Civita tensor. The strong correlation between the anisotropy in the cosmic force field, and the presence of anisotropic features in the density field was extensively discussed by van de Weygaert (2002). It is one of the primary agents behind the cosmic web structure.

There is a strong correlation between the compressional components of the tidal field and the presence of a dense filamentary structure or, similarly less pronounced, wall-like patterns. Therefore, the formation of the web pattern follows the directions outlined by the primordial tidal field, mainly by its compressional components (van de Weygaert 2002). The primeval tidal field is a consequence of the tiny matter density fluctuations in the primordial universe.

The presence of two nearby large mass concentrations resemble a quadrupolar mass distribution. This configuration induces a shear pattern around its surroundings and therefore, a cluster-bridge-cluster system is expected to form. It is then necessary to consider the tidal field when moulding such a system.

8.3 Constrained initial density fields

8.3.1 Imposing CR constraints

The main equation of the Hoffman-Ribak algorithm for generating a constrained field realization is given by Eqn. 8.5. We consider that all M constraints $C_i[f;\mathbf{r}_i]$ imposed on the field $f(\mathbf{r})$ are convolutions of the field itself with a Gaussian kernel $H_i(\mathbf{r};\mathbf{r}_i)$

$$C_i[f;\mathbf{r}_i] = \int \mathrm{d}\mathbf{r}\; H_i(\mathbf{r};\mathbf{r}_i)\, f(\mathbf{r}) = c_i\,. \tag{8.7}$$

The Fourier transforms of the field $f(\mathbf{r})$ and the kernel $H_i(\mathbf{r};\mathbf{r}_i)$ are defined by

$$\begin{aligned} f(\mathbf{r}) &= \int \frac{\mathrm{d}\mathbf{k}}{(2\pi)^3}\hat{f}(\mathbf{k})e^{-\imath\mathbf{k}\cdot\mathbf{r}}\,, \\ H_i(\mathbf{r};\mathbf{r}_i) &= \int \frac{\mathrm{d}\mathbf{k}}{(2\pi)^3}\hat{H}(\mathbf{k})e^{-\imath\mathbf{k}\cdot\mathbf{r}}\,. \end{aligned} \tag{8.8}$$

The first major properties of a peak in a smooth density field are its position and scale. Further characteristics of a peak may be described by up to 18 constraints of 2nd or lower order. Such constraints can be divided into two groups: the first group determines the density field in the immediate vicinity around the peak and are related to the peak height, orientation and shape of the cluster (10 constraints). The second group determines the gravity field around the peak in terms of the smooth peculiar velocity field and shear around the peak (8 constraints).

The peak constraints and the corresponding kernels $\hat{H}$ were filtered with a Gaussian kernel with smoothing length R_G

$$\hat{W}(\mathbf{k}) = e^{-k^2R_G^2/2}\,. \tag{8.9}$$

Each one of the constraints then can be expressed in the following way (see also van de Weygaert & Bertschinger 1996):

1. The peak height (1 constraint)

$$f_G(\mathbf{r}_d) = \nu\sigma_0(R_G)\,, \qquad \hat{H}(\mathbf{k}) = \hat{W}(\mathbf{k})\,e^{\imath\mathbf{k}\cdot\mathbf{r}_d}\,, \tag{8.10}$$

   expressed in terms of the variance of the smoothed field $\sigma_0(R_G) = \langle f_g f_g\rangle^{1/2}$. ν is the desired height of the peak with respect to the variance.

2. Orientation and shape of the clusters (6 constraints)

$$\frac{\partial^2 f_g}{\partial r_i r_j}(\mathbf{r}_d) = -\sum_{k=1}^{3}\lambda_k A_{ki}A_{kj}\,, \qquad \hat{H}(\mathbf{k}) = -k_i k_j\,\hat{W}(\mathbf{k})\,e^{\imath\mathbf{k}\cdot\mathbf{r}_d}\,, \tag{8.11}$$

   where $i,j = 1,2,3$ and λ's are the axis-magnitudes of the triaxial ellipsoid, which constraint the shape of the overdensity. The orientation of the peak with respect to the general coordinate system is described in terms of the Euler angles transformation matrix A_{ij} (Goldstein 1980).

3. The peculiar velocity field of the field $\mathbf{v}_G(\mathbf{r}_d)$ (3 constraints),

$$g_{G,i}(\mathbf{r}_d) = \tilde{g}_i\,\sigma_{g,pk}(R_G)\,, \qquad \hat{H}(\mathbf{k}) = \frac{3}{2}\Omega_m H^2\frac{\imath k_i}{k^2}\hat{W}(\mathbf{k})\,e^{\imath\mathbf{k}\cdot\mathbf{r}_d}\,, \tag{8.12}$$

   where $\sigma_{g,pk}(R_G)$ is the dispersion of the gravitational acceleration of the peak and g_i the $i-$component of $\mathbf{g}$. The factor $\frac{3}{2}\Omega_m H^2$ is introduced via the Poisson equation between the gravity field and the local density perturbation $f(\mathbf{r})$.

4. The tidal shear components (5 constraints),

$$E_{G,ij}(\mathbf{r}_d) = \tilde{\epsilon}\,\sigma_E(R_G)\sum_{k=1}^{3}\mathcal{L}T_{ki}T_{kj}\,, \qquad \hat{H}(\mathbf{k}) = \frac{3}{2}\Omega_m H^2\Big(\frac{k_i k_j}{k^2}-\frac{1}{3}\Big)\hat{W}(\mathbf{k})\,e^{\imath\mathbf{k}\cdot\mathbf{r}_d}\,, \tag{8.13}$$

   where $T_{ki}T_{kj}$ are the components of the various eigenvectors of the tidal tensor given by Eqn. 8.6. For the particular case of peaks, there is a strong tendency of the tidal tensor to align itself along the principal axes of the mass ellipsoid. Therefore, one needs to express the elements with respect to the reference frame specified by these axes. The magnitude of the tidal field along the

principal axes of the tidal tensor is given by its eigenvalues $\mathcal{L}$ and the tide scalar $\tilde{\epsilon}$ (Bertschinger & Jain 1994). Furthermore, because the tidal tensor is traceless, it is sufficient to specify only two eigenvalues. We have expressed the eigenvalues in terms of the dispersion of the off-diagonal elements (σ_E) of the tidal tensor,

$$\sigma_E(R_G) = \frac{3}{2}\Omega_m H^2 \sigma_0(R_G)\sqrt{\frac{1-\gamma^2}{15}} \qquad \text{with} \qquad \gamma \equiv \frac{\sigma_1^2}{\sigma_0\sigma_2}\,, \tag{8.14}$$

where $\sigma_i((R_G)$ are the spectral moments,

$$\sigma_i^2(R_G) \equiv \int \frac{\mathrm{d}\mathbf{k}}{(2\pi)^3} P(\mathbf{k})\,\hat{H}(\mathbf{k})\,k^{2i}\,. \tag{8.15}$$

8.3.2 The real system

The system that we want to model is the one given by two Abell clusters, Abell 222 and Abell 223. They are a close pair of rich galaxy clusters, both having Abell richness class 3 (Abell 1958), separated by 18′, which at the cluster redshift of ~ 0.21 corresponds to 2.6 h^{-1}Mpc. Several studies have confirmed that these are massive clusters (e.g. Wang & Ulmer 1997; David et al. 1999). Proust et al. (2000) observed 4 galaxies at the cluster redshift in the region between clusters, indicating a possible connection between both clusters (bridge) (Dietrich 2002).

In moulding the observational data we have considered each one of the observational aspects and cosmological characteristics of the system. We have performed a set of 10 realizations in a periodic 50 h^{-1}Mpc box. The power spectrum of the random field fluctuations for all simulations was the standard cold dark matter spectrum of BBKS with $\Omega_\Lambda = 0$, $\Omega_m = 1$, $h = 0.5$ and normalized such that $\sigma(8\ h^{-1}\mathrm{Mpc}) = 1.0$ at $a = 1$, the present epoch (Davis & Peebles 1983a). All constrains were imposed over a cubic grid of 64 grid-cells per dimension, and all calculations have been carried out in Fourier space. In the realizations, all constraints were defined on a Gaussian scale of 4 h^{-1}Mpc for both clusters, the "typical" scale that allows to study the properties of protoclusters (e.g. Doroshkevich 1970; Peacock & Heavens 1985; Bardeen et al. 1986; van Haarlem & van de Weygaert 1993). Because we are dealing with rich clusters, we imposed a peak height $f_G = 3\sigma_0$. In all simulations two initial cluster seeds were placed at the center of the simulation box, separated by a distance d (in h^{-1}Mpc) along the $i-$axis. Each simulation contained different combinations from the mentioned 18 constraints.

The first configuration involved spherical clusters at the center of the box with a separation of 3 h^{-1}Mpc. None of the resulting density maps showed a clear filament presence. The next step was to consider oblate clusters (2nd constraint) and separated by larger distances. We constructed both clusters with axis ratios $\lambda_2/\lambda_1 = 0.9$ and $\lambda_3/\lambda_1 = 0.8$ ($\lambda_1 > \lambda_2 > \lambda_3$) and both major axes aligned with each other. The corresponding density fields indicated a weak presence of a bridge between both structures. The next step was to constrain the gravity field around the system by imposing an initial momentum (3 constraints) on both clusters approaching to each other with a relative velocity of 100 km s^{-1} separated at a distance of 12 h^{-1}Mpc. Although this configuration was more successful in reproducing the desired configuration, the bridge signature was not clear enough. The last constraint imposed was the tidal field (5 constraint components). We have imposed a "weak" tidal field in order to produce a realistic field around the clusters. The observed system does not show signatures of objects falling at high velocities towards the potential well. The stretching mode of the tidal field was aligned along the same direction given by the major cluster axes ($x-$axis). The compressional mode was set perpendicular to the bridge axis. This constraint's combination proved to be the most successful one in reproducing (in the linear regime) the configuration presented by the Abell clusters.

Figure 8.1 illustrates the most successful cluster-bridge-cluster configuration. In order to show the relevant characteristics of the field, we have filtered the initial density field with a Gaussian filter of 2 h^{-1}Mpc scale. The low density regions (dark areas) are denoted by dashed lines, while the density regions above the zero contour (bold line) are depicted by continuous lines (light regions). The top-left panel is a slice cut through the central part of the $z-$axis, the top-right panel for the $y-$axis. The

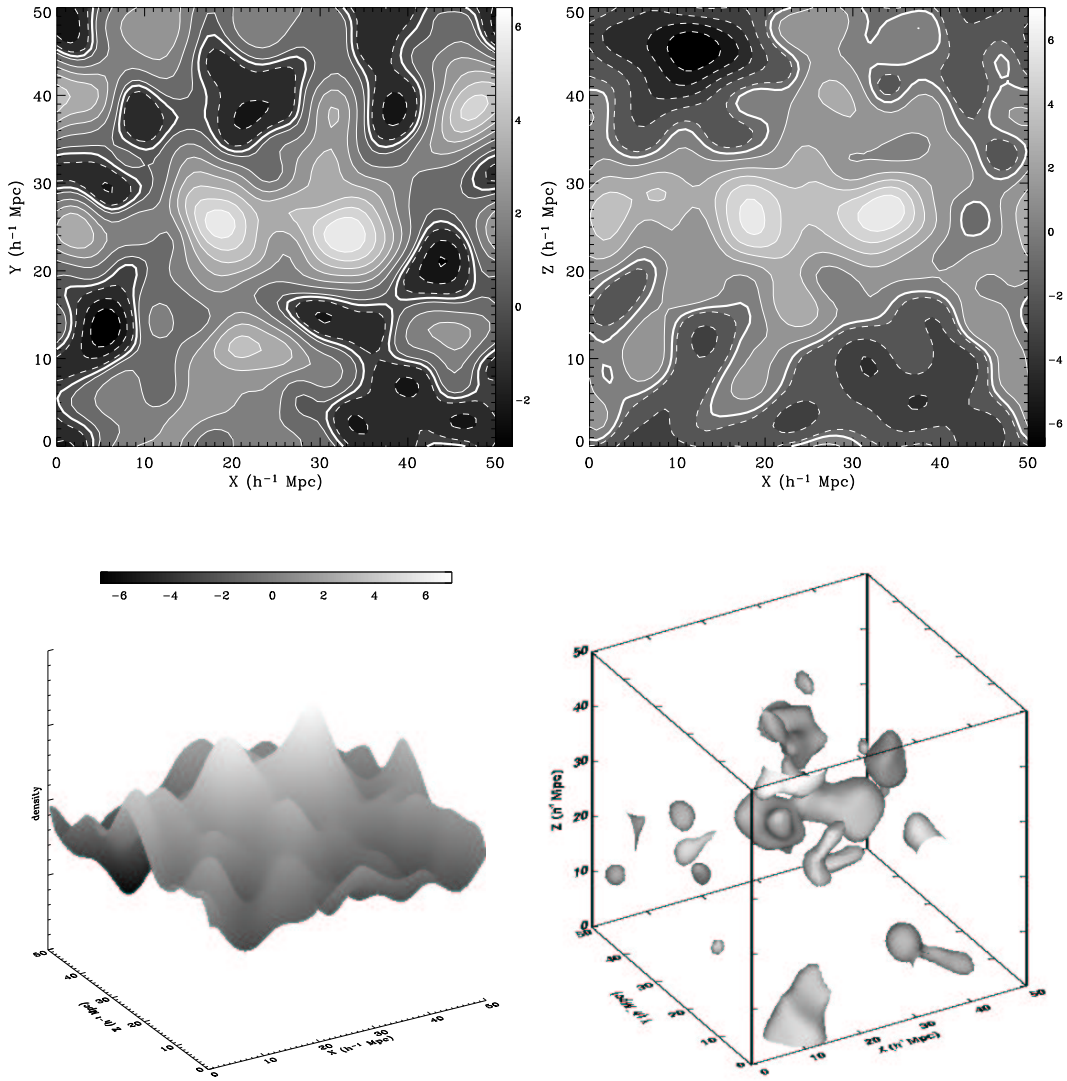

Figure 8.1 — Constrained initial density fields. The top panels present central slices along the z−axis (left) and y−axis (right). Clearly visible are the two imposed clusters at the center of the box and connected by a filament. The lower-left panel shows a surface plot indicating the strength of the clusters. The lower-right panel depicts the 3D configuration of the clusters and confirms the real presence of the bridge connecting them.

presence of the two clusters and a bridge connecting them is very clear in both projections. These plots show that the bridge's presence is not only a projection effect. This can also be noticed by the 3D configuration at the right-bottom panel. The isosurface corresponds to structures at the 2× the mean density level. The two imposed clusters and the bridge connecting them are clearly visible among other unconstrained structures present in the field. The bottom-left panel indicates the strength of both structures in comparison with the other unconstrained random structures along the same plane. The surface plot is scaled with respect to the highest density on the plane. The dominance of both clusters over the projected field is very clear.

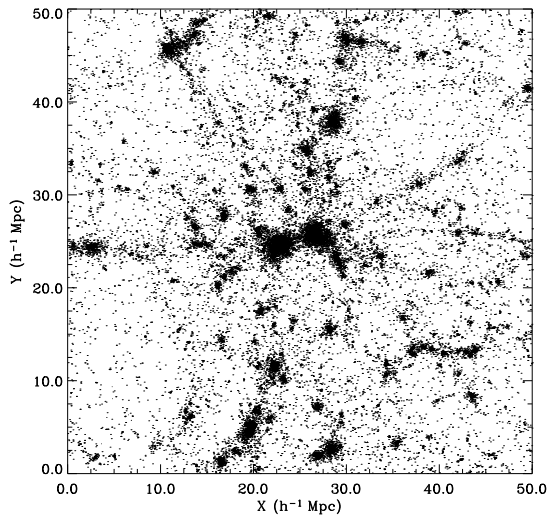

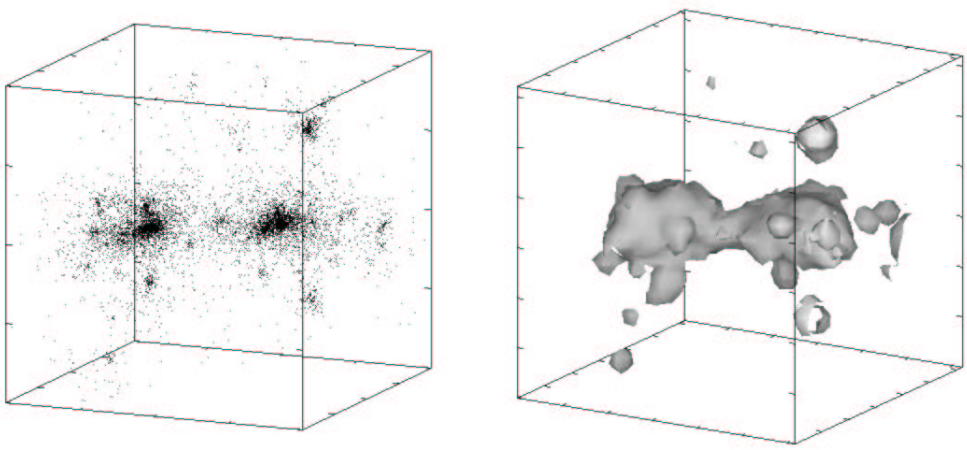

Figure 8.2 — Evolved density fields at $z = 0.21$. The top panel presents the particle distribution projected along the z−axis for a central slice of 5 h^{-1}Mpc thick. Clearly visible are the two imposed clusters at the center of the box connected by a filament. The bottom panels show 3D zooms of the central region enclosing the clusters and bridge from the particle distribution (left-panel), and density field (isosurface), smoothed with a Gaussian filter of 1 h^{-1}Mpc size (right-panel).

8.4 N−body simulations

In order to make suitable the initial density fields for their evolution with an N−body code, particle positions were displaced from a regular cubic grid and velocities assigned according to the Zel'dovich formalism (Zel'dovich 1970).

The evolution of the linear Constrained density field into the non-linear regime was performed by means of a standard P^3M code (Bertschinger & Gelb 1991). The number of grid-cells used to evaluate the particle-mesh force was 128^3, with a particle mass resolution of $3.3 \times 10^{10}\ M_\odot$. We selected 15 time outputs in order to follow the simulation through the non-linear regime, with a time output at redshift $z = 0.21$, to match the observed redshift cluster.

Figure 8.2 depicts the same initial density field presented in Fig. 8.1 evolved to redshift $z = 0.21$. The top panel shows a wide view of the particle distribution projected along the z−axis, with a thickness of 5 h^{-1}Mpc. A clear peanut shape composed by the two clusters and bridge can be distinguished

at the center of the plot. A zoom of the 3D particle distribution is presented at the bottom-left panel, indicating the presence of a connecting bridge between the two structures. This situation is more clearly noticeable at the bottom-right panel, where an isosurface of the same zoomed particle distribution is presented. The surface level corresponds to an isosurface of 2× the mean density. At this output redshift, the cluster are separated by $\approx 2.5\ h^{-1}$Mpc, as required by the observations.

8.4.1 Quantifying Filaments

In order to quantify the presence of a filament and the significance of its detection three problems must be solved. First, due to the correlation of error bars described in Appendix 8.A the significance of a filament in a reconstructed mass map cannot be assessed directly from the reconstruction. Statistics like the aperture mass and aperture multipole moments (Appendix 8.A) allow the calculation of signal-to-noise ratios for a limited spatial region and are thus well suited to quantify the presence of a structure in that region. Aperture statistics, however, integrate over the weighted surface mass density in an aperture. Hence, to quantify the presence of a structure between two galaxy clusters, the aperture has to be chosen such that it avoids the clusters and is limited to the filament candidate. This is the second problem. The third and most fundamental question that has to be answered is, "What is a filament?". How for instance can we distinguish the overlapping halos of two close galaxy clusters from a filament? While in some cases the question whether a structure between two cluster indeed constitutes a filament is easy to answer intuitively, it can be difficult to quantify in many other cases.

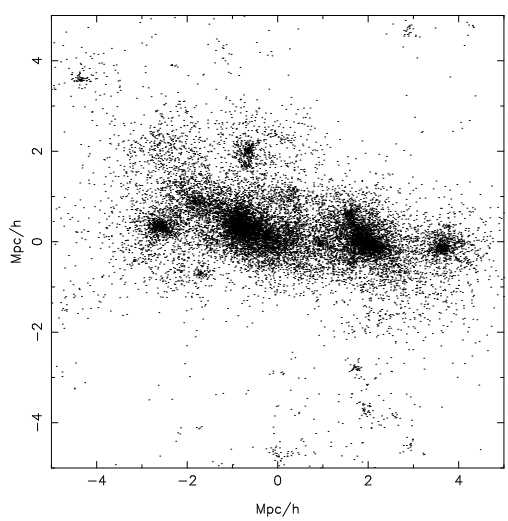

Figure 8.3 — Zoom in on the central $10 \times 10\ h^{-1}$Mpc of an $N-$body simulation. Displayed is the projection of a slice of $2.5\ h^{-1}$Mpc thickness.

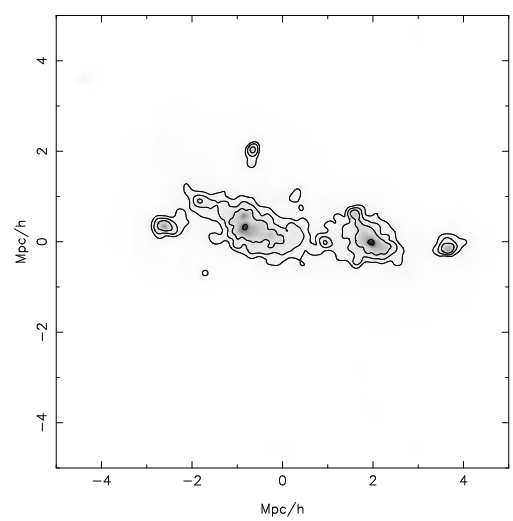

Figure 8.4 — Smooth density distribution of the data in the left panel from the adaptive kernel density estimate. The contours are at $\kappa = \{0.03, 0.05, 0.1, 0.5\}$.

To get density estimates we applied the adaptive kernel method only to an interesting subsample of the simulation showing the galaxy clusters and the filament connecting them. Figures 8.3 and 8.4 show such a subsample and the corresponding smoothed density distribution. The subsample is a $10 \times 10 \times 2.5(\ h^{-1}\text{Mpc})^3$ slice of the $N-$body simulation at a redshift $z = 0.21$. The surface mass density in the right panel was not calculated from the mass of the particles but linearly scaled, such that the surface mass density in the cluster center is just sub-critical.

8.5 Lensing Simulations using $N-$body Data

In this section we will derive the lensing properties of the simulated mass distribution. The lensing formalism will be explained in detail in the Appendix 8.A, together with the main results of the Multipole moments technique and the aperture multipole statistics.

While it is in principle possible to gain the deflection potential and from that the shear by finite integration and differentiation via the dimensionless surface mass density and magnification matrix (Eqs. A8-2 and A8-6), this is a cumbersome and time consuming method. It is much faster and simpler to calculate the shear directly from the simulated surface mass density using its magnification factor (Eqn. A8-9) and the convolution theorem. The Fourier transformation of the complex kernel $\mathcal{D}$ (Eqn. A8-9) reads,

$$\hat{\mathcal{D}}(\vec{k}) = \pi \frac{k_1^2 - k_2^2 + 2\imath k_1 k_2}{|\vec{k}|^2} \tag{8.16}$$

and thus the Fourier transformed shear is given by

$$\hat{\gamma}(\vec{k}) = \frac{1}{\pi}\hat{\mathcal{D}}(\vec{k})\hat{\kappa}(\vec{k}) \,, \qquad \text{for } \vec{k} \neq 0 \,. \tag{8.17}$$

The shear is then calculated via the inverse Fourier transformation and the magnification is easily computed from the right hand side of Eqn. (A8-11).

The Fourier transformation is calculated with the Fast Fourier Transformation (FFT) algorithm (Press et al. 1992b). An implementation that readily computes lensing quantities like the shear and magnification on a grid from discrete κ-maps as outlined above is the `kappa2stuff` program from Nick Kaiser's `IMCAT` package [1]. To account for the finite field size, FFT uses periodic boundary conditions. The surface mass density at the edges of the simulated fields is small enough to not lead to any artifacts due to the boundary conditions.

For the lensing simulation, catalogs of background galaxies were produced. Galaxies were randomly placed within a predefined area until the specified number density was reached. To each galaxy an intrinsic ellipticity was assigned from two Gaussian random deviates. Until noted otherwise all simulations have 30 galaxies/arcmin^2 and a one dimensional ellipticity dispersion of $\sigma_\varepsilon = 0.2$.

Since the shear and magnification is only known on a grid, they were linearly interpolated between the four grid points neighboring each galaxy to compute these quantities at the galaxy position. To simplify the program, galaxies at the edges that have less than four neighboring grid points were removed from the catalog. For each galaxy a uniformly distributed random deviate from the interval $[0;1)$ was drawn. If the random deviate was bigger than $\mu^{-0.5}$ the galaxy was deleted from the catalog.

Figure 8.5 shows a mass reconstruction of the simulated density map in Fig. 8.4 The lensing properties of the simulation were calculated as described above on a 2048×2048 points grid and the computed shear and magnification were applied to a random catalog of background galaxies. The reconstruction was performed on a 206×206 points grid with a $1\farcm3$ smoothing scale.

The quality of the reconstruction is much higher than one would expect for real observational data for a number of reasons.

1. All galaxies in the catalog are indeed background objects. In real data, the catalog of background galaxies would inevitably be contaminated by stars and faint foreground galaxies (mainly dwarf galaxies in the cluster one observes).

2. No effects like atmospheric smearing and distortions of the image by the telescope and/or camera optics deteriorate the determination of the observed galaxy ellipticity.

3. The intrinsic ellipticity dispersion of the background galaxies is too low compared with real data, which suggests $\sigma_\varepsilon = 0.3$ or even higher.

[1] `http://www.ifa.hawaii.edu/~kaiser/imcat/`

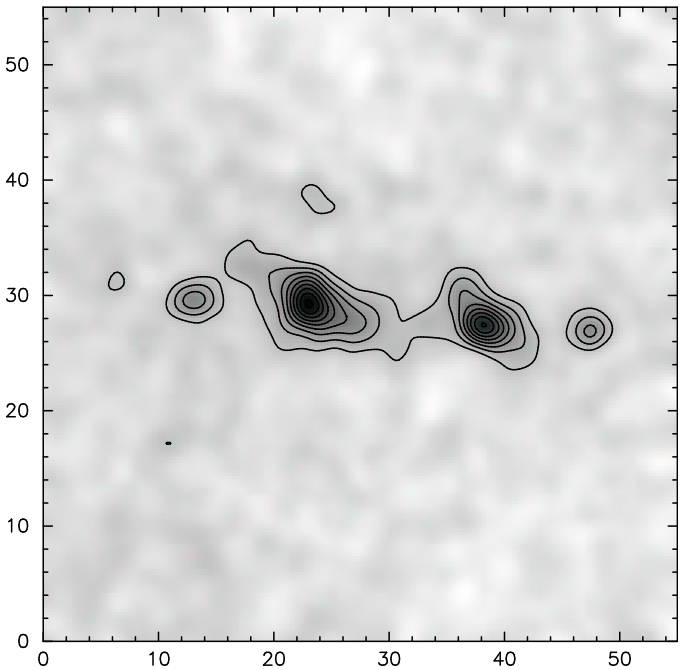

Figure 8.5 — Reconstruction of the mass distribution in Fig. 8.4 on a 206× 206 points grid. The scale of the axes is given in arc minutes. The contours mark an increase of κ in steps of 0.025 above the mean of the edge of the field.

4. Likewise, the assumed number density of background objects is at the high end of what one typically can achieve with ground–based observations.

The few differences between the original mass distribution and the reconstruction thus indicate systematic deviations due to the smoothing and not due to noise caused by the intrinsic ellipticities of galaxies and their random distribution. Of course, some degree of noise is still present in the reconstructed mass distribution but it is not the dominant feature of the reconstruction.

It is immediately obvious that many small scale features present in the simulation are not recovered in the reconstruction. This is due to the smoothing done to the shear data. One can show that in the absence of Poisson noise and under the assumption $g = \gamma$ the smoothing of the shear data is equivalent to a convolution of the mass distribution with the smoothing kernel (van Waerbeke 2000). This also explains that the density peaks in the reconstruction are broader and not as high as in the original mass map.

8.6 Fitting Elliptical Profiles to Galaxy Clusters

With all the tools needed to simulate the weak gravitational lens effect at hand, we can now concentrate on the quantification of a filament. In a first attempt we try to represent the galaxy clusters by elliptical mass profiles. We then define the filament as the part of the mass distribution which is in excess of the mass fitted by the ellipses.

Two different approaches can be used when fitting elliptical profiles to the clusters. First, the fitting can be done to the reconstructed mass distribution. Second, the fitting can be done adjusting the elliptical profiles so that their shear matches the observed shear.

The first method has the advantage that the surface mass density is a much more intuitive quantity than the shear. Problems in the fitting procedure are easier to understand when working with the surface mass density. On the other hand, κ is not an observable. The only observable is the reduced shear and the surface mass density has to be reconstructed from the shear first. As we have seen in the previous section, even in the absence of strong observational noise, the reconstructed mass profile deviates systematically from the true mass profile.

Fitting directly to the shear avoids the additional intermediate step of mass reconstruction and is thus not susceptible to the broadening of the core radius introduced by the smoothing of the shear data. Directly using the shear as the quantity to which the elliptical profiles of the clusters are fitted also has disadvantages. First, the shear at a given position is determined by the surface mass density on the whole field. This makes it much harder to control the fitting process by choosing suitable weight functions that guide the fitting process in the right direction. Second, the profiles for which the shear can be computed analytically are very limited. While fitting to the surface mass density allows one to have a flexible radial profile, one is limited to radial profiles for which analytic expressions for the shear are known, when fitting directly to the shear.

Common to all fitting procedures is that they try to minimize a quantity

$$\chi^2 = \int \mathrm{d}^2\theta \left[f_{\mathrm{true}}(\vec{\theta}) - f_{\mathrm{sim}}(\vec{\theta}) \right]^2 w(\vec{\theta}) \,. \tag{8.18}$$

For example if one fits to the reconstructed surface mass density, $f_{\mathrm{true}}(\vec{\theta})$ is $\kappa(\vec{\theta})$ from the reconstruction, while $f_{\mathrm{sim}}(\vec{\theta})$ is the surface mass density of the fitted ellipses. $w(\vec{\theta})$ is a weight function that can be chosen to guide the minimization procedure in the right direction.

Various methods for multidimensional minimization are available. All programs used for fitting either used the Downhill Simplex or Powell's Direction Set algorithms discussed in detail in Press et al. (1992a). We could not find any systematic differences between the results of the two methods. In general, their results agreed quite well if the same starting values were used.

Common to all algorithms for multidimensional minimization is the problem that they cannot guarantee to find the global minimum but only a local one. One has to choose the starting parameters so that they are already close to the suspected global minimum to help the minimization procedure find the right minimum.

8.6.1 Fitting Elliptical Profiles to the Simulated Surface Mass Density

As a first test to see how well clusters could be represented by elliptical profiles, we fitted two ellipses with a King profile directly to the simulated data. The surface mass density of a circular King profile is given by

$$\Sigma(\theta) = \Sigma_0 \left[1 + \left(\frac{\theta}{\theta_{\mathrm{c}}} \right)^2 \right]^{-1} \,, \tag{8.19}$$

where Σ_0 is the surface mass density in the center, θ_{c} is the core radius of the profile, and θ is the distance from the cluster center. There are 12 parameters that have to be determined in the minimization procedure, 6 for each cluster. The parameters are position of the cluster center, Σ_0, θ_{c}, axis ratio of the ellipse, and orientation of the ellipse. As the position of the clusters in the simulation is well known, the central position can be used as a starting value. This is necessary to avoid that the minimization procedure puts both ellipses on one cluster or even on a small mass peak away from the clusters because this might very well be a local minimum in which we are not interested. It is sufficient to set the starting values of the other parameters to values in the right order of magnitude to achieve reasonable fits.

Figure 8.6 shows the fit of two elliptical King profiles to the simulated data displayed in Fig. 8.3. To reduce the computer time needed for the minimization, which is dominated by the repeated calculation of the integral (8.18), the data was smoothed on a 512×512 points grid instead of the 2048×2048 points grid which was used to calculate the lensing properties of the simulation. The weight function was chosen to be unity on the whole field.

Fig. 8.7 shows the difference between the simulated data in Fig. 8.4 and the fit to the simulation in Fig. 8.6. While the two clusters are not fitted perfectly – after all galaxy clusters are not perfect ellipses – most of the cluster mass is removed in the difference image. An overdensity of the surface

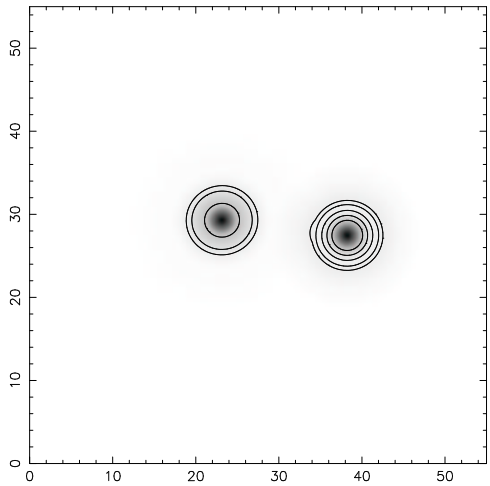

Figure 8.6 — Fit of two elliptical King profiles to the simulation data in Fig. 8.4. The contours are at the same levels as in Fig. 8.4.

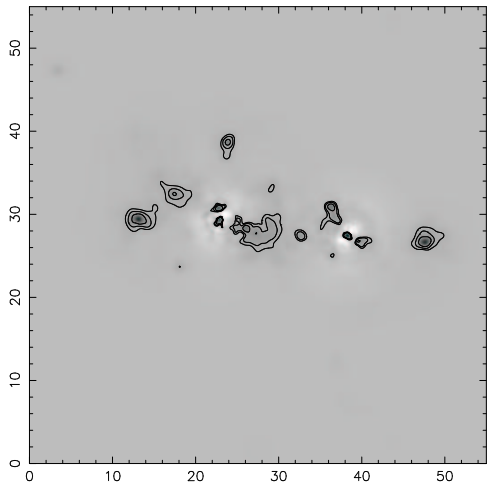

Figure 8.7 — Difference image between the simulated data in Fig. 8.4 and the fit in the left panel. The contours are at the same level as in Fig. 8.4. Clearly visible is an excess in the surface mass density between the two clusters.

mass density is visible between the two clusters, which supports the definition of the filament being the surface mass density that is in excess of the elliptical cluster profiles.

However, the main problem in all fitting procedures is already visible here. Both clusters in the simulation have rather elliptical profiles. The orientation of the major axis of the left cluster is almost parallel to the 1–axis, while the major axis of the right cluster runs from the upper left to the lower right corner. Contrary to the simulation the fitted mass profiles are almost perfectly circular. Finding the right ellipticity and orientation seems to be the crucial difficulty in all fitting procedures.

8.6.2 Fitting Elliptical Profiles to the Reconstructed Surface Mass Density

While the fitting described in the previous section can be used as proof of concept that filaments can indeed be understood as mass that is in excess of elliptical profiles, the true surface mass density is not accessible in the case of observational data. If one wants to use the surface mass density to fit elliptical profiles, only the reconstruction is available.

Figures 8.8 and 8.9 show two such fits to the reconstruction displayed in Fig. 8.5. The only difference between both fits is the starting value for the orientation of the right cluster in the minimization procedure. Again, the weight function was chosen to be unity. One can clearly see the dependence of the orientation of the ellipses on the initial value. Even worse, although two completely different starting values were used, none of them lead to an orientation that is close to the actual orientation of the cluster.

We tried various weighting schemes in order to control this problem. e.g. only regions close to the cluster center were taken into account to reduce the influence of the noise further away from the clusters. None of this lead to more stable solutions. Also the attempt to use flexible radial profiles instead of the King profiles did not lead to positive results.

8.6.3 Fitting Non–Singular Isothermal Ellipses to the Shear

Although fitting elliptical profiles to the surface mass density seemed promising when done directly to the simulated data, it failed when reconstructed mass maps where used. Fitting directly to the

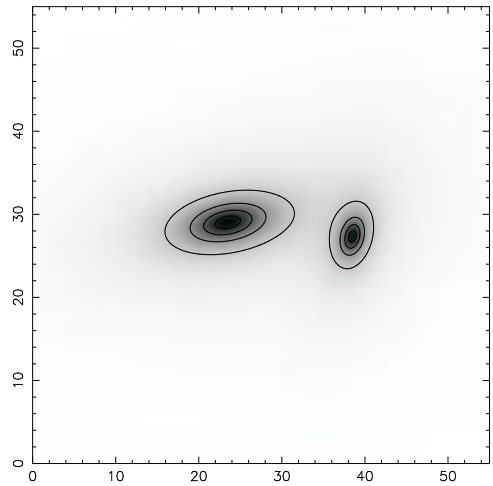

Figure 8.8 — Fit of two elliptical King profiles to the reconstruction shown in Fig. 8.5. The contours are at the same level as in the reconstruction.

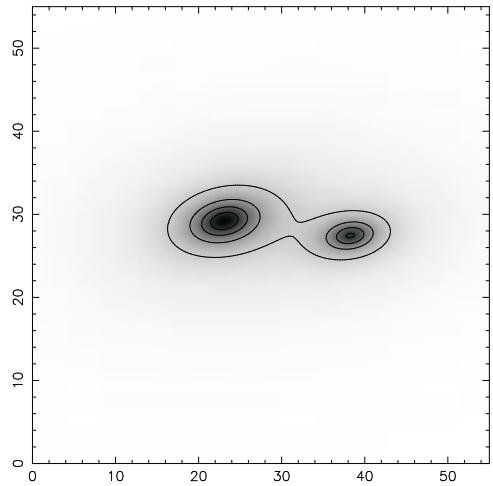

Figure 8.9 — Same as Fig. 8.8 but with different starting value for the orientation of the right cluster.

ellipticities and avoiding the intermediate step of reconstructing the mass distribution may be a remedy for the problems described in the previous section.

An ellipsoidal density distribution for which the shear can be calculated analytically is that of a softened, oblate isothermal ellipse. Consider an oblate spheroid with axis ratio q_3. In projection this becomes an ellipsoidal density distribution with axis ratio $q = (q_3 \cos^2 i + \sin^2 i)^{1/2}$, i being the inclination angle with $i = 90°$ face–on and $i = 0°$ edge–on. If s is the core radius and $e = (1 - q_3^2)^{1/2}$ is the eccentricity of the mass distribution, the density distribution for this model in cylindrical coordinates is

$$\rho = \frac{v_c^2}{4\pi G q_3} \frac{e}{\arcsin e} \frac{1}{s^2 + R^2 + z^2/q_3^2} \,, \tag{8.20}$$

(Keeton & Kochanek 1998). In the limit of $s = 0$ and $q_3 = 1$ this becomes the density distribution of a singular isothermal sphere (SIS). With $b_\mathrm{I} = (2\pi e D_\mathrm{ds} v_c^2)/(D_\mathrm{s} c^2 \arcsin e)$ the dimensionless surface mass density becomes

$$\kappa = \frac{b_\mathrm{I}}{2\sqrt{q^2(s^2 + \theta_1^2) + \theta_2^2}} \,. \tag{8.21}$$

Introducing the abbreviation $\Psi^2 = q^2(s^2 + \theta_1^2) + \theta_2^2$ the shear of this profile can be expressed as

$$\gamma_1 = k_1 \cos^2\varphi - k_2 \sin^2\varphi \,, \tag{8.22}$$

$$\gamma_2 = k_1 \sin^2\varphi + k_2 \cos^2\varphi \,, \tag{8.23}$$

where φ is the angle of the major axis of the ellipse with respect to the 1–axis and

$$k_1 = \frac{b_\mathrm{I}}{2\Psi}[\theta_2^2 - \theta_1^2 - (1 - q^2)s^2]^2 \,, \tag{8.24}$$

$$k_2 = -\frac{b_\mathrm{i}}{\Psi}(\theta_1 \cos\varphi + \theta_2 \sin\varphi)(\theta_2 \cos\varphi - \theta_1 \sin\varphi) \,. \tag{8.25}$$

Unfortunately, it turned out that minimizing the quantity $\chi^2 = \sum_i |\varepsilon_i - \gamma(\vec{\theta}_i)|^2$ is extremely sensitive to the noise introduced by the random orientation of the FBG. While simulations based on catalogs

with circular background galaxies gave reasonable results, simulations based on the small value of $\sigma_\varepsilon = 0.2$ used here did not achieve reasonable fits and were extremely sensitive to the initial values.

Generally, a tendency to over-fit the filament region, so that the difference image had negative surface mass density there, could be observed.

8.7 Using Aperture Multipole Moments to Quantify the Presence of a Filament

Aperture multipole moments (AMM) quantify the weighted surface mass density distribution in a circular aperture. If it is possible to find a characteristic mass distribution for filaments and express it in terms of multipole moments, AMM can be used to quantify the presence of a filament.

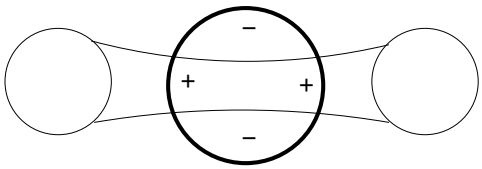

Figure 8.10 — Simple toy model of two galaxy clusters connected by a filament. A quadrupole moment is present in the aperture centered on the filament.

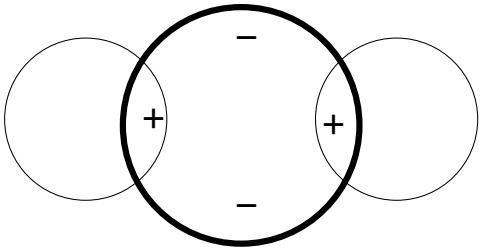

Figure 8.11 — Toy model of two galaxy clusters without a filament, illustrating why it is important to choose the correct size of the aperture.

Fig. 8.10 illustrates with the help of a simple toy model of two galaxy clusters connected by a filament why one expects to find a quadrupole moment in an aperture centered on the filament. Fig. 8.11 illustrates that it is crucial not to choose the aperture too large. If the aperture also covers the clusters a quadrupole moment will be measured even if no filament is present.

Figures 8.12– 8.15 show quadrupole moment $|Q^{(2)}|$ maps calculated from simulated lensing data of the simulation shown in Fig. 8.4. The weight function was chosen to be

$$U(\theta) = \begin{cases} 1 - \left(\frac{\theta}{\theta_{\max}}\right)^2 & \theta \leq \theta_{\max} \ , \\ 0 & \text{else} \ . \end{cases} \tag{8.26}$$

While this weight function is clearly not ideal as it does not closely follow the mass profile of the simulated data, it is sufficient to identify all relevant features. In the quadrupole maps $\theta_{\max}$ increases from 2' to 5' . The maps were computed on 55×55 points grid, so that each grid point is $1' \times 1'$ big. Overlaid are the contours of the surface mass density of the reconstruction of Fig. 8.5.

One clearly sees that the quadrupole moment between the clusters increases as the size of the apertures increases. This is of course due to the growing portion of the clusters in the aperture, that with their large surface mass density dominate the mass distribution.

Most interesting for the quantification of filaments are the two maps in the top panel. The aperture quadrupole moment centered on the middle of the line connecting both clusters does not overlap with what one intuitively would call the galaxy clusters in these two maps. Noteworthy in Figs. 8.12 and 8.13 is also that they show a quadrupole moment on a ring–like structure around the cluster center. This is indeed to be expected for all galaxy clusters because there is a non–vanishing quadrupole moment if the aperture is not centered on the galaxy cluster, but somewhere on the slope of the mass distribution. This now raises the question how we should distinguish the quadrupole moment present around any cluster from that caused by a filamentary structure between the clusters.

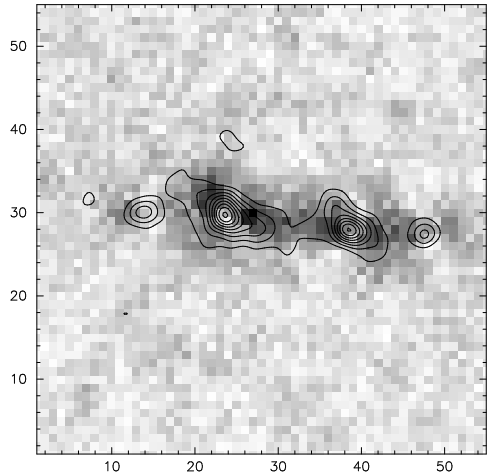

Figure 8.12 — Quadrupole Moment of the simulation in Fig. 8.4 in a circle of 2' radius.

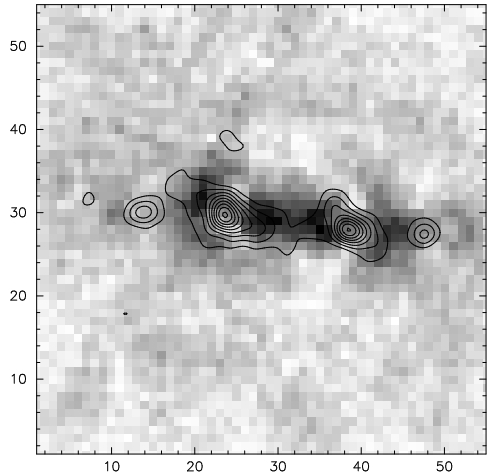

Figure 8.13 — Same as Fig. 8.12 in a 3' radius circle.

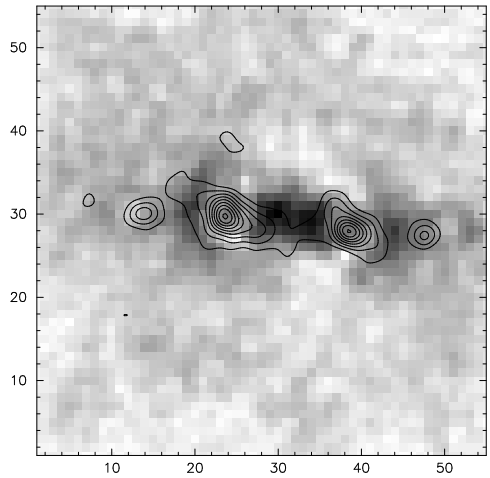

Figure 8.14 — Same as Fig. 8.12 in a 4' radius circle.

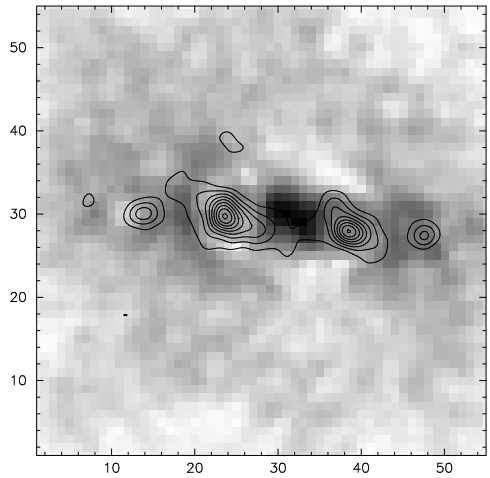

Figure 8.15 — Same as Fig. 8.12 in a 5' radius circle.

The most obvious answer, that the quadrupole moment between the clusters has to exceed the quadrupole moment at the points having the same distance from the cluster center on the axis connecting both clusters outside the filament fails, due to the particular geometry of this simulation. The two small mass clumps to the left and the right of the clusters create a situation similar to that depicted in Fig. 8.11 and thus increase the quadrupole moment to the point where it is roughly equal to that in the filament center. Other simulations without this special geometry show no such behavior and the applicability of this criterion will be discussed below.

However, even in this special case there is evidence that the quadrupole signal in the center is caused by a filament and not by the clusters alone. This evidence is the asymmetry of the quadrupole moment around the galaxy clusters. An almost closed ring, on which the quadrupole moment is lower, is visible around the filament. This ring is easier is to spot in the maps generated from filter functions with larger radii. All aperture statistics act as bandpass filters on structure comparable in size to the filter radius. As the ring has a radius of $\sim 7'$ it is better visible in the maps generated from larger filters. Still, the asymmetry is well visible in Fig. 8.13 and less well visible but still present in Fig. 8.12. Thus, the quadrupole maps clearly indicate that the measured quadrupoles on the filament are not caused by

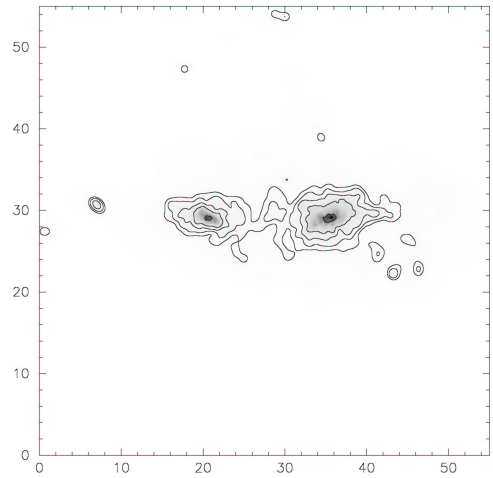

Figure 8.16 — Smoothed surface mass density distribution of a second simulation. The projection parameters are the same as in Fig. 8.3. An additional contour line is drawn at $\kappa = 0.02$ because this filament is weaker.

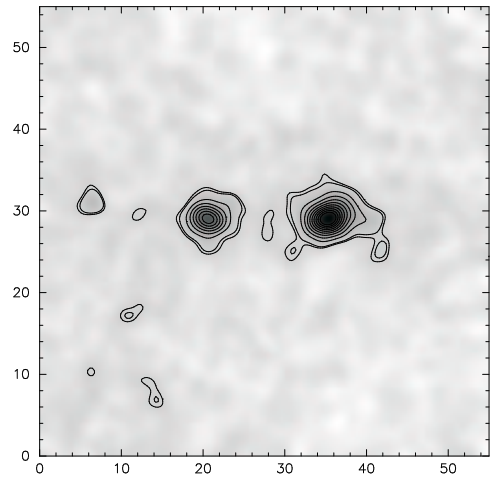

Figure 8.17 — Same as Fig. 8.5 for the simulation in Fig. 8.16 with an additional contour at $\kappa = 0.02$.

a symmetric situation, that two galaxy clusters without filament would constitute.

The geometry of the simulation displayed in Fig. 8.16 is less peculiar than that of the previous simulation but poses other challenges to the quadrupole statistics. As can be seen in the figure, the surface mass density of the filament connecting both clusters is lower than that of the simulation in Fig. 8.4. A continuous filament is only visible because an additional contour line at $\kappa = 0.02$ was added. As a consequence only the small peak in the filament rising to $\kappa \simeq 0.03$ is visible in the reconstruction, but only at the level of the noise fluctuation, as we can infer from the spurious peaks in the lower left corner of Fig. 8.17.

Figure 8.18 shows a quadrupole map from simulated lens data for this simulation. The aperture quadrupole moment was computed in a 3' radius. Again the size of the aperture was chosen such that the aperture in the middle between both clusters does not cover what one intuitively would identify as part of the clusters. The two lowest contours, which are partly covered by the aperture in the filament center, do not belong to the region that obviously belongs to the cluster.

Again we see a quadrupole moment on the filament and around the galaxy clusters. As there are no small mass clumps on the connecting axis outside the clusters we can test the hypothesis that the quadrupole moment in the filament region exceeds the quadrupole moment on the corresponding point on the cluster slope. Fig. 8.19 shows the absolute value of the quadrupole moment in Fig. 8.18 along a line running through both cluster centers from the left edge of the image to the right. Points which are not exactly on a grid point were approximated by linear interpolation. The same was done for the error bars, which were calculated from 1000 randomizations of the galaxy orientations. The points are connected by straight lines.

Clearly visible is the broad central double peak on the filament bounded by the two minima of the cluster centers. The quadrupole moment on the slope of the left, less massive cluster is well below that of the filament. The center of the filament corresponds to the small minimum left of the little "bump" in the middle of the broad double peak (at $\sim 27'$). Although the maximum of the quadrupole moments is on the outer slope of the massive right cluster, the quadrupole moment having the same distance from the cluster center as the filament center is below the value in the filament center (at $\sim 43'$).

The double peak structure of the quadrupole moment on the filament is probably caused by the small mass concentration in the filament. The quadrupole moment in aperture centered on this peak will be lower than that of aperture which covers this peak and already part of the cluster and thus leads

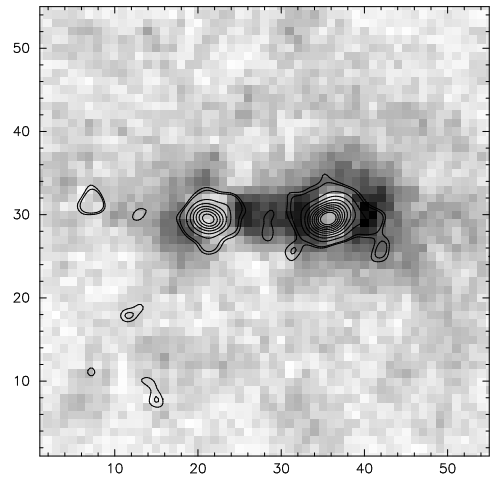

Figure 8.18 — Aperture quadrupole moment in a 3' radius. Overlaid are the contours of Fig. 8.17.

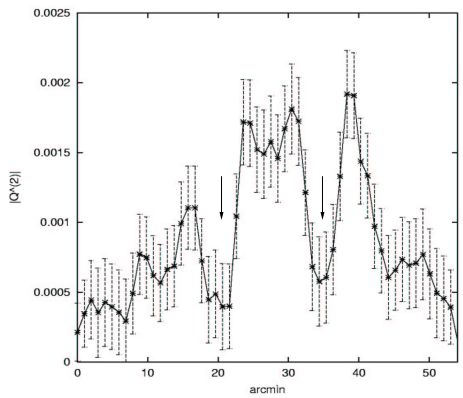

Figure 8.19 — Absolute value of the aperture quadrupole moment along a line running through the centers of both clusters from the left edge to the right edge of Fig. 8.18. The arrows mark the cluster center.

to a situation comparable to that of Fig. 8.11 with one cluster replaced by the small peak.

It is interesting to note that the quadrupole statistics gives a positive result if the reconstruction fails to show a filament. In fact, until now we have ignored the possibility that the clusters could have filamentary extensions that do not join.

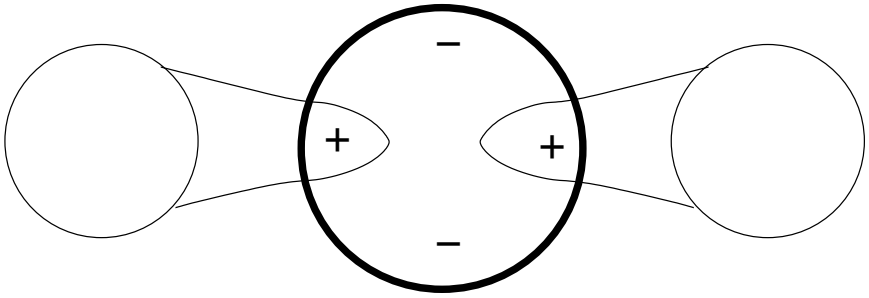

Figure 8.20 — Quadrupole moment of filamentary extensions of cluster that do not join.

An observer not knowing the true mass distribution of Fig. 8.16 would conclude to observe the case illustrated in Fig. 8.20. This example shows, that while the quadrupole moments can be used to quantify the significance of a filament by computing the significance of the quadrupole moment, measuring a quadrupole moment alone is not sufficient. Ideally, the filament is also visible (and significant) in a map of the aperture mass with the same filter radius.

8.7.1 Defining Cluster and Filament Regions

While in the attempt to separate the clusters and filament by fitting elliptical profiles to the clusters, the filament was defined as the surface mass density excess above the clusters. There is no criterion in the AMM statistics that defines cluster and filament regions. Much of the discussion of the quadrupole statistics in the last section was based upon "intuitive separation" of clusters and filament. In many cases this can be a problem, as seen from Fig. 8.16. While the contours show a continuous connection between the clusters, one could argue that the clusters in this simulation overlap. The right-hand cluster has a mass extension to the right, whose maximum spatial extension from the cluster center is

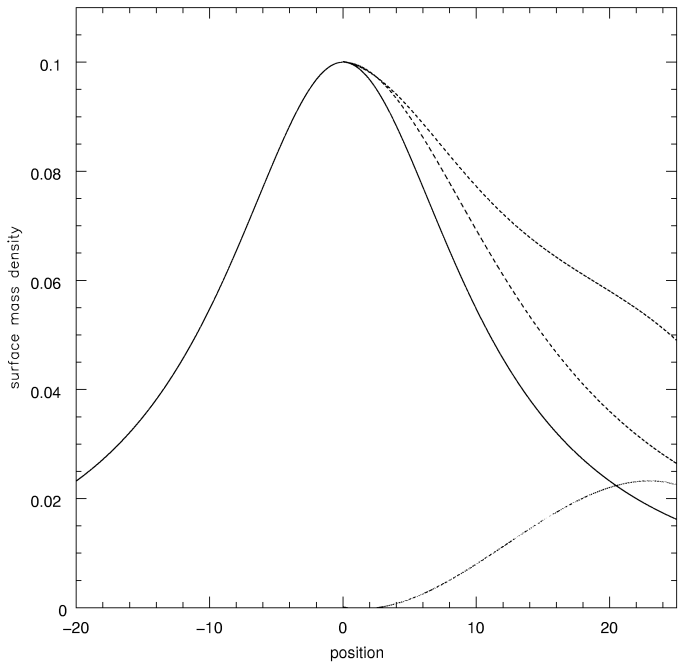

Figure 8.21 — Simple model of the surface mass density distribution of an elliptical cluster and a filamentary extension along the main axis of the system. The axes are labeled in arbitrary units.

comparable to the distance of the peak in the filament from the cluster center. The situation for the left-hand cluster is approximately the same. This illustrates the need for a more objective criterion to separate the clusters from a possible filament, which we try to develop in this section.

Fig. 8.21 shows a simple one–dimensional toy model of the mass distribution of a cluster with a filamentary extension. The model consists of the following components: We assume a cluster with a King profile. This is the solid line in Fig. 8.21. In all simulations we see that the clusters are not circular but stretched and have their major axes oriented approximately towards each other. We attribute this to tidal stretching and account for it in the model by stretching the right half of the King profile (long dashed line) by a factor, which has to be determined. This factor will be called the "stretch factor". The contribution of the filament (dotted line) is added to the stretched King profile. The result is the observed surface mass density profile on the right–hand side (short dashed).

We tried to define the "start" of the filament and the "end" of the cluster by the following procedure: The unstretched King profile, observed on the left–hand side, is stretched by a factor, to model the influence of tidal stretching. By this step we try to obtain the (unobservable) cluster profile on the right side without the contribution of the filament. This stretched profile is then compared to the observed profile containing the contribution of the filament by computing the goodness of fit

$$\chi^2 = \sum_{i=i_0}^{N} \left(\frac{\kappa_{\rm stretch}(\theta_i) - \kappa_{\rm true}(\theta_i)}{\sigma_i} \right)^2 , \tag{8.27}$$

at sample points θ_i in the reconstruction along the main axis of the system. σ_i is the estimated error in κ at the ith point and the summation is carried out from the i_0th point to the Nth point. χ^2 is repeatedly computed for increasing values of N. Unless noted otherwise, $i_0 = 1$. We can define the end of the cluster and the start of the filament by the point N, where the probability that $\kappa_{\rm stretch}$ is a good representation of $\kappa_{\rm true}$ falls below a predefined level ("cut–off confidence level").

We now have to find a way to determine the stretch factor. We assume that the inner portion of the observed profile on the right–hand side is a fair representation of the (unobservable) stretched profile. The stretch factor can then be determined by fitting the unstretched profile to the inner portion of the observed profile. This "stretch factor fit" was done using a χ^2 minimization with linear interpolation between the observed sample points. The size of the inner region to be used in the stretch factor fit

was measured in units of the core radius of the unstretched profile. Its value is called the "cut–off parameter".

The cut-off parameter and the cut–off confidence level have to be determined from simulations.

Figure 8.22 shows the mass profiles to the left and right of the center of the cluster on the left in the reconstruction displayed in Fig. 8.5 along the main axis of that system. For simplicity the error bars were assumed to be equal to the standard deviation of a reconstructed mass map of a randomized catalog of background galaxies.

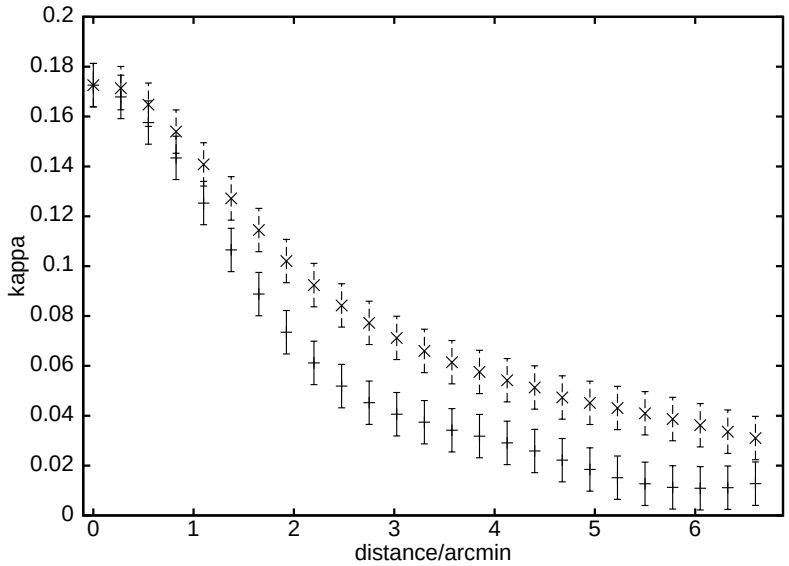

Figure 8.22 — Surface mass density profiles of the cluster on the left in the reconstruction displayed Fig. 8.5 along the main axis of the system. The crosses mark the surface mass density in the filament part, the dashes the surface mass density on the left-hand side of the cluster. The x–axis denotes the distance from the cluster center in arc minutes.

We determined several combinations of the cut–off parameter and confidence level that match the visual impression of filament beginning and cluster end. However, if these were applied to other clusters, the separation point between cluster and filament was placed at non–sensical positions.

We also modified the starting value i_0 in the summation in eq. (8.27). First, we placed it at the point closest to the cut–off parameter of the stretch factor fit in order to exclude the central region, which by definition of this procedure has a small χ^2. Second, we calculated χ^2 in a moving window of fixed size and set the separation point between cluster and filament to the start of the window for which χ^2 fell below the cut–off confidence level. This was done for various window sizes and confidence levels. Again, parameters that worked well for one cluster failed horribly for others.

8.8 Conclusions

In this chapter we have investigated two main aspects concerning to filaments. The first point was to set up proper initial conditions for N–body simulations in order to create bridges between two neighbouring clusters at a given redshift. By using the approach of Constrained Realizations, we have been capable of producing controlled and carefully designed initial density fields in order to get the desired configuration.

The aim was to recreate as close as possible the environment presented by the Abell clusters 222 and 223, with a connecting bridge between the two clusters. We have considered every observed feature available in order to model the initial density fields. We found that in order to reproduce successfully such configuration, a set of 18 conditions imposed over each cluster seed were needed. Those constraints were position, distance, shape, orientation, peculiar velocity and tidal shear. The shape was specified by the axis ratios of the triaxial density peaks. The clusters were aligned in such way that their corresponding major axes will point out toward each other. An initial kick was given in order to approach the system in a smoothly way avoiding violent interaction between the two clusters.

The tidal field was constructed in such a way that its stretching mode was aligned along the same main axis-system direction and a compressional mode perpendicular to this main axis. Under these constrictions, the linear initial density fields showed the desired configuration.

The evolved density fields satisfyingly reproduced the main observed system features, showing beyond doubt the effectiveness of the CR algorithm to study and reproduce cosmic observed features. Without the use of the CR formalism, it would be very difficult to find in a $N-$body simulation the right situation required for the weak lensing analysis.

The second part of the chapter consisted in quantify the presence of the bridge between the clusters. For this, the use of weak lensing analysis was employed, in particular the circular aperture method. The Aperture multipole moments [AMM] technique was used in order to quantify the weighted surface mass density distribution from the circular aperture method.

The lensing reconstruction results showed that while the quadrupole moments can be used to quantify the significance of a filament by computing the significance of the quadrupole moment, measuring a quadrupole moment alone is not sufficient. In an attempt to separate the clusters and filament by fitting elliptical profiles to the clusters, the filament was defined as the surface mass density excess above the clusters. However, such criterion failed with the AMM statistics since there is none criterion to define cluster and filament regions with this technique. The aperture quadrupole moment statistics in principle has the power to quantify the presence of a filament-shaped structure. To objectively apply this technique, one needs to be able to separate clusters from filaments. We did not find an objective way to do this and had to resort to subjectively defining the sizes of the apertures used.

We would like to stress that this is not a problem of the weak lensing technique but stems from the fact that we were unable of giving an objective criterion to define a filament. The visual impression of what a filament is, is often sufficient in simulations or redshift surveys where filaments stretching long distances between clusters are seen. In the case of close pairs of clusters -where we can hope to see filaments with today's telescopes- a more objective criterion is important, but difficult to find.

8.A Aperture multipoles moments

8.A.1 Definitions

Let $\vec{\theta}$ be the position angle of a lensed object and $\vec{\beta}$ its undeflected position, the two angles are related to each other via the lens equation:

$$\vec{\beta} = \vec{\theta} - \vec{\alpha}(\vec{\theta}), \tag{A8-1}$$

where $\vec{\alpha}$ is the scaled deflection angle.

Depending on the surface mass density ($\Sigma(D_d\vec{\theta})$, which is defined as the projection of the 3D density distribution of the lens onto a plane perpendicular to the line of sight, eq. A8-1 can have multiple $\vec{\theta}$ for a given $\vec{\beta}$. The dimensionless surface mass density $\kappa(\vec{\theta})$ is defined as:

$$\kappa(\vec{\theta}) = \frac{\Sigma(D_d\vec{\theta})}{\Sigma_{cr}}, \tag{A8-2}$$

where Σ_{cr} is the *critical surface mass density*,

$$\Sigma_{cr} = \frac{c^2}{4\pi G}\frac{D_s}{D_d D_{ds}}. \tag{A8-3}$$

D_d denotes the angular-diameter distances between observer and deflector (lens), D_s between observer and source, and D_{ds} from the deflector to the source.

The value of κ in eq. A8-2 gives a qualitative description of the lens. If $\kappa > 1$ for a given region in the lens plane, the lens is said to be *strong* and it can produce multiple images of the background source. If $\kappa \ll 1$ the lens is called *weak* and cannot produce several images of the source.

The scaled deflection angle can be written in terms of κ

$$\vec{\alpha}(\vec{\theta}) = \frac{1}{\pi}\int \mathrm{d}^2\theta'\,\kappa(\vec{\theta}')\frac{\theta-\theta'}{|\theta-\theta'|^2}\,.$$

From this equation is easy to see that the scaled deflection angle can be written as the gradient of a two dimensional potential, $\vec{\alpha} = \nabla\psi$

$$\psi(\vec{\theta}) = \frac{1}{\pi}\int \mathrm{d}^2\theta'\,\kappa(\vec{\theta}')\ln|\theta-\theta'|\,, \tag{A8-4}$$

following the analogy with Newtonian theory, ψ satisfies the Poisson equation:

$$\nabla^2\psi(\vec{\theta}) = 2\,\kappa(\vec{\theta})\,. \tag{A8-5}$$

An important characteristic of Eq.A8-1 is its non-linearity. Therefore, a gravitational lens will not only change the position of the source image, but also its shape. The local properties of the lens mapping are described by its Jacobian matrix, or *magnification matrix*

$$\mathcal{A} = \frac{\partial\vec{\beta}}{\partial\vec{\theta}} = \left(\delta_{ij} - \frac{\partial^2\psi(\vec{\theta})}{\partial\theta_i\partial\theta_j}\right) = \begin{pmatrix} 1-\kappa-\gamma_1 & -\gamma_2 \\ -\gamma_2 & 1-\kappa+\gamma_1 \end{pmatrix}. \tag{A8-6}$$

The trace-free part of $\mathcal{A}$ is defined as the *shear*,

$$\gamma = \gamma_1 + \imath\,\gamma_2 = |\gamma|\,e^{2\imath\varphi}\,, \tag{A8-7}$$

and it is related to the deflection potential as

$$\gamma_1 = \frac{1}{2}(\psi_{,11} - \psi_{,22})\,, \qquad \gamma_2 = (\psi_{,12})\,. \tag{A8-8}$$

The magnification factor of an image is given by the inverse of the determinant of the Jacobian:

$$\mu = \frac{1}{\det\mathcal{A}} = \frac{1}{(1-\kappa)^2 - |\gamma|^2}\,. \tag{A8-9}$$

The tensor of the quadrupole moment of the two-dimensional mass distribution $\kappa(\vec{\theta})$ with respect to the point $(\vec{\theta}_0)$ is defined as (Schneider & Bartelmann 1997),

$$Q_{ij} = \int \mathrm{d}^2\theta\,\kappa(\vec{\theta}+\vec{\theta}_0)\,w(|\vec{\theta}|)\,\theta_i\,\theta_j\,, \tag{A8-10}$$

for $i, j = 1, 2$, where $w(|\vec{\theta}|)$ is a radial weight function. The shape of an image can be quantify in terms of the components of the tensor Q_{ij} via the complex number:

$$\epsilon = \frac{Q_{11} - Q_{22} + 2\imath Q_{12}}{Q_{11} + Q_{22} + 2(Q_{11}Q_{22} - Q_{12}^2)^{1/2}}\,, \tag{A8-11}$$

which is called the *complex ellipticity* (Bonnet & Mellier 1995).

8.A.2 Multipole moment in terms of the shear

The trace-free and trace parts of eq. A8-10 can be written in a very general way for higher multipole orders. Schneider & Bartelmann (1997) defined the complex nth-order multipole moment (trace-free) by

$$Q^{(n)} = \int_0^\infty \mathrm{d}\theta\,\theta^{n+1}w(\theta)\int_0^{2\pi}\mathrm{d}\varphi\,e^{n\imath\varphi}\kappa(\vec{\theta}_0+\vec{\theta})\,, \tag{A8-12}$$

and the *mass moments* (trace),

$$M^{(n)} = \int_0^\infty \mathrm{d}\theta\,\theta^{n+1} w(\theta) \int_0^{2\pi} \mathrm{d}\varphi\,\kappa(\vec{\theta}_0 + \vec{\theta}), \tag{A8-13}$$

where $w(\theta)$ is a radially symmetric weight function.

Kaiser (1995) shown by suitably combining third-order derivatives of φ in eq. A8-5, that the gradient of κ can be written in terms of the derivatives of the shear components:

$$\nabla\kappa = \begin{pmatrix} \gamma_{1,1} + \gamma_{2,2} \\ \gamma_{2,1} - \gamma_{1,2} \end{pmatrix}. \tag{A8-14}$$

This relation can now be used to express the multipole moments just defined in terms of the shear γ. Since the shear is directly observable from the distortions of the images of faint background galaxies (in the case of weak lensing, i.e. $\kappa \ll 1$), the multipole moments can be written directly in terms of observables.

Schneider & Bartelmann (1997) defined the *tangential shear* $\gamma_t(\vec{\theta};\vec{\theta}_0)$ and the *radial shear* $\gamma_r(\vec{\theta};\vec{\theta}_0)$ at positions $\vec{\theta} = \theta e^{\imath\varphi}$ relative to position $\vec{\theta}_0$ by

$$\begin{aligned} \gamma_t(\vec{\theta};\vec{\theta}_0) &= -[\gamma_1 \cos(2\varphi) + \gamma_2 \sin(2\varphi)] = -\Re[\gamma(\vec{\theta} + \vec{\theta}_0)\, e^{-2\imath\varphi}], \\ \gamma_r(\vec{\theta};\vec{\theta}_0) &= -[\gamma_2 \cos(2\varphi) - \gamma_2 \sin(2\varphi)] = -\Im[\gamma(\vec{\theta} + \vec{\theta}_0)\, e^{-2\imath\varphi}], \end{aligned} \tag{A8-15}$$

where $\Re$ and $\Im$ denote the real and imaginary parts of the given complex quantity.

By integrating by parts eq. A8-12, transforming it into polar coordinates and by doing some partial integrations and algebraic manipulation, it is possible to show that one can get a local estimation of the aperture multipole moment in a circle of radius R from

$$Q^{(n)} = \int_0^R \mathrm{d}\theta\,\theta^{n+1} w(\theta)\, g_t(\theta) + \frac{\imath}{n} \int_0^R \mathrm{d}\theta\,\theta^{n+1} [n\, w(\theta) + \theta\, w'(\theta)]\, g_r(\theta), \tag{A8-16}$$

here $w'(\theta)$ is the derivative of $w(\theta)$, and we have defined

$$g_t(\theta) = \int_0^{2\pi} \mathrm{d}\varphi\, e^{n\imath\varphi}\, \gamma_t(\vec{\theta};\vec{\theta}_0), \qquad g_r(\theta) = \int_0^{2\pi} \mathrm{d}\varphi\, e^{n\imath\varphi}\, \gamma_r(\vec{\theta};\vec{\theta}_0). \tag{A8-17}$$

In the case of dealing with real data, the integral is replaced by a sum over individual galaxy ellipticities to compute the aperture multipole statistics.

$$Q^{(n)}(\vec{\theta}_0) = \frac{1}{n_g} \sum_{i=1}^{N} e^{n\imath\varphi_i} \left\{ \theta_i^n\, w(\theta_i)\, \epsilon_{ti} + \imath \frac{\theta_i^n [n w(\theta_i) + \theta w'(\theta_i)]}{n} \epsilon_{ri} \right\}, \tag{A8-18}$$

where n_g is the number density of galaxies in the circle, (θ_i, φ_i) are the polar coordinates of the ith galaxy with respect to $\vec{\theta}_0$, and

$$\epsilon_{ti} = \Re(\epsilon_i\, e^{-2\imath\varphi_i})\,; \qquad \epsilon_{ri} = -\Im(\epsilon_i\, e^{-2\imath\varphi_i}), \tag{A8-19}$$

are the tangential and radial components of ellipticity of the ith galaxy with respect to the origin of the coordinate system.

The significance of a multipole moment measurement can in the absence of lensing (expectation value of $Q^{(n)} = 0$) be computed from

$$\sigma^{(n)} = \frac{\sigma_\epsilon}{\sqrt{2} n_g} \left\{ \sum_{i=1}^{N} \left[(\theta_i^n\, w(\theta_i))^2 + \left(\frac{\theta_i^n\, [n\, w(\theta_i) + \theta\, w'(\theta_i)]}{n} \right)^2 \right] \right\}^{1/2} \tag{A8-20}$$

where it has been used, in the absence of lensing,

$$\langle \epsilon_{ri}\, \epsilon_{rj} \rangle = \frac{\sigma_\epsilon^2}{2} \delta_{ij} \qquad \text{and} \qquad \langle \epsilon_{ti}\, \epsilon_{rj} \rangle = 0, \tag{A8-21}$$

and σ_ϵ is the dispersion of the intrinsic source ellipticity.

9

The DTFE density and velocity fields of the PSC*z* catalog

E. Romano-Díaz, R. van de Weygaert, W. E. Schaap & E. Branchini.

We apply the Delaunay Tessellation Field Estimator to reconstruct the density and velocity fields of the linear model of the full sky galaxy survey PSC*z*. The characteristics of the DTFE technique have allowed us to trace the density and velocity fields at both high and low density regions without losing resolution. A characteristic of the DTFE method is that velocity-gradient related quantities can be computed in a straightforward manner. We have reconstructed the DTFE divergence and shear components of the reconstructed velocity field. Our results show a great consistency between the velocity field and the density field.

9.1 Introduction

Within the gravitational instability scenario, large-scale flows of galaxies are a response to the underlying matter distribution and thus, peculiar velocity measurements are a critical probe for cosmology and large scale structure. Under the assumption that galaxies trace the matter distribution it is possible to reconstruct self-consistently density and velocity fields from a galaxy-redshift catalog. Comparison of the modeled velocity field with a real measured velocity field allows to test the gravitational instability picture, to measure the relative distribution of luminous and dark matter and to determine the parameter $\beta = \Omega_m^{0.6}/b$, where Ω_m is the cosmological mass density parameter, and b is the bias of the galaxy distribution relative to the underlying matter density (Peebles 1980).

A common problem when performing this comparison is the fact that the sampled objects in the velocity and galaxy surveys are not the same. Although one could assume that both fields faithfully trace their respective underlying velocity and density fields, this might not be the case. It is therefore necessary to perform such analysis by counting with volume-weighted velocities that properly sample the surveyed region.

Reconstructing a continuous volume-weighted velocity field from a sparse sample of peculiar velocities is a challenging task. One needs to interpolate the peculiar velocities into those regions devoid of data, overcome shot-noise effects and to preserve the large and small scale characteristics of the peculiar velocities. Several authors (e.g. Bertschinger et al. 1990; Juszkiewicz et al. 1995; Lokas et al. 1995; Baker et al. 1998; Branchini et al. 1999; Dekel et al. 1999) filtered galaxy peculiar velocities with a Gaussian kernel of a fixed length to obtain the velocity field onto a regular grid. However, the use of a filtering algorithm smears out all the velocity information contained on scales smaller than the filter size. Also, in most of the cases, the smoothing procedures are implicitly mass-weighted.

Bernardeau & van de Weygaert (1996) showed that for the velocity field, conventional reconstruction techniques are unable of recovering this field accurately over its whole range of values from small-scale to large-scale. They introduced a tessellation based method to recover fully volume-covering and volume-weighted velocity field, the Voronoi and Delaunay tessellation methods. They demonstrated the success in reproducing analytical predictions by the Delaunay method. In particular this concerned the ability to reproduce the velocity-divergence distribution in the quasi linear regime. Based on the work of Bernardeau & van de Weygaert, Schaap & van de Weygaert (2000) and Schaap (2005) developed a reconstruction method based on the geometrical concept of the Delaunay tessellation (Delaunay 1934), the *Delaunay Tessellation Field Estimator* [hereafter, DTFE]. The method enables a natural reconstruction of the density field from the sampling point set. In Chapter 6 we presented an extension of DTFE for peculiar velocities along the line of Bernardeau & van de Weygaert. The method has been tested on $N-$body simulations. Given a discrete set of peculiar velocities, the processed DTFE velocity field is able to maintain the small and large scale characteristics of the peculiar velocities. It obtains continuous full coverage volume-weighted estimates. Implicitly, the method involves the computation of the velocity field gradient. This makes velocity related quantities such as the velocity divergence, shear and vorticity quite straightforward to compute.

In order to compute a self-consistent reconstruction of the density and velocity fields one needs to consider a uniform whole-sky sample with complete redshift information. This requirement has lead to the use of the IRAS catalogs. Here we concentrate on the last and best defined survey, the PSC*z* survey (Saunders et al. 2000). The intrinsic characteristics of the IRAS-PSC*z* catalog such as depth and sky coverage have made its reconstructed density and velocity fields into faithful representations of both fields in our nearby universe (Branchini et al. 1999; Schmoldt et al. 1999; Branchini et al. 2001; Teodoro et al. 2003).

In this chapter, we apply the DTFE velocity interpolation method to the linear modeled PSC*z* velocity field of Branchini et al. (1999) [hereafter, B99]. Our main aim is to reconstruct in a volume-weighted fashion the discrete PSC*z* velocity field, to uncover the intricate velocity pattern in the local universe and to show the virtues of the DTFE method with "real" data. Testing the performance of the method with the well controlled spatial reconstructed PSC*z* catalog should give us confidence for applying the DTFE technique to the forthcoming surveys such as 2MASS and 6dF.

9.2 The DTFE method

The DTFE interpolation method was introduced by Schaap & van de Weygaert (2000) (see also Schaap 2005), for rendering fully volume-covering and volume-weighted physical fields from a discrete set of sampled field values. The method is self-adaptive and does not make use of any artificial smoothing procedure. It followed the pioneering work by Bernardeau & van de Weygaert (1996) for using the Delaunay tessellation of the point set as a natural and self-adaptive interpolation frame for recovering the continuous velocity field sampled by the velocities at those points. Schaap & van de Weygaert (2000) and Schaap (2005) extended this to the recovery of the density or intensity field when one assumes it to be fairly sampled by the spatial point distribution.

The DTFE algorithm as a linear multidimensional field interpolation scheme is the linear first-order version of the natural neighbouring algorithm for spatial interpolation (see Sibson 1981; Okabe et al. 2000). Related procedures have been implemented in a variety of other applied sciences. Successful examples may be found in geophysics (see e.g. Braun & Sambridge 1994; Sambridge 1999) and engineering mechanics (Sukumar 1998).

The primary ingredient of the DTFE method is the Delaunay tessellation of the particle distribution. The Delaunay tessellation of a point set is the uniquely defined and volume-covering tessellation of mutually disjunct Delaunay tetrahedra. A Delaunay tetrahedron is defined by the set of four points whose circumscribing sphere does not contain any of the other points in the generating set (Delaunay 1934) (triangles in 2D). The Delaunay tessellation is intimately related to the Voronoi tessellation of the point set, i.e. they are each others *dual*. The Voronoi tessellation of a point set is the division of space into mutually disjunct polyhedra, each polyhedron consisting of the part of space closer to the defining point than any of the other points (Voronoi 1908; Okabe et al. 2000)

It is straightforward to appreciate that on the basis of their definitions both Delaunay and Voronoi tessellation fully adapt to the local point distribution. Moreover, the minimal coverage characteristics of the Delaunay tessellation imply it to be optimal for defining a network of multidimensional interpolation intervals. The point in case for its pattern tracing characteristics is provided by the right-hand panel of Figure 9.1. It shows the 2-Dimensional Delaunay triangulation for a section along the z-supergalactic plane through the PSCz catalog, the galaxy set which we analyze in this work.

9.2.1 DTFE density and velocity fields

One of the important properties of a processed DTFE density field is that it resolves two of the main characteristics of gravitational structure formation. It objectively reproduces any anisotropic patterns in the density distribution without diluting their intrinsic geometrical properties. This is a great advantage when seeking to analyze the cosmic matter distribution, characterized by prominent filamentary and wall-like components linking up into a *cosmic web*. Also, it manages to outline the full hierarchy of substructures present in the sampling point distribution. Since we assume that structure in the Universe arose through the gradual hierarchical buildup of matter concentrations, the benefits of an objective tracer of such features are obvious. In addition, it has been recognized that the low density regions, e.g. the voids in the galaxy distribution, are evenly rendered as regions of slowly varying, moderately low density values through the interpolation definition of the DTFE field reconstruction. It manages to suppress automatically the shot noise in such sparsely sampled regions (see Schaap 2005).

The linear interpolated DTFE velocity field retains the same characteristics as that of the corresponding DTFE density field. In this thesis we have demonstrated that the DTFE velocity method has indeed the ability to resolve both small and large scale features of the velocity field. Note that a succesfull DTFE velocity field interpolation does not demand it to be uniformly sampled from an underlying density field. In this work, however, we assume that they do. The DTFE velocity fields are continuous and fully volume-covering. Bernardeau & van de Weygaert (1996) introduced the Delaunay method for velocity field interpolation in an attempt to reproduce *volume-weighted* velocity field estimates. The latter was deemed essential for testing theoretical predictions. Most analytical results concerning the statististics of velocity field related quantities, as they develop gravitationally from a primordial

Gaussian perturbation field, concern explicit volume-weighted expressions.

Bernardeau & van de Weygaert (1996) explicitly applied the Delaunay method to the velocity divergence field to test the validity of the second order perturbation theory results. This was particularly interesting as a mildy non-Gaussian velocity divergence distribution would enable the breaking of the degeneracy between the cosmic matter density Ω and the bias b between the matter and galaxy distribution (Bernardeau 1994; Bernardeau et al. 1995). The later work by Schaap & van de Weygaert (2003) showed the first results on the succesfull reproduction by DTFE of the physical and spatial correlation between cosmic density and velocity fields in a large GIF $N-$body simulation (Kauffmann et al. 1999) (also see Schaap 2005). The corresponding density and velocity maps provide convincing evidence of the detailed tracing of the velocity flows in and around the cores of high-density regions. Within the same simulations, the voidlike regions were rendered as super-Hubble expanding bubbles, consistent with our view of void dynamics (Icke 1984; Sheth & van de Weygaert 2004).

9.2.2 The DTFE general reconstruction

The DTFE field reconstruction method can be summarized in the following sequence of steps:

1. Construction of the Delaunay tessellation from the point distribution.
2. In the case of estimating the density from the point distribution itself, with the extra requirement of the latter being an unbiased sample of the underlying density field, we first estimate the density values at the sampled points from the Voronoi tessellation.
3. Calculation of the field (velocity) gradient $\widehat{\nabla f}|_j$ in each Delaunay tetrahedron j by inversion on the basis of the field values and positions of the tetrahedron vertices.
   (a) In the case of the velocity field $\mathbf{v}$, we may in each Delaunay tetrahedron, directly infer velocity gradient related quantities such as the velocity divergence, shear and vorticity.
4. Processing. This may involve various operations. The most important ones are *"image reconstruction"* and, subsequently, *"filtering"*. Image reconstruction consists of two steps:
   (a) For a set of image points (usually grid points) determine in which Delaunay tetrahedra they are located.
   (b) By (linear) interpolation compute field values at each of these points. For a point $\mathbf{x}$ in a Delaunay tetrahedron j, having $\mathbf{x_0}$ as one of its vertices, the resulting DTFE field value $\hat{f}(\mathbf{x})$ becomes:
$$\hat{f}(\mathbf{x}) = f(\mathbf{x_0}) + \widehat{\nabla f}|_j \cdot (\mathbf{x} - \mathbf{x_0}) . \tag{9.1}$$

9.3 The PSC*z* catalog

The IRAS-PSC*z* catalog (Saunders et al. 2000) is an extension of the 1.2-Jy catalog (Fisher et al. 1995a). It contains ~ 15 500 galaxies with a flux at 60μm larger than 0.6-Jy. For a full description of the catalog, selection criteria and the procedures used to avoid stellar contamination and galactic cirrus, we refer the reader to Saunders et al. (2000). For our purposes the most important characteristics of the catalog are the large area sampled (~ 84% of the sky), its depth with a median redshift of 8 500 km s^{-1}, and the dense sampling (the mean galaxy separation at 10 000 km s^{-1} is $\langle l \rangle$ = 1 000 km s^{-1}).

Because of the flux-limited nature of the PSC*z* catalog, there is a decrease in the objects' sampling as a function of distance from the observer. This is quantified by the radial selection function of the catalog, $\psi(r)$, where the selection function is defined as the fraction of the galaxy number density that is observed above the flux limit at some distance r. To recover the proper number density of objects one needs to weight each galaxy by the inverse of the selection function. In this work we adopt the selection function of B99 (see also Chapter 5).

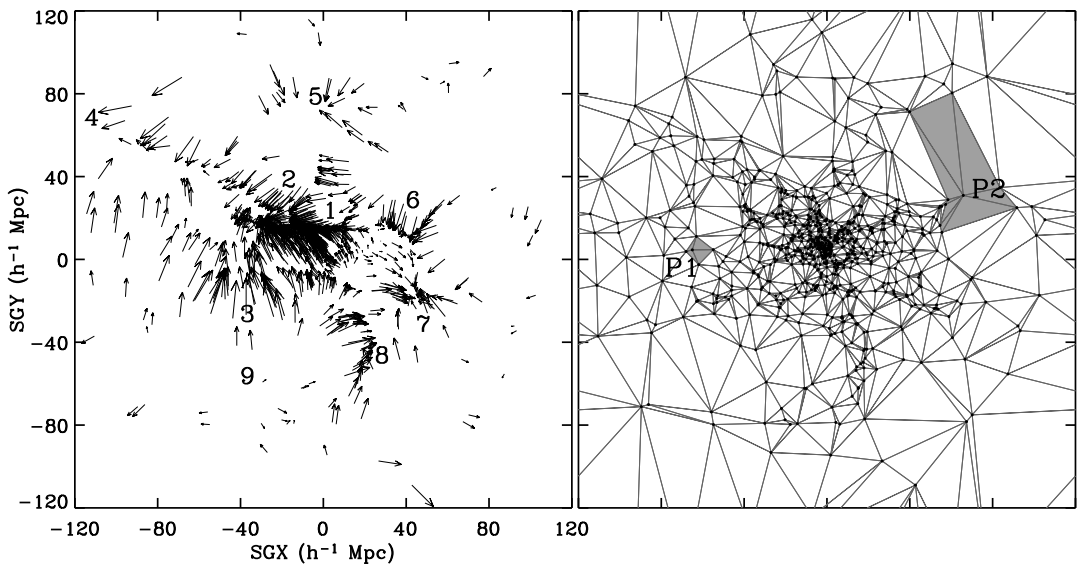

Figure 9.1 — Modeled peculiar velocity field at the galaxy positions (left-hand panel). The plot represents a slice of 2.5 h^{-1}Mpc thickness centered along the z−supergalactic plane. Numbers indicate the major visible structures along the cut. 1- Local supercluster, 2- Great attractor region, 3- Pavo-Indus-Telescopium complex, 4- Shapley supercluster, 5- Coma cluster, 6- Camelopardalis cluster, 7- Perseus-Pisces supercluster, 8- Cetus wall, 9- Sculptor void. (From Branchini et al. 1999). The right-hand panel shows the respective Delaunay tessellation of the galaxy distribution. The shadowed regions illustrate the "contiguous Voronoi cell" concept for two given points (P1 & P2).

To correct for the selection function, as well as for the 16% of the missing sky devoid of data due to the cirrus emission and unobserved areas and to correct for redshift distortions, we have used the spatial reconstructed PSCz catalog of B99. The positions and velocities in real space were computed following the *method I* of B99. In this approach, the technique of Yahil et al. (1991) was implemented to minimize redshift-space distortions (see B99 for a more complete explanation of the method).

9.3.1 The linear modeled PSCz catalog

An important constraint in the spatial reconstructed model of B99 is the fact that the reconstruction is valid only in the limit of small density fluctuations. The gravity field was smoothed with a top-hat filter of radius 500 km s^{-1} to assure the validity of linear theory and thus to obtain the smoothed peculiar velocity at each galaxy position.

The end product of such procedure is the real spatial position and peculiar velocity for each individual galaxy for a given value of the β parameter ($\mathrm{v} \propto \beta \mathbf{g}$). In our adopted reconstructed catalog $\beta = 0.5$, in agreement with the results of Branchini et al. (2001) and Zaroubi et al. (2002) from density-density and velocity-velocity comparisons. Velocity predictions were made in the Local Group frame [LG, hereafter] to minimize the uncertainties derived from the lack of information on scales larger than the PSCz catalog.

The final spatial positions and peculiar velocities can be seen in the left-hand panel of Figure 9.1, in which a slice of 2.5 h^{-1}Mpc thickness centered along the z−supergalactic plane is shown. Velocities are displayed at the galaxy positions and normalized to the maximum amplitude within this slice. The Local Group is located at the origin. The main large-scale structures have been labeled and can be easily recognized by their gravitational effects in their surroundings. Cluster such as Coma and Camelopardalis, and superclusters like the Local supercluster, the Great Attractor region (GA, Hydra-Centaurus supercluster, H-C), the Pavo-Indus-Telescopium (P-I-T) complex, Shapley and the Cetus

wall are noticeable in the map. Also, underdense regions such as the Sculptor void can be identified. A peculiar characteristic of the modeled velocity field is the lack of a backflow in the GA region, implying that the Shapley supercluster is still a major source of the LG velocity field (e.g. Rowan-Robinson et al. 2000; Plionis & Kolokotronis 1998; Basilakos & Plionis 1998).

Around high density regions (cluster of galaxies) where shell crossing might have occurred, there are tripled-valued regions. In Chapter 5 we addressed this problem by considering two different samples, one where tripled-valued regions were collapsed, and another without collapsing them. Results showed that the smoothing procedure used to linearized the data minimized this effect. Differences between collapsed and uncollapsed samples are less than 10% for their bulk flow and velocity shear components, and consistent at the 1σ level. The velocity model we have chosen leaves tripled-valued regions uncollapsed. In this way, we reduce a source of error at high-density regions in the DTFE procedure.

Since the PSC*z* velocities have been linearized, the vorticity modes in the peculiar velocity field have been minimized, although not completely erased. Dekel et al. (1999) employed a Gaussian kernel of 12 h^{-1}Mpc in order to linearize completely the measured velocity field from the Mark III catalog (Willick et al. 1997a). The reliability of the modeled density and velocity fields has been confirmed in several studies and in density-density and velocity-velocity comparisons with other surveys (e.g. Branchini et al. 2001; Zaroubi et al. 2002).

9.4 DTFE reconstruction of the PSC*z* density and velocity fields

In order to reconstruct the continuous volume-weighted DTFE density and velocity fields from the PSC*z* catalog, we have made use only of the linearized data within a spherical volume of radius 180 h^{-1}Mpc. This radius is large enough to enclose the main sources that contribute to the local velocity field (e.g. B99, see also Chapter 5). The selected number of galaxies at this radius is 13432. The DTFE density and velocity reconstruction was performed following the steps described in Section 9.2. In our analysis we only present DTFE density and velocity maps up to a radius of 120 h^{-1}Mpc in order to have a more qualitative comparison with those from B99 and Schmoldt et al. (1999). At this radius, the sample contains 10651 galaxies with an inter-object separation of $\approx 14\ h^{-1}$Mpc.

9.4.1 The DTFE PSC*z* density field: Cosmography

The spatial DTFE density field is shown in Figure 9.2. The density field has been smoothed with a Gaussian filter of $\sqrt{5}\,h^{-1}$Mpc size in order to match the linearized velocity field[1]. The isosurface level corresponds to structures at 3 times the smoothed mean density. Two major matter concentrations along the $z = 0$ plane dominate the field. The complex formed by the P-I-T and the H-C with its extension toward the Shapley concentration dominates the left side region. The PP and the Cetus wall located at the opposite side overshadow the other structures. There is a thin filamentary structure connecting both massive matter concentrations, the Local Supercluster.

A cut along the 3D density field is presented in Figure 9.3. The slice corresponds to the $z-$supergalactic plane. The color density contours represent the density field. The superimposed arrows correspond to the DTFE reconstructed velocity field discussed in Section 9.4.2. Also here the density field has been convolved with a Gaussian kernel of $\sqrt{5}\ h^{-1}$Mpc. The right-hand color bar indicates the amplitude of the density fluctuations.

High-density regions (reddish regions) as well as low density ones (dark zones) can be easily recognized along the map. Very conspicuous is the filamentary structure running from the Camelopardalis cluster ($[SGX, SGY] \approx [45, 20]\ h^{-1}$Mpc) toward the Shapley supercluster ($[SGX, SGY] \approx [-120, 70]\ h^{-1}$Mpc) and connecting the Local Supercluster with the Hydra-Centaurus supercluster. The Pavo-Indus-Telescopium supercluster is barely noticeable at ($[SGX, SGY] \approx [-40, -10]\ h^{-1}$Mpc). The Perseus-Pisces supercluster is well defined at ($[SGX, SGY] \approx$

[1]We have used the fact that $R_G = R_{TH}/\sqrt{5}$ (Suto & Fujita 1990). In our case, $R_{TH} = 5\ h^{-1}$Mpc

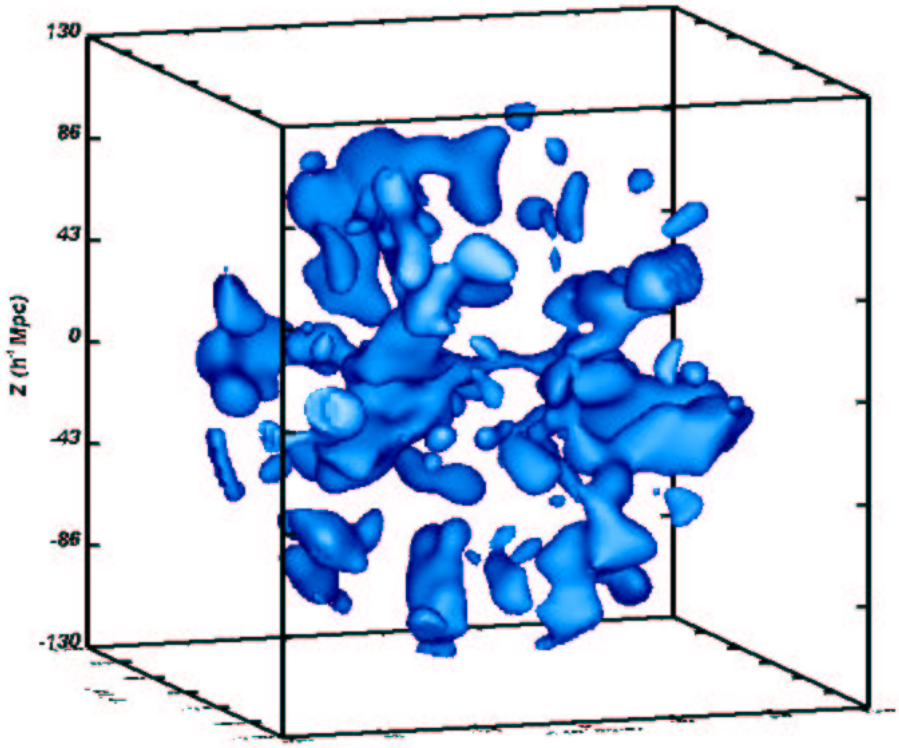

Figure 9.2 — 3D reconstructed DTFE PSC*z* density field. The field has been smoothed with a Gaussian kernel of 5 h^{-1}Mpc. The isosurface represents structures at the 2 level of the mean density. Notice the two huge density concentrations around the $z = 0$ plane, the PP and Cetus wall complex to the right, and the H-C and P-I-T to the left side. A well delineated bridge connects both structures, the Local Supercluster.

$[45,-20]$ h^{-1}Mpc). Also recognizable is the Cetus wall ($[SGX,SGY] \approx [20,-40]$ h^{-1}Mpc) which connects with the barely visible Sculptor wall ($[SGX,SGY] \approx [0,-80]$ h^{-1}Mpc). At the top of the plot, the Coma cluster ($[SGX,SGY] \approx [0,70]$ h^{-1}Mpc) is the only major concentration visible. A glimpse of the Coma wall can also be seen.

We can also clearly recognize the voids. The Sculptor void, surrounded by the P-I-T complex and the Sculptor and Cetus walls is one of the most conspicuous empty features along the supergalactic plane. The Fornax void is located just at the bottom of the plot ($[SGX,SGY] \approx [10,-110]$ h^{-1}Mpc). The small void located between the Coma cluster and the H-C region is clearly well defined.

9.4.2 The DTFE PSC*z* velocity field

We have reconstructed the continuous volume-weighted DTFE velocity field of the PSC*z* catalog. Because the input velocities have been linearized prior to the DTFE processing, we did not have to smooth the velocity field any further. This will also constraint our reconstruction in the sense that velocity flows smaller than the kernel size ($\sqrt{5}$ h^{-1}Mpc) will not be recovered.

In Figure 9.3 the projected DTFE velocity field along the same density cut is presented. The velocity arrows have been normalized to the maximum plotted velocity amplitude. Notice that both density and velocity fields are strongly correlated with each other. The processed DTFE velocity field

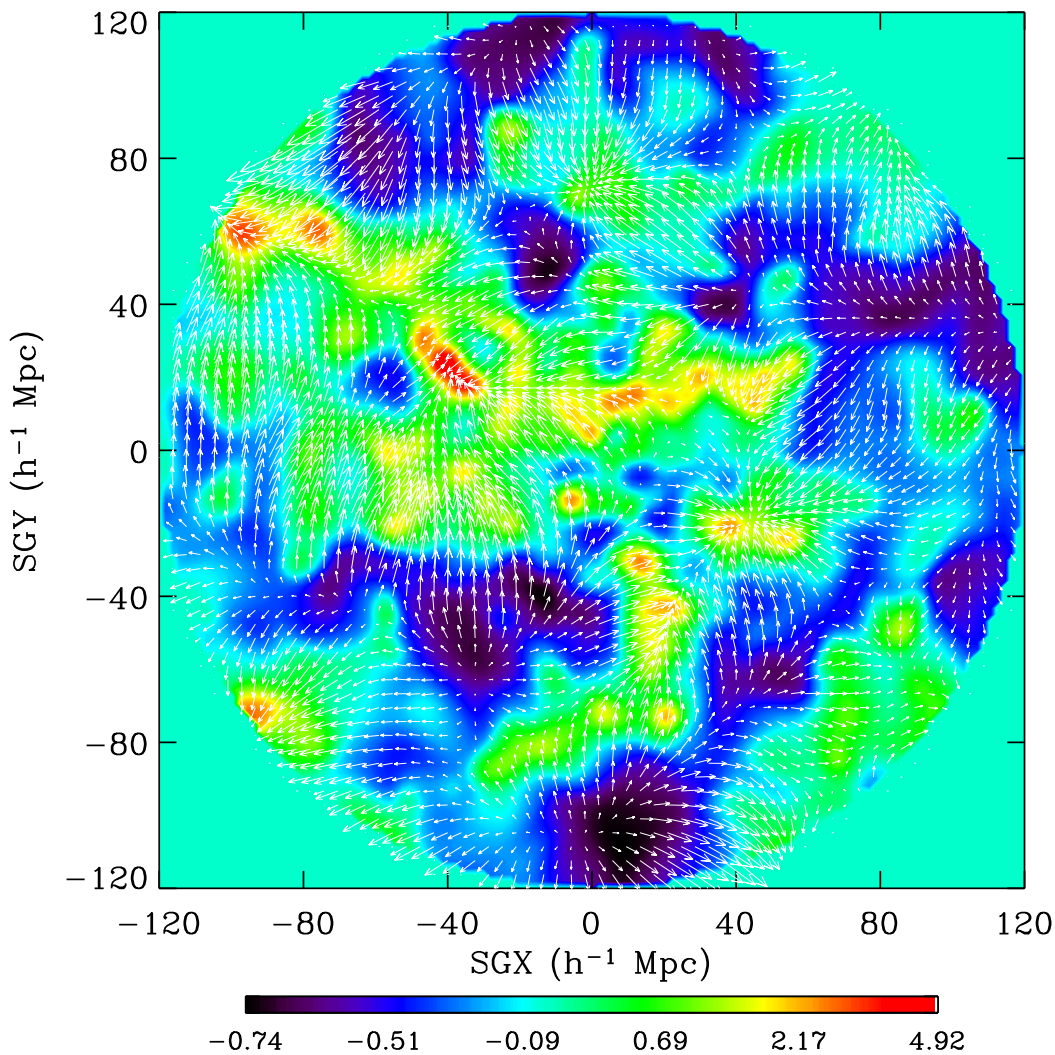

Figure 9.3 — DTFE density and velocity fields projected along the z−supergalactic plane in a thin slice. The color bar indicates the plotted density scale. Velocities have been normalized to the maximum plotted velocity.

reveals intricate details along the whole volume. Large scale bulk flows, distortion patterns such as shear, expansion and contraction modes of the velocity field are clear features uncovered by our DTFE technique.

Positive velocity divergence modes within voids resemble very well the dips in the density field. Velocity shear patterns are also clearly visible in the map. Significant quadrupolar patterns in the matter distribution are correlated with corresponding shear patterns.

The gravitational influence of the H-C supercluster over its surroundings is more than evident. A pronounced bulk flow toward the H-C region dominates the general LG region motion. At the top of the plot the Coma cluster exerts the main gravitational attraction in the surrounding region.

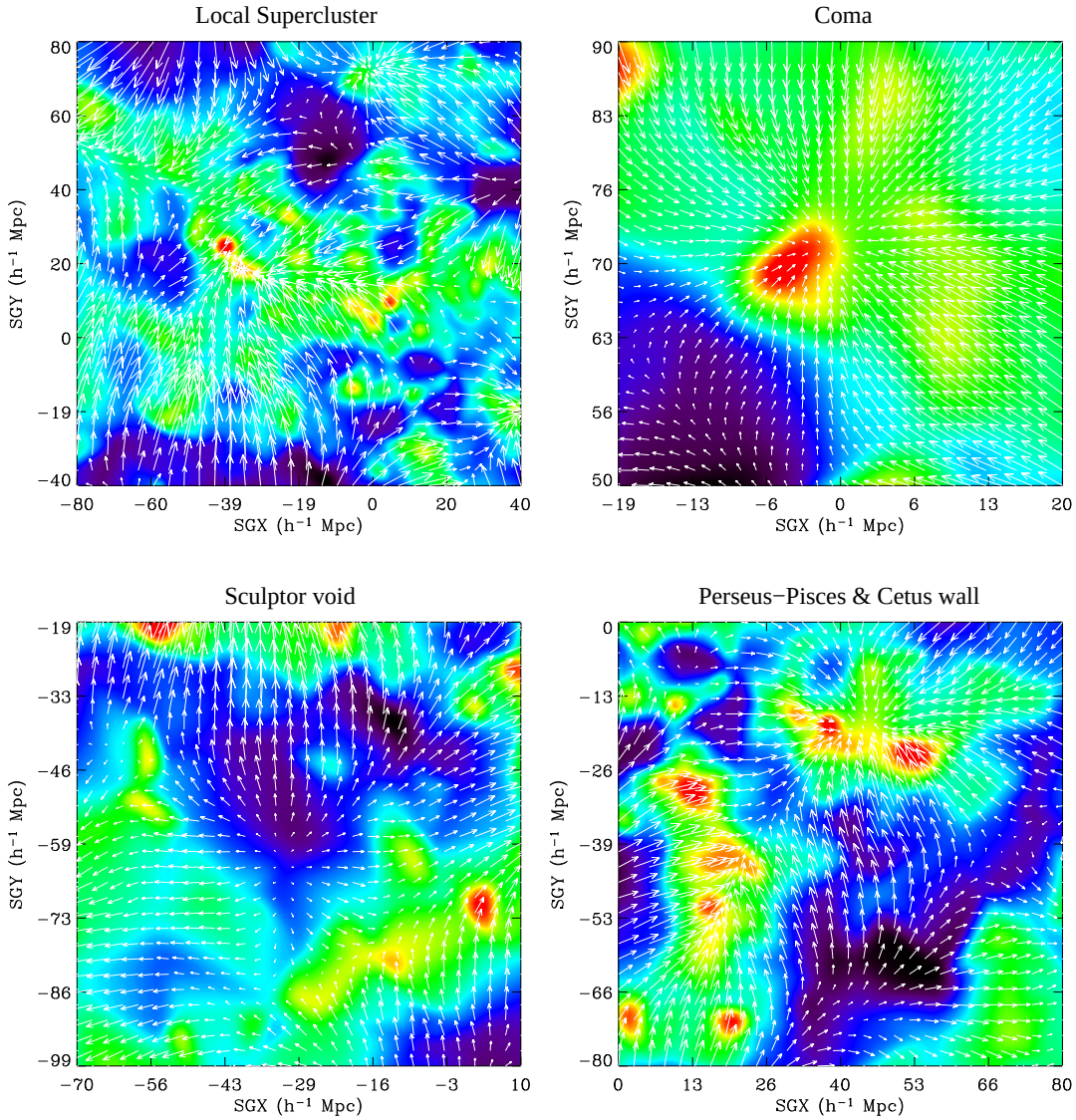

Figure 9.4 — Density and velocity zooms for four different regions along the supergalactic plane indicated by the labels at the top of each frame. The density field has been convolved with a Gaussian kernel of 1 h^{-1}Mpc for a better impression of such field. The normalization of the velocity field is the same for the four panels.

9.4.3 Small-scale details in the DTFE reconstructed fields

The ability of the DTFE method to resolve both small and large scale field characteristics can be appreciated from Figure 9.4. This four-panel plot zooms into four different regions of our supergalactic plane. To get more detail the density field has been smoothed with a Gaussian kernel of 1 h^{-1}Mpc.

The top-left panel shows the complex velocity field in and around the Local Supercluster. The Virgo cluster is located just above the LG. Noteworthy is the presence of the Great Attractor region and its influence on the velocity field. It can be noticed that at the location of the LG there is a very pronounced velocity shear pattern, exerted by the influence of the GA and PP supercluster (e.g. see

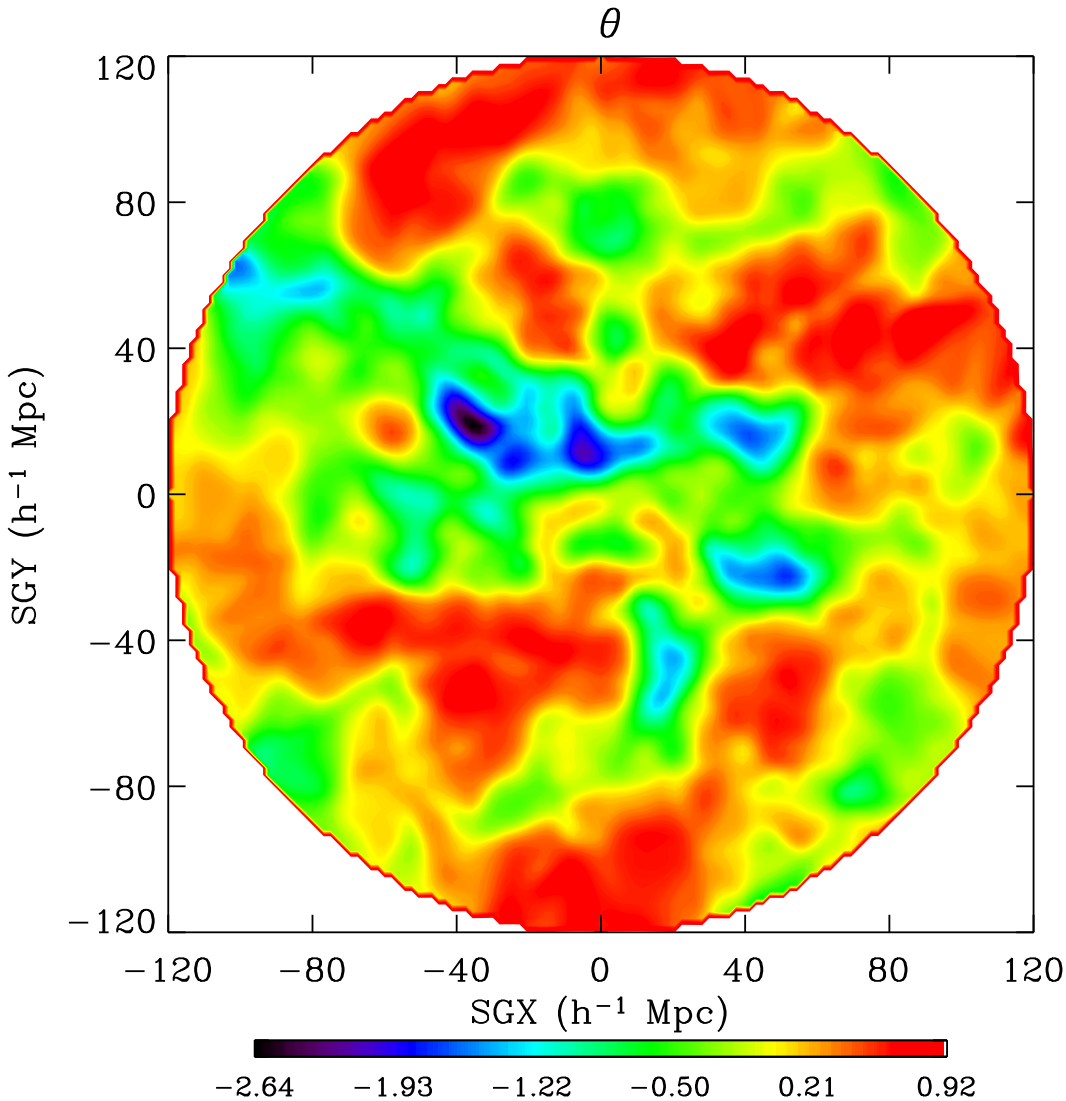

Figure 9.5 — DTFE velocity-divergence field projected along the z−supergalactic plane. The thin slice corresponds to the one presented in Fig. 9.3. The velocity-divergence is in units of the Hubble parameter. The color bar indicates the plotted velocity-divergence scale.

Chapter 5). Other shear patterns are easily recognized. An example is the region located between the Coma cluster and the Centaurus wall. The velocity field around the Centaurus wall clearly traces such filamentary structure. A prominent flow can also be observed near the P-I-T complex. The combined action of the nearby expanding void and the gravitational attraction of the heavy matter concentration itself generate a massive stream towards the latter. The top-right hand panel depicts how the Coma cluster, embedded within the Coma wall, distorts the velocity field in its surroundings. Infalling velocity patterns follow the density distribution. The shear pattern at the bottom-left corner is the response to the contrasting matter distribution around this region.

The bottom-right frame concerns the Perseus-Pisces supercluster and Cetus wall. Infalling velocity patterns following the cluster and filamentary structure show a clear dynamical connection between these two structures. Their gravitational influence can be recognized along the whole zoomed region. The velocity field around the underdense region located at ($[SGX, SGY] \approx [45, -60]$ h^{-1}Mpc) is completely distorted by these two massive structures. At the top-left corner (near the LG location) a shear

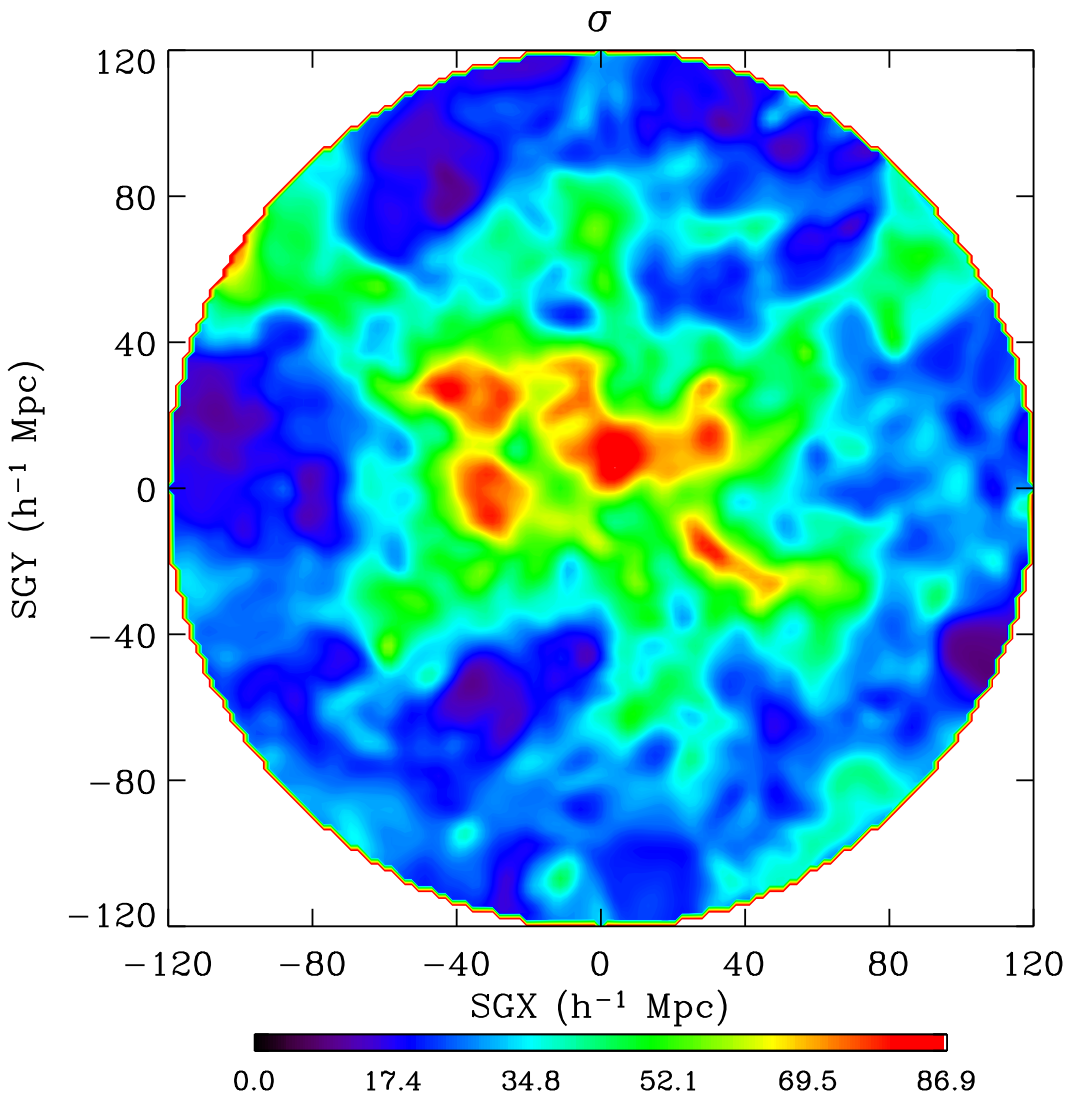

Figure 9.6 — DTFE velocity shear field projected along the z−supergalactic plane. The slice corresponds to the one presented in Fig. 9.3. We have plotted the velocity shear amplitude in units of the Hubble parameter. The color bar indicates the plotted scale.

pattern can also be recognized.

Finally, the bottom lefthand frame zooms in on the Sculptor void. The lowest measured DTFE density contrast value (smoothed at 1 h^{-1}Mpc) in this region is ≈ -0.78 at the deepest of the void[2]. At the smoothed scale of $\sqrt{5}\,h^{-1}$Mpc the DTFE density threshold is -0.74, in agreement with the reported value by Plionis & Basilakos (2002) of -0.69. The velocity field of this almost "empty" expanding region is distorted by the surrounding matter distribution. Small, yet detectable, distortions delineate the dynamical borders of this void with its surrounding matter distribution, the Sculptor wall.

[2]The theoretical expectation for a mature and shell-crossing void, with a characteristic inverse tophat density profile, is an underdensity of $\Delta \approx -1. + (1./1.7)^3$.

9.5 DTFE velocity-gradient related fields

Here we reconstruct and present these quantities for the same plane projection (z-supergalactic plane) as in Fig. 9.3.

In order to compute the full spatial peculiar velocity field it is necessary to calculate the nine elements of the velocity gradient matrix. At each Delaunay tetrahedron the velocity field gradient is constant. Therefore, the recovered velocity divergence, shear and vorticity are not continuous. However, they are volume-weighted and fully volume-covering. Having smoothed the velocity divergence, shear and vorticity fields with the same kernel as in the case of the reconstructed density field has provided them with the sense of continuity seen in Figure 9.5 & 9.6.

9.5.1 The DTFE PSCz velocity divergence

The velocity divergence computed with DTFE is the sum of the trace of the velocity-gradient matrix given by:

$$\nabla \cdot \mathbf{v} = \left(\frac{\partial \mathrm{v}_x}{\partial x} + \frac{\partial \mathrm{v}_y}{\partial y} + \frac{\partial \mathrm{v}_z}{\partial z} \right), \tag{9.2}$$

The velocity divergence and the density contrast are related via the continuity equation (Peebles 1980). In the linear regime this is a strict linear relation. In the quasi-linear and mildly nonlinear regime the one-to-one correspondance between the two fields remains intact, be it that it involves higher order terms (see Bernardeau et al. 2002, for an extensive review about the topic). The density and velocity-divergence maps will therefore look very similar. This is why the density map and the velocity-divergence map are almost each other negative (see Figure 9.3).

The expanding and contracting modes of the velocity field can be discerned in Figure 9.5 where we have plotted the normalized divergence θ of the velocity field, $\theta = (\nabla \cdot \mathbf{v})/H_0$. Here H_0 is the Hubble constant[3]. Positive divergence modes, indicated by red to yellow tones, mark the location of the expanding voids. Clearly recognizable are the Sculptor and Fornax voids and the underdense regions around the Coma cluster. Other expanding regions like the one above the Camelopardalis cluster located at ($[SGX, SGY] \approx [40, 45]\ h^{-1}$Mpc) and the one at the right of the Cetus wall at ($[SGX, SGY] \approx [50, -55]\ h^{-1}$Mpc) are also notorious.

By constrast, negative divergence modes indicate infalling motions. These modes delineate the peaks of the density field. The largest contracting regions, represented by the blue tones are clearly identified with the most massive structures located along this slice. The H-C is the most prominent infalling region. Other clusters such as Virgo, Camelopardalis, Coma, PP, Cetus wall, P-I-T, and partly Shapley can be recognized.

The green scale contours delineate density regions just above the mean density contrast. Notice how all large scale structures are connected through a filamentary velocity-divergence pattern.

9.5.2 The DTFE PSCz velocity shear

Velocity shear can be due to the intrinsic asphericity of evolving structures and/or due to the external tidal stresses exerted by the surrounding large scale matter distribution. Bond, Kofman, & Pogosyan (1996) (see also van de Weygaert 2002) pointed out that the filamentary web is a consequence of the distribution and spatial coherence of the shear field in the medium. Hence, shear is expected to be present at linear, quasi- and non-linear regions. The recovered shear from the processed DTFE velocities corresponds to the symmetric traceless part of the velocity-gradient matrix given by

$$\sigma_{ij} = \frac{1}{2} \left\{ \frac{\partial \mathrm{v}_i}{\partial x_j} + \frac{\partial \mathrm{v}_j}{\partial x_i} \right\} - \frac{1}{3} (\nabla \cdot \mathbf{v}) \delta_{ij} \,. \tag{9.3}$$

[3]We have adopted a value of $h = 0.7$ ($H_0 \equiv 100\ h$ km s^{-1} Mpc^{-1}) in agreement with the last reported measurements (e.g. Lahav & Liddle 2004).

In Figure 9.6 we have plotted the shear amplitude, $\sigma = (\Sigma\sigma_{ij}\sigma_{ij})^{1/2}$, along the supergalactic plane. Clearly visible is the presence of a strong shear measured around the LG region, which is mainly exerted by the large scale quadrupolar matter distribution (H-C and PP) surrounding it (see Chapter 5 and references therein). The major matter concentrations (H-C, PP, P-I-T, Camelopardalis) exert a strong shear distortion onto their surrounding velocity fields. In general there is a non-negligible shear contribution tracing the overdense regions. At the large empty regions the shear is very small as expected (Hoffman 1986; Bertschinger & Jain 1994).

9.6 Conclusions

The DTFE reconstruction of the PSCz catalog has been shown to represent a marked improvement over the previous field interpolations of B99 and Schmoldt et al. (1999). One of the main advantages of using DTFE is its large dynamic range for tracing small and large scale characteristics. DTFE traces underdense regions better and deeper. In addition, it clearly resolves high-density regions on small scales.

The estimated velocity field of B99 and Schmoldt et al. (1999) did not show small scale details because of their employed interpolation techniques. The diverse features of the linear velocity field have been exposed in detail by the DTFE technique. The self-adaptive nature of DTFE tracing the galaxy distribution without loosing resolution and preserving the characteristics of both large and small scale contributions are also reflected in the reconstructed velocity field. The reconstructed DTFE velocity field has unveiled the expected infall, expansion and shear motions in our nearby universe.

One of the main virtues of the method is its ability to compute any quantity related to the velocity-gradient matrix in a very straightforward manner. The divergence and shear maps showed a great consistency with the reconstructed density field. Large scale structures can be recognized by their gravitational distortions reflected in the divergence and velocity shear components.

In order to explore in more detail the velocity field of our nearby universe, it would be desirable to compute the quasi-linear contributions to the velocity field. Techniques like the FAM$-z$ of Branchini et al. (2002) combined with the DTFE algorithm applied to the forthcoming surveys such as 6dF will help us to understand more the dynamics of our nearby universe.

Deze zon, genaamd 4 Beweging, is onze Zon, waar we nu wonen.
En hier is zijn teken, zoals hij viel in het Vuur van de Zon,
in de goddelijke oven, daar in Teotihuacan.
Deze was ook de Zon van onze Prins, in Tula, van Quetzalcoatl.
De vijfde Zon, 4 Beweging is zijn teken,
wordt de Zon van beweging genoemd, omdat hij beweegt, hij volgt zijn pad.

Azteeks gedicht over de creatie van de Vijfde Zon (fragment, Codex Chimalpopoca).

Nederlandse Samenvatting

Waarschijnlijk hebben er al voor het begin van de beschaafde wereld mensen 's nachts naar de sterren aan de hemel gestaard en zich verwonderd over de wereld waarin zij leefden. De mensheid heeft zich al eeuwen bezig gehouden met vragen als "Hoe is het heelal ontstaan?" en "Hoe is alles daarna gevormd?". Door de eeuwen heen zijn er allerlei verklaringen gegeven, want bijna elke beschaving en samenleving heeft zijn eigen kosmogonie en verklaring voor het heelal gegeven. Deze zoektocht is krachtig doorgezet tot in de moderne tijd. Het is zelfs zo dat tegenwoordig de mensheid voor het eerst dichtbij een alomvattend wetenschappelijk verantwoord antwoord op deze eeuwenoude vragen lijkt te zijn, op basis van een grote hoeveelheid wetenschappelijke kennis waaronder een voortdurend toenemende en ontzagwekkende hoeveelheid observationeel bewijs.

In het huidige kosmologische model wordt verondersteld dat het heelal waarin wij leven 13,7 miljard jaar geleden is ontstaan, geboren uit een enorme expanderende vuurbal die we de *Hot Big Bang* noemen. Op dat moment zijn ruimte en tijd, net als alle materie en energie die het heelal omvat, ontstaan. Het vroege heelal was extreem heet en dicht, geleidelijk afkoelend en verdunnend terwijl het uitdijde. De theoretische beschrijving van deze gebeurtenis is gebaseerd op twee cruciale aannames. De eerste is dat de dynamische ontwikkeling volledig bepaald wordt door de zwaartekracht, die beschreven wordt door Einstein's algemene relativiteitstheorie. Volgens deze theorie is de zwaartekracht de manifestatie van de kromming van het systeem. Het Big Bang heelal is gebaseerd op de aanname dat de geometrie van het heelal sterk beperkt wordt door het kosmologische principe. Dit stelt dat het heelal homogeen en isotroop is. Met andere woorden, het heelal heeft overal gelijke eigenschappen, zowel wat betreft de verdeling van de materie als wat betreft de fysische wetten die er gelden, terwijl het heelal er bovendien in elke richting hetzelfde uit moet zien. Er zijn maar drie geometriën die aan deze eisen voldoen. In combinatie met de vergelijkingen van de algemene relativiteitstheorie vinden we dat er drie corresponderende oplossingen zijn, de Friedmann-Robertson-Walker-Lemaitre [FRWL] modellen, die het theoretische kader vormen voor de ontwikkeling van het uitdijende heelal. De ontdekking door Hubble in 1929 van het systematisch van ons afbewegen van melkwegstelsels vormde het eerste bewijs voor de juistheid van deze kijk op de dynamische kosmos.

De directe gevolgtrekking van de ontdekking van Hubble was en is dramatisch: de kosmos moet een begin hebben! Op basis van de FRWL kosmologische modellen en onze kennis van de wetten van de natuurkunde hebben kosmologen de volledige thermische geschiedenis van het heelal kunnen reconstrueren tot op een fractie van een seconde na zijn geboorte. Dit is wat we de *Hot Big Bang* theorie noemen. De resulterende voorspellingen voor een verscheidenheid van belangrijke gebeurtenissen en fenomenen tijdens de ontwikkeling van het heelal hebben ons een waarlijk indrukwekkende hoeveelheid bewijzen opgeleverd voor de geldigheid van de *Hot Big Bang* theorie. Wellicht de meest indrukwekkende voorspelling is de kosmische achtergrondstraling, het overblijfsel van de straling die ons uit elke richting van de hemel bereikt en die afkomstig is van 379,000 jaar na de Big Bang. De ontdekking hiervan in 1965 door Penzias & Wilson wordt terecht gezien als een van de belangrijkste wetenschappelijke doorbraken van de 20^{e} eeuw. Met een huidige temperatuur van slechts $2.725^{\circ}K$ is deze vrijwel perfect isotroop en vertoont temperatuursvariaties over de hemel van kleiner dan 1 op 10^5, een meer dan indrukwekkende bevestiging van het kosmologische principe. Het vroege heelal was bijna perfect homogeen.

Terwijl de bewijzen ten gunste van het Hot Big Bang heelal zich opeen hebben gestapeld, werden

Figuur 1 — Voorbeelden van sterrenstelsels in ons heelal, een spiraalstelsel (linkerpanel; Met dank aan: G.F. Benedict, A. Howell, I. Jorgensen, D. Chapell, J. Kenney en B.J. Smith en NASA) en een elliptisch sterrenstelsel (rechterpanel, met dank aan: NOAO,AURA,NSF). In het middelste panel wordt een cluster van sterrenstelsels getoond die bestaat uit enkele tientallen sterrenstelsels (Met dank aan: NOAO,AURA,NSF).

wij geconfronteerd met het raadsel dat op relatief kleine schalen het heelal helemaal niet homogeen is, lokaal niet eens isotroop. De kosmos wemelt daarentegen van rijke en sterk wisselende structuren. Iedereen kent planeten en sterren. Zij zijn met honderden miljarden, samen met gas en stof gegroepeerd in wat beschouwd kunnen worden als de meest fundamentele bouwstenen van het waarneembare heelal, de *sterrenstelsels*. Sterrenstelsels maken op hun beurt deel uit van nog grotere en massievere structuren, *groepen* en *clusters* van sterrenstelsels (zie Figuur 1). Deze zijn ook onderdeel van een hiërarchie van steeds grotere systemen, op schalen van tientallen en zelfs honderden Megaparsecs vormen ze *superclusters*, die zelf onderdeel zijn van een patroon dat eruit ziet als een kosmisch web dat zich uitstrekt door het volledige waarneembare heelal.

Een van de belangrijkste vraagstukken uit de hedendaagse kosmologie is daarom het verklaren van de onregelmatige verdeling van de materie die zich op schalen kleiner dan honderd Megaparsec bevindt, en wel binnen de context van de Big Bang kosmologie. In dit proefschrift proberen we deze vraag te beantwoorden, en kijken we in het bijzonder naar zaken die verband houden met de samenhangende stromen van materie in het heelal, tot op een afstand van ongeveer 100 h^{-1}Mpc. Hierbij volgen we de standaardleer van structuurvorming in het heelal, de theorie van gravitationele instabiliteit. Deze vormt een uitbreiding van de standaard Hot Big Bang theorie met een extra element. Dit stelt dat hoewel het vroege heelal vrijwel volledig glad was, dit toch niet helemaal het geval was. In plaats daarvan vertoonden de verdeling van materie en de kosmische uitdijing kleine fluctuaties. Deze werden versterkt door de zwaartekracht en groeiden uit tot de rijkdom aan structuur die we door onze telescopen zien. Ook hiervoor bestaat een ruime hoeveelheid bewijs, waarbij het weer waarnemingen van de kosmische achtergrondstraling en de detectie van kleine temperatuursschommelingen door de COBE en WMAP satellieten waren die ons voorzien hebben van voldoende vertrouwen om het onderzoek uit te voeren dat in dit werk wordt gepresenteerd.

De Hot Big Bang

Tot aan het begin van de twintigste eeuw werd aangenomen dat het heelal statisch was. In 1916 stelde Albert Einstein de algemene relativiteitstheorie op, samen met de vergelijkingen die de dynamica van het heelal beschrijven. Einstein ontdekte dat volgens deze vergelijkingen het heelal uit moet dijen of moet krimpen, volledig in strijd met het bestaande beeld van een statisch heelal[1].

[1] Hij geloofde deze resultaten niet en stelde daarom voor om een extra term aan zijn bewegingsvergelijkingen toe te voegen, zodat het heelal toch statisch is. Deze term wordt de *kosmologische constante* genoemd en wordt aangegeven met de Griekse letter Λ.

Friedman slaagde erin om de bewegingsvergelijkingen voor algemene homogene en isotrope modellen van het heelal op te lossen binnen de context van de algemene relativeitstheorie. Voortbouwend op dit uiterst belangrijk maar destijds onvoldoende erkende werk, was het de Belgische priester Georges Lemaitre die niet alleen onafhankelijk dezelfde vergelijkingen in 1927 oploste, maar zich bovendien ook de natuurkundige gevolgen realiseerde. Terugrekenend in de tijd zag hij in dat een uitdijend heelal een begin gehad moet hebben in een extreem hete en dichte toestand met de naam ”Oeratoom”. Spoedig daarna, in 1929, ontdekte Edwin Hubble dat sterrenstelsels van ons af bewegen met een snelheid die toeneemt naarmate ze op grotere afstand van ons staan. Dit universele verband staat bekend als *de wet van Hubble*. Zonder twijfel vormt deze ontdekking een van de grootste wetenschappelijke revoluties in de menselijke geschiedenis, die het eerste duidelijke en overtuigende bewijs leverde voor het feit dat ons heelal niet statisch is, maar “uitdijt”! In de afgelopen paar jaar heeft de nauwkeurigheid van moderne satellieten geleid tot een convergentie van de geschatte uitdijingssnelheid van het heelal naar een waarde in het smalle bereik rond $H_0 \approx 71$ km s^{-1} Mpc^{-1} (de *Hubble constante*). Voor elke Megaparsec[2] verder weg lijkt de snelheid van een ver weg staand object in de richting van ons toe te nemen met 71 km s^{-1}.

Met het nieuwe bewijs voor een uitdijend heelal werd de astronomische gemeenschap geconfronteerd met een volledig nieuw stel vragen. Wat was de aard van deze uitdijing? Zal de uitdijing eeuwig voortduren? Zal het heelal geleidelijk uitdijen tot deze een dynamisch evenwicht bereikt en vanaf dat moment voor eeuwig in een statische toestand blijven? Zal het heelal een kritiek punt bereiken waarna het weer begint samen te trekken als een omgekeerde Big Bang, de *Big Crunch*? Deze vragen bleven lange tijd onbeantwoord, aangezien er geen waarnemingen waren die ze overtuigend konden beantwoorden.

Eén aspect van het uitdijende heelal blijkt voor ons van essentieel belang te zijn om de fysische omstandigheden en processen in zowel het vroege als het toekomstige heelal te onderzoeken. De FRWL modellen corresponderen alle met adiabatische uitdijing, hetgeen ons in staat stelt om de temperatuur en dichtheid van de inhoud van het heelal op ieder moment te voorspellen. Met andere woorden, terwijl het heelal uitdijt, koelen straling en materie af en, omgekeerd, als het heelal zou krimpen, dan zouden dichtheid en temperatuur toenemen. Dit heeft ons in staat gesteld om tijdens de afgelopen decennia een indrukwekkende hoeveelheid bewijzen te verzamelen voor de Hot Big Bang theorie door verschillende van de natuurkundige voorspellingen te testen.

Hoewel er een verscheidenheid aan tests is, vormen vier tot vijf ervan de meest solide pilaren van de Big Bang theorie. Wellicht de meest eenvoudige is het feit dat de Big Bang een verklaring geeft voor een verbazingwekkend eenvoudige waarneming door Olbers in de vroege 19^{e} eeuw: de nachtelijke hemel is donker. Alleen in een heelal met een eindige leeftijd en een eindige lichtsnelheid kan dit worden begrepen. Het is duidelijk dat Hubble’s (isotrope) uitdijende heelal niet alleen een belangrijke bevestiging vormt van de werkelijkheid van de FRW beschrijving, maar dat deze ook beschouwd kan worden als het begin van de kosmologie als “natuurwetenschap”. Wellicht het meest interessant zijn de twee waarnemingsresultaten die tot de vroegste tijden van onze kosmos reiken. De ongelooflijke precisie waarmee de Big Bang theorie de uitkomst en resultaten van de allervroegste fase van de primordiale nucleosynthese van de lichte chemische elementen weet te voorspellen, brengt ons terug naar de eerste drie minuten van het heelal. De voorspelling van een isotrope deken van kosmische thermische straling, met een ongelooflijk nauwkeurig spectrum van een zwart lichaam met een temperatuur van $T \approx 2.725^{\circ}K$, heeft ons in staat gesteld om de ontdekking hiervan in 1965 om te zetten in de uiteindelijke bevestiging van de werkelijkheid van de Big Bang. De bijnaam is omgezet in een eervolle titel!

Ongeveer drie minuten na de Big Bang, toen de temperatuur van het heelal afgekoeld was naar een paar miljard graden, was het heelal gevormd tot een enorme kernreactor. De lichte chemische elementen Deuterium, ^{3}Helium en ^{4}Helium, evenals een kleine hoeveelheid Lithium, waren net gevormd voordat de uitdijing de kernreactor uitzette. De voorspelling van de Big Bang theorie voor de gevormde hoeveelheid van deze elementen komt heel goed overeen met de waarnemingen, een zeer

[2]Mpc = Megaparsec ≈ 3 260 000 lichtjaar ≈ 30 800 000 000 000 000 000 *km*

overtuigende overwinning!

In de daaropvolgende honderdduizenden jaren hebben de fotonen, in een nauwe wisselwerking met het kleine overblijfsel aan elektronen en protonen[3], een evenwicht bereikt en hun energie verdeeld over een bijna perfect zwartelichaamsspectrum. Ongeveer 279,000 jaren hierna was de temperatuur van het heelal afgekoeld tot slechts $3000°K$, waarna protonen en elektronen samen waterstofatomen vormen tijdens deze zogenaamde *Recombinatie"*[4]. De resulterende *"ontkoppeling"* van straling en materie vond vrijwel gelijktijdig plaats. Niet langer door vrij rondzwevende elektronen verstrooid, konden fotonen hun lange reis door de diepten van een vrijwel doorzichtig heelal beginnen. Deze fotonen van de *kosmische achtergrondstraling*, die hun vrijwel perfecte zwartelichaamsspectrum hebben behouden, lijken hun oorsprong te vinden op het *oppervlak van laatste verstrooiing*. Dit oppervlak markeert de positie van de atomen die de waargenomen fotonen van de komische achtergrondstraling als laatste hebben verstrooid[5]. Daarna is de geleidelijke afkoeling van het heelal samengegaan met een corresponderende afkoeling van de temperatuur van de fotonen.

Een voortdurend toenemende vloed van nieuwe kosmologische waarnemingen, afkomstig van grotere en grotere diepten van het heelal, heeft geleid tot een convergerende concensus met betrekking tot het heelal waarin wij leven. Met een indrukwekkende nauwkeurigheid is een nogal opvallende verzameling waarden voor de cruciale kosmologische parameters te voorschijn gekomen, nu algemeen bekend onder de naam *Concordance Model*. Satellietexperimenten, zoals COBE en MAP, in samenhang met ballonexperiment Boomerang, hebben het embryonisch heelal ten tijde van de recombinatie in groot detail in kaart weten te brengen. Niet alleen hebben ze de geldigheid van de Hot Big Bang aangetoond, ze hebben ons ook overtuigd dat het heelal *vlak* is, de leeftijd nauwkeurig vastgesteld op 13,7 miljard jaar en onafhankelijk de baryoninhoud bevestigd waar ook de primordiale nucleosynthese op wees. Mede dankzij de grote roodverschuivingsstudies die vanaf de grond plaatsvinden, waarvan we hier de honderduizenden sterrenstelselposities noemen die door 2dFGRS en SDSS gemeten zijn, hebben we de (donkere) materie inhoud van het heelal kunnen bepalen. De grootste verrassing werd geleverd door de programma's om Supernova Ia explosies tot op grote diepten in het heelal waar te nemen en te meten. Deze hebben geleid tot de bijna onontkoombare conclusie dat een ongrijpbare maar alomtegenwoordige "donkere energie" moet bestaan.

Dit brengt ons tot de toestand dat hoewel het Concordance Model een goede beschrijving van de werkelijkheid lijkt te vormen er nog steeds een groot aantal onopgeloste raadsels overblijft. Het standaard FRW model kan bij lange na niet verklaren waarom het heelal vrijwel "vlak" is, een probleem dat gewoonlijk aangeduid wordt met de naam "Flatness Problem". Evenzo blijft het de vraag waarom de kosmische achtergrondstraling in elke richting dezelfde temeratuur heeft, hoewel de kosmische horizon tijdens recombinatie niet groter is dan $\approx 1°$. Dit probleem staat bekend als het "Horizon Problem". In samenhang met andere samenlopen van omstandigheden hebben deze vragen geleid tot een uitbreiding van de *Hot Big Bang* theorie met een inflatie fase-overgang waarin het zeer vroege heelal exponentieel is uitgedijt met een factor van 60 ordes van grootte. Evenzo, zoals we zullen zien in de volgende paragraaf, zou inflatie kunnen helpen om de oorsprong van structuur te verklaren.

Kosmische Inventaris: Materie en Donkere Materie

Als we naar het heelal kijken is het licht dat door sterren wordt uitgestraald het eerste dat we zien. Hoewel sterren wellicht de meest opvallende en zichtbare bewoners van ons heelal zijn, blijken ze slechts een heel klein gedeelte van de totale hoeveel materie in de kosmos te representeren. Volgens de laatste schattingen zijn bevatten sterren niet meer dan $0,25\%$ van de totale hoeveelheid energie, $0,9\%$ van de totale hoeveelheid materie en zelfs maar 5% van het totale aantal baryonen in het heelal. Planeten,

[3]Het is goed om te beseffen dat ons heelal een heel uitzonderlijk fysisch systeem is in de zin dat er twee miljard fotonen zijn voor iedere baryon!

[4]Deze gebeurtenis heeft deze naam om historische redenen gekregen. Het is duidelijk geen toepasselijke naam, wat het was de eerste keer dat elektronen en protonen samen waterstofatomen vormden.

[5]Sommige van deze fotonen zijn verantwoordelijk voor $\sim 1\%$ van de ruis van onze TV-toestellen.

manen, asteroïden en stof die om deze sterren draaien, corresponderen met een nog bescheidenere fractie. In het verleden is er wel gespeculeerd dat een grote hoeveelheid extreem zwakke sterren, bruine dwergen of objecten die net niet tot sterren zijn gevormd, gezamenlijk een veel grotere hoeveelheid massa bevatten, maar er is geen overtuigend bewijs voor deze stelling gevonden. Ook is er geen bewijs gevonden voor een grote hoeveelheid materie in een kerkhof van overleden sterren, zwarte gaten of uitgedoofde witte dwergen. Naast de honderden miljarden sterren die zich in sterrenstelsels bevinden, bevatten deze echter ook grote hoeveelheden gas. Radiotelescopen hebben het diffuse neutrale waterstof en de dichtere en massievere moleculaire gaswolken in kaart gebracht. Infrarood- en submillimetertelescopen hebben in de kern van deze wolken gekeken, de plek waar sterren geboren worden. Alles bij elkaar vinden we op deze manier niet meer dan nog eens 30% van de massa in sterren. Een veel grotere hoeveelheid baryonen is ontdekt binnen rijke clusters van sterrenstelsels. Deze bevatten grote hoeveelheden extreem heet geïoniseerd intra-cluster gas. Bij temperaturen van ongeveer honderd miljoen graden K zendt dit gas röntgenstraling uit. Dit gas bevat ten minste drie keer zoveel materie als de sterrenstelsels zelf die in dezelfde cluster bewegen. In totaal zou dit gas maximaal $0,7\%$ van de hoeveelheid materie in het heelal kunnen bevatten.

Gas en sterren zijn gemaakt van hetzelfde materiaal als wijzelf, baryonische materie die voornamelijk uit protonen en neutronen bestaat. Eén van de grote successen van de Hot Big Bang theorie is de voorspelling geweest dat de totale hoeveelheid baryonen in het heelal een magere $4,4\%$ bedraagt van de totale hoeveelheid massa die nodig is voor een vlakke geometrie van het heelal. Als we alle boven beschreven bijdragen bij elkaar optellen dan vinden we dat de meeste baryonische materie nog niet ontdekt is. Een bijzonder opwindende gedachte daarbij is dat wellicht 80% van de baryonen door de uitgestrekte structuren van het kosmische web zweeft, en wel in de vorm van een warm of een koud plasma.

Een ontnuchterende gedachte is dat de materie die uit baryonen bestaat slechts een klein onderdeel vormt van de totale kosmische inventaris. Door de bewegingen van sterren en gas in melkwegstelsels te bestuderen, evenals de bewegingen van melkwegstelsels in de kosmos, hebben we ontdekt dat deze bewegingen veroorzaakt moeten worden door de gravitationele actie van veel grotere hoeveelheden materie. Waarnemingen laten zien dat terwijl baryonen niet meer dan $4,4\%$ van de kritieke massa van het heelal kunnen bevatten, de totale hoeveelheid materie 27% van deze kritieke massie moet bedragen.

De eerste twee aanwijzingen voor het bestaan van een gravitationeel dominante donkere materiecomponent werden beschreven door Oort en Zwicky in de jaren 30 van de 19e eeuw. Oort ontdekte dat de sterren in onze Melkweg sneller loodrecht ten opzicht van het vlak van de Melkweg bewegen dan alle sterren in het Galactische vlak samen kunnen verklaren. De baanbewegingen van sterren en gaswolken in de buitendelen van sterrenstelsels duiden op zelfs nog grotere hoeveelheden donkere materie, in een donkere materie halo om sterrenstelsels heen. Het werk van astronomen uit Groningen (Van Albada & Sancisi) heeft hierbij sleutelrol gespeeld. Op grotere massaschalen werden zelfs nog sterkere discrepanties tussen de gravitationele en zichtbare materie aangetroffen. Fritz Zwicky ontdekte in 1930 dat de snelheden van de sterrenstelsels in de Coma clusters zo hoog waren dat de cluster niet bijeen zou kunnen worden gehouden door de onderlinge zwaartekracht van de sterrenstelsels. Als er niet meer dan 100 keer zoveel materie aanwezig was dan zichtbaar in sterren dan zou de cluster uiteen vliegen. In de jaren hierna is een vergelijkbare hoeveelheid materie aangetroffen in elk waargenomen cluster van sterrenstelsels. De aanwezigheid van deze materie kon niet alleen afgeleid worden uit de bewegingen van de sterrenstelsels binnen de clusterpotentiaal, maar ook uit de thermische toestand van het hete intra-cluster gas dat in het röntgen straling uitzendt, als ook uit het effect dat de cluster heeft op de lichtpaden van lichtdeeltjes, afkomstig van achtergrondstelsels, die de cluster passeren (afbuiging door gravitatielenzen). Deze trend zet zich voort op de nog grotere Megaparsec scalen: de kosmische stromen van sterrenstelsels evenals de recent gemeten zwakke afbuigingen van het licht dat door de inhomogene Megaparsec materieverdeling beweegt, duiden op een vergelijkbare of wellicht iets grotere hoeveelheid donkere materie.

Aangezien de totale hoeveelheid kosmische materie ongeveer zeven keer groter is dan de maximale hoeveelheid baryonische materie, moet de gedetecteerde donkere materie *"niet-baryonische materie"* zijn. Tot op heden hebben we geen directe en duidelijke aanwijzingen voor de aard van deze materie

gevonden. In de loop van de tijd is een groot aantal soorten potentiële kandidaten de revue gepasseerd. Gedurende een korte tijd vormden de *massieve neutrino's* een serieuze kandidaat, om snel daarna vervangen te worden door een klasse van koude en niet botsende *exotische* deeltjes met een lange levensduur, de zogenaamde *Koude Donkere Materie*. De identiteit van deze donkere materiedeeltjes is nog steeds onbekend, hoewel er allerlei speculaties gaande zijn. De brede, speculatieve klasse van zwak wisselwerkende en massieve deeltjes, WIMPs genaamd, of een heel licht deeltje dat *axion* wordt genoemd behoren tot op heden beiden tot de favorieten.

Op dit moment lijkt *Materie* 27% van de hoeveelheid energie in het heelal voor zijn rekening te nemen, waarvan het merendeel in de vorm van *Donkere Materie*. Sinds enkele jaren weten we dat *Donkere Energie* een nog groter gedeelte, 73%, in beslag neemt, hoewel de aard hiervan vrijwel volsterkt onbekend is. Wat we echter wel weten is dat deze gelijkmatig over het heelal verdeeld is en niet samenklontert, waardoor de donkere energie een onbelangrijke rol speelt bij de vorming van structuur. Het is dus zo dat terwijl zowel de donkere energie als de donkere materie de uitdijing en daarmee het lot van het heelal bepalen, alleen de donkere materie kan samenklonteren en structuren vormen. Daarom is de *Donkere Materie* de bepalende factor voor de uitkomst van de structuurvormingsprocessen in het heelal, die de kern vormen van het werk dat beschreven wordt in dit proefschrift.

De vorming van structuur

De vraag is nu hoe alle planeten, sterren, sterrenstelsels en clusters van sterrenstelsels hebben kunnen ontstaan in een vrijwel perfect homogeen heelal. Het meest plausibele antwoord dat we hebben is via structuurvorming middels *gravitationele instabiliteit*.

Kleine dichtheids- en snelheidsverstoringen werden steeds groter onder invloed van hun onderlinge gravitationele aantrekkingskracht. Onder invloed van de netto resulterende gravitatiekracht werd materie aangetrokken door gebieden met een hoger dan gemiddelde dichtheid, waardoor zich op die plaatsen in de loop van de tijd steeds meer materie opeen heeft gehoopt. Deze hierdoor hoger geworden dichtheid betekent een sterkere zwaartekracht, waardoor het effect sterker wordt, hetgeen uiteindelijk leidt tot een vicieuze cirkel: gravatiationele instabiliteit. Andersom zullen gebieden met een lager dan gemiddelde dichtheid een kleinere gravitationele aantrekkingskracht op hun omgeving uitoefenen. Daardoor zal materie uit deze gebieden wegstromen naar gebieden met een hogere dichtheid, hetgeen een steeds leger wordend gebied met een steeds lagere dichtheid achterlaat.

Tijdens de eerste fase van dit proces, wanneer de dichtheidsverstoringen nog relatief klein zijn, is de resulterende materieverdeling voornamelijk een versterkte versie van de oorspronkelijke verdeling. Deze fase noemen we het *lineaire regime*. Op het moment dat de dichtheidsverstoringen substantieel hiervan af beginnen te wijken, ontkoppelt de expansie van materieconcentraties van de globale kosmische expansie en beginnen deze samen te trekken. De daaropvolgende ineenstorting verloopt volgens een reeks van karakteristieke anisotrope patronen. In het begin nemen ze een vlakke wandachtige structuur aan, gevolgd door een samentrekking tot een uitgerekte filamentaire vorm, voordat uiteindelijk de volledige ineenstoring en virialisatie tot een klomp van materie plaats heeft. De fysische eigenschappen van de primordiale dichtheidsfluctuaties zijn verantwoordelijk voor een tweede belangrijke aspect van gravitationele structuurvorming, namelijk de *hiërarchische* aard ervan. Omdat de fluctutaties op kleine schalen sterker zijn dan die op grote schalen, zullen de vroegst gevormde objecten klein zijn. Grotere objecten vormen doordat kleine, eerder gevormde objecten, samen klonteren. Dit proces van *hiërarchische structuurvorming* lijkt inderdaad overeen te komen met hetgeen we waarnemen: *sterrenstelsels* zijn veel ouder dan de massievere en recentelijk ineengestorte *clusters* van sterrenstelsels. Op een nog grotere schaal hebben *Superclusters* nog niet eens de ineenstortingsfase bereikt of ze zijn net begonnen met samentrekken.

De manier waarop deze hiërarchisch ingebedde structuren zichzelf hebben geordend in het heelal bevat een rijkdom aan informatie over het structuurvormingsproces. Ze lijken gegroepeerd te zijn in vlakke of filamentaire, gedeeltelijk samengetrokken superclusters. Deze zijn onderling verbonden middels een uitgestrekt webachtig systeem, gescheiden door enorm grote en lege gebieden. Dit kos-

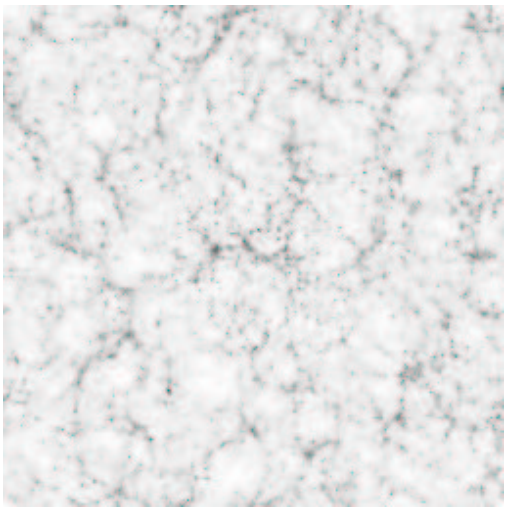

Figuur 2 — Voorstelling van een gedeelte van het heelal dat gecreëerd is door een computersimulatie

mische web strekt zich uit over het gehele waarneembare heelal.

Om de theorie van gravitationele instabiliteit te testen, hebben we daarvoor relevante structuren en fenomenen nodig. Deze zouden bij voorkeur een directe link met de primordiale omstandigheden in het heelal moeten hebben, zodat we de resulterende informatie relatief eenvoudig kunnen interpreteren. Er is een verscheidenheid aan zulke *kosmische fossielen*. Een belangrijk voorbeeld zijn de temperatuurschommelingen in de kosmische microgolfachtergrondstraling, een directe reflectie van de kleine embryonische kosmische verstoringen van waaruit structuur is gegroeid. Een ander belangrijk voorbeeld is gerelateerd aan de kaart van de verdeling van materie op Megaparsec schalen, het hedendaagse produkt van het structuurvormingsproces. Op basis van de veronderstelling dat de sterrenstelselverdeling een goede weerspiegeling is van de onderliggende materieverdeling, vormen kaarten van de ruimtelijke sterrenstelsverdeling wellicht het meest geanalyseerde *kosmische fossiel*. De hiermee samenhangende kosmische stromen representeren een ander belangrijk fossiel. De studie van de eigensnelheden van sterrenstelsels vormt daarom een cruciale aanvulling op bovengenoemde analyses.

Computersimulaties van het heelal

Theoretische kosmologische modellen doen voorspellingen over het structuurvormingsproces in het heelal. De kosmische structuren die door astronomen worden waargenomen, zijn de eindprodukten van een lang en gecompliceerd evolutionair proces. Om de verschillende structuurvormingssceniaro's te testen, nemen kosmologen hun toevlucht tot computersimulaties die de evolutie van het heelal modelleren.

Het gebruik van computersimulaties heeft zich ontwikkeld tot een belangrijk hulpmiddel voor studies van de grote schaal structuur. Computersimulaties volgen de evolutie en vorming van kosmische structuren overeenkomstig de theorie van gravitationele instabiliteit. *N-deeltjes* simulatiepogramma's vormen het belangrijkste gereedschap om de verschillende aspecten van deze evolutie te volgens. In dit berekende heelal worden deeltjes of vloeistofelementen - die hetzij donkere hetzij lichtgevende materie representeren - op lokaties neergezet waar ze zich in het zeer vroege heelal hebben moeten bevinden. Door de zwaartekracht in rekening te brengen, wordt het systeem van deeltjes geëvolueerd in de tijd. Ook meer gecompliceerde fysische processen zijn in ogenschouw genomen, waardoor het mogelijk is om te bepalen hoe en wanneer sterrenstelsels gevormd worden en waar het meeste gas in het heelal zich bevindt.

Figuur 2 laat het resultaat van een $N-$deeltjes simulatie zien. De grijswaarden geven de dichtheid (het aantal deeltjes) aan. Op deze manier correspondeert zwart met gebieden met een grote concen-

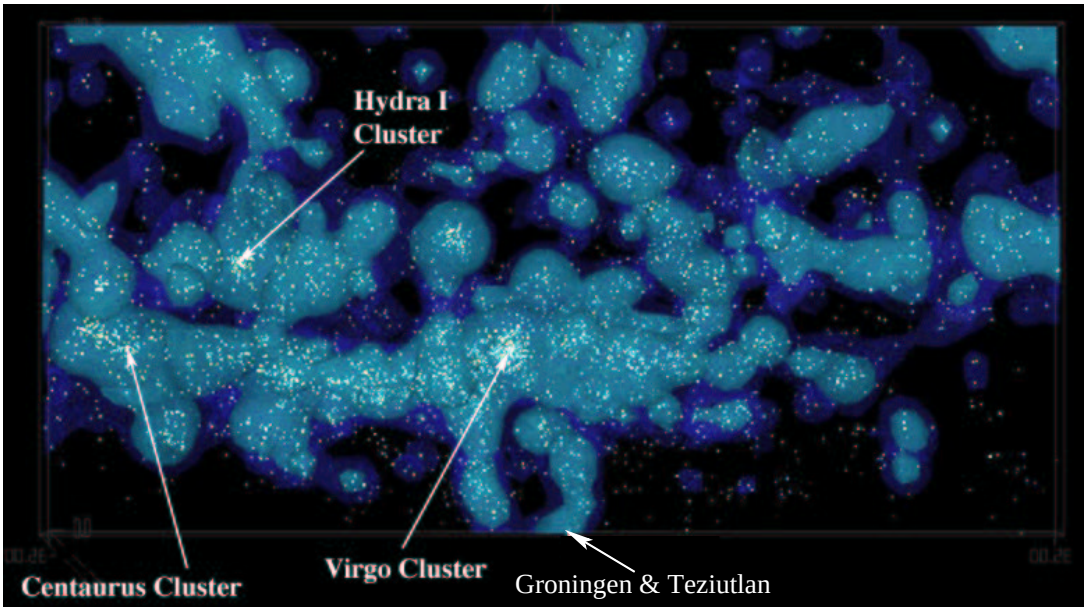

Figuur 3 — Symbolische voorstelling van de Lokale Supercluster. Elk puntje representeert een sterrenstelsel. De grijze gebieden bevatten meer dan een gemiddelde hoeveelheid sterrenstelsels. De meest in het oog springende clusters van sterrenstelsels worden aangegeven met labels, evenals de lokatie van de Melkweg. (Met dank aan Brent Tully, zie www.ifa.hawaii.edu/ tully/outreach)

tratie van materie (clusters van sterrenstelsels), grijs met superclusters, lichtgrijs met filamenten en wit met lege gebieden. De filamentaire structuur (het kosmische web) is duidelijk te zien. De goede overeenstemming tussen de resultaten van $N-$deeltjes simulaties en het waargenomen heelal is een geruststellend succes van de theorie voor de evolutie van het heelal.

De grote schaal structuur van het heelal

Als we om ons heen kijken, dan zien we dat sterrenstelsels de fundamentele bouwstenen van het heelal vormen. Deze grote en waarlijk magnifieke verzamelingen van honderden miljarden sterren bevinden zich overal in het waarneembare heelal. Een algemene aanname is dat hun verdeling de onderliggende verdeling van materie weerspiegelt. Daarom vormen ze een uitstekend hulpmiddel om de structuur en infrastructuur van het heelal in kaart te brengen.

Sterrenstelsels vertonen een ruime verscheidenheid aan soorten en maten. Vele hebben een schijfachtige vorm. Binnen de schijf kunnen we vaak heldere spiraalarmen herkennen, oplichtend door jonge en blauwe sterren. In de kern van zulke sterrenstelsels vinden we een “bulge”, een geel-rode ellipsoïde concentratie van oudere sterren. Een kleiner gedeelte van sterrenstelsels heeft een bolvormige of elliptische vorm, de “elliptische” stelsels. Deze bevatten een voornamelijk oudere sterpopulatie, met veel minder gas dan de “spiraal”stelsels (zie Figuur 1). De meeste stelsels behoren niet tot deze twee hoofdklassen en zijn veel kleiner. Vaak hebben ze een onregelmatige en slecht-definieerbare vorm, hoewel een flink aantal een elliptische vorm heeft.

Onze Melkweg is een spiraalstelsel met ongeveer 200 miljard sterren. Onze zon is een gemiddelde gele dwergster in de schijf van de Melkweg, ronddraaiend op een straal van $\approx 8,5$ kpc van het centrum van de Melkweg[6].

Sterrenstelsels zijn verre van gelijkmatig verdeeld over het heelal. Op schalen van tientallen Megaparsecs vertonen ze een intrigerend schuimachtig patroon, het *kosmische schuim*, dat zich uitstrekt

[6]Een “kpc” is een kiloparsec. 1 kpc $\approx$ 30 860 000 000 000 000 *km*

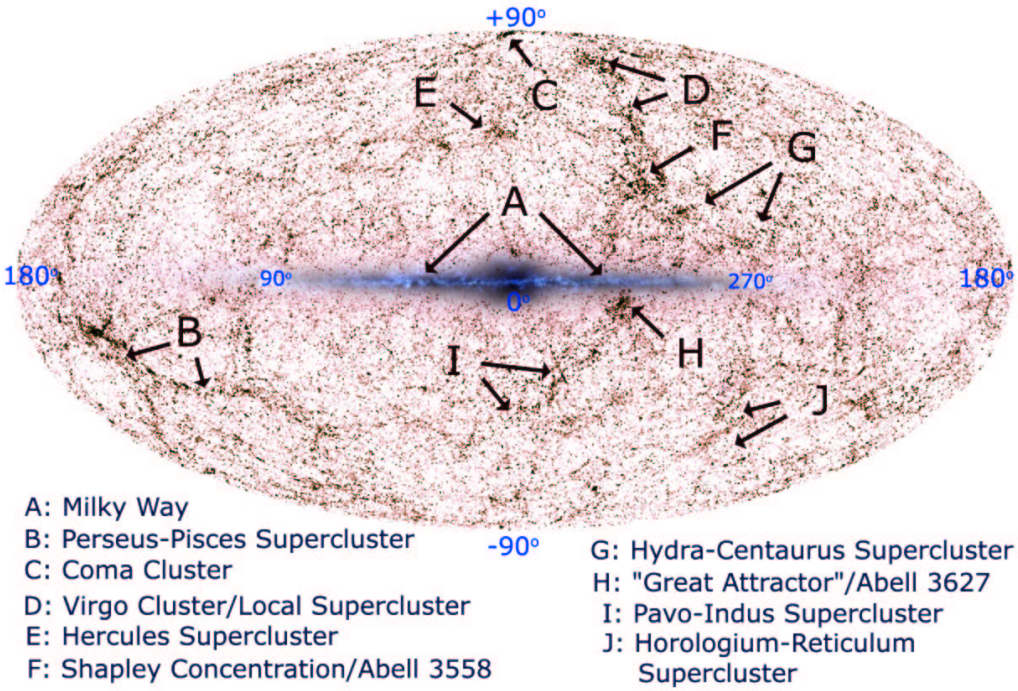

Figuur 4 — Kaart van de verdeling van sterrenstelsels, oriëntatie en lokatie van de grote schaal structuur in het lokale heelal, geprojecteerd aan de hemel. Clusters en superclusters van sterrenstelsels, filamenten en enkele lege gebieden zijn duidelijk zichtbaar. (Met dank aan: 2MASS Extended Source Catalog, T. Jarret en 2MASS/UMass/IPAC-Caltech/NASA/NSF)

over het gehele waarneembare heelal. Op de nog grotere schaal van $\approx 200\ h^{-1}$Mpc kunnen we geen structuren meer herkennen: op deze schalen bereikt het heelal de homogeniteit die vereist wordt door het kosmologische principe. Op kleinere schalen treffen we echter een ingewikkelde hiërarchie van structuren aan.

Individuele sterrenstelsels worden vaak in *groepen* en *clusters* aangetroffen, die op hun beurt meestal deel uitmaken van nog grotere structuren, *superclusters*. Groepen van sterrenstelsels bestaan uit minder dan 50 leden, voornamelijk spiraalstelsels. Alleen in hele dichte en compacte groepen kunnen ook elliptische stelsels worden aangetroffen. Clusters van sterrenstelsels zijn groter en bestaan uit honderden tot duizenden leden. Ze vormen de meest massieve en meest recent volledig ineengestorte objecten in het heelal. In het centrum van clusters bevinden zich voornamelijk elliptische stelsels, terwijl spiraalstelsels en onregelmatige stelsels zich voornamlijk in de buitengebieden ophouden. De omvang van superclusters is in de orde van 20 h^{-1}Mpc of groter. Ze hebben een dichtheid van een paar tot tien maal de gemiddelde kosmische dichtheid. Dynamisch gezien is de expansie van een deel van de superclusters net gestopt. Het zal echter nog even duren voordat deze structuren volledig ineenstorten.

Een goede illustratie van deze hiërarchische inbedding van structuren op allerlei schalen vormt onze eigen Melkweg. Deze behoort tot een kleine groep van sterrenstelsels, *de Lokale Groep*. Van de ongeveer 40 leden zijn de twee meest massieve stelsels, Andromeda en de Melkweg, verreweg het grootst. De Lokale Groep bevindt zich aan de buitenrand van een groter systeem van sterrenstelsels dat bekend staat als de *Lokale Supercluster*. Deze bestaat uit verschillende groepen van sterrenstelsels, enkele kleinere clusters en één hele rijke cluster in zijn kern, de *Virgo Cluster*. Figuur 3 geeft een beeld van de Lokale Supercluster, waarbij elk witte puntje een sterrenstelsel representeert. Wij bevinden ons aan de onderkant van de figuur. De belangrijkste clusters zijn aangegeven met labels.

De kosmische materieverdeling zou bepaald kunnen worden door kaarten van de verdeling van sterrenstelsels te bestuderen. Als het mogelijk zou zijn om een panoramisch beeld van de verdeling van

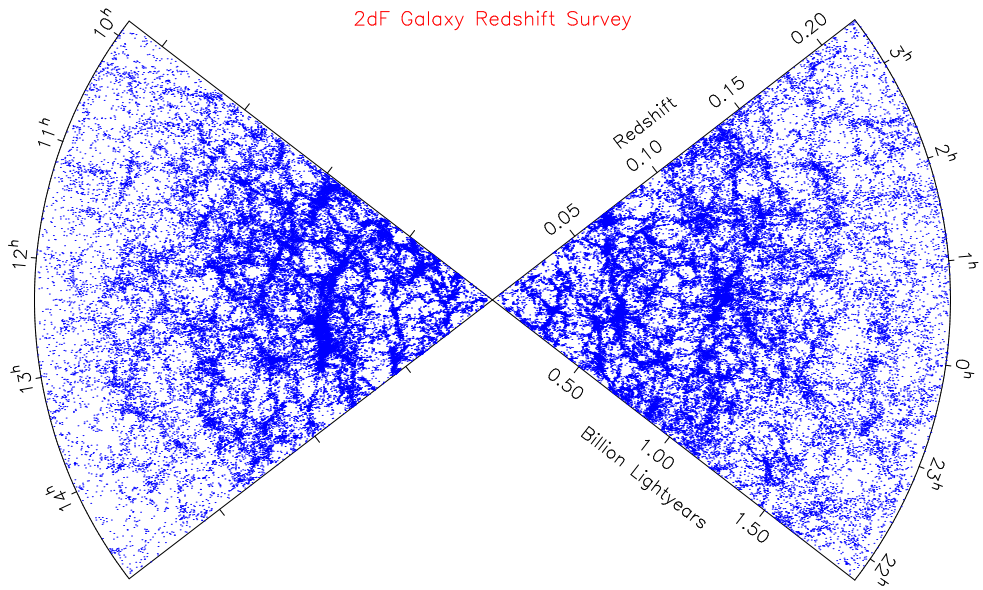

Figuur 5 — Kaart van de verdeling van sterrenstelsels in de ruimte als functie van hun afstand tot ons volgens de 2dFGR Survey. Merk op hoe de materie concentraties vormt in bepaalde gebieden (clusters en superclusters van sterrenstelsels), terwijl er ook lege gebieden zijn. (Met dank aan het 2dF Galaxy Redshift Survey team).

sterrenstelsels voorbij de Melkweg te bekijken, dan zou het resultaat op Figuur 4 lijken. Deze afbeelding is opgebouwd uit de meer dan 1,6 miljard sterrenstelsels (aangegeven met puntjes) die vermeld staan in de All-Sky Survey Extended Source Catalog van de Two Micron All Sky Survey (2MASS). Belangrijke nabijgelegen concentraties van materie zijn voorzien van een label. De vele overdichte gebieden zijn duidelijk zichtbaar. Deze bestaan uit clusters van en superclusters van sterrenstelsels, die de grote schaal van het nabije heelal voor een belangrijk deel bepalen. Merk op dat ons heelal lokaal helemaal niet isotroop lijkt. Het is belangrijk om te beseffen dat de schijnbaar grootte van onze Melkweg in deze projectie een artefact is, resulterend door de nabijheid van de Melkweg. Vanwege onze positie in de schijf van de Melkweg wordt ons uitzicht in het zichtbare licht geblokkeerd door het stof dat zich ook in de schijf bevindt. Met de 2MASS kaart die op microngolflengte is gemaakt, hebben we ineens een veel duidelijker beeld van onze omgeving gekregen. Voorheen onttrokken aan onze aanblik vormt de aanwezigheid van de Great Attractor (H in Figuur 4) een duidelijk voorbeeld hiervan.

Voor een volledig ruimtelijk beeld van de verdeling van sterrenstelsels is het van belang hun afstanden te kennen. Deze zijn lastig om op een directe wijze te meten. Hierbij komt echter de Hubble uitdijing van het heelal ons te hulp. Volgens de Hubble uitdijing is de snelheid van ons af direct evenredig aan de afstand. Door de snelheid te meten, kunnen we dus de afstand bepalen. De snelheid is veel eenvoudiger te meten dan de afstand, vanwege de *roodverschuiving* van het door het stelsel uitgezonden licht. Deze valt te vergelijken met de lagere toon van de sirene van een ambulance die van ons af beweegt. Evenzo wordt het licht van een stelsel roder als het stelsels van ons af beweegt.

Figuur 5 laat de verdeling van sterrenstelsels zien in de Two degree Field Galaxy Redshift Survey (2dFGRS) in een strook aan de hemel. Op deze kaart ligt de Melkweg in het midden van de twee kegels en worden individuele sterrenstelsels aangegeven met een punt. De positie van elk stelsel op de kaart wordt bepaald door zijn roodverschuiving en positie aan de hemel[7] Het resultaat is een ruimtelijke kaart van de verdeling van sterrenstelsels en materie in ons lokale heelal. Sterrenstelsels, clusters en superclusters vormen samen een webachtig patroon. Hierin markeren superclusters de filamentaire bruggen en vlakke wanden in dit netwerk, terwijl clusters zich op de dichte knooppunten

[7]Merk op dat het lijkt dat er minder stelsels zijn naarmate je verder van de Melkweg komt. Dit is echter een schijneffect, omdat het veel moeilijker is om verder weggelegen en daarom minder heldere stelsels waar te nemen dan dichtbijstaande.

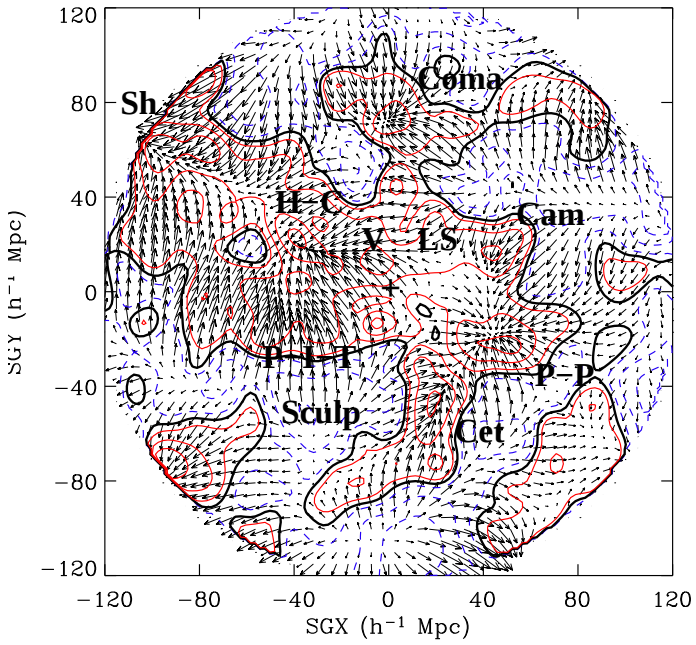

Figuur 6 — Model van de eigensnelheden zoals afgeleid uit de verdeling van materie. De pijltjes geven de richting en grootte van het snelheidsveld aan. De ononderbroken lijnen laten de materieverdeling zien, waarbij compacte gebieden die omsloten worden door een lijn massieve structuren aanduiden, terwijl gestreepte lijnen wijzen op lege gebieden. De labels markeren de posities van de grootste structuren in het veld: V: Virgo cluster, LS: Lokale Supercluster, H-C: Hydra-Centaurus, Sh: Shapley, P-P: Perseus-Pisces, P-I-T: Pavo-Indus-Telescopium, Cet: Cetus wand, Sculp: Sculptor leegte. (Uit E. Romano-Díaz et al. 2004, met data van E. Branchini)

van het netwerk bevinden. Samen omvatten deze uitgestrekte bolvormige gebieden waar zich vrijwel geen sterrenstelsels bevinden, de *leegten*. Tegenwoordig weten we dat dit *Kosmische Web* een van de belangrijkste karakteristieken van ons heelal is.

Kosmische stromen

Hoewel op grote schalen het heelal ongeveer met eenzelfde snelheid uitdijt (de Hubble stroom), is dit niet waar voor afzonderlijke sterrenstelsels. Snelheidsmetingen van afzonderlijke stelsels laten zien dat deze afwijken van de Hubble stroom. Deze afwijkingen worden de *eigensnelheden* van deze sterrenstelsels genoemd.

Migratiestromen van kosmische materie zijn een belangrijke manifestatie van de groei van kosmische structuren. Verondersteld dat kosmische structuren afkomstig zijn van kleine dichtheidsfluctuaties die versterkt werden door de zwaartekracht, zijn eigensnelheden en materieverstoringen nauw aan elkaar gerelateerd. De kosmische stromen verplaatsen materie richting gebieden waar zich steeds meer materie opeenhoopt, alwaar zich geleidelijk de structuren vormen die we tegenwoordig waarnemen in het heelal.

Aangezien eigensnelheden het resultaat zijn van de gecombineerde zwaartekracht van alle materieconcentraties in het heelal samen, weerspiegelen ze niet alleen de lokale materieverdeling maar ook verder weggelegen structuren. Aangezien zowel lichtgevende als donkere materie de zwaartekracht uitoefenen, bevatten kosmische stromen bovendien informatie over de totale materieverdeling. In principe zou daarom het snelheidsveld gebruikt kunnen worden om het corresponderende dichtheidsveld te bepalen of vice versa.

Er is veel energie gestoken in het nauwkeurig meten van eigensnelheden en het corrigeren voor mogelijke willekeurige of systematische fouten. Hiervoor is het noodzakelijk om de echte afstanden tot sterrenstelsels te meten in plaats van hun roodverschuivingen. Studies van eigensnelheden zijn daarom beperkt tot een kleiner gebied dan studies van roodverschuivingen.

Het snelheidsveld is veel gevoeliger voor fluctuaties in de kosmische materieverdeling op grote dan op kleine schalen. Hierdoor is het voor reconstructties van het eigensnelheidsveld van groot belang om een voldoende groot volume in aanmerking te nemen. Dit volume moet zo groot zijn dat het alle

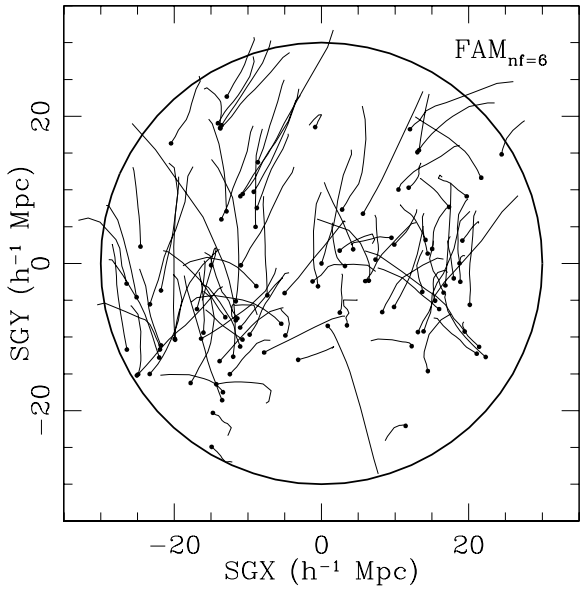

Figuur 7 — Reconstructie van de banen van sterrenstelsels op basis van het Least Action Principle. De punten representeren de huidige posities van de sterrenstelsels, terwijl de stroomlijnen hun banen terug in de tijd volgen.

relevante materieconcentraties bevat die het eigensnelheidsveld zouden kunnen beïnvloeden.

Een van de meest massieve en nabije materieconcentraties, de *Great Attractor*, werd ontdekt door onderzoek aan eigensnelheden. Niet zichtbaar op optische afbeeldingen van de hemel waren het de eigensnelheden die ons wezen op het gebied dat verstopt ligt achter het vlak van onze Melkweg. Dit gebied is grotendeels verantwoordelijk voor onze kosmische beweging. Inmiddels weten we dat het bestaat uit een massieve dichtbijstaande cluster, A3627, die zicht uitstrekt tot de Hydra-Centaurus supercluster.

De Point Source Catalog Redshift (PSC*z*) is een goed voorbeeld van de relatie tussen de materieverdeling en het snelheidsveld. In Figuur 6 bevindt onze Lokale Groep van sterrenstelsels zich in het midden. De ononderbroken lijnen geven gebieden met een hoge dichtheid aan, de gestreepte lijnen gebieden met een lager dan gemiddelde dichtheid. Met behulp van labels hebben we de belangrijkste structuren aangegeven. De pijltjes geven de richting en grootte van het snelheidsveld aan. Let op de sterke invalsnelheden in de richting van de meest massieve concentraties. Ook de lege gebieden beïnvloeden de kosmische snelheden, zoals we bijvoorbeeld kunnen zien in het gebied rond de Sculptor leegte waaruit materie richting gebieden met een hogere dichtheid stroomt. De kaart laat bovendien zien dat onze Lokale Groep in de richting van de Great Attractor beweegt, die onderdeel uitmaakt van de H-C supercluster.

Dit proefschrift

Ik heb de omgevings- en dynamische effecten bestudeerd die de grote schaal structuur van het heelal heeft op enkele van de belangrijke grote kosmische structuren zoals clusters van sterrenstelsels en filamenten. In het bijzonder heb ik het eigensnelheidsveld van sterrenstelsels en de materieverdeling in de Lokale Supercluster bestudeerd. Hiertoe heb ik het Least Action Principle toegepast en de nieuwe DTFE methode uitgebreid om een volledig ruimtebedekkend snelheidsveld te verkrijgen.

Hoewel het merendeel van de data die in dit proefschrift wordt gebruikt geproduceerd is door computerprogramma's, besluiten we met toepassingen van de betreffende technieken op data van het echte heelal.

Voorbij het lineaire regime: het Least Action Principle

Tijdens het structuurvormingsproces worden de dichtheden in materieconcentraties op een gegeven moment hoger dan de gemiddelde waarden die beschreven worden door de lineaire theorie. Ook voor deze gevorderde, niet-lineaire fases is het mogelijk om de corresponderende kosmische stromen te beschrijven. Eén van de schema's waarmee ook in deze fases de materieverdeling gevolgd kan worden is het *Least Action Principle*. Met deze methode kunnen de banen van sterrenstelsels terug in de tijd gevolgd worden, gegeven hun huidige posities en onder de aanname dat hun beginsnelheden gelijk aan nul zijn (een voorwaarde waaraan wordt voldaan omdat het vroege heelal bij benadering homogeen en bewegingsloos was). Met deze methode is het mogelijk om op elk tijdstip de snelheid van ieder object te schatten. Figuur 7 illustreert de reconstructie van de banen van een groep sterrenstelsels (puntjes). De stroomlijnen geven de bewegingen van deze sterrenstelsels aan terwijl het heelal evolueerde. Merk op hoe in dichte gebieden de banen sterker worden afgebogen dan die van meer geïsoleerde sterrenstelsels, hetgeen laat zien waarom het moeilijker is om eigensnelheidsvelden te bestuderen in gebieden met een hoge dichtheid.

Van een stel "test"-catalogi verkregen uit N-deeltjes simulaties hebben we de eigensnelheidsvelden gemodelleerd. Hiervoor hebben we een efficiënte implementatie van het Least Action Principle, de Fast Action Minimization [FAM] methode, gebruikt. Het belangrijkste voordeel van FAM is dat het mogelijk is om de beweging van deeltjes in gebieden met een hoge dichtheid te volgen, zelfs voor een groot aantal deeltjes[8]. Om de betrouwbaarheid van deze gemodelleerde snelheidsvelden te bepalen, hebben we ze vergeleken met de "echte" snelheidsvelden van de N-deeltjes experimenten.

De belangrijkste resultaten van dit deel van mijn onderzoek zijn:

- In het eerste deel van dit proefschrift hebben we het eigensnelheidsveld (van N-deeltjes simulaties) bestudeerd in gebieden die op onze Lokale Supercluster lijken. We hebben de invloed van de massaverdeling buiten onze Lokale Supercluster op de lokale dynamica bestudeerd. De resultaten geven aan dat in alle plausibele kosmologische scenarios de massaverdeling buiten onze Lokale Supercluster de lokale dynamica significant beïnvloedt. We hebben laten zien dat het mogelijk is om rekening te houden met deze effecten, en dat deze door een paar dynamische termen beschreven kunnen worden. De nauwkeurigheid van onze resultaten hangt af van het kosmologische model en de precieze configuratie van het systeem.

- Om meer concrete conclusies te kunnen trekken over de invloed van de externe materieverdeling op de dynamica van de Lokale Supercluster hebben we de *Constrained Random Field* methode gebruikt. De correct gemodelleerde beginomstandigheden, ontworpen om de massaverdeling in ons lokale heelal zo goed als mogelijk te beschrijven, werden geëvolueerd door middel van een N-deeltjes programma. Onze simulaties zijn erin geslaagd om enkele eigenschappen van de grote schaal structuur van ons heelal te reproduceren. Zo hebben we structuren die lijken op de Great Attractor, Perseus-Pisces en Hydra-Centaurus in onze simulaties aangetroffen. Uit een gedetailleerd onderzoek van deze simulaties blijkt bovendien dat ze het dynamische gedrag van het waargenomen heelal goed beschrijven.

- Door het resulterende eigensnelheidsveld in de "constrained" simulaties te modelleren, hebben we aangetoond dat de massaverdeling die onze kosmische omgeving (de Lokale Supercluster) omgeeft goed beschreven wordt door de gemiddelde snelheid en de zogenaamde "shear". De gemiddelde snelheid beschrijft hoe de ingesloten materie als geheel beweegt onder invloed van de omliggende externe materieverdeling. De shear beschrijft de verstoring van het snelheidsveld door de structuren die buiten het in ogenschouw genomen gebied liggen.

- We hebben de FAM techniek toegepast om het eigensnelheidsveld van echte data te modelleren, waarbij we de Point Source Catalog redshift survey (PSCz) hebben gebruikt. Hierbij hebben we

[8] Desalniettemin faalt ook deze methode in het reproduceren van de bewegingen van sterrenstelsels in de centrale gebieden van clusters, waar de dichtheid zeer hoog is, hoewel dit probleem geen invloed heeft op onze belangrijkste conclusies

gezocht naar de belangrijkste structuren die verantwoordelijk zijn voor het eigensnelheidsveld van ons Lokale Superclustergebied. De resultaten geven aan dat de clusters die op gemiddelde afstand staan, zoals Hydra-Centaurus en Perseus-Pisces (Fig. 4 en 6), de dynamica van de Lokale Supercluster bepalen. Ook structuren op grotere afstanden, zoals de Shapley Structuren, hebben nog steeds een effect op onze lokale kosmische omgeving.

Continue snelheidsvelden: het DTFE snelheidsalgoritme

In het tweede deel van het proefschrift hebben we voortgebouwd op een nieuwe techniek om vanuit een discreet gesampeld snelheidsveld een continu en ruimtebedekkend snelheidsveld te verkrijgen.

De vergelijking van waargenomen en gesimuleerde snelheidsvelden met de voorspellingen van theoretische modellen is alleen mogelijk onder de aanname dat de waargenomen velden een goede beschrijving vormen van het onderliggende snelheidsveld. In werkelijkheid is dit niet het geval. De eigensnelheden zijn alleen bekend op de lokaties waar zich waargenomen sterrenstelsels of simulatiedeeltjes bevinden. Theoretische voorspellingen zijn gebaseerd op de veronderstelling dat het snelheidsveld continu en goed gedefinieerd is binnen het volume dat beschouwd wordt. De resulterende vergelijking met theoretische voorspellingen is daarom niet altijd goed gedefinieerd. De velden die met elkaar worden vergeleken zijn daarom niet altijd gelijk!

Bij het vergelijken van theorie en waarnemingen wordt het gemeten snelheidsveld geïnterpoleerd naar alle andere posities in het gesampelde volume, waaronder gebieden met weinig of geen data. Conventionele interpolatiemethoden maken gebruik van kernels die de snelheden van de deeltjes in de kernel middelen. De prijs van deze benadering is dat signalen met een kleinere afmeting dan de grootte van de kernel worden uitgewist. Hiermee gaat informatie in gebieden met een hoge dichtheid verloren. In veel gevallen is de interpolatiemethode bovendien niet in staat om gebieden met weinig data te beschrijven. Daarom is naast de interpolatie ook een *smoothing* operatie noodzakelijk. Deze zorgt er onder andere voor dat er snelheidswaarden worden toegewezen aan gebieden met weinig data. De prijs van deze smoothing operatie is dat er opnieuw informatie verloren gaat, ditmaal op schalen kleiner dan de afmetingen van de smoothing kernel.

Idealiter zou alle informatie op zowel grote als kleine schaal behouden blijven, zodat een consistente bestudering van het eigensnelheidsveld mogelijk is. De analyse van de eigensnelheidsvelddispersie op kleine schaal bevat bijvoorbeeld informatie over de totale hoeveelheid materie en volledige dynamische toestand binnen een gegeven gebied. Als deze uit de deeltjesverdeling zelf zou worden bepaald, dan zouden wellicht misleidende conclusies kunnen worden getrokken. Deze studie geeft immers veel gewicht aan hoge dichtheidsgebieden die relatief goed gesampeld zijn. Een veel betere benadering is om een gelijkwaardige significantie toe te kennen aan de slecht gesampelde lage dichtheidsgebieden door een continu en ruimtebedekkend snelheidsveld te gebruiken.

Wij hebben een geavanceerd interpolatieschema ontwikkeld dat zich automatisch aanpast aan de geometrie van de deeltjesverdeling, en dat zowel op kleine als op grote schaal snelheidsvelden oplost. Van deze Delaunay Tessellation Field Estimator [DTFE] (zie Schaap 2005) techniek is het bekend dat de hiermee gereconstrueerde snelheidsvelden goed bepaalde statistische eigenschappen hebben (Bernardeau & van de Weygaert 1996). De DTFE is gebaseerd op een driehoekig netwerk, bekend onder de naam Delaunay tessellatie, die naburige punten verbindt op een volledige adaptieve en objectief gedefinieerde manier.

Voortbouwend op de introductie van de DTFE laat Figuur 8 een discreet snelheidsveld zien dat gesampeld is op de deeltjesposities. Het is gemodelleerd met behulp van de materieverdeling zoals gemeten in de PSCz catalogus van ons nabije heelal. De snelheidspijlen die in het rechterframe worden aangegeven zijn het resulterende DTFE snelheidsveld. Alle structuren die aanwezig zijn in de discrete kaart zijn ook aanwezig in de DTFE kaart, maar ook de gebieden zonder eigensnelheidsdata worden volledig beschreven.

De belangrijkste resultaten van de analyse van DTFE snelheidsvelden kunnen als volgt opgesomd worden:

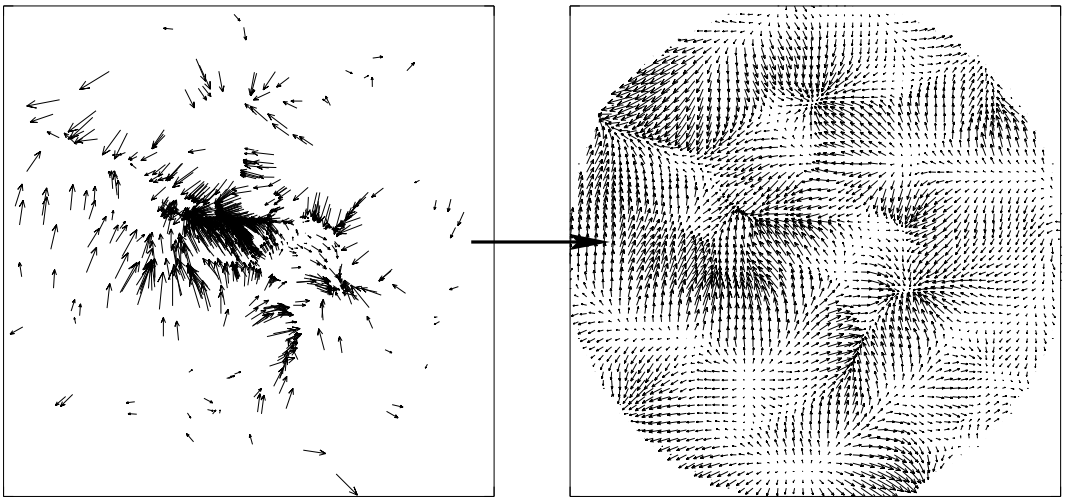

Figuur 8 — Eigensnelheden zoals afgeleid uit de werkelijke snelheidsverdeling van de verdeling van sterrenstelsels volgens de PSCz catalog van ons nabije heelal. Het linkerpanel toont het discrete snelheidsveld, het rechterpanel het continue ruimtebedekkende snelheidsveld dat door het DTFE snelheidsalgoritme is gereconstrueerd.

- De DTFE snelheidsmethode kan zowel op kleine als op grote schaal de karakteristieke elementen van het eigensnelheidsveld reconstrueren. De DTFE snelheidsvelden hebben de vereiste eigenschappen, namelijk dat ze continu en volumebedekkend zijn over het gehele gesampelde volume. Met onze implementatie kunnen gerelateerde grootheden als de uitdijing of samentrekking van het snelheidsveld eenvoudig berekend worden, evenals de rotatie, uitrekking en compressie. Vergelijkingen van DTFE snelheidsvelden met theoretische voorspellingen komen zeer goed met elkaar overeen. De resulaten laten zien dat deze techniek een belangrijke stap voorwaarts is bij het analyseren van kosmische eigensnelheden op zowel kleine als grote schalen. Hetzelfde geldt voor studies van de dynamica van het kosmische web.

- Met de DTFE techniek hebben we bestudeerd hoe “koud” de Lokale Supercluster is, i.e., hoe groot of klein de snelheidsafwijkingen van een pure Hubble stroom zijn. De grootte van deze afwijkingen hangt af van het kosmologische model. Waarnemingen geven aan dat ons lokale heelal koud is. Onze methode heeft ons in staat gesteld om objectievere conclusies te trekken, omdat we de stroom over het gehele gesampelde volume kunnen schatten en bestuderen. De resultaten geven aan dat onze kosmische omgeving inderdaad vrij koud is. De snelheidsafwijkingen zijn erg klein, en onze algemene beweging wordt bepaald door een sterke coherente stroom die uitgeoefend wordt door een zeer massieve structuur, de Great Attractor.

Detectie van het kosmische web: filamenten

In een project met J. Dietrich en P. Schneider hebben we de zwakke lenseigenschappen van het kosmische web bestudeerd met als doel het detecteren van filamenten die twee dicht bij elkaar gelegen clusters met elkaar verbinden. De massaverdeling in de buitendelen van clusters van sterrenstelsels is veel moeilijker te onderzoeken dan in de binnendelen van clusters. We hebben de nauwkeurigheid en de betrouwbaarheid van een methode getest waarmee het in principe mogelijk is om de zwakke lenssignalen van filamenten te meten. We hebben dit gedaan door filamentaire configuraties te onderzoeken waarvan de beginomstandigheden door de Constrained Field techniek bepaald zijn. Deze simulaties zijn zo ontworpen dat ze zo dicht mogelijk in de buurt komen van de werkelijke configuratie van twee dichtbij elkaar liggende clusters met een filament die ze verbindt. De resultaten laten zien dat

er inderdaad een klein maar detecteerbaar signaal van filamenten is. Dit signaal is ook gedetecteerd voor de dubbele cluster A222 en A223.

Conclusies en vooruitblik

Het centrale thema van dit proefschrift is het begrijpen van de oorsprong en de belangrijkste eigenschappen van het lokale eigensnelheidsveld van sterrenstelsels. Hiertoe behoren de grote schaal structuren die de dynamica van de Lokale Supercluster beïnvloeden. Het onderzoek van grote schaal structuur boekt nog steeds snelle vooruitgang door het beschikbaar komen van nieuwe data en dit zal voorlopig zo blijven met de ambitieuze surveys die in de komende jaren uitgevoerd zullen worden. Met betere data en nieuwe theoretische en computergereedschappen kunnen kosmologen vooruit kijken naar het beantwoorden van enkele van de raadsels die ons huidig kosmologisch wereldbeeld omringen. Tot de meest belangrijke hiervan behoren vragen die direct gerelateerd zijn aan de oorsprong en het lot van ons heelal: wat is de aard van de donkere materie en de donkere energie?

This sun, called 4 Movement, is our Sun, where we live now.
And here is its mark, as it fell into the Sun's Fire,
in the divine furnace, there in Teotihuacan.
This was also the Sun of our Prince, in Tula, of Quetzalcoatl.
The fifth Sun, 4 Movement is its sign,
it is called Sun of movement because it moves, it follows its path.

Aztec poem of the creation of the Fifth Sun (fragment, Codex Chimalpopoca).

English Summary

Probably from even before the dawn of civilization humans have been gazing at the starry nights and wondered about the world in which they found themselves living. Questions that have occupied humanity were ones like "How did the universe begin?" "How had everything come into being?". Many explanations have been given throughout the eons, as nearly every culture and society forwarded its own cosmogony and understanding of the universe. This quest has been vigorously pursued up to the modern age. Indeed, for the first time humanity appears to come close to an all-encompassing scientifically justified answer to these age-old questions, on the basis of a vast body of scientific knowledge supported by an ever-increasing and impressive amount of observational evidence.

Within the current cosmological model, it is assumed that the universe we inhabit came into being 13.7 billion years ago, born in a massive expanding fireball which we have named the *Hot Big Bang*. In this event space and time, as well as all the matter and energy that the universe contains came into being. The pristine universe was extremely hot and dense, gradually cooling and diluting as it expanded. The theoretical description of this event rests on two crucial assumptions. The first one is that its dynamical evolution is entirely dictated by the force of gravity, which has been encapsulated in Einstein's Theory of General Relativity. According to this theory, the force of gravity is the manifestation of the curvature of a system. The Big Bang Universe is based on the assumption that the Universe's geometry is severely constrained by the Cosmological Principle. It states that the universe is homogeneous and isotropic. In other words, the universe has the same properties everywhere, both concerning its matter distribution as well as the physical laws pertaining throughout its realm. In addition, it also looks the same in every direction. Only three geometries obey these restrictions, and when working out their repercussions within the context of General Relativity we find that the corresponding solutions, the Friedmann-Robertson-Walker-Lemaitre [FRWL] models, provide the correct theoretical framework for the evolution of the expanding Universe. Hubble's finding in 1929 of the systematic recession of galactic nebulae established for the first time the reality of this view of a dynamic cosmos.

The immediate implication of Hubble's discovery was and is dramatic: the cosmos should have a beginning ! On the basis of the FRWL cosmological models and our knowledge of the laws of physics cosmologists have even been able to reconstruct the full thermal history of the Universe up to a fraction of the second after its birth. This is what we describe as the *Hot Big Bang* theory. The resulting predictions for a variety of major events and phenomena in the course of the Universe's evolution have provided us with a truly impressive body of evidence for the validity of the *Hot Big Bang* theory. Arguably the most impressive prediction has been that of the Cosmic Microwave Background, the remnant of radiation reaching us from every direction on the sky and originating from the time 379,000 years after the Big Bang. Its discovery in 1965 by Penzias & Wilson, is rightfully regarded as one of the major scientific breakthroughs of the 20th century. With a current temperature of only $2.725^{\circ}K$ it is almost perfectly isotropic, displaying temperature variations over the sky smaller than 1 in 10^5, a more than impressive confirmation of the Cosmological Principle. The early Universe was almost perfectly featureless.

While the evidence in favor of the Hot Big Bang Universe has been accumulating to impressive levels, we are left with the riddle that on scales much smaller than the radius of the visible Universe it looks far from homogeneous, locally even far from isotropic. The cosmos is teeming with a rich and highly varied internal structure. Planets and stars are familiar to everyone, hundreds of billions

Figure 1 — Examples of galaxies in our Universe, a spiral galaxy (left panel; Credits: G.F. Benedict, A. Howell, I. Jorgensen, D. Chapell, J. Kenney, and B.J. Smith, and NASA) and an elliptical galaxy (right panel, Credits: NOAO,AURA,NSF). At the central panel a galaxy cluster is shown (Credits: NOAO,AURA,NSF), which consists of tens of galaxies.

of them aggregate together with gas and dust into what may be regarded as the fundamental building blocks of our observational Universe, the *galaxies*. The galaxies themselves clump together into even larger and more massive structures, *groups* and *clusters of galaxies* (see Figure 1). They are part of a hierarchy of ever larger systems, on scales of dozens and even hundreds of Megaparsecs grouping into *superclusters*, which themselves are structural elements of a pattern resembling a cosmic web which pervades throughout the observable Universe.

One of the key dilemma's of modern cosmology is therefore to explain the irregular matter distribution on scales smaller than a hundred Megaparsec within the context of the cosmological worldview of the Big Bang. It is in this thesis that we pursue this question, and in particular explore issues concerning the related flows of matter along the local Universe, out to a distance of around 100 h^{-1}Mpc. In this we will follow the standard lore of structure formation in the Universe, the theory of Gravitational Instability. This extends the standard Hot Big Bang theory with an extra element, stating that although the early Universe was nearly completely smooth it was not perfectly so. Instead, it did contain some tiny variations in the matter distribution and the cosmic expansion. These got amplified by gravity and grew into the wealth of structure we see through our telescopes. Also this view has been accumulating convincing evidence, and again it was the observation of the Cosmic Microwave Background and the detection of tiny temperature variations by the COBE and WMAP satellites which have provided us with sufficient confidence to set out on the investigation presented in this work.

The Hot Big Bang

Up to the beginning of the 20th century it was believed that the Universe was static. In 1916, Albert Einstein proposed his theory of general relativity and the equations that describe the dynamics of the Universe. Einstein found in those equations that the Universe should be expanding or contracting, something entirely incompatible with the prevailing notion of a static universe[1].

In 1923 Friedman managed to solve the equations of motion for general homogeneous and isotropic Universe models within the context of General Relativity. Following his seminal yet at the time insufficiently recognized contributions, it was the Belgian priest Georges Lemaitre who not only independently solved the same equations in 1927 but also realized its physical ramifications. Extrapolating backward in time he saw that an expanding Universe should have had a beginning in an extremely hot and dense phase. With some measure of imagination, he indicated this primordial state by the name

[1]He did not believe these results, and hence, introduced an extra term into his equations of motion in such way to produce a static Universe. This term is called the *Cosmological constant* and its denoted by the Greek letter Λ

of 'Primeval Atom'. Soon thereafter, in 1929, these theoretical ideas found a firm root in reality when Edwin Hubble discovered that galaxies recede from us with a velocity increasing as they are located at a larger distance. This universal relation we commonly know as *Hubble Law*, and since Hubble's early results it has been followed throughout the observable Universe as our instruments managed to peer into larger and larger depths. Without doubt this discovery has been one of the greatest scientific revolutions in human history, providing the first clear and conclusive evidence that our Universe is not static, but "expanding"! In the past few years the accuracy of modern space instruments have lead to a convergence of the estimated expansion rate of the Universe to a value in a narrow range around $H_0 \approx 71$ km s^{-1} Mpc^{-1} (known as the *Hubble constant*). For each Megaparsec[2] of distance, the recession velocity of a distant object appears to increase by 71 km s^{-1}.

With the new observational evidence of an expanding universe, a whole new set of questions confronted the astronomical community. What was the nature of this expansion? Would the expansion last forever? Would the Universe expand gradually until reaching a dynamical equilibrium remaining in a static state forever? Would the universe reach a critical point from which it will start to contract until reaching the opposite point of the Big Bang, the *Big Crunch*? These questions remained unanswered for a long time, since there were no conclusive observations which could answer them convincingly.

One aspect of the expanding Universe proves to be of instrumental importance in our ability to explore the physical circumstances and processes in both the early as well as the future Universe. The FRWL Universes all involve an adiabatic expansion, which enables us to predict the temperature and density of its constituents at each instant of time. In other words, the radiation and matter constituents cool down as the universe expands. Reversely, as we extrapolate backward in time and the universe shrinks in size we see both its density and temperature rising. Over the past half century this proved to be the key for accumulating an impressive amount of evidence in support of the Hot Big Bang theory.

Amongst a range of tests, some four to five pieces of observational evidence have become the most solid pillars of the Big Bang cosmology. Perhaps the most straightforward one is the fact that the Big Bang offers an explanation for an amazingly simple observation by Olbers in the early 19th century: the sky at night is dark ! Only in a Universe with a finite age and with a finite velocity of light this may be understood. Evidently, it was Hubble's (isotropically) expanding universe which not only forms a telling confirmation of the reality of the FRW description but may also be regarded as the beginning of cosmology as a "physical science". Maybe most tantalizing are the two observational results reaching to much earlier epochs of our cosmos. The incredible precision with which the Hot Big Bang theory manages to predict the products of the very early phase of primordial nucleosynthesis of light chemical elements brings us back to the first three minutes of the Universe. The prediction of an isotropic blanket of cosmic thermal radiation, with a mind-boggling precise blackbody spectrum with a temperature of $T \approx 2.725^\circ K$, enabled us to turn its discovery in 1965 into the final conclusive proof of the Hot Big Bang's reality. The nickname coined by Fred Hoyle in 1950 had turned into a honorary title !

Some three minutes after the Big Bang, when the temperature of the Universe had cooled down to a few billion degrees, the Universe had turned into a gigantic nuclear reactor. The light chemical elements of Deuterium, ^{3}Helium and ^{4}Helium, as well as a trace of Lithium, managed to form before the cosmic expansion turns off its "nuclear power". The fact that the Hot Big Bang offers the explanation for the fact that 24% of the mass of all baryons in the world is one of its most convincing victories.

In the subsequent hundreds of thousands of years photons, in close interaction with a tiny residual of electrons and protons[3], reached equilibrium and distributed their energy into an almost perfect blackbody spectrum. Around 279,000 years after the fact the temperature of the Universe had cooled to a mere $3000^\circ K$, upon which protons and electrons manage to combine into forming Hydrogen atoms during this *"Recombination"* event[4]. Almost coincidental is the resulting *"decoupling"* of radiation and matter. No longer scattered by freely floating electrons, photons assume a long journey along

[2]One parsec is 3.26 light-years. Mpc = Megaparsec ≈ 3 260 000 light-years ≈ 30 860 000 000 000 000 000 *km*.

[3]It is good to realize that our Universe is a highly abnormal physical system in that it has 2 billion photons for each baryon !

[4]For historic reasons, this resulted into the epoch acquiring the name "Recombination". Evidently, this is a misnomer as it was the very first time electrons and protons went in communion.

the depths of a virtually transparent Universe. These photons of the *Cosmic Microwave Background* [CMB], having retained their almost perfect blackbody spectrum, appear to have originated from the *surface of last scattering*. This surface marks the location of the atoms from which the observed CMB photons were last dispersed[5]. Since then, the gradual expansion of the Universe goes along with a proportional cooling down of the photon temperature, having reached a present-day value of $T \approx 2.725^{\circ}K$.

A continuously rising flood of new cosmological observations, stemming from larger and larger depths in the Universe, has lead to a converging consensus regarding the Universe we are living in. With impressive accuracy a rather remarkable set of values for the crucial cosmological parameters has emerged, now commonly known by the name of *"Concordance Model"*[6]. Satellite experiments such as COBE and WMAP, in conjunction with balloon-borne experiments such as Boomerang, have managed to map in great detail the embryonic Universe at around the recombination epoch. Not only did they show the validity of the Hot Big Bang, but they also convinced us that the Universe is *flat*, accurately determined its age to 13.7 billion years and independently confirmed the baryon content suggested by primordial nucleosynthesis. In combination with the ground-based mapping efforts of large redshift surveys of galaxies, of which we may as yet mention the $100,000$s of galaxy positions determined by 2dFGRS and SDSS, we have been able to track the (dark) matter content of the Universe. The greatest surprise got delivered by the programs for detecting and measuring Supernova Ia explosions out to large depths in the Universe. They lead to the almost inevitable conclusion of the existence of an elusive yet omnipresent "Dark Energy". This mysterious medium would represent no less than 73% of the energy content of the Universe. Ever since it started to dominate the dynamics of our Universe, only as recent as some 7 Gigayears after the Big Bang, it has been propelling an acceleration of the expanding Universe !!!!

Leaves us to state that even while the *"Concordance Model"* appears to form a good description of reality we are left with a large number of unsolved riddles. The standard FRW model would go nowhere to explain why the Universe appears to be so very close to *"flat"*, an issue which is commonly indicated with the name of *Flatness Problem*. Also, it remains a puzzle why the Cosmic Microwave Background has the same temperature in every direction while the cosmic horizon at recombination is no larger than $\approx 1^{\circ}$. This is known as the *Horizon Problem*. In conjunction with other possible coincidences these issues have lead to an extension of the *Hot Big Bang* theory by an inflationary phase transition during which the very early Universe got exponentially inflated by a factor of 60 orders of magnitude. Also, as we will see in the subsequent section, it may help in explaining the origin of structure.

Cosmic Inventory: Matter and Dark Matter

When we look into the Universe the first thing we see is the light and radiation emitted by the stars. Although they may be the most conspicuous and visible denizens of our Universe, they turn out to represent only a minute fraction of the cosmic matter content. The latest estimates are that the stars represent not more than 0.25% of the total cosmic energy content, 0.9% of its total matter content and even no more than 5% of all baryons in the Universe. Planets, moons, asteroids and dust encircling such stars represent an even more humbling fraction. There have been speculations that a highly abundant population of extremely faint stars, brown dwarfs, or objects that just failed to ignite as a star would make up for far more mass, but no convincing evidence to that end has been found. Neither have the claims materialized for a vast amount of matter hidden in a graveyard of deceased stars, black holes or extinguished white dwarfs. In addition to the hundreds of billions of stars which galaxies harbor, they contain large amounts of gas. Radio telescopes have been able to map the diffuse neutral hydrogen and the denser and more massive molecular gas clouds. Infrared and sub-millimeter wavelength telescopes have peered into the cores of the latter, the birth cradles of the stars. Altogether, however, this accounts

[5] Some of these photons are responsible for $\sim 1\%$ of our tv-set's noise

[6] A probably more healthy and modest attitude would resort to the name of *"Benchmark Model"* (Ryden 2003)

for not more than 30% of the mass found within the stars. A far larger amount of baryons has been found within rich galaxy clusters. They contain huge amounts of extremely hot ionized intra-cluster gas. At temperatures of around hundred of million degrees K this gas radiates at X-ray wavelengths. It represents at least three times more matter than the galaxies roaming around within the same cluster potential well. In total it may account for up to 0.7% of matter in the cosmos.

Gas and stars are made of the same material as we, baryonic matter mainly made up by protons and neutrons. One of the great successes of the Hot Big Bang theory has been the prediction of the total amount of baryons in the Universe, a mere 4.4% of the amount of mass needed to flatten the geometry of the Universe. Adding up the above contributions, we find that most of baryonic matter has as yet not been found. Really exciting is the accumulating evidence that perhaps up to 80% of the baryons is swirling within the vast structures traced out by the Megaparsec cosmic web, in the form of a warm or cool plasma.

A sobering thought is the realization that matter made up of baryons is only a minor constituent of the cosmic inventory. By studying the motions of stars and gas in galaxies and that of galaxies in the cosmos we have come to realize that they must be induced by the gravitational action of vastly larger amounts of matter. While baryons cannot account for more than 4.4% of the critical mass of the Universe, observations indicate that the total amount of matter should account for up to 27%.

The two first observational indications for the existence of a gravitationally dominant dark matter component were forwarded by Oort and Zwicky in the 1930s. Oort found the stars in our Galaxy to move faster perpendicular to the plane of the Milky Way than could be accounted for by all the stars in the Galactic plane. Orbital motions of stars and gas clouds in the outer realms of galaxies appear to hint at even larger quantities contained in an extended surrounding dark matter halo. In particular the work by Groningen astronomers (van Albada & Sancisi) has played an instrumental role in reaching these conclusions. Even more perplexing and stark were the discrepancies between gravitational and luminous matter on even larger mass scales. Fritz Zwicky found in 1930 that the velocities of galaxies in the Coma clusters were much too high for the cluster to remain gravitationally bound. If it were not for the presence of at least 100 times more matter than seen in the form of stars, the cluster would fly apart. Ever since, the presence of similar amounts of cluster matter has been found in every observed cluster of galaxies. Not only this came to be inferred from the motions of the galaxies within the cluster potential, but also from the thermal state of the heated X-ray emitting intra-cluster gas and from the bending effect that the cluster has on the light paths of passing radiation emitted by background galaxies (gravitational lensing). The trend continues on even larger Megaparsec scales: the cosmic flows of galaxies as well as the recently measured *cosmic shear*, the "weak lensing" of light as it travels through the inhomogeneous Megaparsec matter distribution, indicate similar or even slightly larger amounts of dark matter.

As the total amount of cosmic matter is some seven times larger than the maximum amount of baryonic matter, the detected dark matter has to be a form of *"nonbaryonic matter"*. As yet we do not have any direct and compelling evidence for what it may be. A large variety of potential candidates have been forwarded as dominant matter component in nature. For a short time *massive neutrinos* were a serious candidate, soon to be replaced by a class of *exotic* particles that are long-lived, cold and collisionless, *Cold Dark Matter* (CDM). The identity of these dark matter particles is still unknown. Nonetheless, speculations rife. The broad and speculative class of weakly interacting and massive particles, WIMPs, or a very light particle called *axion* are as yet amongst the favorites.

At present *Matter* appears to account for 27% of the energy content of the Universe, of which *Dark Matter* take up the major share. Since some years we have come to realize that *Dark Energy* has an even larger share of 73%, although its nature is almost completely unknown. What we do know, however, is that its nature does not allow it to cluster and therefore it does play a minor role in the structure formation process. However, the latter is distributed evenly throughout the Universe and because of its special nature (equation of state) it is unable to cluster. Thus, while both dark energy and dark matter are both instrumental in steering the expansion and fate of the Universe, only *matter* is able to cluster and therefore evolve structure. We therefore find *Dark Matter* as the decisive agent for shaping the outcome of the structure formation process which lies at the core of the work presented in

this thesis.

Gravitational Structure Formation

How then did all the planets, stars, galaxies and clusters of galaxies arise in an almost perfectly homogeneous Universe? The most plausible answer we have at is that of structure formation through *gravitational instability*.

Tiny density and velocity perturbations got amplified by their mutual gravitational interaction. Under the influence of the net resulting gravitational force, matter starts to migrate to slightly overdense regions where more and more matter accumulates. In turn, this growing overdensity represents an even stronger gravity excess, amplifying the effect and ultimately leading to a runaway process: gravitational instability. By contrast, regions with a density deficit have a slightly lower than average gravitational attraction. Matter will stream out of these depressions towards the higher density regions, leaving a gradually emptying and expanding void.

In the first phase of gravitational clustering, when the density perturbations are still moderate, the resulting matter distribution is merely a more pronounced version of the initial circumstances. This we call *linear regime*. Once the density fluctuations start to deviate substantially, matter concentrations come to a halt, decouple from the global cosmic expansion, and start to contract. The subsequent collapse proceeds along a sequence of characteristic anisotropic patterns. At first they acquire a planar wall-like shape, followed by a contraction onto an elongated filamentary shape before reaching full collapse and virialization into a clump of matter. The nature of the primordial fluctuations is responsible for a second key aspect of gravitational structure formation, its *hierarchical* nature. Because the fluctuations on small scales are more pronounced than the ones on large scales, the first objects to form are the smaller ones. The larger ones form through the merging of smaller ones that had already formed. This process of *hierarchical structure formation* seems indeed what we observe: *galaxies* are much older than the more massive and more recently collapsed *clusters* of galaxies. On an even larger scale, *Superclusters* have not even reached a collapse stage, at best they started to contract.

The way in which these hierarchically embedded structures have arranged themselves in the Universe contains a wealth of information on the structure formation process. They appear to be grouped in planar or filamentary partially contracted superclusters, interconnected into a vast web-like configuration, interspersed by huge and empty void regions, stretching out along the observable Universe.

For testing the theory of gravitational instability we do need to find suitable structures and phenomena. Preferably these should still retain a direct link to the primordial circumstances in the Universe, so that we can interpret the resulting information rather directly. There is a variety of such *cosmic fossils*. A major one are the temperature fluctuations in the microwave background, a direct reflection of the tiny embryonic cosmic perturbations out of which structure has grown. A crucial one concerns a map of the matter distribution on Megaparsec scales, the present-day product of the structure formation process. On the basis of the assumption that the galaxy distribution is a fair reflection of the underlying matter distribution, maps of the spatial galaxy distribution are perhaps the most widely analyzed *cosmic fossil*. Propelled by the dynamics of the process, we may hope to find ample information in the induced cosmic flows. They do indeed represent another important fossil, making the study of the related peculiar velocities of galaxies a crucial additional field of attention.

Computer Simulations of the Universe

Theoretical cosmological models make predictions about the structure formation process of the universe. The cosmic structures that astronomers observe are the end products of a long and complicated evolutionary process. For testing the structure formation scenarios cosmologists resort to computer simulations that model the evolution of the Universe.

The use of computer simulations have developed into a major instrument for the study of the large scale structure. They follow the evolution and formation of cosmic structures according to the theory

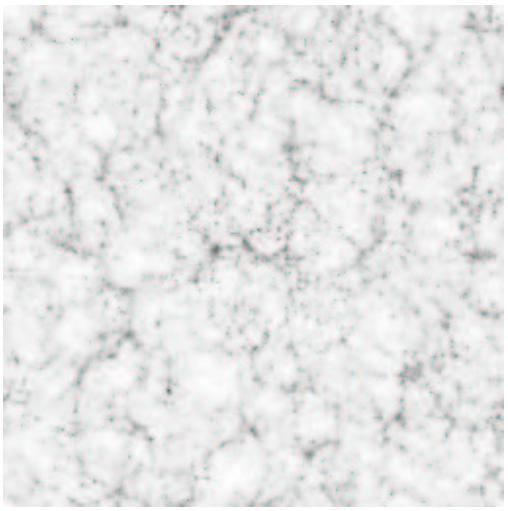

Figure 2 — Representation of a portion of the Universe created by a computer simulated model.

of gravitational instability. $N-body$ simulation codes have become the major workhorse for following the various aspects of this evolution. In this computed universe, particles or fluid elements -which represent either dark or luminous matter- are placed at locations where they were supposed to be at very early times of our universe. By prescribing the force of gravity the system of particles is evolved in time. Also more complex physical processes have been incorporated, enabling us to follow how and when galaxies formed, or where most of the gas in the Universe is located.

Figure 2 shows the result of an $N-$body simulation. The gray scale is an indication of the density (number of particles). In this way, black represents regions where there is a high concentration of matter (galaxy clusters), gray for superclusters, light gray for filaments, and the lightest tone represents the empty regions, voids. The filamentary structure (cosmic web) is clearly distinguishable. The good agreement between the results from $N-$body simulations and the observed Universe is an ensuring success for the theory of the evolution of the universe.

The Large Scale Structure of the Universe

When looking around, we notice that the basic constituents of the Universe are the galaxies. These huge and truly magnificent agglomerations of up to hundreds of billions of stars are distributed throughout the observable Universe. A common assumption is that their distribution reflects the underlying matter distribution. This makes them an excellent tracer for mapping the structure and infrastructure of the Universe.

Galaxies show a wide variety of sizes and morphologies. Many of them have a disk-like shape. Within the disk we can often recognize bright spiral arms highlighted by young and blue stars. In the center of such galaxies we find a bulge, a yellow-reddish ellipsoidal concentration of older stars. A smaller fraction of galaxies are so-called “ellipticals”, whose spherical or elliptical body contains mostly an aged star population, and with far less gas than the “spirals” (see Figure 1). While accounting for most of the starlight in the Universe, in terms of numbers most of the galaxies are far smaller than these two major classes. Often these have a more irregular and ill-defined shape, although a fair fraction of these dwarfs appears to have an elliptical shape.

Our galaxy resembles a spiral galaxy, containing around 200 billion stars. Our Sun is an average yellow dwarf star in the disk of the Galaxy, orbiting at a radius ≈ 8.5 kpc from the Galactic center[7].

Galaxies themselves are far from evenly distributed throughout the Universe. On scales of tens of Megaparsecs they appear to delineate an intriguing foamlike pattern that pervades the whole of

[7] A “kpc” is a kiloparsec. 1 kpc $\approx$ 30 860 000 000 000 000 *km*

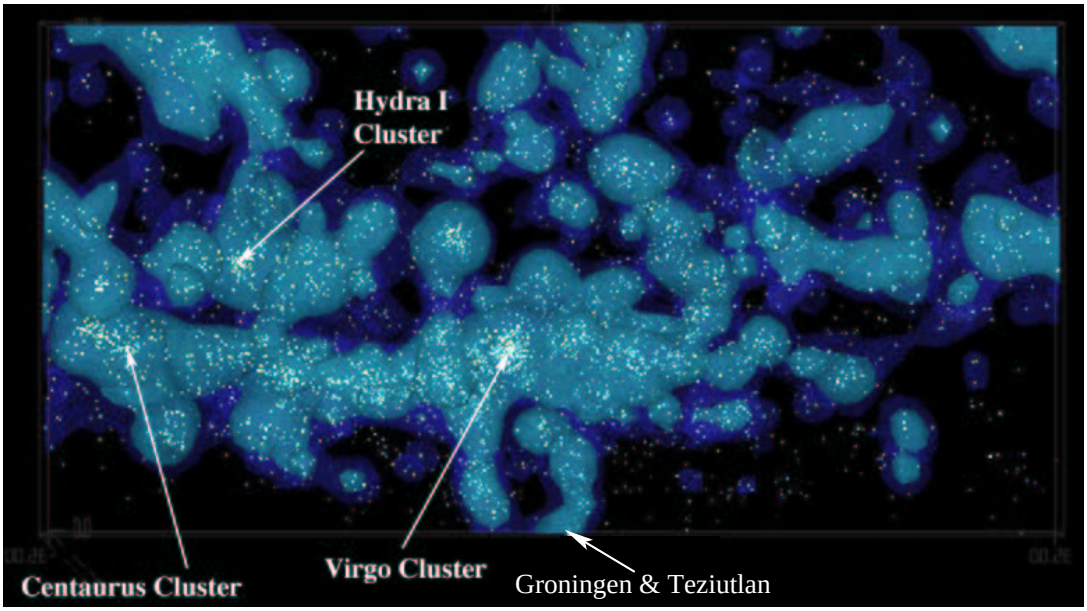

Figure 3 — Symbolic view of the Local Supercluster. Each dot represents a single galaxy. The gray surfaces outline regions where there are more galaxies than the average number of objects. The most prominent galaxy clusters are indicated by labels as well as the location of the Milky Way. (Credits: Brent Tully, The Large Scale Structure of the Universe, www.ifa.hawaii.edu/ tully/outreach).

the observable Universe, the *Cosmic Foam*. On even larger scales, over $\approx 200\ h^{-1}$Mpc, we cannot recognize any real structure: on those scales the Universe reaches the homogeneity demanded by the Cosmological Principle. On smaller scales, however, we find an intricate hierarchy of structures.

Individual galaxies are hardly ever isolated. Galaxies are usually found in *groups* and *clusters*, which typically form part of still larger structures, *superclusters*. Groups of galaxies have fewer than 50 members, most of them spirals, except in very dense and compact groups in which many ellipticals can be found. Clusters of galaxies are larger systems with more than 50 members up to thousands of galaxies within a sphere of radius of $4\ h^{-1}$Mpc. They are the most massive and most recent fully collapsed objects in the Universe. The centers of the clusters are mainly populated by elliptical galaxies, while spirals and irregulars populate the outskirts and surroundings.

Galaxies, groups and rich clusters are generally incorporated into larger structures known as *superclusters*. Their sizes are in the order of $20\ h^{-1}$Mpc or more and with a density in the order of a few to ten times the average cosmic density. Dynamically these structures are on the verge of halting their expansion, while a lot of them started contracting already, although as yet far removed from collapse.

A nice illustration of this hierarchical embedding is provided by our own Milky Way. It belongs to a small group of galaxies, *the Local Group*. Among its approximately 40 members it is mainly dominated by the two most massive galaxies, Andromeda and the Milky Way. The Local Group sits near the outer edge of a bigger association of galaxies known as the *Local Supercluster*. It consists of several groups of galaxies, a few poor clusters and one very rich cluster at its center, the *Virgo Cluster*. Figure 3 provides a view of its structure, with each white dot representing a galaxy. We are located at the bottom of the plot. The prominent clusters are indicated by labels along with our location at the bottom of the figure.

One way of assessing the cosmic matter distribution is through the study of maps of the galaxy distribution. If one could see a panoramic view of the distribution of galaxies beyond the Milky Way, the result will resemble Figure 4. This image is composed of over 1.6 million galaxies (represented by dots) listed in the survey All-Sky Survey Extended Source Catalog of The Two Micron All Sky Survey (2MASS). Major nearby matter concentrations are labelled. Quite evident are the many overdense

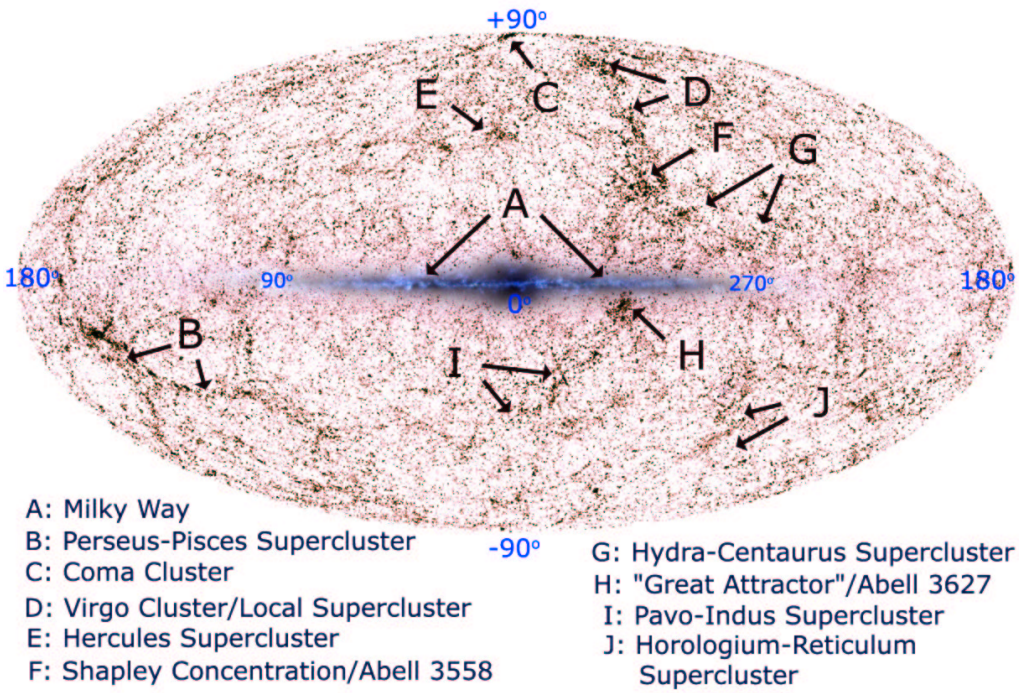

Figure 4 — Chart showing the galaxy distribution, orientation and location of Large Scale Structure in the local Universe projected on the sky. Clusters and superclusters of galaxies, filaments and some "empty" regions can be noticed in the map (Credits: 2MASS Extended Source Catalog, courtesy of T. Jarret and 2MASS/UMass/IPAC-Caltech/NASA/NSF).

regions, prominent galaxy clusters and superclusters, characterizing the large-scale structure of the nearby universe. Note that locally our Universe looks far from isotropic. It is important to realize that the apparent large projected size of our Galaxy is only an artifact of its proximity. Because of our location within the disk of the Milky Way our view in the visible light got obstructed by the dust it contains. Now with the micron wavelength 2MASS map we are suddenly confronted with a much clearer view of our surroundings. Previously hidden from view, the presence of the Great Attractor (H in Fig. 4) forms a telling illustration.

For a full spatial view of the galaxy distribution we need to know the distances to the galaxies. Direct distances are difficult to measure. Here the Hubble expansion of the Universe proves a great help. While it says that the recession velocity of a galaxy is directly proportional to its distance, we may hope to estimate its distance from its velocity. The latter is a lot easier to measure on the basis of the *redshift* of the light emitted by the galaxy. Akin to the lower tone of an ambulance's siren when it speeds away from us, the light of a galaxy becomes redder the faster it moves away from us. Hence, measuring the redshift of a galaxy is a useful shortcut to determining its distance.

We have been gradually revealed the intriguing patterns in the galaxy distribution shown in Figure 5. It depicts the galaxy distribution by the Two degree Field Galaxy Redshift Survey (2dFGRS) in a strip of the sky. In this map, the Milky Way is located at the center of the two cones and single galaxies are represented by points. The position of each galaxy in the map is given by its redshift and its position in the sky[8] (cf. Fig. 4). The result is a true spatial map of the distribution of galaxies and matter in our local Universe. Galaxies, clusters and superclusters are embedded in a web-like pattern. The superclusters mark the filamentary bridges and planar walls in this network, with the clusters located at the densest nodes. These structures surround large roundish regions nearly devoid of galaxies, the

[8]Notice that in this figure it looks as if there are less galaxies far away from us. However, this is a mere artifact because it is much harder to observe more distant galaxies than nearby ones. Distant galaxies are fainter and thus harder to detect.

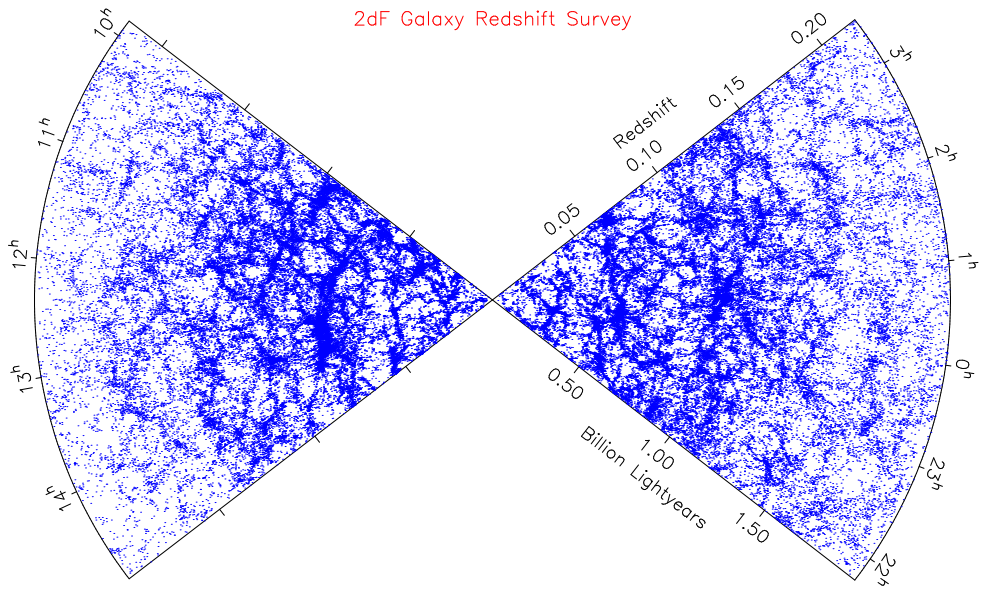

Figure 5 — Map of how galaxies are distributed in space as a function of distance from us according to the 2dFGR Survey. Notice how matter is clumped at some specific regions (clusters & superclusters of galaxies), while there are also empty regions (voids). (credits: 2dF Galaxy Redshift Survey team).

voids. We have come to realize that this *Cosmic Web* is indeed one of the most dominant characteristics of our Universe.

Cosmic flows

While on large scales the Universe expands roughly at the same rate (called the *Hubble flow*), this is not true for individual galaxies. Velocity measurements of individual galaxies show that they deviate from the Hubble flow. These deviations are called *peculiar velocities* of galaxies.

Migration flows of cosmic matter are one of the major manifestations of cosmic structure growth. Indeed, under the assumption that cosmic structure originated from small-amplitude density fluctuations that were amplified by gravity, peculiar velocities and matter perturbations are intimately coupled. The cosmic flows move out matter toward regions where ever more matter accumulates, gradually assembling the structures we observe in the universe.

Because peculiar velocities are the result of the combined gravitational force of all matter concentrations in the Universe, they are not only tracing the local matter distribution but also the surrounding and more distant structures. Also, as gravity is induced by luminous as well as dark matter, the cosmic flows form a direct probe of the total matter distribution. Potentially one can use the velocity field to reconstruct the corresponding density field and vice versa.

Substantial efforts have been directed toward accurately measuring peculiar velocities and to correcting possible random and systematic errors. It is necessary to determine the real galaxy distances instead of redshifts, which also reflect the involved peculiar velocities. Surveys of peculiar velocities are therefore limited to a considering smaller region than those of galaxy redshift surveys.

The velocity field is more sensitive to the large scale modes of the cosmic matter distribution, and less so to the small scale details in the density field. This renders it crucial for sensible reconstructions of the peculiar velocity field to reach out to sufficiently large volumes. These should include all relevant matter concentrations that may influence the peculiar velocity field.

One of the most massive nearby matter concentrations known as the *Great Attractor* was first discovered through the study of peculiar velocities. Unknown from optical images of the sky, it were

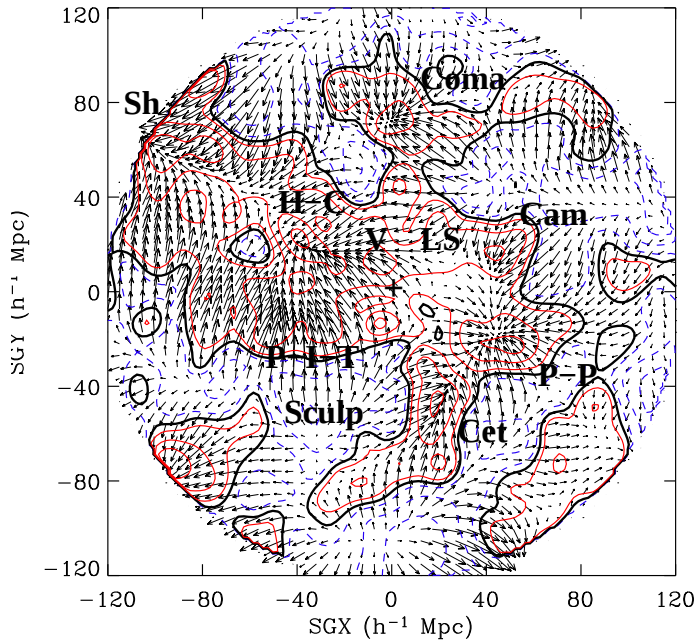

Figure 6 — Model of galaxy peculiar velocities inferred from the matter distribution. Velocities are represented by arrows which are proportional to their magnitude. The continuous lines (contours) delineate the matter distribution, small areas enclosed by contours indicate very massive structures, dashed lines indicate voids. The labels mark the position of the largest structures in the field: V: Virgo cluster, LS: Local Supercluster, H-C: Hydra-Centaurus, Sh: Shapley, P-P: Perseus-Pisces superclusters, P-I-T: Pavo-Indus-Telescopium complex, Cet: Cetus wall, Sculp: Sculptor void (Credits: E. Romano-Díaz et al. 2004, with data from E. Branchini).

the peculiar velocity flows which pointed us to a region hidden behind the plane of the Milky Way as the dominant source of our cosmic motion. Now we have learned that this region consists of a massive nearby cluster, A3627, extending out to the Hydra-Centaurus supercluster.

Arguably one of the best illustrations of the intimate relationship between the matter distribution and the velocity field is that inferred from the Point Source Catalog Redshift (PSC*z*). In Figure 6 our local group of galaxies is located at the center of the plot. The solid lines indicate overdense regions, the dashed lines surround the underdense voids. By means of labels we have indicated the major matter structures. The arrows indicate the direction and amplitude of the velocity field. Notice the strong infall velocities into the most massive concentrations. Also the voids influence the cosmic velocities as maybe discern from the region around the Sculptor void we see matter streaming out of the voids towards the high density regions. The map shows our local group is rushing towards the Great Attractor region inside the H-C supercluster.

This thesis

I have studied the environmental and dynamical effects that the large scale structure of the Universe exerts upon some of the main large cosmic structures such as clusters of galaxies and filaments. I have specifically studied the peculiar velocity field of galaxies and the matter distribution within the Local Supercluster. For these purposes I have applied the Least Action Principle and applied and extended the new DTFE method to obtain a fully volume-covering velocity field.

While most of the data used in this thesis is simulated data produced by computer codes, we conclude with applications of the involved techniques to data of the real Universe.

Beyond the linear regime: the Least Action Principle

As the structure formation process evolves with time, matter concentrations increase their density beyond the moderate density values prone to the description of linear theory. Even for such advanced non-linear stages, it has proven to be possible to predict the corresponding cosmic flows. One such scheme for following the evolving matter distribution into a more advanced state is the *Least Action*

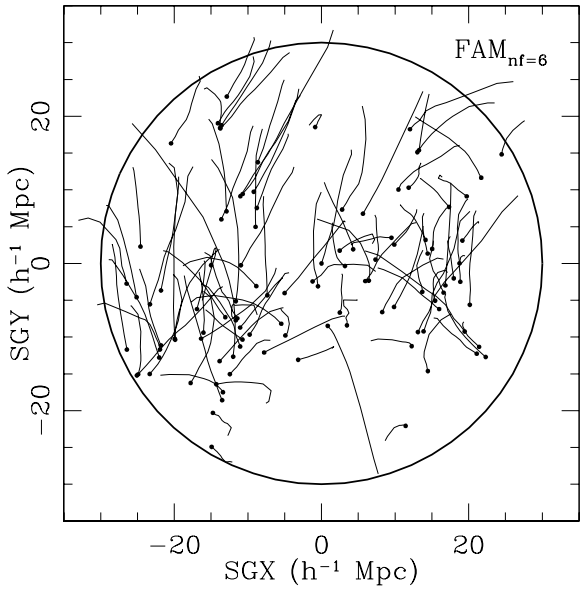

Figure 7 — Reconstruction of galaxy orbits by means of the Least Action Principle. The dots represents the actual galaxy positions, while the stream lines indicate their trajectories back in time.

Principle. This method can trace galaxy orbits back in time, given the current positions and requiring that the peculiar velocities initially vanish (a condition fulfilled because the Universe was relatively smooth and motionless in early epochs). With this method it is possible to estimate the velocity of each object at any epoch. Figure 7 illustrates the orbits reconstruction of a set of test galaxies (dots). The stream lines indicate the galaxy motions as the universe evolved. Notice how at dense regions the orbits become more deflected than those of more isolated galaxies, emphasizing why it is more difficult to study peculiar velocity fields in very dense regions.

From a set of mock catalogs obtained from $N-$body simulations, we have modeled peculiar velocity fields. An efficient implementation of the Least Action Principle, the Fast Action Minimization method [FAM], was used to achieve this. The main benefit of using FAM is that it allows one to follow the motion of particles into dense regions, even for a large number of particles[9]. In order to assess the reliability of these modeled velocity fields, we have compared them with the "real" velocity fields from the $N-$body experiments.

The most important results of this part of my research are:

- In the first part of this thesis we have analyzed the peculiar velocity field (from $N-$body simulations) of regions similar to our Local Supercluster. We have studied the influence of the mass distribution beyond the Local Supercluster on the local dynamics. Results show that in all plausible cosmological scenarios the mass distribution outside the Local Supercluster does significantly affect the local dynamics. We have shown that it is possible to account for this effect and to characterize this external influence by means of only a few dynamical terms. The accuracy of our results depends on the cosmological model considered and the exact configuration of the system.

- In order to draw more concrete conclusions about the influence of the external large scale matter distribution on the dynamics of the Local Supercluster, we used the *Constrained Random Field* method. The properly moulded initial conditions, designed to match the mass distribution in our Local Universe as closely as possible, were evolved by means of an $N-$body code. Our simulations have successfully reproduced some of the large scale features that shape our universe. Clusters similar to the Great Attractor, Perseus-Pisces and Hydra-Centaurus, could be

[9]Nevertheless this method still fails in reproducing the galaxy motions at the dense cores of galaxy clusters, although this problem does not affect our main conclusions.

recognized in our simulations. A detailed inspection of the simulations shows that they recover the dynamical behavior of the real observed universe very well.

- The modeling of the resulting peculiar velocity field of the constrained simulations showed that the mass distribution surrounding our cosmic neighbourhood (Local Supercluster) can be characterized to a great extent by its bulk flow and velocity shear. The former characterizes how the enclosed matter moves as a whole due to the surrounding external matter distribution. The latter describes the distortion of the velocity field by the structures located beyond our sample.

- We have applied the FAM technique to model the peculiar velocity field from real data using the Point Source Catalog redshift (PSC*z*) survey. In this study, we have searched for the main structures responsible for moulding the peculiar velocity field of our Local Supercluster region. Results indicated that at intermediate distances clusters like Hydra-Centaurus and Perseus-Pisces (Fig. 4 and 6) play a dominant role over the Local Supercluster dynamics. At large distances, structures like the Shapley Supercluster still influence our local cosmic vicinity.

Continuous velocity fields: the DTFE velocity algorithm

Having tested and elaborated upon the FAM method to trace galaxy orbits into the more advanced stages of evolution, we follow up with an elaboration of a novel technique to process discretely sampled velocities into a continuous volume-weighted velocity field.

Comparison of observed or simulated velocity fields with predictions from the theoretical models is possible only if one makes the assumption that the observed fields faithfully trace the underlying velocity field. In reality this is not the case. One only knows the peculiar velocities at the positions of observed galaxies or simulation particles. Theoretical predictions are based on the assumption that the velocity field is continuous and well defined within the considered volume. The resulting comparison with theoretical predictions is therefore not always clearly defined. The compared fields may not really be the same thing !

When comparing theory and observations, the measured velocity field is interpolated to all locations within the sampled volume, including the regions poorly sampled or devoid of data. Conventional interpolation methods make use of kernels which in essence “average” the velocities of the particles contained within the kernel. The cost of this approach is to erase any signal smaller than the kernel size and to lose information at high-density regions. In many cases the interpolation procedure alone is not enough, mainly at regions where the sampling is very poor. In addition the interpolation needs to be follow up by a *smoothing* procedure. This assures one of a theoretically well defined scale for the processed velocity field while it takes care of the assigning velocity values to poorly sampled regions. The price of this smoothing procedure is the loss of any signal smaller the smoothing kernel.

Ideally, one would like to preserve the large and small scale regimes in order to allow consistent studies of the peculiar velocity field. For example, the analysis of the small scale peculiar velocity dispersion contains information on the total matter content and dynamical state within a given region. When directly determined from the particle distribution itself it will lead to misleading conclusions since the study will be biased toward regions where the sampling is good. A far better approach, assigning equivalent significance to the poorly sampled low density regions is to determine a continuous covering velocity field.

Here, we work out an advanced interpolation scheme which adapts itself automatically to the geometry of the particle distribution, resolving both small and large scale velocity fields. This Delaunay Tessellation Field Estimator [DTFE] (see Schaap 2005) technique for peculiar velocities has been demonstrated to have very reliable velocity field statistics (Bernardeau & van de Weygaert 1996). The DTFE is based upon a triangular network, known as Delaunay tessellation, which connects neighbouring points in a fully adaptive and objectively defined fashion.

Following up on the introduction of DTFE, Figure 8 illustrates a discrete velocity field, sampled at particle positions. It is modeled from the matter distribution as measured by the PSC*z* catalog for our nearby Universe. The velocity arrows depicted in the right-hand frame, is the resulting DTFE velocity

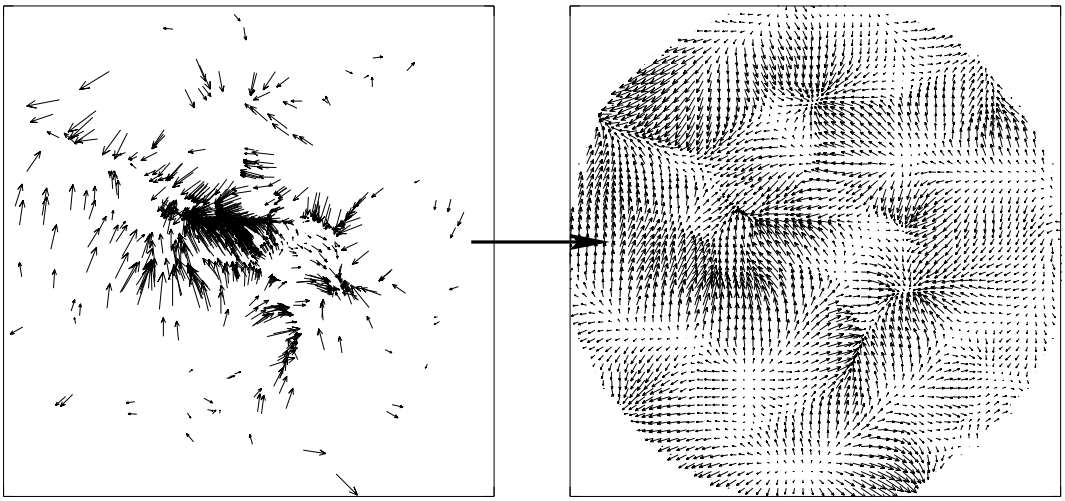

Figure 8 — Peculiar velocity field as inferred from the real galaxy distribution from the PSC*z* catalog in our nearby universe. The left-hand panel shows the discrete velocity field, while the right-hand panel the continuous volume-covering velocity field reconstructed by means of the DTFE velocity algorithm.

field. All structures present in the discrete map are also present in the DTFE map, but also the regions without peculiar velocity data are fully covered.

The main results from the analysis of DTFE processed velocity fields can be summarized as follows:

- The DTFE velocity method can reconstruct small and large scale characteristics of the peculiar velocity field. The processed DTFE velocity fields have the required characteristics that they are continuous and volume-weighted over the whole sampled volume. With our actual implementation, velocity-related quantities such as the expansion or contraction of the velocity field, its rotation, stretching and compression can be straightforward computed. Comparisons of DTFE velocity fields to the theoretical predictions are in very good agreement. Results showed that this technique is a major step forward in analyzing cosmic peculiar velocities at both small and large scales, and studying the dynamics of the cosmic web.

- With the DTFE technique, we have studied how "cold" the local Supercluster is, i.e., how large or small the velocity deviations from a pure Hubble flow are. The magnitude of these deviations depends on the cosmological model. Observational studies have indicated that our local universe is cold. Our method allowed us to draw more objective conclusions as we can estimate and study the flow throughout the sample volume. Results indicated that our cosmic neighborhood is indeed rather cold. The velocity deviations are very small, and our general movement is governed by a strong coherent flow exerted by a very massive structure, the Great Attractor.

Detecting the cosmic web: filaments

In a project with J. Dietrich and P. Schneider, we have explored the weak lensing properties of the cosmic web in order to detect filaments connecting two neighbouring clusters. Probing the mass distribution in the outskirts of galaxy clusters is much harder than close to the cluster centre. We have tested the accuracy and reliability of a method that in principle allows one to measure weak lensing signals from filaments. We have done so by exploring filamentary configurations whose initial conditions were set up by the Constrained Field technique. The constrained simulations were designed to mimic as close as possible a real configuration of neighbouring clusters and a filament between

them. Results showed that there is indeed a small yet detectable lensing signal from the filament that has indeed been detected for the double cluster A222 and A223.

Significance and Prospects

The central theme of this thesis has been to help understand the origin and main characteristics of the local peculiar velocity field of galaxies. This includes the large scale structures which influence the dynamics of the Local Supercluster. The study of large scale structure is still advancing rapidly from forthcoming new data, and will do even more so on the basis of more ambitious forthcoming surveys. With better data and new theoretical and computational tools, cosmologists have the prospect of solving several of the enigmas besetting our modern cosmological worldview. Amongst the most important ones are the questions directly related to origin and fate of our universe: what is the nature of dark matter and what is the nature of the dark energy?

Bibliography

Aaronson, M., Huchra, J., Mould, J., Schechter, P. L., & Tully, R. B. 1982a, ApJ, 258, 64
Aaronson, M., et al. 1982b, ApJS, 50, 241
Abell, G. O. 1958, ApJS, 3, 211
Baker, J. E., Davis, M., Strauss, M. A., Lahav, O., & Santiago, B. X. 1998, ApJ, 508, 6
Bardeen, J. M., Bond, J. R., Kaiser, N., & Szalay, A. S. 1986, ApJ, 304, 15
Basilakos, S. & Plionis, M. 1998, MNRAS, 299, 637
Baugh, C. M., et al. 2004, MNRAS, 351, L44
Baugh, C. M., Gaztanaga, E., & Efstathiou, G. 1995, MNRAS, 274, 1049
Berlind, A. A., Narayanan, V. K., & Weinberg, D. H. 2000, ApJ, 537, 537
Bernardeau, F. 1992, ApJ Lett., 390, L61
—. 1994, ApJ, 433, 1
Bernardeau, F., et al. 1999, MNRAS, 309, 543
Bernardeau, F., Colombi, S., Gaztanaga, E., & Scoccimarro, R. 2002, Physics Reports, 367, 1
Bernardeau, F., Juszkiewicz, R., Dekel, A., & Bouchet, F. R. 1995, MNRAS, 274, 20
Bernardeau, F. & van de Weygaert, R. 1996, MNRAS, 279, 693
Bernardeau, F., van de Weygaert, R., Hivon, E., & Bouchet, F. R. 1997, MNRAS, 290, 566
Bertschinger, E. 1987, ApJ Lett., 323, L103
—. 1998, ARA&A, 36, 599
Bertschinger, E. & Dekel, A. 1989, ApJ Lett., 336, L5
Bertschinger, E., Dekel, A., Faber, S. M., Dressler, A., & Burstein, D. 1990, ApJ, 364, 370
Bertschinger, E. & Gelb, J. M. 1991, Computers in Physics, 5, 164
Bertschinger, E. & Jain, B. 1994, ApJ, 431, 486
Binney, J. & Quinn, T. 1991, MNRAS, 249, 678
Bistolas, V. & Hoffman, Y. 1998, ApJ, 492, 439
Bond, J. R. 1995, Physical Review Letters, 74, 4369
Bond, J. R., Efstathiou, G., Lubin, P. M., & Meinhold, P. R. 1991, Physical Review Letters, 66, 2179
Bond, J. R., Kofman, L., & Pogosyan, D. 1996, Nature, 380, 603
Bonnet, H. & Mellier, Y. 1995, A&A, 303, 331
Bouchet, F. R. & Hernquist, L. 1988, ApJS, 68, 521
Branchini, E. & Carlberg, R. G. 1994, ApJ, 434, 37
Branchini, E., Eldar, A., & Nusser, A. 2002, MNRAS, 335, 53
Branchini, E., et al. 2001, MNRAS, 326, 1191
Branchini, E., et al. 1999, MNRAS, 308, 1
Braun, J. & Sambridge, M. 1994, Earth and Planetary Science Letters, 124, 211

Brown, M. E. & Peebles, P. J. E. 1987, ApJ, 317, 588

Bunn, E. F., Fisher, K. B., Hoffman, Y., Lahav, O., Silk, J., & Zaroubi, S. 1994, ApJ Lett., 432, L75

Burstein, D., Faber, S. M., & Dressler, A. 1990, ApJ, 354, 18

Canavezes, A., et al. 1998, MNRAS, 297, 777

Carlberg, R. G., Couchman, H. M. P., & Thomas, P. A. 1990, ApJ Lett., 352, L29

Clowe, D., Luppino, G. A., Kaiser, N., Henry, J. P., & Gioia, I. M. 1998, ApJ Lett., 497, L61+

Cole, S., Hatton, S., Weinberg, D. H., & Frenk, C. S. 1998, MNRAS, 300, 945

Cole, S., Weinberg, D. H., Frenk, C. S., & Ratra, B. 1997, MNRAS, 289, 37

Coles, P. & Lucchin, F. 2002, Cosmology: the origin and evolution of cosmic structure (Cosmology: the origin and evolution of cosmic structure/ Peter Coles, Francesco Lucchin. 2nd ed. Chichester, England: John Wiley & Sons, c2002.)

Coles, P. C. & Sahni, V. 1996, The Observatory, 116, 25

Colless, M., et al. 2001, MNRAS, 321, 277

Couchman, H. M. P., Thomas, P. A., & Pearce, F. R. 1995, ApJ, 452, 797

Courteau, S., Willick, J. A., Strauss, M. A., Schlegel, D., & Postman, M. 2000, ApJ, 544, 636

Croft, R. A. C. & Gaztanaga, E. 1997, MNRAS, 285, 793

Cutri, R. M., et al. 2003, VizieR Online Data Catalog, 2246

da Costa, L. N., et al. 2000a, ApJ Lett., 537, L81

da Costa, L. N., et al. 2000b, AJ, 120, 95

David, L. P., Forman, W., & Jones, C. 1999, ApJ, 519, 533

Davis, M., Efstathiou, G., Frenk, C. S., & White, S. D. M. 1985, ApJ, 292, 371

Davis, M., Nusser, A., & Willick, J. A. 1996, ApJ, 473, 22

Davis, M. & Peebles, P. J. E. 1983a, ApJ, 267, 465

—. 1983b, ARA&A, 21, 109

de Lapparent, V., Geller, M. J., & Huchra, J. P. 1986, ApJ Lett., 302, L1

de Vaucouleurs, G. & Peters, W. L. 1981, ApJ, 248, 395

Dekel, A. 1994, ARA&A, 32, 371

Dekel, A. 1999, in Formation of Structure in the Universe, 250–+

Dekel, A., Bertschinger, E., & Faber, S. M. 1990, ApJ, 364, 349

Dekel, A., et al. 1999, ApJ, 522, 1

Dekel, A. & Rees, M. J. 1994, ApJ Lett., 422, L1

Delaunay, B. N. 1934, Bull. Acad. Sci. USSR: Clase Sci. Mat., 7, 793

Dietrich, J. P. 2002, Master's thesis, Rheinischen Friedrich-Wilhelms-Universität Bonn

Doroshkevich, A. 1970, Afz, 6, 581 [Astrophys., 1973, 6, 320]

Doroshkevich, A., Tucker, D. L., Allam, S., & Way, M. J. 2004, A&A, 418, 7

Dressler, A., et al. 1987, ApJ Lett., 313, L37

Dunn, A. M. & Laflamme, R. 1993, MNRAS, 264, 865

Ebeling, H., Barrett, E., & Donovan, D. 2004, ApJ Lett., 609, L49

Efstathiou, G., Davis, M., White, S. D. M., & Frenk, C. S. 1985, ApJS, 57, 241

Eke, V. R., Cole, S., & Frenk, C. S. 1996, MNRAS, 282, 263

Ekholm, T., Baryshev, Y., Teerikorpi, P., Hanski, M. O., & Paturel, G. 2001, A&A, 368, L17

Euler, L. 1759, Letter dated October 27, 1759, from Euler to Lagrange, Opera postuma, 2, 559

Evrard, A. E., et al. 2002, ApJ, 573, 7

Faber, S. M. & Burstein, D. 1988, in Large-Scale Motions in the Universe: A Vatican study Week, 115–167

Faber, S. M. & Jackson, R. E. 1976, ApJ, 204, 668

Fall, S. M. & Jones, B. J. T. 1977, in IAU Colloq. 37: Decalages vers le Rouge et Expansion de L'Univers, 141–+

Fisher, K. B., Huchra, J. P., Strauss, M. A., Davis, M., Yahil, A., & Schlegel, D. 1995a, ApJS, 100, 69

Fisher, K. B., Lahav, O., Hoffman, Y., Lynden-Bell, D., & Zaroubi, S. 1995b, MNRAS, 272, 885

Ganon, G. & Hoffman, Y. 1993, ApJ Lett., 415, L5

Geller, M. J. & Huchra, J. P. 1989, Science, 246, 897

Giavalisco, M., Mancinelli, B., Mancinelli, P. J., & Yahil, A. 1993, ApJ, 411, 9

Gingold, R. A. & Monaghan, J. J. 1977, MNRAS, 181, 375

Giovanelli, R., et al. 1997a, AJ, 113, 53

Giovanelli, R., et al. 1997b, AJ, 113, 22

Giovanelli, R., Myers, S. T., Roth, J., & Haynes, M. P. 1986, AJ, 92, 250

Gnedin, N. Y. 1995, ApJS, 97, 231

Goldstein, H. 1980, Classical mechanics, 2nd edn. (Addison-Wesley World Student Series, Reading, Mass.: Addison-Wesley, 1980)

Governato, F., Moore, B., Cen, R., Stadel, J., Lake, G., & Quinn, T. 1997, New Astronomy, 2, 91

Gray, M. E., Taylor, A. N., Meisenheimer, K., Dye, S., Wolf, C., & Thommes, E. 2002, ApJ, 568, 141

Groth, E. J., Juszkiewicz, R., & Ostriker, J. P. 1989, ApJ, 346, 558

Guth, A. H. 1981, Physical Review D, 23, 347

Hamilton, A. J. S. & Tegmark, M. 2002, MNRAS, 330, 506

Hamilton, A. J. S., Tegmark, M., & Padmanabhan, N. 2000, MNRAS, 317, L23

Han, M. & Mould, J. 1990, ApJ, 360, 448

Harrison, E. R. 1970, Physical Review D, 1, 2726

Haynes, M. P., et al. 1999a, AJ, 117, 2039

Haynes, M. P., et al. 1999b, AJ, 117, 1668

Hockney, R. W. & Eastwood, J. W. 1988, Computer simulation using particles (Bristol: Hilger, 1988)

Hoffman, Y. 1986, ApJ, 308, 493

Hoffman, Y. 2000, in ASP Conf. Ser. 218: Mapping the Hidden Universe: The Universe behind the Mily Way - The Universe in HI, 161–+

Hoffman, Y., Eldar, A., Zaroubi, S., & Dekel, A. 2001, ArXiv Astrophysics e-prints

Hoffman, Y. & Ribak, E. 1991, ApJ Lett., 380, L5

Hubble, E. 1929, Proceedings of the National Academy of Science, 15, 168

Hudson, M. J., Dekel, A., Courteau, S., Faber, S. M., & Willick, J. A. 1995, MNRAS, 274, 305

Hudson, M. J., Lucey, J. R., Smith, R. J., Schlegel, D. J., & Davies, R. L. 2001, MNRAS, 327, 265

Hudson, M. J., Smith, R. J., Lucey, J. R., & Branchini, E. 2004, MNRAS, 352, 61

Hudson, M. J., Smith, R. J., Lucey, J. R., Schlegel, D. J., & Davies, R. L. 1999, ApJ Lett., 512, L79

Icke, V. 1984, MNRAS, 206, 1P

Jackson, J. D. 1975, Classical electrodynamics (92/12/31, New York: Wiley, 1975, 2nd ed.)

Jain, B., Seljak, U., & White, S. 2000, ApJ, 530, 547

Joeveer, M. & Einasto, J. 1978, in IAU Symp. 79: Large Scale Structures in the Universe, 241–250

Juszkiewicz, R., Vittorio, N., & Wyse, R. F. G. 1990, ApJ, 349, 408

Juszkiewicz, R., et al. 1995, ApJ, 442, 39

Kaiser, N. 1987, MNRAS, 227, 1

—. 1991, ApJ, 366, 388

—. 1995, ApJ Lett., 439, L1

Kaiser, N., Wilson, G., Luppino, G., & Dahle, H. 1999, ArXiv Astrophysics e-prints

Kang, H., et al. 1994, ApJ, 430, 83

Karachentsev, I. D., et al. 2003, A&A, 398, 479

Karachentsev, I. D., et al. 2002, A&A, 389, 812

Kauffmann, G., Colberg, J. M., Diaferio, A., & White, S. D. M. 1999, MNRAS, 303, 188

Keeton, C. R. & Kochanek, C. S. 1998, ApJ, 495, 157

Kepner, J. V., Summers, F. J., & Strauss, M. A. 1997, New Astronomy, 2, 165

Klypin, A., Hoffman, Y., Kravtsov, A. V., & Gottlöber, S. 2003, ApJ, 596, 19

Klypin, A. A. & Shandarin, S. F. 1983, MNRAS, 204, 891

Kogut, A., et al. 1993, ApJ, 419, 1

Kolatt, T., Dekel, A., Ganon, G., & Willick, J. 1996, ApJ, 458, 419

Kolb, E. W. & Turner, M. S. 1990, The early universe (Frontiers in Physics, Reading, MA: Addison-Wesley, 1988, 1990)

Kraan-Korteweg, R. C., Sandage, A., & Tammann, G. A. 1984, ApJ, 283, 24

Kravtsov, A. V., Klypin, A., & Hoffman, Y. 2002, ApJ, 571, 563

Kudlicki, A., Chodorowski, M., Plewa, T., & Różyczka, M. 2000, MNRAS, 316, 464

Lagrange, J. L. 1762, Oeuvres de Lagrange, 1, 151

Lahav, O., et al. 2002, MNRAS, 333, 961

Lahav, O., Fisher, K. B., Hoffman, Y., Scharf, C. A., & Zaroubi, S. 1994, ApJ Lett., 423, L93+

Lahav, O. & Liddle, A. R. 2004, ArXiv Astrophysics e-prints

Lahav, O., Rees, M. J., Lilje, P. B., & Primack, J. R. 1991, MNRAS, 251, 128

Lauer, T. R. & Postman, M. 1994, ApJ, 425, 418

Liddle, A. R. & Lyth, D. H., eds. 2000, Cosmological inflation and large-scale structure

Lilje, P. B., Yahil, A., & Jones, B. J. T. 1986, ApJ, 307, 91

Lokas, E. L., Juszkiewicz, R., Weinberg, D. H., & Bouchet, F. R. 1995, MNRAS, 274, 730

Lucy, L. B. 1977, AJ, 82, 1013

Lynden-Bell, D., et al. 1988, ApJ, 326, 19

Lynden-Bell, D. & Lahav, O. 1988, in Large-Scale Motions in the Universe: A Vatican study Week, 199–217

Möller, P. & Fynbo, J. U. 2001, A&A, 372, L57

Maddox, S. J., Efstathiou, G., & Sutherland, W. J. 1996, MNRAS, 283, 1227

Mathewson, D. S. & Ford, V. L. 1994, ApJ Lett., 434, L39

Mathis, H., et al. 2002, MNRAS, 333, 739

Nagamine, K., Ostriker, J. P., & Cen, R. 2001, ApJ, 553, 513

Noh, W. F. 1964, Methods Comput. Phys., 3, 117

Nusser, A. & Branchini, E. 2000, MNRAS, 313, 587

Nusser, A. & Colberg, J. M. 1998, MNRAS, 294, 457

Nusser, A., et al. 2001, MNRAS, 320, L21

Nusser, A. & Dekel, A. 1992, ApJ, 391, 443

—. 1993, ApJ, 405, 437

Nusser, A., Dekel, A., Bertschinger, E., & Blumenthal, G. R. 1991, ApJ, 379, 6

Okabe, A., Boots, B., Sugihara, K., & Nok Chiu, S. 2000, Spatial tessellations : concepts and applications of voronoi diagrams. 2nd ed. (Chichester ; Toronto : John Wiley & Sons, 2000.)

Ostriker, J. P. & Suto, Y. 1990, ApJ, 348, 378

Padmanabhan, T. 1993, Structure formation in the universe (Cambridge, UK: Cambridge University

Press, —c1993)

Peacock, J. A. 1999, Cosmological physics (Cosmological physics. Publisher: Cambridge, UK: Cambridge University Press, 1999. ISBN: 0521422701)

Peacock, J. A. & Heavens, A. F. 1985, MNRAS, 217, 805

Peacock, J. A. & The 2dFGRS Team. 2001, in 20th Texas Symposium on relativistic astrophysics, Austin, Texas, Vol. 586. Edited by J. Craig Wheeler and Hugo Martel. p.245, 245–+

Peebles, P. J. E. 1976, ApJ, 205, 318

—. 1980, The large-scale structure of the universe (Research supported by the National Science Foundation. Princeton, N.J., Princeton University Press, 1980. 435 p.)

—. 1987, ApJ, 317, 576

—. 1988, ApJ, 332, 17

—. 1989, ApJ Lett., 344, L53

—. 1990, ApJ, 362, 1

—. 1993a, Principles of physical cosmology (Princeton Series in Physics, Princeton, NJ: Princeton University Press, —c1993)

—. 1993b, in Texas/PASCOS '92: Relativistic Astrophysics and Particle Cosmology, 84–+

—. 1994, ApJ, 429, 43

Peebles, P. J. E., Phelps, S. D., Shaya, E. J., & Tully, R. B. 2001, ApJ, 554, 104

Peebles, P. J. E. & Yu, J. T. 1970, ApJ, 162, 815

Pelupessy, F. I., Schaap, W. E., & van de Weygaert, R. 2003, A&A, 403, 389

Pen, U. 1998, ApJS, 115, 19

Phelps, S. D. 2000, PhD thesis, Princeton University

Pierce, M. J. & Tully, R. B. 1988, ApJ, 330, 579

Plionis, M. & Basilakos, S. 2002, MNRAS, 330, 399

Plionis, M., et al. 2000, MNRAS, 313, 8

Plionis, M. & Kolokotronis, V. 1998, ApJ, 500, 1

Plionis, M. & Valdarnini, R. 1991, MNRAS, 249, 46

Pogosyan, D., Bond, J. R., Kofman, L., & Wadsley, J. 1996, Bulletin of the American Astronomical Society, 28, 1289

Pogosyan, D., Bond, J. R., Kofman, L., & Wadsley, J. 1998, in Wide Field Surveys in Cosmology, 14th IAP meeting held May 26-30, 1998, Paris. Publisher: Editions Frontieres. p. 61., 61–+

Press, W. H., Teukolsky, S. A., Vetterling, W. T., & Flannery, B. P. 1992a, Numerical recipes in C. The art of scientific computing (Cambridge: University Press, —c1992, 2nd ed.)

—. 1992b, Numerical recipes in FORTRAN. The art of scientific computing (Cambridge: University Press, —c1992, 2nd ed.)

Proust, D., et al. 2000, A&A, 355, 443

Raychaudhury, S. 1989, Nature, 342, 251

Raychaudhury, S. & Lynden-Bell, D. 1989, MNRAS, 240, 195

Riess, A. G., Davis, M., Baker, J., & Kirshner, R. P. 1997, ApJ Lett., 488, L1+

Romano-Díaz, E., Branchini, E., & van de Weygaert, R. 2004, Submitted

Rowan-Robinson, M., et al. 1990, MNRAS, 247, 1

Rowan-Robinson, M., et al. 2000, MNRAS, 314, 375

Rubin, V. C., Roberts, M. S., Graham, J. A., Ford, W. K., & Thonnard, N. 1976a, AJ, 81, 687

Rubin, V. C., Roberts, M. S., Thonnard, N., & Ford, W. K. 1976b, AJ, 81, 719

Rybicki, G. B. & Press, W. H. 1992, ApJ, 398, 169

Ryden, B. 2003, Introduction to cosmology (Introduction to cosmology / Barbara Ryden. San Fran-

cisco, CA, USA: Addison Wesley, ISBN 0-8053-8912-1, 2003, IX + 244 pp.)
Sahni, V. & Coles, P. 1995, Phys. Rep., 262, 1
Sambridge, M. 1999, Geophysical Journal International, 138, 479
Sandage, A. 1986, ApJ, 307, 1
—. 1999, ApJ, 527, 479
Santiago, B. X., et al. 1995, ApJ, 446, 457
Saunders, W., et al. 2000, MNRAS, 317, 55
Schaap, W. E. 2005, PhD thesis, Rijksuniversiteit Groningen
Schaap, W. E. & van de Weygaert, R. 2000, A&A, 363, L29
Schaap, W. E. & van de Weygaert, R. 2003, in Statistical Challenges in Astronomy, 483–+
Schechter, P. L. 1980, AJ, 85, 801
Schlegel, D., Davis, M., Summers, F., & Holtzman, J. A. 1994, ApJ, 427, 527
Schmoldt, I. M., et al. 1999, AJ, 118, 1146
Schmoldt, I. M. & Saha, P. 1998, AJ, 115, 2231
Schneider, P. & Bartelmann, M. 1997, MNRAS, 286, 696
Shandarin, S. F. & Zeldovich, Y. B. 1989, Reviews of Modern Physics, 61, 185
Sharpe, J., et al. 2001, MNRAS, 322, 121
Shaya, E. J., Peebles, P. J. E., & Tully, R. B. 1995, ApJ, 454, 15
Shectman, S. A., et al. 1996, ApJ, 470, 172
Sheth, R. K. & van de Weygaert, R. 2004, MNRAS, 350, 517
Sibson, R. 1981, in Interpreting Multi-variate Data, 21–+
Sigad, Y., Eldar, A., Dekel, A., Strauss, M. A., & Yahil, A. 1998, ApJ, 495, 516
Spergel, D. N., et al. 2003, ApJS, 148, 175
Stoyan, D., Kendall, W. S., & Mecke, J. 1995, Stochastic Geometry and its Applications (John Wiley & Sons, Chichester)
Strauss, M. A., Cen, R., & Ostriker, J. P. 1993, ApJ, 408, 389
Strauss, M. A., Davis, M., Yahil, A., & Huchra, J. P. 1992, ApJ, 385, 421
Strauss, M. A., Ostriker, J. P., & Cen, R. 1998, ApJ, 494, 20
Strauss, M. A. & Willick, J. A. 1995, Phys. Rep., 261, 271
Sukumar, N. 1998, PhD thesis, Northwestern University, Evanston, IL, USA
Sutherland, W., et al. 1999, MNRAS, 308, 289
Suto, Y., Cen, R., & Ostriker, J. P. 1992, ApJ, 395, 1
Suto, Y. & Fujita, M. 1990, ApJ, 360, 7
Tadros, H., et al. 1999, MNRAS, 305, 527
Tegmark, M., Zaldarriaga, M., & Hamilton, A. J. 2001, Physical Review D, 63, 43007
Teodoro, L., Branchini, E., & Frenk, C. 2003, ArXiv Astrophysics e-prints
Tonry, J. L., Blakeslee, J. P., Ajhar, E. A., & Dressler, A. 2000, ApJ, 530, 625
Tonry, J. L. & Davis, M. 1981, ApJ, 246, 666
Tormen, G. & Bertschinger, E. 1996, ApJ, 472, 14
Tully, B. & Shaya, E. 1999, in Evolution of Large Scale Structure : From Recombination to Garching, 296–+
Tully, R. B. 1988, Journal of the British Astronomical Association, 98, 316
Tully, R. B. & Fisher, J. R. 1977, A&A, 54, 661
Tully, R. B. & Shaya, E. J. 1984, ApJ, 281, 31
Valentine, H., Saunders, W., & Taylor, A. 2000, MNRAS, 319, L13

van de Weygaert, M. A. M. 1991, Voids and the geometry of large scale structure (Leiden: Rijksuniversiteit, —c1991)

van de Weygaert, R. 1994, A&A, 283, 361

van de Weygaert, R. 2002, in ASSL Vol. 276: Modern Theoretical and Observational Cosmology, 119–+

van de Weygaert, R. & Babul, A. 1994, ApJ Lett., 425, L59

van de Weygaert, R. & Bertschinger, E. 1996, MNRAS, 281, 84

van de Weygaert, R. & Hoffman, Y. 1999, in Evolution of Large Scale Structure : From Recombination to Garching, 178–+

van de Weygaert, R. & Hoffman, Y. 2000, in ASP Conf. Ser. 201: Cosmic Flows Workshop, 169

van de Weygaert, R. & van Kampen, E. 1993, MNRAS, 263, 481

van Haarlem, M. & van de Weygaert, R. 1993, ApJ, 418, 544

van Waerbeke, L. 2000, MNRAS, 313, 524

Verde, L., et al. 2002, MNRAS, 335, 432

Vogeley, M. S., Park, C., Geller, M. J., Huchra, J. P., & Gott, J. R. I. 1994, ApJ, 420, 525

Voronoi, G. 1908, J. reine angew. Math., 134, 167

Wang, Q. D. & Ulmer, M. P. 1997, MNRAS, 292, 920

Webster, M., Lahav, O., & Fisher, K. 1997, MNRAS, 287, 425

Weinberg, S. 1972, Gravitation and cosmology: Principles and applications of the general theory of relativity (New York: Wiley, —c1972)

White, S. D. M., Efstathiou, G., & Frenk, C. S. 1993, MNRAS, 262, 1023

Whitehurst, R. 1995, MNRAS, 277, 655

Wiener, N. 1949, Extrapolation and Smoothing of Stationary Time Series (New York: Wiley)

Willick, J. A., et al. 1997a, ApJS, 109, 333

Willick, J. A. & Strauss, M. A. 1998, ApJ, 507, 64

Willick, J. A., Strauss, M. A., Dekel, A., & Kolatt, T. 1997b, ApJ, 486, 629

Xu, G. 1997, MNRAS, 288, 903

Yahil, A., Strauss, M. A., Davis, M., & Huchra, J. P. 1991, ApJ, 372, 380

Zaroubi, S. 2002, in XIII Recontres de Blois ”Frontiers of the Universe”

Zaroubi, S., Branchini, E., Hoffman, Y., & da Costa, L. N. 2002, MNRAS, 336, 1234

Zaroubi, S., Hoffman, Y., & Dekel, A. 1999, ApJ, 520, 413

Zaroubi, S., Hoffman, Y., Fisher, K. B., & Lahav, O. 1995, ApJ, 449, 446

Zehavi, I., et al. 2002, ApJ, 571, 172

Zel’dovich, I. B., Einasto, J., & Shandarin, S. F. 1982, Nature, 300, 407

Zel’dovich, Y. B. 1970, A&A, 5, 84

—. 1972, MNRAS, 160, 1P

Acknowledgments

Fiuuu... what a ride!

Many people have contributed in one or another way to the completion of this thesis. Chapter 10 could be easily just about thanking all of you who helped me in this process. The realization of a PhD in science not only involves scientific interaction with other people but also social. The latter being of utmost importance for a little Mexican in Europe, where customs, mentality, food and weather are so different to what I was used to.

First of all, I want to thank my supervisor and friend Prof. dr. Marinus Adrianus Maria van de Weijgaert (aka Rien). Without knowing me (and me to him), we together decided to start this adventure some time ago. We have had rough times as in any human process. Fortunately, they never overshadowed our relationship. I have learned a lot from you boss. It always has amazed me your ability to see beyond the results. I thank you for pushing me to try to do good science and to explore new research paths. Thanks for your patience and for always helping me when I needed it. I have enjoyed our discussions about science, politics, history and life. We have passed from the student-supervisor relation to the collaborators one. I am looking forward to continue with this collaboration and to extend it along the tessellation path. My English has certainly been benefited with your help, at the cost of lowering my Spanglish! I will never forget when you told me that doing a PhD will be a one life time experience, thanks to you, it certainly has been so!

The Consejo Nacional de Ciencia y Tecnología (CONACyT, México) and the Mexican people are deeply acknowledged for their financial support along the first three years of my PhD. I also want to thank the Ubbo Emmius Scholarship program at the Rijksuniversiteit Groningen and the Kapteyn Institute for their financial support during my PhD research. The Leids Kerkhoven Bosscha Fonds is acknowledged for funding travels to conferences, working visits and ice creams.

Back in time, while I was happily living in Puebla, two people were important in helping me to search for my goals, Alejandro González and Omar López Cruz. Omar, thanks for your support at the first stages of this PhD. Without you, I would have ended up somewhere else in astronomy. I enjoyed a lot discussing with you about life and long-distance relationships. Alex, thanks for introducing me to the fascinating world of cosmology and $N-$body simulations.

A very important person in the setting and defining some of the projects in this thesis was Enzo Branchini. Thanks Enzo for your help and for answering all my questions about peculiar velocity fields. I enjoyed having dinners at your place both here and in Rome and watching movies. My gratitude for your hospitality while I visited you in 2001 and for your friendship.

Special thanks go to Frank Briggs and Bob Sanders who “adopted” me temporarily at the beginning and the end of this thesis and helped me to go through the bureaucratic procedure of the university. I also want to thank those who had to pass through my thesis, my reading committee: Profs. Tjeerd van Alvada, Thijs van der Hulst and Manolis Plionis. Their comments and suggestions helped to improve the scientific content of this thesis. I also want to thank Bernard Jones for showing great enthusiasm about my work. Discussing science and other topics with you has been a very motivating experience. I also benefited from discussions about peculiar velocity fields with Saleem Zaroubi. Thanks Saleem for sharing with me your point of view about the Palestinian-Israeli political situation. Jesús Galindo is acknowledged for his help with the cover images. Richard Powell, Tom Jarret and Brent Tully thanks for letting me use some of your images for my summary.

A big part of this thesis would not have been possible without the help of my collaborators: Willem E. Schaap, Enzo Branchini, Yehuda Hoffman and Joerg Dietrich. Thanks Yehuda for letting me use your initial constrained realizations of the local universe which gave a more realistic touch to this thesis. I am looking forward to start a new stage in my scientific life there at Jerusalem working with you. Joerg, it was fun to work with you. Designing $N-$body simulations that matched your data was not so easy as I thought. I hope that we will continue collaborating in the "lensed" future.

The help of the system computer managers is deeply acknowledged. Kor, Wim, Martin, Danny and Eite always helped me with all my computer-related problems. Also, the secretary staff for their kindness and help in all bureaucratic, money refunding and legal stuff matters. Greta, Hennie, Jackie and Gineke thank you very much. Georg Comello, thanks for always being friendly and speaking spanish to me.

Ante todo, quiero agradecer a mi familia, mi mamá, mamá tita y los telerín: Juan, Elizabeth, Emilio, Karla y Juan. Todos ustedes han sido un soporte constante a lo largo de este tiempo. Sin su ayuda, amor y comprensión nada de esto hubiera sido posible. Gracias por haber estado ahí cuando más los necesitaba y porque siempre han creído en mi. Esta tesis no es solo logro mío, sino de todos nosotros. Dios me ha bendecido con una hermosa familia.

A very important person in my life here in Groningen has been my office mate, Willem E. Schaap, my compadre! I have enjoyed your company since the first day I arrived to the institute. Having lunches at MacDonald's, listening good music and no discussing science was great! It has been awesome discovering the Delaunay world with you. I wish you the best for you and Paula in this new stage of your lives. I will never forget the trips to Vancouver, Marseille and the NAC. We are still the record holders my friend.

Leon, I greatly appreciate your friendship. Ole, I hope one day we could continue with what once started together. Hans, I enjoyed your friendship and sense of humor. I thought Neanderthals were extinct until I met you. Jelte, it was great fun having you as my friend, your (constant) interruptions along the last stages of my thesis helped me to relax at those moments, thanks also for your help whenever I needed to translate dutch documents. Nasser, I admire your determination to do things, chatting with you has been a lot of fun.

My gratitude for all of you who helped me along the "dark" moments of my thesis, specially in the last stages. Jero, Willem, Pablo, Miguel and Sjou, thank you very much.

The party animals are also acknowledged, Macho-man (Wilfred) and Peter. Liesbeth, Christiaan, Chris and Niels, it was great to enjoy the night life in Groningen with you.

My house mates with whom I enjoyed being at home doing nothing: César, Jacquie, Alvaro, Pablo, Román, Emily, Miguel and Volker. I greatly enjoyed chatting, playing PS2, watching cartoons and movies, discussing about life and having dinner with all of you. Román, fue una grata experiencia compartir casa contigo, gracias a ti y a Emily por su amistad. Espero que algún día podamos continuar con nuestras discusiones sobre ciencia y política mexicana. Gracias por tu apoyo y animo. Jacquie thanks for trying to share your passion about Rugby with me, even though I always felt asleep watching the matches. Still, I belive that American Football is more exciting, don't you think so Sir Xander Tielens? You were one of the very few people who knew about real sports. I enjoyed chatting with you about real and very important matters. My office mates who had to deal with me along this time, Willem and Katarina. Willem, What else can I say? Without your help in science, computing, dutch and serious matters (and not so serious) about life I would be lost. Kata, it has been "amaaazing" sharing office with you. Nic, thank you for showing me the bright side of England, I really enjoyed it.

The environment at the institute could not be great without the PhD students and postdocts. The large diversity of nationalities give a very international taste to the institute and the opportunity to learn new traditions, ways of thinking and taste different food. Hanadi, Jocelyn, Mercedes, Nicola, Dieter, Henrik, Giuseppina, Michiel, Fabrice, Edo, Rense, Mirella, Bjorn, Alvaro, Kambiz, Nissim, Neil, Bruno, Isabel, Henk, Joris, Diah, Martin, Rolf, Roelof, Gert, Aaron, Scott, Amina, Eline and Renso thank you very much. Annette, we should go more often to Rumba. Jan and Els, thank you very much for your friendship and for showing me how beautiful your country is. I would like to thank the Amnesty International student group in Groningen, especially to Inma, Sanders, Patricia and Harold.

In October 1999 torrential rains stroke México. In particular my home town Teziutlán. The lack of a secure civilian town development planning and the negligence of the local authorities provoke a catastrophe over there. Many people suffered the consequences. In an attempt to help my people I organized a money collect at the Kapteyn Institue. The generous response was very touching. The money was directed to buy medicines and toys for the affected children. In the name of my people I want to deeply thank all of you.

The spanish community at the institute me moló un mogollón. Iñigo, César, Lourdes, Jorge, Isabel, Leticia, Carlos, Alvaro, Isabel y Jero, fue una gran sorpresa descubrir que el peor español que se habla es en España. Iñigo, la sensación de libertad al escalar paredes contigo, filosofar sobre la vida, el viaje a Ibiza, las cenas vegetarianas, y las largas noches de juerga, son solo algunas de las cosas que te agradezco mucho. César, compartir casa contigo fue genial (tambien lo del coco). Gracias a ti y a Lulu por las cenas, por enseñarme a hacer paella y tortilla de patatas y por tu ayuda en las últimas etapas de la tesis, aprecio mucho vuestra amistad y espero visitarlos por aquellas islas. Leticia y Carlos, disfrute de vuestra amistad, y sí Leti, soy más de 5cm alto que tu. Alvaro, el tiempo que convivimos juntos, tus correos y tus visitas esporádicas a Groningen las he disfrutado mucho. Espero que nuestra amistad continue y suerte con la señorita Williams. Gracias a ti descubrí que los chistes de españoles tienen algo de cierto. Candar mi bicicleta con tu candado y luego perder la llave a media noche no es muy inteligente que digamos.

Het verkennen van de Salsa wereld was leuk en "produktief". Gonny en Marjolijn, bedankt voor jullie vriendschap, de uitgaansnachten en voor één van de beste ritjes in een achtbaan die ik ooit heb gehad. Gonny, ik zal je steun in die "donkere" momenten nooit vergeten.

Miguel y Pablo, ha sido muy entretenido estar con ustedes. Su amistad hizo más llevadero para mi los últimos meses de esta tesis. Gracias Miguel por tu gran ayuda en la elaboración de la portada. Espero que algún dia podamos continuar con las clases de guitarra. Pablo, disfruté mucho nuestras pláticas y caminatas en la madrugada. Gracias por estar conmigo hasta en los últimos momentos de esta tesis. Espero que nuestra amistad perdure y que podamos continuar colaborando en nuestros proyectos. Los espero en Israel.

To my friend, Padeli Papadopoulos. Destiny has gave us the chance to meet from both sides of the ocean. Along this years, you have become like my older brother, not because of your (lack of) wisdom, but because you always gave me your hand and support. Your friendship is a very valuable treasure for me. One of the most amazing experiences along my PhD was visiting you and your family there in Athens. My concept of "fasting" changed completely after being there. Mama *Κατινα* and Dad *Χρήστος*, your kindness, love and hospitality have been one of the most rewarding experiences while being here in Europe. *Σας ευχαριστώ από τα βάθη της καρδιάς μου.*

A mis amigos en México que siempre estuvieron ahí apoyándome para salir adelante. Héctor, me enorgullese ser tu amigo. Gracias por la oportunidad que me has dado de conocerte y de abrirme las puertas de tu casa, pero sobre todo, por la oportunidad de conocer a Dios a través de ti. Emmanuel, siempre te llevo en mi corazón. Lo aprendido contigo y tu amistad siempre han hecho de mi, una persona más completa. Mario y Luis Felipe, espero que podamos seguir disfrutando de nuestra amistad y de ser del mismo equipo. Amelia, Chisco, Chucho, Armando, Soco y Leti gracias por compartir su tiempo y amistad conmigo. P. Reyes, muchas gracias por su apoyo. Tere, esto es el culmen de un largo sueño que ahora se hace realidad. En gran medida esto ha sido gracias a ti. Tus correos, apoyo y detalles personales siempre me ayudaron a salir adelante. Te lo agradezco de todo corazón. Andrés Ballesteros, gracias por tu apoyo hacia mi y a mi familia. Don Filli Pérez Villa, muchas gracias por creer siempre en mi.

Aaron, Pipos y Xochitl, las cosas que hemos compartido juntos a lo largo de esta amistad han sido exquisitas. Gracias por que a pesar de la distancia, siempre han estado ahí. Dios los bendiga. Alonso, he disfrutado mucho nuestra amistad. Eileen, siempre he disfrutado tus correos y hablar por teléfono contigo, que nuestra amistad perdure por siempre. José Manuel Vázquez "Mestizo", tú fuiste el primero que me enseñó a pensar de una manera distinta hacia la ciencia. Parte de mi gusto hacia la física y las matemáticas te lo debo a ti. Gracias también a Hugo Reyes Castañeda quien me enseño que la ciencia tambien puede ser divertida. Jorse Isaac, gracias por motivarme siempre a echarle ganas a

esto, valoro mucho tu amistad. Franco, el gran detalle que tuviste para conmigo antes de dejar México lo llevo siempre conmigo, muchas gracias. El contacto vía correo electrónico con Arturo Méndez (mi tio), Ivan Portillo, Jackito, Andres, Daniel (el mostro), César Alvarez, Laura Colombón, Roberto (mi primo) han hecho esto más divertido.

Jero, tío, te echo de menos. Convivir contigo ha sido una de las mejores cosas de todo el doctorado. Las parrandas, la ps2, el curre, el eclipse solar del 99, Ibiza, Storm, los tequilas (y si que fueron muchos), las potas, los amaneceres, las cenas, los correos, ir de caza y que me tradujeras el dia de la bestia han hecho de nuestra amistad un lazo de unión que ha traspasado las fronteras. Gracias por estar conmigo en los malos momentos y por nunca dejarme solo. Se que nos volveremos a encontrar muchas veces en nuestras vidas y nos pondremos las botas. Gracias por ser mi amigo.

Doña Afke, Don Mintsje, Wytske en Nolke, betanke foar alles. Jim doar stie foar my iepen. En noch belangryker, dat jim my opnamen by jim yn de famylje. Ik ha genietsje kinnen fan jim selskip en jim hûs yn Fryslân en hoopje dat it sa bliuwe mei. Ek betanke dat jim my de wûnderen fan de fryske natoer sjen litten ha.

Ta beslút, mar net as lêste, Sjou, ha ik gjin wurden om dy te betankjen foar al dyn moed en stipe foar my yn dizze lêste tiid. As ik it net mear sitten seach wiest do der om my op te fleurjen. As ik my iensum fielde wiist do it dy't my selskip hâlde. Do wiest de fonk dy't myn libben ferljochte. Do nômst it beslút om mei my troch it libben te gean. Do jûchst my dyn leafde. Sûnder dy is myn libben leech. Ik hâld fan dy Sjou.

Emilio Romano Díaz, Groningen, September 2004.